Kiwifruit Flower Pollination –

Wind Pollination Efficiencies
and Sprayer Jet Applications

A thesis

submitted in fulfillment

of the requirements for the Degree

of

Doctor of Philosophy

in

Chemical and Process Engineering

by

Michael J.W. Hii

UC

UNIVERSITY OF
CANTERBURY
Te Whare Wānanga o Waitaha
CHRISTCHURCH NEW ZEALAND
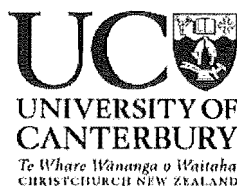
2004

ABSTRACT

There has been a move in the kiwifruit industry to pollinate by machine, allowing orchardists flexibility in timing, and other advantages. The traditional pollinators, bees, are unreliable and are susceptible to diseases such as the varroa mite. No measurements have been done on the efficiency of single-flower collection of pollen and the influence of airjet characteristics, to put this activity on a firm quantitative basis. For predictive purposes, a robust model of pollen behaviour around a single Green kiwifruit flower (*Actinidia deliciosa*) was built in this study by using a commercial computational fluid dynamics (CFD) package. The theoretical study first looked at the wind pollination of flower buds at different opening stages. Within the range of draft velocity recorded in the orchards, stigma are predicted to capture more pollen in a wind approaching from the front than from the side and back. Also, the pollen deposition on stigma increases as the bud opens wider and loses its petals. An estimation based on the predicted pollen collection efficiency indicated that wind pollination alone is insufficient to produce a minimum exportable fruit, which is in agreement with the observations reported in the literature. The question whether kiwifruit is a wind-pollinated plant is also discussed. Experimental checks of the modelling were carried out. Visualization of flow paths around a real kiwifruit flower in a wind tunnel compared well with the CFD predictions.

The machine pollination employs a jet of air. CFD simulations of pollen-loaded air jets were carried out to study the effect of different jet-nozzle configurations, namely the jet direction onto the flower, nozzle-to-flower distance, diameter of nozzle and initial jet velocity. A frontal spray gives the most efficient pollen delivery to the stigma. Further gain is accomplished by introducing the pollen cloud closer to the flower, from a smaller nozzle and at higher initial jet velocity. These trends, except for that of nozzle size, have been validated experimentally through the pollen spraying of single real kiwifruit flower in the laboratory. Recommended ways of airjet spraying are suggested based on the CFD results. From the stigma collision efficiency, it is more advantageous to apply pollen when most of the flowers have lost their petals.

Additional inclusion of an electrostatic influence into the pollen-loaded air jet simulations indicate that corona charging, but not tribo-charging, gives enhanced pollen

collection by the stigma. The enhancement depends on the strength of electric field established between the nozzle and the flower. The spraying tests with tribo-charged pollen in laboratory indicated that an improved pollen collection may be possible with a greater charging of pollen. The benefit however was not realized consistently in all experimental conditions.

The simulations assumed complete stickiness i.e. complete capture of pollen by the stigma on collision. This study also measured the force necessary to remove pollen in contact with stigma. The stickiness measurements of the stigma of Gold and Green kiwifruit flowers found that both flowers have equally sticky stigma. Stickiness increased with the aging of flowers. A reason is proposed related to the sugar in the exudate film. Overall, the variation of stickiness was statistically insignificant during the day. However, some older stigma were found to be stickier in the afternoon, which is in contrast to the general view that stigma are stickier in the morning. The gain in stickiness by the older stigma supports the recommendations for carrying out machine pollination after the petal fall.

The last section of the work was done in an orchard, and studied the characteristics of large jet spraying (without pollen) at the T-bar and pergola trained vines. Recommendations on the designs of jet have been provided.

ACKNOWLEDGEMENTS THANK YOU!

I like to express my gratitude to my supervisor, Assoc. Prof. John Abrahamson for his guidance and brilliant enlightenment that have been invaluable to me, not just in overcoming many problems encountered during this project but also in shaping up my research skills. I am grateful to my associate supervisor, Dr Pat Jordan, for his suggestions and support, particularly with the CFD and conference papers.

Also, many thanks to:

- Peter Mulligan (project mentor) and Dr Alistair Mowat, of Zespri for their enthusiasm and advices
- David Brown and Grace for the wonderful field trips to Nelson, which has yielded many important experimental data
- Trevor Berry, Bob Gordon, Franks Weert, Ron Boyce, Glenn Wilson and Paul Tolson for their technical assistances
- Tony Allen for his treasured helps in setting up the demanding computational resources for running the CFD package
- David Fletcher, James Hart and particularly Darrin Stephens, of ATD International for the valuable support of CFD
- EastPack Te Puke Packhouse and Bill Stevens for allowing me to carry out my work in their orchards
- Dr Ross Ferguson (from HortResearch) and Dr Senti Senthilmohan for their thoughtful views on the exudates
- Jill Hamlyn from Kiwipollen for supplying the pure kiwifruit pollen
- Peter Malcolm (dentist), whom the candidate and his supervisor greatly appreciate his help in building a metal version of an actual kiwifruit flower
- My fellow postgraduate colleagues particularly Nohemi Q-Ch, as knowing you has made this postgraduate life more cherish
- My mum, dad and brothers for their precious emotional supports
- Those whom I have not mentioned their names

TABLE OF CONTENTS

CHAPTER 1: INTRODUCTION

Kiwifruit[1] is one of New Zealand's most important horticultural exports[2], with a net sale of NZ$831 million during 2002-03 (Zespri Kiwifruit Annual Report, 2003). The success of the international market can be tracked back to the tight quality control of crop, which begins in the orchards. Apart from the general vine maintenances such as the soil nutrition, irrigation, pruning, frost prevention, pesticide and disease control, the value of the crop also depends significantly on the level of pollination. Insufficient pollination is known to lead to unsatisfactory fruit size, shape and uniformity (Goodwin, 2000; Stevens & Forsyth, 1982; Wilson, 1990), which represents a decreased marketable value. Unreliability of natural pollinators (wind and bees) has driven up the use of machine pollination across the industry. Among different types of wet or dry spray-based machine application, the dry air jet appears to be more promising due to its simplicity. There is however a need to improve its technique. This is the initiative of this work which begins with the studies of the collection of windborne pollen by a single kiwifruit flower. It is followed by the identification and optimization of the important parameters to maximize the pollen collection efficiency in artificial pollination using the dry air jet.

1.1. Objectives

The main objective was to build a robust model of pollen behaviour around a single kiwifruit flower for predictive purposes. This was carried out by using a commercial computational fluid dynamics (CFD) package to simulate the air field and pollen flow around a full scale flower model. The work started with the simulation of wind pollination and then progressed to the simulation of a pollen-loaded air jet. The latter was used to study the influence of jet characteristics and the charging of pollen grains in pollen collection.

---

[1] Also called Chinese gooseberry because it is native to China. See review by Huang & Ferguson (2001).
[2] $ 618.4 million for the year ended June 2002 (New Zealand Horticulture Facts & Figures - Fruits, Flowers & Vegetables 2002, 2002). This accounts for 29 % of New Zealand total horticultural exports.

The next objective was to verify the simulations by tracing the flow paths around the flower using smoke in a wind tunnel. A single kiwifruit flower was also placed in a jet of air carrying charged or uncharged pollen and the number of pollen grains deposited on the stigma was counted.

In the third objective, the outputs of the modelling and the experiments were used to investigate the practical aspects of pollination by machine applicator. This includes the studies of the behaviour of a large air jet under the vines trained on the T-bar and Pergola system using smoke visualizations.

The last objective was to look into the stickiness of a maturing flower over the pollination period. This arose from the interest among the growers to know whether the presence of exudates on stigma may assist the deposition of sprayed pollen grains. The exudates were sampled and analysed for their composition, particularly for the sugars which were thought as the major contributors to the stickiness of exudates.

1.2. Kiwifruit flowers and pollen

The kiwifruit industry is dominated by the 'Hayward' pistillate cultivar (*Actinidia deliciosa* (A. Chev) C.F. Liang *et* A.R. Ferguson). It is commonly known as the green kiwifruit because of its flesh colour. The recent years see an increasing cultivation of the higher-priced gold kiwifruit or 'Hort16A' cultivar (*Actinidia chinensis*). Other females such as 'Abbott', 'Bruno' and 'Monty' are grown to a very limited extent (< 1% of production). Male clones 'Chieftain', 'Matua', M51, M52, M56 and 'Tomuri' are the pollinizers for 'Hayward' in New Zealand (Hopping, 1981; McNeilage *et al*, 1991; Sale, 1990). The botanical nomenclature and the domestication of the important members of *Actinidia* family can be found in Ferguson (1990b) and Ferguson & Bollard (1990) respectively. Detailed morphological description of these staminate and pistillate clones has been reported by Zhang & Thorp (1986) and Martyn & Hopping (1988).

The 'Hayward' flower is focussed on in this work because of the market dominance of green kiwifruit and its more demanding pollination requirements than the 'Hort16A'. It is anticipated that any improvement on the pollination of 'Hayward' can be realized on the 'Hort16A'. Unless specified, 'Hayward' kiwifruit flowers are referred to in this work.

Kiwifruit is functionally dioecious i.e. staminate and pistillate flowers are borne on separate vines[3]. The vines are either trained on T-bar or Pergola system (see details in Sale, 1990). The flower loading ranges from 1500 to 3000 flowers per pistillate vine (Hopping, 1990a) and 3700 to 8000 per staminate vine (Palmer-Jones & Clinch, 1974). However excess of 1500 flowers per pistillate vine is regarded overcropping (Mills *et al*, 1986). Fig. 1-1 shows the components of male and female flowers in which the male can be distinguished by the absence of styles, stigma and a swollen ovary.
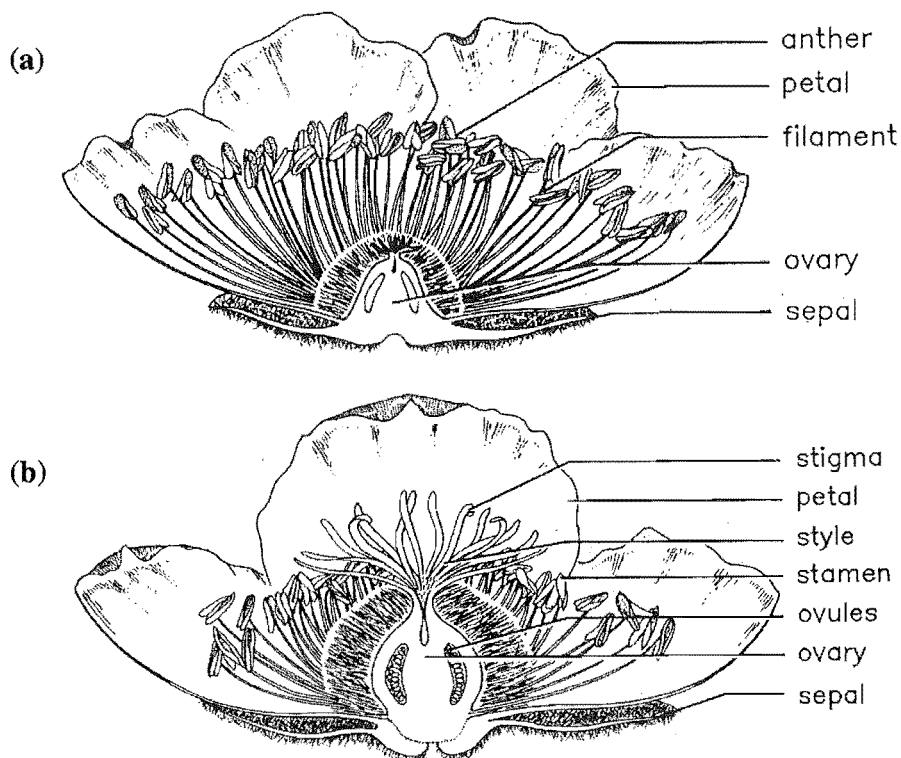
Fig. 1-1: Longitudinal section of a kiwifruit (a) male (staminate – only stamens) and (b) female (pistillate – pistils and stamens) flower (Hopping, 1990a). Pistil consists of stigma, style and ovary. Stamen consists of filament and anther.

---

[3] There is however a small number of self-fertile or hermaphroditic clones (Bellini *et al*, 1991).

In New Zealand, the evocation[4] of 'Hayward' flowers begins in February. The flower bud initiation takes place from late August onwards and it takes about 70 days from the active bud initiation to full bloom (see details in Brundell, 1973; Brundell, 1975a; Brundell, 1975b; Brundell, 1975c; Davison, 1974; Snowball, 1996; Stevens & Forsyth, 1982). Depending on the geographic location, altitude and season (Goodwin, 2000), 'Hayward' flowering generally starts in early to mid November in the North Island and late November to beginning of December in the South Island. The 'Hort16A' flowering is about a month earlier. The duration from the bud break to flowering depends on the local temperature (Morley-Bunker & Salinger, 1987; Salinger & Morley-Bunker, 1988; Warrington & Stanley, 1986), and ranges from 30 to 120 days when the mean temperature drops from 19 to 10 ^{O}C (McPherson et al, 1988).

The flowerings of 'Hayward' and 'Hort16A' in individual vines last 7 – 10 days (Ferguson & Davison, 1986) or 10 – 12 days (B Stevens, 2003, personal communication), but up to 17 – 18 days had been reported by Brundell (1975d), Hopping & Jerram (1980b) and Patterson et al (1991). Increasing temperature was found to lead to a shorter flowering duration by McPherson et al (1988). The blossom period is compacted to 4 – 7 or 6 – 7 days if Hi-Cane (hydrogen cyanamide) is used (Goodwin, 2000; Patterson, 2000). Hydrogen cyanamide is used to enhance the break of bud dormancy particularly if the winter chilling is insufficient (Richardson et al, 1994; Nee, 1991). Flower quantity and quality depend on the level of winter chilling received (Brundell, 1976; Davison, 1974; Davison, 1977; Ferguson & Davison, 1986; Stevens & Forsyth, 1982), being better for lower temperatures.

Fig. 1-2 shows the sequential changes to a 'Hayward' flower during the blossom season in Te Puke in 2001. The petals are creamy-white (sometimes with yellow patches) when first opened, but they gradually change to dirty gold colour (Ferguson & Davison, 1986; Zhang & Thorp, 1986). They fall off 3 – 4 days after opening. The varying corolla shape of a maturing flower is expected to influence the aerodynamics and pollen flow around it. Appearance of different aged pistillate Hort16A flowers can be found in Goodwin et al (2000) where the petal fall takes place from day 4 to 6.

---

[4] The induction of flowering i.e. the changing of a meristem to begin reproductive development (Hopping, 1990a).
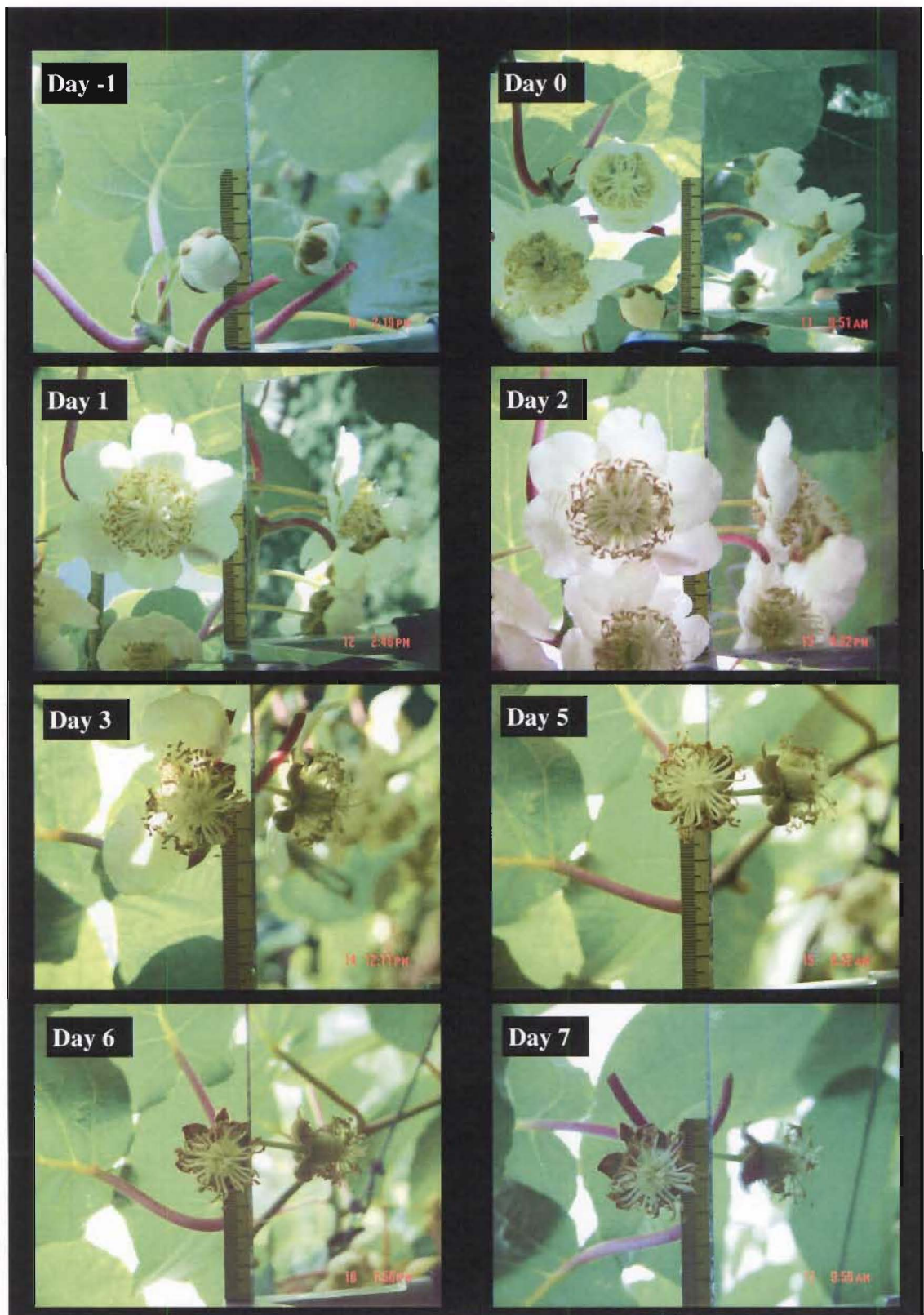
Fig. 1-2: Development of a 'Hayward' flower after opening. Shown are front (to left) and side views (to right) taken in an orchard in Te Puke in November 2001.

93.5 % of 'Hayward' inflorescences[5] (see diagrammatic representation in Hopping, 1990a) consist of one terminal flower (Brundell, 1975d). The maximum number of flowers in 'Hayward' inflorescence is three but only 1.2 % of inflorescences bear the additional two lateral flowers on the same peduncle[6]. Henzell & Allison (1993) found that the T-bar trained vines have more lateral flowers than Pergola-trained vines. The side flowers are often thinned for increased export production (Henzell & Allison, 1993; Sale, 1986; grower, personal communication in Motueka, 2003). During the 2001 field trip to Te Puke, the lateral flowers were observed to open 4 - 7 days later than the terminal flower and a number of them ceased development before the full initiation of their petals (as reported too by Hopping, 1990a). The use of Hi-Cane also results in less number of lateral flowers (Henzell & Allison, 1993; Patterson, 2001). For these reasons, inflorescence bearing more than one flower is not considered in this work.

Pistillate flowers have more stamens than staminate flowers (Hopping & Jerram, 1979), but their stamens produce non-viable pollen. A single staminate flower produces 2 - 3 million pollen grains (Hopping, 1981a) and the pollen shedding lasts for 1 - 3 days after opening (Hopping, 1990a; Goodwin, 1986a; Sale, 1981). The pollen grain has an oblate spheroidal shape, 25.9 µm along the polar axis and 18.1 µm along the equatorial axis (Dickison *et al*, 1982; Schmid, 1978); or 26.56 µm in length and 13.23 µm in diameter (Ferguson & Pusch, 1991). Staminate pollen are binucleate whereas pistillate pollen are enucleate and shrivelled (see Fig. 1-3a & b). The smooth exine surface that is pock marked with concave dimples (Fig. 1-3c) is likely to have similar drag-reduction function of dimples as on a golf ball that promotes longer travelling distance (Ferguson & Pusch, 1991; The Visualization Society of Japan, 1993).

---

[5] The reproductive shoot; the part of a plant that consists of the flower-bearing stalks and their flowers (Hopping, 1990a).
[6] The stalk of a flower cluster or inflorescence, or of a single flower (Hopping, 1990a).
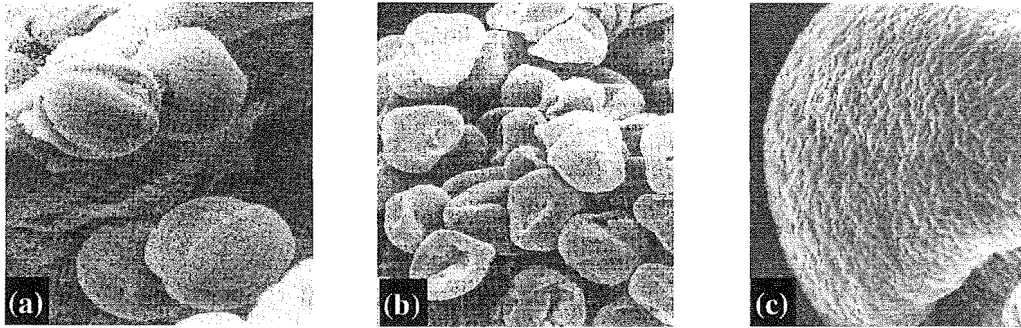
Fig. 1-3: (a) staminate and (b) pistillate pollen grains (Hopping, 1990a); (c) close-up view of exine surface of a staminate pollen (Dickison *et al*, 1982).

1.3. Pollination requirement and limitation

Hopping & Jerram (1979) reported that within 7 hr after landing on the stigma, the staminate pollen grains germinated and the pollen tubes penetrated into the styles. They observed that the pollen tubes reached the style base and fertilised the ovules inside the ovary by 31 hr and 43 hr respectively. The progression of pollen tubes to the ovary still took place after 72 hr. All or most of the flowers on the vine are capable of developing into an exportable fruit (Davison, 1977; Hopping & Hacking, 1983a) and the basal flowers have the maximum growth potential (Ryugo *et al*, 1988).

Gonzalez *et al* (1995a) observed that the stigma were highly receptive to pollen at anthesis[7]. There are variances among the reported duration of stigma receptivity. Works by Gonzalez *et al* (1995a, 1995b, 1997) in Spain showed that the stigmatic receptivity remained high for the first 4 days after anthesis before declining to nil on day 7. They attributed this to the loss of papillar integrity i.e. the unicellular papillae[8] that cover the stigma began to rupture. According to Sale (1981), pistillate flowers in New Zealand are receptive for 7 – 9 days after opening. This longer period is also reported by Goodwin (2000) where the relatively constant and high receptivity was displayed for the first 8 days before dropping. Goodwin (2000) found that the seed set still happened on day 10. Even though kiwifruit has a highly efficient reproductive

---

[7] The period of flowering in plants; more specifically, the time of flower bud opening and expansion when pollination takes place (Hopping, 1990a).
[8] Small projection of tissues (Hopping, 1990a).

system (Gonzalez *et al*, 1996), Gonzalez *et al* (1995b) pointed out that this short stigmatic receptivity period is likely to limit the fruit set.

The fruit size and weight at harvest depend strongly on the number of seeds set during the pollination. Seed-derived hormones are required to promote fruit growth (Anon., 1983; Hopping, 1976; Stevens & Forsyth, 1982; Woolley *et al*, 1988). The final fruit size however is also affected by the management factors such as irrigation, nutrients, crop loadings, type of training systems, beehives management and shelter management; the position of the fruit on the vines in any particular training system, time of anthesis, flower quality, leaf to fruit ratio, length of shoot and orchard microclimate i.e. amount of sunshine received (Clinch, 1984a; Goodwin, 2000; Lawes *et al*, 1990; Lees, 1986; McPherson *et al*, 2001; Patterson *et al*, 1991; Patterson *et al*, 1999; Pyke & Alspach, 1986; Richardson & McAneney, 1990; Sale, 1986; Underwood, 2001; Woolley *et al*, 1988). The number of seeds is in turn related to the number of viable pollen deposited on the stigma. Even though a successful mating of a pollen tube with an ovule produces a seed, the number of pollen grains needed per seed ranges from 3.0 to 5.2 depending on the male clones (Hopping & Martyn, 1990). This is because some pollen tubes die during the passage through the style. For this reason, the selection of superior male clones (e.g. M51, M52, M56, Chieftain) that produce high quality pollen i.e. less number of pollen grains needed per seed set is important and has attracted many researches or breeding programs (e.g. see Hopping, 1981; Hopping, 1985a; Hopping & Martyn, 1986b; McNeilage & Seal, 1990; Gonzalez *et al*, 1994).

The important question in kiwifruit pollination is the number of pollen grains that needs to be deposited on the fertile stigma or the number of seeds that needs to be set in order to:
1. produce a minimum export size of 70 g (Pyke & Alspach, 1986; Testolin *et al*, 1991; which will make the Class I according to *International Standardisation of Fruit and Vegetables*, 1992);
2. produce a preferred export size of 100 g or more (Hopping, 1986; which will make Class "Extra" that requires a minimum of 90 g according to *International Standardisation of Fruit and Vegetables*, 1992);
3. fully pollinate the flowers i.e. produce a fruit to its maximum potential which is up to 120 g (Goodwin, 2000).

Table 1-1 is a list of the requirements reported in the literature. For minimum exportable fruit weight, roughly at least 700 seeds and > 2000 pollen are necessary. The seed and pollen number increase to > 1000 and possibly > 3000 – 4000 respectively for the desired export weight. Fully pollinated fruit containing > 1300 seeds will need fertilization by at least 12000 pollen grains. The ranges in Table 1-1 vary to some extent particularly for the category of desired exportable weight. To obtain a more definite number of the required pollen grain for use in the following chapters, it is decided to re-do the estimation based on the fundamental data available in the literature.

Table 1-1: Numbers of seeds and pollen in a kiwifruit that are recommended in the literature for achieving different export criteria of crops. * if pollen are from superior males.

Sources	Export criteria	Required no. of seed	Required no. of pollen
Anon. (1985)	Minimum export grade	800	–
Clinch (1990)	Minimum export grade	525 - 740	–
Sheat et al (1982)	Minimum export grade	–	2880
Hopping & Hacking (1983a)	Minimum export grade	700 - 800	–
Hopping (1986)	Minimum export grade	850	–
Kiwi Pollen Limited (1993)	Minimum export grade	≥ 800	
Stevens & Forsyth (1982)	Minimum export grade	750	≥ 3000
Lawes & Lupton (1982)	> 72 g	750 - 1000	2000 - 3000
Hopping (1979)	49 tray-count, ~ 72 g	250	~ 1000
Hopping (1979)	39 tray-count, ~ 93 g	> 1000	> 12000
Hopping (1982b)	36 tray-count, ~ 101 g	1150	2000 - 3000
Hopping (1980, cited in Craig & Stewart, 1988a)	Export grade	> 1000	1870 - 2960
Hopping & Hacking (1983a)	Export grade	1200 - 1400	2000 - 12000
Hopping (1986)	100 g	1150	~ 12000
Anon. (1984)	100 - 110 g	1150 - 1200	Up to 12000
Kiwi Pollen Limited (1993)	100 - 110 g	≥ 1150	> 12000
		800 – 1000 *	4000 – 6000 *
Goodwin & Haine (1995)	Fully pollinated	1300 - 1600	15000
Hopping (1981)	Fully pollinated	1400	~ 2500
Hopping (1976)	Fully pollinated	1400	–

Table 1-2: Estimation of number of seeds (to the nearest ten) required for 70-g and 100-g fruits based on the correlation between the seed number and fruit weights from various sources. * = more than one set of data are reported by the author(s).

Sources	Approximate number of seeds needed for a	
	70-g fruit	100-g fruit
Costa et al (1993) *	240	750
	200	700
Goodwin (2000)	710	1070
Hopping (1976)	750	1290
Hopping (1986)	300	930
Hopping & Hacking (1983b)	820	1150
McAneney et al (1984)	840	1160
Pyke & Alspach (1986)	330	1050
Testolin et al (1991)	370	800
Woolley et al (1988) *	180	620
	320	980
	430	1050
Average =	458	963
Standard deviation (s.d.) =	250	206
Average + 1 s.d. =	707	1169
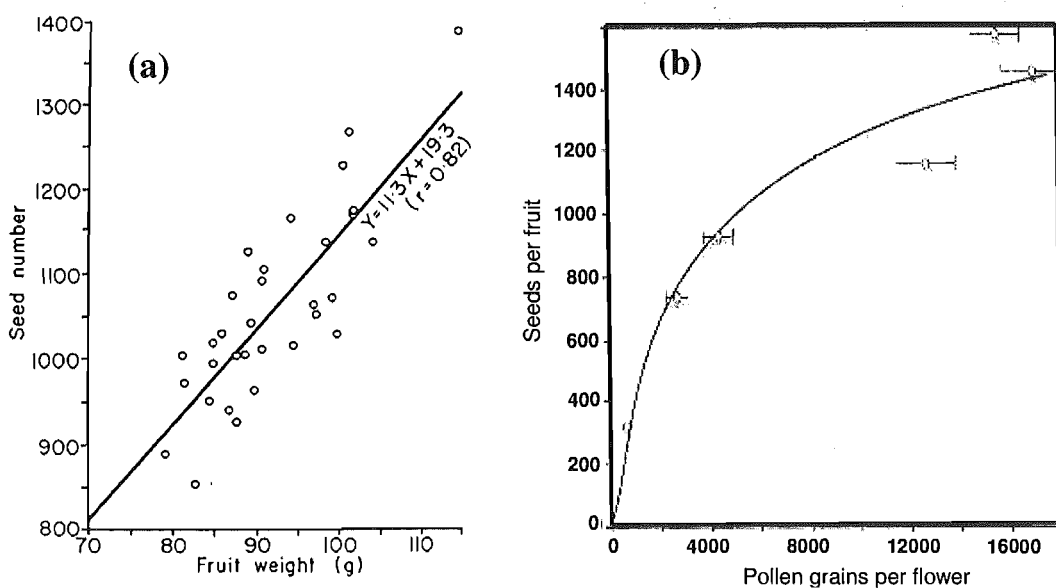
Fig. 1-4: (a) Relationship between seed number and fruit weight (Hopping & Hacking, 1983b). (b) Relationship between seed number and number of pollen grains landed on the stigma per flower (Goodwin, 2000).

There are a number of published relationships between the fruit weight and the number of seed per fruit[9], as listed in Table 1-2. The seed-to-fruit relationships from these sources display very large scatter and either linear or non-linear positive correlation (one of them is shown in Fig. 1-4a). This is thought due to the influence of other factors such as the age of vine (Hopping, 1986) and loading of vine (Testolin *et al*, 1991). These correlations are compared in Table 1-2 in the number of seeds expected in a 70-g or 100-g kiwifruit.

Table 1-2 shows that the estimated values exhibit a wide range particularly for the 70-g fruit where the standard deviation is almost half of the average. For a conservative estimate, the "average + 1 standard deviation" rather than the "average" is considered here. Thus, a minimum export size of 70-g must have at least 707 seeds while a 100-g fruit will require at least 1169 seeds. This means, according to Fig. 1-4b, at least 2300 and 7900 viable pollen grains need to be delivered to each female flower in order to produce the 70-g and 100-g fruits respectively. The seed and pollen numbers estimated in this exercise are within the recommended ranges in Table 1-1. No comparison is done for a fully pollinated fruit as ≥ 12000 appears to be a consistent target number of pollen grains.

Overpollination, for example, through repeated pollinations with large amount of pollen grains, is not desirable because it was found to result in fewer seeds per fruit and hence smaller fruit size (Hopping, 1979, 1982a). High pollen loading results in excessive numbers of pollen tubes competing for growing space and nutrients within the styles (Hopping, 1982a). The newly deposited pollen from the successive pollinations are also thought to inhibit the growth of pollen tubes already taking place in the style (Hopping, 1982b). This affects the fertilization of ovules, leading to small crop.

1.4. Natural pollinators of kiwifruit

Wind is one of the natural pollinating vectors available at no cost. However, its effectiveness is greatly reduced by the wind shelters in the orchard (Burge *et al*, 1988).

---

[9] Or the weight of seed per fruit (Clinch, 1984a; Lawes *et al*, 1990; Pyke & Alspach, 1986).

The windbreaks, either artificially made from polyethylene fabric sheets or comprising of rows of shelter-belt trees, are aimed to protect the tender young shoots, replacement canes and flower shoots; avoid fruit abrasion; reduce premature defoliation; promote bee activity; and provide a suitable microclimate for vegetative growth and fruit development (Hathaway, 1990; Hawes & Lupton, 1982; Paterson, 1995; Sale, 1990; Sale & Lyford, 1990).

Donovan (1983), Donovan (1987) and Palmer-Jones & Clinch (1974) reported that 'Hayward' flowers were visited by honeybees (*Apis mellifera* L.), bumble bees (*Bombus* sp.), thrips (*Thrips (Isothrips) obscuratus* Crawford), hover flies (*Syrphus novae-zealandiae* Macquart), native bees (*Leioproctus* and *Lasioglossum*), beetles and moths. Among them, Clinch (1984a), Donovan (1983), Palmer-Jones & Clinch (1974) and Vaissiere *et al* (1996) identified honeybees as the most numerous insects visiting kiwifruit flowers. Honeybees carry up to half a million pollen grains on their bodies (Donovan, 1983). Kiwifruit flowers are considered as buzz-pollinated by bumble bees (Corbet *et al*, 1988) and the vibratory pollen collection mechanism had been described by King (1993), King & Ferguson (1994) and King & Lengoc (1993).

A large number of bee visits are required for sufficient pollen deposition on stigma. The seed number increases with the number of bee visits (Goodwin & Haine, 1995) and the number of days of which the flowers are exposed to bees (Goodwin, 1986c, Goodwin & Ten Houten, 1989). According to Goodwin & Haine (1995), full pollination can be attained from one bee visit but 40 visits are usually expected. The foraging commences when the anthers dehisce[10] around 8 am and reaches the peak at midday (Goodwin, 1986d).

The required stocking rate of honeybees is high where normally 8 – 12 hives/ha is recommended depending on the level of floral competition (Clinch, 1979; Clinch, 1990; Goodwin, 1986b; Lyford & Underwood, 1992; Palmer-Jones & Clinch, 1976; Paterson, 1995). Hives are brought into the orchards at 10 – 15 % or 10 – 20 % female bloom (Bryant, 1986; Clinch, 1990; Lyford & Underwood, 1992; Sale, 1981). In the presence of strong floral competition, some colonies will be introduced at 15 % bloom with the

---

[10] The breakdown of the anther wall to expose the pollen (Goodwin, 2000).

balance at 50 – 60 % bloom (Bryant & Vardy, 1985; Goodwin, 1995b). They are usually placed in a warm, sunny and sheltered spot to maximize the bee activities (Goodwin, 1995b; Sale, 1981).

It is necessary to feed honey bee colonies with sugar syrup inside the hives in order to boost the bee foraging activities (Goodwin & Ten Houten, 1991; Goodwin et al, 1991). This doubles the collection of kiwifruit pollen but does not increase significantly the collection of other types of pollen (Goodwin, 1986b; Goodwin, 1987; Goodwin & Ten Houten, 1988). Another method to increase kiwifruit pollen collection by bees is the use of pollen traps, but Clinch (1984b) found that the gain was inconsistent among seasons. Removal of pollen stores from honey bee colonies had been observed to significantly increase the pollen collection by Tsirakoglou et al (1997).

A good distribution of male vines is essential for both wind and bee pollination. Male vines are typically inter-planted with female vines at a ratio of 1:8 (Sale, 1981), occupying about 10 % of the orchard canopy (Lawes & Lupton, 1982). Males are sometimes trained above female vines to allow easier access by bees. The seed number and fruit weight were found to decline sharply with the increasing distance from a male vine (Clinch, 1982; Goodwin et al, 1992a) and moderately with the increasing distance between staminate vines (Goodwin et al, 1992a; Goodwin et al, 1999). This can be explained by the knowledge that honeybees usually forage in small areas (Goodwin, 1986c, Jay, 1982) and by the decreasing wind-borne pollen concentration in the air.

There is a handful of published literature attempting to elucidate the relative importance between the wind and bees in kiwifruit pollination. Craig & Stewart (1988a, 1988b) supported the important role of wind in pollination. Their rationale is based on the findings by other researchers that the fruit size is significantly larger near the male vines and is significantly larger downwind of male plants than it is upwind. Their review of the floral architecture and pollination biology of kiwifruit suggested that the evidence for wind pollination is as much as for the insect pollination.

However, Wilson (1990) observed that in two isolated orchards without bee hives placed, the resulting crop is useless; indicating that wind pollination alone is insufficient. Field trials by Hopping (1981a) and Hopping et al (1984) found that wind

pollination contributed little or none to the final fruit size. In Burge *et al* (1988), Clinch & Heath's (1985) and Heath *et al*'s (1984) experiments, 90 – 100 % of the un-exportable fruits came from wind pollinated flowers. According to Costa *et al* (1993) and Testolin *et al* (1991), although wind pollination led to an appreciable fruit set, fruit weight was low and below minimum exportable weight.

Works by Clinch *et al* (1985) found that wind pollination could also occur with the male pollen released at night and 40 % of the resulting fruits reached 72 g (exportable weight). They interpreted their results as indicating wind-mediated pollination is an important component of the pollination ecology of kiwifruit but insufficient for higher crop production.

On the other hand, experiments by Palmer-Jones (1974) and Palmer-Jones & Clinch (1975) indicated that virtually all pollinations were provided by honey bees. This is echoed by the results from Costa *et al* (1993), Gonzalez *et al* (1998) and Vaissiere *et al* (1996) that the resulting fruit set and final fruit weight are significantly more with the participation of honeybees than with just wind.

In short, the presence of honeybees in kiwifruit orchards contributes to good quantity and quality crops (Gonzalez *et al*, 1998; Howpage *et al*, 2001). As pointed out by Burge *et al* (1988), wind pollination alone is inadequate with the current orchard layout in New Zealand.

1.5. Why artificial pollination?

The call for artificial pollination of kiwifruit started in early 1980s because of the prediction that there might be a shortfall in the number of honeybee hives available for this crop (Anon., 1983; Anon., 1984; Ivens, 1982). The feared shortfall did not happen because the growth of bee keeping was greatly underestimated at that time. However, the call 'kicked start' the development in artificial pollination. Cumulative improvement of techniques have made artificial pollination popular among the orchardists nowadays. The reasons, mainly derived from the inadequacies of natural pollinators, that encourage this popularity are given below.

The flowering of most staminate cultivars do not coincide with the 'Hayward' flowering as they usually blossom in advance of Hayward (Hopping, 1981; Brundell, 1975c). Because of this, the pollen from these male flowers will not reach the late opening female flowers even with the presence of bees. Viable pollen are only available from the male flowers for the first 2 – 3 days after opening before the male flowers senesce and die (Sale, 1981).

Jansson & Warrington (1988) pointed out that because of the reduced germination rate and viability of pollen in cold weather during flowering season (when $\leq 12\ ^{O}C$), the bees activities need to be increased. This is hard to achieve because honeybee activities are promoted by the warm, sunny and calm conditions (Bryant, 1986; Hopping, 1979; Jay, 1982; Vaissiere *et al*, 1996). Their activities degrade when the wind velocity exceeds 15 km/h and comes to stagnant at wind speed above 24 km/h (Bryant, 1986).

Rain was found to curtail the foraging activity of bees (Blanchet, 1990; Clinch, 1984a; Clinch & ten Houten, 1986; Ford, 1971; Goodwin *et al*, 1994; Goodwin, 1986c). Adverse weather is thought to reduce the bee flight (Palmer-Jones & Clinch, 1974; Palmer-Jones & Clinch, 1975).

Artificial pollination has been found important for parts of the orchards that are poorly pollinated by bees e.g. where vines are shaded, exposed to draughts, too thick to attract bees, in gullies, experiencing shelter belts effect, next to end assemblies, windy, exposed and having poor male flowering (Hopping, 1979; Hopping, 1982b; Hopping & Martyn, 1986c; Lyford & Goodwin, 1989; Lyford & Underwood, 1992; Underwood, 2001).

Staminate kiwifruit pollen grain is a rich source of crude protein and almost all amino acids required for honeybees (Clark & Lintas, 1992). However, when the honeybees number is low, honeybees prefer to collect the female pollen and ignore the male pollen, resulting in poor pollination (Goodwin, 1986c).

For an isolated orchard, there are likely to be other competing flowers in pasture and waste land surrounding the orchard (Clinch & ten Houten, 1986; Underwood, 2001). Lack of nectar and their dry rather unattractive pollen disadvantage both male and

1-13

female kiwifruit flowers in this floral competition (Palmer-Jones & Clinch, 1974). Pollen of white clover (*Tri-folium repens* L.) and honeysuckle (*Lonicera* sp.) were identified as severe competitors (Clinch, 1982; Clinch, 1984a; Clinch & Schrader, 1984; Goodwin, 1986a). Honeybees display remarkable constancy in foraging on only one plant species per trip and will forsake the plant species they were previously working only if the new environment is dominated by a new crop (Bryant & Vardy, 1985; Bryant, 1986).

As found later in the results of this study, the configuration of petals plays an important role in attracting the windborne pollen to the stigma (see section 3.5). This function however ceases when all the petals drop off after 3 - 4 days, even though the stigma are still receptive for up to 5 more days. In addition, flowers become unattractive to bees after losing their petals (Stevens & Forsyth, 1982). Introduction of artificial pollination here would aid further fertilization after the petal fall-off.

The degrees of wind and bee pollination are not uniform during the day because of the uneven pollen release during the day. Analysis by Heath & Tenquist (1984) showed that more pollen are released from the early morning to early post-noon than from the early post-noon to late afternoon. The pollen liberation is maximum at midday (Goodwin, 1986c). Heath & Tenquist (1984) found that pollen liberated at night was as much as during the day, but this is in contrary to the findings by Malaboeuf *et al* (1997) that airborne pollen at night was only 3 % of the total daily amount.

The pollen collection by honeybees had been found to decline in the afternoon (Blanchet, 1990; Goodwin, 1986a; Goodwin, 1986c) when the foragers have depleted the pollen supply from the male flowers (Goodwin, 1986d; Goodwin, 1995a). Bumble bees were observed to continue foraging in the afternoon but their required stocking rate of more than 1000 hives/ha proves too costly (Pomeroy, 2001).

Artificial pollinations are usually recommended to be used in conjunction with the introduction of reduced number of bee hives. For example, 1 – 2 hives of bees per hectare are hired and followed by artificial pollination at 50 % and 100 % flower opening (Anon., 1984).

Since artificial pollination offers more flexibility to the orchardists in unpredicted weather in such a short stigma receptivity period, it has been developed with the aim to reduce the dependence on bees which require special management. Injudicious spraying of citrus trees which are commonly found near kiwifruit orchards may cause bee mortality (Palmer-Jones, 1974; Palmer-Jones & Clinch, 1974). Bees need to be safeguarded carefully from the application of pre-blossom and post-blossom pesticides as well as fungicides (Reid, 1982; Sale, 1981).

The spread of "chalk brood" in 1980s (Anon., 1984) and the more recent Varroa mite (Keene, 2000a; Keene, 2000b) could threaten the stable supply of beehives. The disease, together with the rising sugar cost, has driven up the cost of hiring beehives (Underwood, 2001).

The application of Hi-Cane compacts the flowering. The shorter flowering period increases the risk of poor pollination from adverse weather (Lyford & Goodwin, 1989). Goodwin et al (1990) found the treatment of hydrogen cyanamide had resulted in less number of bees visiting the flowers. On the other hand, the compressed flowering favours the artificial pollination because more open flowers can be pollinated in less number of applications.

Some orchards have no males at all and rely totally on supplementary pollination (Bay of Plenty Pollen Limited, n.d.). Growers can maximize the fruit output per unit growing area if they remove the male vines and replace them with the fruit-producing females (Brewer, 1988).

Machine pollination is needed when restructuring and improving an existing male vine layout which may take 2 – 3 years (Lyford & Underwood, 1991). Male vines, which are less hardy than the females, may not produce flower in some years as a result of winter injury. In this case, the females will have to be pollinated artificially.

Artificial pollination is best regarded as an insurance to produce good fruit size because the pollination is an one-off event unlike other possible corrective measures such as additional pruning and soil fertilization.

1.6. Types of artificial pollination

There are various pollinating machines varying in size, price, ease of use, complexity, method of operation, speed, and labour and pollen use (Ferguson & Bradley, 1991). They can be categorized into three groups shown in Fig. 1-5. The comparisons among them are summarized in Table 1-2.

```
                          artificial pollination
         ┌─────────────────────────┼─────────────────────────┐
    contact              wet based                    dry based
      ├─ hand pollination    ├── Cambrian sprayer         ├── Airflo
      ├─ Polli               └── airshear                 ├── Turbobee
      └─ Rollon pollinators      ├── tractor mounted      ├── Variflo air pollinator
                                 └── back pack            ├── Dry-pol
                                                          └── Hanakaze
```
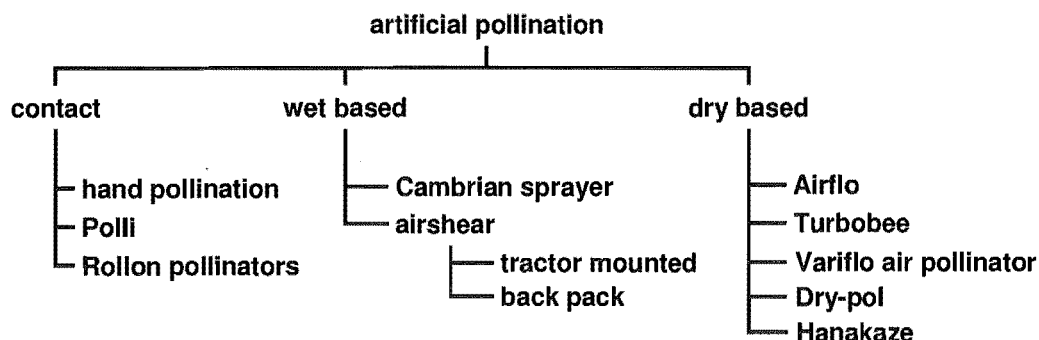
Fig. 1-5: Types of artificial pollination system.

Hand pollination

The just-open male flowers with dehisced anthers are picked and the anthers are brushed across or circularly against the stigma of individual female flowers for $1 - 2$ seconds (Hopping, 1981b; Sale, 1983c). Only female flowers of less than 3 days old and still with attached petals are recommended for hand pollination (Hopping, 1982b). If not used immediately, picked male flowers can be stored at $4 - 6$ $^{\text{o}}$C in air tight plastic bags up to 48 hours (Goodwin, 2000). Hand pollination is only economical for the small canopies with low flower loadings (Hopping, 1979). It is however necessary as a control of maximum potential size (Blanchet, 1990; Hopping, 1990b).

Polli

It consists of two rollers where one of them is fitted with velveteen-like fabric impregnated with pollen (Anon., 1992). The fabric scrolls between the rollers. The fabric strip is rubbed against the flowers, placing excessive amount of pollen (see Fig. 1-6e). Hence, it is not necessary to touch every female flower because bees had been found to carry the excess pollen to other flowers (Anon., 1992). Even though it is

Table 1-2: Comparison of various artificial pollination machines used for pollinating kiwifruit flowers.   *Continued next page...*

	Contact			Wet-based
	Hand pollination [c]	**Polli**	**Rollon pollinators**	**Cambrium sprayer**
No. of operator	1	1	1	1
Rate of application	130 h/ha [a] 181 h/ha [b]	42.8-57.5 h/ha [f, 3] 80 h/ha [g]	104 h/ha [b] 33-74 h/ha [h] 42.2-47.4 h/ha [f, 3]	74 h/ha [b] 66 h/ha [i] 67-95 h/ha [j]
Amount of pollen required	5-6 male flowers for 1 female flower [d]	318-327 g/ha [g]	261-296 g/ha [f, 3] 160 g/ha [p]	760 g/ha [b] 840 g/ha [j]
Pollen source(s)	- freshly picked male flower - stored male flowers	- cartridge holding a fabric strip coated with pollen	- by vacuuming the pollen directly onto the sleeve [c, h]	- commercial pure pollen or BCP [I] - from milled male flowers by growers
Suitable in rain?	Feasible but not recommended [5]	No	No	Yes
Recommended no. of application	2 [a]	1 or 2 [e]	1 or 2 [e]	2 or 3 [j, 8]
Recommended timing of application	30 % and 90-100 % flowering [a]	80 % flowering for single application [e]	80 % flowering for single application [e]	- 40 % and 90-95% flowering [j, 8] - or, 30 %, 60 % and 90 % flowering [j, 8]
Advantages	- achieve full pollination - useful for research - to trouble the pollination problem i.e. whether pollination is a limiting factor - to determine the full potential of fruit	- user-friendly [c, g]	- user-friendly [c]	- can be used in heavy rain - flexible [b]
Disadvantages / limitations	- very labour intensive - physically and psychologically demanding [b] - for small orchards or small area of vines in large orchard	- flowers must be dry during pollination i.e. free from rain and dew [4] - inconsistent pollen application due to the decreasing pollen on the cloth [c] - for small orchards or small area of vines in large orchard [g]	- flower must be dry during pollination i.e. free from rain and dew [4] - inconsistent pollen application due to the decreasing pollen on the cloth [c] - for small orchards or small area of vines in large orchard	- relatively heavy when full [b] - must use deionized water and food grade container [j]
Cost [2]	$ 3100 / ha [b]	$ 412-1399 /ha [e, 3] $ 1262-1399 /ha [f, 3]	$ 550-1318 /ha [e, 3] $ 3100 /ha [b] $ 814-917 /ha [f, 3]	$ 3700 /ha [b] $ 3836-5038 /ha [i] $ 2368 /ha [j, 6] $ 3508 /ha [j, 7]

Table 1-2: Comparison of various artificial pollination machines used for pollinating kiwifruit flowers.   *Continued next page...*

	Wet-based		Dry-based	
	Airshear – tractor mounted	**Airshear – back pack**	**Airflo**	**Turbobee**
No. of operator	5 [b] or 9 [k] (including driver)	1	6 (including driver)	1
Rate of application [h/ha]	108 h/ha [b] 46.8-58.1 h/ha [f, 3] 67-95 h/ha [l]	67-95 h/ha [j]	19.6-46.2 h/ha [f, 3] 20-40 h/ha [e]	2.3-2.5 h/ha [f, 9] 0.25 h/ha [q] < 3 h/ha [c]
Amount of pollen required	368-369 g/ha [f, 3] 420 g/ha [j]	600 g/ha [m] 420 g/ha [j]	371-513 g/ha [f, 3] 500 g/ha [n] 200-500 g/ha [p]	258-302 g/ha [f, 9]
Pollen source(s)	- commercial pure pollen or BCP [l] - from milled male flowers by growers	- commercial pure pollen or BCP [l] - from milled male flowers by growers	- directly from male flowers - pre-collected pollen	- pollen fallen on foliage or ground [q] - directly from male flowers [q] - pre-collected pollen [q]
Suitable in rain?	Yes	Yes	No	Yes [e, q]
Recommended no. of application	2 or 3 [j, 8]	2 or 3 [j, 8]	1 or 2 [e]	N/A
Recommended timing of application	- 40 % and 90-95% flowering [j, 8] - or, 30 %, 60 % and 90 % flowering [j, 8]	- 40 % and 90-95% flowering [j, 8] - or, 30 %, 60 % and 90 % flowering [j, 8]	80 % flowering for single application [e]	Throughout flowering [q]
Advantages	- can be used in heavy rain	- can be used in heavy rain - machine is light and easy to use [b]	- relatively low labour requirement [o] - simple to use [o] - relatively low capital and running cost [o]	- can be used in adverse weather
Disadvantages / limitations	- inflexible when artificially pollinating shelter rows [l] - inefficient labour use in T-bar orchard [l] - must use deionized water and food grade container [j]	- constant depression of trigger can decline the pressure rapidly [b] - must use deionized water and food grade container [j]	- rain water or wet flowers can affect the pollen delivery because of the water running down the tubes [c] - large-diameter tubes are tiring to handle, difficult to manoeuvre and often tipped over by the workers [b]	N/A
Cost [2]	$ 4400 /ha [b] $ 1176-1321 /ha [f, 3]	$ 1660 /ha [j, 6] $ 2228 /ha [j, 7]	$ 415-1323 /ha [e, 3] $ 853-1323 /ha [f, 3]	$ 508-619 /ha [e, 9] $ 508-593 /ha [f, 9]

Table 1-2: Comparison of various artificial pollination machines used for pollinating kiwifruit flowers.

| | Dry-based | | |
	Variflo air pollinator	Dry-pol	Hanakaze
No. of operator	1 or 2 [10]	1	1
Rate of application [h/ha]	1-2 h/ha [r]	63 h/ha [b]	43 h/ha [b]
Amount of pollen required	500 g/ha [r]	480 g/ha [b]	520 g/ha [b]
Pollen source(s)	- commercial pure pollen - pure pollen mixed with diluents [r]	- commercial pollen	- commercial pollen
Suitable in rain?	No	No	No
Recommended no. of application	2 [r]	N/A	N/A
Recommended timing of application	50 % and 90 % flowering [r]	N/A	N/A
Advantages	- relatively less labour intensive [s]	- light weight [t] - easy to use [b]	- light weight [b] - easy to hold and use [b]
Disadvantages / limitations	- need to avoid damp orchard condition [r] - relatively heavy if carried by an individual [s]	N/A	- difficult to discharge pollen as the pollen level in the reservoir decreases [b]
Cost [2]	N/A	$ 2100 /ha [b]	$ 1900 /ha [b]

Notes / remarks:
1. BCP = bee collected pollen
2. refer to the sources for the date
3. depending on the no. of applications and the types of training system (T-bar or Pergola)
4. or else will wet the cloth
5. osmotic effect causes the pollen to burst [j]
6. based on bee collected pollen
7. recalculated based on pure pollen
8. depending on whether the vines are Hi-Cane treated
9. depending on the types of training system (T-bar or Pergola)
10. carried by individual or using a trailer

Sources:
a. Hopping (1985)
b. Ferguson & Bradley (1991)
c. Goodwin (2000)
d. Sale (1990)
e. Goodwin et al (1994)
f. Goodwin et al (1992)
g. Anon. (1992)
h. Anon. (1988b)
i. Hopping et al (1987)
j. Kiwi Pollen Limited (1993)
k. Brewer (1988)
l. Anon. (1991)
m. Kiwi Pollen Limited (n.d. 3)
n. Anon. (1989b)
o. Anon. (1987)
p. Bay of Plenty Pollen Limited (n.d.)
q. Anon. (1989c)
r. Kiwi Pollen Limited (n.d. 2)
s. Grower (personal communication, 2001)
t. Ferguson & King (1991)
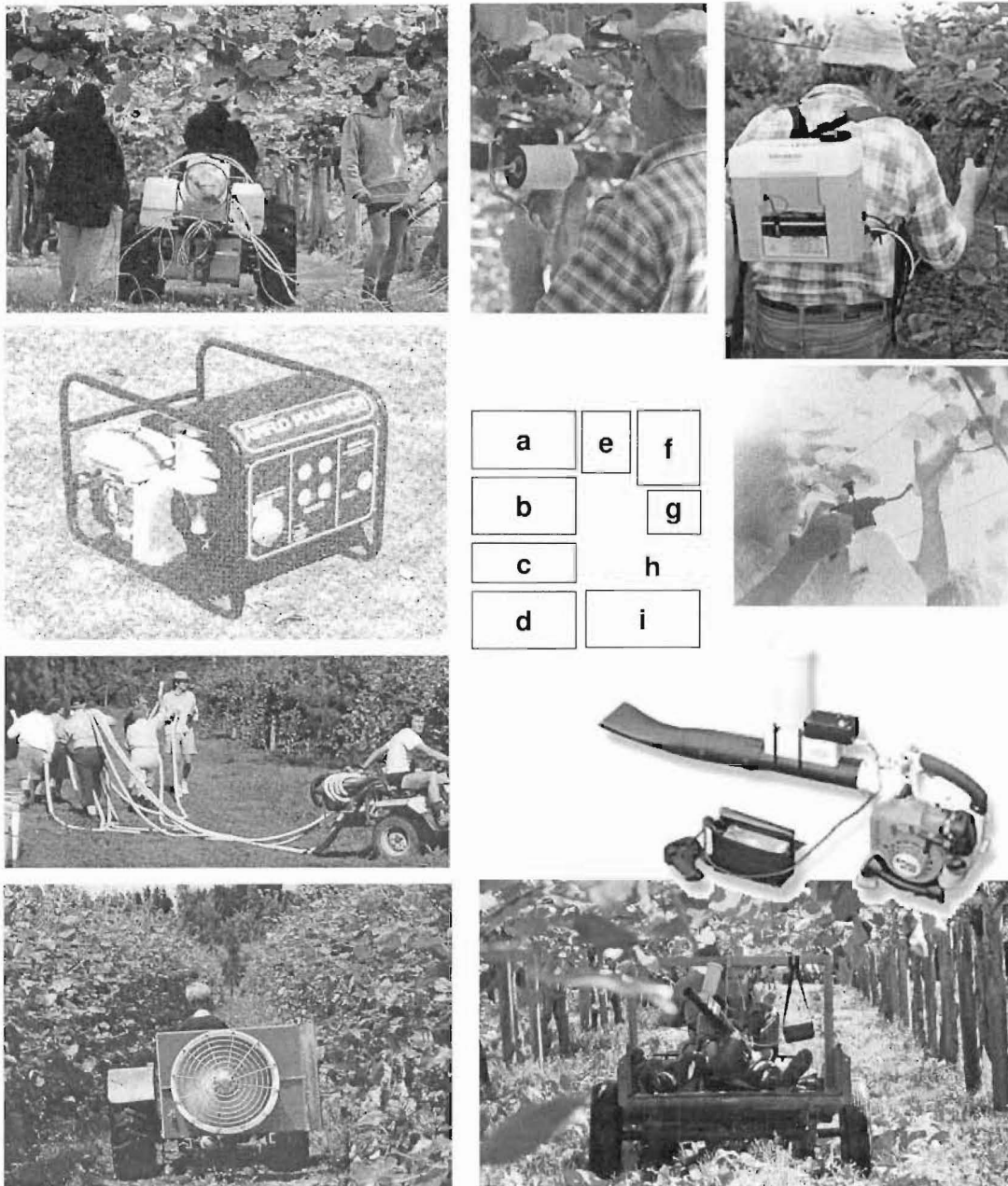
Fig. 1-6: (a) Tractor mounted airshear sprayers; (b) Airflo machine; (c) Airflo machine mounted on tractor and the operators; (d) Turbobee; (e) Polli; (f) Backpack version of airshear sprayer; (g) Cambrium sprayer; (h) Variflo air pollinator; (i) Variflo air pollinator used with a moving trailer. Sources: (b) is from Anon. (1989); (f) and (h) are from Kiwi Pollen Limited (2004); (i) was taken in a Katoa orchard, Te Puke, 2001; and the rest are from Goodwin (2000).

capable of achieving sufficient pollination, Polli is recommended as a supplement to bee pollination.

Rollon pollinators

A pollen-laden sleeve is fitted over a roller that looks like a conical paint roller (Anon,. 1988b). The stigma of individual female flowers are contacted with the sleeve while the roller is turned.

Cambrium (or Cambrian) sprayers

This is based on the Pollenaid system where the pollen are suspended in deionized water (Hopping & Simpson, 1982) mixed with commercial Pollenaid suspension medium. This suspension medium has been formulated to maintain the pollen viability up to one hour (Kiwi Pollen Limited, 2002). The formulation is developed by Hopping (1982a), Hopping & Jerram (1980a) and Hopping & Simpson (1982) based on their work of pollen suspension in CBCA media. CBCA consists of $Ca(NO_3)_2$ + H_3BO_4 + carboxymethyl cellulose (each 0.01 % w/v) + gun acacia (at 0.005 % w/v). A red marker dye is also added to identify the sprayed flowers. Cambrium sprayer (Fig. 1-6g) is based on the existing manual pumping method where the suspended pollen solution is manually pressurized and sprayed in a broad swirl jet towards the individual flowers (Ferguson & Bradley, 1991; Goodwin, 2000; Hopping & Hacking, 1983). Overspraying to drip point will lead to pollen being lost in spray drips from the end of flower styles (Hopping *et al*, 1987).

Airshear – tractor mounted and back pack

Here, the pollen suspended Pollenaid solution is atomized through an airshear nozzle by using the compressed air. The hand gun (or an airshear nozzle) is recommended to introduce the pollen at 100 mm away from individual open flowers for about quarter of a second (Kiwi Pollen Limited, 1993). The tractor mounted unit consists of a 15-L tank, two 25-L jerry cans, a mixer/agitator and a low pressure compressor (Kiwi Pollen Limited, 1993). Up to 8 nozzles can be connected simultaneously to a tractor mounted pump (Brewer, 1988; see Fig. 1-6a). The lighter back pack version has a 3-L tank holding enough pollen for 1 hour use and a battery powered compressor that lasts for 5 hours (Anon., 1991; see Fig. 1-6f).

Airflo

The Airflo machine (Fig. 1-6b) is mounted on a trailer or tractor and has 5 tubes fitted to it (Fruitfed Limited, n.d.; see Fig. 1-6c). One of tubes is used to suck the pollen from the male flowers. The pollen can either be applied instantaneously through other 4 tubes that target individual or small group of flowers, or collected for later use. Ryan & Rhoades (1988) found that the pollen collected in this way displayed similar viability to those collected from the anther in a mill. A polyester pollen cap is used to filter the air stream in order to concentrate the pollen (Atkinson, 1989). Although the system works well without bees (Anon., 1989a), a combination of bees and machine is recommended (Anon., 1987).

Turbobee

Turbobee (Fig. 1-6d) uses a big fan that generates the turbulence to lift the pollen from ground or foliage and disperse it on to female flowers; and to blow the pollen from male to female flowers (Anon., 1989c). Additional pollen can be also introduced into the air stream (Goodwin, 2000). It is generally used in conjunction with bees (Anon., 1989c).

Variflo air pollinator

It utilises a leaf blower to disperse the suspended pollen at a group of flowers. The pollen delivery rate is controlled by using an electric driven pollen dispenser powered by a battery pack (Kiwi Pollen Limited, n.d. 2; see Fig. 1-6h). The unit is designed to be carried by a walking individual. However, under the Pergola trained vines, the unit is hung on a moving trailer and swung from left to right by a worker (personal observation in a Katoa orchard, Te Puke, 2001; see Fig. 1-6i). For the T-bar trained vines, the pollinator is operated by a worker sitting at the back of a motorcycle moving between the rows of vine (grower, personal communication in Motueka, 2003). Variflo is considered as an enhancement to bee pollination (Kiwi Pollen Limited, n.d. 2).

Hanakaze and Dry-pol

Hanakaze is a plastic machine and Dry-pol is a gun-like aluminium machine (Ferguson & King, 1991; King & Ferguson, 1991) that can hold 65 g and 10 – 20 g of pollen respectively (Ferguson & Bradley, 1991). Both are not as well known as others.

Pollen sources for artificial pollinators

As shown in Table 1-2, some of these pollinators rely on the commercial supply of pure pollen (or called anther collected pollen, ACP) and bee collected pollen (BCP). The pollen are relatively costly, about NZ$ 1900 to 2500 per kg of pure pollen (Ferguson & Bradley, 1991; Goodwin et al, 1992b; Goodwin et al, 1994) and around $525 per kg of bee collected pollen.

The bulk commercial pollen supplies are from the male flowers specially grown in a male orchard. The about-to-open flower buds ('pop-corn' shape) are harvested and passed through revolving cutter bars to detach the anthers (Hopping, 1982a; Hopping & Hacking, 1983a; Mills et al, 1986). After screened from flower debris at mill outlet, the fresh anthers are dried and then tumbled in a rotary drum to dislodge pollen. The cyclone separators then collect the pollen from the air stream. According to Hopping (1981a), up to 14 kg of flower buds can be picked from a staminate vine in a commercial orchard in a flowering season. These flower buds produce about 100 g of pollen. Sheat et al (1982) estimated that a specific pollen orchard could produce 30 kg of pollen per hectare annually.

Another pollen extraction method based on the washing with organic solvents (benzene and toluene) had been published by Waki & Takeuchi (1990), but it does not appear to be practiced in New Zealand.

Long term storage of pure pollen are recommended at $-18\,^{O}C$ and 20 %RH (Bomben et al, 1999; Hopping & Hacking, 1983d; Kiwi Pollen Limited, 1993). The recommended temperature for storing bee collected pollen is $4\,^{O}C$. The optimum in vitro pollen germination occurs at $22 - 28\,^{O}C$ (Jansson & Warrington, 1988) but Manandhar & Lawes (1980) stated that the variation on the stigma is insignificant within the range of $14 - 26\,^{O}C$.

Overall comparisons of artificial pollinators

Goodwin et al (1994) evaluated some of these artificial pollination systems and found that only the wet-based method or Pollenaid system gave significant increase in the percentage of flowers producing exportable fruits but with no significant improvement on the average fruit weights. The similar results are also reported by Kiwi Pollen

Limited (n.d. 1). The gain of increase in the export trays however did not happen consistently in every orchard (Anon., 1988a). Earlier extensive field trials by Hopping (1990b), Hopping & Hacking (1983c), Hopping & Jerram (1980a, 1980b), Hopping & Martyn (1986b, 1986c) and Hopping *et al* (1985) had shown that wet-based application or Pollenaid system was nearly as effective as hand pollination.

Despite the success of wet-based (or Pollenaid) systems, spraying dry pollen does have the advantages that the pollen are dispersed more freely and the pollen not used to fertilize one flower (i.e. on the petals) can be delivered to other flowers by bees or wind (Anon., 1988a, King & Ferguson, 1991). Trial results by Kiwi Pollen Limited (n.d. 1) show that the dry pollen application using the Variflo air pollinator produced comparable average tray-count to those using Pollenaid system and hand pollination. Applying pollen in dry form represents a direct use of pre-collected pollen without the need to mix them uniformly in the suspension liquid. Pollen sprayed in liquid medium become unviable after 60 – 80 minutes (Anon., 1988a; Kiwi Pollen Limited, 2002). In contrast, dry pollen at room temperature remains viable for several days, according to Mckay (1978, cited in King & Ferguson, 1991). Even the bee collected pollen, which are stickier than pure pollen, could be used satisfactorily in dry application if mixed with suitable diluent (Alspach *et al*, 1991). If the efficacy of the pollen from the dry air pollinator to attach securely to the stigmatic surfaces is improved to the level achieved by the Pollenaid system and hand pollination, the dry air pollinator such as based on an air jet is expected to benefit the growers in terms of convenience and time saving.

CHAPTER 2: CFD AND FLOWER MODEL

2.1. Background of CFD

The computational fluid dynamic (CFD) is a modelling technique to simulate the motion of fluids described by the mass, momentum and energy transfers. Wide applications are found in various fields such as process industries, architectural design, medical, electronics, agricultural, automobile and aerospace industry (Versteeg & Malalasekera, 1995). It is widely used as an effective tool in the process of design, problem-solving, optimization and research (Bakker *et al*, 2001; Joshi & Ranade, 2003). The still improving technology is becoming more accessible with the release of more advanced yet user-friendly commercial CFD packages and the more powerful computers.

A CFD package generally consists of three components, namely pre-processor, solver and post-processor. The commercial CFD package used in this work is called CFX-5.6 from ANSYS (originally developed by AEA Technology; refer to *CFX-5.6 Manual*, 2003). CFX-5 uses implicit finite volume formulation to construct the discrete equations representing the Navier-Stokes equations for the fluid flow (Esch *et al*, 2003). Its structure is shown in Fig. 2-1.
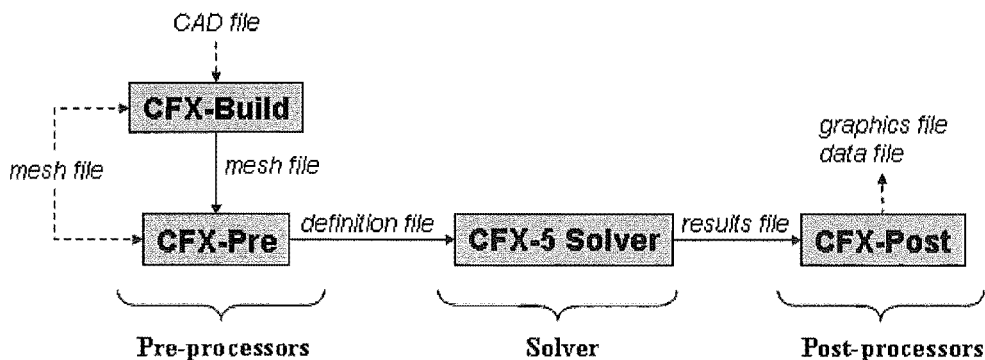
Fig. 2-1: The simulation sequence of modules in CFX-5.6. CAD stands for computer-aided drawing.

CFX-Build is both a solid modeller and mesh generator. The geometry of the region of interest can either be created or imported from third-party CAD packages. Imported geometries usually require the repair of CAD surfaces in CFX-Build prior to meshing. The meshing begins with either the Delaunay or Advancing Front surface meshing and ends with the unstructured volume mesh generation of tetrahedral elements. Local mesh refinement is achieved by using various mesh controls and the generation of prismatic element layers (called inflation layers) in the boundary layer regions.

After importing the mesh produced by either CFX-Build or other mesh generation software, CFX-Pre is used to define the boundary conditions, flow physics, properties of fluids, source terms, initial values and solver parameters. The specifications of flow physics include choosing laminar or turbulence models, nature of simulation (i.e. steady state or transient), number of components and phases, and heat transfer models. CFX-Pre also features additional capabilities such as the multiphase models (Eulerian-Eulerian and Particle Tracking), free surface models, combustion models, radiation models, mesh adaption, built-in expression language for general user-defined functions and support for user-subroutines written in Fortran.

The defined problem then has its partial differential equations discretised (using upwind or a blend of 1st and 2nd order differencing) and solved iteratively for each control volume in CFX-5 Solver. All hydrodynamics equations are solved as a single system by using a coupled algebraic multi-grid solver, which converges more quickly than a segregated solver. CFX-5 Solver Manager is a user interface to

- set the attributes of a run (e.g. parallel or serial run, partitioning details, memory allocation);

- control the execution of CFX-5 Solver (e.g. initiation, termination and continuation of a run); and

- monitor the progress of convergence (e.g. number of iterations or timestep, residuals, % imbalance, convergence rate and user-specified monitor points of interested variables).

The simulation results are then analysed in CFX-Post using different visualizations e.g. vector plots, isosurfaces, contour plots, streamlines, XY graphs and animations. Quantitative calculations (such as the mass flow-based averaging and integration of

interested variables) are performed by using the built-in expressions and the user-defined functions/subroutines written in the built-in expression language and Perl. The generated images and data can be exported in various formats.

2.2. Principles of CFD

The air and pollen flow around a single female kiwifruit flower are simulated by treating the flower as a bluff body in the flow domain. The relevant fluid flow models, associated wall treatments and the multiphase modelling in CFD are reviewed below.

The conservations of mass, momentum and energy form the governing equations in CFD, collectively known as the Navier-Stokes equations. For a compressible Newtonian fluid, these are Equation 2-1 to Equation 2-5 (Versteeg & Malalasekera, 1995).

Mass/continuity $$\frac{\partial \rho}{\partial t} + div(\rho \mathbf{U}) = 0$$ Equation 2-1

x-momentum $$\frac{\partial(\rho u)}{\partial t} + div(\rho u \mathbf{U}) = -\frac{\partial p}{\partial x} + div(\mu \, grad \, u) + S_{Mx}$$ Equation 2-2

y-momentum $$\frac{\partial(\rho v)}{\partial t} + div(\rho v \mathbf{U}) = -\frac{\partial p}{\partial y} + div(\mu \, grad \, v) + S_{My}$$ Equation 2-3

z-momentum $$\frac{\partial(\rho w)}{\partial t} + div(\rho w \mathbf{U}) = -\frac{\partial p}{\partial z} + div(\mu \, grad \, w) + S_{Mz}$$ Equation 2-4

Internal energy $$\frac{\partial(\rho i)}{\partial t} + div(\rho i \mathbf{U}) = -p \, div(\mathbf{U}) + div(k \, grad \, T) \\ + \Phi + S_i$$ Equation 2-5

Where ρ = fluid density; t = time; $\mathbf{U}$ = velocity vector = $[u, v, w]^T$; u = x-component velocity; v = y-component velocity; w = z-component velocity; μ = dynamic viscosity; S_M = momentum source term in x, y or z direction; i = internal (thermal) energy; p = pressure; k = thermal conductivity; T = temperature; Φ = dissipation function; and S_i = internal energy source term.

If density ρ is constant, as in an incompressible flow, Equation 2-1 reduces to Equation 2-6.

$$div(\mathbf{U}) = 0 \qquad\qquad \text{Equation 2-6}$$

Apart from the definition of sensible boundary conditions, the quality of a CFD simulation depends largely on the type of flow models (laminar or turbulence) used. The choice of flow models depends on the dimensionless Reynolds number ($Re = \dfrac{L\,U}{v}$), where L is the characteristic length [m], U is velocity [m/s] and v is kinematic viscosity [m^2/s]. It is a measure of relative importance of non-linear inertial force to viscous force.

Laminar flow is dominated by the viscous force and thus characterized by a low Re number. Laminar flow model is governed by the unsteady Navier-Stokes equations.

When the inertial forces of fluid become more significant, as indicated by a high Re number, the flow becomes turbulent and exhibits random fluctuations in the flow characteristics, particularly velocity and pressure, over the time and space. Turbulence is a three-dimensional continuum phenomenon (Warsi, 1999) that is diffusive i.e. in mass and momentum transports; and dissipative i.e. the energy is cascaded down from large eddies to small eddies where it is removed by the viscous resistance. To model a turbulent field, approximating turbulence flow models are developed because it is unpractical to numerically solve the Navier-Stokes equation for the wide range of turbulent length and time scales found in the turbulent flows.

Since the *mean* flow quantities of the turbulent flow are usually of interest, the modelling of turbulent *fluctuations* can be avoided by statistically averaging the Navier-Stokes equations. This leads to the Reynolds Averaged Navier-Stokes (RANS) models, which are either time-averaged (for steady flows) or ensemble-averaged (for unsteady flows); see details in Warsi (1999) and Ferziger & Peric (1999). RANS models are widely available in the commercial CFD codes such as the CFX-5.6 used in this work and expected to be the workhorse in the foreseeable future.

The more advanced turbulence flow models, namely Direct Numerical Simulation (DNS) and Large Eddy Simulation (LES), are not considered here due to requirements of a high computational resource. Both DNS and LES require very fine grid spacing and very small time steps to capture the large and small eddies (Wesseling, 1991; see Fig. 2-2). DNS is applicable only to simple low-Reynolds-number flows and not considered cost-effective for engineering flows (Rodi, 1993; Sotiropoulos, 2000). Since DNS solves the Navier-Stokes equations for all the motions, it is commonly used to develop/validate the simpler RANS models (Ferziger & Peric, 1999; Sotiropoulos, 2000). Less expensive than DNS, LES solves for only the large eddies directly while the small eddies are modelled heuristically (called subgrid-scale modelling). LES is becoming increasingly popular in simulating moderate Reynolds number flows.
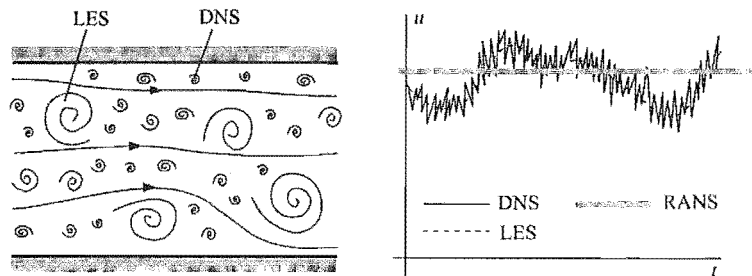
Fig. 2-2: Scale of flow motions modelled by RANS, DNS and LES (Ranade, 2002). Here, u and t refer to instantaneous velocity and time respectively.

Depending on the mathematical treatment of flow isotropy, RANS models can be grouped into Eddy-viscosity Models and Second Order Closure Models (Fig. 2-3). Eddy-viscosity Models employ the Boussinesq approximation which assumes that the eddy viscosity is isotropic (i.e. no sense of directionality; see Warsi, 1999) and proportional to the mean-flow stress-tensor S_{ij}; and the kinematic eddy viscosity v_T is the proportionality constant here. This representation can also be modified into a higher-order and non-linear, as in the Algebraic Stress Model, to account for the anisotropy of flow (Collie et al, 2001; see the explicit and implicit models of the Algebraic Stress Model in Warsi, 1999). On the other hand, Second Order Closure Models actually solve the differential transport equations for each Reynolds-stress which enables it to model anisotropic flow accurately.

2-5

Linear Eddy-viscosity Models are further categorized depending on the number of partial differential equations (PDE), ranging from Zero- to Two-equations (Fig. 2-3). Two-equation models are focussed on in this work because they are more complete than others. They can be applied to a full range of different flow types without the immediate requirement for the specification of turbulent length scales or the calibration of algebraic functions (Collie *et al*, 2001).

Two-equation Models solve a transport equation for the turbulent kinetic energy k [m^2/s^2] and another scale determining transport equation. The capabilities and limitations of five Two-equation Models (Standard k-ε, RNG k-ε, Standard k-ω, Baseline (BSL) k-ω, Shear-stress-transport (SST) k-ω based) and one Reynolds-Stress Model provided in CFX-5.6 are looked at below in order to evaluate their suitability for the simulation of air flow field around a single kiwifruit flower.

2.2.1. Standard k-ε Model

This is the simplest semi-empirical Two-equation model, proposed by Jones & Launder (1972) (see also Launder & Spalding, 1972) and it has since become the most popular model for general engineering flows. Apart from offering reasonable accuracy for a wide range of simple and high Reynolds-number flows, it is computationally economic, numerically stable and robust (Wright & Easom, 1999).

But, it is known for its poor prediction of separation points (either delayed or prevented) under adverse pressure gradients. This is due to the over-prediction of turbulent length scale (and hence eddy viscosity) that results in high wall shear stress in the defect layer (Menter, 1996; Murakami, 1993; Rodi & Scheuerer, 1986). Without taking the effects of molecular viscosity into account, this model is limited to fully turbulent flows (*Fluent User Guide*, 2001). Inaccurate solutions can therefore occur in the viscous sub-layer i.e. in the low Reynolds-number region near wall. In addition, this model fails in rotating flows, streamline curvature, some unconfined flows, stagnation regions, swirl jet, predicting secondary flow based on the differences in normal stresses, flows with large extra strains such as the curved boundary layers and swirling flows (Menter & Grotjans, 2000; Murakami, 1993; Ranade, 2002; Versteeg & Malalasekera, 1995).
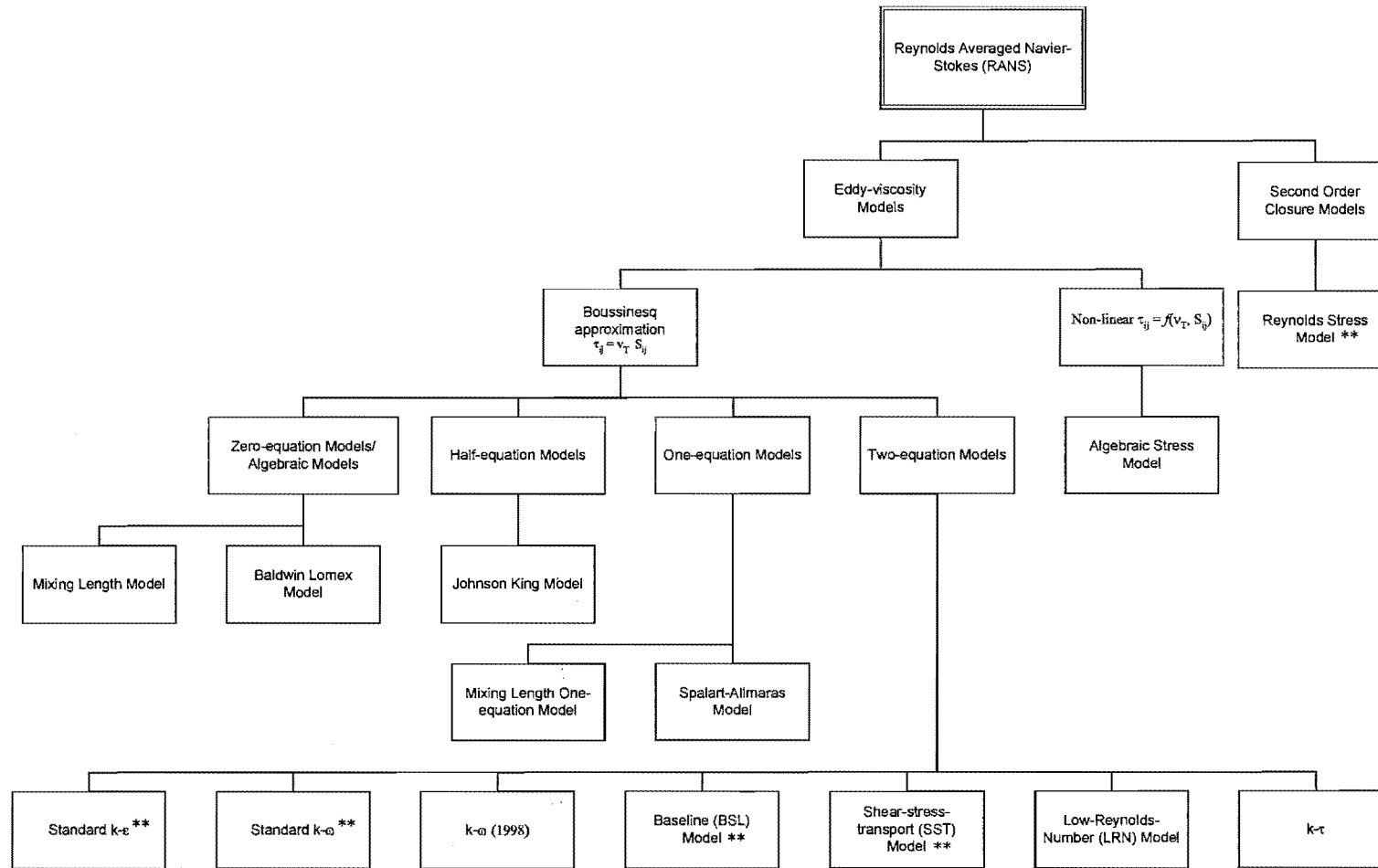
Fig. 2-3: Types of common Reynolds Averaged Navier Stokes (RANS) Models. Models available in CFX-5.6 are marked **. This diagram is prepared based on the review by Collie *et al* (2001).

In the study of blunt obstacles aerodynamics, Laurence (1993) found that the Standard k-ε could model only shear or wall parallel flows and could be 100 % wrong in impinging flows. This was demonstrated by the under-prediction of eddy in a backward facing step problem. The Standard k-ε Model also overpredicts the length of the separation zone behind a square cylinder considerably (Rodi, 1993). In simulating a flow around a cubic building, Wright & Easom (1999) observed that the Standard k-ε Model failed to predict the proper pressure distribution around the bluff body due to the overproduction of turbulent kinetic energy at the impinging area. Thus, the Standard k-ε Model usually requires modifications to improve the simulations around a bluff body such as building (Castro *et al*, 1999). The Standard k-ε Model is also inaccurate for all surface roughness values (Collie *et al*, 2001).

In this model, the second transport equation is solved for the turbulence eddy dissipation ε [m^2/s^3], which is the rate at which the velocity fluctuations dissipate.

The equations in CFX-5.6 based on that of Launder & Spalding (1974) are:

Eddy viscosity
$$\mu_T = C_\mu \rho \frac{k^2}{\varepsilon}$$
Equation 2-7

Turbulent kinetic energy

$$\frac{\partial(\rho k)}{\partial t} + \nabla \bullet (\rho\, U\, k) - \nabla \bullet \left(\frac{(\mu + \mu_T)}{\sigma_k} \nabla k \right) = \mu_T \nabla U \bullet (\nabla U + \nabla U^T)$$

$$- \frac{2}{3} \nabla \bullet U\, (\mu_T \nabla \bullet U + \rho k) - \rho \varepsilon$$
Equation 2-8

Dissipation rate

$$\frac{\partial(\rho \varepsilon)}{\partial t} + \nabla \bullet (\rho\, U\, \varepsilon) - \nabla \bullet \left(\frac{(\mu + \mu_T)}{\sigma_\varepsilon} \nabla \varepsilon \right) = \frac{\varepsilon}{k}\, (C_{\varepsilon 1} \mu_T \nabla U \bullet (\nabla U + \nabla U^T)$$

$$- \frac{2}{3} C_{\varepsilon 1} \nabla \bullet U\, (\mu_T \nabla \bullet U + \rho k) - C_{\varepsilon 2} \rho e)$$
Equation 2-9

Closure coefficients (adopted from Rodi, 1980)

| $C_\mu = 0.09$ | $C_{\varepsilon 1} = 1.44$ | $C_{\varepsilon 2} = 1.92$ | $\sigma_k = 1.0$ | $\sigma_\varepsilon = 1.3$ |

The closure coefficients are appropriate for the plane jets, recirculating flows, confined flows, mixing layers, the flat plate flows, and the free shear flows that are decaying isotropic and homogeneous turbulence (Collie *et al*, 2001; *Fluent User Guide*, 2001; Launder & Spalding, 1974; Rodi, 1980). It is a common practice to change one or more of these closure coefficients for particular flows, such as the change of $C_{\epsilon 1}$ to 1.60 by Morgans *et al* (1999) which yielded better agreement to experimental data of a round jet in a co-flow.

2.2.2. RNG k-ϵ Model

This is one of the variants of the Standard k-ϵ Model which is modified by applying a rigorous statistical technique called Renormalization Group Theory (Yakhot & Orszag, 1986; Yakhot *et al*, 1992; Yakhot & Smith, 1992). It improves the modelling of the adverse pressure gradients, separated flows, homogeneous shear flow, far wake, mixing layers, wall-bounded flow and flows with strong streamline curvature (swirls), vortices and rotation (*Fluent User Guide*, 2001; Menter, 1996; Yakhot *et al*, 1992). The model is not restricted to high-Reynolds-number flows because its differential equation for effective viscosity can handle low-Reynolds-number and near-wall flows (*Fluent User Guide*, 2001).

Compared to the Standard k-ϵ Model, although it generally gives more realistic flow, it can exhibit worse results for some free shear flows i.e. the plane and round jet (Menter, 1996). It also predicts much lower levels of turbulence in the complex geometries (Laurence, 2001). The integration through the viscous layer still requires modification of ϵ-equation (Collie *et al*, 2001) such as the use of viscous damping function in Low-Reynolds-Number k-ϵ Model. In addition, RNG k-ϵ Model is not sufficiently validated (Ranade, 2002) and as stable as the Standard k-ϵ Model (Bakker *et al*, 2001).

The k-equation and ϵ-equation are same as in the Standard k-ϵ model, but with different closure coefficients that are derived explicitly using RNG theory (Yakhot *et al*, 1992). Only the equation of eddy viscosity at high Reynolds number limit is shown here (see

the differential formula in Yakhot & Orszag, 1986; Yakhot *et al*, 1992), which is similar to that of Standard k-ε model.

Eddy viscosity (at high Re number)
$$\mu_T = C_{\mu RNG}\,\rho\,\frac{k^2}{\varepsilon}$$
Equation 2-10

Turbulent kinetic energy
$$\frac{\partial(\rho k)}{\partial t} + \nabla\bullet(\rho\,\mathbf{U}\,k) - \nabla\bullet\left(\frac{(\mu+\mu_T)}{\sigma_{kRNG}}\nabla k\right) = \mu_T\nabla\mathbf{U}\bullet(\nabla\mathbf{U}+\nabla\mathbf{U}^T)$$

$$-\frac{2}{3}\nabla\bullet\mathbf{U}\,(\mu_T\nabla\bullet\mathbf{U}+\rho k) - \rho\varepsilon$$

Equation 2-11

Dissipation rate
$$\frac{\partial(\rho\varepsilon)}{\partial t} + \nabla\bullet(\rho\,\mathbf{U}\,\varepsilon) - \nabla\bullet\left(\frac{(\mu+\mu_T)}{\sigma_{\varepsilon RNG}}\nabla\varepsilon\right) = \frac{\varepsilon}{k}\,(C_{\varepsilon1RNG}\mu_T\nabla\,\mathbf{U}\bullet(\nabla\mathbf{U}+\nabla\mathbf{U}^T)$$

$$-\frac{2}{3}C_{\varepsilon1RNG}\nabla\bullet\mathbf{U}\,(\mu_T\nabla\bullet\mathbf{U}+\rho k) - C_{\varepsilon2RNG}\rho e)$$

Equation 2-12

Where, without showing the extensive equations (which can be found in Yakhot *et al*, 1992),

$$C_{\varepsilon1RNG} = f(\beta_{RNG},\,C_{\mu RNG},\,\rho,\,\mu_T,\,\mathbf{U},\,k)$$
Equation 2-13

Closure coefficients

$C_{\mu RNG} = 0.085$ $C_{\varepsilon12RNG} = 1.68$ $\sigma_{kRNG} = 0.7179$ $\sigma_{\varepsilon RNG} = 0.7179$ $\beta_{RNG} = 0.012$

2.2.3. Standard k-ω Model

The Standard k-ω Model gives promising results for a wide range of flows i.e. free shear flows, separated flows and flat plate boundary layer flows particularly under adverse pressure gradients (Menter, 1992b; Wilcox, 1988). It is known for its proper prediction of wake strength in equilibrium adverse pressure gradient (Menter, 1992a). Its near wall treatment is accurate, robust and does not require viscous damping function for

integration to the wall (Menter & Grotjans, 2000; Wilcox, 1988). Numerically, the ω-equation is more stable and less stiff near the wall than the ε-equation (Collie *et al*, 2001). The wall surface roughness can be incorporated by specifying a finite ω (Wilcox, 1988).

The model however displays a sensitive dependency of ω in the freestream, especially for the free shear flows. Menter (1992a) showed that a reduction of freestream ω could change the eddy viscosity in the boundary and free shear layers by more than 100 %. Thus, an inaccurate freestream boundary specification of ω can deteriorate the model predictions. The streamline curvature effects are also not accounted for in this model (Wilcox, 1988).

In addition to *k*-equation, a transport equation of turbulent frequency ω [1/s] is solved. ω is the characteristic frequency of turbulent decay process.

Eddy viscosity

$$\mu_T = \rho \frac{k}{\omega}$$

Equation 2-14

Turbulent kinetic energy

$$\frac{\partial(\rho k)}{\partial t} + \nabla \bullet (\rho\, \mathbf{U}\, k) = \mu_T\, [\nabla \mathbf{U} + \{\nabla \mathbf{U}\}^T] - \beta'\rho k\omega + \nabla \bullet \left[\left(\mu + \frac{\mu_T}{\sigma_k}\right)\nabla k\right]$$

Equation 2-15

Specific dissipation rate

$$\frac{\partial(\rho\omega)}{\partial t} + \nabla \bullet (\rho\, \mathbf{U}\, \omega) = \alpha \mu_T \frac{\omega}{k}\, [\nabla \mathbf{U} + \{\nabla \mathbf{U}\}^T]$$

$$- \beta\rho\omega^2 + \nabla \bullet \left[\left(\mu + \frac{\mu_T}{\sigma_\omega}\right)\nabla\omega\right]$$

Equation 2-16

Closure coefficients

$$\beta' = 0.09 \qquad \alpha = \frac{5}{9} \qquad \beta = \frac{3}{40} \qquad \sigma_k = 2 \qquad \sigma_\omega = 2$$

2.2.4. Baseline (BSL) k-ω Model

Developed by Menter (1994), this model is an empirical approach of combining the superiority of the Standard k-ω Model in handling adverse pressure gradient and that of the Standard k-ε Model in the wake region of the boundary layer. This is done by multiplying the Standard k-ω Model with a blending function F_1 and the transformed Standard k-ε Model with $(1 - F_1)$, where $F_1 = 1$ in the sub- and log-layer; and $F_1 = 0$ in the wake region of the boundary layer. Thus, this model gradually switches from the Standard k-ω Model to the Standard k-ε Model when moving away from the wall. The transformation of Standard k-ε Model into a k-ω formula introduces a cross diffusion term that is found to enhance the production of ω, which in turn increases the dissipation of k and thus reduces the spreading rates of free-shear layers. The non-linear multiplication of the cross diffusion term with the blending function then eliminates the strong freestream sensitivity that comes from the Standard k-ω Model (Menter, 1994). According to Menter & Grotjans (2000), the BSL model displays a similar performance as the Standard k-ω Model for boundary layer flows and is (almost) identical to the Standard k-ε Model for free shear flows. This model retains the Standard k-ω Model's numerical properties and ability to incorporate the surface roughness (Collie *et al*, 2001; Menter & Grotjans, 2000).

The drawback in this model is the improper prediction of the onset and amount of flow separation from the smooth surfaces, resulted from the over-prediction of the eddy-viscosity by both the Standard k-ω and k-ε Models (Menter, 1994).

Here, the same eddy-viscosity, k- and ω-equations in the Standard k-ω Model are used (Equation 2-14 to Equation 2-16), except that the closure coefficients α, β, σ_k and σ_ω now become α_1, β_1, σ_{k1} and $\sigma_{\omega 1}$ respectively.

The variable ε in the k- and ε-equations of the Standard k-ε Model (Equation 2-15 and Equation 2-16) are now expressed in ω (see Equation 2-17 and Equation 2-18).

Turbulent kinetic energy – Standard k-ε Model

$$\frac{\partial(\rho k)}{\partial t} + \nabla \bullet (\rho\, \mathbf{U}\, k) = \mu_T\, [\nabla\mathbf{U} + \{\nabla\mathbf{U}\}^T] - \beta' \rho k \omega + \nabla \bullet \left[\left(\mu + \frac{\mu_T}{\sigma_{k2}}\right)\nabla k\right] \qquad \text{Equation 2-17}$$

Specific dissipation rate – Standard k-ε Model

$$\frac{\partial(\rho\omega)}{\partial t} + \nabla \bullet (\rho\, \mathbf{U}\, \omega) = \alpha_2 \mu_T \frac{\omega}{k}\, [\nabla\mathbf{U} + \{\nabla\mathbf{U}\}^T] - \beta_2 \rho \omega^2 +$$

$$\nabla \bullet \left[\left(\mu + \frac{\mu_T}{\sigma_{\omega2}}\right)\nabla\omega\right] + 2\rho\sigma_{\omega2}\frac{1}{\omega}\nabla k \nabla\omega \qquad \text{Equation 2-18}$$

The addition of the corresponding k- and ω-equations from the Standard k-ε and k-ω Models, after these models are multiplied by F_1 and $(1 - F_1)$ respectively, gives Equation 2-19 and Equation 2-20.

Turbulent kinetic energy

$$\frac{\partial(\rho k)}{\partial t} + \nabla \bullet (\rho\, \mathbf{U}\, k) = \mu_T\, [\nabla\mathbf{U} + \{\nabla\mathbf{U}\}^T] - \beta' \rho k \omega + \nabla \bullet \left[\left(\mu + \frac{\mu_T}{\sigma_{k3}}\right)\nabla k\right] \qquad \text{Equation 2-19}$$

Specific dissipation rate

$$\frac{\partial(\rho\omega)}{\partial t} + \nabla \bullet (\rho\, \mathbf{U}\, \omega) = \alpha_3 \mu_T \frac{\omega}{k}\, [\nabla\mathbf{U} + \{\nabla\mathbf{U}\}^T] - \beta_3 \rho \omega^2 +$$

$$\nabla \bullet \left[\left(\mu + \frac{\mu_T}{\sigma_{\omega3}}\right)\nabla\omega\right] + (1 - F_1)2\rho\sigma_{\omega2}\frac{1}{\omega}\nabla k \nabla\omega \qquad \text{Equation 2-20}$$

The new coefficients Φ_3 are blended between the closure coefficients Φ_1 and Φ_2 from the Standard k-ω and k-ε Models respectively, according to Equation 2-21.

$$\Phi_3 = F_1\Phi_1 + (1 - F_1)\Phi_2 \qquad \text{Equation 2-21}$$

Where, without showing the extensive equations (which can be found in Menter, 1994; *CFX-5.6 Manual*, 2003),

$$F_1 = f(\beta', k, \omega, y, \nu, \rho, \sigma_{\omega2}) \qquad \text{Equation 2-22}$$

And y is the distance to the nearest wall.

Closure coefficients

Φ_1 (Standard k-ω Model)

$$\beta' = 0.09 \qquad \alpha_1 = \frac{5}{9} \qquad \beta_1 = \frac{3}{40} \qquad \sigma_{k1} = 2 \qquad \sigma_{\omega1} = 2$$

Φ_2 (Standard k-ε Model)

$$\alpha_2 = 0.44 \qquad \beta_2 = 0.0828 \qquad \sigma_{k2} = 1 \qquad \sigma_{\omega2} = 0.856$$

2.2.5. Shear-stress-transport (SST) k-ω based Model

This model (Menter, 1994) consists of the same k- and ω-equations as in BSL k-ω Model, but an additional blending function F_2 is introduced in the eddy-viscosity equation to account for the transport of the principal turbulent shear stress (see Equation 2-23). There is a modified relation of eddy-viscosity based on the Bradshaw's assumption that the Reynolds shear stress in a boundary layer flow is proportional to the turbulent kinetic energy k (Bradshaw *et al*, 1967). Both additions remove the deficiency of BSL k-ω Model i.e. it now predicts the onset and amount of flow separation accurately under the adverse pressure gradients (Menter, 1994; Menter & Grotjans, 2000; Vieser *et al*, 2002). Thus, this model is regarded as the most advanced and promising among the Two-equation models because it combines the strengths and overcomes the weaknesses from the ε- and ω- equations. Both BSL and SST k-ω based Models are reported to be numerically stable in complex applications and the additional computational expense is insignificant compared with the Standard k-ω Model (Menter, 1994).

This model still requires the calculation of a wall distance and does not handle the streamline curvature (i.e. sharply changing streamlines) and strongly anisotropic flows well (Collie *et al*, 2001). For free shear layers, it is identical to the Standard k-ε Model and hence gives under-predicted spreading rates of far wake and over-predicted spreading rates of the round jet (Menter, 1996).

Eddy viscosity
$$\mu_T = \frac{\rho a_1 k}{\max(a_1\omega;SF_2)}$$
Equation 2-23

S is an invariant measure of the strain rate and $a_1 = 0.31$.

Where, without showing the extensive equations (which can be found in Menter, 1994; *CFX-5.6 Manual*, 2003),

$$F_2 = f(\beta', k, \omega, y, \nu)$$
Equation 2-24

F_1 and F_2 have been calibrated with the free-shear and boundary layer flows.

2.2.6. Reynolds Stress Models

Six components of the Reynolds-stress-tensor and the rate of energy dissipation ε are solved using the Reynolds-stress transport equations here (see details in Versteeg & Malalasekera, 1995). Since the Reynolds stress tensor is no longer treated as an isotropic tensor, this makes it excellent for anisotropic flows with large streamline curvature (i.e. swirl), rotation, wall jets, round jets, planar jets, asymmetric channel, non-circular ducts and sudden changes in the strain rate (Bakker *et al*, 2001; *Fluent User Guide*, 2001; Versteeg & Malalasekera, 1995).

The additional seven transport equations require expensive computational time and storage. Compared to the more advanced eddy-viscosity models, little improvements are gained unless there are strong curvature and secondary recirculation regions. In some flows e.g. axisymmetric jets and unconfined recirculating flows, it performs as poorly as the Standard k-ε Model due to the problems with ε equation (Ranade, 2002; Versteeg & Malalasekera, 1995). In the flow over the backward facing step, Reynolds Stress Models were found to underpredict the strength of the recirculation zone in terms of the wall shear stress and give too large a recirculation zone away from the wall (Menter & Grotjans, 2000).

This model requires fine meshes, robust and accurate schemes to capture the fine secondary motions (Laurence, 2002). It is well-known for its high computational cost,

difficulty in converging and numerical instability (Menter & Grotjans, 2000). The former is due to the strong coupling between the Reynolds stresses and the mean flow (*Fluent User Guide*, 2001) while the latter can be due to the physical unsteady behaviour in some cases (Laurence, 2002). It is also not widely validated (Ranade, 2002; Versteeg & Malalasekera, 1995).

There are three versions of differential Reynolds Stress Models in CFX-5, namely LRR-IP, LRR-QI and SSG. They differ in the closure coefficients and the pressure-strain correlation. Only LRR-IP is looked at here.

Reynolds stresses

$$\frac{\partial \rho \, \overline{\mathbf{u'} \otimes \mathbf{u'}}}{\partial t} + \nabla \bullet (\rho \, \mathbf{U} \otimes \overline{\mathbf{u'} \otimes \mathbf{u'}}) = -\rho [\, \overline{\mathbf{u'} \otimes \mathbf{u'}} \, (\nabla \mathbf{U})^{\mathrm{T}} + (\nabla \mathbf{U}) \, \overline{\mathbf{u'} \otimes \mathbf{u'}} \,]$$

$$+ \, \underline{\phi} + \nabla \bullet \left[\left(\mu + \frac{2}{3} c_s \rho \frac{k^2}{\varepsilon} \right) \nabla \, \overline{\mathbf{u'} \otimes \mathbf{u'}} \right] - \frac{2}{3} \rho \varepsilon \delta$$

Equation 2-25

Where **u'** is the fluctuating velocity component in turbulent flow, δ is the Kronecker Delta function and $\underline{\phi}$ is the pressure-strain correlation.

Dissipation rate

$$\frac{\partial (\rho \varepsilon)}{\partial t} + \nabla \bullet (\rho \, \mathbf{U} \, \varepsilon) = \frac{\varepsilon}{k} \left[-C_{\varepsilon 1} \rho \left\{ \overline{\mathbf{u'} \otimes \mathbf{u'}} \, (\nabla \mathbf{U})^{\mathrm{T}} + (\nabla \mathbf{U}) \, \overline{\mathbf{u'} \otimes \mathbf{u'}} \right\} - C_{\varepsilon 2} \rho \varepsilon \right]$$

$$+ \nabla \bullet \left[\frac{1}{\sigma_{\varepsilon RS}} \left(\mu + \rho C_{\mu RS} \frac{k^2}{\varepsilon} \right) \nabla \bullet \varepsilon \right]$$

Equation 2-26

Where, without showing the extensive equations (which can be found in *CFX-5.6 Manual*, 2003),

$$\phi = f(\rho, \, \varepsilon, \, \mathbf{u'}, \, k, \, \delta, \, \mathbf{U}, \, C_{s1}, \, C_{s2}, \, C_{r1}, \, C_{r2}, \, C_{r3}, \, C_{r4}, \, C_{r5})$$

Equation 2-27

Closure coefficients

$C_{\mu RS} = 0.1152$	$\sigma_{\varepsilon RS} = 1.10$	$c_s = 0.22$	$c_{\varepsilon 1} = 1.45$	$c_{\varepsilon 2} = 1.9$
$C_{s1} = 1.8$	$C_{s2} = 0.0$	$C_{r1} = 0.0$	$C_{r2} = 0.8$	$C_{r3} = 0.0$
$C_{r4} = 0.6$	$C_{r5} = 0.6$			

2.2.7. Near wall treatments

In the presence of solid boundaries i.e. the surfaces of the kiwifruit flower, the proper near wall treatments need to be used in conjunction with the abovementioned turbulence flow models in order to model the boundary layer flow behaviours such as flow separation and re-attachment.

Fig. 2-4 is a representation of a wall zone where the inner layer consists of viscous sub-layer and log-law regions. u^+ is the dimensionless near wall velocity and y^+ is the dimensionless distance from the wall. Viscous force is dominant in the viscous sub-layer where the flow is laminar like. In the outer layer (or defect layer), the flow is fully turbulent and can be regarded as inviscid. A gradual change from viscous to the turbulence effects takes place in the log-law region.
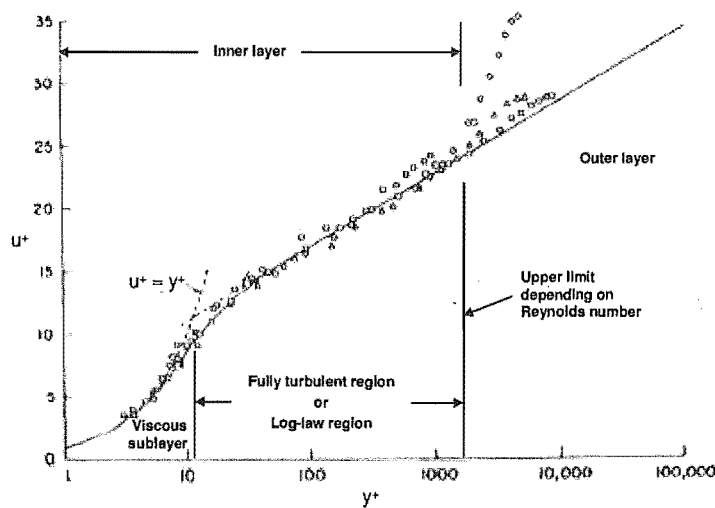
Fig. 2-4: Wall boundary layer (from Cebeci & Smith, 1974) edited based on the schematic diagram of boundary layer from *Fluent User Guide* (2001).

The log-law region can be represented by a logarithmic relation between u^+ and y^+, which is called the standard wall function (Equation 2-28).

$$u^+ = \frac{1}{\kappa} \ln(y^+) + C \qquad \text{Equation 2-28}$$

Where
$$u^+ = \frac{U_t}{u_\tau}$$
Equation 2-29

$$u_\tau = \sqrt{\frac{\tau_\omega}{\rho}}$$
Equation 2-30

$$y^+ = \frac{\Delta y\, u_\tau}{\upsilon}$$
Equation 2-31

κ is the von Karman's constant equal to 0.4187 (Versteeg & Malalasekera, 1995); C is a constant depending on the wall roughness (4.9 to 5.24 for a smooth wall; Warsi, 1999); U_t is the tangential velocity at Δy from the wall; u_τ is the friction velocity; τ_ω is the wall shear stress and υ is the kinematic viscosity.

In the viscous sublayer where y^+ is below 11.067, the standard wall function is no longer applicable because the profile changes from logarithmic to linear i.e.

$$u^+ = y^+$$
Equation 2-32

If the standard wall function is used with the very fine meshes near the wall such that y^+ drops below 11.067, the logarithmic relation will be incorrectly used to represent the supposedly linear profile in the viscous sublayer.

To overcome this fine grid inconsistency, CFX-5 offers two improved wall treatments, namely Scalable Wall Functions and Automatic Near-Wall Treatment for turbulence models based on ε-equation and ω-equation respectively (*CFX-5.6 Manual*, 2003).

Scalable Wall Functions do not allow the computed y^+ to fall below 11.067 and this effectively assumes that the wall coincides with the edge of the viscous sublayer (Esch *et al*, 2003; Menter & Grotjans, 2000; Vieser *et al*, 2002). In other words, the first node on the wall is assumed to be at the boundary of the viscous sublayer and the log-law region. Thus, all grid points near the wall, regardless of their mesh fineness, will be resolved as being outside the viscous sublayer. This allows the use of arbitrarily fine near-wall grids without violating the logarithmic profile assumption.

In contrast, the Automatic Near-Wall Treatment does not neglect the viscous sublayer. It achieves this by automatically switching gradually from a wall function to a low-*Re* near-wall formulation as the mesh is refined (Esch *et al*, 2003; Vieser *et al*, 2002). This is made possible by taking the advantage of the analytical near-wall expression for ω. The Automatic Near-Wall Treatment allows integration right through to the wall using a low-*Re* formulation when the near-wall resolution is high. If the near-wall resolution is insufficient, a wall-function formulation will be used where the first node is treated as being outside the edge of the viscous sublayer. Automatic Near-Wall Treatment is employed when the aim is to model the boundary layer in detail with the use of fine meshes close to the wall.

2.2.8. Comments

The flow past a single kiwifruit flower can be regarded as a free shear layer flow. Some of the turbulence models mentioned above will be selectively compared in the next chapter.

The Standard k-ε Model is usually used as the first qualitative indication of the flow behaviour and as a benchmark of comparisons in many literature papers such as Menter (1996). Although the Standard k-ε Model is robust and stable, it tends to over-predict the turbulent length scale in flows with adverse pressure gradients. This deficiency is improved in RNG k-ε Model while still retaining the numerical robustness. In the Wright & Easom's (1999) test case of a flow past a cubic building, RNG k-ε Model managed to predict flow separation and reattachment on the roof which the Standard k-ε Model and Reynolds Stress Model failed to do so. RNG k-ε Model also produced more accurate results for the wake recirculation zone. Thus, RNG k-ε Model combined with the Scalable Wall Functions is chosen for further comparison.

The ω-equation is known to accurately calculate the turbulent length scale in adverse pressure gradients and thus give an improved prediction of wall shear stress (Wilcox, 1993). However, the Standard k-ω Model shows strong freestream sensitivity, which is unacceptable because the arbitrary choice of the boundary conditions will affect the

solutions undesirably. This problem can be overcome by using a combination of k-ω model near the wall and k-ε model away from the wall in the Baseline (BSL) k-ω Model and Shear-stress-transport (SST) k-ω based Model. Both of them are virtually identical and inherit the strength of Standard k-ω Model in handling the adverse pressure gradient boundary layer. Since the SST k-ω based Model is an improved version of BSL k-ω Model, only the former will be further evaluated together with the Automatic Near-wall Treatment.

Reynolds Stress Models are not expected to yield satisfactory convergence and be computationally economic for the complex kiwifruit flower geometry to be used. Furthermore, according to Laurence (1993) and Murakami (1998), Reynolds Stress Models do not necessarily predict well the flow field around a bluff body. Lasher (2001) found that in his quasi-steady simulations of two-dimensional blocked flow normal to a flat plate, the isotropic eddy-viscosity models gave similar drag prediction to that by anisotropic models such Reynolds Stress Models. The quasi-steady approach is used to resolve unsteady flows when the averages rather than the details of flow transients are of interest (Lasher, 2001). This approach is applied in this work (see more details in section 3.1). Based on the abovementioned reasons, Reynolds Stress Models will not be looked at further.

The localized characteristic Reynolds number ranges from 50 to 4400 based on the dimension of style and the largest overall diameter (ϕ 66 mm) of a full open flower (see section 2.5). Since the localized flow varies from laminar coherent eddying to turbulent, laminar model is considered too.

2.3. Multiphase modelling

Three particle transport models are available in CFX-5.6, namely Eulerian-Eulerian (also called multi-fluid or continuum), Eulerian-Lagrangian (called Particle Tracking Model) and Algrebraic Slip Model (ASM; also called drift-flux model). Each is described below followed by an evaluation of the suitability for simulating the flow of

airborne pollen. This is a dilute gas-solid flow with air and pollen as the continuous and dispersed phase respectively.

2.3.1. Eulerian-Eulerian approach

Both gas and particulate flows are treated as continua and mathematically as two mutually interacting fluids (Tu & Fletcher, 1995). This is a preferred approach for moderate to dense particulate flows or when the volume fraction of particle is more than 10 % (Ranade, 2002), such as in fluidized bed (e.g. Tyler & Mees, 1999) and bubble columns reactors (e.g. Olmos *et al*, 2001). Interphase turbulent dispersion force and particle-particle interactions due to the collisions are readily included in CFX-5.

It is however computationally expensive for poly-dispersed flow i.e. with a wide particle size distribution because of the additional solving of continuity and momentum equations (*CFX-5.6 Manual*, 2003). The solution accuracy is also affected by the incomplete knowledge of diffusion coefficients and when there is change in particle size e.g. due to reactions and evaporations (Ranade, 2002). The Eulerian approach in predicting dilute gas-solid particle flows also needs to consider whether the continuum hypothesis is satisfactory in a limiting computational control volume (Tu & Fletcher, 1995).

For an isothermal flow, the continuity and momentum equations for the gas and solid phase are

Continuity
$$\frac{\partial}{\partial t}\left(\alpha_g \rho_g\right)+\nabla \bullet \left(\alpha_g \rho_g \mathbf{U}_g\right)=0$$
Equation 2-33

$$\frac{\partial}{\partial t}\left(\alpha_s \rho_s\right)+\nabla \bullet \left(\alpha_s \rho_s \mathbf{U}_s\right)=0$$
Equation 2-34

Momentum

$$\frac{\partial}{\partial t}\left(\alpha_g \rho_g \mathbf{U}_g\right)+\nabla \bullet \left(\alpha_g \rho_g \mathbf{U}_g \mathbf{U}_g\right)-\nabla \bullet \left(\alpha_g \mu_g \left[\nabla \mathbf{U}_g + \left(\nabla \mathbf{U}_g\right)^{\mathrm{T}}\right]\right)$$

Equation 2-35

$$=-\alpha_g \nabla p + \beta\left(\mathbf{U}_s - \mathbf{U}_g\right)+S_{Mg}$$

$$\frac{\partial}{\partial t}(\alpha_s\rho_s\mathbf{U}_s)+\nabla\bullet(\alpha_s\rho_s\mathbf{U}_s\mathbf{U}_s)-\nabla\bullet\left(\alpha_s\mu_s\left[\nabla\mathbf{U}_s+(\nabla\mathbf{U}_s)^\mathrm{T}\right]\right)$$

$$=-\alpha_s\nabla p+\beta(\mathbf{U}_g-\mathbf{U}_s)+S_{Ms}$$

Equation 2-36

Where t = time; g and s denote gas and solid phase respectively; α = volume fraction; ρ = density; $\mathbf{U}$ = velocity; μ = dynamic viscosity; p = pressure; S_M = momentum sources due to external body forces; and β = interphase momentum transfer coefficient. The interphase momentum transfer can arise from the interphase drag force, lift force, wall lubrication force, virtual mass force, turbulence dissipation force and solids pressure force.

2.3.2. Particle Tracking Model (Eulerian-Lagrangian approach)

The fluid phase is treated as a continuum by solving the time-averaged Navier-Stokes equations (*Fluent User Guide*, 2003). But, the motions of particles (dispersed phase), which are discretely distributed in the continuous phase, are explicitly calculated using a Lagrangian framework. This gives the trajectories of particles plus useful information such as the residence time and circulation time distributions. Many particle sizes and properties (e.g. shape, density etc) can be specified without hefty increase in computational resources.

The Lagrangian technique is recommended for dispersed phase at less than 10 % in volume fraction (Ranade, 2002), even though the mass loading of the particles may greatly exceed 10-12 % (*Fluent User Guide*, 2003). Large number of particle trajectory however needs to be computed in order to be statistically safe, which can be computationally intensive (*CFX-5.6 Manual*, 2003). Stochastic method (random walk model) is accommodated in CFX-5 to simulate the turbulent particle dispersion due to the presence of turbulent eddies in the continuous phase (more details on Stochastic method can be found in *Fluent User Guide*, 2003). Therefore, none of the tracked particles has identical trajectory.

The fluid models described in section 2.2 are used to predict the gas flow here. Newton's Law is used to determine the motion and position of each particle in the flow

field. The inertial force of a particle equates to the total forces acting on a particle, in which the integration of force balances gives the motion and trajectories of the particle.

$$m_p \frac{dU_p}{dt} = F_D(U_g - U_p) + F_G + \Sigma F_O \qquad \text{Equation 2-37}$$

$$\frac{dx_p}{dt} = U_p \qquad \text{Equation 2-38}$$

Where m_p is mass of the particle; U_p and U_g are velocity vectors of the particle and gas phase respectively; t is time; x_p is the particle location; F_D and F_G refer to the drag force and gravitational force respectively.

F_O refers to other forces which are can be considered negligible in the kiwifruit flower/pollen problem. They are thermophoretic force (due to the large temperature gradient), virtual mass (additional inertia due to the acceleration of continuous phase), Basset history force (due to the development of a boundary layer around the particles), pressure gradient force (from the continuous phase), Saffman lift force (due to the shear or vorticity in the continuous phase) and Brownian motions (significant only for sub-micron particles); see details in Delnoij *et al* (1997), *Fluent User Guide* (2003) and Ranade (2002).

$$F_D = -\frac{\pi}{8} C_D \rho_g D_p{}^2 |U_p - U_g| (U_p - U_g) \qquad \text{Equation 2-39}$$

$$F_G = \frac{1}{6} \pi D_p{}^3 (\rho_p - \rho_c) g \qquad \text{Equation 2-40}$$

ρ_g and ρ_p are the density of gas and particle respectively; D_p is the particle diameter; $|U_p - U_g|$ is the magnitude of the resultant slip velocity i.e. scalar value; g is the gravitational acceleration; and C_D stands for drag coefficient given by

$$C_D = \frac{24}{Re_p} \left[1 + \frac{1}{6} Re_p{}^{0.66} \right] \qquad Re_p < 1000 \qquad \text{Equation 2-41}$$

$$C_D = 0.44 \qquad Re_p > 1000 \qquad \text{Equation 2-42}$$

2-22

$$Re_p = \frac{\rho_c \, D_p \, |U_p - U_g|}{\mu_g} \qquad\qquad \text{Equation 2-43}$$

Where Re_p is the particle Reynolds number and μ_g is the gas viscosity. More correlations for drag coefficient can be found in Ranade (2002).

2.3.3. Algebraic Slip Model (ASM)

ASM assumes that the relatively small particles are always travelling at their terminal velocity i.e. the relaxation time for the particles is much smaller than the flow time scale (*CFX-4.4 Solver Manual*, 2001). Thus, the drag force balances all the body forces exerted on the particles. This enables the determination of phase slip, which is the relative movement between the dispersed phase components and the continuous phase, using a simple algebraic formula (Penrose & Hamill, 2003). Any number of dispersed phases can be modelled and each is regarded as a component dispersed in the continuous phase i.e. they are treated as in a mixture (CFX Consultants, 2002). ASM is less computationally expensive than Eulerian-Eulerian approach for a wide distribution of the dispersed phases (*Fluent User Guide*, 2003). In addition, it is also less complex and thus numerically more stable (*Fluent User Guide*, 2003).

The mixture behaves like a single fluid and the phases are treated as interpenetrating continua (*Fluent User Guide*, 2003). Its local density and viscosity depend on all of the components (including continuous phase) based on their respective mass fraction or volume fraction (*Fluent User Guide*, 2003; Penrose & Hamill, 2003). Each dispersed phase component is represented by a mass-fraction equation and a transport equation (Penrose & Hamill, 2003). ASM is typically used for particle-laden flows with low loading (*Fluent User Guide*, 2003) because particle-particle interaction is assumed negligible.

For a buoyant flow of single particle species in gas, the slip velocity i.e. the difference between the velocities of the gas and particle is solved by (Penrose & Hamill, 2003)

$$(U_p - U_g) \, |U_p - U_g| = \frac{4 \, D_p \, (\rho_p - \rho_c)}{3 \, \rho_g \, C_D} \, [B - g] \qquad\qquad \text{Equation 2-44}$$

Where U_p and U_g are velocity vectors of the particle and gas phase respectively; D_p is the particle diameter; ρ_g and ρ_p are the density of gas and particle respectively; g is the gravitational acceleration; B refers to the total body acceleration of other body forces; and C_D is drag coefficient given by either Equation 2-41 or Equation 2-42. The continuity and momentum equations for mixture, plus the relation between relative velocity and drift velocity can be found in *Fluent User Guide* (2003).

2.3.4. Comments

The pollen flow to be modelled has very low particulate loading. Therefore, one-way coupling between phases is expected i.e. the particles are influenced by the gas flow via drag and turbulence, but have no influence on the gas flow. This means all three models can be used, but Eulerian-Eulerian approach is not recommended because it is the most expensive (*Fluent User Guide*, 2003).

Comparing Particle Tracking model with ASM, the solution visualization from the former is more desirable because the history of particles movements are presented in tracks compared to just local mass or volume fraction representation by ASM. Since the volumetric flow of the gas phase is significantly higher than that of the particulate phase, there is also no advantage in treating the particulate phase as continuum. Others had shown that Particle Tracking method can be used to study particle deposition such as on a square cylinder (Brandon & Aggarwal, 2001), in airway bifurcations (Comer *et al*, 2001; Werner *et al*, 2001) and in the ventilated multizone rooms (Lu *et al*, 1999). Hence, Particle Tracking model is chosen to predict the pollen deposition on the stigma.

2.4. Description of flower models

During the blossom season, the flowering is not uniform on a vine and the spread is a result of the variation in date of flower opening (anthesis) within and among

inflorescences, laterals and canes (Patterson *et al*, 1991). The percentage of flowers open typically reaches a peak before falling off quickly. There is also delay in the flowering at different parts of the orchard due to the microclimate effect. Majority of 1-day-old and 2-day-old pistillate flowers open before 8 a.m. and continue to open widely until midday before starting to close in the afternoon (Goodwin, 1995a). The artificial pollination is usually applied twice at around 40 % and around 90 % flower opening (see Table 1-2). This means the growers are likely to encounter flower buds at different opening stages during the application.

Hence, full scale flower buds with three opening configurations, namely half-open, full-open and flip-back, were constructed in Solidworks, which is a solid modeller program. Their CAD surfaces were then exported in Parasolid or Iges format into CFX-Build to define each flower bud as a bluff body in the flow domain.

The reported morphologies of a 'Hayward' flower in the literature are listed in Table 2-1 and they were found insufficient to create the flower models for simulation in CFD. Thus, more than 200 'Hayward' flowers were photographed in the Te Puke orchard area, New Zealand from 9-10 November 2001. This collection (for examples, Fig. 2-4a to h) was studied to obtain the detailed geometries (shown in Fig. 2-5 to 2-10) for constructing the flower models in Solidworks. The summary of these measured geometries is also included in Table 2-1 for comparison.

Corolla and petals

Although a female flower may have 5 – 7 petals (occasionally more than 7), 6 petals are chosen in this work because this is the most frequent number. Out of 249 randomly selected flowers in Te Puke orchard area in 2001, 62 % of them bear 6 petals.

Each real petal extends outwards from the base of the central ovary. Fig. 2-7 shows that there is a near-linear decrease in thickness from the inner part to the outer part of a petal. However, for computational efficiency, a constant thickness based on the average of the middle and inner parts is assumed i.e. 0.75 mm.

Table 2-1: Dimensions of components of a 'Hayward' flower reported in the literature and measured in this work. Refer Fig. 1-1 for the locations of each flower organ.

Flower organs	From literature				Measured in this work
Pedicel [1] length [mm]	$10 - 20$ [a];	$10 - 40$ [c];	41.2 ± 1.5 [e]		–
Pedicel diameter [mm]	–				$2.73 {\ +0.51 \atop \ -0.50}$; see Fig. 2-6
Flower diameter [mm]	$59.3 - 67.9$ [b];	$35 - 68$ [c];	67.3 ± 0.7 [e]		$74.4 {\ +13.5 \atop \ -19.4}$; see Fig. 2-5
Sepal numbers	5 [a];	$3 - 7$ [c];	$5 - 6$ [d];	6.3 ± 0.2 [e]	$4 - 6$
Sepal length × width [mm]	10×12 [c];	12.7 ± 0.4 (length) [e]			See Fig. 2-10
Petal numbers	$5 - 7$ [c];	$5 - 6$ [d];	6.5 ± 0.1 [e]		5 to ≥7; see text
Petal length × width [mm]	18×22 [c];	$(27.8 \pm 0.4) \times (24.3 \pm 0.5)$ [e]			See Fig. 2-9
Stamen numbers	$166 - 200$ [c];	183 ± 17 [d]			$172 - 187$
Filament length [mm]	$10.3 - 11.3$ [b];	$9 - 13$ [c]			–
Filament diameter [mm]	–				$0.29 {\ +0.12 \atop \ -0.11}$; see Fig. 2-6
Anther length [mm]	4.1 [b];	$3 - 4$ [c]			See Fig. 2-6
Ovary diameter [mm]	$7.5 - 8.2$ [b];	$5.5 - 8.2$ [c]			See text
Style numbers [2]	36 ± 5 [d]				$37.7 {\ +7.3 \atop \ -8.7}$; see Fig. 2-6
Style diameter [mm] [3]	0.75 [c];	0.66 [f]; see Fig. 2-4i	$1.7\text{-}2.1$ [d]		$1.06 {\ +0.77 \atop \ -0.51}$; see Fig. 2-6
Stigma-style length [mm]	$10.3 - 10.8$ [b];	$8 - 9$ [c];	8.4 ± 0.9 [d]		$9.98 {\ +4.29 \atop \ -4.91}$; see Fig. 2-6

[1] Flower stem.

[2] Style number refers to number of styles per flower.

[3] The literature values are approximated by analyzing the pictures of stigma-styles from each source.

Sources:

a. Ferguson & Davison (1986)
b. Brundell (1975b)
c. Hopping (1990a)

d. Hopping & Jerram (1979)
e. Zhang & Thorp (1986)
f. Gonzalez *et al* (1996)
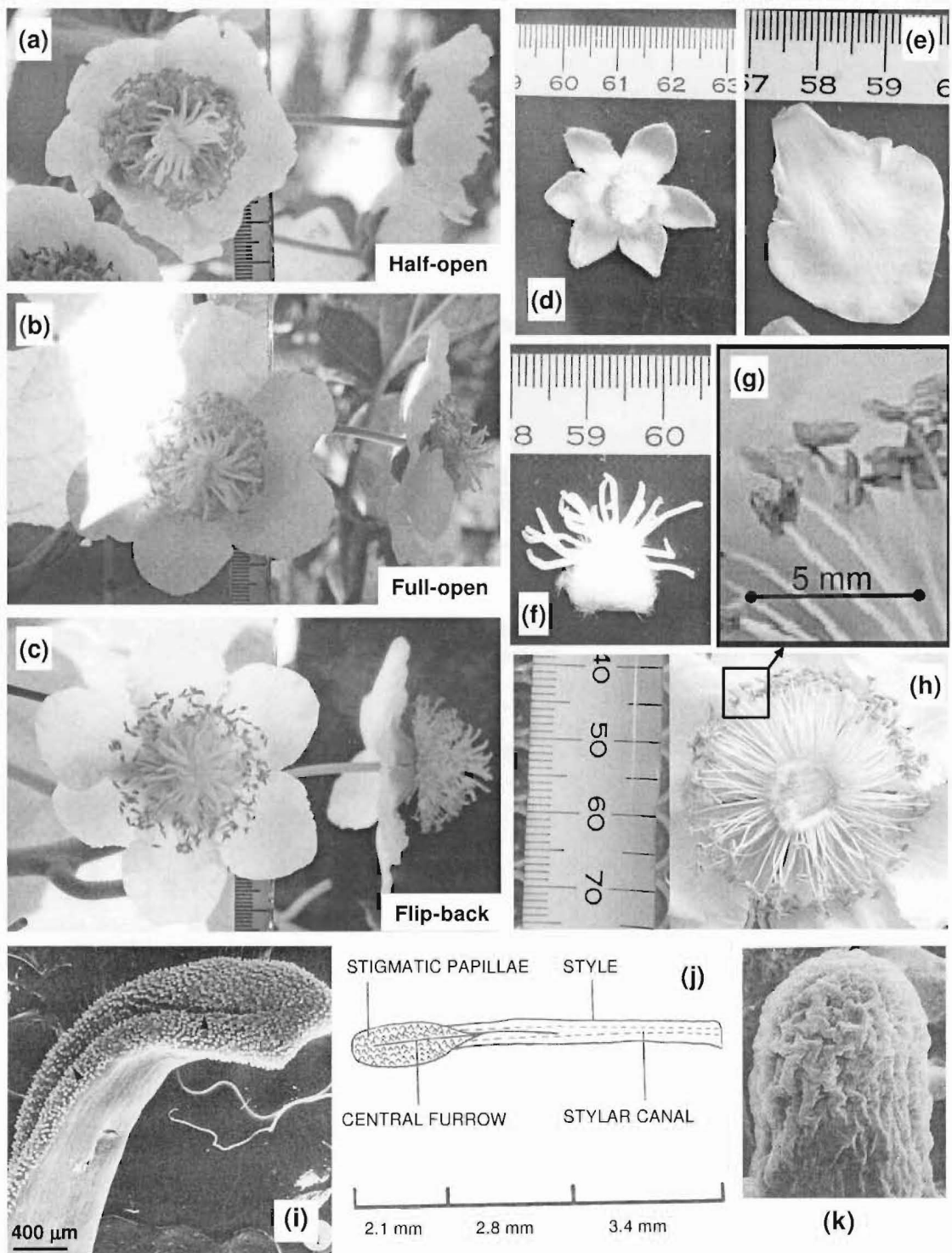
Fig. 2-4: (a), (b) and (c) are the flower buds at half-open, full-open and flip-back stages respectively; (d) sepal; (e) flattened petal; (f) ovary with styles; (g) enlarged view of (h) showing the anthers and filaments; (h) whorls of filaments and anthers; (i) SEM of the tip of a stigma-style; (j) diagrammatic representation of the stigma-style; (k) SEM of an individual papilla. Sources: (a) to (h) were taken in Te Puke orchard area, 2001; (i) is from Gonzalez *et al* (1996); (j) and (k) are from Hopping & Jerram (1979).
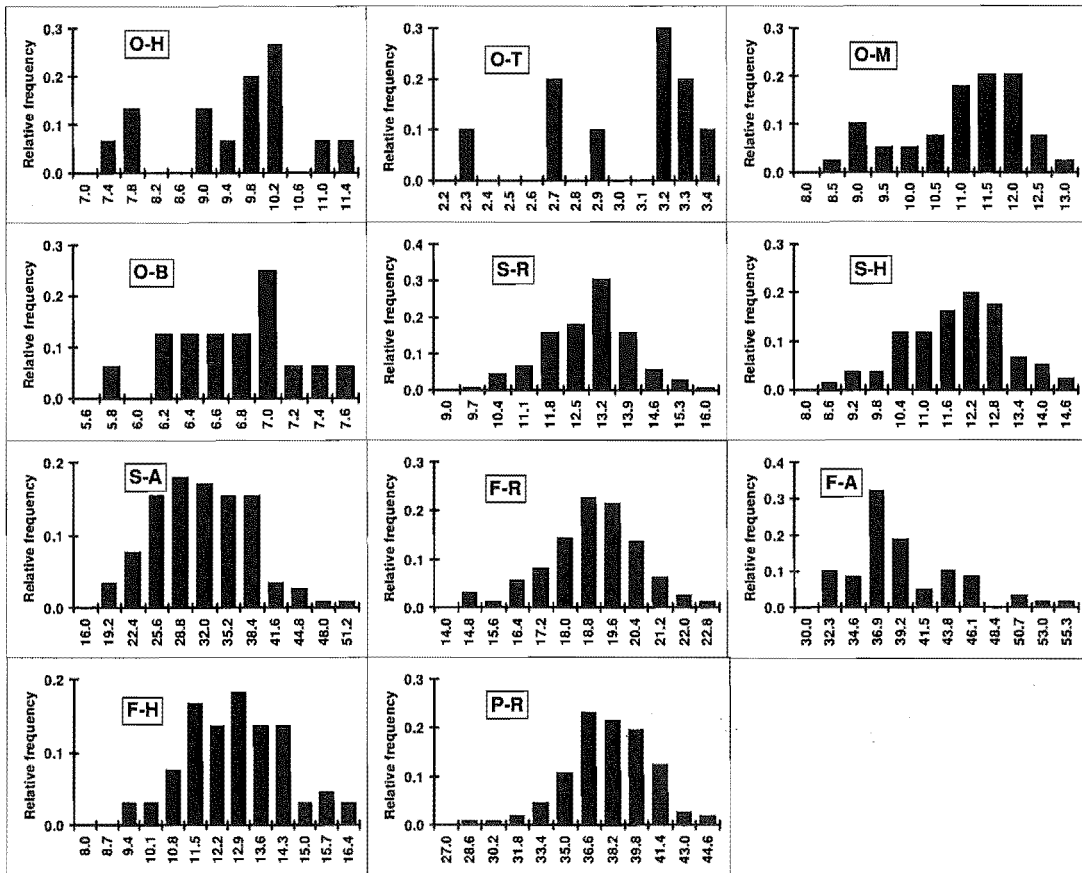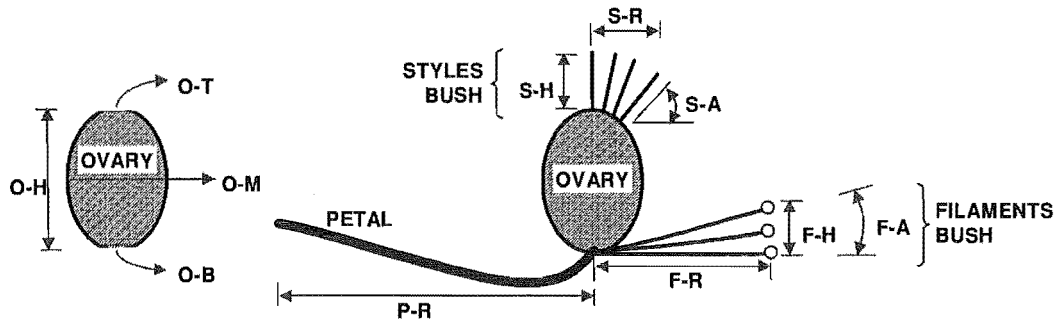
Keys:
O-H = Ovary-Height
O-T = Ovary-Top
O-M = Ovary Middle

O-B = Ovary-Bottom
S-R = Style bush-Radius
S-H = Style bush-Height
S-A = Style bush-Angle

F-R = Filament bush-Radius
F-A = Filament bush-Angle
F-H = Filament bush-Height
P-R = Petal-Radius

	O-H [mm]	O-T [mm]	O-M [mm]	O-B [mm]	S-R [mm]	S-H [mm]	S-A [°]	F-R [mm]	F-A [°]	F-H [mm]	P-R [mm]
mean	9.35	2.97	10.82	6.64	12.48	11.52	30.07	18.54	38.27	12.43	37.20
s.d.	1.20	0.36	1.13	0.49	1.14	1.30	6.34	1.59	5.12	1.58	2.75
count	15	10	39	16	184	136	117	162	59	66	112
min	7.12	2.27	8.47	5.65	9.27	8.37	16.79	14.08	30.87	8.87	27.52
max	11.37	3.34	12.98	7.45	15.79	14.20	49.09	22.43	53.71	16.24	43.97

Fig. 2-5: Statistics of dimensions of ovary, petal, stigma-styles bush and filament-anthers bush measured on the flowers collected from Te Puke orchard area in 2001.

ANTHER and FILAMENT
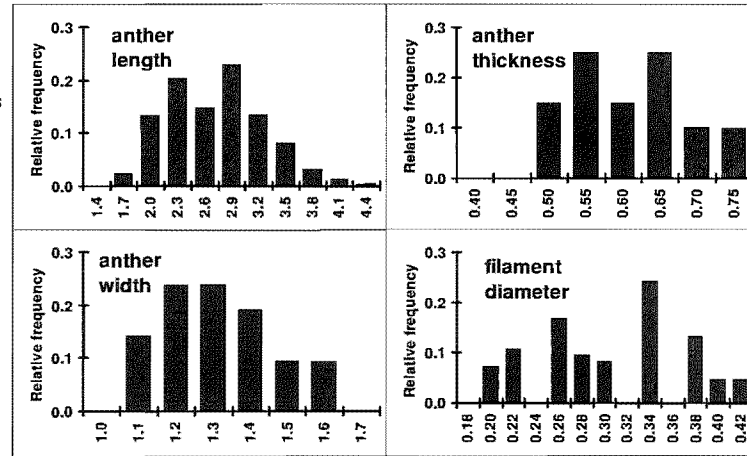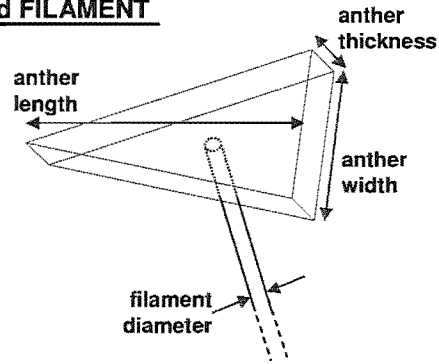
STYLES and PEDICEL
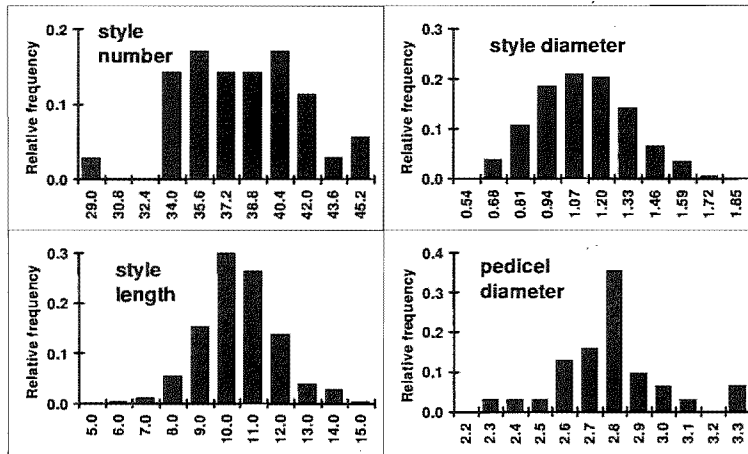
SUMMARY			All dimensions in [mm].		
	mean	s.d.	count	min	max
Anther length	2.58	0.53	285	1.52	4.25
Anther thickness	0.58	0.08	20	0.45	0.73
Anther width	1.25	0.14	21	1.00	1.52
Filament diameter	0.29	0.06	83	0.18	0.41
Style number *	37.7	3.4	35	29	45
Style diameter	1.06	0.23	667	0.55	1.83
Style length	9.98	1.41	670	5.07	14.27
Pedicel diameter	2.73	0.22	31	2.23	3.24

* Style number refers to number of styles per flower.

Fig. 2-6: Statistics of dimensions of style, pedicel, anther and filament measured on the flowers collected from Te Puke orchard area in 2001.
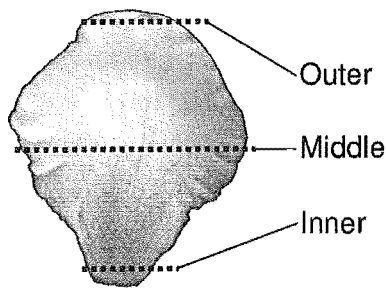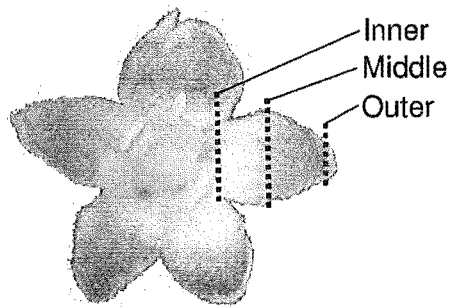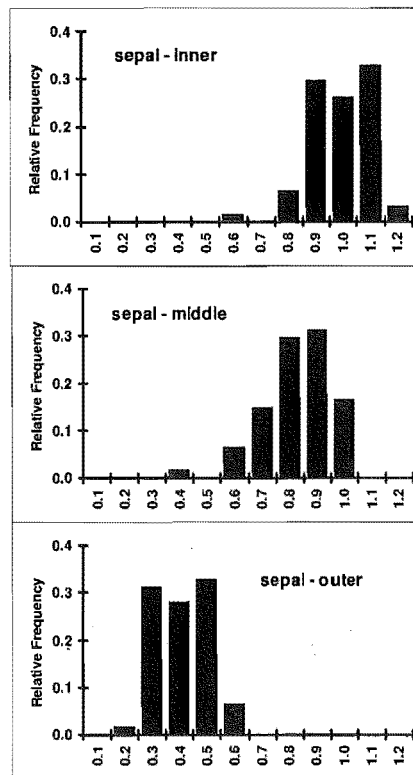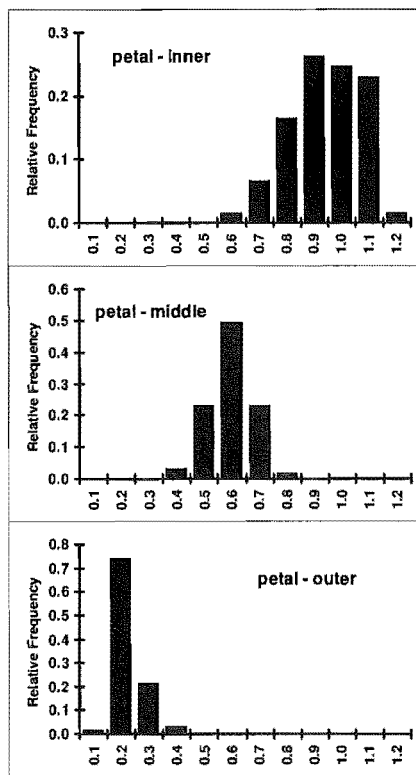
All dimensions are in [mm].

		mean	s.d.	count	min	max
	Inner	0.92	0.12	61	0.60	1.15
Petal	**Middle**	0.57	0.08	61	0.40	0.80
	Outer	0.21	0.05	61	0.10	0.40
	Inner	0.96	0.11	61	0.60	1.20
Sepal	**Middle**	0.80	0.12	61	0.35	1.00
	Outer	0.39	0.09	61	0.20	0.60

Fig. 2-7: Variation of thickness measured at 3 equally spaced cross-sectional lines (called Inner, Middle and Outer) along an individual petal or sepal. Data were collected using a Vernier calliper with resolution of 0.01 mm in Te Puke orchard area, 2001.

STYLES

OVARY

PETAL

gap

PETAL

FILAMENTS

Maximum gap between petals

Relative frequency

0.2

0.1

0.0

3.35 3.55 3.75 3.95 4.15 4.35 4.55 4.75 4.95 5.15 5.35 5.55 5.75

Dimension in [mm].

OL

PL

Ratio of OL / PL

Relative frequency

0.3

0.2

0.1

0.0

0.63 0.66 0.68 0.71 0.73 0.76 0.78 0.81 0.83 0.86 0.88 0.91

OL = projected overlap length
PL = projected petal length
The reference point is the centre of ovary.
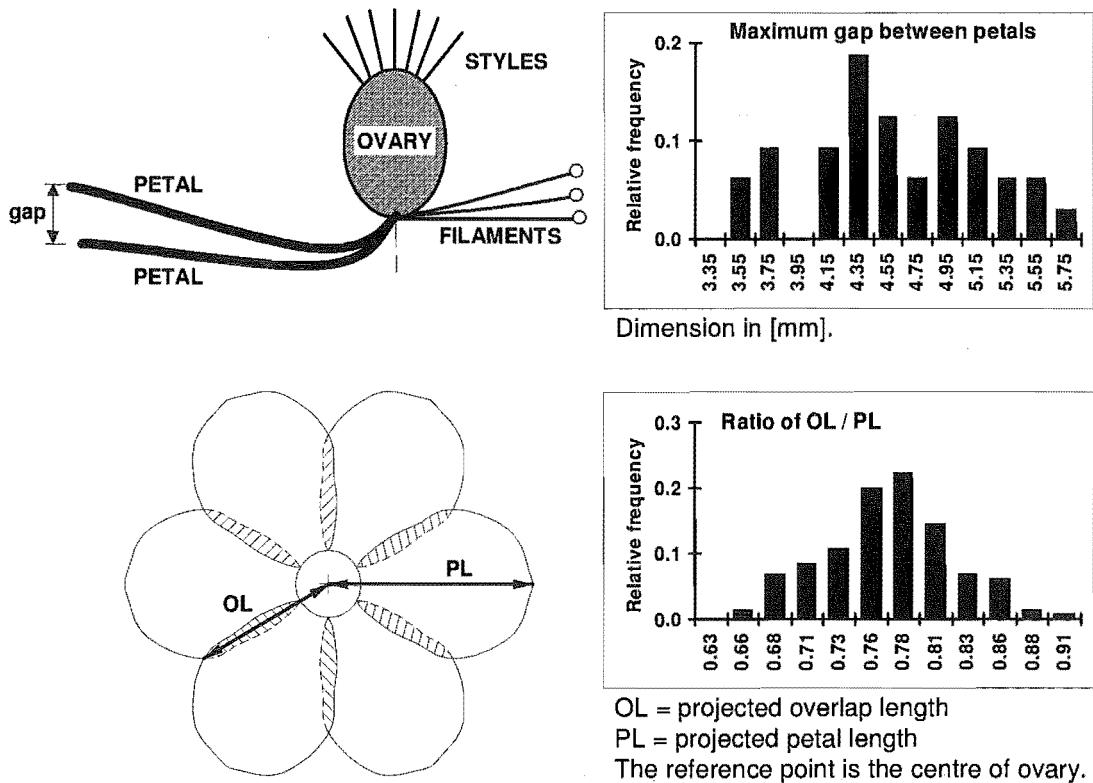
	mean	s.d.	count	min	max
Maximum gap between petals [mm]	4.50	0.60	32	3.37	5.68
Ratio of OL / PL	0.76	0.05	130	0.63	0.88

Fig. 2-8: Statistics of the maximum gap between the petals and the ratio of project overlap length to projected petal length. Data were collected by analysing the photos of flowers taken in Te Puke orchard area, 2001.
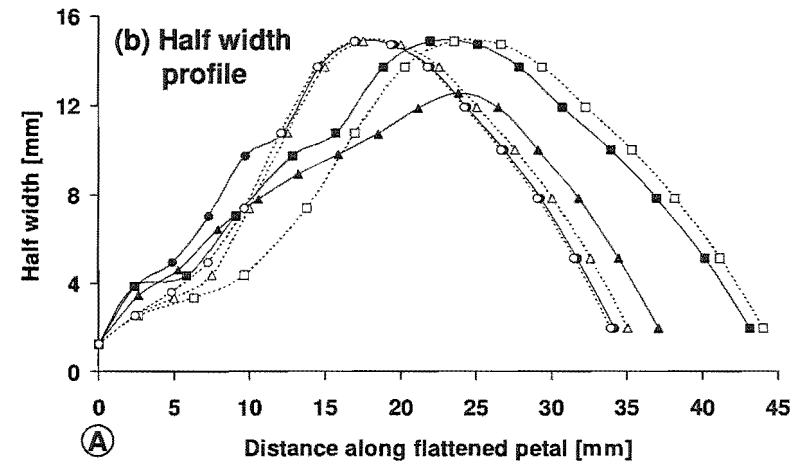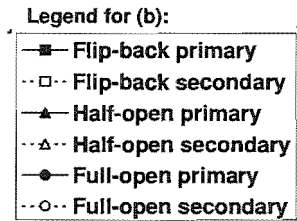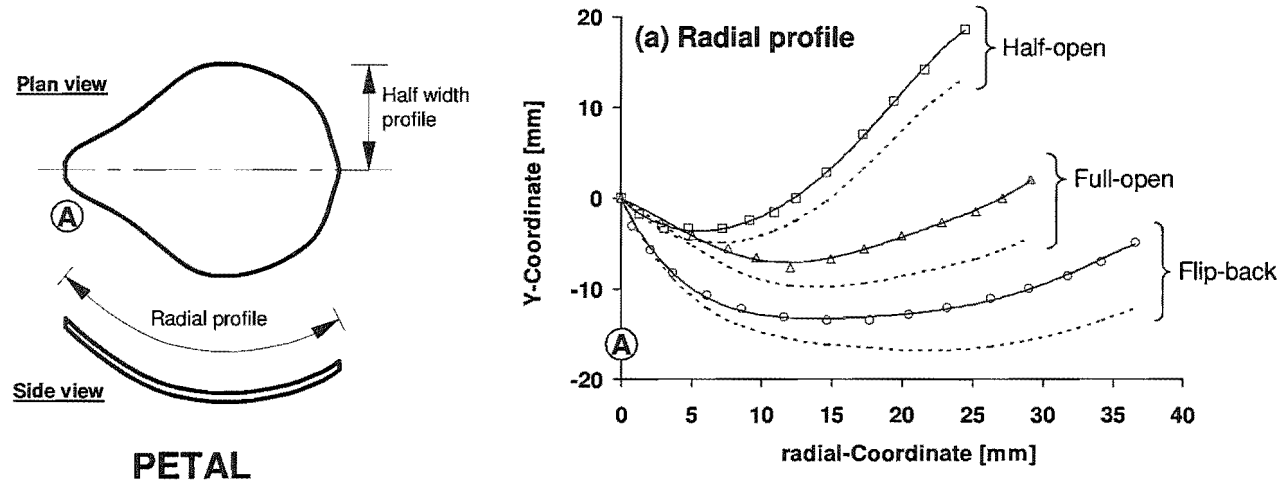
Fig. 2-9: (a) Radial profiles of the centreline of petals at 3 opening stages. Solid lines represent primary petals while dotted lines represent secondary petals. (b) Half width profiles of the symmetrical petal when flattened, at different bud opening.
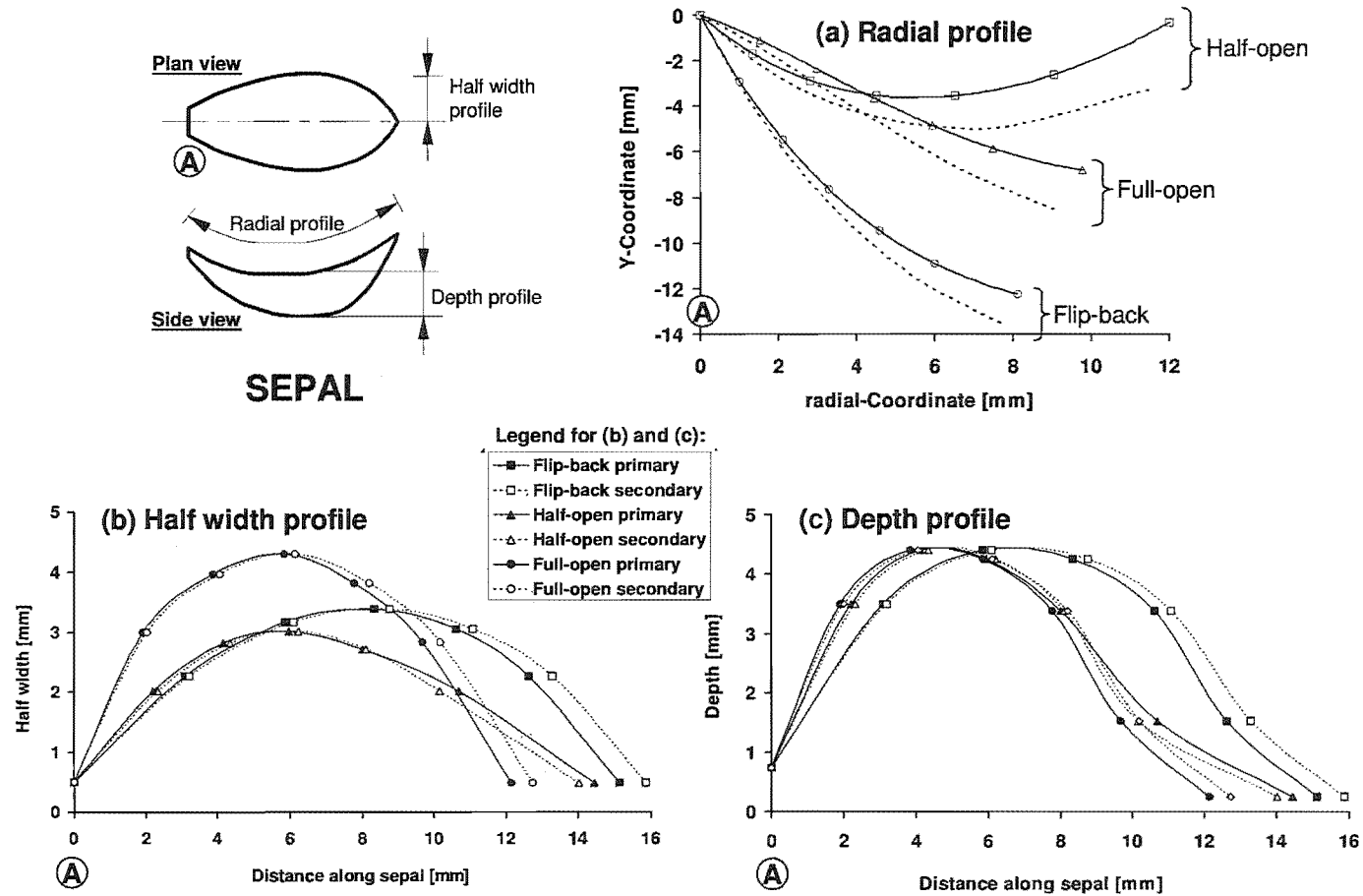
Fig. 2-10: Profiles of sepal at 3 flower opening stages. Solid lines represent primary sepals while dotted lines represent secondary sepals. (a) Radial profiles of the centreline of sepals. (b) Half width profiles of the symmetrical sepal. (c) Depth profiles of the sepal.
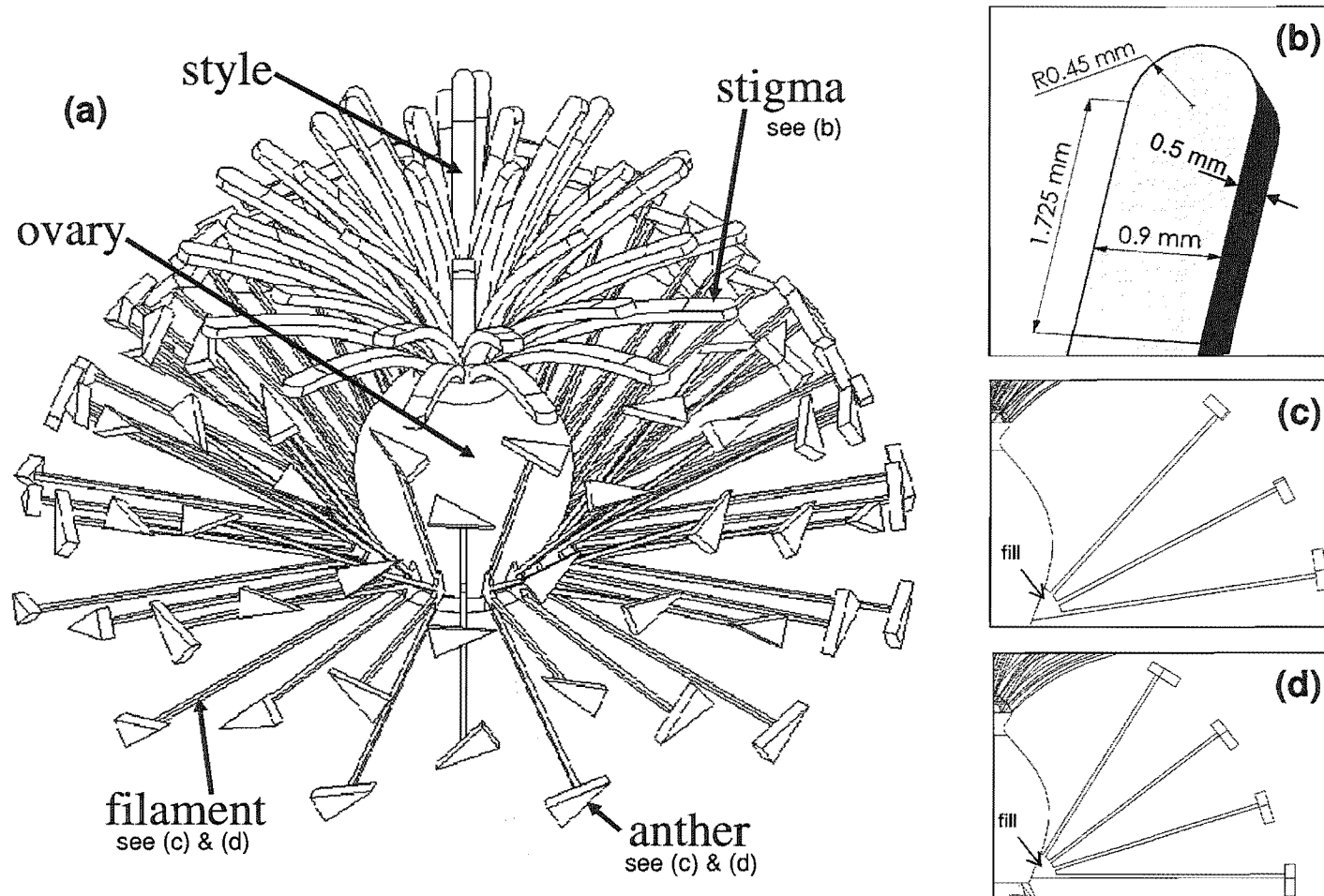
Fig. 2-11: (a) Flower model showing ovary, 36 stigma-styles, 84 filaments and anthers. (b) Shape and dimension of the model's planar stigmatic surface. (c) and (d) are the vertical side views of 3- and 4-filament row respectively.

The petals are mainly overlapping. This is shown by the ratio of OL to PL averaging 0.76 in Fig. 2-8. OL and PL are the projected overlap length and petal length respectively. The maximum gap between the adjacent petals ranges from 3.37 to 5.68 mm with the average of 4.50 mm; see Fig. 2-8.

Fig. 2-7e shows a flattened petal which is described as widely obovate with subentire margin and involute by Zhang & Thorp (1986). Since each model petal was assumed symmetrical, only the half-width profile of this petal was used in all the flower models with slight modifications (see Fig. 2-9b). Additional minor differences were applied among the petals in Fig. 2-9b for ease of meshing.

Fig. 2-4a, b and c are the photos of flower buds from cupped at half-open stage to the stage where the petals flip to the back. Although not captured on camera, some petals had been observed to flip back further 30 $^{\circ}$. The radial variation profiles of these 3 flowers were extracted to represent the corollas at different blossom phases (shown in Fig. 2-9b).

In order to simulate the flow leakage through the gap between petals, each model flower has 3 pairs of overlapped 0.75-mm-thick petals (called primary and secondary) evenly spaced around the ovary. The primary petal was constructed using the radial variation profile obtained from Fig. 2-4a, b and c (see Fig. 2-9b). The secondary petal was drawn such that the petal gap was linear with distance along the overlap with a maximum gap of 5 mm. The edges of the petals were rounded.

Sepals

Sepals are ovate-oblong, brown and mainly overlapping (Hopping & Jerram, 1979; Zhang & Thorp, 1986). They are persistent, covered by a brownish tomentum and develop little after pollination (Ferguson & Davison, 1986). The half-width profile of one of the sepals in Fig. 2-4d was captured (Fig. 2-10b) to draw the symmetrical model sepal.

In the flower model, one sepal is placed below each petal. The sepal follows the radial variation of their respective primary and secondary petals until about 5 mm from the ovary (see Fig. 2-10a). Even though the thickness of sepal had been measured (Fig. 2-

7), each sepal is modelled as a 'filled' boat-shape object instead of as a curly sheet. Each model sepal is then fused onto the bottom of the petal, leaving no gap in between for the unnecessary meshing. The depth profiles of the 'filled' sepals are given in Fig. 2-10c.

Stigma-styles

The styles were described as recumbent and strongly curved above middle at full bloom by Zhang & Thorp (1986). A stigma-style has a V-opening at top end which runs into a central furrow which extends half the length of the style where it joins the stylar canal (Stevens & Forsyth, 1982; see Fig. 2-4j). The upper part of a style is glabrous while its lower part carries dense, long and fine hairs (Ferguson & Davison, 1986; Zhang & Thorp, 1986). Fig. 2-4i is a scanning electron micrograph (SEM) of the stigmatic arm of a pistil. Note that only about half of circumferential surface at the tip of a style is called stigma i.e. area receptive to pollen. The stigma is covered with small unicellular papillae (see Fig. 2-4k) of mostly 100 μm (up to 135 μm) long with 5.5 – 8.0 μm thick walls (Schmid, 1978). Hopping & Jerram (1979) estimated that each stigma was covered with at least 2000 papillae. The stigma is wet with secretion moderate to slight flooding interstices between papillae (Harvey et al, 1987). More SEM views of stigma-styles and papillae can be found in Gonzalez et al (1995a), Harvey et al (1987) and Hopping (1990a).

36 slightly curled and flat stigma-styles (based on the average number on a flower reported by Hopping & Jerram, 1979; cf. 37.7 determined in this work) were evenly spaced on top of the ovary to form an 'expanding bush' (see Fig. 2-11a). The styles bush was drawn based on the parameters S-R, S-H and S-A in Fig. 2-5.

With reference to Fig. 2-4i and for economy of mesh, the styles were not modelled as cylinder but as the rectangular 'French fries' with semi-spherical ends (see Fig. 2-11b). The edges were not filleted. The model stigma-styles are 9.53 – 10.49 mm long, which is within the ranges in Table 2-1.

A pair of planar stigmatic surfaces, which are the area of interest, were defined at the tip of each style i.e. one on top and another on the bottom, to take into account that a real

stigma can orient in any direction. The length the model stigma is 2.175 mm (i.e. 1.725 mm + 0.45 mm), chosen based on Fig. 2-4j.

The reported stigma diameter in the literature ranges from 0.66 to 2.10 mm (see Table 2-1). 667 stigma-styles measured in this work have a range of 0.55 – 1.83 mm with a mean of 1.06 mm (refer to the distribution in Fig. 2-6). Without considering the high-end value from Hopping & Jerram (1979), the average of the listed diameters in Table 2-1 is about 0.82 mm. Thus, for a similar circumference, the width and thickness of the model stigma-style were set as 0.9 mm and 0.5 mm respectively.

Anther-filaments

The filaments are long, slender, greenish white and their top ends are attached dorsally to the middle of the versatile, yellow anthers (Ferguson & Davison, 1986; see Fig. 2-4g). They are tucked neatly under the radiating styles and arranged in spirals around the ovary (Ferguson & Davison, 1986; see Fig. 2-4h).

An anther is approximated as a triangular wedge with its length, thickness and width equal to 2.58 mm, 0.58 mm and 1.25 mm respectively. These parameters are the average values from Fig. 2-6.

84 filaments, with a triangular anther at each end, surround the ovary (see Fig. 2-11a). Although for ease of computation the number of filaments is reduced from an average of 183 on a real flower (Hopping & Jerram, 1979), its density is visually comparable to that of an actual flower shown in Fig. 2-4c. The mean diameter of a filament is 0.29 mm (see Fig. 2-6). Since the cylindrical shape of filament is not considered influential on the flow, each filament is modelled as 0.205 × 0.205 mm square rod (i.e. with diagonal equals to 0.29 mm).

The filament bush (or whorl) was drawn based on the parameters F-H and F-A in Fig. 2-5. Each model filament (14.2 – 15 mm long) extends from the bottom of the ovary. The filament spacing evolves from alternate 3- and 4-filament rows around the ovary as shown in Fig. 2-11c and 2-11d respectively. The base of filaments are 'filled' to avoid sharp corners in mesh generation. Sharp corners lead to elongated computational cells which degrade the quality of simulation.

Ovary

Large numbers of multicellular hairs cover the outer epidermis of the ovary (Ferguson & Davison, 1986; as shown in Fig. 2-4f). The ovary was modelled as a truncated oblate spheroid 9.3 mm high, 9.0 mm diameter, and 3.0 and 7.0 mm diameter top and bottom (see Fig. 2-11). These dimensions were chosen with reference to the average of parameters O-H, O-T, O-M and O-B in Fig. 2-5. A small dome was placed on top of the ovary (see Fig. 2-12) in order to avoid the meshing of sharp corners at the base of the style bush.

A sepal base and a 77-mm long pedicel (ϕ 2.73 mm as measured in this work; see Fig. 2-6) are also included under the ovary. Any isolated or small gaps, particularly in the space between the sepals and the pedicel, are eliminated manually for efficient meshing and better solver convergence. Fig. 2-12 shows all three model flowers which only differ in the configuration of petals and sepals. In addition, a smaller filament bush is drawn to fit within the smaller corolla of the half-open flower bud.

Further simplifications and additions to the flower models

The CFD simulations based on the flower models described above have been reported in the papers attached in Appendices A and B. Towards the end of this project, a new mesh generator called ICEM CFD 4.CFX was released to the users of CFX-5.6. This meshing program is based on the Octree method (see further details in *ICEM CFD 4.CFX Manual*, 2003). It allows the flexible definition of 'thin surfaces' which has been found impossible to be applied to the complex flower models in CFX-Build. 'Thin surfaces' are commonly used in CFD to represent thin objects because the influence of the objects' thickness on the fluid flow is negligible. Its use is mesh-economical because large number of fine cells are not needed to capture the object's thickness. Thus, 'thin surface' approach is applied to the stigma, styles, filaments and anthers which are less than 0.5 mm thick. However, the simplification is found infeasible for the overlapping petals and sepals. All the simulations in the following chapters are based on the flower models with simplified stigma, styles, filaments and anthers.

In addition, a flower model without petal (called 'bold') is added to represent a flower bud that has all its petals fallen off after 3 – 4 days. The sepals are preserved just like on the real flowers (see Fig. 1-2) and they are modeled as 'thin surfaces'.

2-30

Plan view

Front view

y

x
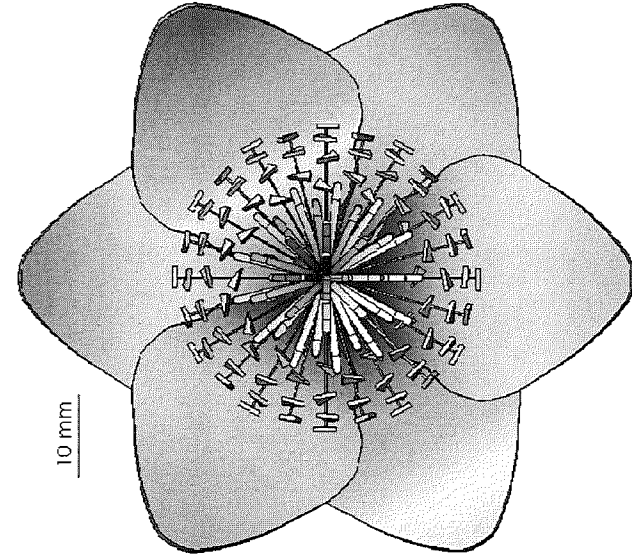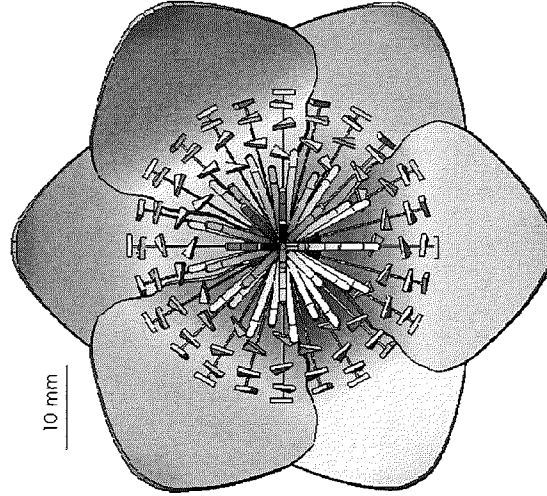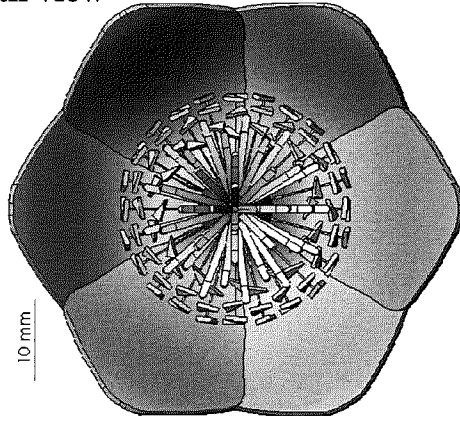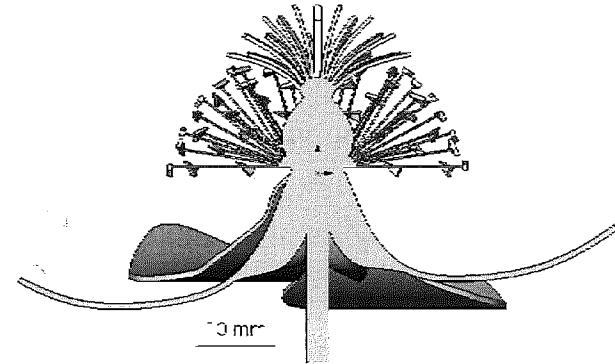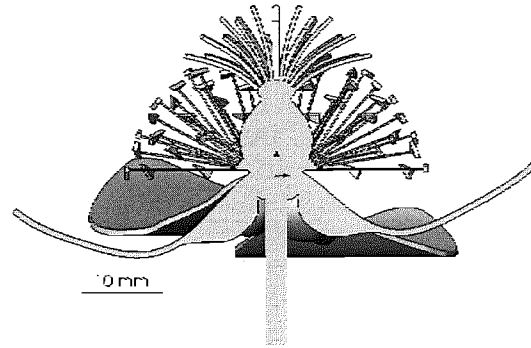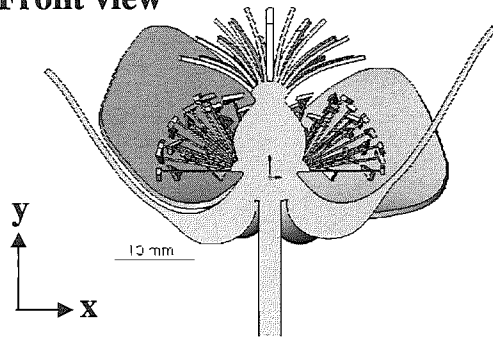
(a) half-open   (b) full-open   (c) flip-back

Fig. 2-12: Flower models created in Solidworks for different bud opening stages: (a) half-open, (b) full-open and (c) flip-back.

CHAPTER 3: SIMULATION OF WIND POLLINATION

There are only a handful of published works on modelling the motion and capture of airborne pollen around a wind-pollinated plant, i.e. Buchmann *et al* (1989), Niklas (1988), Niklas & Buchmann (1987), Niklas & Kerchner (1986). The collection mechanism of windborne pollen by a single kiwifruit flower is simulated in this chapter. In addition, the grid independence, residual independence and particle number independence checks are carried out, in accordance to the common practices in CFD works.

3.1. Wind pollination simulation settings

A uniform air flow of 0.5 – 3 m/s are set to flow onto each of the four flower models (bold[1], half-open, full-open and flip-back) from the front, side and back. These simulate the wind pollination under the vine with the draft in random directions. The average and maximum measured draft speed under the vine are 1 and 3 m/s respectively (cf. maximum of 1.25 m/s recorded by Costa *et al*, 1993; and the range of 0.5 – 1 m/s reported by Wakelin, 1985a). The flower models are assumed rigid up to 3 m/s even though the observations in a wind tunnel showed that this was true only below 1.8 ± 0.1 m/s for a 1-day-old flower. The petals were found to deflect and vibrate above 1.8 m/s.

The computational flow domain is 550 mm long with a 400 mm × 400 mm cross section. The inlet and outlet boundaries are 200 mm and 350 mm away from the centre of the ovary bottom respectively. The other boundaries of the domain are represented as symmetry planes. Fig. 3-1 shows the orientation of a full-open flower relative to the flow domain in the frontal, side and back flows. A uniform velocity (0.5, 1, 2 and 3 m/s) is defined normal to the inlet boundary. The outlet boundary has a relative pressure of 0 Pa. The flower surfaces including the stigma are smooth with no slip (i.e. zero velocity at the surface). The incompressible air flow field is solved at the reference pressure of 101325 Pa and isothermally at 25 $^{\circ}$C. The selection of laminar or turbulence models is to be decided in section 3.4.

---

[1] Refers to the flowers that have lost their petals.

Steady state or transient?

A kiwifruit flower corolla positioned normal to a uniform flow to a first approximation resembles a two-dimensional flow past a sharp-edged flat plate normal to a free stream. Literature was looked up to determine whether this kind of flow is likely to be transient. According to Simiu & Scanlan (1986), the symmetrical vortices that are attached to the back of the flat plate are present in the Reynolds number range of 10 - 250. Above this range, cyclically alternating vortices begin to appear. The shedding however stops and replaced with a generally turbulent wake when the Reynolds number exceeds 1000. Two outer defining edges form a shear layer consisting of a long series of smaller vortices that connect the wake region to the adjacent smooth flow region.

However, transient simulations by Lasher (2001) show that vortex shedding still occurs at Reynolds number of 32200. Even so, depending on the direction of flows approaching the flower, the presence of pedicel, ovary or style bush downstream is likely to eliminate the vortex shedding. This is because the placing of a "splitter plate" in the near wake of the generating body is known to inhibit the establishment of a vortex trail (Simiu & Scanlan, 1986).

Thus, it was decided to carry out simulations in steady state. It must be noted that even if the actual flow still exhibits transient behaviour, the decided modelling approach (so-called quasi-steady) will still suffice based on the comparisons between the quasi-steady and transient solutions by Lasher (2001).

Modelling pollen flow

A maximum daily male pollen flow of 14.5 million grain/m^2/day in the French orchards and 1.58 million grain/m^2/day in a New Zealand orchard had been reported by Malaboeuf *et al.* (1997) and Heath & Tenquist (1984) respectively. Malaboeuf *et al.* (1997) captured the airborne pollen by using the cellulose filters fitted to a wind-vane. The wind-vane was placed at the upper level of the flowers and in the middle of the orchard. Filters were replaced daily. Heath & Tenquist (1984) used microscope slides that had a known area covered with adhesive material. With the adhesive side downwards, the slides were suspended at the same level as the female flowers over 8 hours.

However, both sources did not specify the average daily draft velocity. So, it was decided to use the measured average velocity of 1 m/s in the orchard and this gives ~ 168 grain pollen/m^3 air based on the figure by Malaboeuf *et al.* (1997). This means in the computational domain of 88×10^{-3} m^3, there are only ~ 15 pollen grains at any time and thus only the one-way fluid-particle coupling is considered for wind pollination.

Since the injection of 15 pollen grains on the inlet boundary is not going to give a representative estimation of pollen collection efficiency from wind, 50000 pollens are injected uniformly on a ϕ 66-mm circular plane (with centre at the centre of the inlet boundary; see Fig. 3-1) which represents a projected area of the full-open flower. For the sake of consistency, the same projected area is assumed for the other three flowers. The number of simulated pollen is chosen following the particle number independence study in section 3.5. The pollen passing through this circular plane may possibly collide and collect inertially on the flower.

The pollen, having a solid density of 1330 kg/m^3 (Ferguson & Pusch, 1991), are introduced at the same velocities as the air at the inlet. The pollen grains are assumed to be spherical with a mean diameter of 22 μm based on the reported dimensions by Dickison *et al* (1982) and Schmid (1978). Although the actual pollen are oblate spheroidal, the grains become more spherical when hydrated (Hopping & Jerram, 1979).

It is assumed here that the pollen grains are discretely dispersed in the air. However, King & Ferguson (1994) found that the vibration of fresh male anthers at similar buzz foraging vibration of bumble bees caused the ejection of clumps of pollen joined by small droplets of tapetal fluid. There is no pollenkitt[2] (Ferguson & Pusch, 1991). King & Lengoc (1993) estimated the adhesive force between two pollen connected by an interstitial tapetal liquid bridge to be as strong as 58 kN/m^2. More pollen were released as dry individual grains as the anthers aged and became fully dehiscent (King & Lengoc, 1993). Palmer-Jones & Clinch (1974) and Schmid (1978) reported that the pollen were shed in clumps. Malaboeuf *et al* (1997) had also found aggregated airborne

---

[2] A sticky material, produced by the tapetum, that may hold pollen grains together during dispersal.

3-3

pollen in his pollen collection study. This implies that depending on the state of the anthers, the pollen grains in the orchard air may exist in individual grain or clump.

The pollen trajectories are calculated in steady state using the Lagrangian framework (see section 2.3.2). The simulated pollen experience drag force and turbulent dispersion, but not gravitational force. This is because the pollen settling velocity (~ 14 mm/s; Wakelin, 1985b) is low compare to its superficial velocity of 0.5 - 3 m/s in the simulations. In addition, the random orientation of flowers in the vine makes it hard to decide the direction of the gravity vector.

Turbulent particle dispersion (see section 2.3.2) is included as according to Burrows (1975) and Di-Giovanni & Beckett (1990), the modelled pollen (not of kiwifruit) trajectories were sensitive to the turbulent fluctuations in the carrier wind.

The presence of papillar (Gonzalez *et al*, 1995a) and liquid exudate (in the early morning) mean the pollen will stay on the stigma upon collision. Since it is unknown how the pollen will behave on the other surfaces of the flower, it is assumed that all the contacted pollen are captured. Other pollen leave the domain through the outlet boundaries.

3.2. Meshing

The volume around the flower model is meshed using unstructured grids. Various mesh controls are placed on different model flower surfaces in order to achieve gradual refinement of meshes closer to the surfaces (see Fig. 3-2). These are listed in Table 3-1.

To promote better flow prediction in the region of interest, the stigma are covered with fine prismatic cells. There are four layers of prismatic cells with the first layer being 0.05 mm thick. The layers expand outwards and perpendicularly to the surface at a ratio of 1.3. Pyramidal cells connect the prismatic cells to the tetrahedral cells.

The total number of cells to be used will be decided in the grid independence study in section 3.3.
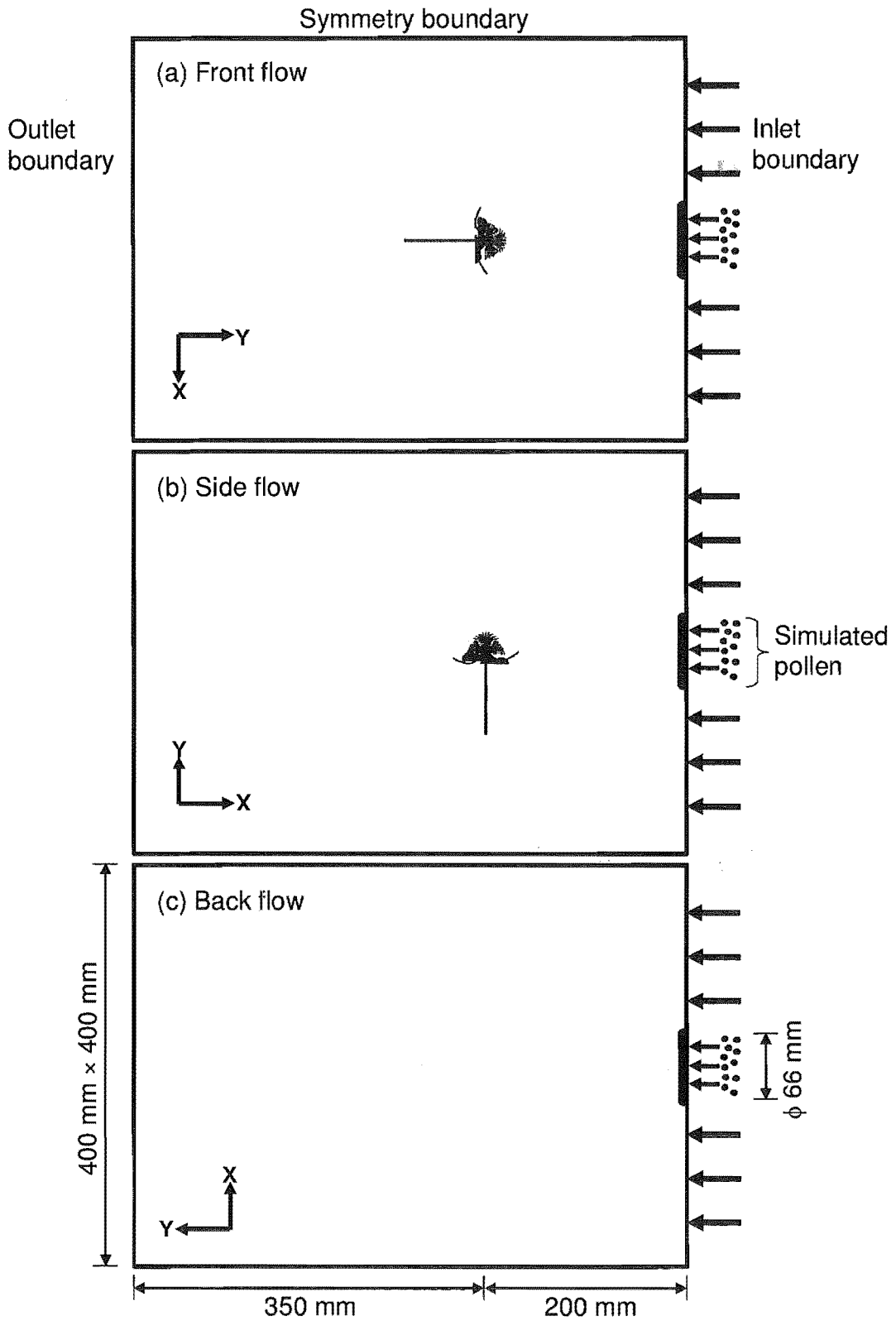
Fig. 3-1: Definition and dimension of the rectangular flow domains for a full-open flower subjected to the uniform inlet flow from different directions. Also shown is the location where the simulated pollen are injected.

2,746,727 cells   1,567,254 cells   1,127,985 cells   915,203 cells   808,284 cells
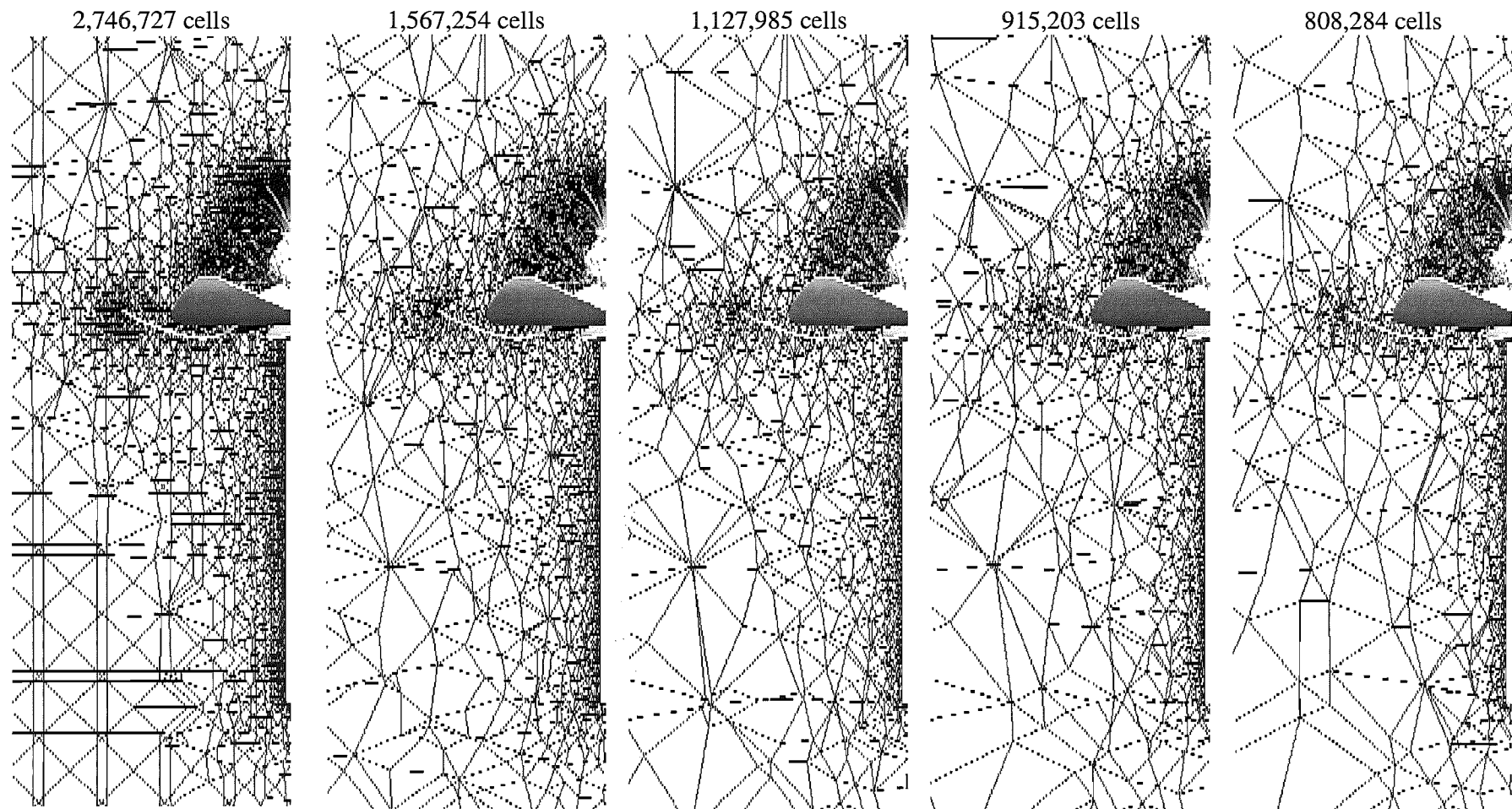
Fig. 3-2: Density of meshes used in the grid independence check.

Table 3-1: Surface mesh controls and their locations.

Locations	Minimum size [mm]	Maximum size [mm]
Ovary	0.3	3.0
Stem	0.75	1.0
Petal tips	0.3	0.75
Petal edges	no control	0.3
Petals	0.5	3.0
Filaments	0.2	0.5
Anthers	0.3	1.0

3.3. Grid independence and residual independence studies

The test case here is based on a full-open kiwifruit flower subjected to a uniform frontal air flow of 1 m/s without any pollen. RNG k-ε model is selected arbitrarily here and an inlet turbulence intensity of 3.7 % is assumed in the absence of field data. Five mesh resolutions are used (0.81, 0.92, 1.13, 1.57 and 2.75 millions; see Fig. 3-2) and the simulations are terminated at four different RMS[3] residual levels (5×10^{-3}, 1×10^{-3}, 5×10^{-4} and 1×10^{-4}), giving a total of 20 combinations. Different mesh resolutions are obtained through successive coarsening. The RMS residual (x-, y- and z-momentum; and pressure-mass) curves have been observed to level out around 1×10^{-4}.

The run having the densest mesh (2.75 millions) and the tightest convergence (RMS residual of 1×10^{-4}) is expected to give the most accurate solution. It is taken as the 'reference run' and used to examine how different the other runs (based on the less dense meshes and higher RMS residuals) are from it. This is done by comparing the velocity profiles across the centre of the style bush and at about ¾ flower diameter downstream from the flower centre (shown as Lines F1 and F2 respectively in Fig. 3-3a). Line F2 strikes through the large downstream recirculation, providing a good mean for comparison.

---

[3] Root-mean-square.

All the velocity profiles are plotted in Fig. 3-4a to d (for Line F1) and Fig. 3-5a to d (for Line F2). At each RMS residual level, all five mesh sizes give similar flow patterns. The velocity differences across the middle of the style bush (Line F1) are smaller and less pronounced than the ones at about ¾ flower diameter downstream (Line F2). This is expected because most of the automatic mesh coarsening takes place outside the style bush region. In a way, this also indicates that the meshes in the style bush region are locally fine enough.

For a comparison to the 'reference run', the velocity differences of each runs are calculated using Equation 3-1 for Lines F1 and F2.

$$\frac{U(S) - U_{Ref}(S)}{U_{Ref}(S)} \qquad \text{Equation 3-1}$$

U(S) is the resultant velocity at location S along the line locators of the velocity profile. $U_{Ref}(S)$ is the reference velocity given by the 'reference run'. Equation 3-1 expresses the velocity difference as a fraction of the reference velocity. Overall, it is found that the velocity differences are becoming smaller with the smaller mesh sizes and the lower RMS residuals. This indicates the solutions are converging steadily but the total grid and residual independences have not been achieved yet.

To provide a better view of the influence of mesh size and RMS residuals on the convergence, the velocity differences of each run are averaged using Equation 3-2. This equation first computes the absolute velocity differences as a fraction of the reference velocity and then averages them over the length of Lines F1 and F2 (both 80 mm long).

$$\frac{\int \frac{|U(S) - U_{Ref}(S)|}{U_{Ref}(S)} dS}{\int dS} \qquad \text{Equation 3-2}$$

The results are surface-plotted in Fig. 3-6a and b for the comparisons at Lines F1 and F2 respectively. Both plots clearly show the improvements on the velocity differences through the use of more cells and lower RMS residuals. Fig. 3-6a indicates that the solutions have converged reasonably well at Line F1, due to the presence of small cells locally. Note that this is the critical one for the pollen collection on the stigma.
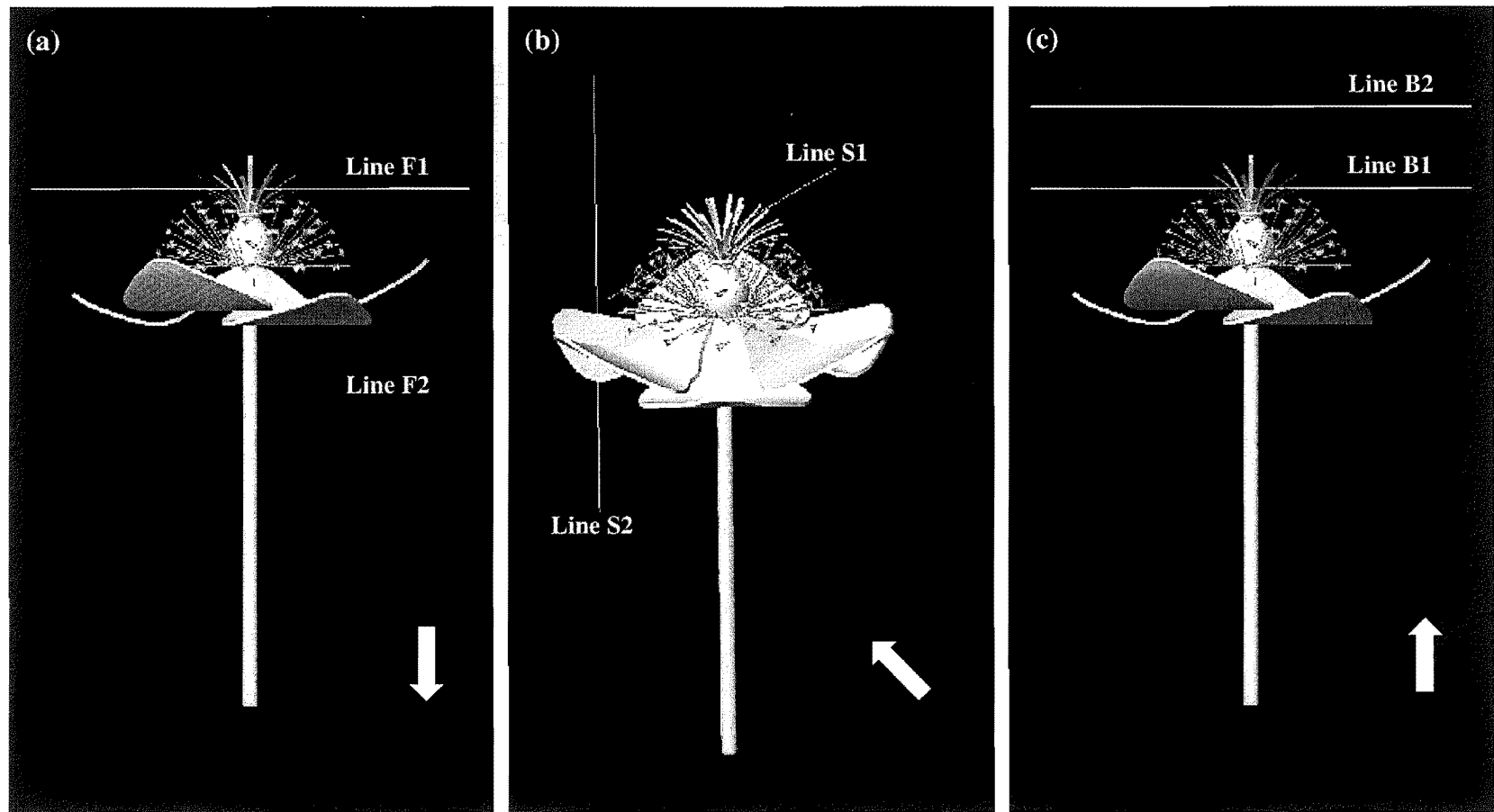
Fig. 3-3: Lines indicating the locations of the velocity profiles extracted from the air flow field around a full-open flower under a (a) frontal flow, (b) side flow or (c) back flow. The arrows show the bulk air flow direction.
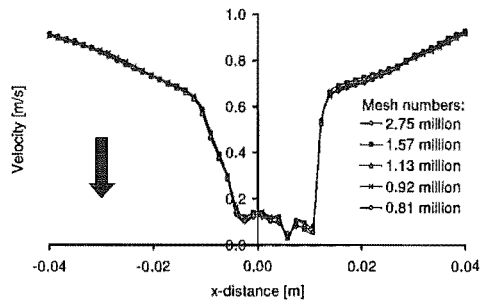
(a) RMS residual = 5×10^{-3}
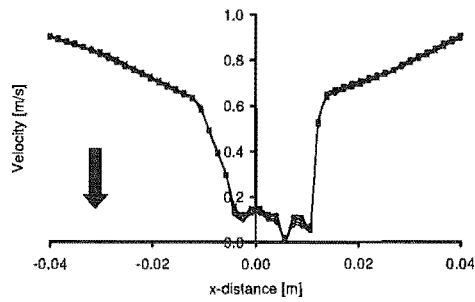
(b) RMS residual = 1×10^{-3}
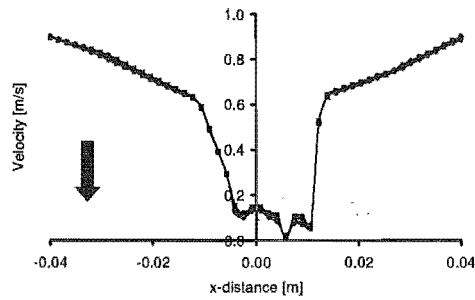
(c) RMS residual = 5×10^{-4}
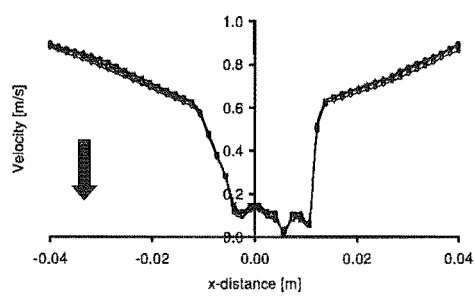
(d) RMS residual = 1×10^{-4}

Fig. 3-4: Mesh and residual independence study. (a) to (d) are the velocity profiles through the middle of the style bush (Line F1 in Fig. 3-3a). The arrows show the bulk air flow direction.
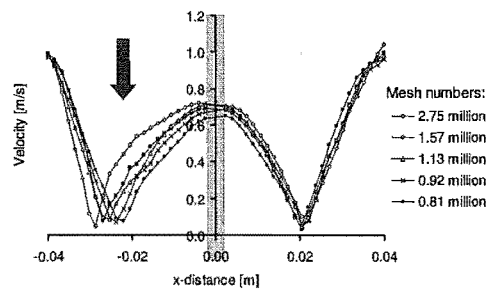
(a) RMS residual = 5×10^{-3}
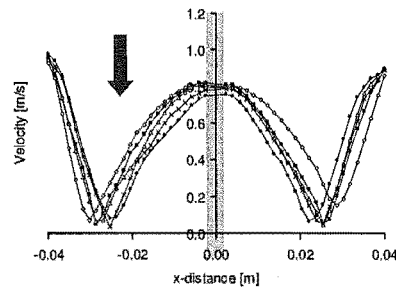
(b) RMS residual = 1×10^{-3}
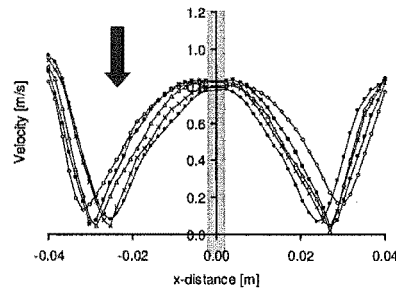
(c) RMS residual = 5×10^{-4}

(d) RMS residual = 1×10^{-4}
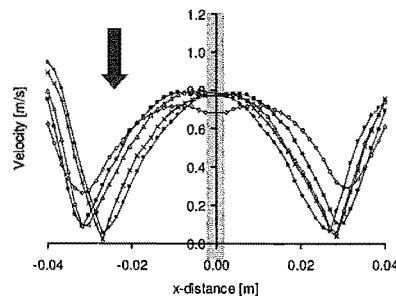
Fig. 3-5: Mesh and residual independence study. (a) to (d) are the velocity profiles at about ¾ flower diameter downstream the flower centre (Line F2 in Fig. 3-3a). The arrows show the bulk air flow direction. Grey region is the stem.

(a) at Line F1
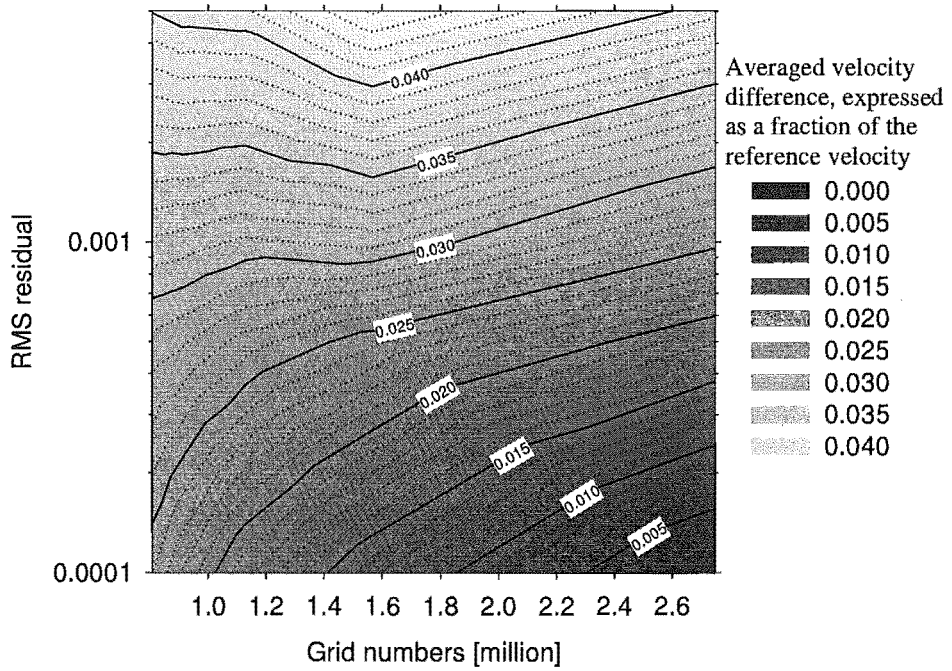
(b) at Line F2
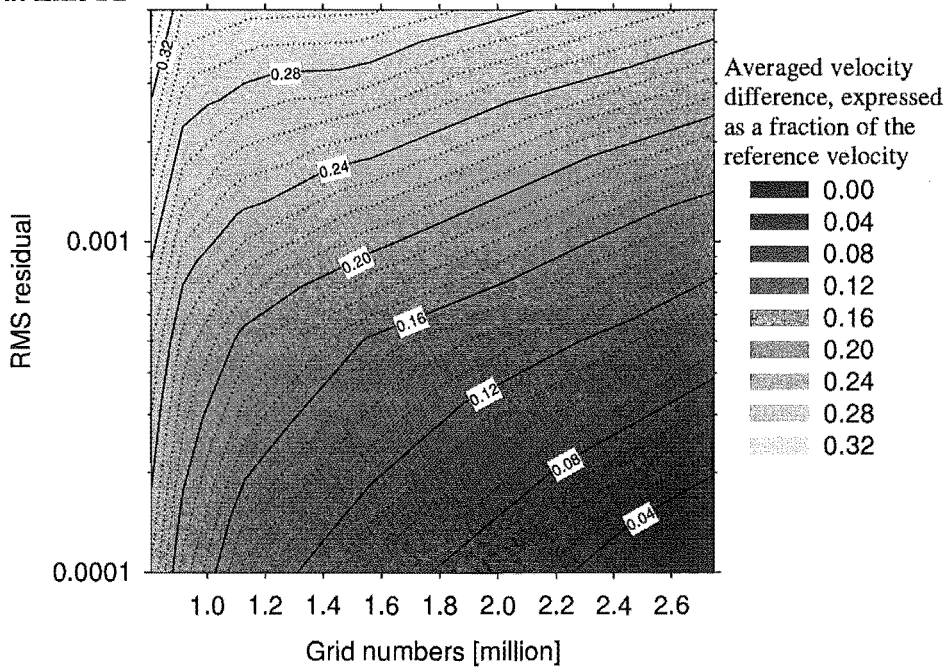
Fig. 3-6: The contour plots of the averaged velocity difference compared to the reference velocity at different RMS residuals and grid numbers, for the velocity profiles at (a) Line F1 and (b) Line F2. The flow is from the front.

This is however not the case at Line F2 (see Fig. 3-6b) i.e. either needs the mesh size to be increased or the RMS residual to be set lower.

Fig. 3-7 shows the solver time taken for each combination. The CPU clock appears to surge when low RMS residual and high mesh number are applied.
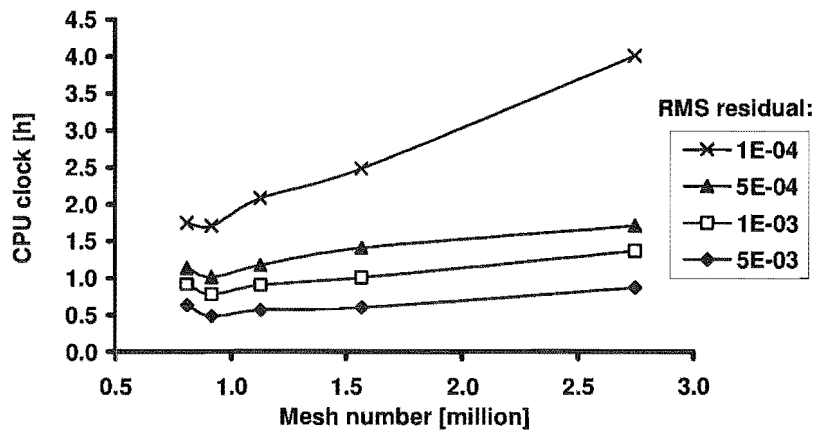
Fig. 3-7: Solver time needed to achieve various RMS residuals for different mesh numbers. System specification: Pentium 4, 2.0 GHz, 2 GB RAM, Window 2000.

It is preferred to set the RMS residual as low as possible i.e. 1×10^{-4} while keeping the mesh size below 2 million, which will otherwise requires large computational memory. Even with the mesh number below 2 millions, some cases (not in this section) took up to five and a half hours to reach a RMS residual of 1×10^{-4}.

Thus, based on Fig. 3-6b, in order to achieve an averaged velocity difference of not more than 10 % compared to the 'reference run', at least 1.55 million cells must be used. All the succeeding runs will be based on a mesh size of ≥ 1.55 million cells and a RMS residual of $\leq 1 \times 10^{-4}$.

3.4. Choosing the flow models

A full-open flower is approached by a 1-m/s air flow from the front, side and back. The flow is solved without pollen by using the Laminar, RNG k-ε and SST models (more

details in sections 2.2, 2.2.2, 2.2.5 and 2.2.8). The solutions given by each flow model are compared in Fig. 3-8 to 3-10 using the same methods described in section 3.3. For the side and back flows, the velocity profiles are extracted from the Lines S1, S2, B1 and B2 in Fig. 3-3b and c. For each flow, one of the lines is along the middle of the style bush while the another lies across the downstream recirculation. In using Equation 3-1, the runs that are solved using the Laminar model which is chosen arbitrarily as the 'reference run'.

All three flow models give very similar velocity profiles except for the RNG k-ε model in the side flow (see Fig. 3-9a and b). Overall, the solutions computed from the Laminar and SST models are closer to each other compared to the ones from the RNG k-ε model. A suggested reason here is that the ω equation in the SST model can better handle the flow transition from the locally laminar behaviour near the flower region to the turbulent bulk flow region compared to the RNG k-ε model which is strictly for fully turbulent flow.

Fig. 3-8b shows that the predictions of RNG k-ε model near the wall (the surface of the stem) are also markedly different from those of the Laminar and SST models. This is likely due to the forced minimum y^+ of 11 by the scalable wall treatment in the RNG k-ε model. On the other hand, like the laminar model, the automatic wall treatment in SST fully resolves the fine cells present near the wall of the stem.

However, the performance of the SST model is not consistently as reliable as the Laminar and RNG k-ε models. SST model occasionally caused the solver to terminate with integration errors in the linear solver. Trial-and-error work suggested that these errors were likely due to the incapability of the SST model in handling a small number of high aspect ratio cells (less than 0.002 % of the total cells) located at the edges of the petals and the sharp corners. The attempt to remove these 'bad' cells through further local cell refinements was found to be very mesh expensive and it did not consistently prevent the integration errors from occurring. The integration error was also thought to be caused by the stiffness encountered in the integration of ω-equation, particularly on the highly curved surfaces in this work. Thus, it was decided not to use the SST model.
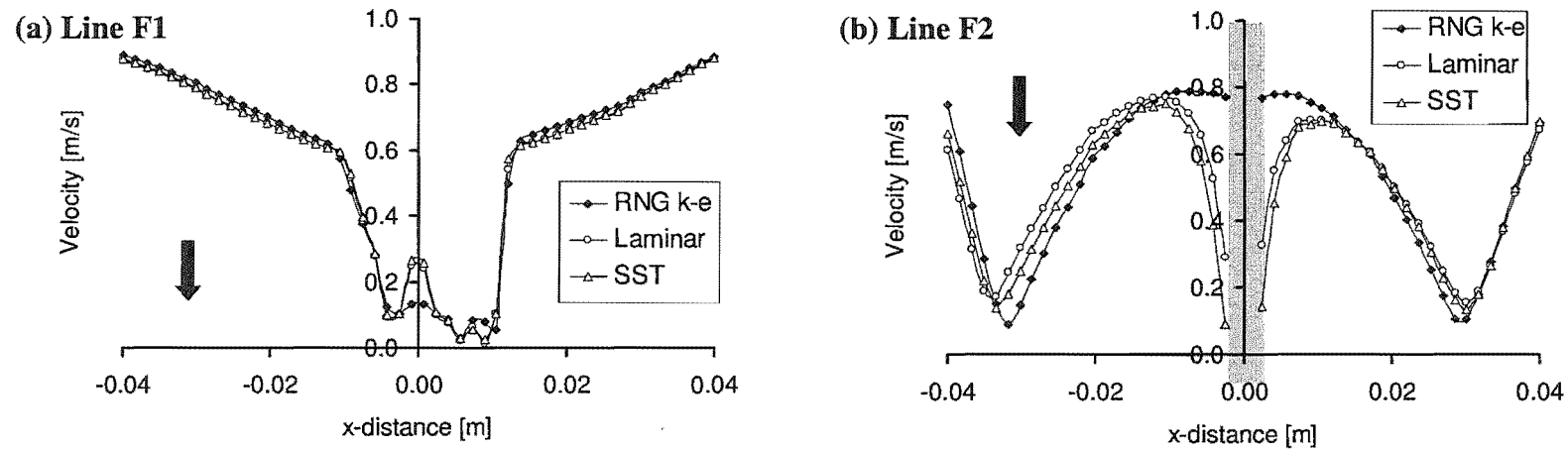
Fig. 3-8: Comparison of velocity profiles calculated using different flow models for a full-open flower under a 1-m/s frontal flow. Locations of velocity profiles: (a) through the middle to style bush (Line F1 in Fig. 3-3a); (b) downstream the flower centre (Line F2 in Fig. 3-3a). Grey region is the stem. The arrows show the bulk air flow direction.
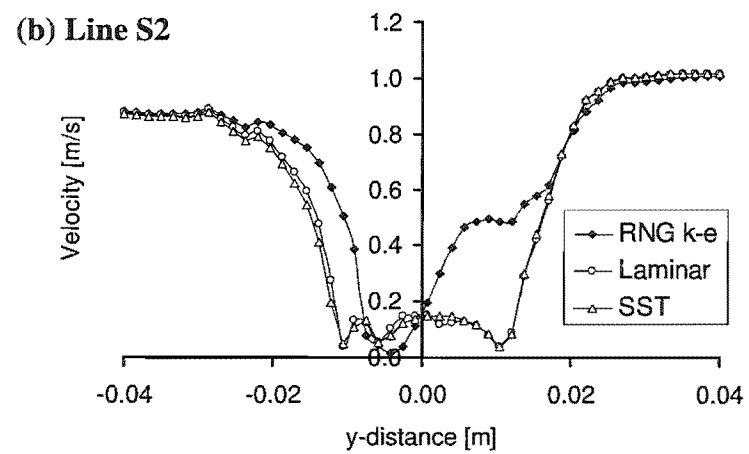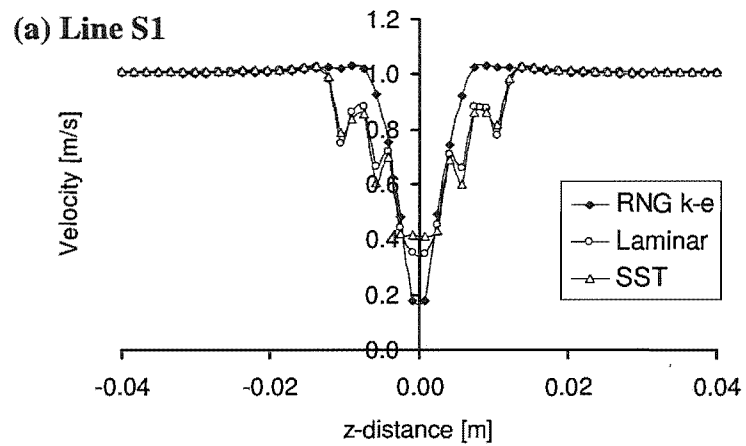
Fig. 3-9: Comparison of velocity profiles calculated using different flow models for a full-open flower under a 1-m/s side flow. Locations of velocity profiles: (a) through the middle to style bush (Line S1 in Fig. 3-3b); (b) downstream the flower centre (Line S2 in Fig. 3-3b). The arrows show the bulk air flow direction.

(a) Line B1
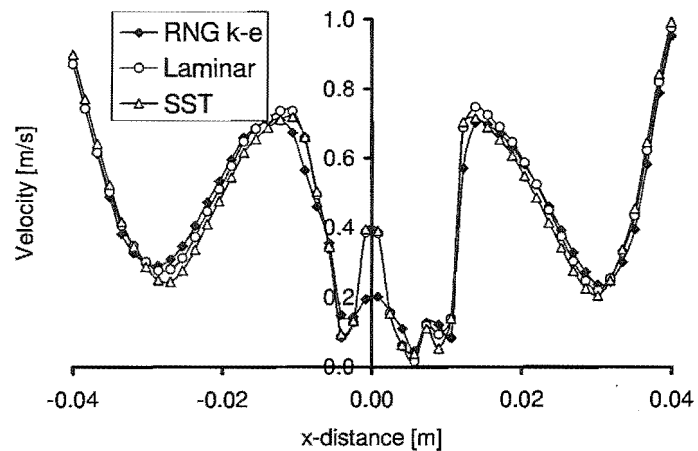
(b) Line B2
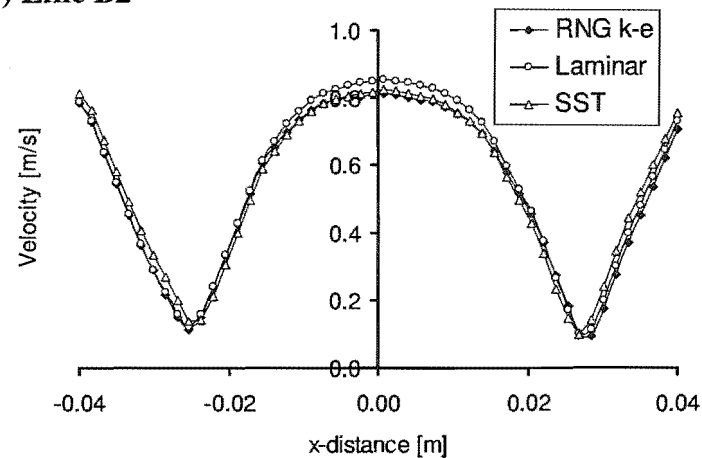
Fig. 3-10: Comparison of velocity profiles calculated using different flow models for a full-open flower under a 1-m/s back flow. Locations of velocity profiles: (a) through the middle to style bush (Line B1 in Fig. 3-3c); (b) downstream the flower centre (Line B2 in Fig. 3-3c). The arrows show the bulk air flow direction.

The choice between the Laminar and the RNG k-ε models was made based on the Reynolds number of the flower. With the diameter of the flower (66 mm) selected as the characteristic length, the Reynolds number is ~ 4400 at 1 m/s of air flow. This suggests that the flow around the flower is likely in the turbulent region i.e. RNG k-ε model is more appropriate. Judging from the comparisons in Fig. 3-8 to 3-10, the predicted air flow by the RNG k-ε model is likely to be as adequate as the Laminar and SST models for modelling the pollen collection on the stigma. RNG k-ε model is employed in all the succeeding runs.

3.5. Particle number independence study

Different quantities of simulated pollen are injected in front of a full open flower submerged in 1-m/s frontal air flow. The percentages of simulated pollen that land on stigma, style and other parts of the flower become relatively constant and independent of the number of pollen introduced when ≥ 20000 pollen are simulated (see Fig. 3-11).
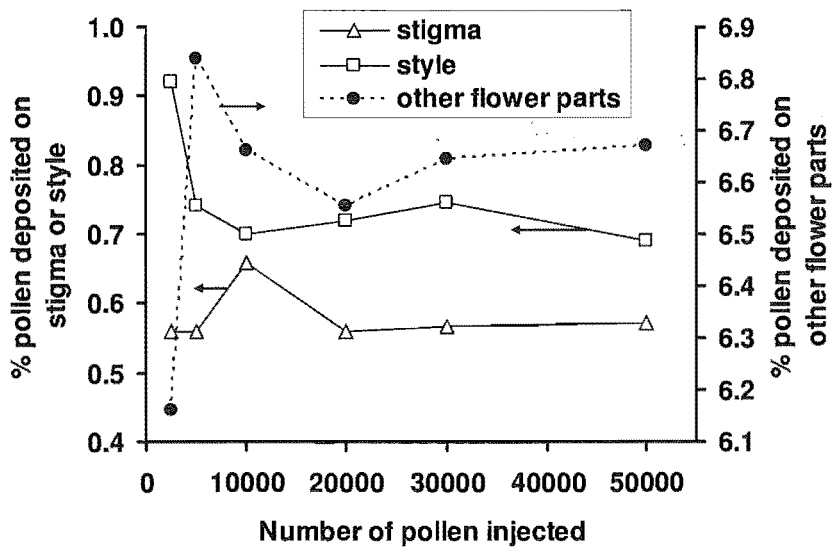
Fig. 3-11: Percentage of the injected particles that are deposited on the stigma, styles and other flower parts.

3-9

However, Fig. 3-12 shows that the proportions of the stigmatic and stylar surfaces (total of 72 faces for each) that have collected the pollen in the simulation continue to rise with the increasing number of pollen injection. In reality, depending on the locations and orientations of a stigmata, not all the stigma may capture the airborne pollen. For a conservative estimate of the collection efficiency, it is assumed that all stigma and styles have equal chances of collecting the simulated pollen. According to Fig. 3-12, large number of pollen will need to be simulated to hold this assumption. At 50000 pollen injection, nearly all the stigmatic and stylar surfaces show deposition of at least one pollen grain. Since it is not economical in memory usage to track more than 50000 pollen, all the succeeding runs are decided to be based on 50000 of simulated pollen.
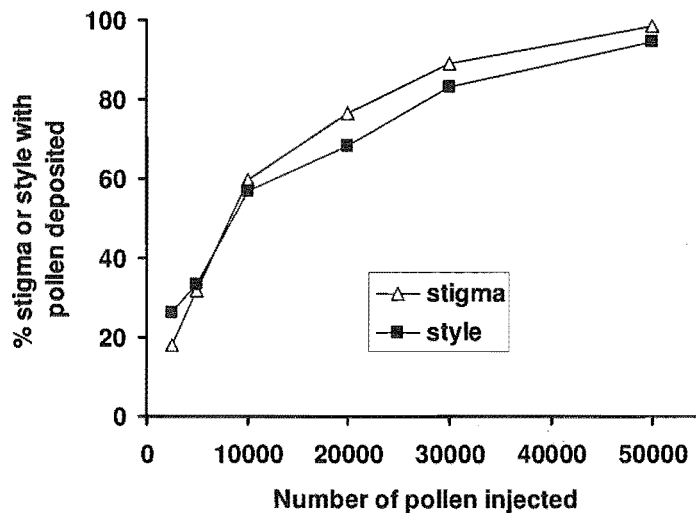
Fig. 3-12: Percentage of all the stigma and styles that have collected simulated pollen when different numbers of particles are introduced.

3.6. Wind pollination simulation results

The lateral view of the total velocity fields around the four flower models are visualized in contour and vector plots in Fig. 3-13 to 3-15 for the frontal, side and back flows respectively. Note that only the runs with an approach velocity of 1 m/s are presented here.

3-10

(a) Bold

(b) Half-open

(c) Full-open

(d) Flip-back
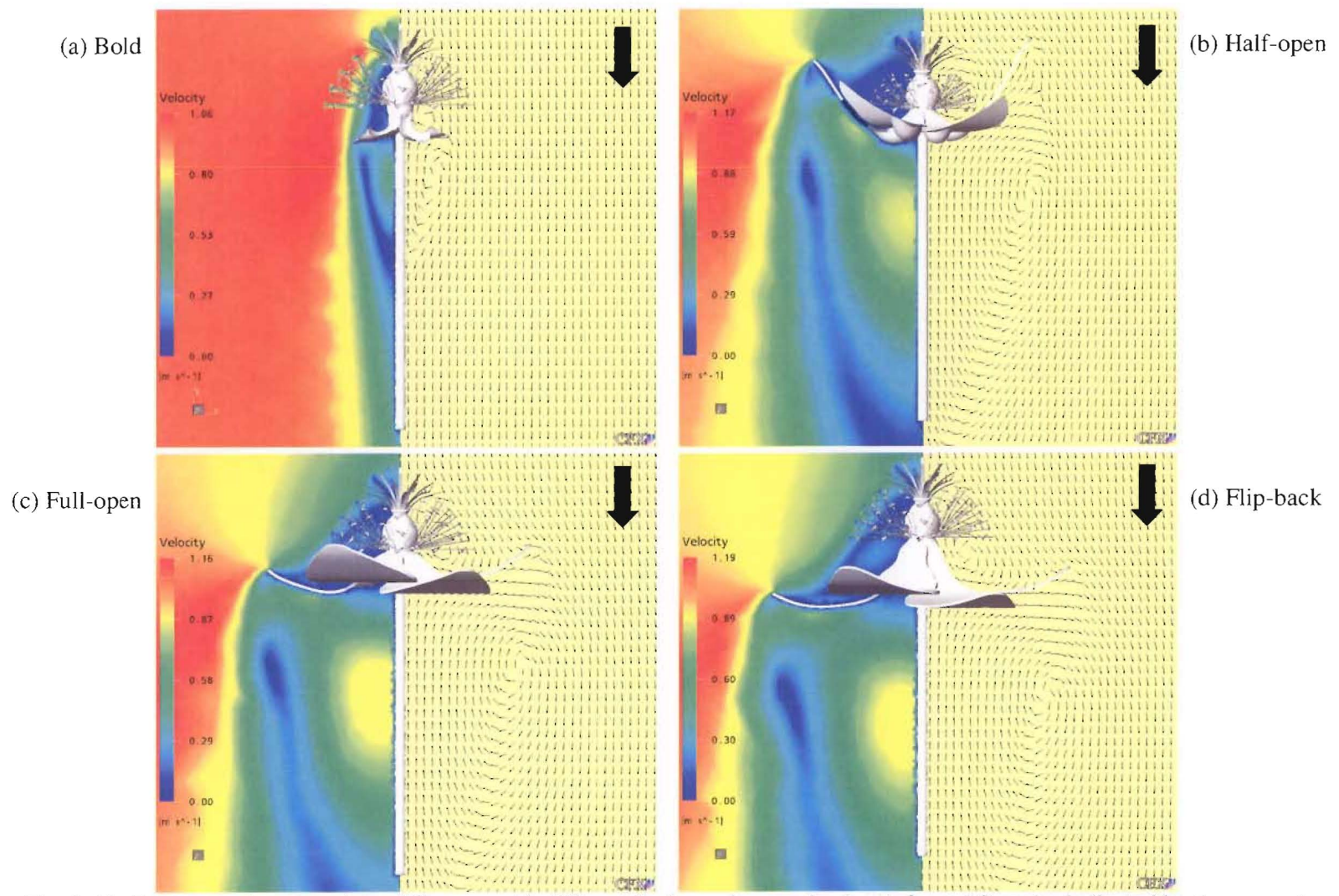
Fig. 3-13: Contour and vector plots of flowers with different bud openings under 1-m/s frontal flow (as indicated by the arrows).
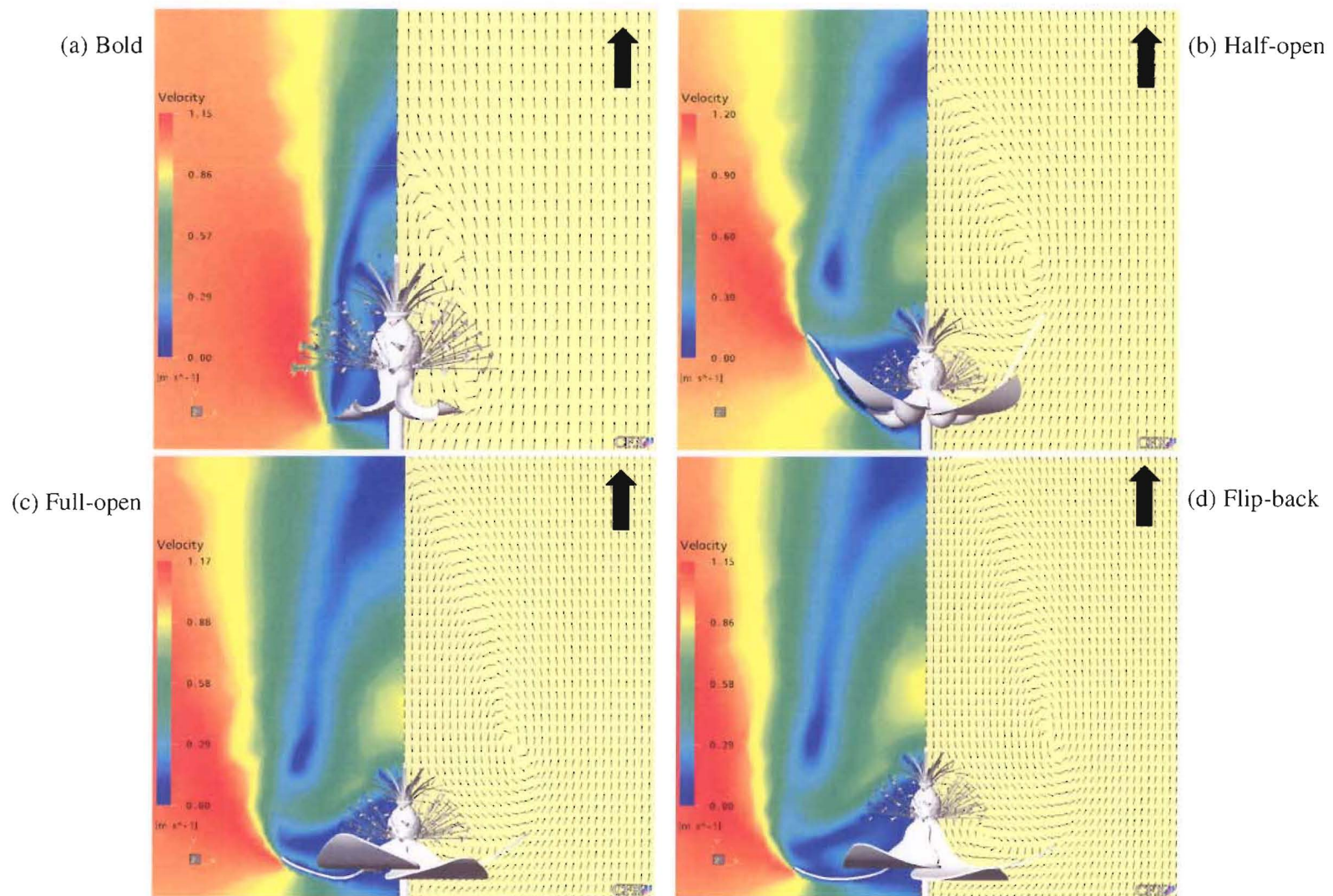
Fig. 3-14: Contour and vector plots of flowers with different bud openings under 1-m/s back flow (as indicated by the arrows).
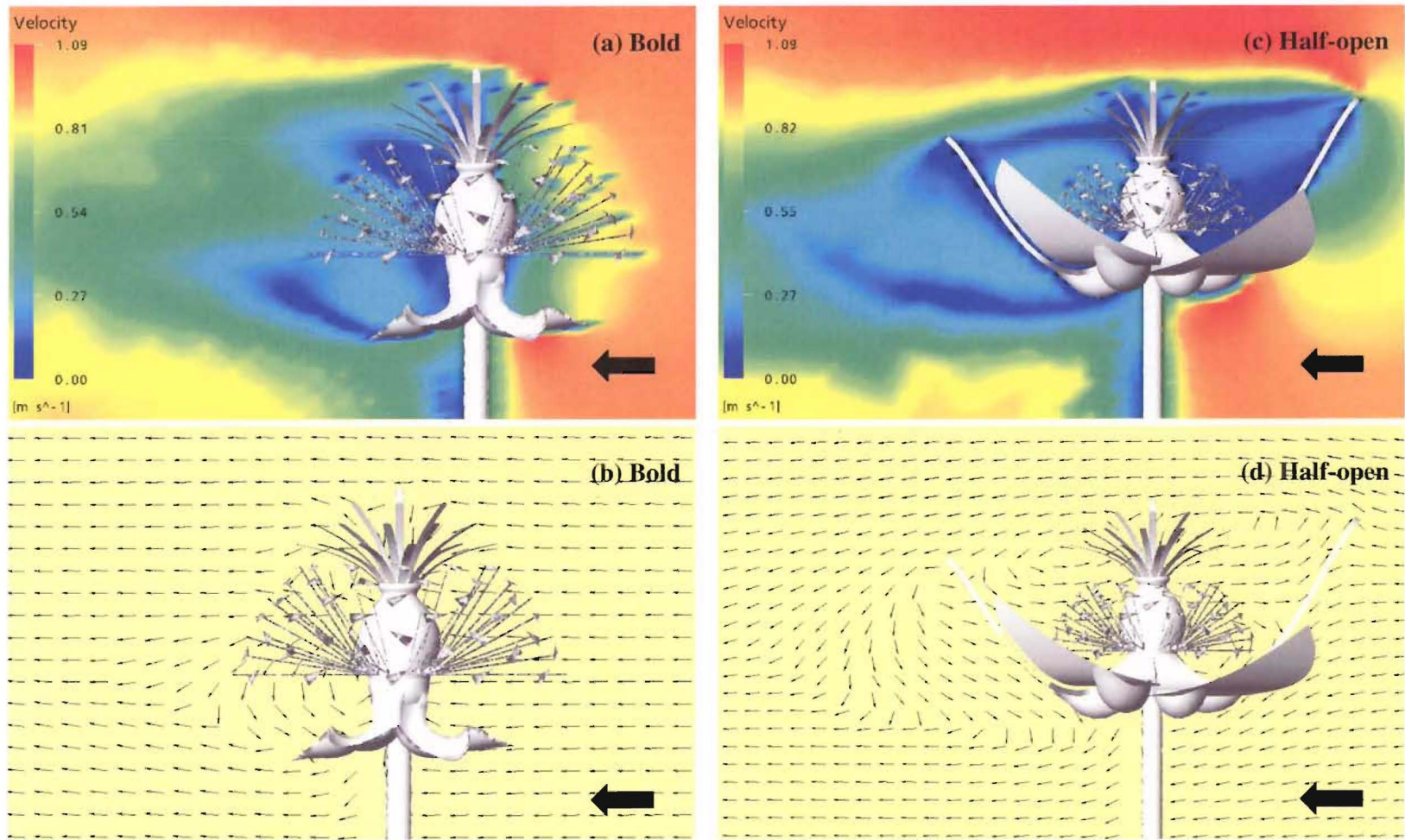
Fig. 3-15: Contour and vector plots of flowers with different bud openings under 1-m/s side flow (as indicated by the arrows).

continue...
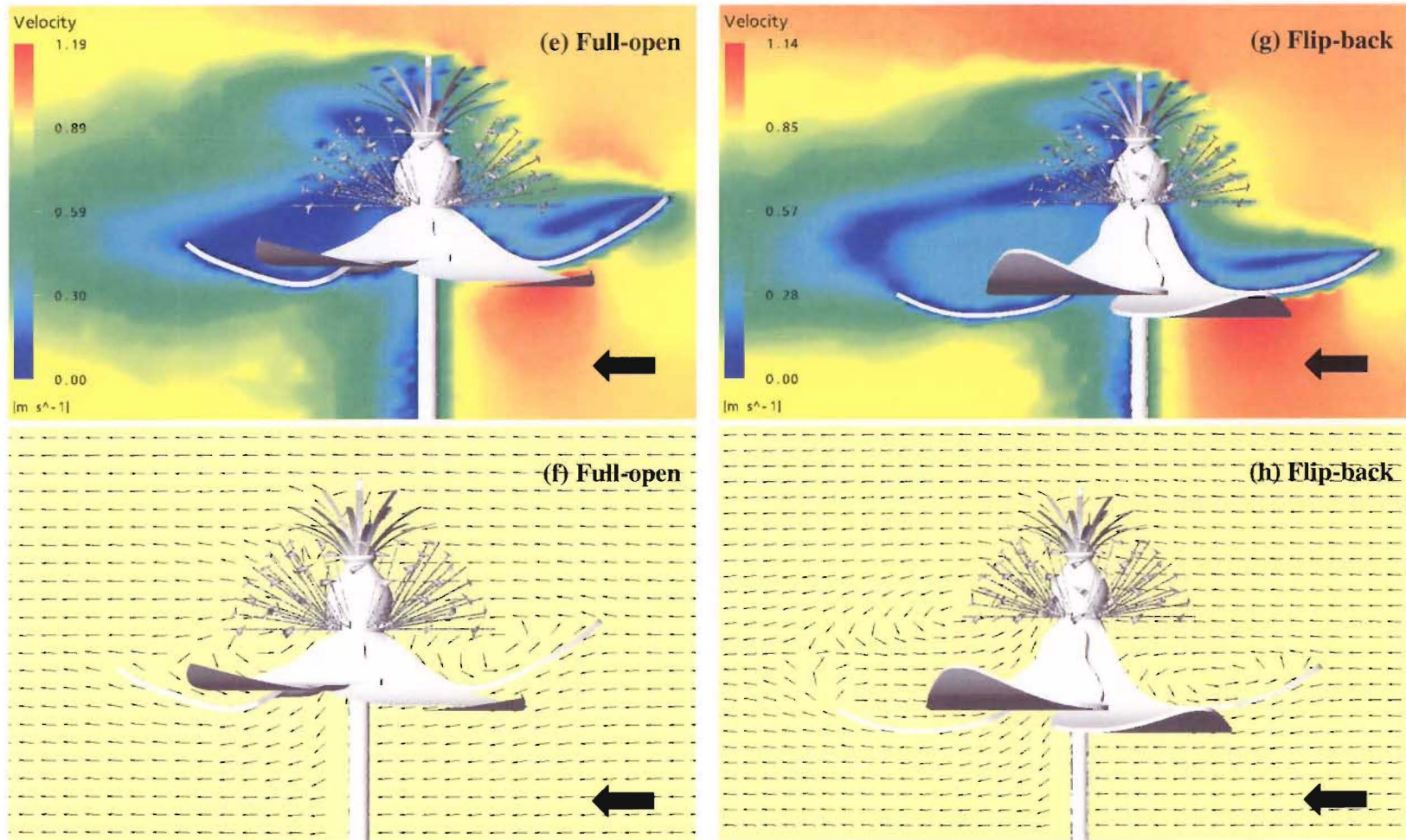
Fig. 3-15: Contour and vector plots of flowers with different bud openings under 1-m/s side flow (as indicated by the arrows).

Fig. 3-16 to 3-18 show the air velocity profiles across the centre of the style bush exposed to the frontal, side and back flows respectively. These velocity profiles are located at Lines F1, S1 and B1 in Fig. 3-3. The velocities have been normalized by the corresponding freestream velocities. The approach velocities from 0.5 to 3 m/s give similar recirculation patterns with the magnitudes in proportion to the freestream velocity.

The time-averaged streamlines and the corresponding pollen trajectories around the bold, half-open, full-open and flip-back flowers are displayed respectively in Fig. 3-19 to 3-22.

Half-open flower

The streamline plots in Fig. 3-20a and c show that there are at least two non-symmetrical recirculation regions under the frontal and back approaches respectively. They are the larger recirculation downstream of the flower and the small eddies in the airspace between the stigma and the petals, which can also be recognized in Fig. 3-13b and 3-14b. The spiralling large wakes extend up to 1.5 and 1.3 flower diameters downstream from the flower centre (bottom of the ovary) for the front and back flows respectively.

The vectors in Fig. 3-13b indicate that the incoming frontal air impinges on the stigma-style bush before being diverted to the sides. The orientation of the stigma-style bush is such that the incoming flow is almost perpendicular to the stigma at the end of the styles. This maximizes both the exposure of the stigma to the pollen-laden wind (see Fig. 3-20d) and the inertial collision of the pollen on the stigma. The air then recirculates vertically in the vicinity of the filament bush and just below the stigma-style bush, resulting in the small eddies that trap the pollen (Fig. 3-20d). The eddies climb upwards against the ovary wall and contact with the outermost styles. Although this is expected to present more chances for trapped pollen to be deposited on the stigma, this simulation (as well as the others) did not find any pollen collected in this way. This is because the filament and anther surfaces are assumed sticky. Thus, the trapped pollens are filtered by the filament and anther surfaces before they reach the stigma.

The pollen tracking calculations with frontal flow (Fig. 3-20a) show that the large downstream wakes redirect the pollen back to the flower. However, the petals prevent the pollen from reaching the stigma.

Under the back flow, the role of the downstream wake becomes very important because all collection of pollen on stigma rely on this wake. The large downstream vortices are found to incorporate the pollen grains and direct them straight to the stigma (Fig. 3-20f). The pattern of the airflow approaching and passing through the style bush exhibits similarity to that in the frontal flow. Fig. 3-14b shows that the airflow deflects at quite a distance above the style bush. It then gains speed (shown by the colour of the velocity field) and impinges the style bush in a straight vertical manner. As with the frontal flow, the approaching streamlines are almost normal to the stigma (Fig. 3-20c) i.e. enabling maximum pollen collection by inertial impaction.

When the wind blows tangentially to a cup-like shaped half-open flower, the air is trapped within the petal enclosure (Fig. 3-20b). There is a cyclonic flow centred around the ovary. The transverse view in Fig. 3-15d shows that there are at least three recirculation regions vertically. The first two are the pair of vortices occurring at about the same level as the style bush (one windward while another leeward of the style bush). They rotate in a direction opposite to each other. The last one happens near the bottom of the bud. Due to the significantly lower velocity within the bud (see the velocity contour field in Fig. 3-15c), the pollen grains are entrained into the region inside the bud (Fig. 3-20e). The cyclonic motion increases the probability of these pollen grains colliding with the stigma. The disordered steady state streamlines behind the flower bud in the flow simulation shown in Fig. 3-20d indicate that in the real situation, chaotic eddies are expected to occur at the back of the bud. This expectation of real flow is supported by the smoke-visualized flow shown in Fig. 4-4e and observation of complex vortex shedding by the author. According to Fig. 3-15d, these chaotic eddies are likely to move downwards. Like the frontal flow, no pollen is directed back to the stigma due to the impedance from the petals (see Fig. 3-20e where the pollen grains are collected on the leeward petal surfaces).
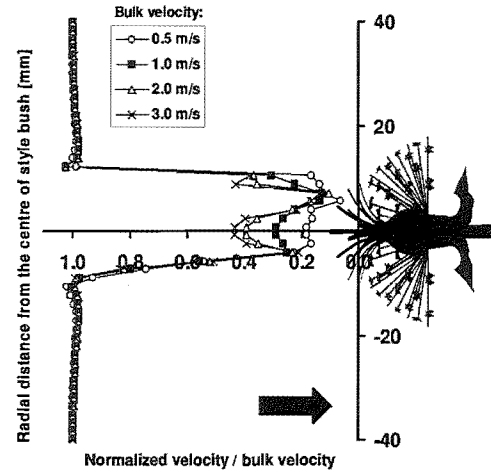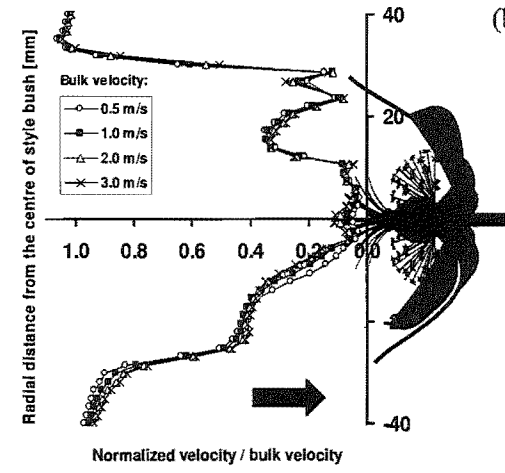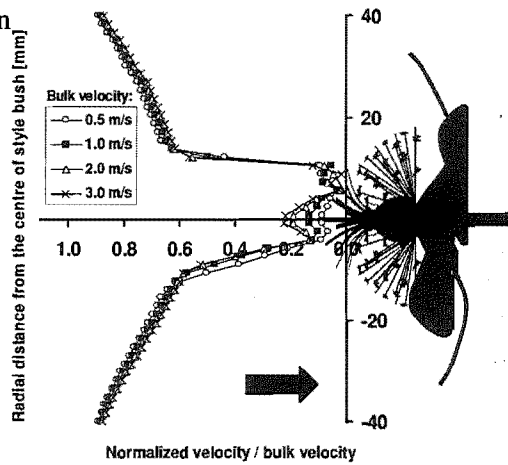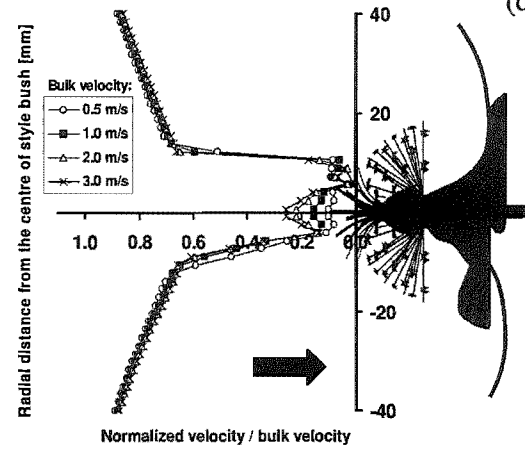
Fig. 3-16: Absolute velocity profiles across the style bush of flowers with different bud openings under frontal flow (indicated by the arrows). RNG k-ε model is used at a convergence to RMS = 1×10^{-4}.
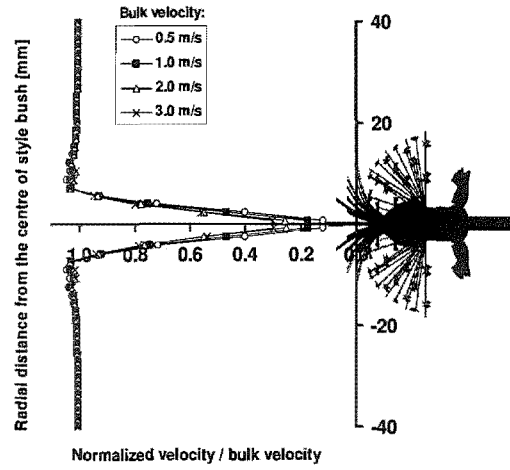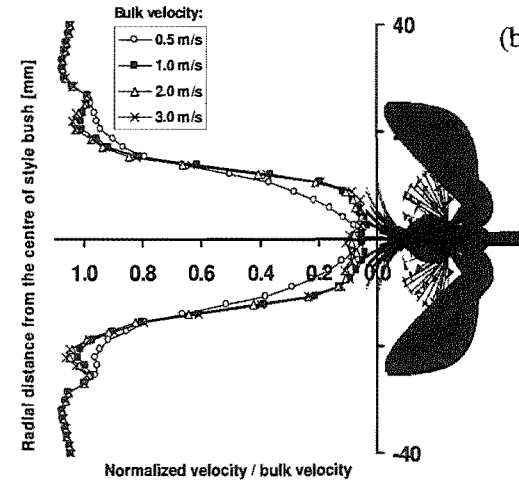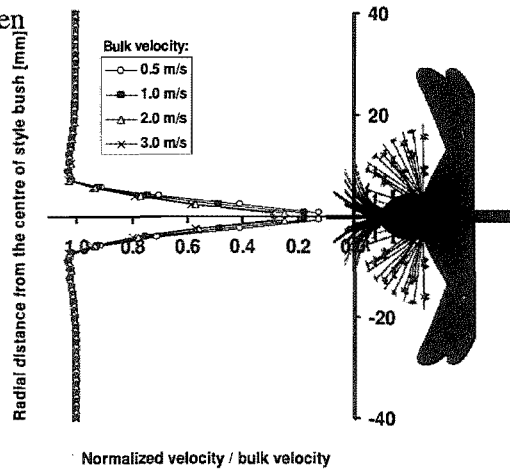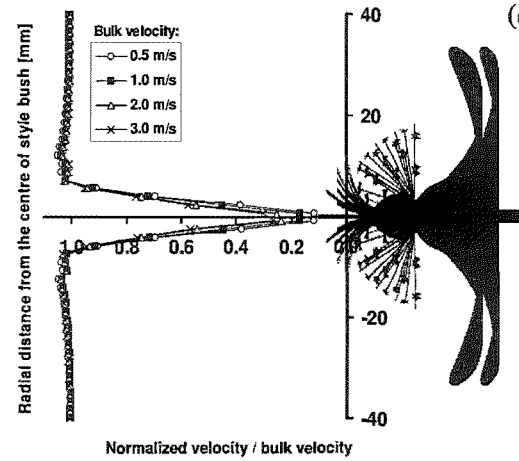
Fig. 3-17: Absolute velocity profiles across the style bush of flowers with different bud openings under side flow. The flow is into the page. RNG k-ε model is used at a convergence to RMS = 1×10^{-4}.
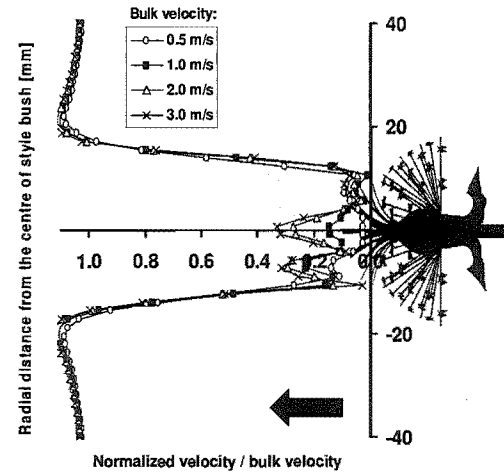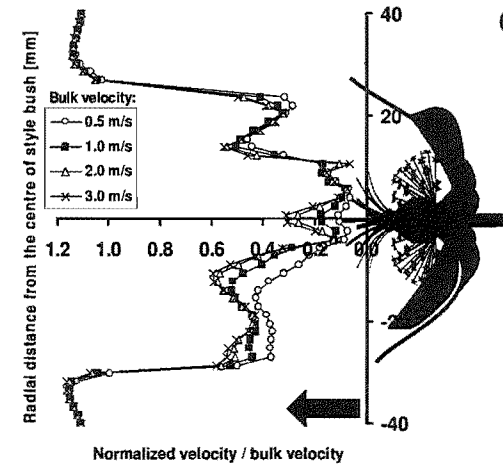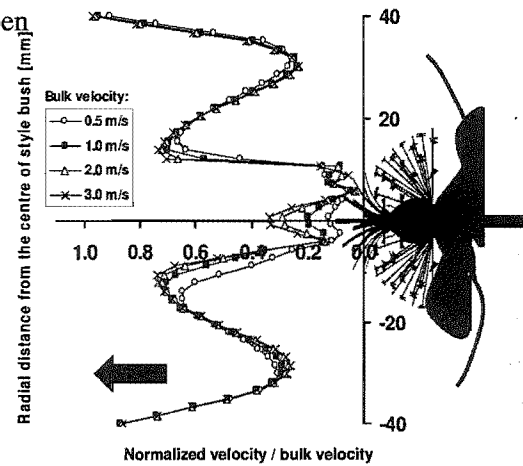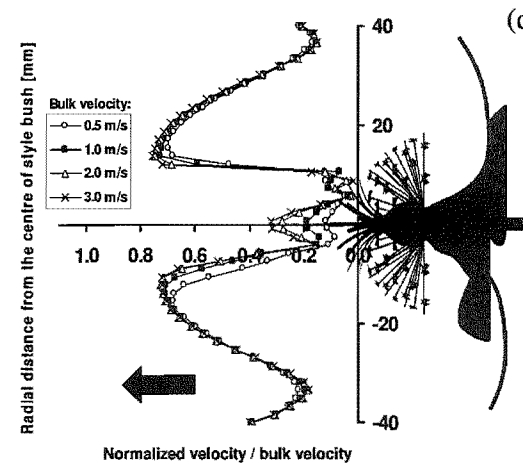
Fig. 3-18: Absolute velocity profiles across the style bush of flowers with different bud openings under back flow (indicated by the arrows). RNG k-ε model is used at a convergence to RMS = 1×10^{-4}.
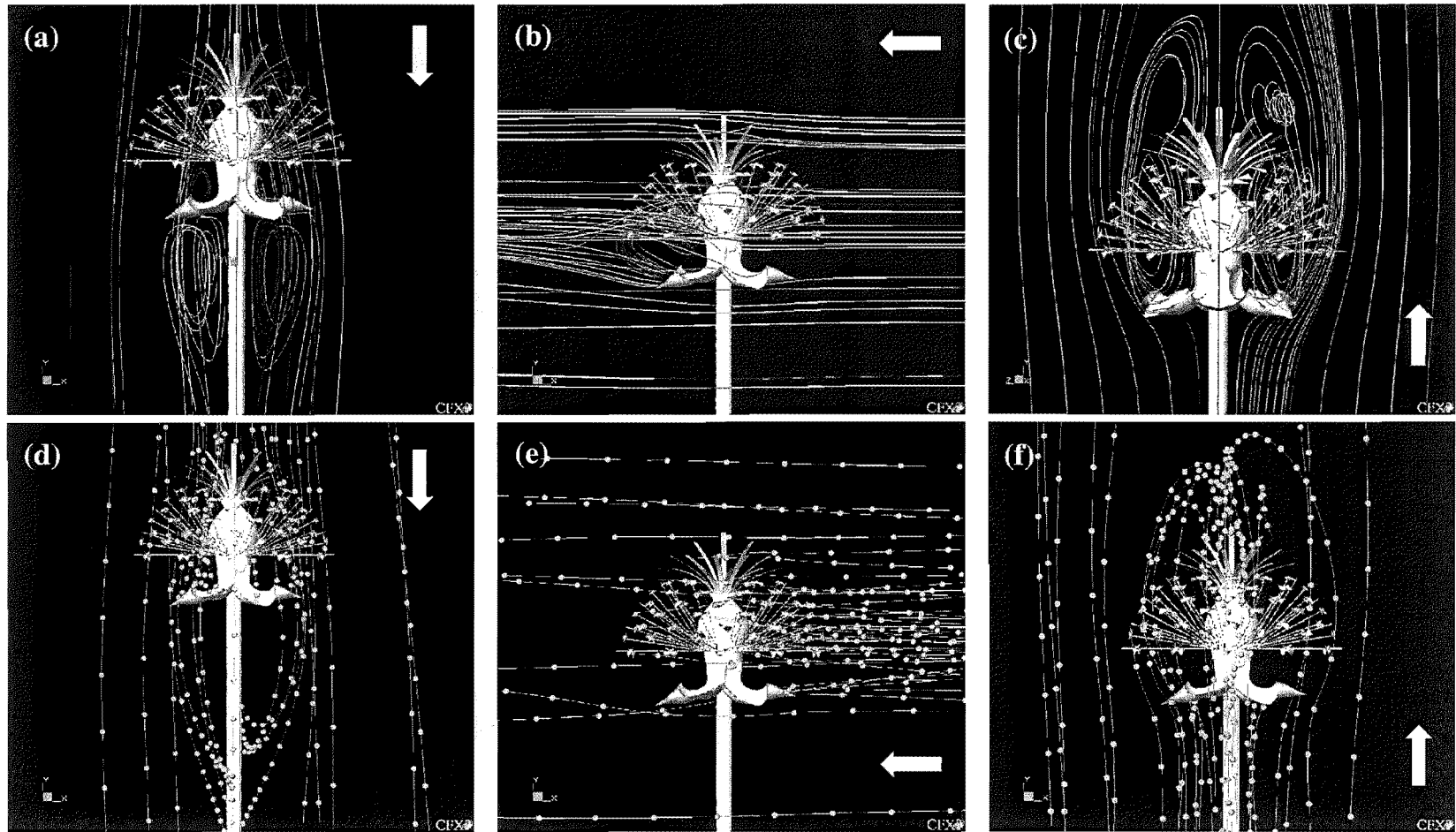
Fig. 3-19: (a), (b) and (c) are the predicted air flow field around a single bold flower under 1-m/s flow from the front, side and back respectively (as shown by the arrows). The corresponding calculated trajectories of a cloud of pollen are shown in (d), (e) and (f). The separation between pollen along a trajectory is 0.01 s.
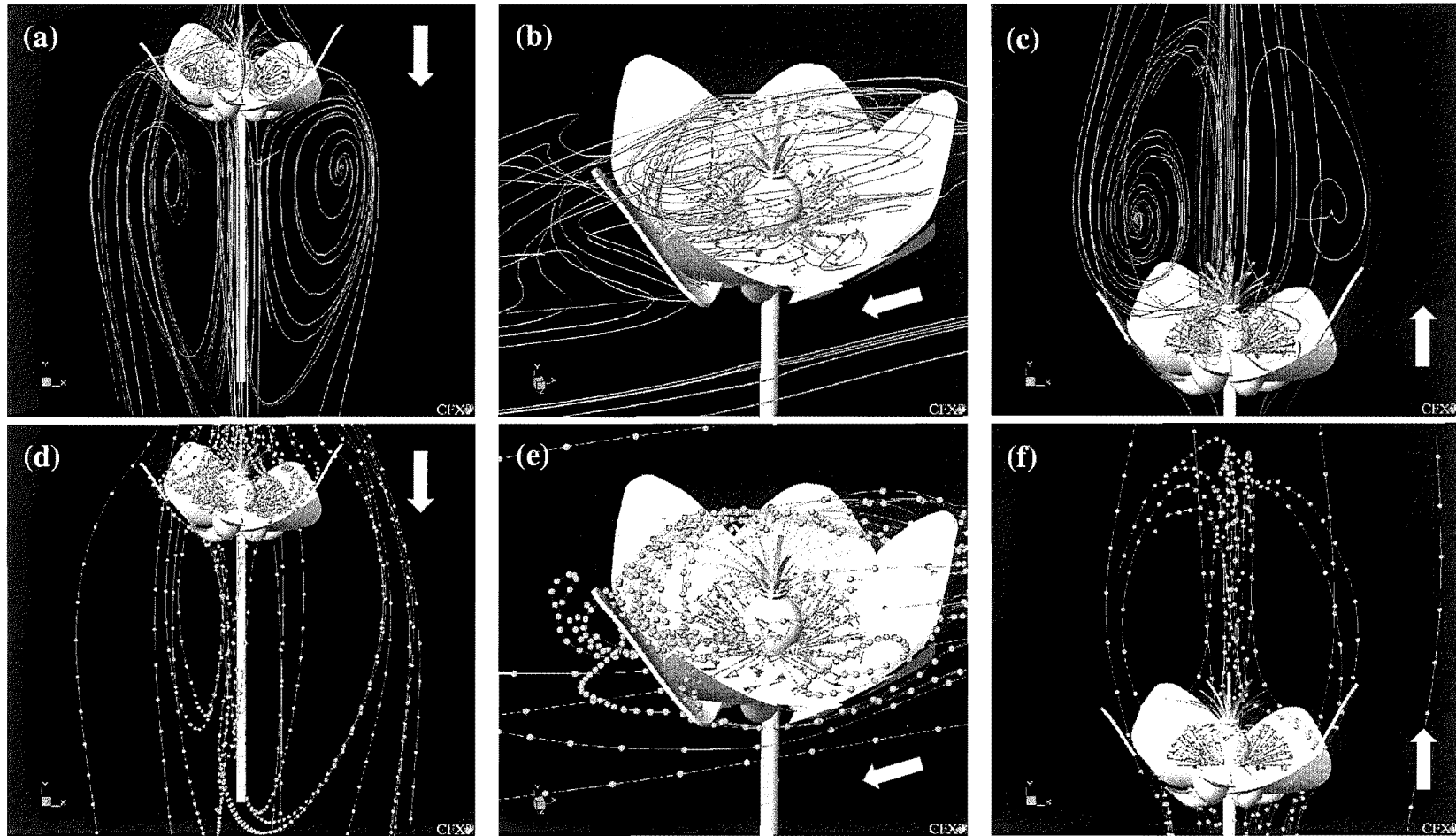
Fig. 3-20: (a), (b) and (c) are the predicted air flow field around a single half-open flower under 1-m/s flow from the front, side and back respectively (as shown by the arrows). The corresponding calculated trajectories of a cloud of pollen are shown in (d), (e) and (f). The separation between pollen along a trajectory is 0.01 s.
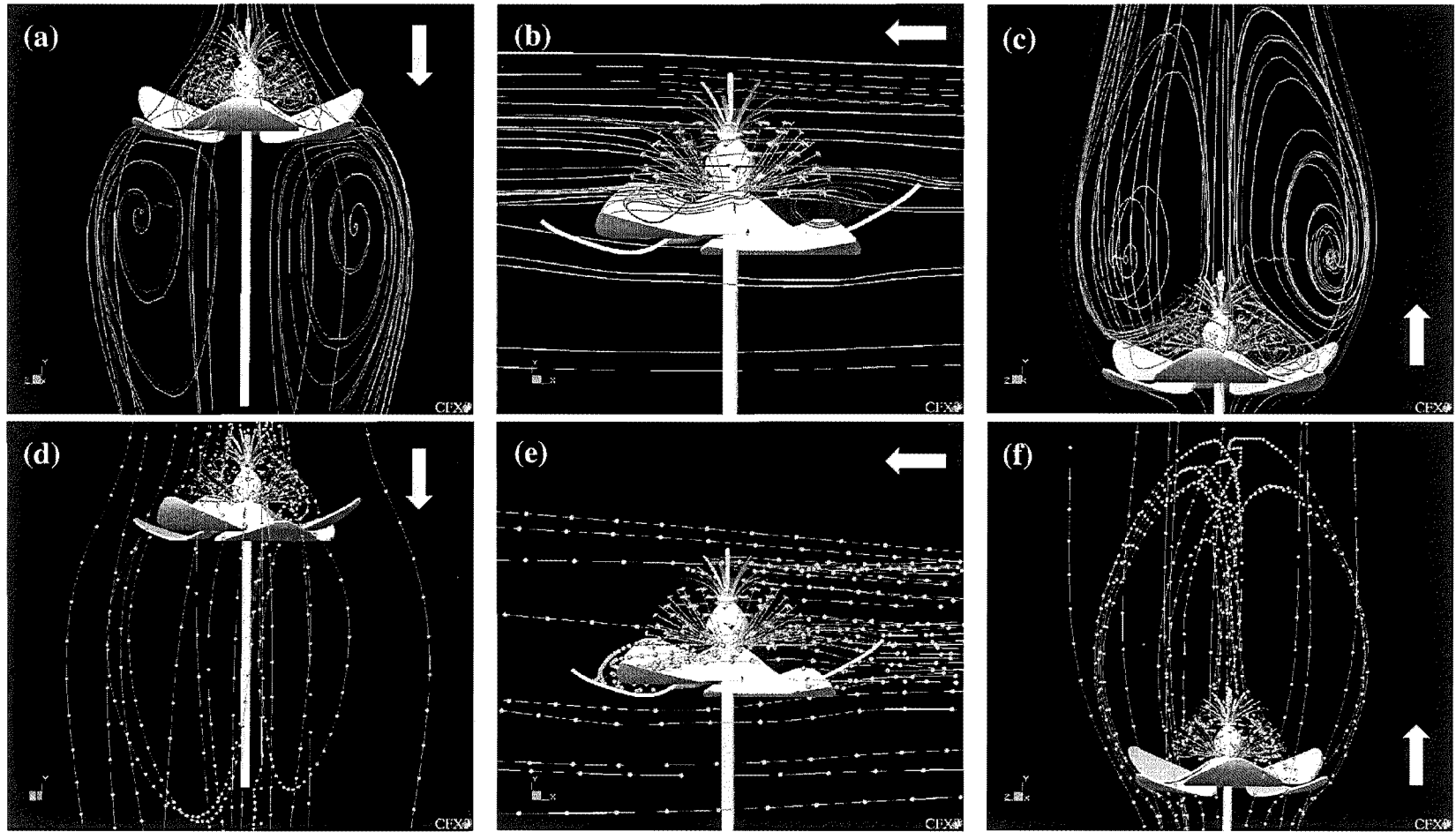
Fig. 3-21: (a), (b) and (c) are the predicted air flow field around a single full-open flower under 1-m/s flow from the front, side and back respectively (as shown by the arrows). The corresponding calculated trajectories of a cloud of pollen are shown in (d), (e) and (f). The separation between pollen along a trajectory is 0.01 s.
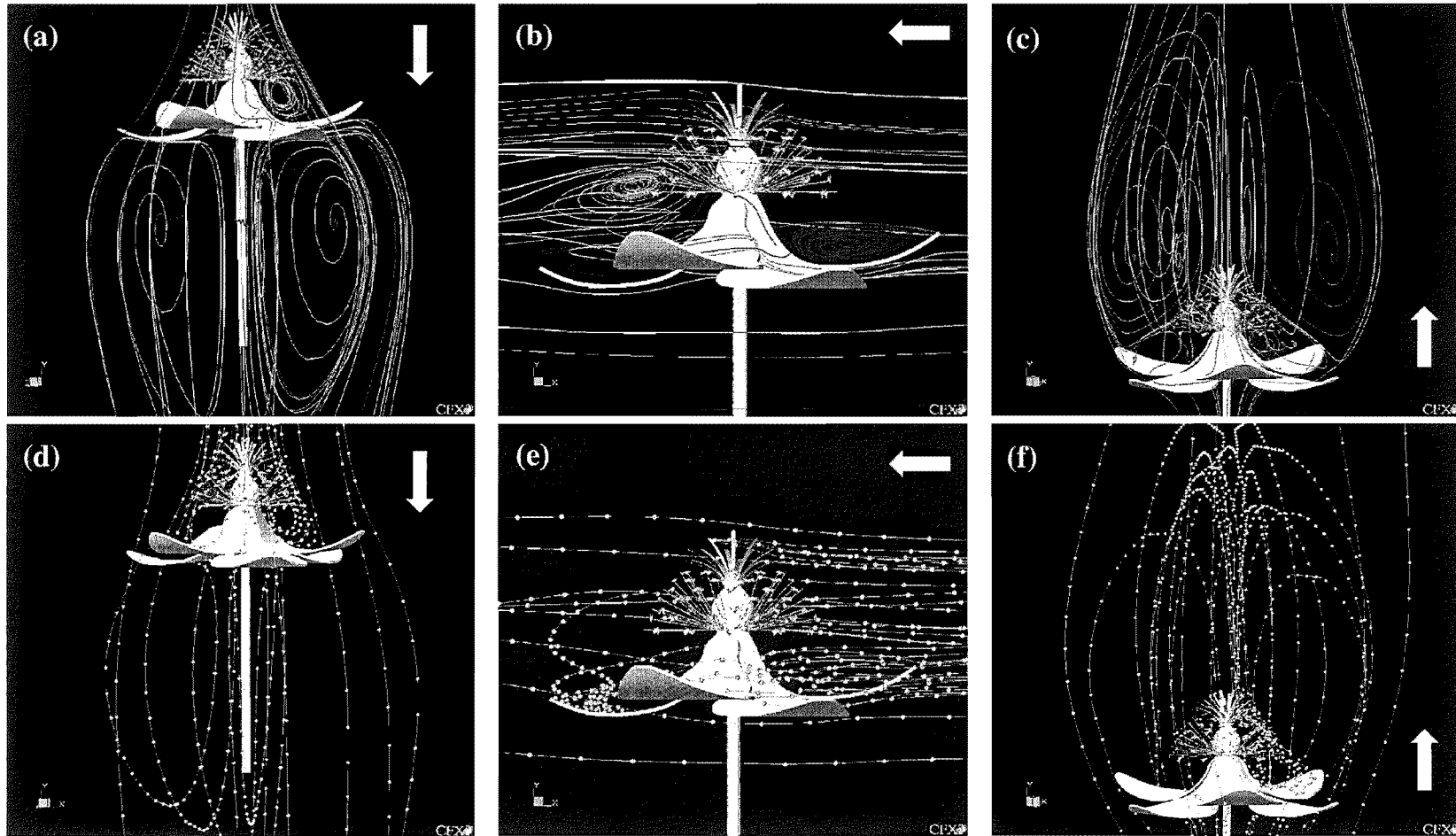
Fig. 3-22: (a), (b) and (c) are the predicted air flow field around a single flip-back flower under 1-m/s flow from the front, side and back respectively (as shown by the arrows). The corresponding calculated trajectories of a cloud of pollen are shown in (d), (e) and (f). The separation between pollen along a trajectory is 0.01 s.

Full-open and flip-back flowers

Even when the bud has developed further to the full-open and flip-back states, the frontal and back flows still give similar features i.e. large downwind wakes and small eddies around the ovary (see Fig. 3-13c, d; 3-14c, d; 3-21a, c; 3-22a, c). Under a frontal flow, the large downstream wakes stretch up to 1.5 and 1.6 flower diameters away from the flower centre for the full-open and flip-back flowers respectively. This stretches to 1.5 flower diameters for both flowers in the back flow.

For both flow directions, the currents carrying the pollen grains sweep past the stigma almost perpendicularly to maximize the inertial collision (Fig. 3-21d, f; 3-22d, f). Likewise, the large downstream wakes generated in the back flow are solely responsible for bringing the pollen grains to the stigma.

In contrast to a half-open bud, the influence of petals is not so profound when the full-open and flip-back flowers are subjected to a tangential flow (Fig. 3-21b, 3-22b). The windward petals induce vortices just below the filament bushes (see also Fig. 3-15f, h). The simulation results give an expectation (derived from the vortex shedding observed in the smoke visualization) that in real flow, there will be eddies being shed off from the leeward part of the filament bushes and the ovary. The style bush allows the air to penetrate without significant distortion to the flow. As can be seen in Fig. 3-21e and 3-22e, most of the pollen grains are expected to be captured by the stigma located at the windward, distal and central parts of the bush.

Bold flower

After the falloff of petals, the sepals take over the limited function of the petals in generating the larger downstream wakes and the smaller vortices near the ovary (Fig. 3-13a; 3-19a, c). Due to the smaller span compared to the petals, the downstream wakes do not stretch as far. While the downstream wakes created by the sepals fail to deliver back to the stigma in the frontal flow, they efficiently channel the pollen grains to the stigma in the back flow (Fig. 3-19d, f).

The side flow pattern (Fig. 3-15b, 3-19b) shows resemblance to that of the full-open and flip-back flowers except for the flow disturbance by the petals. Similarly, the pollen grains are mostly captured by the windward, distal and central stigma (Fig. 3-19e).

3-13

Pollen capture efficacy of stigma

The pollen collection efficiencies of stigma are calculated based on the total number of pollen injected. The pollen are injected randomly within a circular cross sectional area of 3.42×10^{-3} m^2 i.e. projected area of flower. These efficiencies are then halved because a pair of stigmatic surfaces is defined at the end of each style. The averaging here gives a conservative prediction of pollen collection efficiency.

The influences of three factors are looked at here:

(i)   the morphology of the bud or the degree of the petal opening, as shown in Fig. 3-23;

(ii)   the approach flow directions, as shown in Fig. 3-24; and

(iii) the wind velocity, as shown in both Fig. 3-23 and 3-24.

Irrespective of the petal opening state, the stigma are expected to capture the most pollen grains in a frontal flow (Fig. 3-24). This is followed by the side flow and then the back, with the exception for a half-open flower (Fig. 3-24b). The drop in efficiency is significant when the approaching wind direction varies from the front to the side and then to the back.

In a front approaching pollen cloud, the predicted efficiency rises as the petals flip backwards and fall off eventually (Fig. 3-23a). The gain in efficiency however declines with the increasing wind speed and appears to level off beyond 3 m/s.

For the side flow, except for a half-open flower whose petals are shielding the stigma, the stigma of all flowers are found to give similar pollen collection efficiency (Fig. 3-23b). In the absence of petal shielding, the bold, full-open and flip-back flowers receive same exposure to a side flow, as shown the velocity profiles across the centre of respective style bush in Fig. 3-17. The petal shielding on a half-open flower greatly limits the pollen from reaching the stigma. There is no improvement in collection efficiency above 2 m/s.

The importance of petals in deflecting the pollen grains back to the stigma in a back flow can be seen in Fig. 3-23c. More pollen grains are deposited on stigma as the corolla expands outwards. The deposition is the worst in the absence of petals i.e. on a

3-14

(a) Front flow

(b) Side flow

(c) Back flow

—○— Flip-back —■— Half-open —△— Bold —✕— Full-open
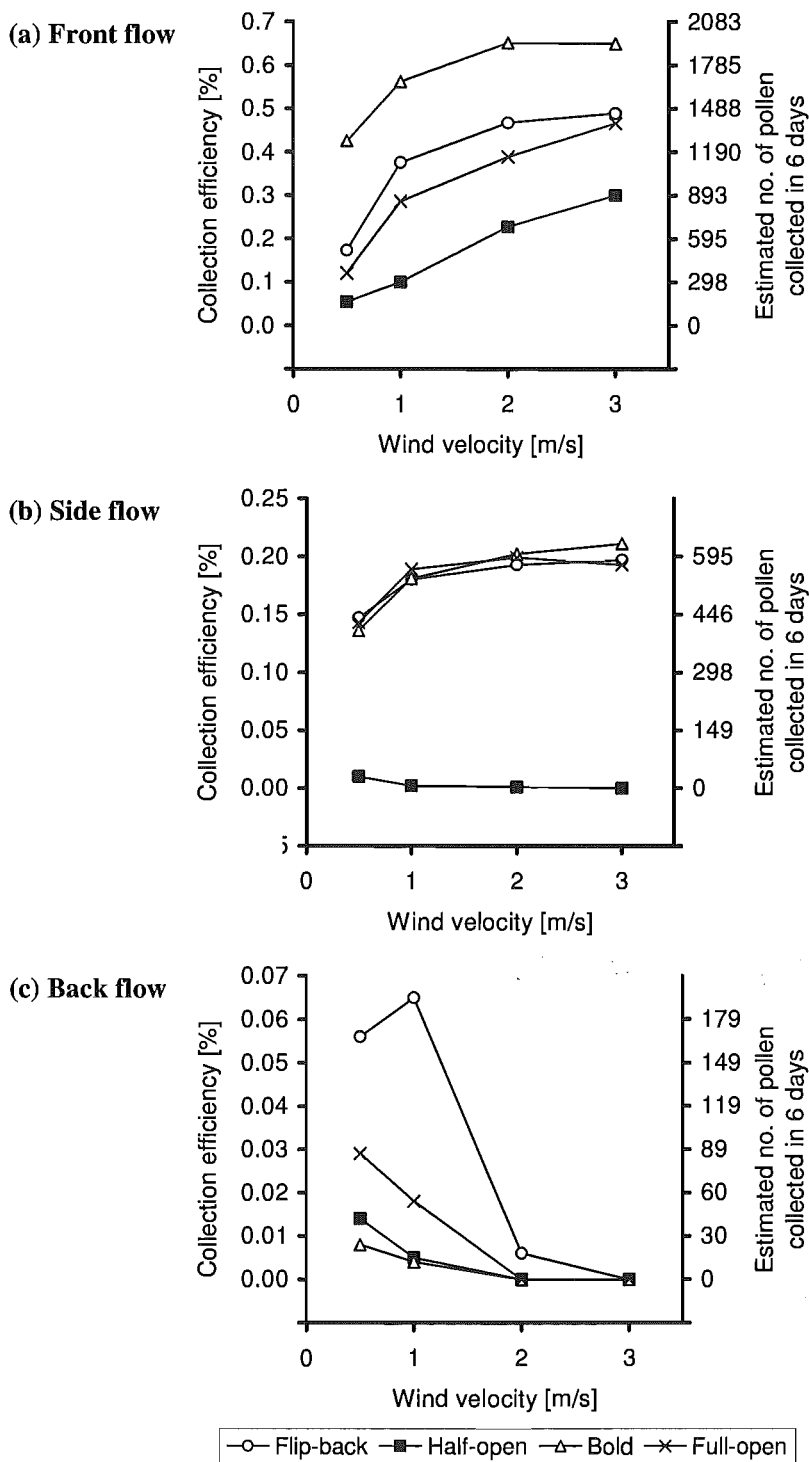
Fig. 3-23: The predicted pollen collection efficiency by stigma of flowers with four different bud openings when subjected to (a) front, (b) side and (c) back flow. Pollen collected in 6 days is based on a constant flux of 14.5×10^6 pollen/m^2/day.
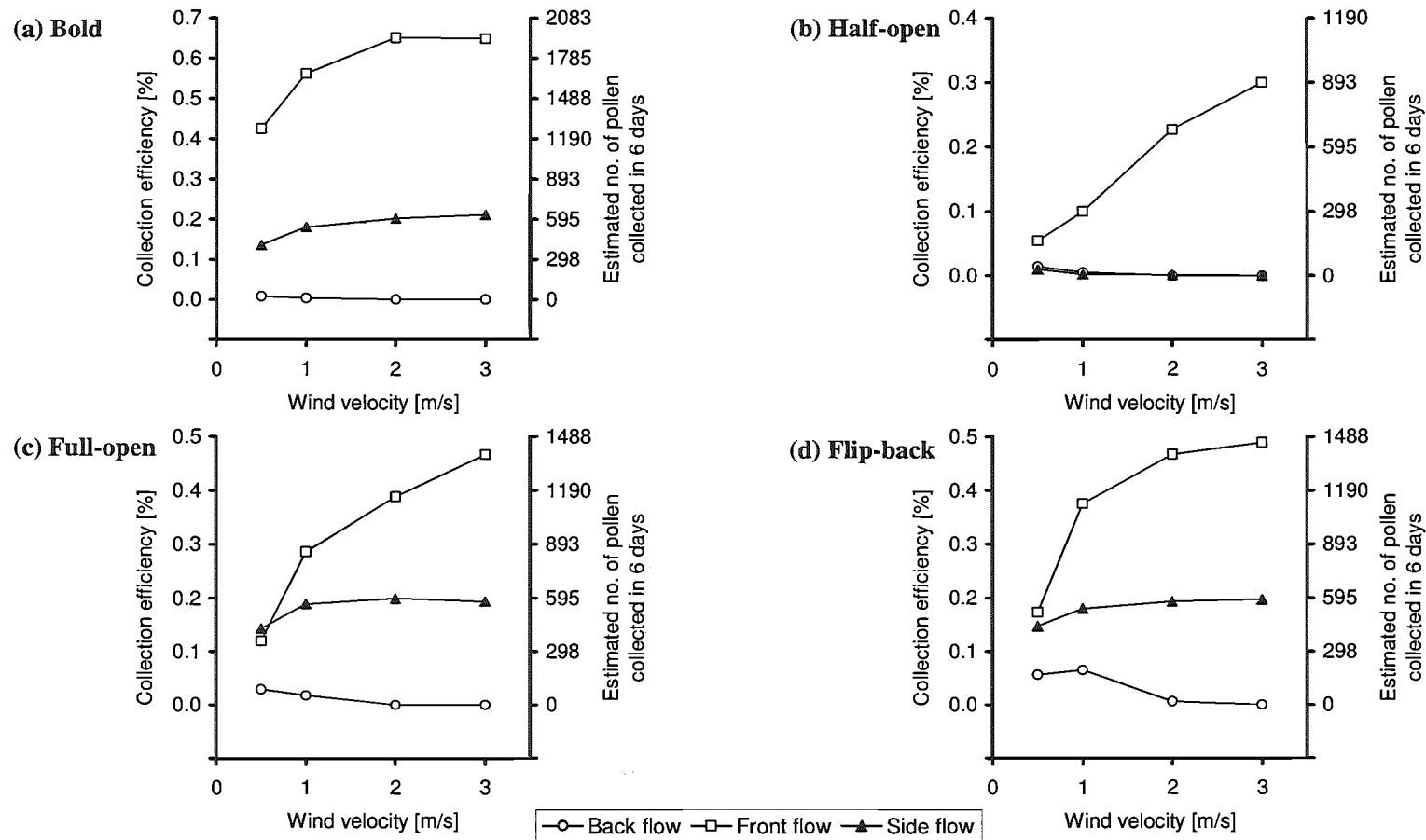
Fig. 3-24: The predicted pollen capture efficiency by the stigma of a (a) bold, (b) half-open, (c) full-open, (d) flip-back flower in the wind from the front, side and back. Pollen collected in 6 days is based on a constant flux of 14.5×10^6 pollen/m²/day.

bold flower. The computed collection efficiency deteriorates with the stronger wind where nearly no deposition is anticipated beyond 2 m/s. The simulations predict a peak in collection efficiency by a flip-back flower around 1 m/s.

The number of windborne pollen collected by inertial impaction over 6 days[4] under the maximum pollen loading flux of 14.5×10^6 pollen/m^2/day reported by Malaboeuf et al (1997) is estimated using Equation 3-3. This is plotted on the secondary y-axis in Fig. 3-23 and 3-24.

$$N_p = 14.5 \times 10^6 \text{ pollen/m}^2\text{/day} \times A_f \times \eta_f \times 6 \text{ days} \qquad \text{Equation 3-3}$$

Where N_p = number of pollen collected, A_f = projected area of flower = 3.42×10^{-3} m^2, and η_f = pollen collection efficiency.

Even under the most favourable situation i.e. exposed to a pollen cloud from the front and at the maximum reported flux and wind speed of 3 m/s for 6 continuous days, no more than 2000 pollen grains are predicted to be captured. This is close to but still below the required number of 2300 for to produce a minimum export size of 70 g (refer section 1.3). In a way, this agrees with the field observations by other researchers (see section 1.4) that wind pollination alone is simply not enough to produce the exportable crop.

The author wishes to note that constant pollen flux is used here because there is no concentration data available in the literature. There is a lack of understanding of the pollen shedding mechanism. Here, the use of constant flux assumes that the mechanism of pollen dispersal from the anthers is flexible and easily accomplished by the wind. In other words, the pollen flux in the orchard is limited by the rate of pollen supply. Like the female flowers, the blossom of male flowers is uneven during the flowering season. It starts off gradually and then reaches a peak before dropping off. Maximum flux is chosen to give an estimation of pollen deposition on the high end. From the calculations above, it can be seen that the pollen delivered to the stigma by wind is not

---

[4] Length of stigma receptive period reported by Gonzalez et al (1995a, 1995b, 1997). See more details in section 1.3.

even sufficient at maximum flux. This further implies that the female flowers are unlikely to be adequately fertilized with just the wind-borne pollen in the orchard.

3.7. Discussion

Air and pollen flow patterns

Although the draft in the vine is likely to have larger eddies than the flower itself, the simulated flow fields based on a uniform incoming flow are not expected to be significantly different to the actual ones. The simulated pollen grains generally follow the course of the air currents. As expected, slight deviation exists due to the drag forces and turbulent dispersions.

The back flow past a half-open flower develops a flow pattern similar to the aerosol visualization test carried out by Ferguson & Pusch (1991) i.e. there were non-symmetrical vortices immediately downstream of the stigma-style bush.

The simulations indicate that the separation points of the large leeward vortices are at the edges of petal (e.g. see Fig. 3-13c and 3-14c). This is similar to a two-dimensional flow past a thin flat plate normal to the freestream where the wakes behind the plate are initiated by the production of circulation at the tips of the plate (Koumoutsakos & Shiels, 1996; Luchini & Tognaccini, 2002).

Based on the experimental observations, Taylor (1987) and Hongladarom (1988) reported that the airstream was directed to pass through the stigma bush of a kiwifruit flower, which maximized the pollen-stigma contact. This agrees with the simulated flow fields. For examples, in the back flow (e.g. Fig. 3-14b), the deflected airstream converges centrally onto the style bush; and in both the frontal and back flows (e.g. Fig. 3-13c and 3-14c), the incoming flow is almost normal to the stigma, which is considered to maximize the collection of pollen. In other words, the shape of the style bush gives an efficient aerodynamic filtration

The simulations demonstrate that the structure of the kiwifruit flower creates an aerodynamic pattern that favours the pollen deposition onto reproductive stigma. The

channelling of airstream to the reproductive organs also happens commonly on other plants. Niklas (1982, 1984, 1985a, 1985b, 1987b) and Niklas & Paw U (1983) reported that the structure of female pinecones are naturally engineered to channel the pollen grains to the receptive micropyles which are buried at the inner base of the scales. Niklas & Buchmann (1986), Niklas & Kerchner (1986) and Niklas *et al* (1986) studied the behaviour of airborne pollen around the ovules of sympatric species of *Ephedra* and found that the trajectories of the pollen grains were focussed to collide with pollination droplets. This is similar to the convergence of pollen flow to the stigma where the exudates (equivalent to pollination droplets) are secreted.

In addition, the generation of downstream eddies that help to deflect the pollen backward for impaction on the reproductive components is not limited to the kiwifruit flowers. This has been found to occur on the female pinecones (Niklas, 1982, 1984, 1985a, 1985b, 1987b; Niklas & Paw U, 1982, 1983), *Ephedra* species (Niklas & Buchmann, 1987; Niklas *et al*, 1986), *Taxus cuspidate* ovulate shoot (Niklas, 1985c), *Cyclad megastrobili* (Niklas & Norstog, 1984), *Pistacia vera* (Niklas & Buchmann, 1988), carpellate flowers of jojoba plant (Niklas & Buchmann, 1985) and grass spikelets (Niklas, 1985b).

The localized regions of turbulent flow within the corolla of a half-open flower (Fig. 3-15c, d) is very similar to the flow visualized by Niklas (1981a, 1981b, 1983a, 1985b) on the models of early seed plant ovules and cupules. The pollen chamber or salphinx at the middle are surrounded by the preintegumentary lobes which leave only an opening on the top for pollen to enter. The localization of airflow turbulence by the lobes greatly reduces the velocity and hence forms a sink for airborne pollen to be directed towards to the pollen chamber. Another similar example is seen inside the spathe of the skunk cabbage, *Symplocarpus foetidus*, which has a cup-like shape and asymmetrical opening margins i.e. resembling a conch-shell (Camazine & Niklas, 1984). The airflow is deflected into the spathe, creating a cyclonic vortex around the spadix which has both stigma and anthers on it. This cyclonic flow inside the spathe helps to disperse the pollen grains from the anthers onto the stigma.

Experimental validations of flow pattern using the smoke visualization have been carried out in this work and these are described in Chapter 4.

Pollen capture efficacy of stigma

The frontal collection efficiency improves with the increasing deflection of petals up to the loss of all petals (Fig. 3-23). The velocity contour plots in Fig. 3-13b to d show that the presence of petals leads to a low velocity airspace around the ovary under a frontal flow. This resembles the direct impingement of an incoming flow onto a surface where a near-stagnant region is created at the core of the impingement and the flow is directed to the sides (Baughn & Shimizu, 1989; Lytle & Webb, 1994). This near-stagnant region in the vicinity of the ovary causes the incoming pollen to be diverted away to the sides and thus reducing the uptake of pollen by the stigma. The stagnation effect is most pronounced at the half-opening stage, which has a cup shape that expeditiously creates a large near-stagnant airflow space within the petals enclosure (Fig. 3-13b). It must however be noted that when the wind direction has switched to the side, this large near-stagnant airflow space will act as a pollen sink. Fig. 3-16 shows that as the petals unfold and fall off, the velocity approaching the centre of style bush starts to build up. Higher approaching velocity here represents better chances of pollen collection by inertial impaction.

The petals exist only for only 3 out of 7 days of the stigma receptive period (can be up to 9 days; see section 1.3). The simulations of frontal pollen collection here may offer a reason as to why the petals fall off so quickly, that is the petals are actually impeding the pollen collection efficiency. Even though the petals are important in the back flow, the overall pollen collection in the back flow is significantly less compared to the frontal and side flows (see Fig. 3-23). However, it must be noted that the stigma-style wither and shrink with aging. The morphological change in the stigma is not reflected in the simulation models, but the results are still expected to serve as a useful explanation.

The simulations suggest that the collection efficiency does not improve at higher wind speed. This may not be true on the real flowers due to the assumptions and limitations in the flower models. For instance, the petals are assumed to remain rigid up to 3 m/s in the simulations. Ferguson & Pusch (1991) reported that unpollinated flowers increase the exposure of the stigma to the airstream by shedding their petals rapidly in strong wind. The wind speed was not stated by them but they suggested this would promote the pollen capture through impaction.

The flower models are stationary in the simulation domains. However in the orchards, the random undulations of flowers had been observed in the occasional strong gust of wind. But the threshold wind speed that onsets the movements had not been determined experimentally. It is possible that the undulation of individual flowers may increase the pollen deposition by the same 'scrubbing' mechanisms observed on the pinecones (Niklas, 1987b) and grass panicles (Niklas, 1985a, 1985b, 1987b, 1992). The pinecones, grown at the tip of the branch, were noticed to undulate in a nearly circular path. This enables the cone to harvest airborne pollen from various levels of the air. The harmonic oscillatory motion of grass panicles allows the flowers to intercept the pollen moving in the vicinity, resulting in an increased pollen uptake. It also varies the approach angle, giving more coverage of the stigma bush.

The predicted pollen collection by this modelling takes into account only the small scale airflow patterns generated by the floral parts, but not the large scale aerodynamic patterns generated by the vegetative parts near the flowers, such as the foliage leaves. Niklas & Buchmann (1985) found that the foliage leaves of a jojoba plant (*Simmondsia chinensis*) step-up the pollen collection on the stigma by creating an airborne pollen 'shower' towards the carpellate flowers. Niklas & Buchmann (1985) also found that the individual carpellate flowers deflect the pollen grains towards the more distal downwind flowers. Since the layout of kiwifruit flowers is similar to those of a jojoba plant, the actual collection efficiency may be facilitated by the presence of the non-receptive vegetative parts and adjacent flowers that help in concentrating and conveying the pollen to the stigma.

The influence of petals or corolla shape in directing the pollen flow to the stigma has an implication on the experimental method used by Clinch & Heath (1985) and Gonzalez *et al* (1998) to assess the effectiveness of wind pollination, where the flowers were mutilated (i.e. de-petalled) in order to make the flowers unattractive to insects. The mutilation must be practised cautiously as the simulations show that it will alter the air current around the flower and affect the collection of wind-borne pollen.

Pollen deposition pattern on the whole flower
The percentages of injected pollen that are deposited on other parts of the flower are plotted in Fig. 3-25 to 3-27 for the flow directions from the front, side and back

respectively. The values for the 84 anthers and filaments in the model have been adjusted proportionally to take into account of the average of 183 on a real flower.

Like the stigma, the pollen depositions on other non-receptive floral parts depend on the wind directions, bud opening states and wind velocities. Except for the bold flower, the petals are predicted to collect the most and significantly more than other floral parts (~ 27 times more than the stigma by median). In the absence of petals, the filaments and the anthers of a bold flower will accumulate the most captured windborne pollen (~ 6 times more than the stigma on median). Due to the larger exposed areas, the styles are found to pick up ~ 5 times more pollen than the stigma on median.

In this work, the coefficient of restitution of pollen is assumed to be zero on every surface of the flower so that there is no rebound upon collision. The coefficient of restitution is the ratio of the immediate particle velocity prior to and after the impingement. This assumption is expected to be valid for the wet stigma and styles, but is not certain for the other floral surfaces as there is a lack of experimental data.

Paw U (1983) studied the rebound of 20- to 40-μm biological particles (Lycopodium spores and Ragweed pollen) on natural surfaces (the leaves of American elm and Tulip poplar). The critical rebound speed (impingement velocity at which 50 % contacted particles had rebounded) ranged from 0.68 to 5.3 m/s. Similar to the behaviour of the non-biological particles on artificial surfaces (Brach & Dunn, 1992, 1995, 1998; Dunn et al, 1995; John, 1995; Li et al, 1999), the coefficient of restitution initially increased with the increasing impingement velocity and then became constant above certain velocities, which were around 1.5 to 2 m/s. The average coefficients of restitution were 0.636 and 0.514 for the Lycopodium spores and Ragweed pollen respectively. Aylor & Ferrandino (1985) studied the same particles on the wheat stem and found a critical rebound speed range of 0.59 to 3.5 m/s.

Judging from these reported critical rebound speeds, it is likely that the pollen will remain on the unreceptive flower surfaces within the velocity range used in the simulations. The pollen spraying experiments in the laboratory (see section 6.1) have detected the deposition of male pollen on the petals and the filaments. However, it is possible that the pollen may be re-entrained and re-dispersed by orchard wind (see
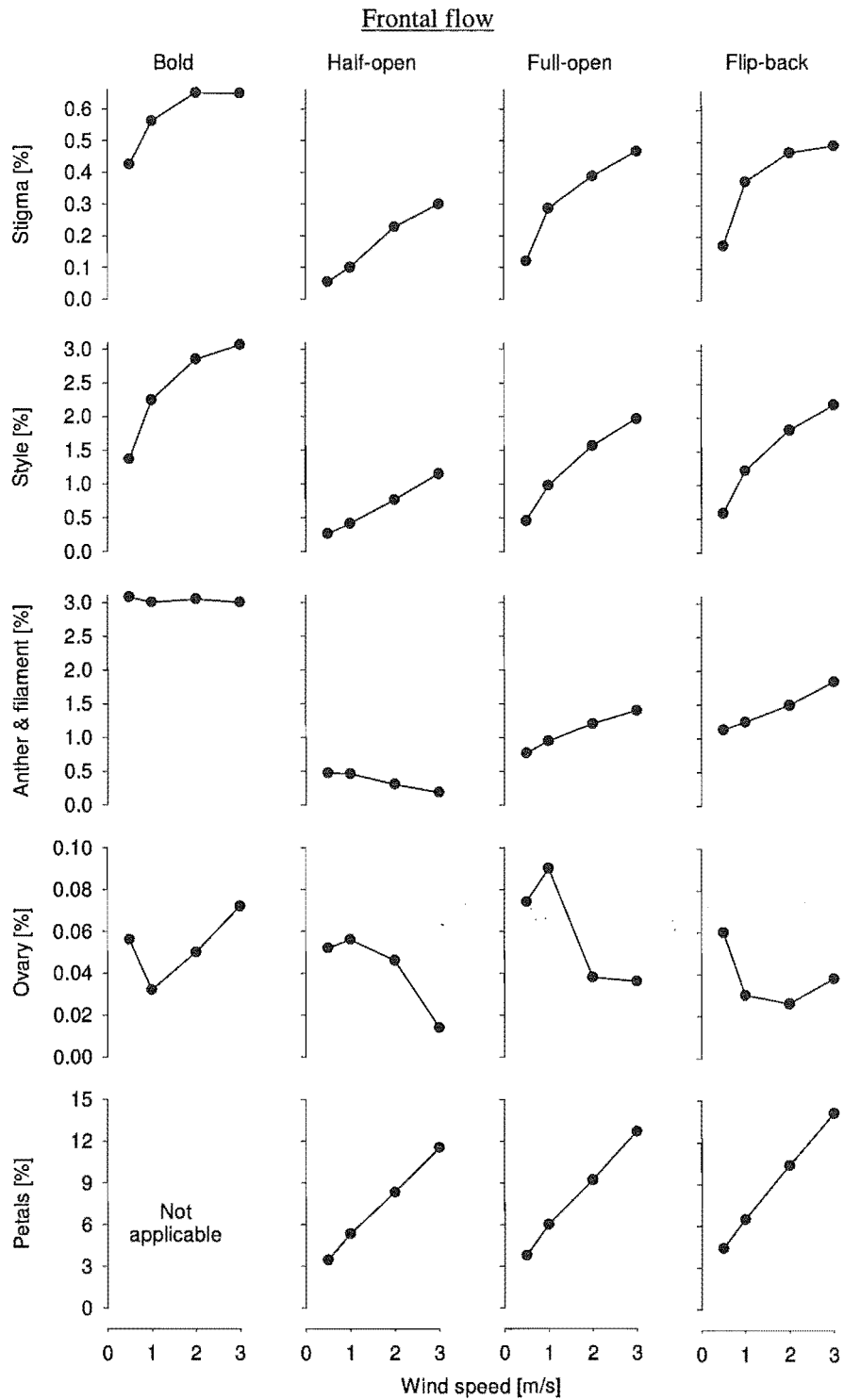
Fig 3-25: Percentage of injected pollen that are deposited on different parts of the flower in the simulation. Each flower, with different bud openings, is approached by a frontal flow of different velocities.
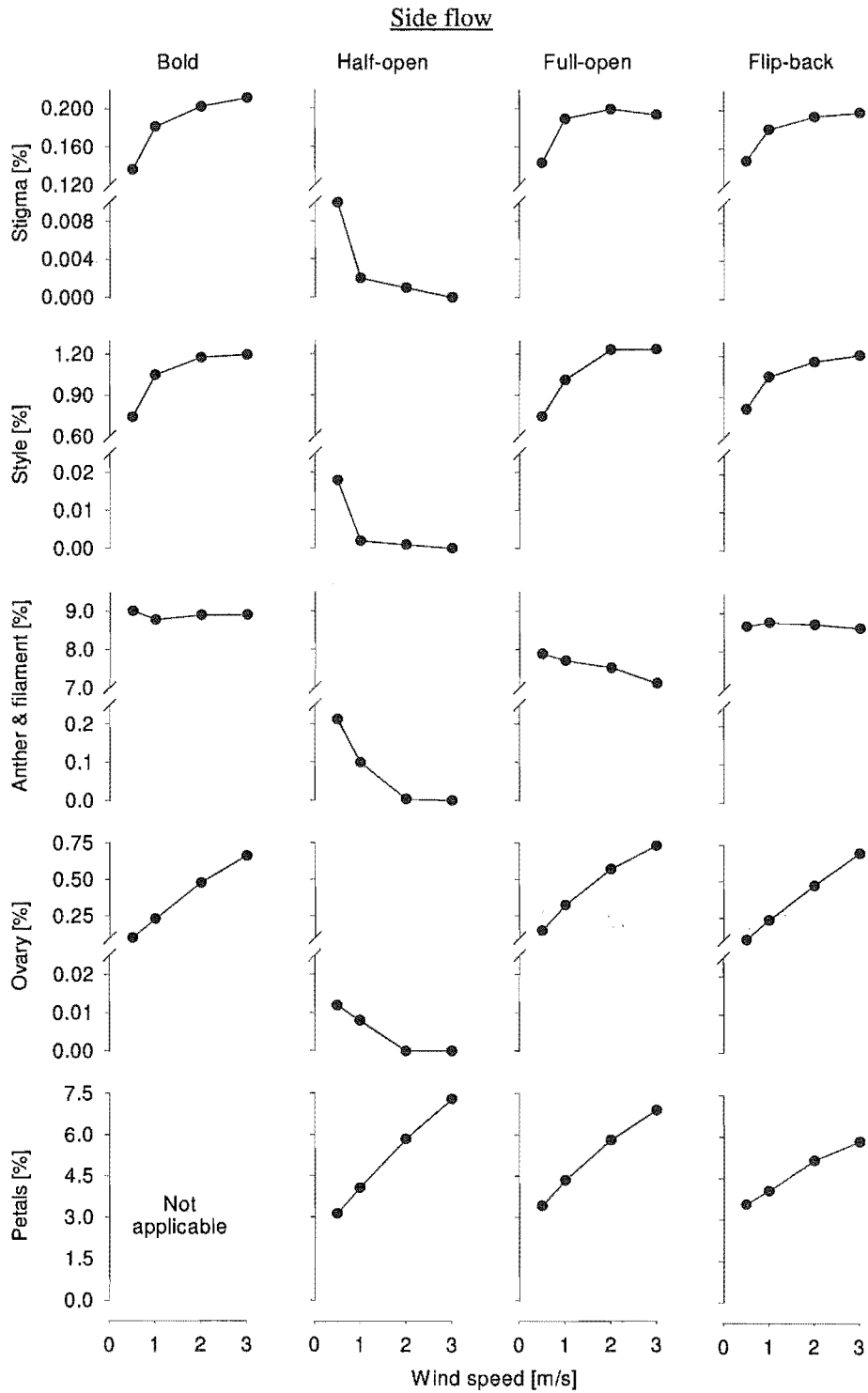
Fig 3-26: Percentage of injected pollen that are deposited on different parts of the flower in the simulation. Each flower, with different bud openings, is approached by a side flow of different velocities.
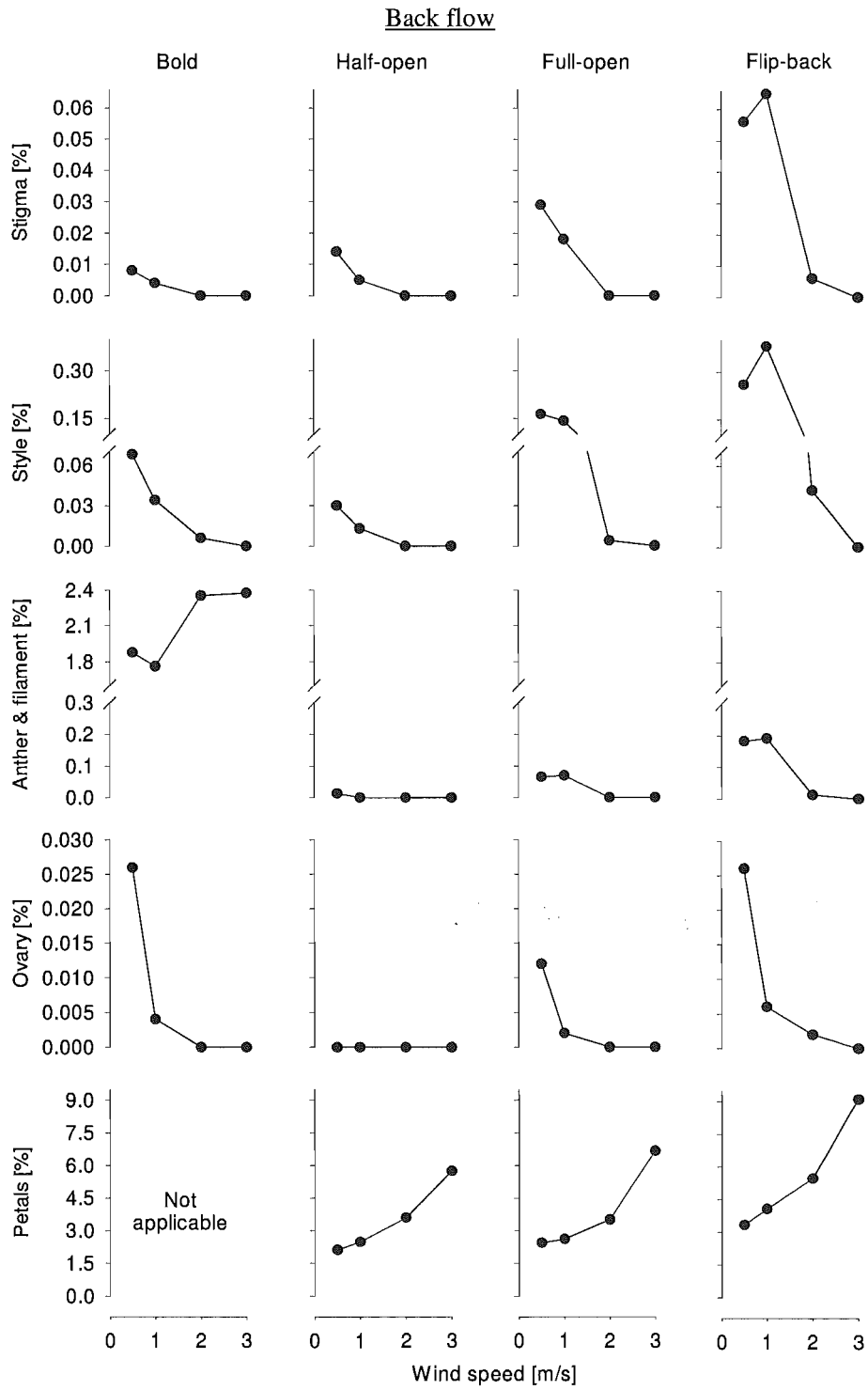
Fig 3-27: Percentage of injected pollen that are deposited on different parts of the flower in the simulation. Each flower, with different bud openings, is approached by a back flow of different velocities.

section 1.6), particularly from the petals whose large surfaces have gathered significantly more pollen than the stigma and where the flower is being shaken by the wind. Pomeroy (1988) pointed out that it is possible that honey bees can help to transfer the pollen from these so-called intermediate locations, such as the stamenoids[5] of the female flowers, to the stigma.

As one means to improve the prediction of pollen deposition, it is recommended to carry out an impaction analysis of pollen on different surfaces of a kiwifruit flower. This can be done by using methods used by Dunn *et al* (1996), Li *et al* (1999), *Poppe et al* (2000), Wall *et al* (1990).

In relation to the wind pollination

This section aims to seek an answer from the simulations for the question of whether kiwifruit is a wind-pollinated plant. The first clue can be deduced from the original habitat in China, where the vines had been seen to climb more than 7 m up to the tops of forest trees (Ferguson, 1990a). This not only gives the plant access to the light but also the wind.

Craig & Stewart (1988a, b) analysed the architecture or floral features of the kiwifruit flowers in an attempt to distinguish whether the wind or the bees are the likely pollen vectors. Several morphological evidences were brought up to support that the kiwifruit is an anemophilous[6] plant, such as the pollen grains are not coated with pollenkitt; high pollen:ovule ratio of 2000:1; the flowers are pendulous; the stigma are large and multi-branched; and the stigma are receptive up to 9 days compared to most of the insect-pollinated stigmas which are receptive for 2-3 days. In addition, before the male flowers are fully open to allow the physical access to bees, half of the pollen has already been released.

In this work, the predicted pollen trajectories and collection show that the kiwifruit flowers are efficient in capturing the windborne pollen. This ties in with the view by Niklas (1987b) that many wind-pollinated plants are aerodynamically designed to filter larger amounts of pollen from the air.

---

[5] Pollenless stamens.
[6] Wind-pollinated.

As discussed above, the results of the simulation may explain why the kiwifruit flowers lose the petals so quickly. The natural de-petalling significantly increases the pollen collection efficiency in the frontal flow. The field study in Chapter 7 also shows that the stigma gain stickiness with their aging. The gain in stickiness compliments well with the gain in collection efficiency. This can be viewed as an adaptation to wind pollination.

In short, the theoretical studies on the windborne pollen capture by the flowers at different flower openings indicate that kiwifruit flowers are adapted to wind pollination. There is no doubt that bees are important pollen vectors i.e. both wind and bees play significant roles in kiwifruit pollination. But as mentioned before in section 1.4, the contribution from wind pollination is significantly impeded by the layout of commercial orchards.

Recommendations for future work

The morphological study here can be extended to examine the influence of flower size on the pollination efficiency. The results may be useful for breeders to target a desired flower size of the new cultivars (personal communication with Karl Niklas, 2004).

For fundamental scientific interest, the simulations can be carried out for pollen of different shapes, size and density, in order to see whether the kiwifruit flowers also selectively captured the conspecific pollen as in other plants such as the pinecones (Linder & Midgley, 1996; Niklas, 1985a, 1987b, 1992; Niklas & Paw U, 1983) and the *Ephedra* species (Buchmann *et al*, 1989; Niklas & Buchmann, 1987; Niklas & Kerchner, 1986). This may be of interest as many competing flowers (see section 1.5) are commonly found close to the commercial kiwifruit orchards. This study will require the collection of morphometric characteristics of the pollen from the competing flowers.

Another field that is not well studied so far is the pollen shedding mechanism on the male anthers (personal communication with Karl Niklas, 2004). The long and slim filaments resemble the grass stem, which has been found to vibrate in the wind during the pollination (Niklas, 1987a, 1992). With the addition of moving mesh capability in the CFD program, it is now possible to study the function of the filament vibration in the pollen release.

CHAPTER 4: FLOW VALIDATION IN WIND TUNNEL

The last chapter presents the simulated air flow fields around a single kiwifruit flower subjected to a uniform air flow. Here, the experimental validations are carried out using the classical smoke visualization method in a wind tunnel.

4.1. Equipment layout

Fig. 4-1 shows the smoke injection system, camera and lighting setup around a glass wind tunnel. A smoke rake is placed inside the wind tunnel which has a cross section of 215 × 340 mm. The blower air supply can attain a superficial velocity of up to 2.5 m/s. The velocity was measured using a pitot tube and controlled using a butterfly valve. The background of the test section is either covered with black cardboard or painted with non-glossy black paint in order to minimize undesirable light reflection.

Smoke generation and injection

There are different methods of generating smoke reported in the literature i.e. from the reaction between titanium chloride ($TiCl_4$) and moisture, heating oil-coated wire giving smoke (smoke-wire), vaporization of kerosene and paraffin, and burning of cigarette, pine wood, rotten wood and wheat straw (Merzkirch, 1987; Mueller, 1983a; Mueller, 1983b; Mueller et al, 1983). However, none of the methods is perfect. For example, smoke-wire requires complex electronic synchronization and the use of $TiCl_4$ produces toxic titanium dioxide (TiO_2). In this work, a commercial fog generator (DSE, model M-6000) that is fed with a commercial glycol + water fog juice is used to give a non-toxic white smoke of satisfactory optical reflectivity. A custom-made transparent perspex injector (ϕ 100 mm) transfers the white smoke to the smoke rake at a controlled and consistent rate.

The procedures of smoke injection are (with reference to Fig. 4-1):
1. First, unplug the rubber bung. Close V1 and V3 but leave V2 open.
2. Turn on the fog generator. The smoke will fill the injector when the piston is drawn backwards slowly.

3. After the filling, put the rubber bung on. Open V3 and V4 to introduce the dry compressed air that has been preset to the desired pressure and flow rate.

4. Close V2 and the pressurization will move the piston forwards at a constant rate. At the same time, open V1 so that the smoke is released to the smoke rake.

The use of a rubber bung provides a pressure relief and prevents a dangerous pressure build-up inside the injector. The piston disc is coated with Vaseline to give a smooth movement. After 3 continuous runs, the smoke rake is purged with dry compressed air in order to clear the condensed smoke.

Smoke rake

A smoke rake was designed to direct eleven smoke filaments towards the flower (see Fig. 4-2). This was achieved by using a row of eleven 20G stainless steel hyperdermic tubing of 1 mm ID. The horizontal dimensions of individual tubing are shown in Fig. 4-2. A movable spacer was used to keep each tube 10 mm apart. Its presence has not been found to alter the flow field.

The smoke comes in from the bottom and goes up a ϕ 6.5-mm (ID) stainless steel tube. It is then distributed evenly to each hyperdermic tubing. The top of the ϕ 6.5-mm (ID) stainless steel tube, which is needed to drain the condensed smoke, is plugged with a rubber bung. The whole tubing connection is attached to a locator block at the bottom which can be slide along a channel on the stainless steel base plate. This allows the vertical row of smoke filaments to be directed towards the centre of the flower.

A single fresh Gold or Green kiwifruit flower is placed on a flower rake which can be moved along another channel on the base plate. This enables the adjustment of flower-to-hyperdermic tubing distance.

Three flower rakes were made of stainless steel rods bent to the desired dimensions, in order to let the smoke approaches the flower from the front, side and back. The Green kiwifruit flower tests used an additional flower rake with a flexible rotating rod design, which allows the flower to be oriented at any 2D angle relative to the hyperdermic tubing row. The stem of a fresh flower was removed before the flower was spiked by the sharpened end of the rod from the sepal base, and mounted on it.
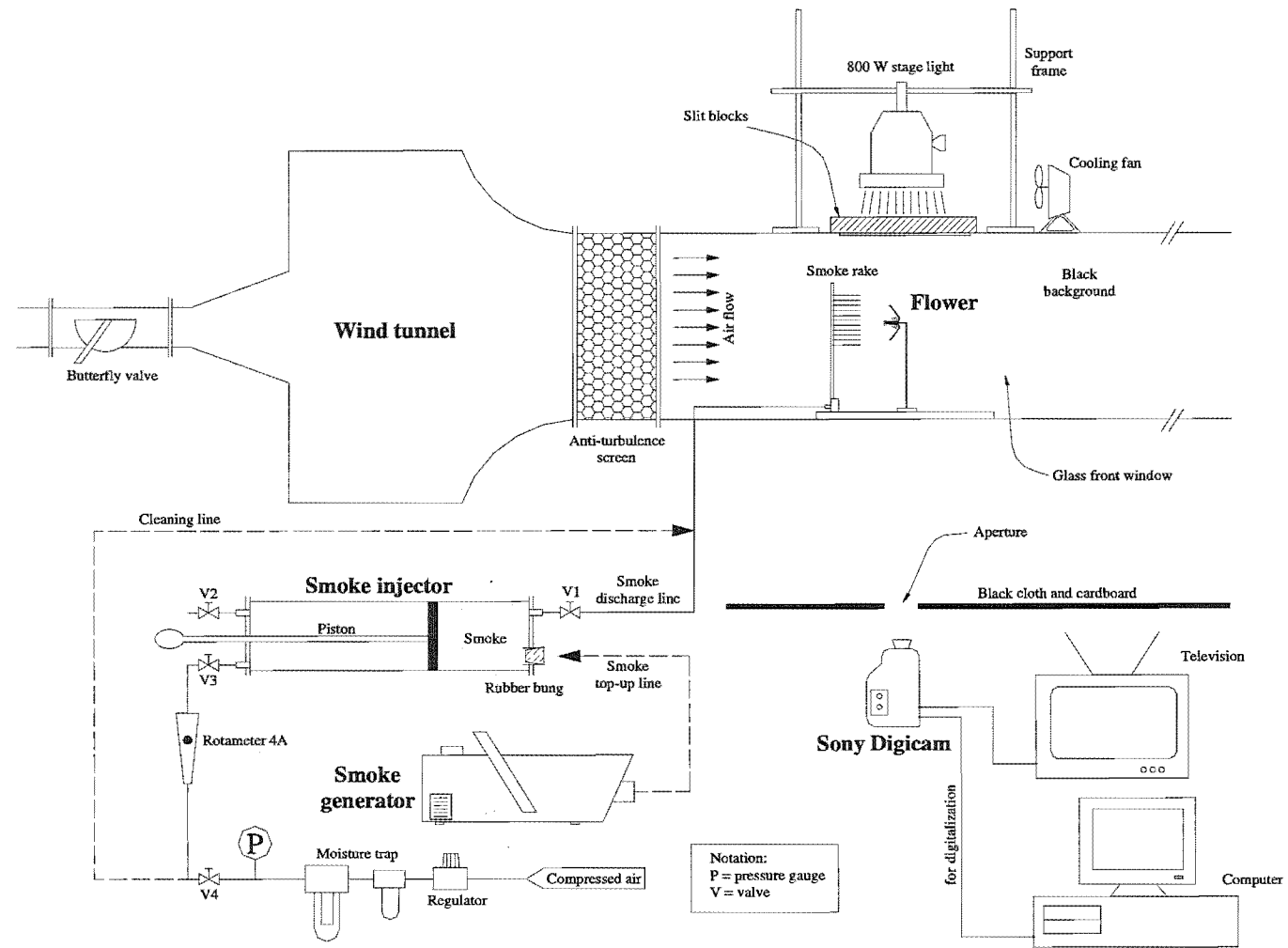
Fig. 4-1: Equipment layout for smoke visualization of air flow around a single kiwifruit flower in the wind tunnel.
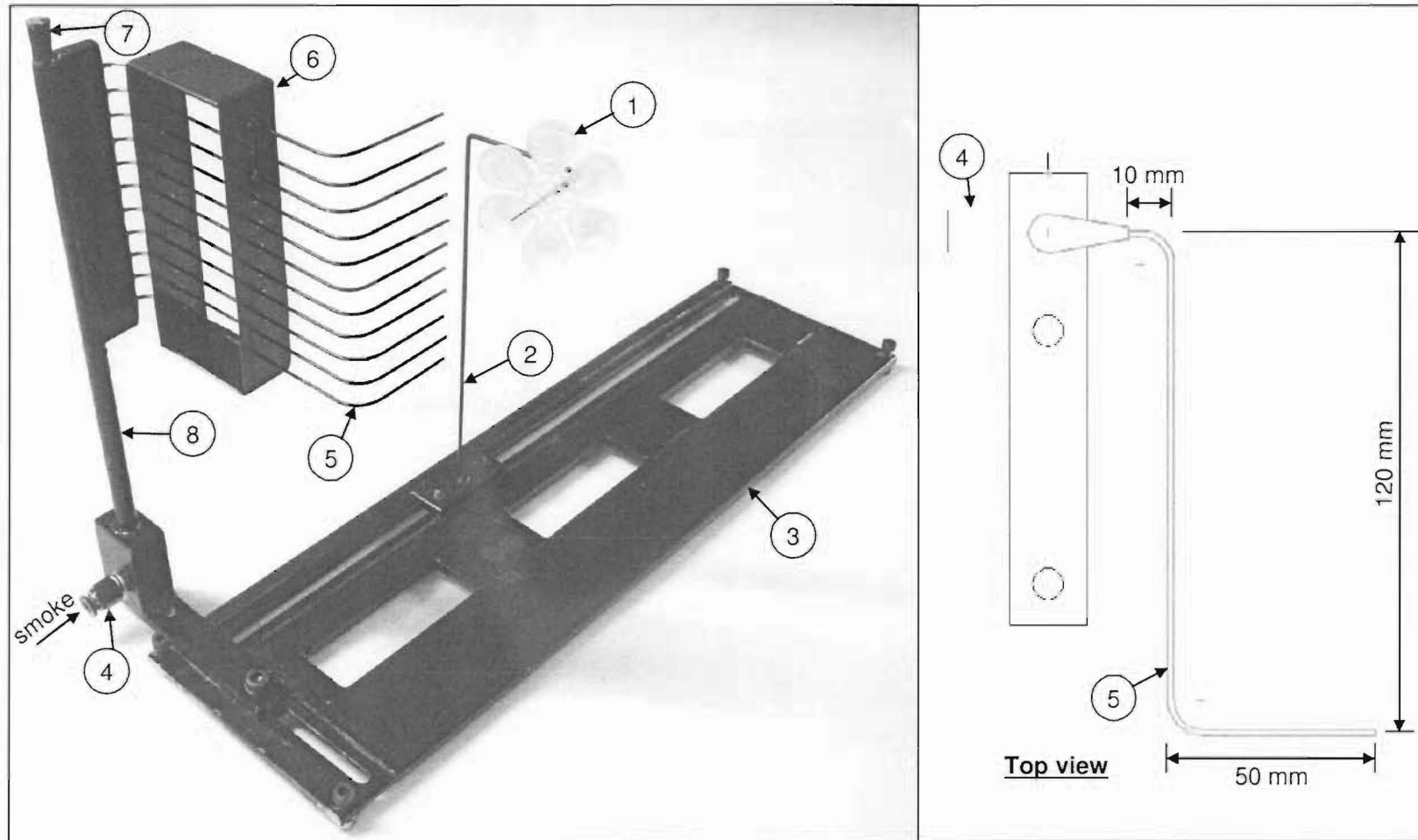
Fig. 4-2: Perspective and top views of smoke rake. (1) flower (shown here is an artificial flower); (2) flower rake; (3) stainless steel base plate; (4) air fitting and smoke inlet; (5) eleven 20G stainless steel hyperdemic tubing, ID ≈ 1.0 mm and OD ≈ 1.1 mm; see horizontal dimensions in Top view; (6) hyperdemic tubing spacer and support; (7) rubber bung to block the cleaning hole; (8) stainless steel tube.

Before securing the flower onto the rake, the Green kiwifruit flowers were painted with non-glossy acrylic paint. This was done only after it was found that the unpainted Gold kiwifruit flowers reflected too much light during the tests. Every part of both the smoke and flower rakes was also painted with non-glossy black acrylic paint.

Lighting

An 800-W lamp is positioned on top of the wind tunnel where there is a small glass window. The light passed through a slit between two black rectangular blocks. This created a light sheet (~ 5 mm thick) that illuminated the smoke filaments that passed through the centre of the flower. A cooling fan was used to dissipate the intense heat produced by the lamp.

Video capturing and processing

The flow motion was captured using Sony Digital Handycam DCR-TRV33E at 30 fps. During the videoing, the soft rubber hose of the smoke discharge line was squeezed and released to create pulses of smoke. This concentrated the smoke for better visualization. Real time videos were shown on a TV for the purpose of fine-tuning the camera exposure, zoom and focus. Selected video segments were then digitalized and reduced to frames for analyses.

4.2. Results

The preliminary tests were carried out using single Gold kiwifruit flowers. The snapshots of the flow field under a 1.2 ± 0.1 m/s bulk flow from the front, side and back are shown in Fig. 4-3a to c.

When the tests were repeated for the Green kiwifruit flowers (Fig. 4-4a, c, e, g and i), two additional approach flow directions were added, namely inclined leeward and backward angles of 45°. These are then compared with the CFD simulated flow fields shown in Fig. 4-4b, d, f, h and j.

4.3. Discussions

Green kiwifruit flower

Under a frontal flow, the smoke test reveals the downstream eddies due to the obstruction of flow by the petals (Fig. 4-4a). After the smoke passes the flower, it is dispersed instantaneously behind the petals due to the intensive turbulent mixing induced by the local recirculation. The downstream recirculation can be identified clearly on the video playback. However, the snapshots such as Fig. 4-4a that show the core of downstream eddies is generally taken at the first instance the smoke filaments were introduced i.e. before the total dispersion of smoke takes place behind the flower as happens in the bottom half part of Fig. 4-4a. Comparison with the simulated streamlines in Fig. 4-4b gives satisfactory agreements in the location of downstream recirculation and the displacement of smoke filaments around the flower (see the top part of Fig. 4-4a).

The smoke test does not show any small eddies predicted by the CFD simulation in the vicinity of the stigma-style and anther-filament bushes. This does not necessarily imply an inaccurate CFD calculation as this is likely to be a limitation of the visualization technique here. The small number of smoke filaments and the large spacing between them may be insufficient to unveil the small eddies. In addition, the distractive light reflection by the ovary, stigma-style and anther-filament bushes further impairs the visibility of the localized eddies, if any.

When the flower is rotated clockwise by 45° in Fig. 4-4c, large eddies are generated immediately under the inclined flower. The top four smoke filaments and the dispersed smoke cloud behind the flower indicate that the downstream flow is being deflected upwards. All these characteristics are also in the CFD computed field in Fig. 4-4d.

In contrast, the smoke filaments do not experience much disturbance when approaching the flower from the side (Fig. 4-4e). Some degree of turbulence after contacting with the ovary, stigma-style and anther-filament bushes is indicated by the dispersion of smoke in the wake. Similar to the CFD prediction in Fig. 4-4f, the petals virtually do not generate any eddies here.
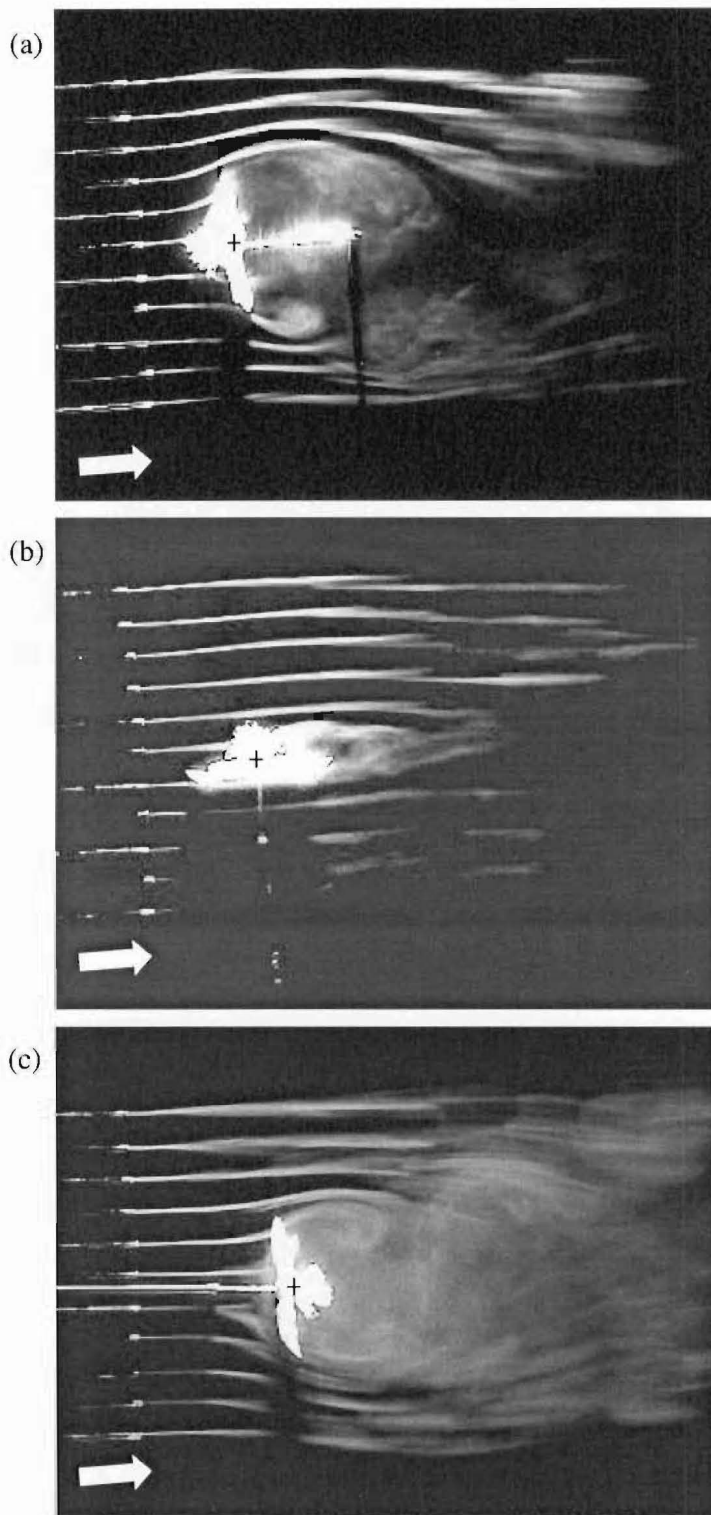
Fig. 4-3: Smoke visualization of flow field around a single full-open Gold kiwifruit flower subjected to a uniform 1.2 ± 0.1 m/s flow from the (a) front, (b) side and (c) back. The arrows and the '+' mark indicate the flow direction and flower centre respectively.
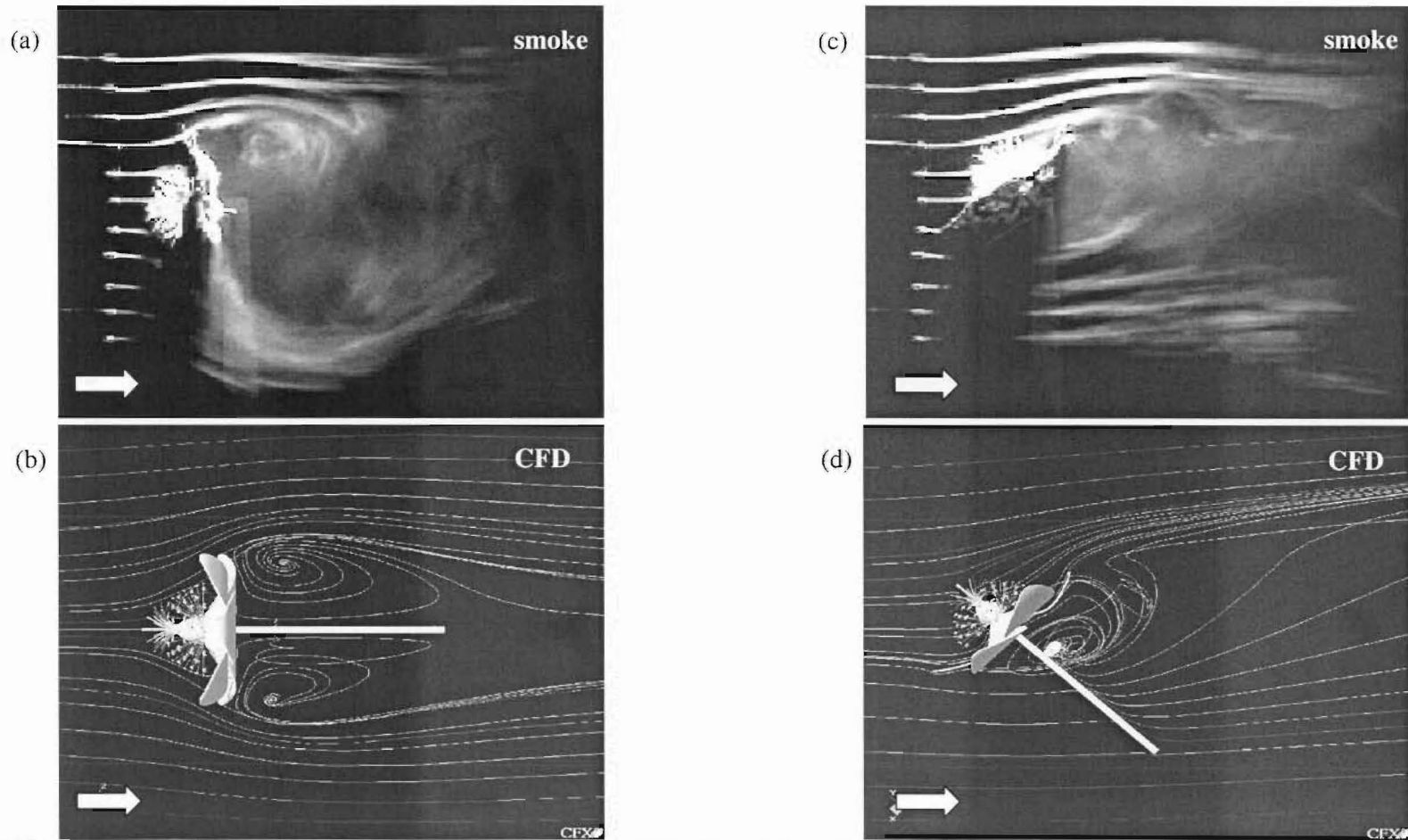
Fig. 4-4: Smoke visualization of flow field around a single full-open Green kiwifruit flower under a uniform 1.2 ± 0.1 m/s flow (a) from the front and (c) at an inclined leeward angle of 45°. The corresponding CFD simulated flow fields are shown in (b) and (d) respectively. The arrows indicate the flow direction.
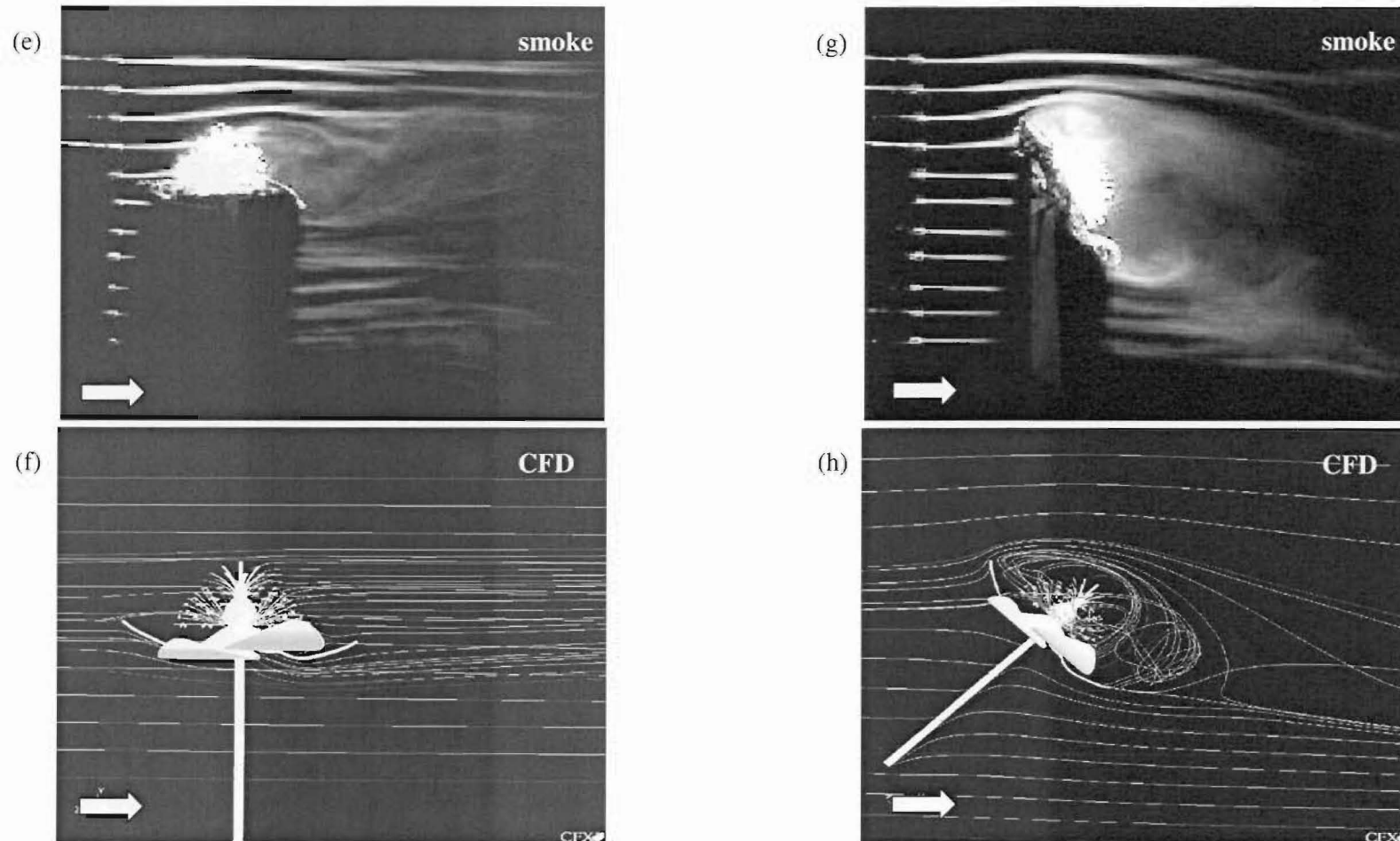
Fig. 4-4: Smoke visualization of flow field around a single full-open Green kiwifruit flower under a uniform 1.2 ± 0.1 m/s flow (e) from the back and (g) at an inclined backward angle of 45°. The corresponding CFD simulated flow fields are shown in (f) and (h) respectively. The arrows indicate the flow direction.
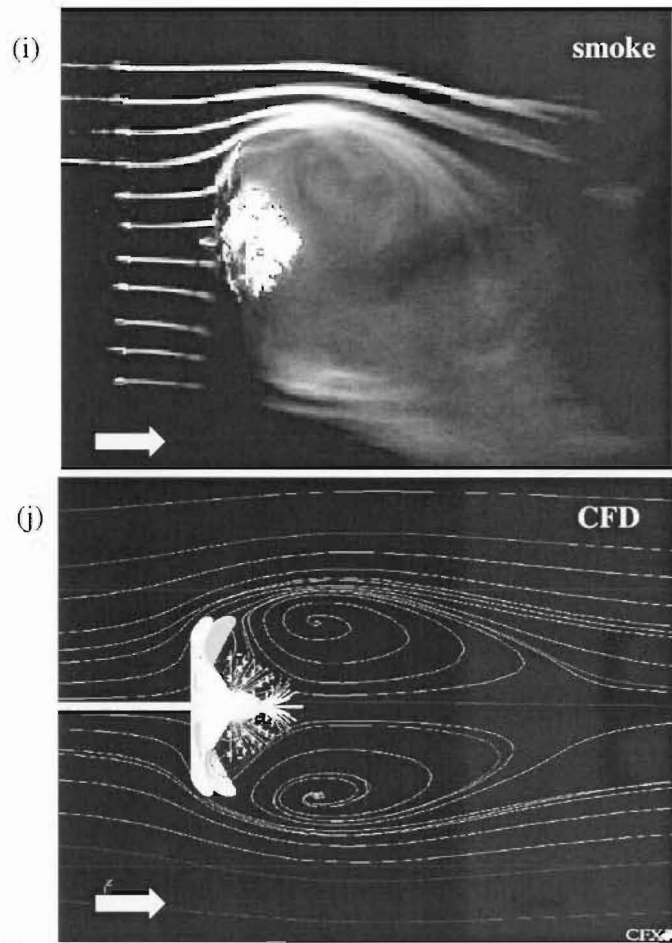
Fig. 4-4: Flow field around a single full-open Green kiwifruit flower under a uniform 1.2 ± 0.1 m/s flow from the back, from (i) smoke visualization and (j) CFD simulation. The arrows indicate the flow direction.

The downstream eddies reappear with a 45° rotation backwards (Fig. 4-4g). As can be seen in Fig. 4-4h too, the eddies are initiated at the tip of the top and bottom petals. The violent and large recirculation takes place within the enclosure of the corolla and around the ovary. The recirculation was observed to trap the smoke for a further 5 to 6 seconds after the smoke supply was stopped.

Similar but more axisymmetrical downstream swirls are exhibited in a back flow (Fig. 4-4i). Focussing on the top half part of Fig. 4-4i, the smoke filaments near the top petal edge are first diverted to the top before proceeding downwards to form the swirls. The big swirls lead to turbulent mixing downwind of the flower. The streamline pattern in Fig. 4-4j resembles this smoke rendered flow pattern.

Gold kiwifruit flower

There was no CFD simulation carried out for the smaller-sized Gold kiwifruit flower. Fig. 4-3 shows that the flow structures in all three directions are similar to those of the Green kiwifruit flower. For examples, large downstream eddies can be seen behind the petals in the frontal and back flows (Fig. 4-3a, c), while the side flow displays only small turbulence leeward of the ovary, style and filament bushes.

Study of natural draft around a single female Green kiwifruit flower

The smoke visualization test was carried out in a commercial orchard (East Pack) in Te Puke in November 2001. The flowers were borne on Pergola training. The wind approached the flower from random directions and displayed chaotic pattern upon contact. This is shown by the trails of smoke videoed using Sony F-707 digital camera at 25 fps. Impulses of sulphuric acid smoke were introduced by using the Drager Air Current Tubes. The white smoke was generated when the fuming sulphuric acid reacted with the moisture in the air. The time sequence of video snapshots in Fig. 4-5 and 4-6 show the dispersion of the smoke which was trapped within the enclosure of the flower for up to 2 seconds. However, no large recirculation as simulated in CFD or as visualized in the wind tunnel was able to be captured by the smoke test in the field. This is presumably due to the fast diffusion of smoke. Similar smoke test was re-attempted on the smaller Gold kiwifruit flowers using the fog machine (see Chapter 8) during the field trip to Motueka in November 2003. Similar results were observed but they are not shown here due to their poor picture quality.

4-5

4.4. Recommendations

The author has attempted to use a digital high speed camera to capture the kiwifruit pollen trajectories around a single Green kiwifruit flower. The pollen grains were observed to follow flow paths similar to those shown in the smoke tests. However, images of satisfactory quality have not been obtained because the lighting problem could not be resolved before the flowering season ran out. Even though the flower had been coated with non-glossy paint, it still reflected a huge amount of light under the high speed flash lamp. This made the tracking of surrounding pollen motions impossible. Yet, this part of the work is important in validating the simulated pollen flow. More efforts need to be invested in minimizing the undesirable reflection by the flower.

Although the smoke filaments produced here have given sound visualization of the air flow patterns, better results are expected by using smaller and greater quantity of filaments. It is not feasible to use hyperdermic tubing of smaller diameter to achieve finer resolution due to the high pressure drop limitation. An alternative here is the smoke-wire method.

The validations here are qualitative. The future work should explore the quantitative aspects. There are many well-known methods to achieve this. For instance, the laser Doppler anemometry (LDA) is appropriate for measuring the velocity field close to the flower, which will otherwise be inaccessible by pitot tube or hot-wire anemometry. Particle tracking velocimetry (PTV) is another effective technique to obtain a complete data of the airflow field. Also worth considering is the use of neutrally buoyant helium bubbles that have been successfully applied by Niklas (1981a, 1982, 1983a) in studying the wind pollination of plants in the wind tunnel.
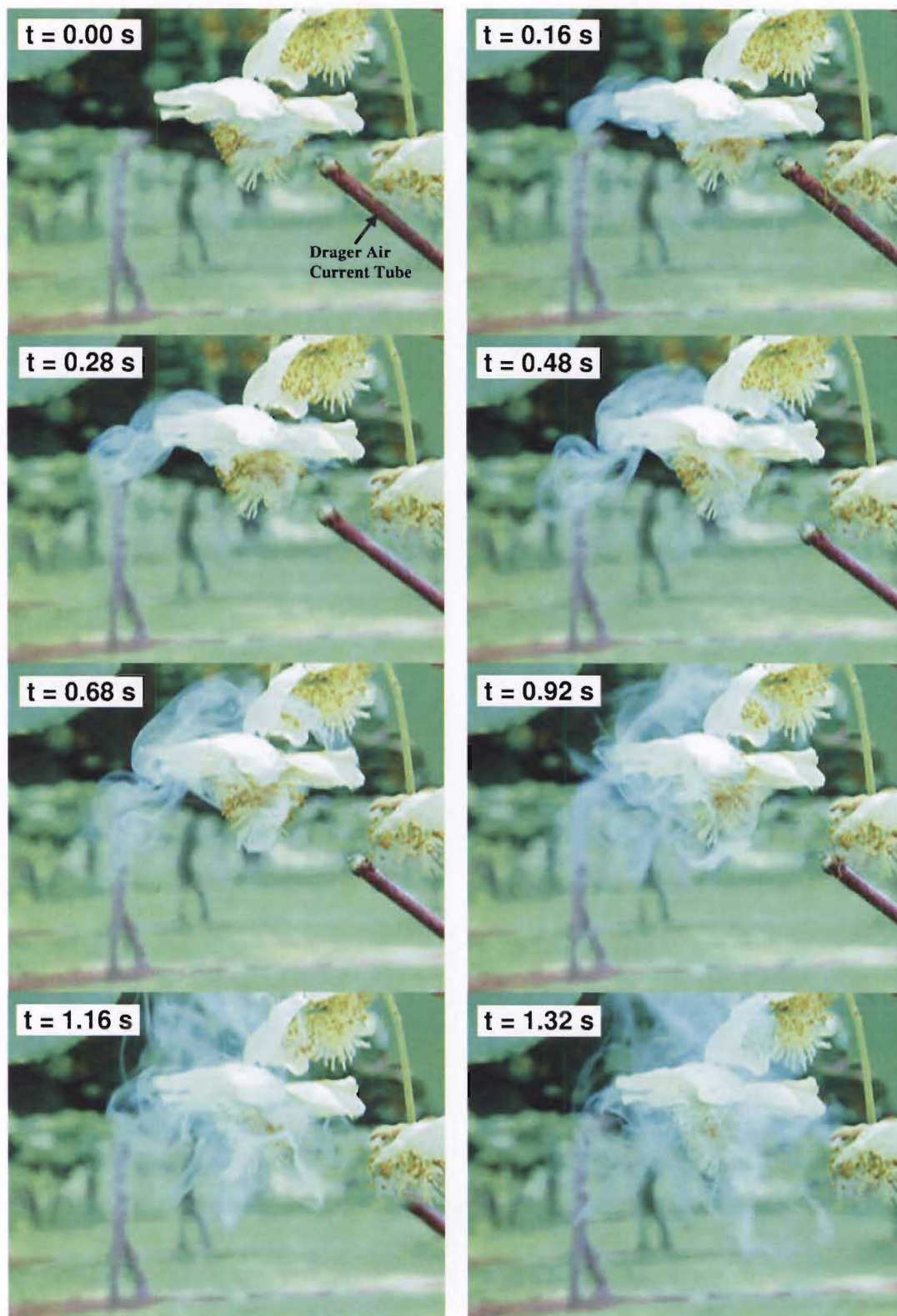
Fig 4-5: Development of smoke pulse around a single female Hayward flower under natural draft in the orchard. Elapsed times are shown.
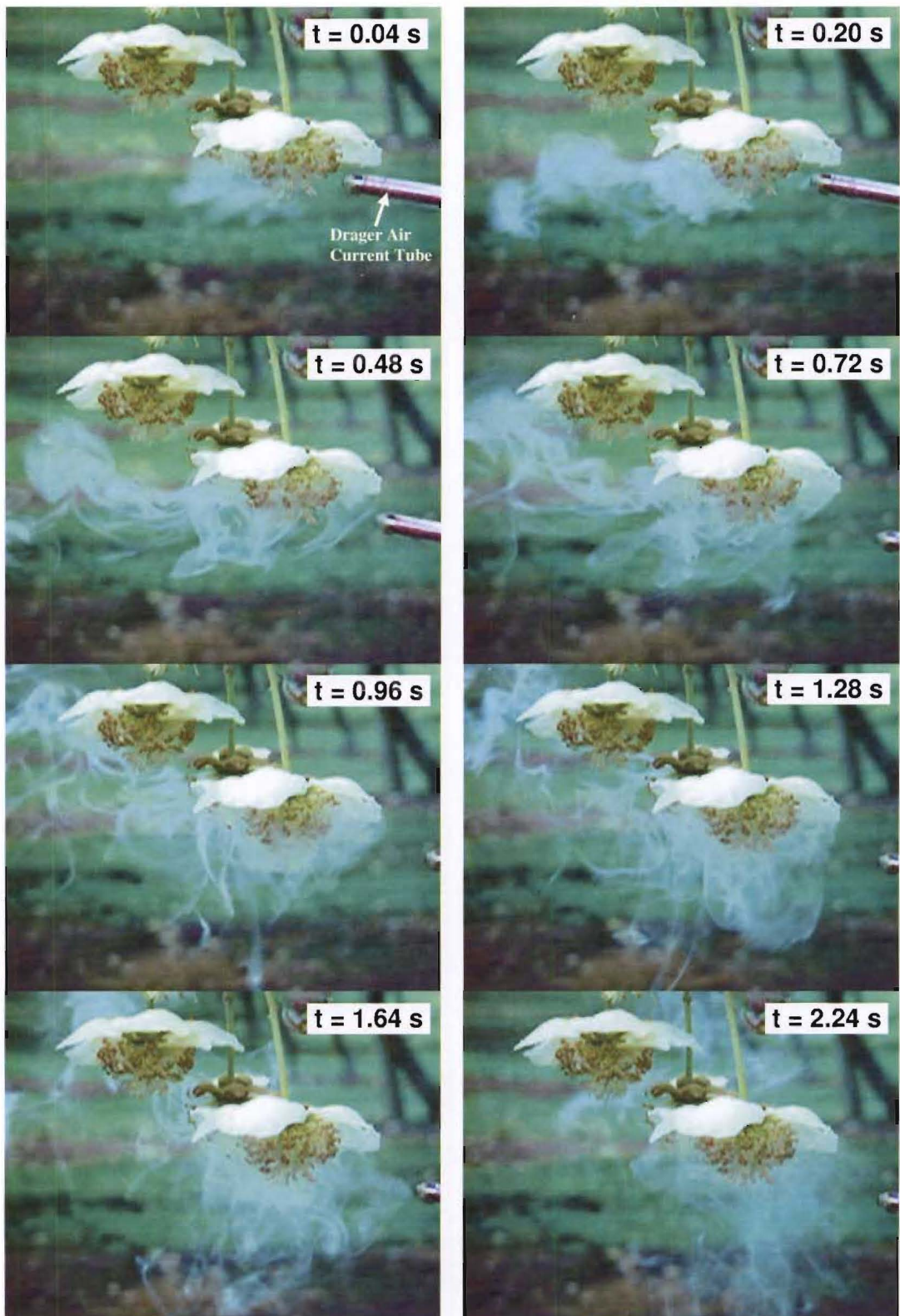
Fig 4-6: Development of smoke pulse around a single female Hayward flower under natural draft in the orchard. Elapsed times are shown.

CHAPTER 5: SIMULATION OF POLLEN-LOADED AIR JET

The CFD flower models are applied here to study the flower collection efficiency of airborne pollen grains that are dispersed by a dry air jet.

Showering individual kiwifruit flowers with a small pollen-laden air jet is an effective way of transferring the pollen onto the targeted stigma. Referring to section 1.6, two types of air jet applicators can be identified in orchard kiwifruit pollination – dry and wet. The gun-like machines, Hanakaze and Dry-pol, are dry applicators because they utilize dry air jets to disperse the pollen directly. They are however much less popular than the Cambrium and airshear sprayers which apply the droplets of pollen-suspended solution. An airshear nozzle was found to perform better because its atomization produces a narrow jet of small droplets ranging from 50 to 200 μm (Goodwin, 2000) compared to a broad swirl jet by a Cambrium sprayer. Still, the dry air sprayers are promising because of its simplicity and other advantages mentioned in section 1.6.

There is a lack of quantification of mechanism and efficiency of air jet spraying of kiwifruit pollen onto a single kiwifruit flower. To the author's best knowledge, the only relevant work is reported by Hopping *et al* (1984) who built an artificial canopy in the laboratory by hanging the preserved female flowers. They tested Curtis applicator with airshear droplets and found that the effectiveness depended on the flower presentation and shielding by "leaves", distance of flower from the centre of the spray pattern, droplet size and the velocity of delivery air. This chapter aims to gain a better understanding of the spraying performance by theoretically studying different jet-nozzle parameters. Although only dry pollen spraying is considered here, the results are expected to be useful for the wet-based sprayers too.

5.1. Computational method

Only two out of the four flower models are chosen for further air jet analyses here, namely the full-open and bold flowers. The full-open flower represents the pollen applications at 50 % flowering and the bold flower is selected because of its highest efficiency predicted in the simulations of wind pollination in Chapter 3.

The aspects of air jet spraying that are studied numerically are:
1. direction of the jet i.e. from the front, side and back;
2. diameter of the nozzle i.e. 30 and 90 mm;
3. nozzle-to-flower distance i.e. 100, 200 and 300 mm;
4. initial velocity of jet i.e. 0.5, 1, 2 and 3 m/s.

The combination gives a total of 144 runs with two flower models.

Since the spraying time for each flower in the orchard is so short (1 to 2 seconds) and the jet itself is moving (see section 5.2), it is assumed that the influence of occasional background draft is not included here. In addition, the inclusion of draft in the steady state simulation is likely to introduce an unrealistic exaggerated effect on the jet.

The definition of computational domain is similar to that in the wind pollination simulation, except for the addition of a circular nozzle. Fig. 5-1a and b shows the domains with a ϕ 30-mm and ϕ 90-mm nozzle respectively. The tubular flow is allowed to develop slightly longer inside the ϕ 90-mm nozzle. The nozzle, located at the centre of the indicated domain in Fig. 5-1, is modelled as a thin-surface cylinder.

To handle the expanding air jet, all the side boundaries of the domain are assigned to be of the 'Opening' type with a relative pressure of 0 kPa. An 'Opening' boundary allows the air to flow in and out, whereas an 'Outlet' boundary (Dirichlet type) only permits the air to leave the domain. Preliminary trials found that the use of 'Outlet' boundary had led to errors in the Solver. This is because the presence of jet has induced an air flow from outside the domain. The air flow field is solved in steady state using the RNG k-ε model. The nozzle wall and all the flower surfaces are regarded as smooth and no slip.
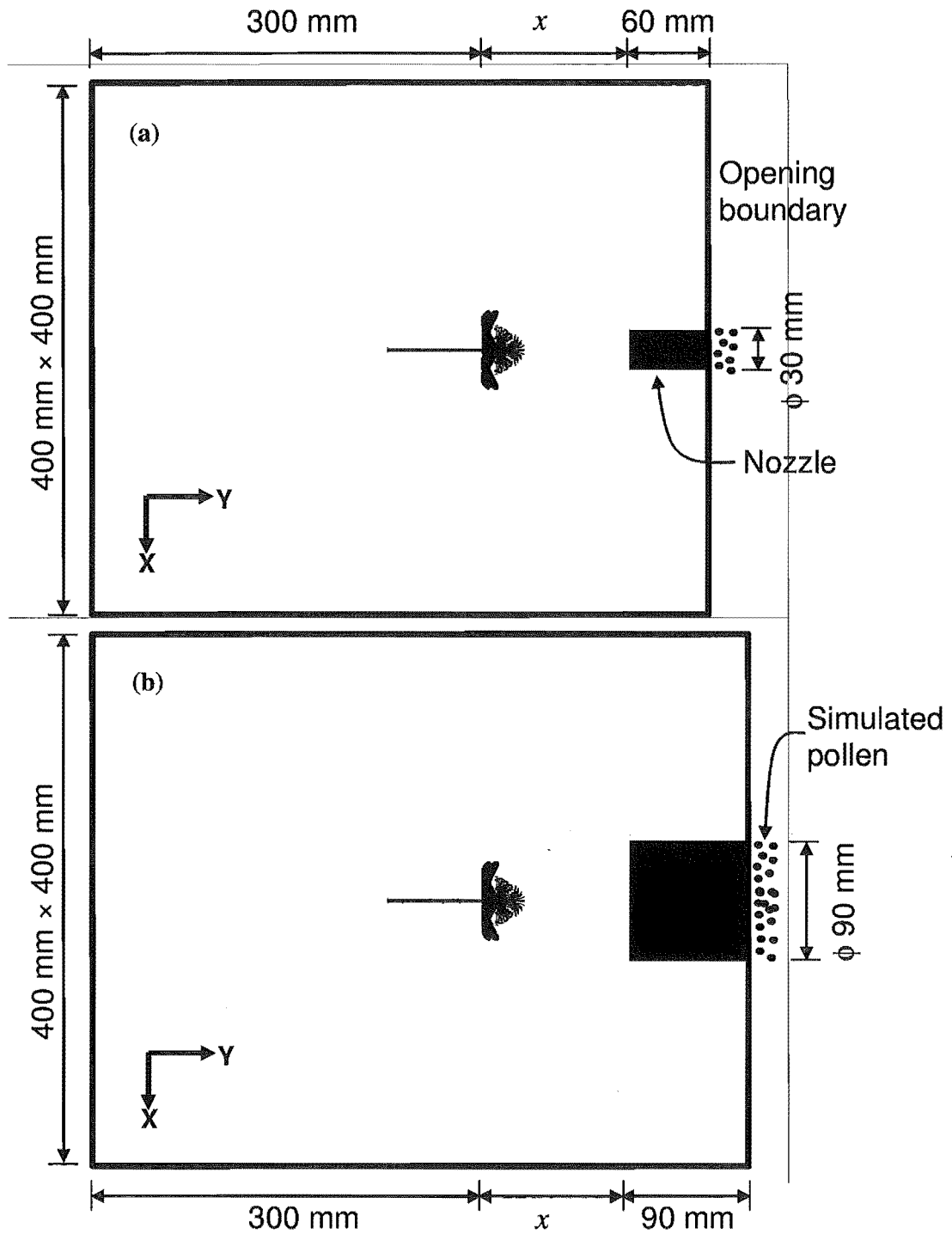
Fig. 5-1: Definition and dimension of the rectangular flow domains with an air jet nozzle of φ 30 mm (a) and φ 90 mm (b) in front of a full-open flower. The simulated flower-to-nozzle distances (x) are 100, 200 and 300 mm.

50000 non-coupled pollen grains are introduced and tracked using the steady state Lagrangian approach. It must be noted since the same number of pollen is injected in each scenario, this is effectively an assessment of pollen collection efficiency at the same pollen mass flow rate. The simulated pollen number density varies depending on the nozzle diameter and the jet velocity.

To assess the effect of momentum coupling between the air and the pollen, 12000 pollen grains are assumed to be required by each flower (see section 1.3). At a collection efficiency of 2.5 % (obtained from the preliminary trials), this means 480000 pollen grains or 3.6-mg pollen/flower need to be sprayed. Field trials by Alspach *et al* (1991) using bee collected pollen either suspended in liquid or in dry application with diluent showed that the mean fruit weights were above 90 g at pollen rate slightly above 0.5 mg/flower. Further increased pollen rate above 2 mg/flower did not result in any significant gain in fruit size. Thus, the pollen rate of 3.6 mg/flower should be conservative enough for the purpose here.

A 1-second spray per flower via a ϕ 30-mm nozzle gives a mass loading of 0.14 to 0.84 %wt in an air jet of 0.5 to 3 m/s inside the nozzle. Despite this low mass loading, the two-way coupling is still tested by employing a smaller set of pollen number (1000; using the recommendation in *CFX-5.6 Manual*, 2003) with a specified pollen mass flow rate of 3.6 mg/s. It has been found that this does not alter the air flow field. The particle-particle interaction is unlikely because the pollen volume fraction inside the nozzle is 0.002 to 0.01 in this initial jet velocity range.

All the walls, except for the jet nozzle, are assumed to be sticky to the pollen. The particle tracking also finishes at Opening boundaries.

5.2. Results

Air and pollen flow around a full-open flower

Fig. 5-2 are the predicted air streamline and particle trajectories plots for a single full-open flower when sprayed with a pollen-laden air jet at 1 m/s. In order to compare with the wind pollination modellings where the inlet is 200 mm away from the flower centre, only the runs with a 200-mm nozzle-to-flower distance are plotted.

With a frontal air jet coming out of a ϕ 30-mm nozzle, the downstream eddies (Fig. 5-2a) are not as tidy and axisymmetrical as in the wind pollination simulation that has a uniform flow inlet defined (see Fig. 3-21a). The downstream vortices in Fig. 3-21a have their centres along the ring of abut the same diameter as the flower. The pollen loaded air jet also spreads more widely than is the case with uniform front flow after the impingement on the petals. Small eddies in the vicinity of style and filament bushes as predicted in the wind pollination simulations are not found in Fig. 5-2a. They are replaced by the large upstream eddies generated as the jet contacts with the flower. The difference here is likely due to the absence of surrounding flow in the jet simulations. While not shown here, it is found that the degree of spread depends on the strength of the jet. The flow patterns are also markedly different in terms of the eddies sizes and positions for different initial jet velocities.

The pollen trajectories under an air jet (Fig. 5-2d) follow the overall pattern of streamlines to some degree but not the exact path. They appear to be more chaotic than those under the uniform velocity inlet (Fig. 3-21d). There are a significant number of pollen grains trapped in the downstream vortices. The petals however prevent any of this pollen from being recollected by the stigma.

A side jet (Fig. 5-2b) gives a similar flow pattern to that in wind pollination (Fig. 3-21b). The air passes the flower with little disturbances near the petals. The airborne pollen grains are captured by the stigma situated at the windward, distal and central parts of the bush.
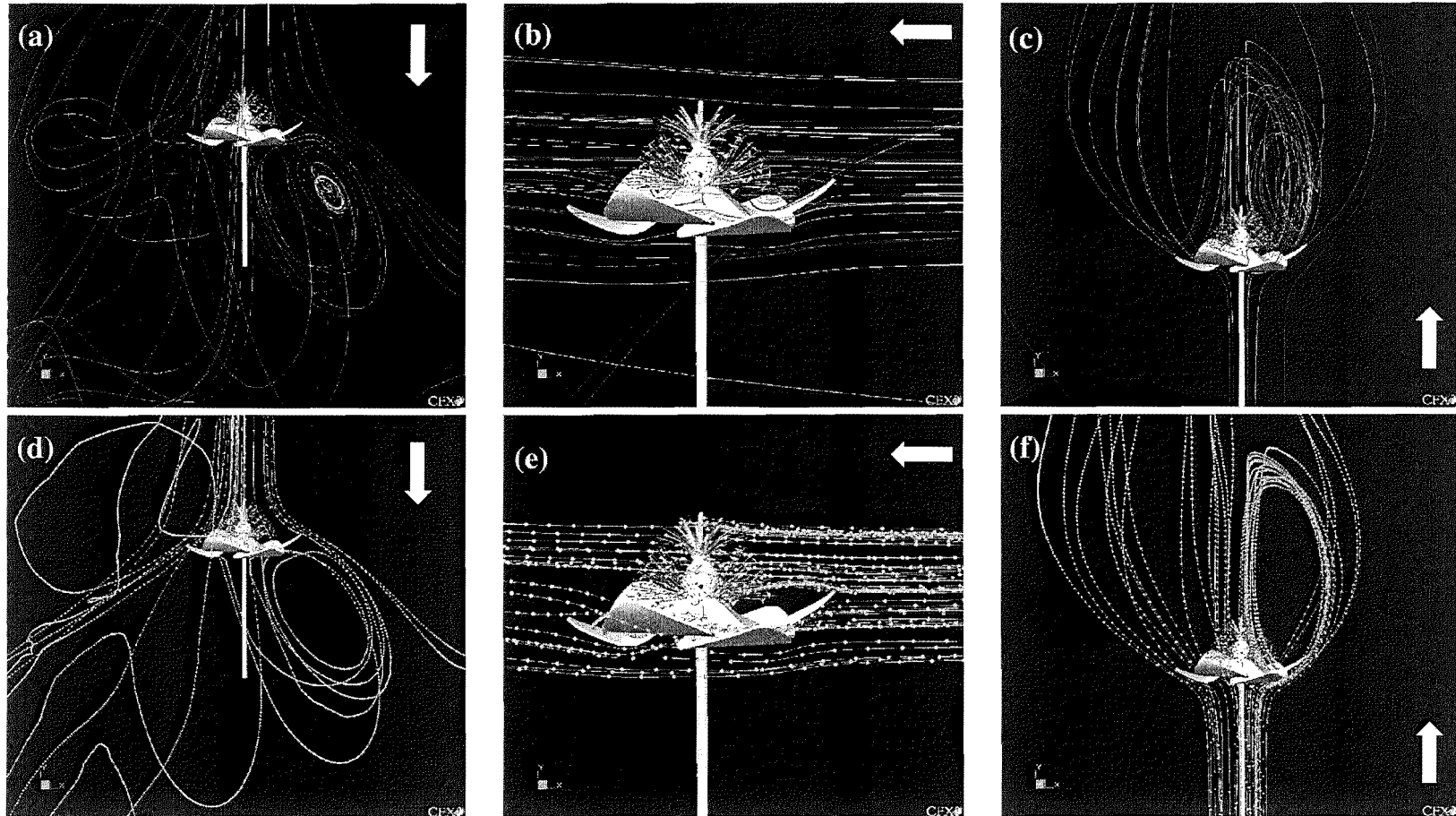
Fig. 5-2: (a), (b) and (c) are the predicted air flow field around a single full-open flower under 1-m/s air jet from the front, side and back respectively (as shown by the arrows). The air jet exits a 30-mm diameter nozzle located at 200 mm away. The corresponding calculated trajectories of a cloud of pollen are shown in (d), (e) and (f). The separation between pollen along a trajectory is 0.015 s.

As in the wind pollination runs (see Fig. 3-21c), large downstream recirculation are predicted (Fig. 5-2c) and they are solely responsible for directing the pollen backwards onto the stigma (Fig. 5-2f). From the pollen trajectory plot, it can be seen that the pollen have been significantly slowed down in the vortices. This 'recycling' method of pollen collection ceases when the jet velocity is increased to ≥ 2 m/s (see Fig. 5-13c). The success of pollen deposition onto the stigma depends on whether the passing pollen can be drawn into the downstream eddies well. At high velocity, for example at ≥ 2 m/s, the pollen grains possess more inertia. Thus, most of the pollen, which are in the projection of impacting onto the flower, will be deposited on the petals (which are defined as sticky) rather than being diverted to the sides and directed to downwind. If these pollen do not collide with the petals, their increased momentum does not allow them to be 'sucked' into the eddies well. Instead, they will follow the course of the deflected jet flow and get entrained into it.

Switching to a ϕ 90-mm nozzle sees flow patterns (Fig. 5-3) that show more resemblance to the wind pollination (Fig. 3-21). This is because the jet diameter exiting the nozzle is now larger than the diameter of the flower (66 mm). In another word, the flower is almost totally immersed at the centre of the jet cf. the uniform velocity inlet in wind pollination.

A frontal jet produces tidy small and large eddies above and below the petals respectively (Fig. 5-3a). There is however no pollen trapped by the downstream vortices (Fig. 5-3d). Not much variation can be identified in a side jet modelling here (Fig. 5-3b, e). Like the frontal jet case, the large downwind eddies fail to attract any pollen i.e. no pollen are being deposited onto the stigma in a back jet application (see Fig. 5-3f).

Air and pollen flow around a bold flower
These are shown in Fig. 5-4 and 5-5 for a 1-m/s air jet released from a ϕ 30-mm and ϕ 90-mm nozzle respectively. Similar to the full-open flower above, both air and pollen flows brought by a larger jet come closer to those predicted in the wind pollination (see Fig. 3-19).

For instance, the larger air jet in Fig. 5-5a induces eddies leeward of the sepals, similar to those observed in the wind pollination runs (Fig. 3-19a). These eddies do not appear with the smaller jet in Fig. 5-4a. Fig. 5-4a further shows that the jet has swung to one side.

The prediction of jet swinging was unexpected prior to the simulations. It happened randomly among the scenarios studied, but consistently within a scenario for both flowers. Examinations of the flow fields of all runs discover that none of the jets are perfectly axisymmetrical. In some cases, the jet sways to such extent that it totally misses the flower. An example of this is given in Fig. 5-6c where the jet from a ϕ 90-mm nozzle moves upwards and bypasses the bold flower in the middle. At other initial jet velocities (Fig. 5-6a, b, d), the jets also deviate from the centreline but not so severely.

The validity of this jet-swinging phenomenon is nevertheless questionable. At first reaction, it was thought that the jet swinging is likely to be a result of interaction between the flower and the jet. In an attempt to justify this opinion, the associated pressure fields of Fig. 5-6a and c were plotted and examined in Fig. 5-6e and f respectively. There is no sign in Fig. 5-6e and f showing any apparent interaction between the flower and the jet. For 2.0 m/s jet velocity showing strong jet swinging, the pressure field indicates the asymmetric disturbance has originated upstream of flower. Thus it is unlikely that the flower has led to this asymmetric flow. This led the author to believe that the jet may be interacting with the domain boundaries of the solution. In numerical simulations, the boundaries of the computational domain, despite being specified as non-wall types, may behave like artificial solid walls which induce an artificial Coanda effect. In other words, the jet swinging is regarded as a computational artefact or numerical instability which leads to a display of the Coanda effect.

Coming back to Fig. 5-4a, numerous streamlines can be seen coming from the left. They represent the air flow from outside of the flow domain, which has been mentioned in section 5.1 in relation to the stability of computation. According to Fig. 5-4d, the pollen are swept to one side after a portion of them has been captured by the stigma.
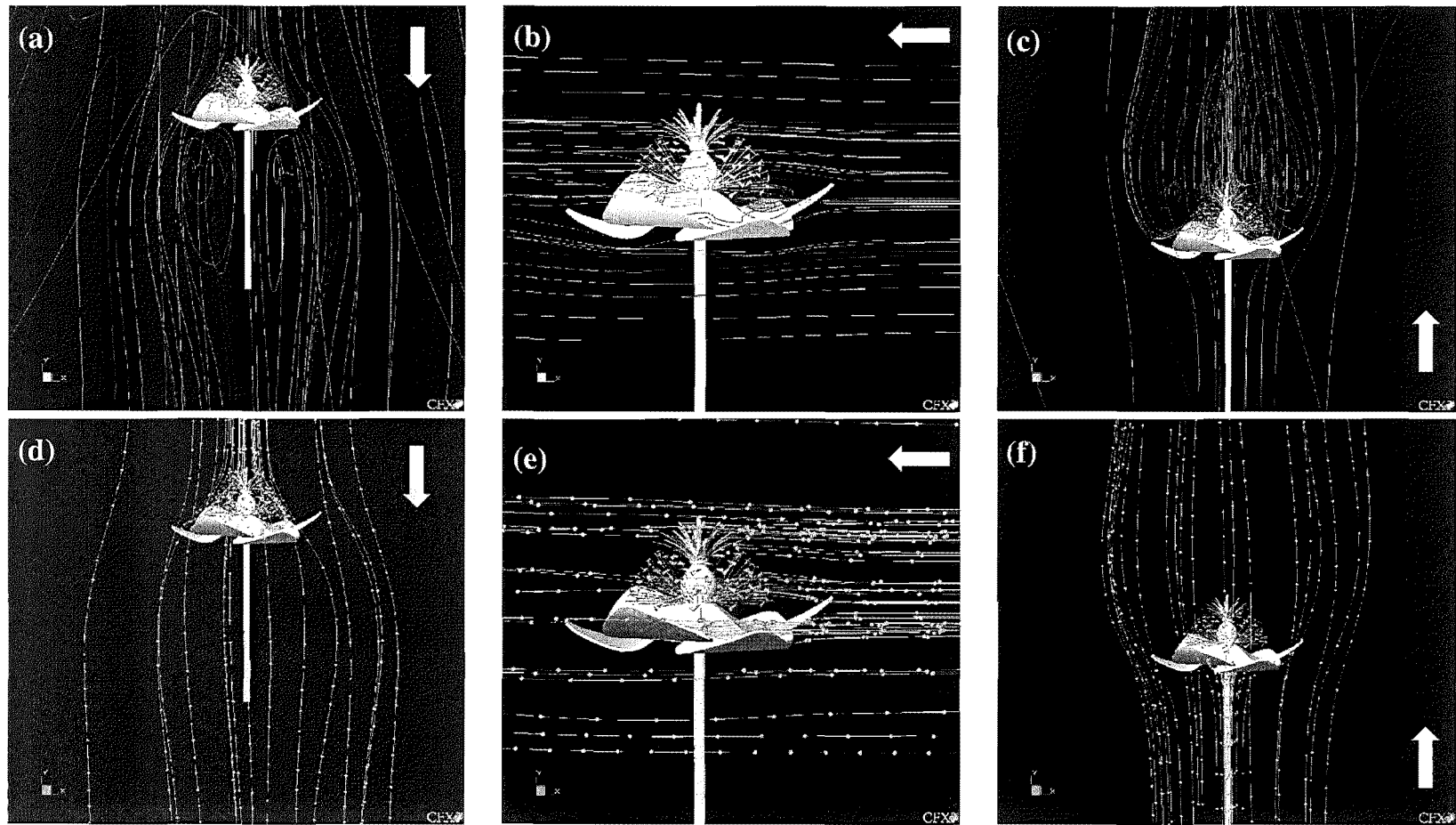
Fig. 5-3: (a), (b) and (c) are the predicted air flow field around a single full-open flower under 1-m/s air jet from the front, side and back respectively (as shown by the arrows). The air jet exits a 90-mm diameter nozzle located at 200 mm away. The corresponding calculated trajectories of a cloud of pollen are shown in (d), (e) and (f). The separation between pollen along a trajectory is 0.015 s.
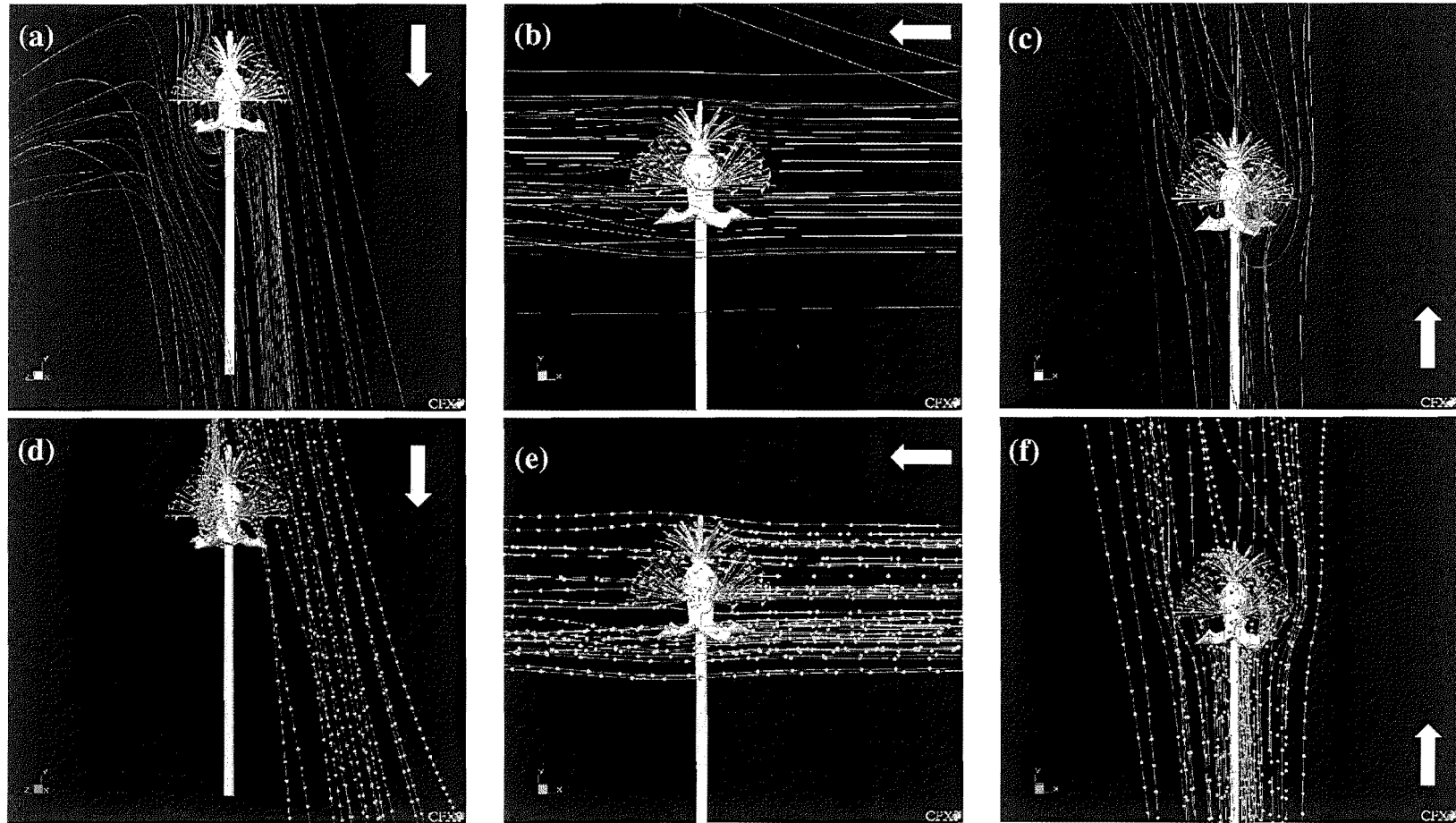
Fig. 5-4: (a), (b) and (c) are the predicted air flow field around a single bold flower under 1-m/s air jet from the front, side and back respectively (as shown by the arrows). The air jet exits a 30-mm diameter nozzle located at 200 mm away. The corresponding calculated trajectories of a cloud of pollen are shown in (d), (e) and (f). The separation between pollen along a trajectory is 0.015 s.
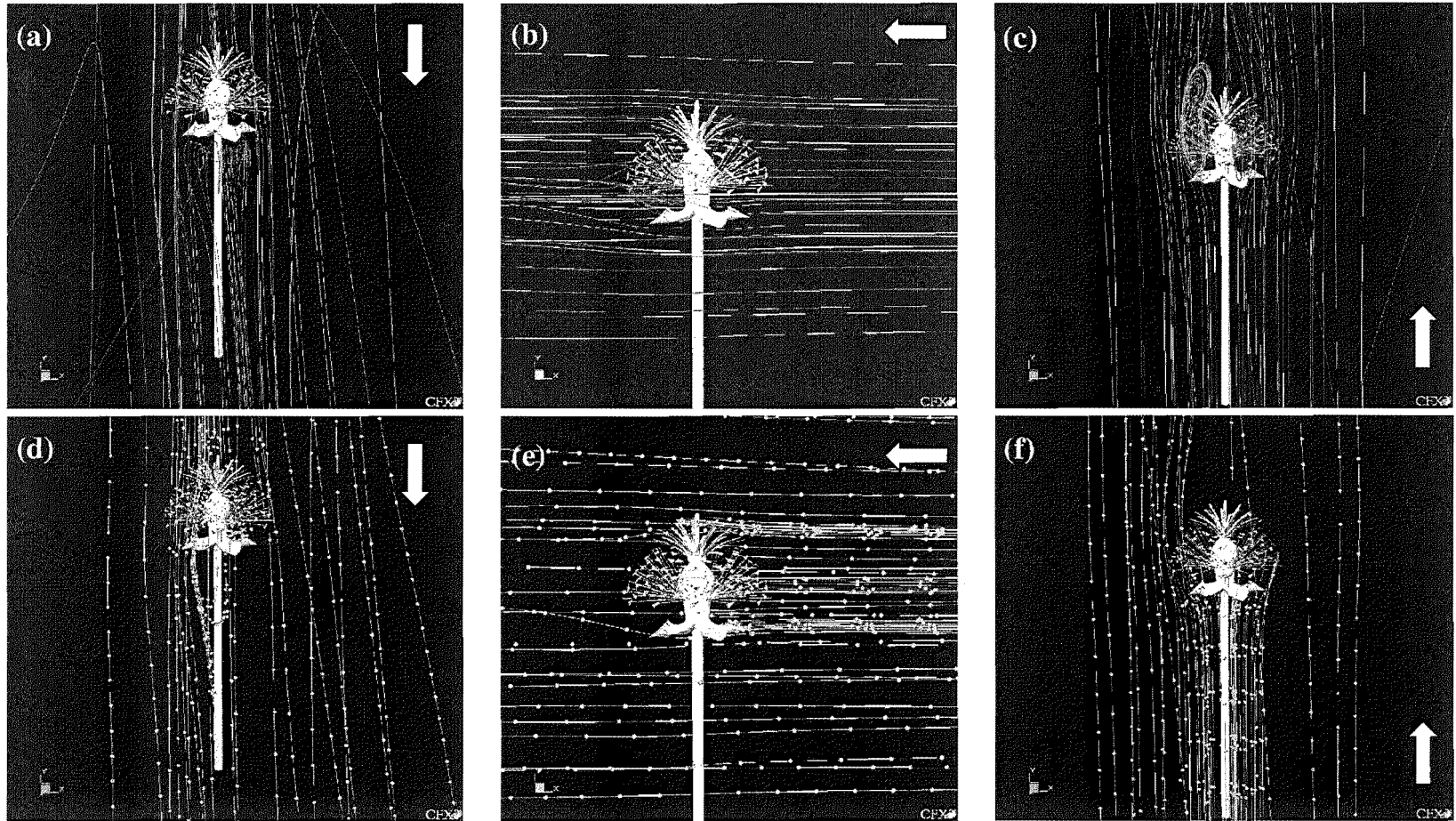
Fig. 5-5: (a), (b) and (c) are the predicted air flow field around a single bold flower under 1-m/s air jet from the front, side and back respectively (as shown by the arrows). The air jet exits a 90-mm diameter nozzle located at 200 mm away. The corresponding calculated trajectories of a cloud of pollen are shown in (d), (e) and (f). The separation between pollen along a trajectory is 0.015 s.
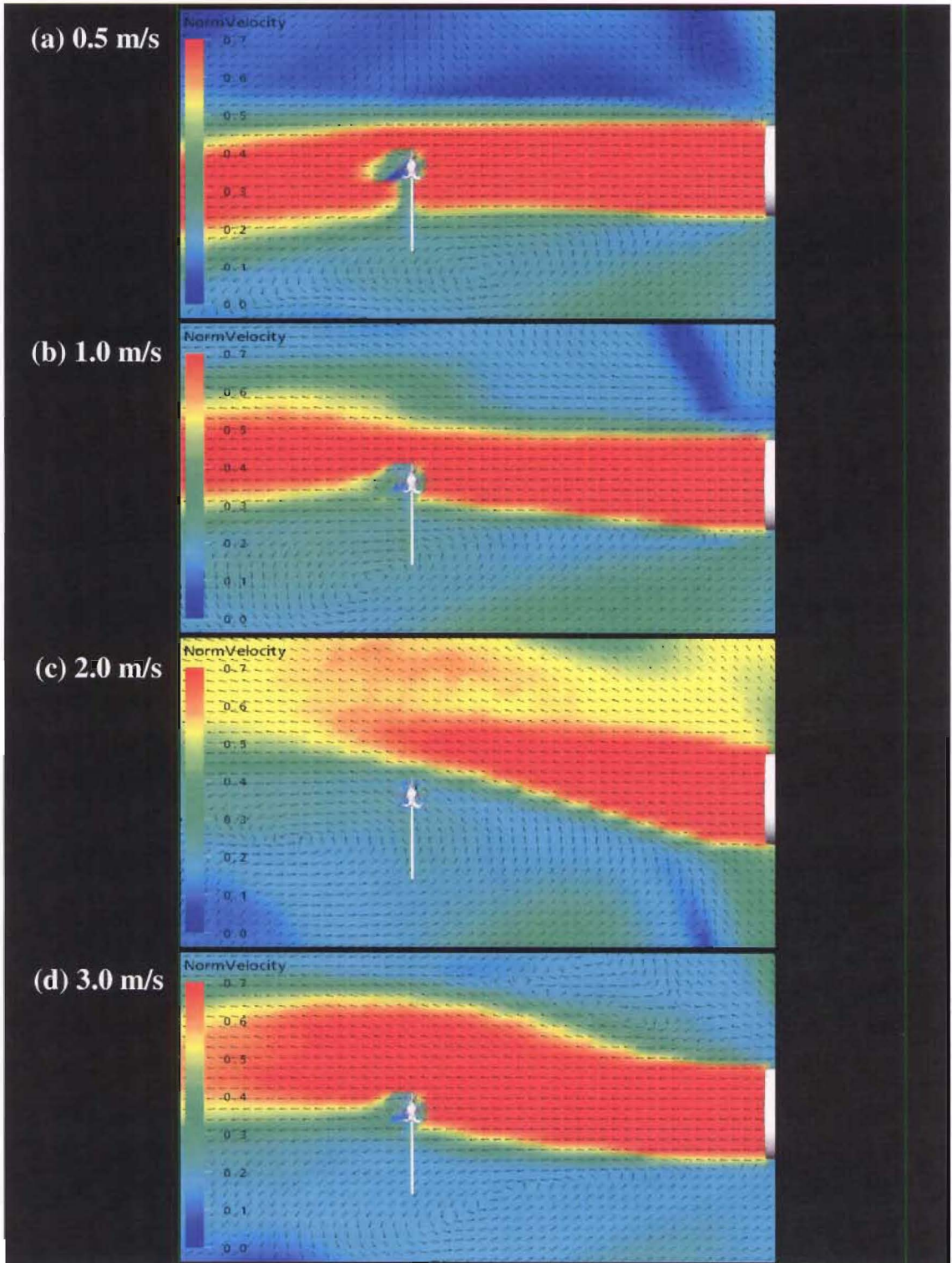
Fig. 5-6: Normalized velocity field around a single bold flower in an air jet from a φ 90-mm nozzle (on the right). Shown are the initial jet velocities. ......continue

(e) 0.5 m/s

Pressure

	1.9e-002
	1.6e-002
	1.3e-002
	1.0e-002
	7.6e-003
	4.8e-003
	2.1e-003
	-6.9e-004
	-3.4e-003
	-6.2e-003
	-9.0e-003
	-1.2e-002
	-1.4e-002
	-1.7e-002
	-2.0e-002

[Pa]

(f) 2.0 m/s

Pressure

	4.8e-001
	4.2e-001
	3.6e-001
	3.0e-001
	2.3e-001
	1.7e-001
	1.1e-001
	5.1e-002
	1.0e-002
	-7.1e-002
	-1.3e-001
	-1.9e-001
	-2.6e-001
	-3.2e-001
	-3.8e-001
	-4.4e-001
	-5.0e-001

[Pa]
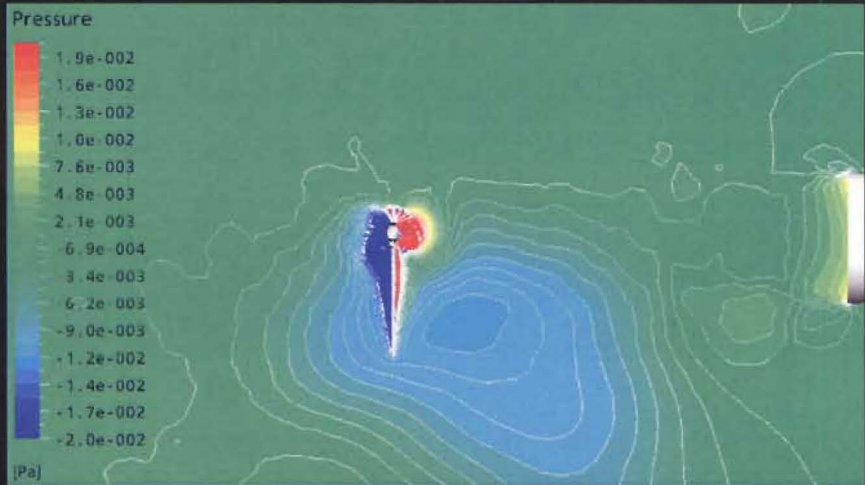
Fig. 5-6: The corresponding pressure fields of (a) and (c). The air jet is released from a ϕ 90-mm nozzle (on the right). Shown are the initial jet velocities.

For both small and large side jets (Fig. 5-4b, e; 5-5b, e), the air and pollen flow paths are almost identical to the wind pollination cases in Fig. 3-19b and e. No remarkable recirculation exists.

The 'peanut' shaped downstream recirculation surrounding the ovary, which is predicted in the wind pollination runs (Fig. 3-19c), emerges in the large back jet (Fig. 5-5c) but not in the small jet (Fig. 5-4c). Even though the 'peanut' shaped recirculation convey the pollen to the stigma at low wind speed (Fig. 3-23c), there is no pollen deposition here (see Fig. 5-14f and Fig. 5-5f). The rather chaotic downstream eddies in Fig. 5-4c, on the other hand, direct the pollen to the stigma region (Fig. 5-4f).

Velocity of jet approaching the stigma region

The changes in air velocity up to 100 mm away from the style bush centre of a full-open flower are plotted in Fig. 5-7, 5-8 and 5-9 for the frontal, side and back jets respectively. These are repeated for a bold flower in Fig. 5-10, 5-11 and 5-12. Note that the velocities have been normalized with the initial jet velocity. In the case of frontal and side jets, the tracked velocities here are along the direction to the nozzle. For a back jet, since the air flow reverses at some points downwind before proceeding to the stigma region, the approaching velocities after the reversal are of interest.

Under a frontal jet applied to a full-open flower (Fig. 5-7), all the normalized velocity profiles exhibit quite similar exponential decay. The exception is for the curve having an initial jet velocity of 2 m/s in Fig. 5-7c, due to the jet swinging. The jets released from ϕ 30-mm nozzle decay more than the ones from ϕ 90-mm nozzle at the same nozzle-to-flower distance. Unlike the jets from ϕ 30-mm nozzle, Fig. 5-7d, e and f show that the normalized velocity profiles are alike at different nozzle-to-flower distances. At around 30 to 40 mm before the style bush centre, there is a sudden drop of velocity. This distance may be regarded as the impaction distance for the pollens to decelerate and be collected by the stigma.

The above interpretations are also applicable to the bold flower in Fig. 5-10. However, the impaction distance is shortened to around 25 to 30 mm. This is perhaps due to the absence of petals which will otherwise significantly slow down the airspeed around the ovary (see discussion in section 3.7).

5-7

The impaction distance is even shorter in a side jet for both full-open and bold flowers (see Fig. 5-8 and 5-11 respectively) i.e. slightly less than 20 mm. The streamline plots in Fig. 5-2b, 5-3b, 5-4b and 5-5b indicate that the side jet penetrates through the style bush with little resistance. This is why the bulk air jet velocity can be sustained closer to the style bush centre. Another observation to note here is more side jets are predicted to swing than the frontal and back jets. The swinging is indicated by the different decay patterns among the curves in Fig. 5-8 and 5-11.

The approaching velocity profile of a back jet is rather untidy (Fig. 5-9 and 5-12), which is expected owing to the presence of large downstream recirculation in the region. The impaction distance is hard to define. With the exception of the jets from ϕ 30-mm nozzle onto a bold flower in Fig. 5-12, the air flow regains the speed at 10 to 25 mm away from the style bush centre before experiencing a sharp decline.

Pollen collection efficiency by the stigma

The predicted pollen depositions on the stigma of a single full-open and bold flower are graphed in Fig. 5-13 and 5-14 for the spraying using ϕ 30-mm and ϕ 90-mm nozzles respectively.

Considering the pollen-loaded jets from ϕ 30-mm nozzle in Fig. 5-13, the frontal approach transfers significantly more pollen onto the stigma than the side and back directions. This is the same as the trend predicted for the wind pollination (Fig. 3-23).

For a frontal jet, except for the run with a nozzle-to-flower distance of 200 mm and initial jet velocity of 3 m/s in Fig. 5-13b, the collection efficiencies degrade with the increasing nozzle-to-flower distance. This is a result of the dispersion of pollen plume. Overall, the efficiencies improve as the jets are made stronger. However, as the nozzle is placed further away from the flower, an opposite trend is predicted. Comparison between Fig. 5-13a and 5-13d shows that it is more advantageous to apply the spray pollination after the petal fall-off.

A side jet gives varying collection characteristics (Fig. 5-13b and e). There seems to be a lot of interactions between the factors of nozzle-to-flower distance and initial jet
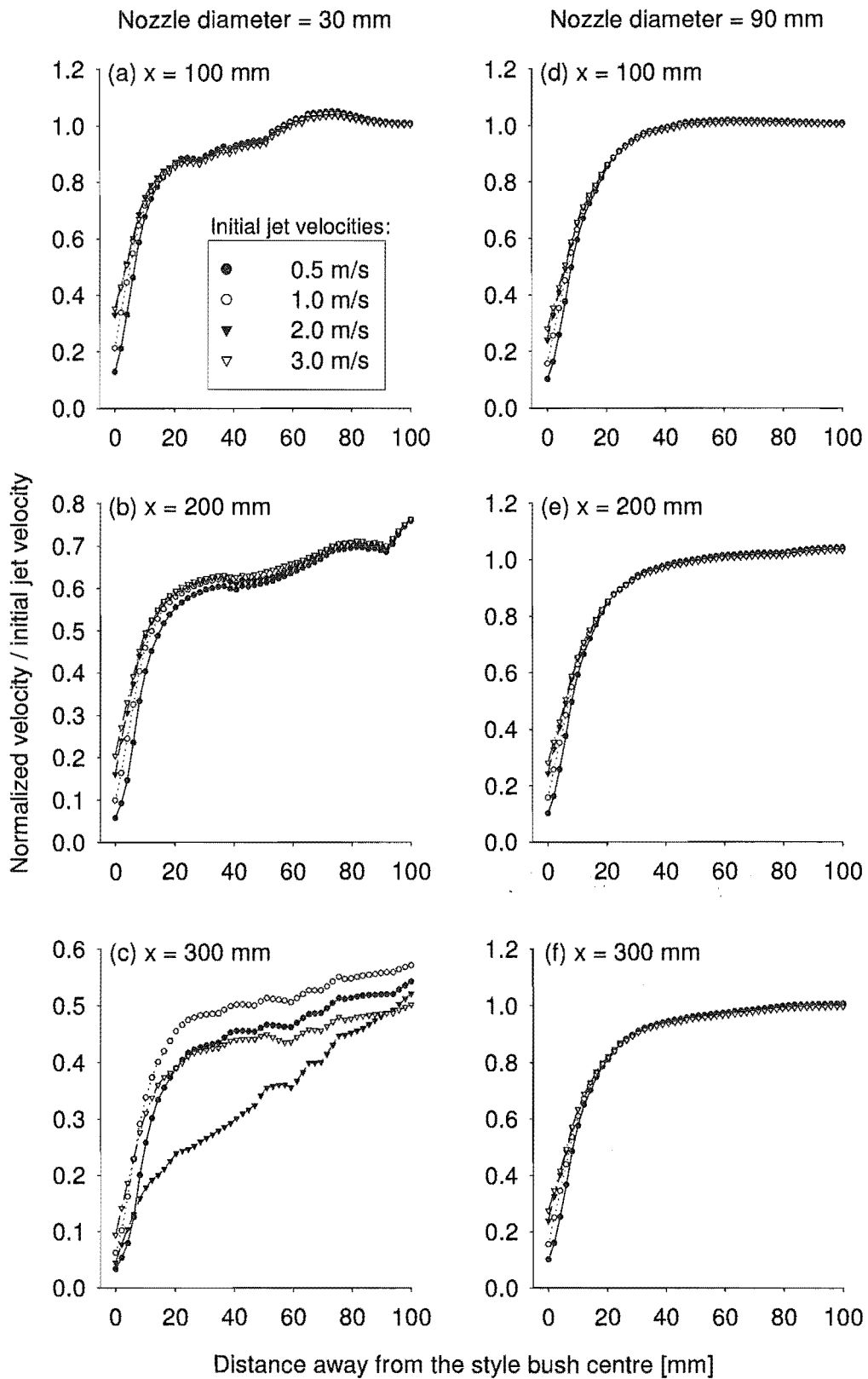
Fig. 5-7: Velocity profile of a frontal jet approaching the centre of the style bush of a full-open flower. x refers to the distance between the flower and the nozzle.
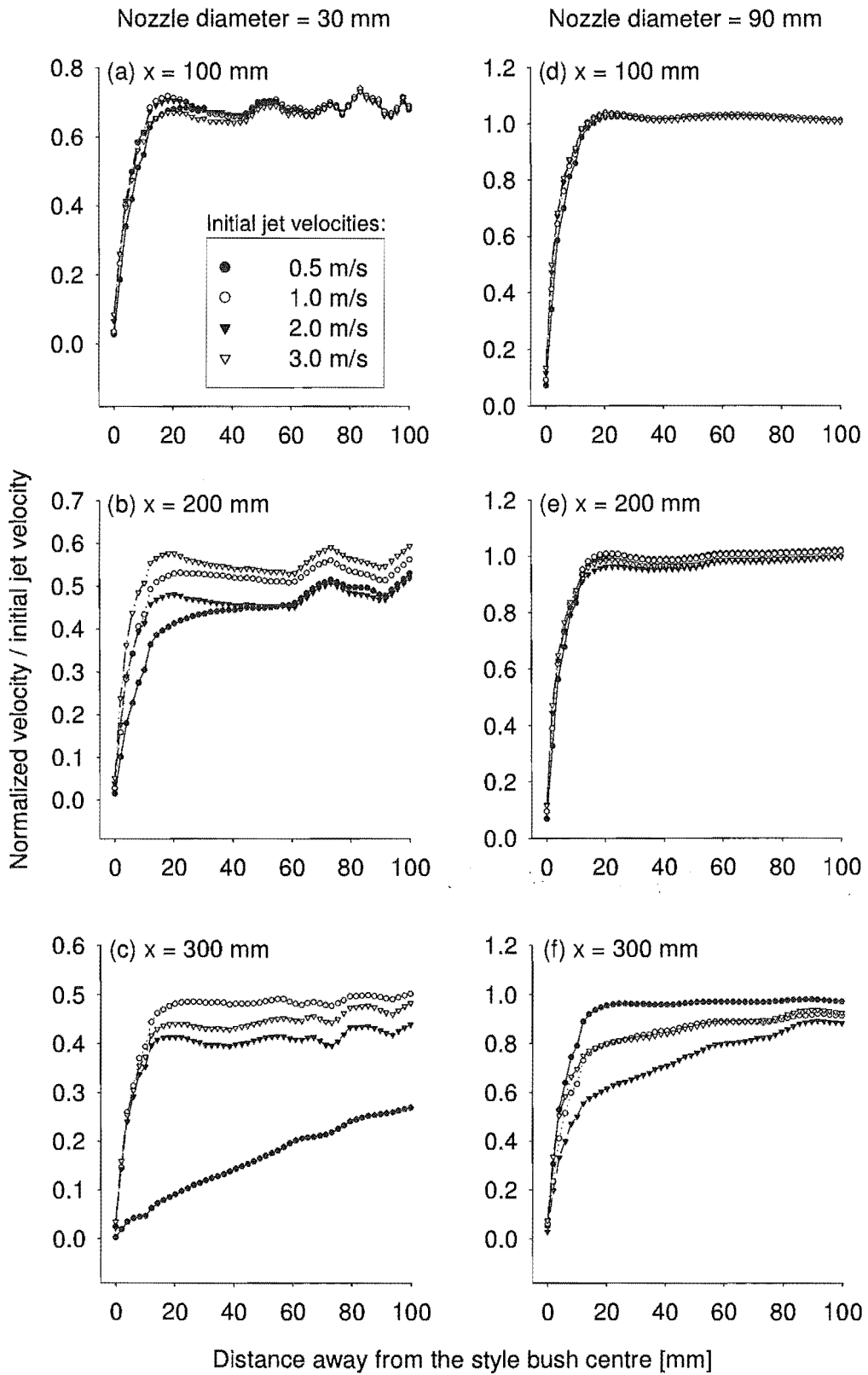
Fig. 5-8: Velocity profile of a side jet approaching the centre of the style bush of a full-open flower. x refers to the distance between the flower and the nozzle.
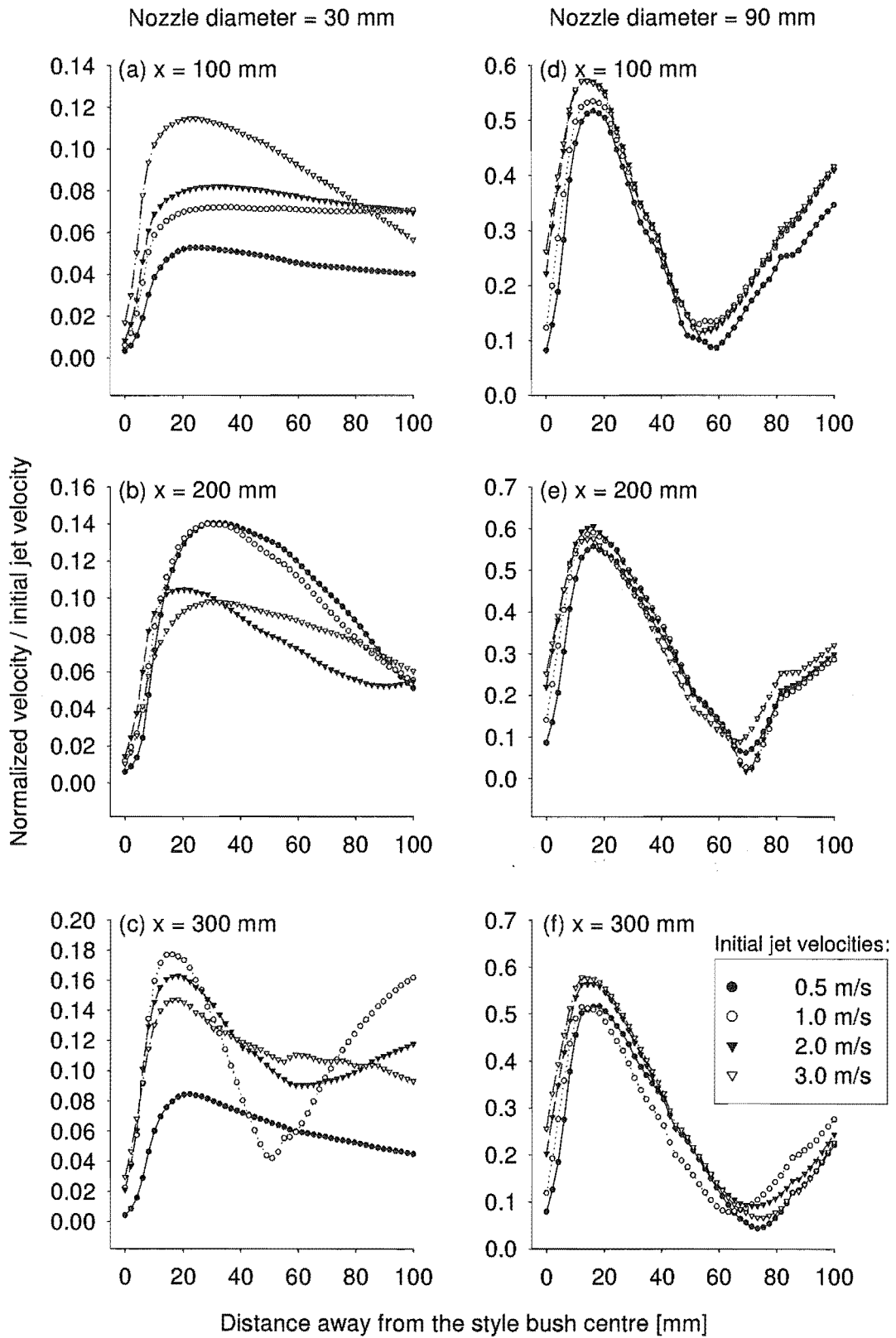
Fig. 5-9: Velocity profile of a back jet approaching the centre of the style bush of a full-open flower. x refers to the distance between the flower and the nozzle.
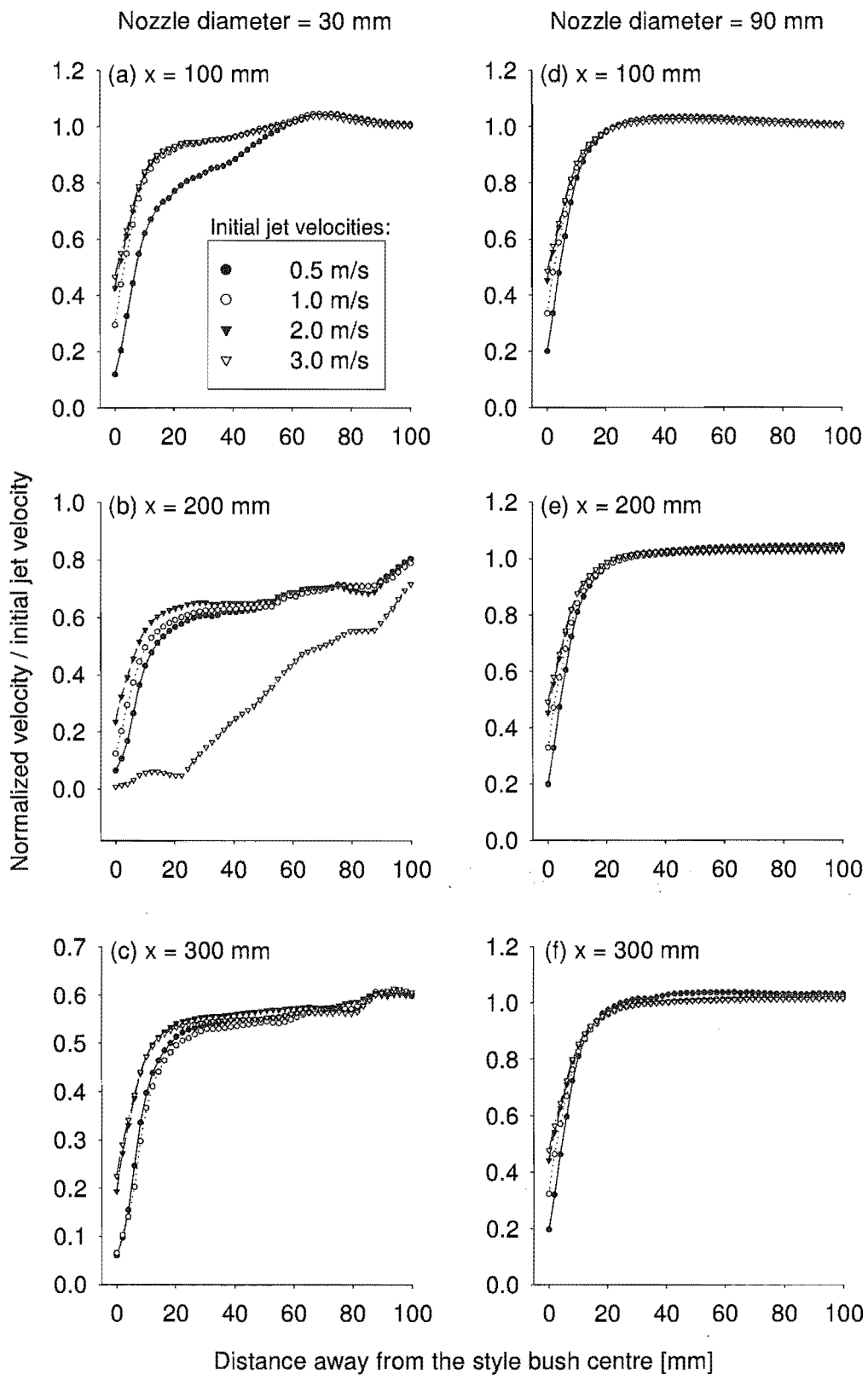
Fig. 5-10: Velocity profile of a frontal jet approaching the centre of the style bush of a bold flower. x refers to the distance between the flower and the nozzle.
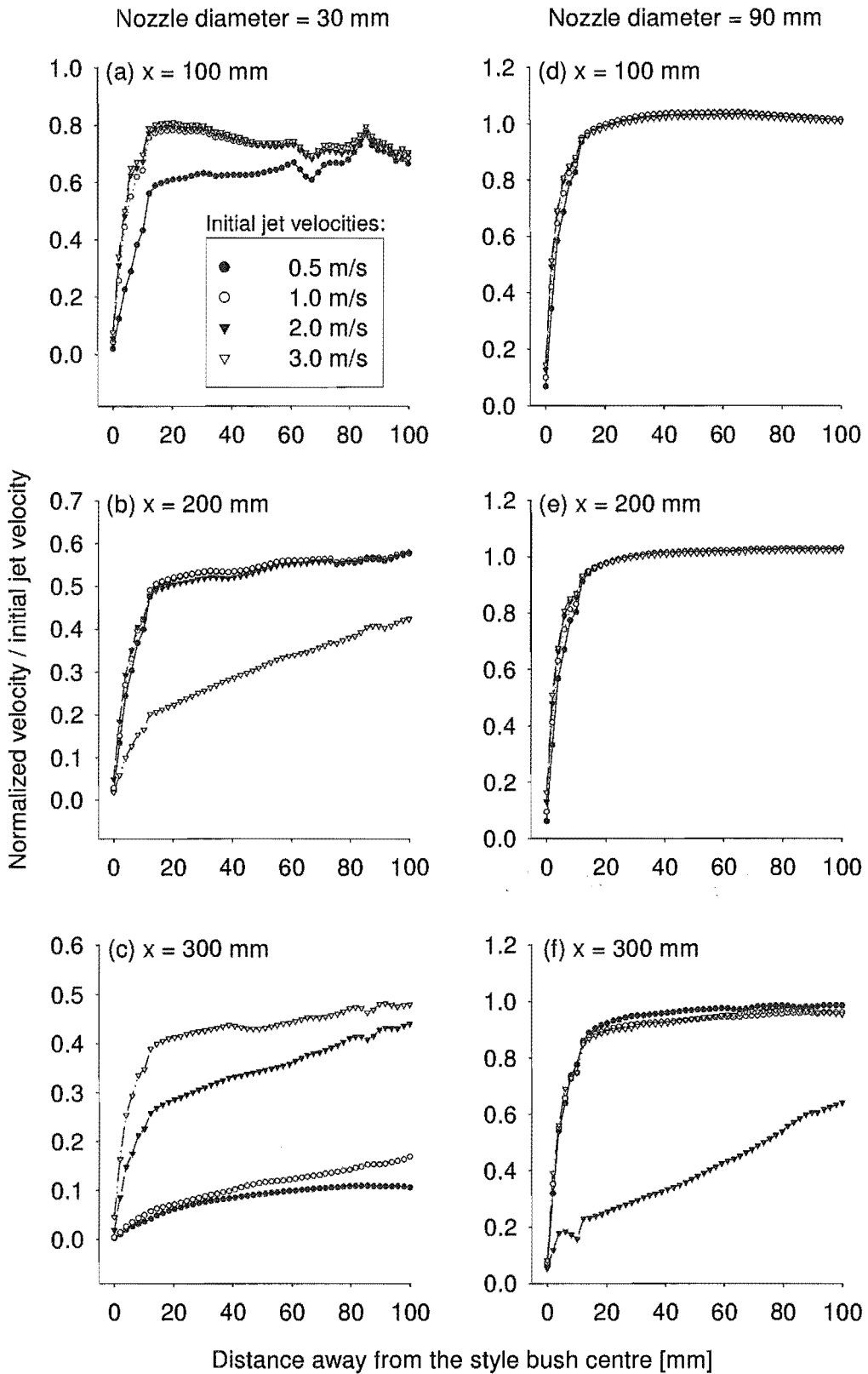
Fig. 5-11: Velocity profile of a side jet approaching the centre of the style bush of a bold flower. x refers to the distance between the flower and the nozzle.
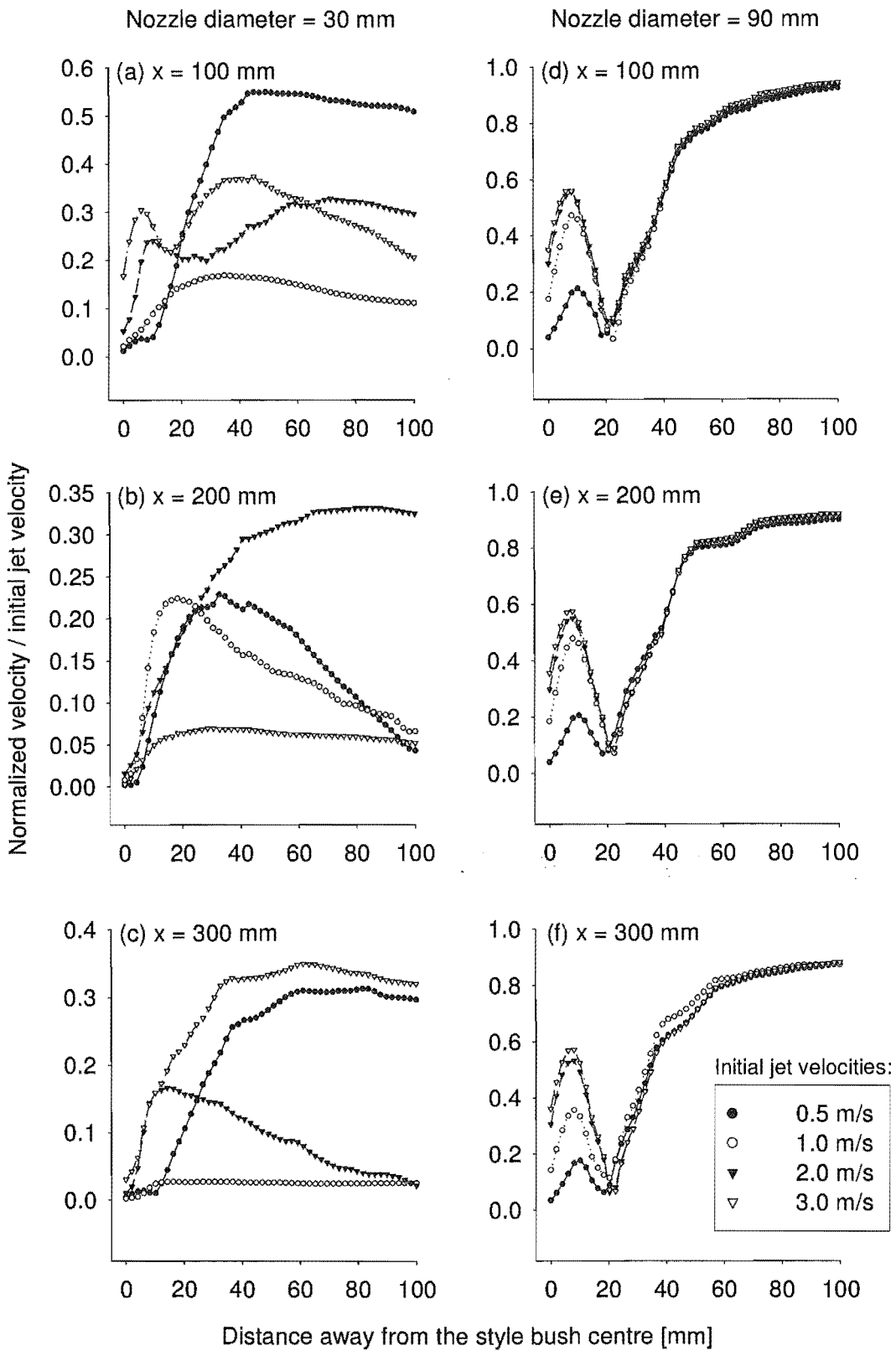
Fig. 5-12: Velocity profile of a back jet approaching the centre of the style bush of a bold flower. x refers to the distance between the flower and the nozzle.
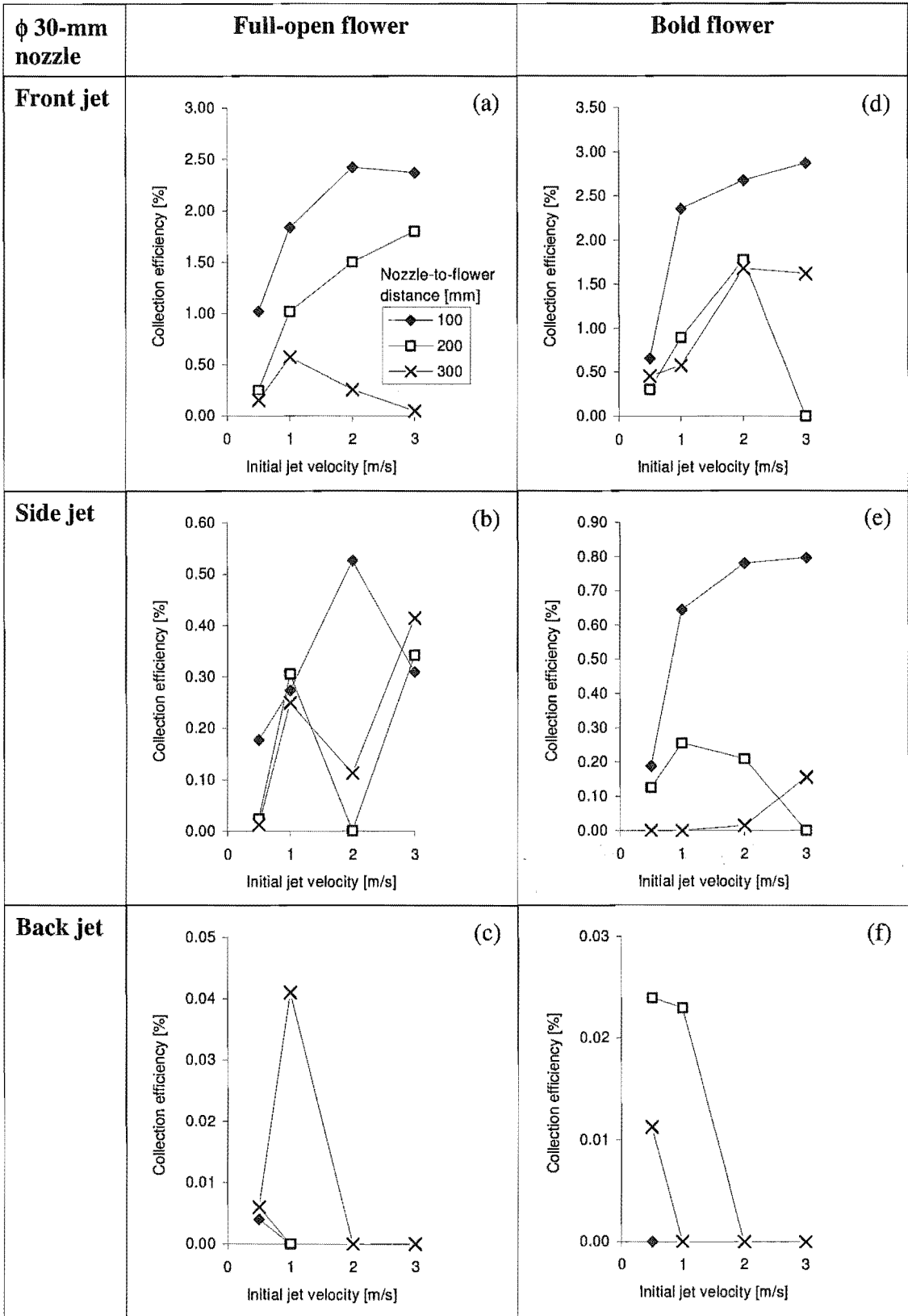
Fig. 5-13: Predicted pollen efficiency of stigma for a single full-open or bold Green kiwifruit flower under a pollen-laden air jet from the front, side and back. The jet comes from a nozzle of 30 mm in diameter. Efficiency = Collected / Fed in jet.

φ 90-mm nozzle	Full-open flower	Bold flower
Front jet	(a)	(d)
Side jet	(b)	(e)
Back jet	(c)	(f)
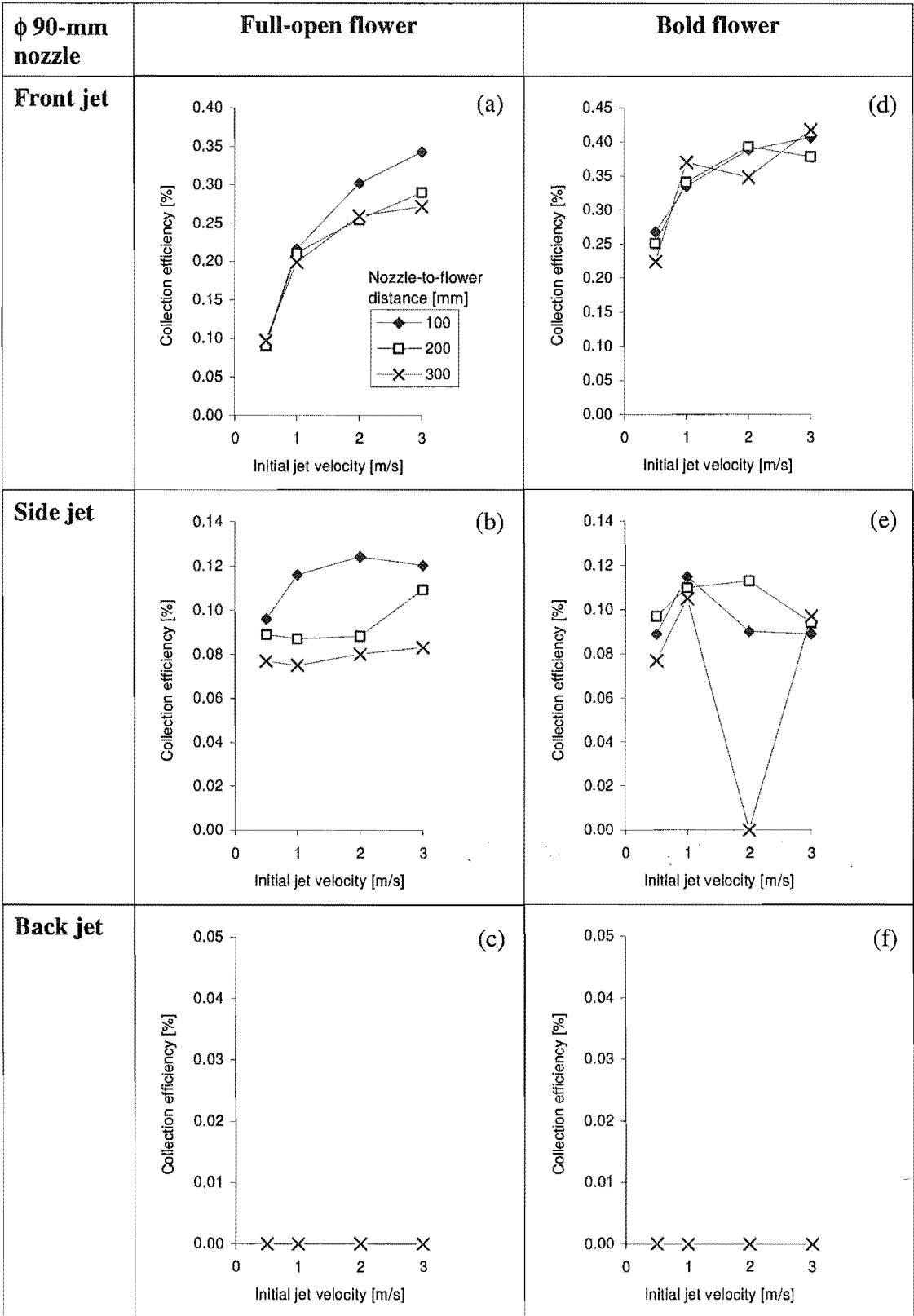
Fig. 5-14: Predicted pollen efficiency of stigma for a single full-open or bold Green kiwifruit flower under a pollen-laden air jet from the front, side and back. The jet comes from a nozzle of 90 mm in diameter. Efficiency = Collected / Fed in jet.

velocity. On a full-open flower under a 2 m/s jet (Fig. 5-13b), a peak exists at 100 mm nozzle-to-flower distance whilst the valley points are predicted at other two nozzle-to-flower distances. It must be noted that the valley points do not result from the jet swinging. Repeated computations with different number of pollen injection still yield these valley points. With the exception of these valley points, the efficiencies improve with the faster side jets. The influence of nozzle-to-flower distance is more clearly displayed on a bold flower (Fig. 5-13e). The incline or decline in efficiencies with the increasing jet velocity also depends on the nozzle-to-flower distance.

For a back jet, very minute amount of sprayed pollen is expected to be captured by the stigma (Fig. 5-13c, f). This is reduced to none as the jet speed is increased to more than 1 or 2 m/s. An usually high collection on a full-open flower is predicted for a nozzle-to-flower distance of 300 mm and initial jet velocity of 1 m/s.

A switch from ϕ 30-mm nozzle to ϕ 90-mm nozzle still sees the stigma of both full-open and bold flowers gather more pollen using a frontal jet than both side and back jets (Fig. 5-14). Note that this is based on the same number of pollen fed and distributed evenly over the jet. The simulations of back jets find no pollen deposition on the stigma (Fig. 5-14c, f). Varying nozzle-to-flower distance does not significantly alter the collection efficiency, which is more dependent on the initial jet velocity. This can be inferred from the normalized velocity approach in Fig. 5-7d, e, f; 5-8d, e, f; 5-9d, e, f and 5-10d, e, f, where the initial jet velocity is maintained up to the stopping distance. For the bold flower, a side jet of more than 1 m/s leads to lower pollen capture efficacy (Fig. 5-14e). The 'outlier' point at 2 m/s in Fig. 5-14e is due to the effect of jet swaying.

Overall, the pollen collection efficiencies given by the jets from a ϕ 90-mm nozzle (Fig. 5-14) are lower than those from a ϕ 30-mm nozzle (Fig. 5-13). This is attributed to the larger cross sectional area of ϕ 90-mm nozzle, which means a lower pollen number density per unit area. The gain in cross-sectional area by ϕ 90-mm nozzle is nine times.

Pollen depositional pattern on other parts of the flower

The amounts of pollen landed on the styles and other parts of a single full-open flower (Fig. 5-15) demonstrate a similar trend but differing magnitude to those on the stigma (Fig. 5-13). The exception is in the back jet application in Fig. 5-15i and l, which find significant pollen accumulation on the petals but not on the stigma or style.

The above is similar for a single bold flower, by comparing Fig. 5-14 to Fig. 5-16. However, in contrast to the full-open flower, the anther-filament bush replaces the petals as the biggest pollen sink.

As mentioned before in section 1.6, a pollen deposition on other parts of the flower may enhance the deposition on the stigma since the pollen applied using dry air jet may get re-entrained into the airspace near the style bush. An examination of the pollen deposition on the styles presents a useful indirect indication of the collection by the stigma which are in the same vicinity. Fig. 5-15 and 5-16 suggests that an air jet application at the bold-flower stage definitely favours more pollen deposition on the styles, hence likely advantage on the stigma. However, in the absence of petals, a whole bold flower does not collect as much pollen as a whole full-open flower. Re-entrainment is not an issue with a spraying of pollen-suspended liquid as it is difficult to realize. In addition, the wetted pollen become non-viable after two hours.

Selection of nozzle diameter

It is found that, except for the back jet, the pollen collection efficiency by the stigma is positively and linearly correlated to the normalized velocity at the stigma bush centre (Fig. 5-17). However, the degree of dependence (i.e. the slope) varies with the nozzle size and the jet directions. Since the collection efficiency by the back jet is so low, it will not be analysed further. For a frontal jet from either ϕ 30-mm or ϕ 90-mm nozzles, Fig. 5-17a and d show that better pollen collection by the stigma of a bold flower comes from a higher normalized velocity at the style bush centre.

Since the normalized velocity at the stigma bush centre is positively correlated with the pollen collection efficiency, it is intended to be able to choose a nozzle diameter and initial jet velocity that will give a desired normalized velocity at the stigma bush centre. Fig. 5-18 shows the normalized velocities at the style bush centre achieved with
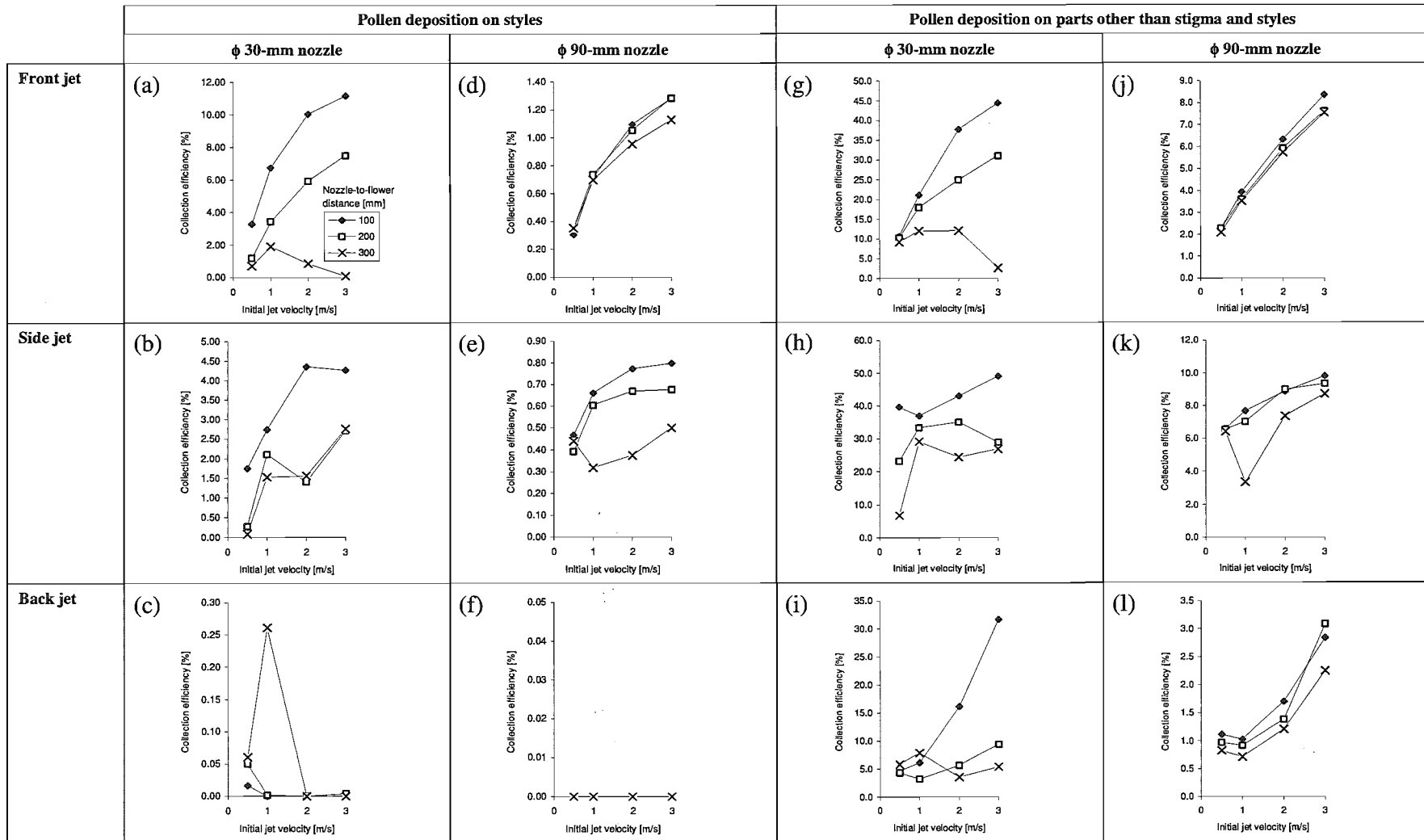
Fig. 5-15: Predicted pollen deposition on the style and other parts of a full-open Green kiwifruit flower under a pollen laden air jet.
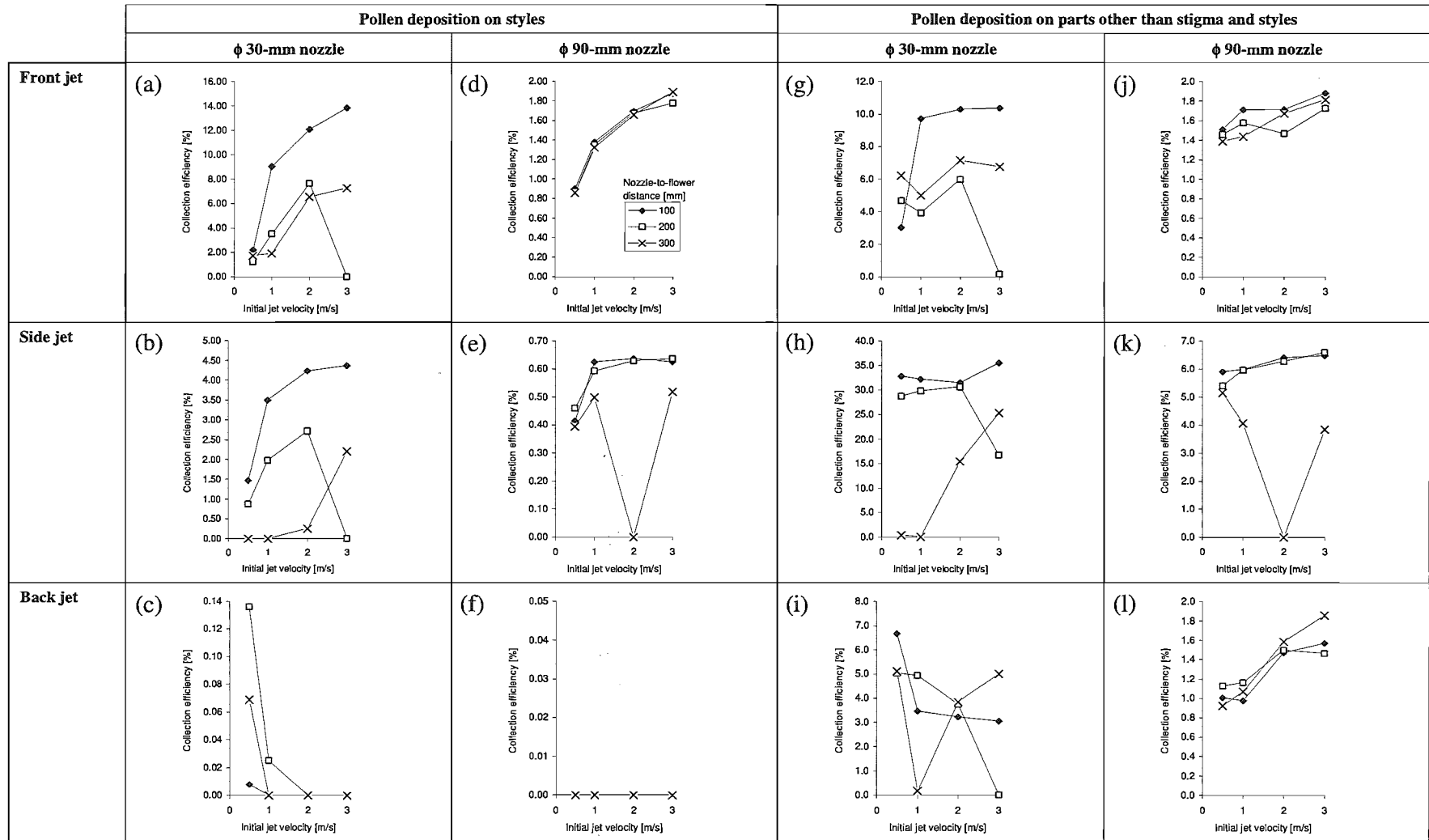
Fig. 5-16: Predicted pollen deposition on the style and other parts of a bold Green kiwifruit flower under a pollen laden air jet
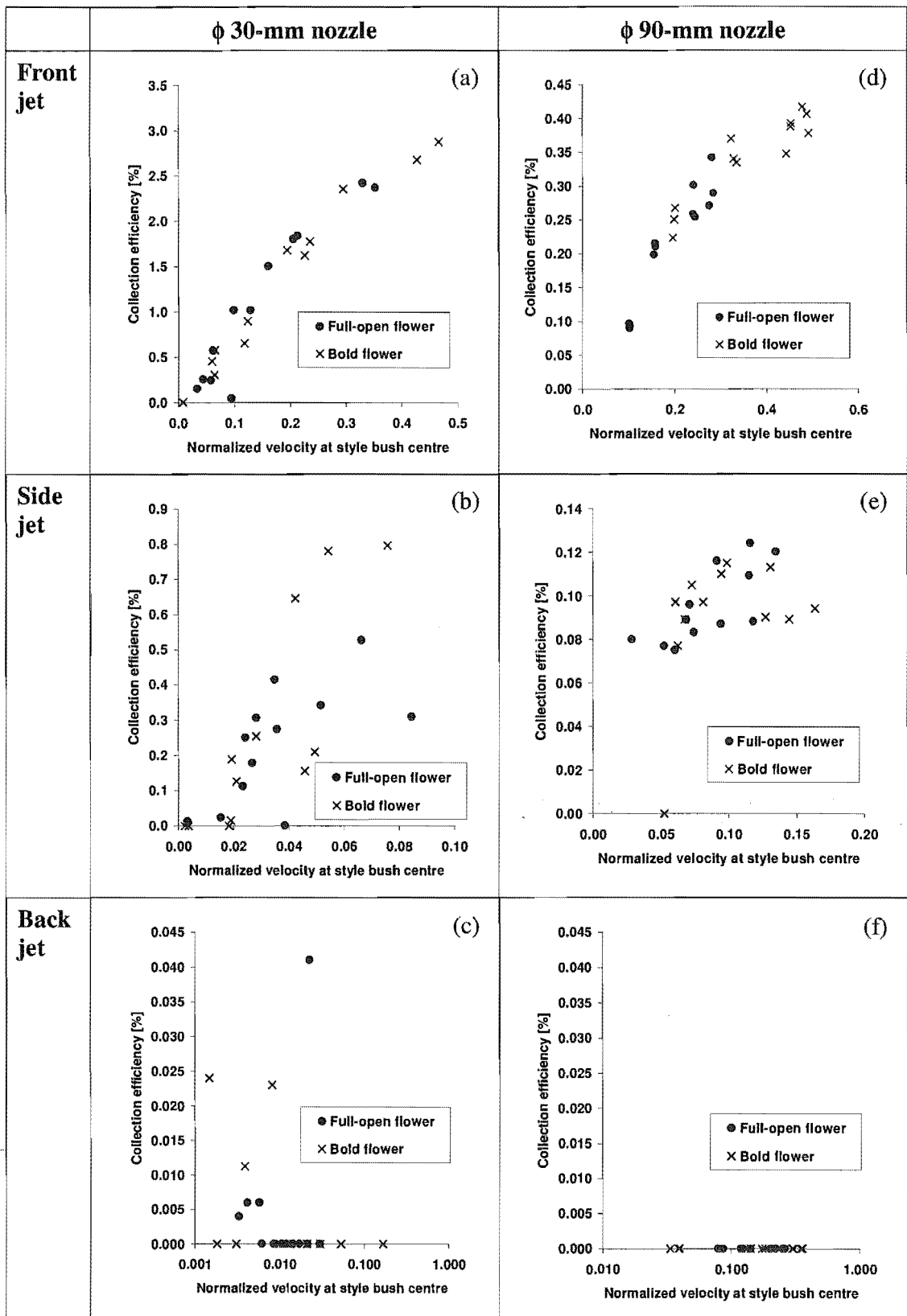
Fig. 5-17: Predicted pollen collection efficiency by the stigma at different normalized velocity at the style bush centre of a single Green kiwifruit flower.
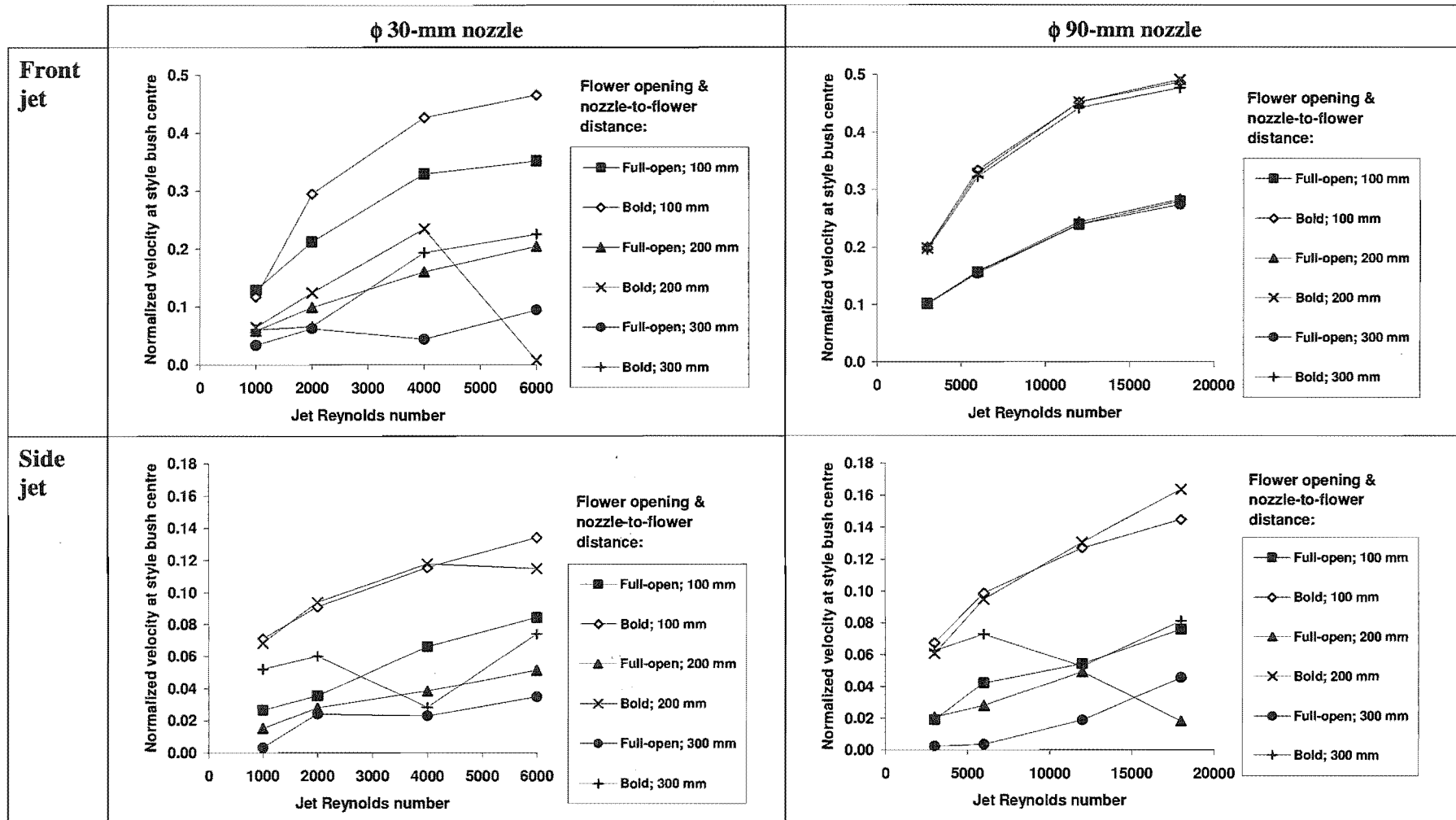
Fig. 5-18: Normalized velocity at the style bush centre of a single Green kiwifruit flower, attained at different jet Reynolds numbers.

different jet Reynolds numbers (calculated based on the nozzle diameters and initial jet velocities), for the frontal and side jet applications. With the exception for a bold flower located at 300 mm away from the nozzle, the normalized velocity at the style bush centre increases with the jet Reynolds numbers. In preparing Fig. 5-18, it is observed that there does not appear a continuation of the plots from Re range of 1000-6000 to Re range of 3000-18000 resulted from a change of φ 30-mm nozzle to φ 90-mm nozzle. This is presumably due to the very different flow patterns established by φ 30-mm and φ 90-mm nozzles. Thus, additional computations are needed when nozzle sizes of other than 30 and 90 mm are to be implemented.

5.3. Discussion and recommendations

The simulations of pollen-loaded air jet show that:
- the jet should be applied in front of the flower, instead of from the side or back;
- at the same pollen mass feed rate, the use of φ 30-mm nozzle is preferred to φ 90-mm nozzle. Smaller nozzle produces a smaller jet that focuses the pollen onto the stigma region;
- the spraying nozzle should be kept close to the flowers such as the 100 mm nozzle-to-flower distance studied here. It is not considered physically practical to have the nozzle much less than 100 mm away from the flowers;
- an initial jet velocity of 3 m/s is suggested. There does not seem to be any significant gain in pollen collection beyond this velocity;
- for a better collection efficiency, pollen should be sprayed after most of the flowers have lost their petals. At jet velocity of 3 m/s and nozzle-to-flower distance of 100 mm, this will lift the efficiency by 21 % according to Fig. 5-13. Although the stigma receptivity is not a concern here, there is a potential risk that the wait may coincide with the unexpected adverse weather. In the orchards where two rounds of machine pollination are carried out, it is recommended to schedule the later according to the percentage of de-petalled flowers.

The simulated pollen collection efficiencies by the stigma with a φ 30-mm nozzle placed at 100 mm away from a single full-open and bold flower can be used to estimate

the pollen loading of the spray jet. Referring to section 1.3, the required number of pollen grains for 100-g and fully-pollinated fruits are 7900 and 12000 respectively. Table 5-1 shows the recommended pollen feed rate for the jets applied onto a single full-open and bold flower for 1 second.

According to Table 5-1, an increase of air jet from 0.5 m/s to 2 m/s (which gives the best pollen collection efficiency) will enable at least 1.4 more full-open flower to be sprayed for the equivalent amount of pollen. The saving is even greater for a bare flower where elevating the jet from 0.5 m/s to 3 m/s results in a coverage of 4.4 more flowers. The better gain in pollen collection efficiency through the adjustment of jet velocity offers another reason to support scheduling the spray pollination after the petal fall-off.

There are however some practicality issues with the ϕ 30-mm nozzle. It is hard and time-consuming to target individual flowers with a small nozzle. There is also a risk of losing track of which flowers have been sprayed[1]. In addition, since the jet is swinging in some conditions, a small jet (such as from a ϕ 30-mm nozzle) may miss the flower easier than a larger jet (say, from a ϕ 90-mm nozzle).

This has prompted the author to look at the ϕ 90-mm nozzle further. Table 5-2 shows the recommended pollen feed rate for a single full-open and bold flower under a frontal jet. Comparison with Table 5-1 for 3-m/s jet indicates that, for both full-open and bold flowers, the higher efficiency by the ϕ 30-mm nozzle enables 6 more flowers to be covered with the same amount of pollen. However, this information can be misleading without considering the larger coverage provided by the larger jet from ϕ 90-mm nozzle.

Say the stigma coverage by the jet is defined as the cross-sectional area in which the jet velocity within is equal to or more than half of the initial jet velocity. This will be the coverage just before the jet contacts with the stigma-style bush[2]. For a nozzle-to-flower distance of 100 mm and under a frontal jet of 3-m/s, the diameters of the coverage are

---

[1] In the liquid system using airshear nozzles, this risk is greatly reduced with the use of a red dye. The equivalent result can be achieved by using the pink-colour lycopodium pollen as indicators.
[2] The diameter of the stigma-style bush is about 24 mm.

		Target = 100-g fruits		Target = fully-pollinated fruits	
Air jet velocity [m/s]	Collection efficiency [%]	Required no. of pollen per spray of one flower	Required mass flow rate of pollen [mg/s]	Required no. of pollen per spray of one flower	Required mass flow rate of pollen [mg/s]
Full-open flower					
0.5	1.02	7.7E+05	5.7	1.2E+06	8.7
1.0	1.84	4.3E+05	3.2	6.5E+05	4.8
2.0	2.42	3.3E+05	2.4	5.0E+05	3.7
3.0	2.37	3.3E+05	2.5	5.1E+05	3.8
Bold flower					
0.5	0.66	1.2E+06	8.9	1.8E+06	13.6
1.0	2.36	3.4E+05	2.5	5.1E+05	3.8
2.0	2.68	3.0E+05	2.2	4.5E+05	3.3
3.0	2.87	2.7E+05	2.0	4.2E+05	3.1

Table 5-1: Recommended pollen loading at different jet velocities onto a single full-open and bold flower. The jets are released from a ϕ 30-mm nozzle at 100 mm away from the flower.

		Target = 100-g fruits		Target = fully-pollinated fruits	
Air jet velocity [m/s]	Collection efficiency [%]	Required no. of pollen per spray of one flower	Required mass flow rate of pollen [mg/s]	Required no. of pollen per spray of one flower	Required mass flow rate of pollen [mg/s]
Full-open flower					
0.5	0.09	8.5E+06	63.0	1.3E+07	95.7
1.0	0.22	3.7E+06	27.1	5.6E+06	41.2
2.0	0.30	2.6E+06	19.4	4.0E+06	29.5
3.0	0.34	2.3E+06	17.1	3.5E+06	26.0
Bold flower					
0.5	0.27	2.9E+06	21.9	4.5E+06	33.2
1.0	0.34	2.4E+06	17.5	3.6E+06	26.6
2.0	0.39	2.0E+06	15.1	3.1E+06	22.9
3.0	0.41	1.9E+06	14.4	3.0E+06	21.9

Table 5-2: Recommended pollen loading at different jet velocities onto a single full-open and bold flower. The jets are released from a ϕ 90-mm nozzle at 100 mm away from the flower.

about 35 mm and 110 mm for φ 30-mm and φ 90-mm nozzles respectively. This is found to be the same for both full-open and bold flowers. In the orchard, the flowers are borne along the canes. Depending on the growth of the canes, there can be patches of flowers. The analyses of the photos taken during the field trip to Te Puke, New Zealand in 2001 indicate that the distance between adjacent flower centres ranges from 47 mm to 73 mm, or 60 mm on average.

A sketch on a piece of paper with these dimensions show that, under an ideal situation where the adjacent flowers are packed close to one another, the jet from φ 90-mm nozzle is able to 'cover' about five more flowers around the targeted flower at the centre. The benefit from the extra coverage here is one flower less than that offered by the φ 30-mm nozzle. However, the saving in labour time (and hence cost) will be substantial. Since this is based on the ideal estimation here, more careful evaluations on the benefits of using a large jet to target an array of flowers are needed. This is because during the field trip to Nelson in 2003, the author learned from the growers that pure pollen was in short supply. In another word, an efficient pollen delivery to the stigma outweighs the saving in labour cost.

The outputs of modelling agree with the field trials by King & Ferguson (1991), in which the amount of pollen deposited on the stigma was found to increase at high air velocity from the boom sprayer. King & Ferguson (1991) further reported that the deposition did not depend on the concentration of pollen sprayed. The concentration factor has not been studied here but can be included in the future work.

The studies by Heath (1984) found that the pollen tube growth happened most readily in pollen clumps and almost none in monolayers of discrete pollen grains. All these suggest that it may be advantageous to spray the pollen in clumps. The pollen clumps can be represented in numerical simulations by specifying a larger pollen size and reduced density.

Similar simulations can also be performed to see whether an air-blasting can enhance the pollination of *Actinidia Arguta*, which has a hermaphroditic (self-pollinated) flower.

CHAPTER 6: STUDY OF ELECTROSTATIC SPRAYING

There is reported evidence that electrostatics enhances natural pollination whether by wind or by bees. This attractive feature has been applied by others to improve pollen collection efficiency during artificial pollination. For this reason, the potential benefits from applying charged pollen onto a single kiwifruit flower are looked at here.

6.1. Background

6.1.1. Electrostatics and pollination

Plants possess small negative surface charges on a clear fair day (Vaknin *et al*, 2000). The surrounding atmospheric fields are weak and positive (Erickson & Buchmann, 1983). The polarity of the surface charges and atmospheric fields change during stormy weather. The electric fields are the strongest at sharp protrusions such as plant extremities like flowers (Dai & Law, 1995), and are least on broad flat surfaces like leaves. The strength of electric fields around the plants is affected by the environment and the chemical composition, height, size and shape of plants (Erickson & Buchmann, 1983). Electrostatic attraction of pollen onto stigma occurs in both wind and bee pollination.

According to Erickson & Buchmann (1983), windborne pollen grains contain a small negative charge when shed from the plant. However, they acquire strong positive charge as they are passively carried by the wind. They are then attracted to electrically conductive plant extremities e.g. flowers which are earthed.

Insects such as bees acquire surface electrical charges through contact with biotic and abiotic substrates, and their flight through the atmosphere (Erickson & Buchmann, 1983). Hardin (1976) reported that bees carry positive potentials after an active flight, with charge of about 23 pC on average (Gan-Mor *et al*, 1995). When a bee approaches a grounded flower, an electric field is induced between them when a quantity of charge

of opposite sign is forced to flow up from the earth into the flower i.e. image charging (Vaknin *et al*, 2000). This leads to the detachment of negatively charged pollen grains from the anthers and deposition onto the bee body. Likewise, there is also detachment of positively charged pollen grains from bee body to stigma.

Corbet *et al* (1982) used silken threads to hold down a living bumblebee onto a cork on a wax block. Sprinkling of oilseed rape pollen over the bee resulted in the pollen grains in the vicinity of the bee drifting towards the bee and adhering to its body. This was attributed to electrostatic attraction. Further experiments by Corbet *et al* (1982) using electrode-mounted bees and flower parts showed that pollen grains could jump from anther to bee and from bee to stigma. This is supported by observations by Gan-Mor *et al* (1995) indicating that an active honeybee could accumulate enough charge to detach avocado and eucalyptus pollen. The extent of electrostatic force in enhancing dry pollen transfer from anthers to stigma via bee depends on the magnitude and spacing of the charge source, the dielectric properties of the media, the flower geometry, atmospheric ion concentration and mobility, and local components of the earth's ambient electric field (Vaknin *et al*, 2000).

Kiwifruit is regarded as a buzz-pollinated flower because bumble bees are involved in the pollen transporting process (Corbet *et al*, 1988). Based on the mechanism reported by Buchmann (1983), Corbet *et al* proposed a model describing the role of electrostatics in the pollen transfer between a flower and a bumble bee. The electrostatic field created by wind vibration attracts the male pollen from anthers to the bee. The charge on a bee leaks away gradually but the ungroomed and insulating pollen on the bee's body hairs may acquire this charge, making the pollen repellent to bees. Upon arrival on a female flower, the charged pollen may be displaced to the stigma that have the lowest impedance paths to earth due to coverage of wet exudates.

The promising aspect of electrostatics in enhancing pollen deposition onto the stigma has prompted the machine spraying of charged pollen. Electrostatic spraying is commonly practised in numerous industrial and agricultural operations, e.g. powder paint coating (Bailey, 1998; Bright *et al.*, 1978; Cross, 1987), pesticides spray (Coffee, 1974; Law, 1983, 1995a, 1995b), fungicidal sprays onto postharvest fruits and

vegetables (Law & Cooper, 2001), and etc. The electrostatic forces minimize the wastage by attracting the charged particulates to the targeted surfaces.

Three types of pollen charging have been reported in the literature, namely induction charging, tribo-charging and corona charging.

Banerjee & Law (1996) applied induction charging on a conductive carrier liquid holding suspended almond pollen grains. The chargeability (i.e. charge-to-mass ratio) was up to 10 mC/kg. Induction charging is achieved by placing an isolated conductor in an electric field (Cross, 1987). Separate positive and negative charges are created within the conductor. When the conductor is earthed in the electric field, the free charges are lost to the ground leaving a net charge on the conductor. Law *et al* (1996, 2000) found that although the induction charging of almond pollen-liquid mixture enabled more deposition of pollen (overall 5.6 times), there was also 19 % relative loss in germinability (i.e. more pollen became non-viable).

Banerjee & Law (1995, 1998) studied the tribo-chargeability of pecan and lycopodium pollen grains using Teflon and nylon chargers. Tribocharging occurs when there are frictional contacts between solid materials (Cross, 1987; Jonassen, 1998). Teflon chargers produce positive charges while nylon chargers give the opposite charges. The pecan and lycopodium pollen grains were charged up to 11.52 mC/kg and 7.59 mC/kg respectively. Measurements by Roberts (1997) and Kardos (1998) indicate that pure kiwifruit pollen can be tribo-electrically charged up to ~3 mC/kg using a Teflon charger. Bee-collected pollen can attain higher chargeability (~ 6.8 mC/kg), but they tend to easily clog the sprayer. Banerjee & Law (1995, 1998) found that chargeability with a Teflon charger did not degrade on continuous exposure to moist air. This suggested a suitable outdoor use as the carrier air does not then need additional drying treatment.

In corona charging, a sharp electrode is used. The high voltage causes an electrical breakdown (called a 'corona' discharge) in a region close to the sharp electrode tip (Bright *et al.*, 1978; Cross, 1987). This produces an ionized field which charges any pollen grains that pass through as they are bombarded with the ions. Field experiment carried out by Bechar *et al* (1999) found the application of date pollen grains which

were corona charged at 40 to 80 kV had increased the fruit yield by 85 to 157 %. Electrostatic dusting of larch pollen deposited three times more pollen on the flowers (Philippe & Baldet, 1997; cited in Vaknin *et al*, 2000). Trials with almond pollen charged at 50 kV reported an improvement by 13 % in fruitlet set (Vaknin *et al*, 2001a).

The ideas of utilising electrostatics to enhance the pollen captured by stigma have also been trialled in the kiwifruit industry. The Airflo pollinator (see section 1.6) has a polyester sock attachment over the distribution nozzle that is intended to electrostatically charge the pollen by contact.

Hopping & Hacking (1983a), in their field trials, found that the electrostatic charging of pollen-loaded spray droplets from a boom sprayer (fitted with conventional T-jets) significantly improved the percentage of exportable weight fruit compared to the same but uncharged application. Their evaluations on the controlled droplets application (CDA) spinning disc contact charger and corona discharge (Hopping & Hacking, 1983c) found that the former gave insufficient pollen deposition on stigma while the latter increased pollen deposition by 39 %. However, the pollination level was still less than half that attained by hand pollination. Hopping *et al* (1984) found that the Laws electrostatic sprayer that had an embedded electrode at 1 kVA[1] improved substantially both fruit set and the percentage of exportable fruit compared to an airshear based Curtis applicator. Hopping *et al* (1985) further tested a prototype sprayer that had 6 atomising nozzles independently contact-charged to 37.5 kV along a 2-m boom and found that the charging did not result in any improvement in pollen deposition on stigma. They concluded from the measurement of spray discharge current, that this was because the charging of this prototype was not as effective as previous ones. This implies that the level of enhancement in pollen deposition depends on the degree of electrostatic charging. The use of electrostatics may not always obtain any improvement, as shown by trials with apple pollen reported by Williams & Legge (1979).

Studies by Bechar *et al* (1999), Dai & Law (1995) and Vaknin *et al* (2001b) on electrostatic spraying using either metallic artificial flowers or numerical modelling of very simplified flower geometries have produced some insights. Maximum electric

---

[1] Note that this reported value is unusually low compare to other corona charging devices.

field was predicted on the pistil top. Uncharged pollen were found to be evenly deposited on the whole flower. Charged pollen on the other hand were concentrated on the stigma. Another interesting finding is that wider petal-opening angle promotes a greater electric field near the stigma and correspondingly less intense electric fields near petal edges. In other words, the strongest electric field prevails when the flower is more open and the stigma are more exposed. However, Vaknin *et al* (2001b) pointed out that as the petals flipped backwards after attaining the flat shape, there was a drop in pollen deposition. The interaction between stigma and the petals in influencing the electric field will be looked at for the kiwifruit flowers as this may give important implications on the best flowering stage to apply the charged pollen.

Overall comments

With respect to the dry kiwifruit pollen spraying in an air jet, both corona charging and tribo-electrification are feasible to charge the pollen. Although corona charging is more reliable, predictable and gives a stronger electric field (Adamiak, 1997a), the need to have a mobile high voltage generator during the spraying in the field can be a major drawback, particularly so during wet days. A corona charging module is likely to be limited to a small vehicle rather than a back-pak design.

The success of electrostatic pollen spraying also relies on a conductive path from the stigma to the earth. Measurements by Corbet *et al* (1982) on a rape plant which was grown in a pot of wet soil showed that stigma had the lowest impedance to earth. Anthers gave the highest impedance reading, about 25000 times higher than that of stigma. Similar exercise was carried out for the kiwifruit flowers in the next section.

6.1.2. Resistance measurement of different flower parts of kiwifruit

The presence of water in the kiwifruit vine (in the form of xylem sap) provides an electrically conductive path from the different parts of the plant to the earth. Here, the resistance of this path was measured for the components of the kiwifruit flowers (i.e. stigma, petal, anther and sepal) and the adjacent 'neighbours' to the flower (i.e. flower stem, leaf stem, leaf and branch). This is to assess whether there is any competition for electrostatic pollen deposition among them, particularly with respect to the stigma. The

work was carried out in a Green kiwifruit orchard in Te Puke, New Zealand from 12 to 19 November 2001.

Measurement method

A multimeter capable of measuring up to GΩ was used. A brass rod, after being sandpapered on the surface, was pushed about 20 cm into the soil to be used as an earth probe. To improve the earthing, the penetration area was wetted with tap water saturated with table salt. A metallic alligator clip was used to attach to the desired part of the plant to complete the conductive path. The internal loop excluding the plant parts had a resistance of less than 0.20 Ω.

To prevent the overloading of the multimeter range, the earth probe was placed close to the trunk of the vine and only the nearby flowers were selected. Depending on the nature of the targets, the time to reach steady reading ranged from half to four minutes. For example, flower stem, leaf stem and branch measurements were usually the quickest while sepal measurements displayed the most instability. It took one to two minutes to obtain a steady reading for stigma, which was reasonably stable.

First, a flower with desired opening stage was chosen as a primary target base. Apart from its components, the flower stem, the leaf and its leaf stem on the same shoot and the branch were also measured for the resistance of the path to earth (see Fig. 6-1).

A = anther
B = branch
FS = flower stem
L = leaf
LS = leaf stem
P = petal
SM = stigma
SP = sepal
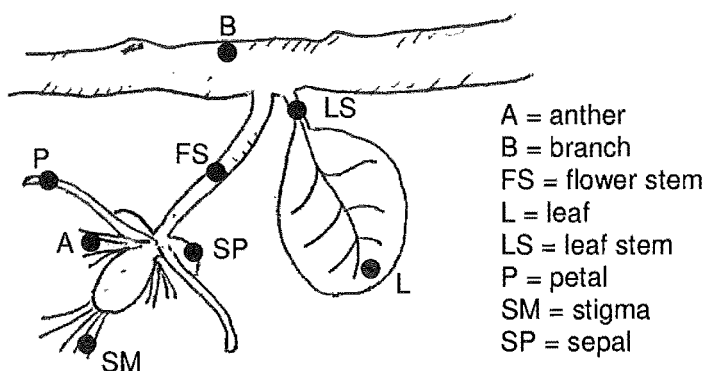
Fig. 6-1: Placement of alligator clip on the different targets.

Assumptions used are:
- Good electrical contact between the alligator clip and the targets;
- Sufficient earthing by using brass rod with salt water;

Results

Most of the readings are in $M\Omega$ with the rest in $k\Omega$. Since the actual resistance will depend on the distance from the targets to earth and the torsions experienced on the electrical path, any comparison between flowers is meaningless. Since the readings actually include the resistance of the surface state (i.e. the cleanliness, the conductivity of the skin layer, the existence of any biological deposition or liquid) of the targets, the flower stem cannot be used as a reference to calculate the actual resistance of the flower components (as shown by the negative value after subtraction).

Therefore, the focus is between the stigma and its adjacent flower components, plus the nearby parts as mentioned before. Since the surface resistance is included, this probably presents a closer to actual picture when charged pollen approaches a flower.

Fig. 6-2 is the statistical distribution of the ratios of the resistance of the different targets to earth with respect to the stigma-earth resistance, based on a single flower. The 31-set data of all flowers (with opening ranges from 25% to petal-fall status) are lumped here. In Fig. 6-2, region above the ratio of 1 means higher resistance compared to stigma-earth path, and vice versa.
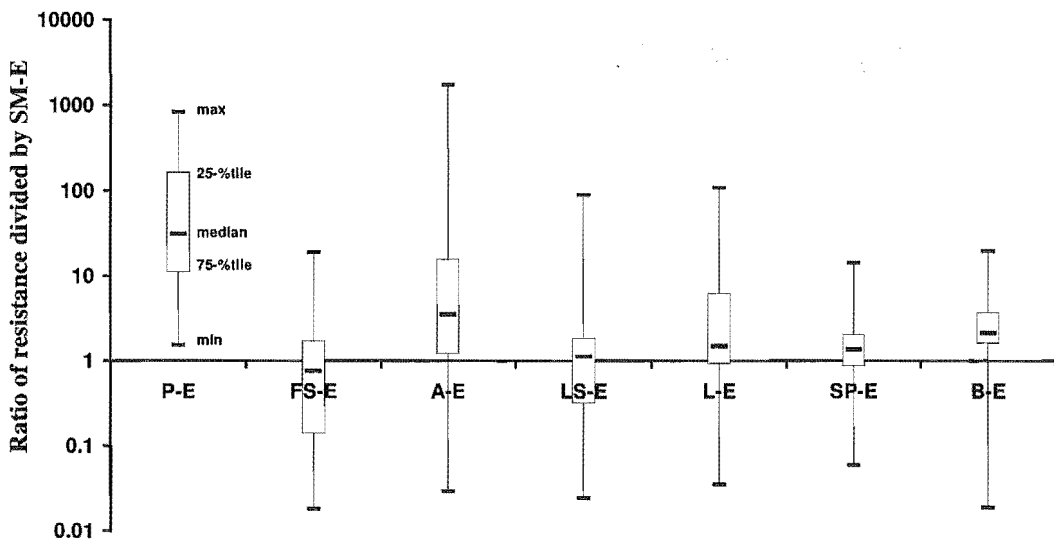
Fig. 6-2: Comparison of resistance of different parts of flower to earth with respect to stigma-earth (SM-E) path; P=petal, FS=flower stem, A=anther, LS= leaf stem, L=leaf, SP=sepal, B=branch, E=earth

Discussion

Apart from the petal-earth path (P-E), other paths in Fig. 6-2 have shown resistance lower and higher than stigma-earth path (refer to the min and max extremes). This can be attributed to the contact surface factor, if the sap flow path through the vine tissue has a significantly lower resistance.

The concentration of the readings (as shown by the median, 25-percentile and 75-percentile) however shows that most of the paths except FS-E and LS-E have resistance frequently above that of stigma-earth.

It is known that when charged pollen approach a flower, the development of mirror charge will force opposite charge to flow from earth to the flower (Vaknin *et al*, 2001b). The lower resistance of stigma-earth path compare to other floral components (petal, anther and sepal) mean quicker mirror charge build-up in the stigma and hence a stronger field between stigma and the pollen, which helps to direct pollen to the desired stigma zone.

Since all the targets measured have shown readings within range of the meter i.e. they are not insulated from earth, there is unlikely to be a huge charge build-up on their surfaces. So, the rate of establishment of mirror charge on the different parts of the vine becomes the influential factor in competing for electrodeposition of pollen.

Although most tests on flower stems and leaf stems have shown a lower resistance path to earth compared to tests on stigma, deposition of pollen on them could be hindered by the shielding of the comparatively larger-area petals and leaf. The fall of petals which takes place after 3-4 days however may remove this hindrance.

The resistance readings here are comparable to the range (i.e. in MΩ) obtained by Ferguson & Pusch (1991) on damp kiwifruit flowers. According to Ferguson & Pusch, the dry petals acted as insulators and the anthers gave readings 2 to 3 times higher than those of stigma. All the readings made on the petals in this work however indicate electrical connection to the earth. 'A-E' in Fig. 6-2 has a median of 3.5, which is within the range of measurements by Ferguson & Pusch.

Other aspects recommended for future study include the changes of resistance at different times of the day i.e. due to the sap movement and its distribution at different time; and the changes of resistance after a shower or after irrigation, i.e. due to the increase in water content of the vine.

In short, electrostatic spraying is applicable since different parts of a Green kiwifruit flower can establish a conducting path to earth. However, unlike the rape plant, there is no clear evidence which indicates that stigma-earth path has the lowest impedance.

6.2. Simulation of electrostatic spraying

6.2.1. Literature review of numerical computation methods

The area of interest in this work is the numerical modelling of the transport of charged pollen from the gun to the target i.e. a kiwifruit flower. Similar numerical simulations have been found to be increasingly popular in the electrostatic powder coating systems and for the electrostatic precipitator (ESP). Two common charging systems - corona and tribo-electrification, are considered here. Note that the term 'particle' below refers to the pollen grain.

In a corona system, the potential difference between the charging gun and the grounded target induces an electric field. The ions from the electric breakdown around the charging electrode dominate the space charge field when compared with the contribution from the particle charge. At the same time, the particles in the field are acquiring further charges and this is called field charging. The acquired charge, q can be calculated using the limit of Pauthenier equation (Pauthenier & Moreau-Hanot, 1932) assuming that the charging has been maximized and the pollen is a medium insulating material (see Cross, 1987; Bechar $et\ al$, 1999).

$$q = 6\pi(r_p)^2\varepsilon_o E \qquad\qquad \text{Equation 6-1}$$

r_p is the particle radius; ε_o is permittivity of the free-space; and E is the local electric intensity.

However, most of the field charging take place in the limited small ionization zone in the vicinity of the charging electrode and thus further field charging outside this zone can be assumed negligible. This is the simplification taken by many researchers and in this work.

The corona needle can be positive or negative in polarity, but a negative polarity is preferred on account of a higher breakdown voltage (e.g. -100 kV in Ali *et al*, 2000).

In a tribo-electrification system, the electric field results from the potential difference between the particle cloud exiting the nozzle and the grounded target. Since there is no ion from an electric breakdown, there is no field charging. Thus, the electric field distribution depends on the space charge density which in turn depends on the local concentration of the particles in the cloud (Adamiak, 1997a, 1998, 2001b; Adamiak & Mao, 1995; Adamiak *et al*, 1992, 1994).

Each simulation, whether of corona or tribo-charging systems, consists of the calculations of (1) the electric field and (2) the particle trajectories through force balances on the particle.

Electric field

The potential difference between the charging gun and the grounded target induces an electric field, E which can be represented by Laplace's equation.

$$\nabla^2 \Phi = 0 \qquad\qquad \text{Equation 6-2}$$

$$E = -\nabla \Phi \qquad\qquad \text{Equation 6-3}$$

Φ is the potential. In the presence of ions (which come from the electric breakdown around the charging electrode) and charged particles, the space charge effects must be considered and this gives Poisson's equation (Choi & Fletcher, 1998).

$$\nabla^2 \Phi = -\frac{\rho}{\varepsilon} \qquad\qquad \text{Equation 6-4}$$

Where
$$\rho = \rho_{ion} + \rho_{pc} \qquad \text{Equation 6-5}$$

$$\varepsilon = \varepsilon_r \times \varepsilon_o \qquad \text{Equation 6-6}$$

ρ_{ion} and ρ_{pc} represent the ion and particle charge density respectively; ε is the permittivity of the field (which is air here); and ε_r is the relative permittivity of the field (which is ≈ 1 for air or gas). Air has a permittivity coefficient, ε_o, of 8.85×10^{-12} F/m. The volumetric particle charge density, ρ_{pc}, for any small control volume, is a product of the particle mass concentration, C in [kg/m^3] and the charge-to-mass ratio of the particle, q in [C/kg].

In a corona system, the ions dominate the space charge field i.e. ρ_{pc} can be optionally neglected. On the other hand, the absence of an ion wind in a tribo-electric system means that the space charge density depends only on ρ_{pc}.

A more comprehensive modelling can optionally include the conservation of charge and the current density equation (Ali *et al*, 2000).

$$\frac{\partial \rho}{\partial t} = \nabla \bullet \mathbf{J} = 0 \qquad \text{Equation 6-7}$$

$$\mathbf{J} = b\,\rho\,\mathbf{E} - D\,\nabla\rho \qquad \text{Equation 6-8}$$

Where $\mathbf{J}$ is the current density; b is the ion mobility; and D is the diffusivity of ions (can be assumed negligible).

Streamler *et al* (1990) showed that an electrostatic field equation can be solved analogously as a heat transfer problem (see later).

Particle transport

The motion of a particle can be taken as the consequences of the resultant balance between the aerodynamic (drag) force, gravitational force and electrostatic force. Other forces are assumed negligible. The Particle Tracking Method, described by Equations 2-37 to 2-43, is the most widely adopted method.

The electrostatic force is the sum of Coulombic force, image charge force, dielectrophoretic force (from the dipole induced by the electric field), the dipole-dipole force (Bottner & Sommerfeld, 2002) and the dipole-monopole force (Abrahamson & Marshall, 2002).

$$F_E = q_p E + \frac{m_p\, q^2}{16\pi\, \varepsilon_o\, y'^2} + \frac{q_p\, E\, D_p^{\,3}}{16\, y'^3} - \frac{3\, \pi\, m_p\, \varepsilon_o\, E^2\, D_p^{\,6}}{128\, y'^4}$$ Equation 6-9

q_p is the charge on a particle; q is the charge-to-mass ratio; E is electric field; m_p is the mass of a particle; ε_o is permittivity of free space (8.854×10^{-12} F/m); and y' is the spacing between the particle and the surfaces.

In the presence of an external electric field (such as in a corona charger and in electrostatic precipitators), only Coulombic force is regarded as dominant and thus the only term included in numerical simulations e.g. Bottner & Sommerfeld (2002), Choi & Fletcher (1998) and Ali et al (2000). This is because the other forces are short-range and significant only in the vicinity of the substrate surface. Dielectrophoretic force and dipole-dipole force, in particular, cannot be resolved fully if the mesh resolution of the wall boundary layer is low. Implementing high density mesh on the stylar surfaces of the kiwifruit flower will be computationally too expensive. Thus, only the first term in Equation 6-9 is employed in this work.

Solver methods

There are four approaches found (listed below), differing mainly in the means of calculating the space charge, ρ. In all the approaches below, particles are assumed not to be field-charged outside the ionization zone i.e. Equation 6-1 is not used. Since Ye et al (2002) obtained very good agreement between computed and experimental results using Approach Three, this approach is favoured for this work. Note that the success of Approach Three depends on the ion charge concentration being negligible over most of the volume, compared with the charge concentration of the particles.

Approach one

This is applicable to both corona and tribo-electrification systems, assuming that the space charge, ρ is negligible. This assumption is valid for dilute particle flow in trib-electrification but doubtful with the ion flux in a corona system.

1. Thus, solve only Equations 6-2 and 6-3 to get electric field, **E**.

2. Then, get particle trajectories from Equations 2-37 to 2-43 and Equation 6-9 using the experimentally measured q.

Approach two (Ali *et al*, 2000)

For a corona system, the volumetric space charge density, ρ is assumed to be attributed to the ion flux only i.e. ρ_{ion}.

1. Start with $\rho = 0$, i.e. solve Equation 6-2, followed by Equation 6-3 to get the initial electric field, **E**.

2. Make an initial guess of ρ, and calculate the ρ distribution in the field from the calculated **E** using Equations 6-7 and 6-8.

3. From this calculated ρ distribution, calculate **E** using Equations 6-3 and 6-4.

4. Repeat step 2 and 3 until the solution is self-consistent.

5. There is an additional criterion to stop the iteration, which is to compare the **E** at the ionization region with an experimentally measured value. If there is no match, repeat step 2 to 4 with a different initial guess of ρ.

6. Then, get particle trajectories from Equations 2-37 to 2-43 and Equation 6-9 using the experimentally measured q.

Approach three (Ye *et al*, 2002)

For both corona and tribo-electrification systems, the space charge field is contributed by the particle charge only i.e. $\rho_{ion} = 0$.

1. Solve the electric field with $\rho = 0$ using Equation 6-2, followed by Equation 6-3 to get the initial electric field, **E**.

2. Then, determine the particle trajectories from Equations 2-37 to 2-43 and Equation 6-9 using the experimentally measured q.

3. Calculate the space charge density distribution in the field due to the particle charge.

4. Using the calculated ρ distribution, solve for the electric field, **E** using Equations 6-3 and 6-4.

5. Repeat step 2 to 4 until the solution of the space charge field is convergent.

Approach four (Choi & Fletcher, 1998)

This is based on the simulation of an electrostatic precipitator, so it can be applied to a corona system. The space charge field now is contributed by both ρ_{ion} and ρ_{pc}. Only important parts of the solver procedure, including the iteration for ρ_{ion} and the use of relaxation factor, are given by Choi & Fletcher (1998). But, these can be combined with the abovementioned Approaches Two and Three.

1. Solve the electric field with $\rho = 0$ using Equation 6-2, followed by Equation 6-3 to get the initial electric field, **E**.

2. Make an initial guess of ρ (= ρ_{ion} only), and calculate the ρ distribution in the field from the calculated **E** using Equations 6-7 and 6-8.

3. From this calculated ρ distribution, calculate **E** using Equations 6-3 and 6-4.

4. Repeat step 2 and 3 until the solution is self-consistent.

5. There is an additional criterion to stop the iteration, which is to compare the ion charge density at the wire with that calculated from the Peek's formula in Cross (1987). If there is no match, repeat step 2 to 4 with a different initial guess of ρ. If the iteration condition is fulfilled, this shall give a distribution of ρ_{ion}.

6. Determine the particle trajectories from Equations 2-37 to 2-43 and Equation 6-9 using the experimentally measured q.

7. Calculate the space charge density distribution in the field due to the particle charge and then Equation 6-5 by including the calculated ρ_{ion} from step 5.

8. Using the calculated ρ distribution, solve for the electric field, **E** using Equations 6-3 and 6-4.

9. Repeat step 2 to 8 until the solution of the space charge field is convergent.

6.2.2. CFD simulations in this work

The pollen-laden jet simulations in Chapter 5 indicate that the highest pollen depositions on stigma of both full-open and bold flower models occur when a ϕ 30-mm nozzle is placed in front of the flower (see Fig. 5-13). This nozzle layout is further studied here under the influences of corona charging and tribo-charging. The main difference between two charging applications lies in the electric field computation.

Corona charging

The domains defined in Chapter 5 (see Fig. 5-1) are used here. The only addition here is a ϕ 1-mm electrode situated in the middle of the ϕ 30-mm nozzle. For mesh economics, the electrode is represented by an 'infinitely thin sheet' of 1 mm in width and 65 mm in length. The electrode exserts the nozzle by 5 mm.

The air flow field is solved isothermally at 25 ^{O}C by using RNG k-ε model. The case study looks at jets at two initial velocities (1 m/s and 3 m/s) from a 30-mm diameter nozzle located at 100, 200 and 300 mm away from the flower centre.

The electric potential is computed as a scalar Additional Variable in [V]. It is solved by using the Additional Variable transport equation under the option of "Poisson equation". Since the transport equation is volumetric based, a conversion factor of 1 [kg^2 m^2 s^{-5} A^{-2}] is applied for unit consistency. The kinematic diffusivity of the transport equation is specified as (permittivity coefficient of air) / (density of air) $\times$ (conversion factor). Due to the low kinematic diffusivity, a large physical timescale of 6×10^8 s is allowed in solving the potential.

Three Additional Variables called Ex, Ey and Ez (in [V/m]) are created to represent the electric field in x, y and z directions (see Equation 6-3). A user-Fortran script calculates the gradients of the potential in x, y and z directions, and then passes on the values to Ex, Ey and Ez.

The electrode has a fixed potential of 50 kV while the whole flower is grounded i.e. at 0 V. A 'zero flux' option is selected for the nozzle i.e. a nozzle made of dielectric

material. To represent the potential at infinite space (i.e. as if the iso-potential lines will extend infinitely), the same option is specified for the Inlet boundary and all the 'Opening' type boundaries around the flow domain.

The electrostatic forces on the pollen, as given by Equation 6-9 (without the last three terms on the right), are included as momentum sources (i.e. $q_p \times Ex$, $q_p \times Ey$, $q_p \times Ez$) when solving for the pollen trajectories. This is achieved by using a user subroutine written in user-Fortran. The field charging of pollen, which is usually calculated using Equation 6-1, is not included. Each pollen grain is assumed to have a charge-to-mass ratio of 3 mC/kg from the close initial corona region, which then gives 2.23×10^{-14} C of charge per pollen grain (q_p).

As in previous simulations, the pollen, which are simulated using the Lagrangian approach, experience turbulent dispersion. The test in section 5.1 has shown that a two-way momentum coupling between the air and pollen is not needed for the low pollen loading to be sprayed. In another words, a one-way coupling representing the influence of air flow on the pollen (but not the other way round) is sufficient. However, it was found that, with the inclusion of electrostatic force as an additional momentum source, the CFX-5 computation required a full momentum coupling between the air and pollen. This severely limits the number of the pollen to be simulated due to the high demand on the computational memory. It was decided to arbitrarily set the pollen injection to 1000, which has been found to use up to 1.8 GB of RAM.

The pollen are however not introduced deep inside the nozzle because of the assumption that the pollen are already charged. As mentioned above, in an actual corona charging system, the majority of the charging takes place in the small ionization region around the tip of the electrode. Ali *et al* (2000) specified an ionization region diameter three times of that of the electrode. The electric field is maintained at the onset electric field value within this region. Thus, the simulated pollen are injected uniformly at 1 or 3 m/s on a ϕ 30-mm plane which is located at 3 mm downstream of the electrode tip. This presents a more realistic model i.e. the pollen have passed through the ionization region and are charged to a constant level.

Every part of the flower including the stigmatic surfaces is sticky to the pollen. On the other hand, a restitution coefficient of 1 (for both parallel and perpendicular components) is imposed on the central electrode and nozzle to avoid pollen deposition. The pollen grains are considered to leave the flow domain once in contact with the Opening boundaries.

Tribo-electrification

The domain and all the boundaries including the flower surfaces are defined in the same way as for the corona charging, except that the electrode is excluded. The only addition here is the inclusion of space charge density as a source term to the Poisson equation in solving for the electric potential (see details in section 6.2.1).

The specification of space charge density requires the knowledge of the local mass fraction/volume fraction of the pollen cloud. It was found that the distribution of volume fraction of pollen given by the Lagrangian calculation is only available to the post-processor but not to the solver. To get around this, the Algebraic Slip Model (ASM; see section 2.3.3 and *CFX-5.7 Manual*, 2004) is used simultaneously with the Lagrangian particle tracking. ASM calculates the mass fraction of the pollen cloud, which is then used in the computation of the electric potential.

In ASM, an ideal variable composition mixture is created from 'air' and 'pollen_asm'[2]. 'Air' refers to the air at 25 °C and atmospheric pressure. 'Pollen_asm' is specified as a pure component having a density of 1330 kg/m^3. 'Air' is the continuous phase and its composition is constrained by the dispersed phase, 'pollen_asm'. Algebraic slip equations calculate the transport of the dispersed phase using the Schiller Naumann drag force prediction (Equations 2-41 to 2-43).

A pollen feed rate in term of mass fraction needs to be supplied to the ASM. Referring to the recommended pollen loading in Table 5-1, a pollen feed of 3.8 mg/s is considered sufficient in providing an estimate of the distribution of the mass fraction of the pollen cloud around the flower. This gives an inlet mass fraction of 'pollen_asm' of 4.48×10^{-3} and 1.49×10^{-3} under an initial jet velocity of 1 and 3 m/s respectively, from

---

[2] Named differently to 'pollen' in the Lagrangian particle tracking in order to avoid confusion.

a ϕ 30-mm nozzle. It must be noted that ASM removes the dispersed phase on the flower surfaces and artificially replaces it with the equivalent quantity of continuous phase.

To implement the source term into the Poisson equation, a sub-domain is created. The space charge density, in [C/m^3], equals to (local mass fraction of 'pollen_asm') × (charge-to-mass ratio of pollen) × (local density of the 'air' and 'pollen_asm' mixture). As in the corona charging model, a constant charge-to-mass ratio of 3 mC/kg is assumed here. The source term is specified as (space charge density) × (conversion factor). This is the same conversion factor used in the corona charging model above.

Following the computation of the electric field, the Lagrangian framework tracks 1000 pollen under the turbulent dispersion effect and influence of electrostatic force. The pollen are introduced inside the nozzle as in reality, the frictional-charging occurs during the conveying inside a tribo-charging device.

Uncharged application

For a consistent comparison, the simulations above are repeated with 1000 uncharged pollen. Particle number independence in the computation is not of concern here since the interest is to determine the relative gain in pollen deposition on the stigma under the charging compared to uncharged application.

6.2.3. Results

Electric fields

Fig. 6-3 shows the iso-potential lines around a single full-open and bold flower when a ϕ 30-mm nozzle with a 50-kV electrode is placed 100 mm in front of the flower. Highly dense iso-potential lines are found around the electrode at the top of the figures. This is reflected by an intense electric field (E$_{rms}$) near the electrode in Fig. 6-3 i.e. like a glowing region. E$_{rms}$ refers to the resultant of electric field in three directions i.e. $\sqrt{Ex^2 + Ey^2 + Ez^2}$.

**(a)
full-open
flower;
corona
charging**

Erms [V/m]

≥ 1139733

1013096

886459

759822

633185

506548

379911

253274

126637

0

**(b)
bold
flower;
corona
charging**

Erms [V/m]

≥ 1605079

1426737

1248395

1070053

891711

713368

535026

356684

178342

0
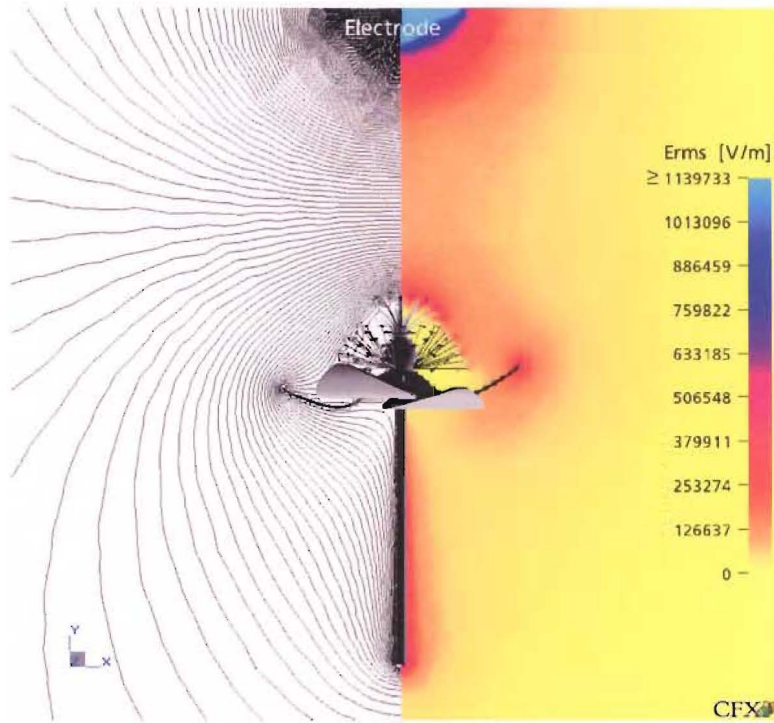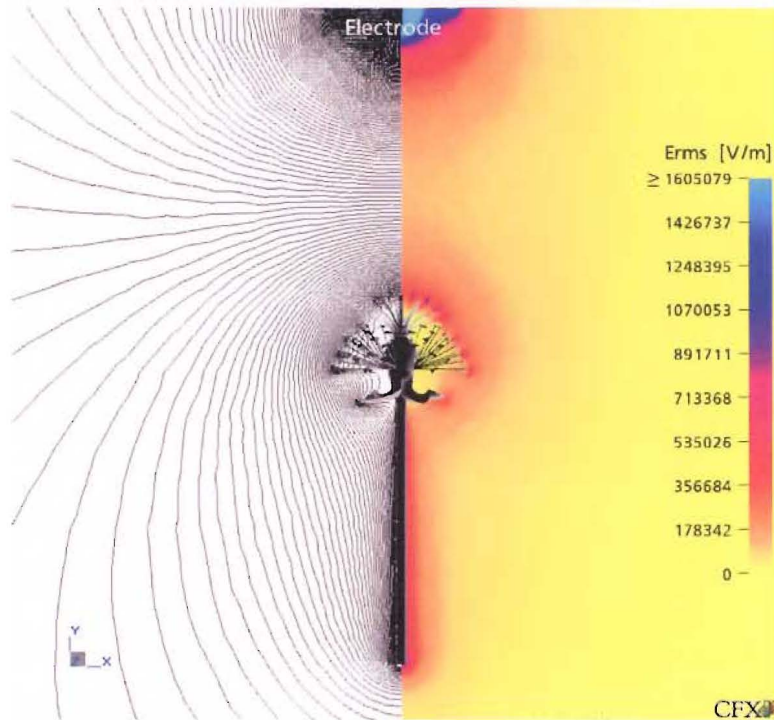
Fig. 6-3: Equipotential contour plots around a single (a) full-open and (b) bold flower, exposed to a 50-kV electrode. Contour interval = 100 V. The electrode is in the middle of a φ 30-mm nozzle (at the top of the figures) located 100 mm away from the flower centre. The corresponding electric fields (E$_{rms}$) are shown on the right.

In the absence of an electrode as in a tribo-electrification, the magnitude of the electric potential depends on the local mass fraction of the pollen in the jet (see the plots of potential and mass fraction of 'pollen_asm' in Fig. 6-4 and 6-5). Higher potential exists at the core of the jets where there are more concentrated 'pollen_asm'. The potential reduces to zero as the jet disperses laterally. The difference between Fig. 6-4 and 6-5 is the location of the nozzle. Due to the greater dispersion of pollen cloud before contacting the flower, the electric potentials around the flowers in Fig. 6-5 are less than those in Fig. 6-4.

As expected for both full-open and bold flowers, the density of iso-potential lines and E_{rms} plots in Fig. 6-3, 6-4 and 6-5 indicate the highest electric field acting on the sharp terminal parts of the flowers such as the tips of the stigma, anthers, petals and sepals (for bold flower only). Tables 6-1 and 6-2 list the maximum E_{rms} values of these flower parts under corona and tribo-charging respectively. Note that E_{rms} is in [V/mm] in Table 6-1 and [V/m] in Table 6-2.

According to Tables 6-1 and 6-2, under both charging methods, the stigma experience a significantly greater electric field than that on the tip of the anthers, petals and sepals. It is observed that, under corona charging, the stigma closer to the centre of the stigma-style bush display higher electric field. There does not appear to be a relationship between the position of the stigma and the electric field acting on them in tribo-charging simulations.

A corona spray gives a stronger electric field on these parts compare to that in a tribo-charged spray (see Tables 6-1 and 6-2). This is because of the low pollen feed rate (i.e. giving a low space charge density and hence a weak source term to the Poisson equation) in the tribo-charging scenario. Boosting the strength of electric field with tribo-charging using a pollen feed rate higher than the recommended rate based on aerodynamic efficiency (given in Table 5-1) is not an option for the expensive pollen. However, the addition of large amount of cheap powder diluent may offer a feasible alternative here.

The presence of petals has a great influence on the distribution of electric potentials and hence the electric field around the flower. In a corona-charged application (Fig. 6-3), a

pollen spray carried out after the petal-fall will achieve a stronger electric field in the vicinity of the stigma (see Table 6-1).

For the tribo-charged pollen-laden jet, the complex air flow field determines the distribution of pollen cloud. Fig. 6-4a shows that as the petals deflect the charged pollen cloud sideways, there is virtually no electric potential downstream of the petals. On the other hand, the entire bold flower is totally immersed in the pollen cloud (Fig. 6-4b) and thus has an electric field evolved around the whole flower. Overall, similar to the corona charging, a greater electric field is predicted on the stigma of a bold flower (see Table 6-2).

Pollen collection and trajectories

Fig. 6-6 shows the percentage of pollen fed that are predicted to land on the stigma of a single full-open and bold flower. Note that there is no correction done to take into account of the fact that there are 72 stigmatic surfaces on the flower models cf. 36 on a real flower. This was done in the previous chapters but not here, because, as mentioned before, the purpose is to determine the potential benefits from the charged applications.

The percentages of pollen captured by other parts of the flower are plotted in Fig. 6-7. Again, for the same reason stated above, no correction is done for the difference between the number of anther-filaments on the flower model and on the real flower.

The patterns of uncharged and charged pollen-laden jet approaching both full-open and bold flowers are shown in Fig. 6-8 to 6-11. In Fig. 6-8 and 6-9, the ϕ 30-mm nozzle is placed 100 mm in front of the flower. The nozzle-to-flower distance is 300 mm in Fig. 6-10 and 6-11.

Tribo-charging

The deposition of tribo-charged pollen on stigma follows the trend of the uncharged application where the percentage of collection drops with the increasing nozzle-to-flower distances (see Fig. 6-6). This decreasing trend is not 'smooth' in Fig. 6-6c and d due to two occurrences of jet swinging. The first jet swinging happens at a nozzle-to-flower distance of 300 mm in Fig. 6-6c where the jet totally misses the stigma-style

(a) Full-open flower; tribo-charging
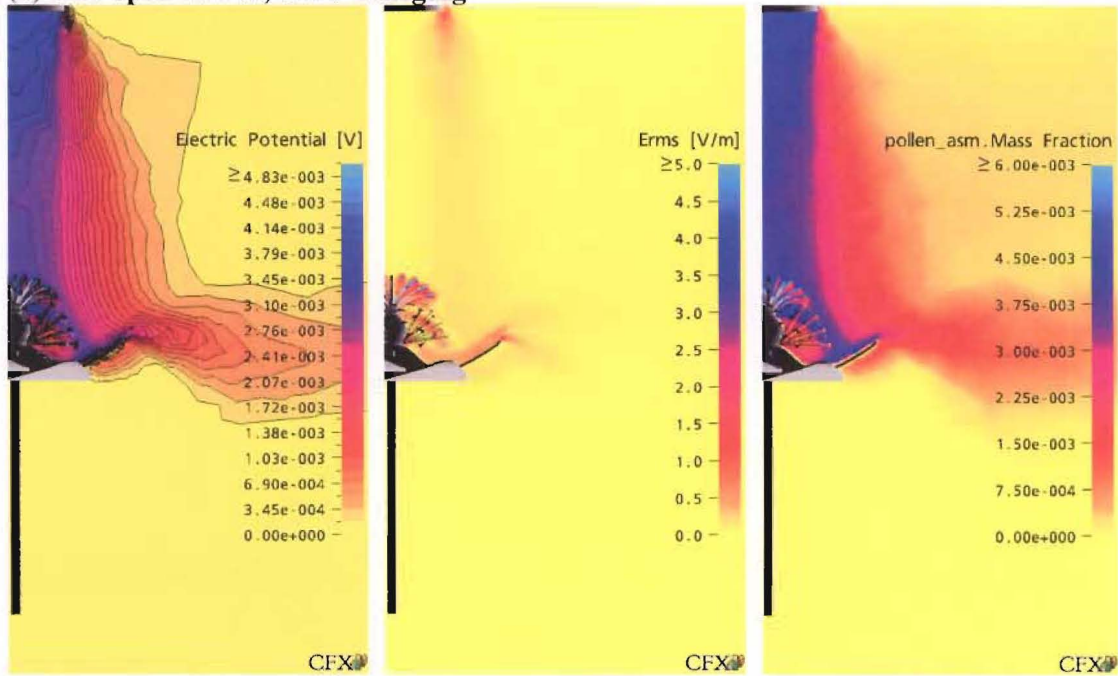
(b) Bold flower; tribo-charging
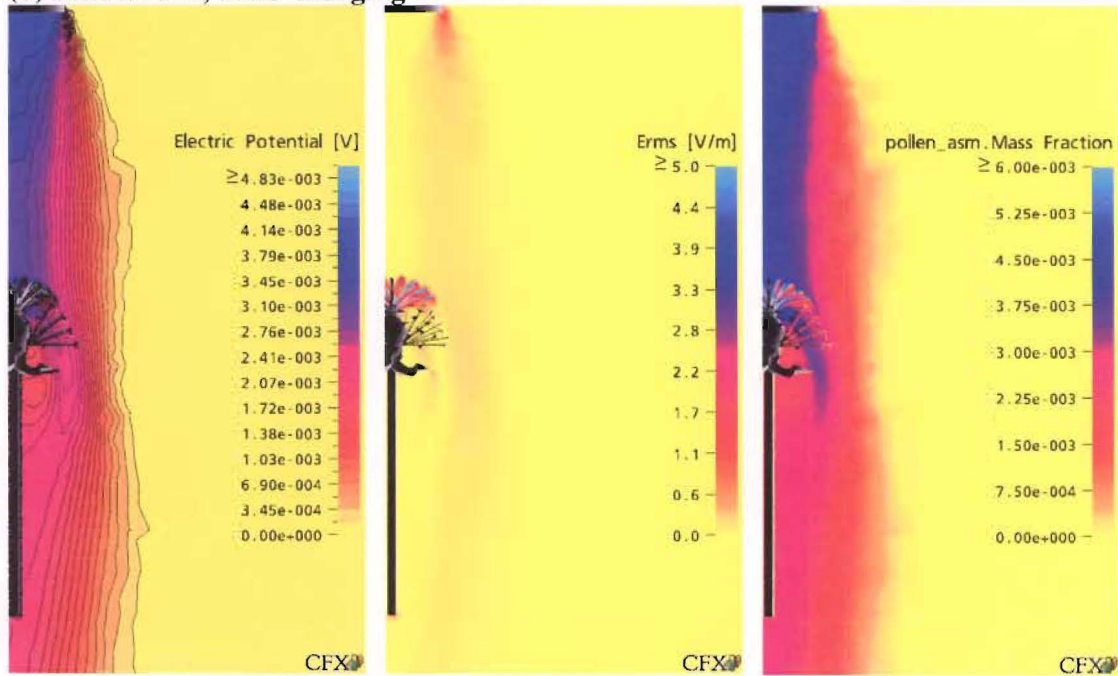
Fig. 6-4: Equipotential contour plots around a single (a) full-open and (b) bold flower, under a tribo-charged pollen cloud. The 1-m/s pollen-laden jets are from ϕ 30-mm nozzle (at the top of the figures) located 100 mm away from the flower centre. The corresponding electric fields (E_{rms}) and mass fraction of 'pollen_asm' are also shown.

(a) Full-open flower; tribo-charging
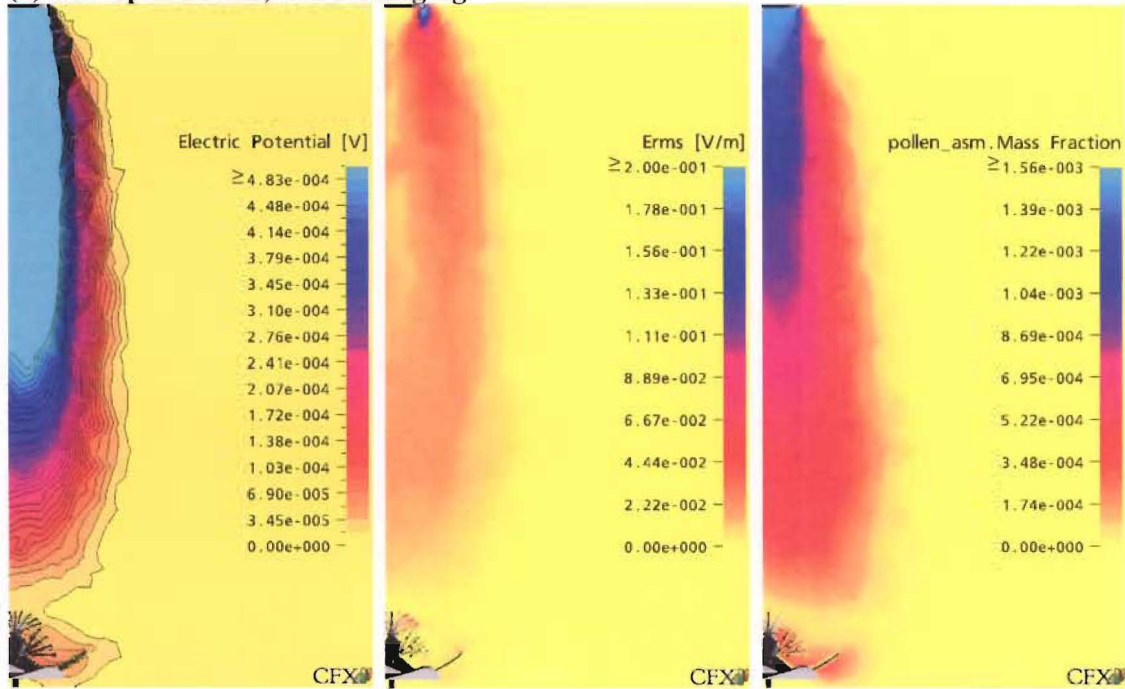
(b) Bold flower; tribo-charging
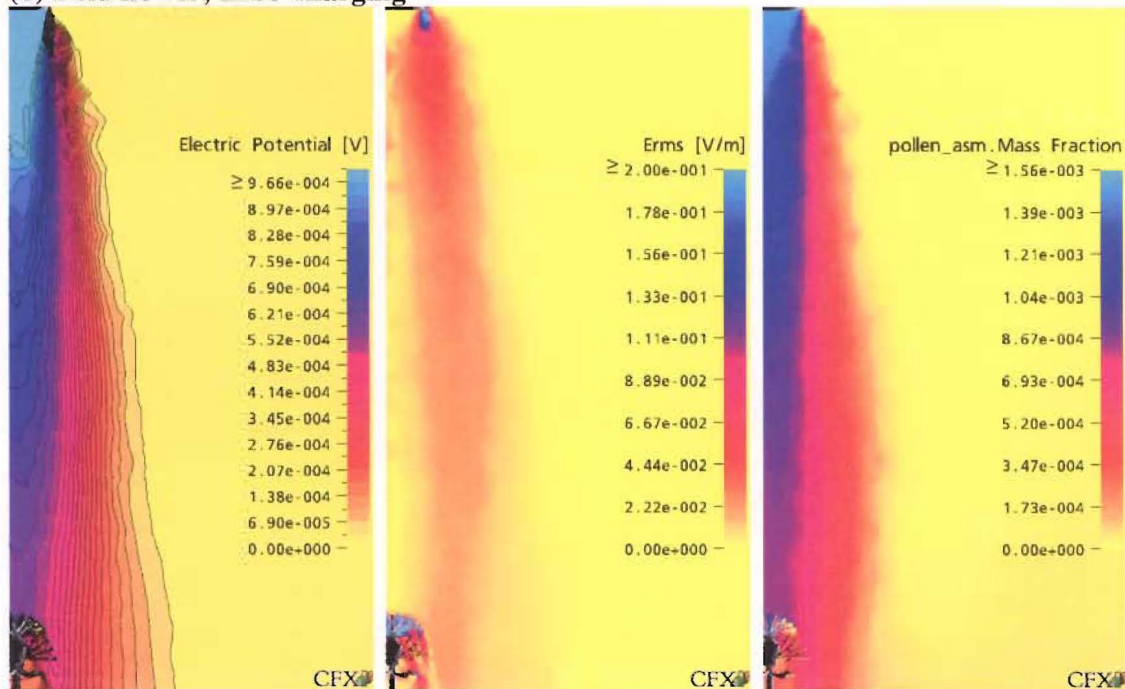
Fig. 6-5: Equipotential contour plots around a single (a) full-open and (b) bold flower, under a tribo-charged pollen cloud. The 3-m/s pollen-laden jets are from φ 30-mm nozzle (at the top of the figures) located 300 mm away from the flower centre. The corresponding electric fields (E_{rms}) and mass fraction of 'pollen_asm' are also shown.

Types of flower	Full-open flower		
Nozzle-to-flower distance [mm]	100	200	300
Stigma	1164 – 1467	1020 – 1213	974 – 1210
Anthers	449	317	298
Tip of petals	762 – 787	684 – 743	677 – 690

Types of flower	Bold flower		
Nozzle-to-flower distance [mm]	100	200	300
Stigma	1871 – 2298	1774 – 1850	1515 – 1873
Anthers	1091	958	899
Tip of sepals	504	468	478

Table 6-1: Maximum E_{rms} values [V/mm] on different parts of a single full-open and bold flower in a corona-charged application.

Types of flower	Full-open flower					
Nozzle-to-flower distance [mm]	100		200		300	
Initial jet velocity [m/s]	1	3	1	3	1	3
Stigma	41 – 206	75 – 922	26 – 37	17 – 268	18 – 25	0.4 – 1.1
Anthers	0.8	0.5	0.2	0.3	0.2	0.01
Tip of petals	8.3 – 10	8.2 – 25	8.2 – 25	4.5 – 12	1.6 – 2.6	0.2 – 0.6

Types of flower	Bold flower					
Nozzle-to-flower distance [mm]	100		200		300	
Initial jet velocity [m/s]	1	3	1	3	1	3
Stigma	58 – 403	217 – 1274	27 – 46	0.3 – 1.9	20 – 22	15 – 303
Anthers	2.0	0.9	0.5	0.3	0.3	0.4
Tip of sepals	0.4	0.2	0.3	0.1	0.1	0.2

Table 6-2: Maximum E_{rms} values [V/m] on different parts of a single full-open and bold flower in a tribo-charged application.

Pollen deposition on stigma

(a) Full-open flower, Vo=1 m/s

(b) Bold flower, Vo=1 m/s

(c) Full-open flower, Vo=3 m/s

(d) Bold flower, Vo=3 m/s

Legend: Uncharged, Corona, Tribo-charged

Axes: % pollen collected vs Nozzle-to-flower distance [mm]
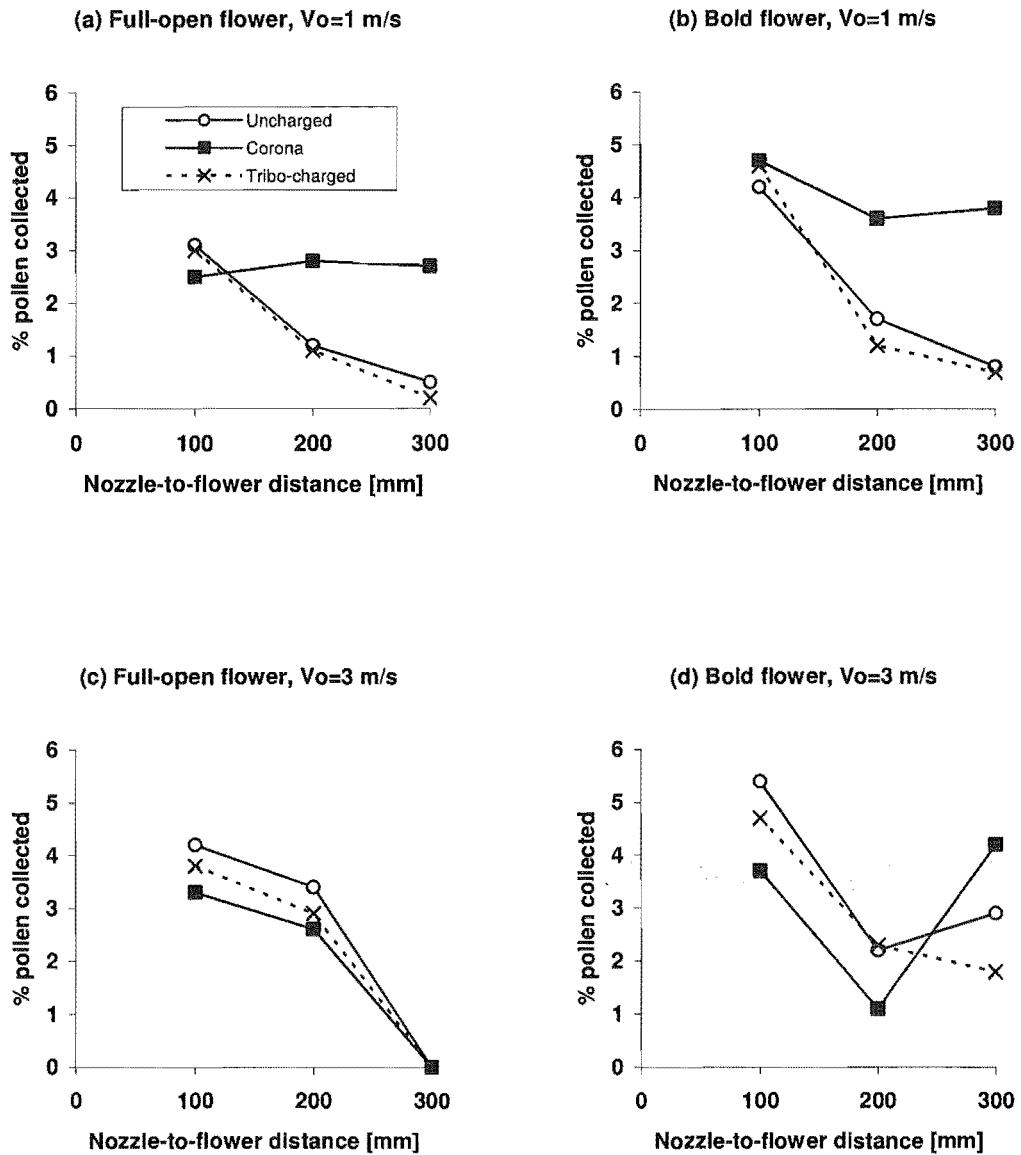
Fig. 6-6: The predicted pollen collection by the stigma of a single full-open and bold flower under uncharged, corona-charged and tribo-charged applications. 1000 pollen are fed in a frontal jet from a ϕ 30-mm nozzle which is placed at various distances away from the flower centre. V_0 refers to initial jet velocity. See text for more details.

Pollen deposition on flower parts other than stigma

(a) Full-open flower, Vo=1 m/s

(b) Bold flower, Vo=1 m/s

(c) Full-open flower, Vo=3 m/s
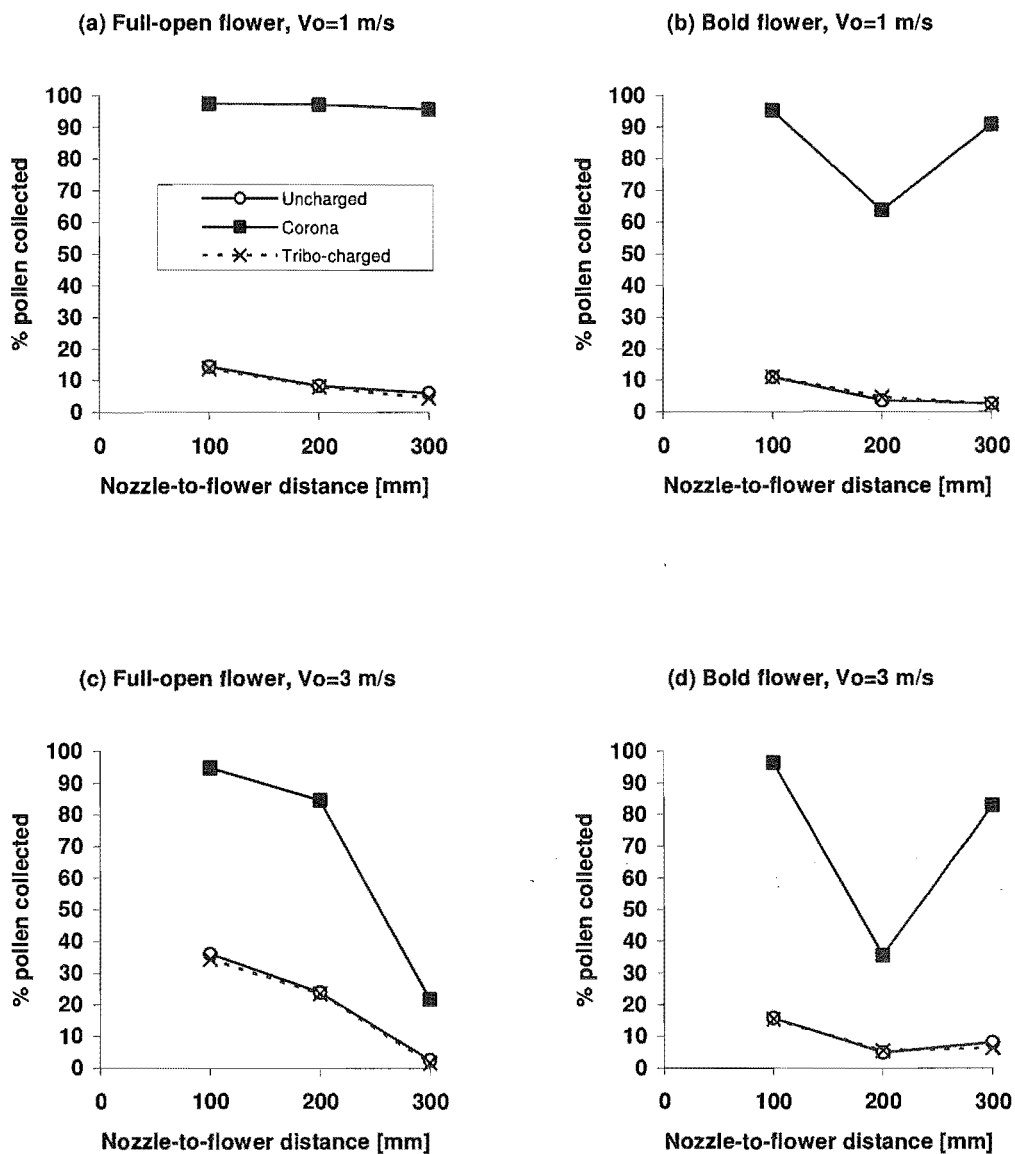
(d) Bold flower, Vo=3 m/s

Fig. 6-7: The predicted pollen collection by other parts of a single full-open and bold flower (i.e. without stigma) under uncharged, corona-charged and tribo-charged applications. 1000 pollen are fed in a frontal jet from a ϕ 30-mm nozzle which is placed at various distances away from the flower centre. V_0 refers to initial jet velocity. See text for more details.

No charging   **Corona charging**   **Tribo-charging**
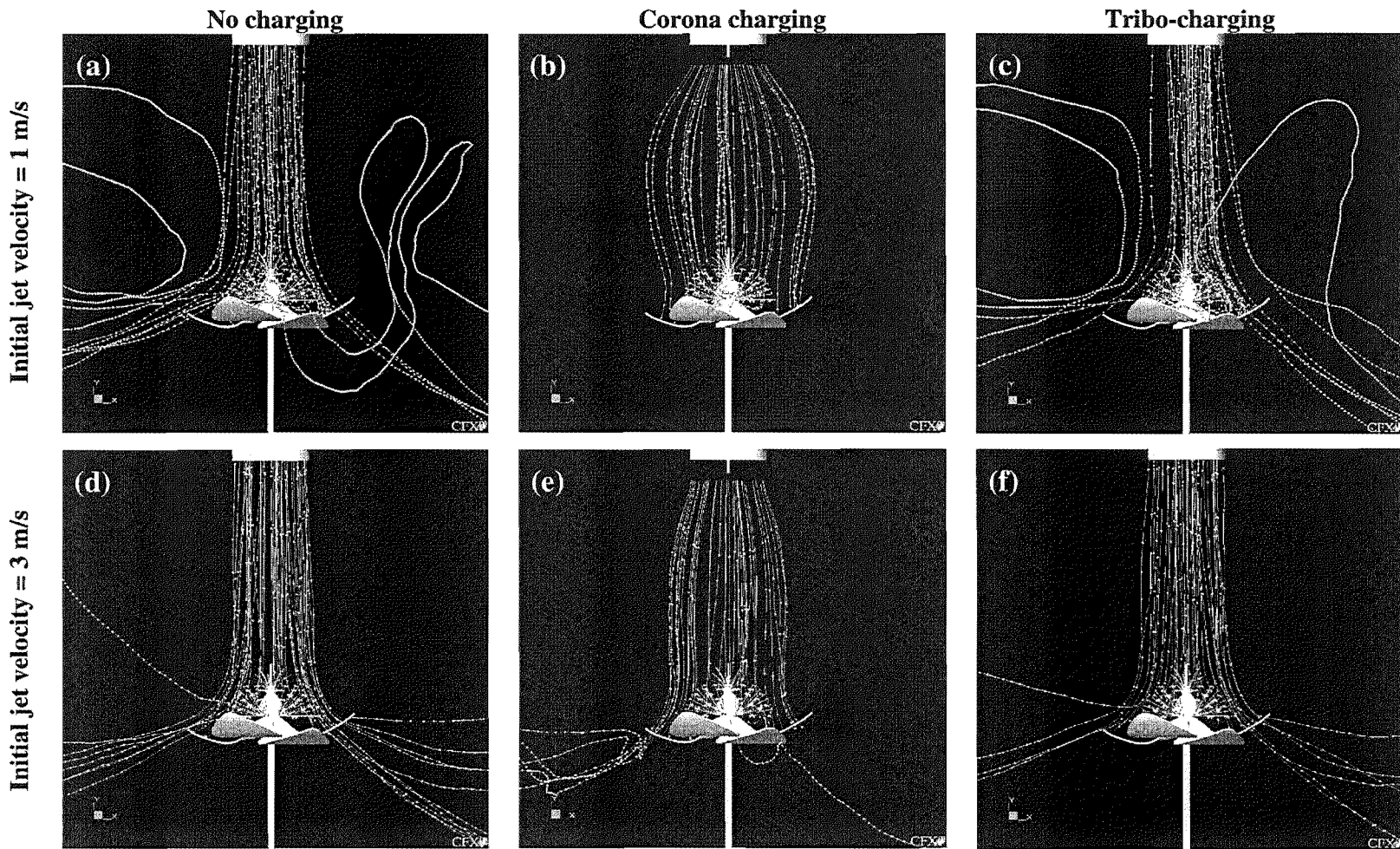
Fig. 6-8: The predicted trajectories of uncharged, corona-charged and tribo-charged pollen grains. The pollen-laden jet is released from a ϕ 30-mm nozzle (at the top of the figures) located 100 mm away from the centre of a full-open Green kiwifruit flower. The separation between pollen along a trajectory is 0.075 s.
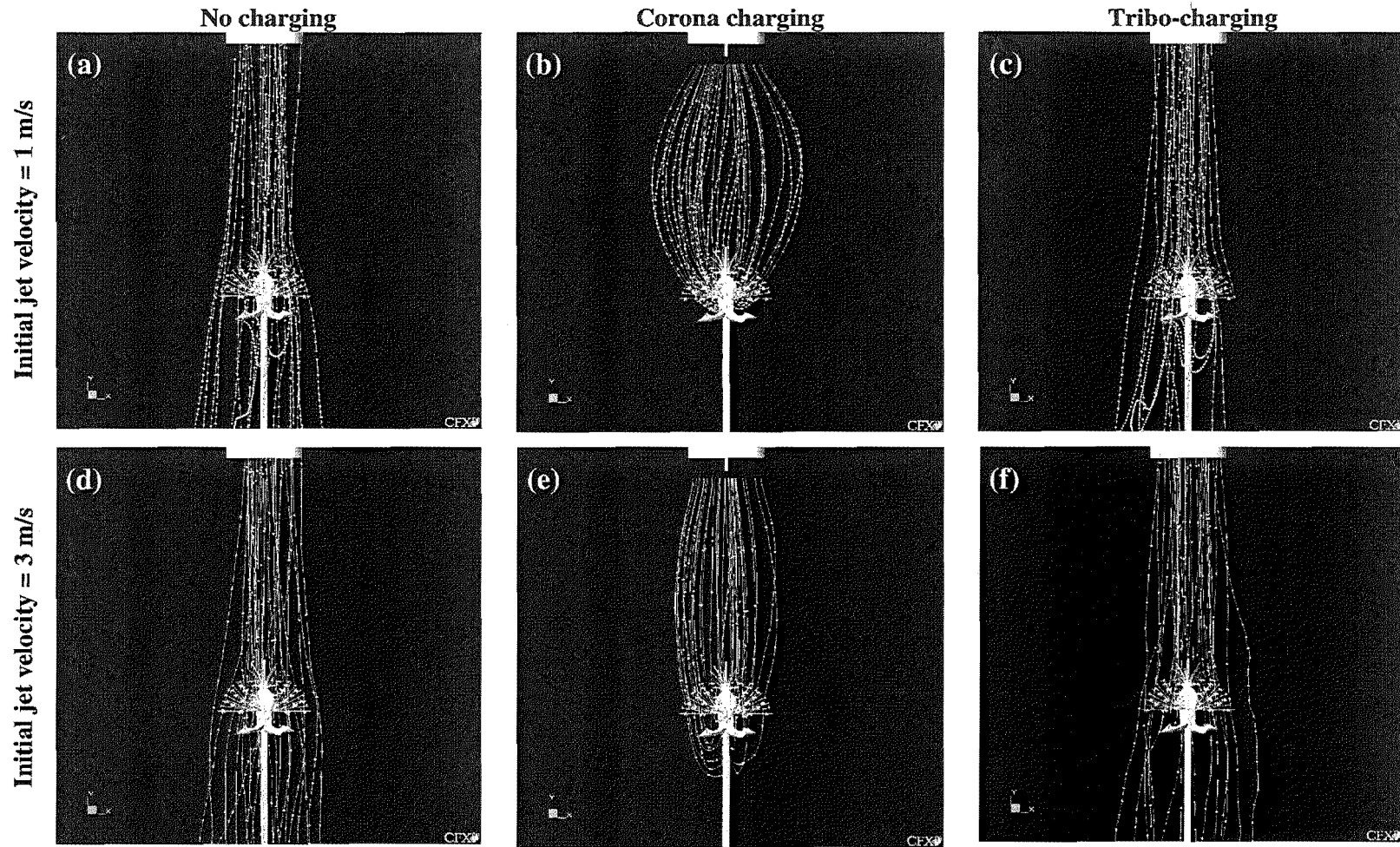
Fig. 6-9: The predicted trajectories of uncharged, corona-charged and tribo-charged pollen grains. The pollen-laden jet is released from a ϕ 30-mm nozzle (at the top of the figures) located 100 mm away from the centre of a bold Green kiwifruit flower. The separation between pollen along a trajectory is 0.075 s.
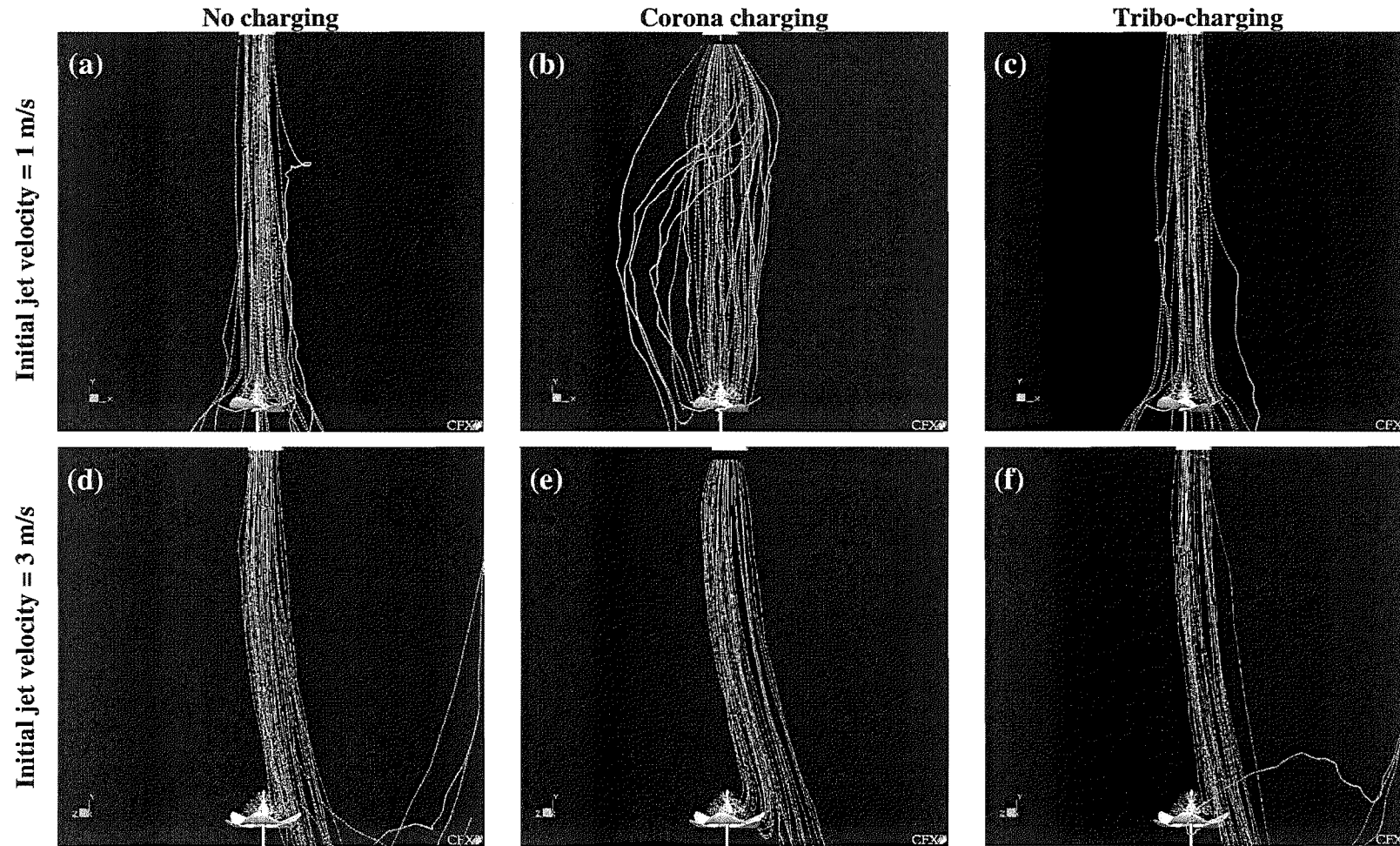
Fig. 6-10: The predicted trajectories of uncharged, corona-charged and tribo-charged pollen grains. The pollen-laden jet is released from a φ 30-mm nozzle (at the top of the figures) located 300 mm away from the centre of a full-open Green kiwifruit flower. The separation between pollen along a trajectory is 0.075 s.
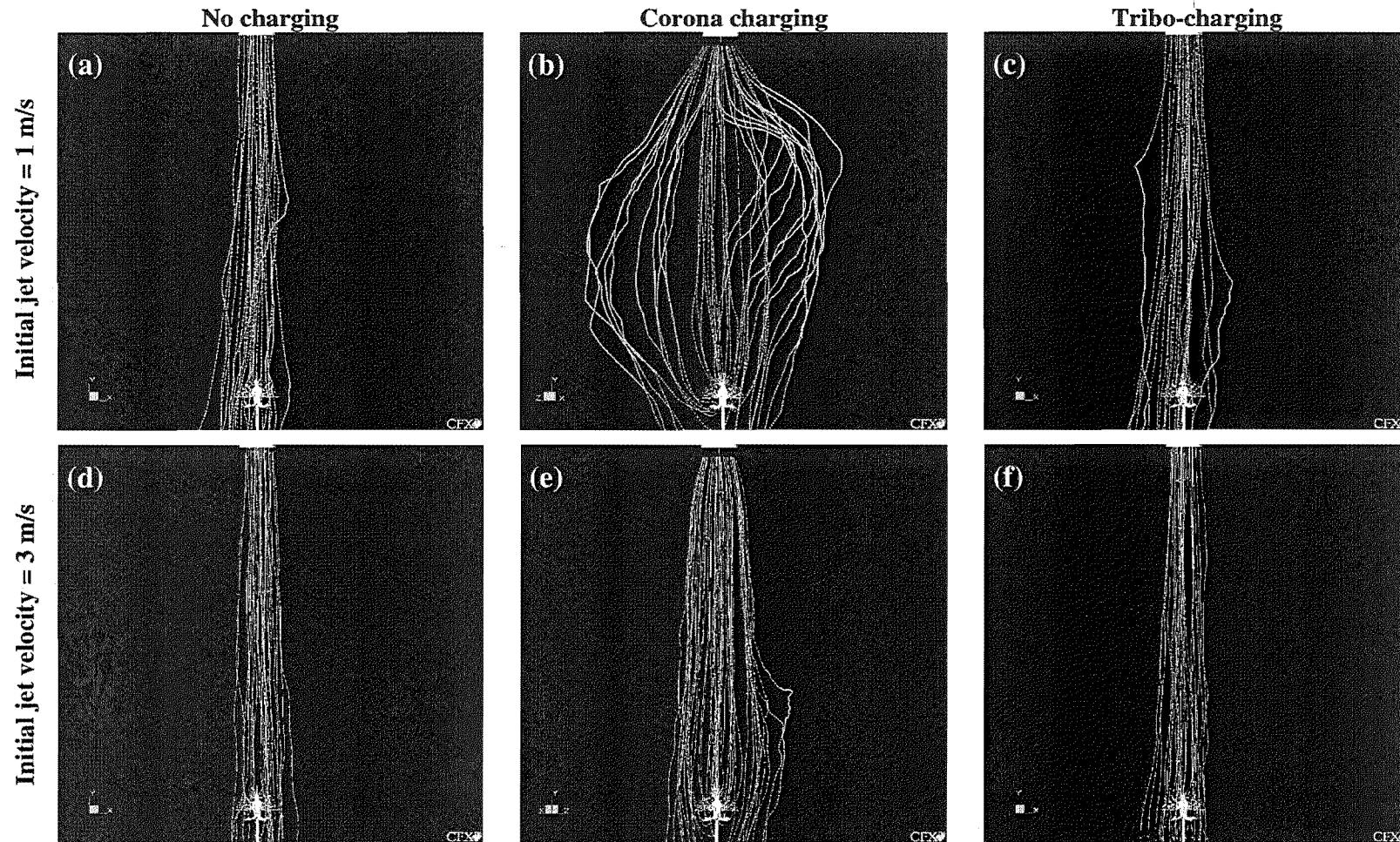
Fig. 6-11: The predicted trajectories of uncharged, corona-charged and tribo-charged pollen grains. The pollen-laden jet is released from a φ 30-mm nozzle (at the top of the figures) located 300 mm away from the centre of a bold Green kiwifruit flower. The separation between pollen along a trajectory is 0.075 s.

bush, which can be seen in Fig. 6-10d and f. The second occurrence gives unusual saddle points at a nozzle-to-flower distance of 200 mm in Fig. 6-6d.

The collections from the uncharged and tribo-charged pollen clouds are indistinguishable in Fig. 6-8 to 6-11. However it appears that, except for a nozzle-to-flower distance of 100 mm in Fig. 6-6b, the performances of tribo-charged pollen are equal to or poorer than those of uncharged pollen in all of the jet-nozzle configurations studied here. An examination on the electric potential plots in Fig. 6-4 and 6-5 reveals that this is possibly because of the higher electric potential around the stigma-style bush, which is immersed inside the core of the jet. The higher potential is given by presence of higher pollen mass fraction calculated by ASM at the core of jet. As a result, this pushes the pollen away from the stigma-style bush and to the sides where the electric potentials are lower. In other words, the electrostatic force has acted in an undesirable direction.

The author wishes to point out that this undesirable electrostatic force action may be partly due to the simplified modelling approach in this work. ASM is used to compute the distribution of pollen around the flower assuming that there is no electrostatic force influencing the pollen movement. The electric potential is then calculated based on this distribution of pollen. Following this calculation, the electrostatic force is added to Lagrangian particle tracking model. The deficiency of this modelling technique is a result of the whole process being one-way i.e. there is no two-way coupling between the pollen in ASM and the electric potential calculation. A further iteration would give the two-way coupling. Inability of including two-way coupling here may have caused an over-estimated pollen mass fraction around the stigma-style bush.

Nonetheless, the calculated electric fields in Fig. 6-4 and 6-5 suggest that the fields are too weak compared to the corona charging (Fig. 6-3) and thus unlikely to provide a contribution matching the corona-charged application. The depositional pattern of corona-charged pollen is looked at below.

Corona charging

The enhancement of pollen capture by the stigma through corona charging is affected by the nozzle-to-flower distance and the speed of the jet.

When the nozzle with a 50-kV electrode is positioned 100 mm in front of a full-open flower, the charged pollen introduced at 1 and 3 m/s are found to be marginally less likely to be captured by the stigma than the uncharged pollen (see 100-mm points in Fig. 6-6a and c). This is because the pollen grains are strongly repelled away from the electrode, leading to low pollen deposition on the stigma at the central and abundant deposition on the other parts of the flower (see Fig. 6-8b and e). This undesirable repulsion cannot be compromised with the use of a low voltage because high voltage breakdown is needed to create the ionized field for charging the pollen.

For the 1-m/s jet in Fig. 6-6a, the electrostatic attraction begins to improve the pollen deposition on stigma when the nozzle is pointed from ≥ 200 mm away from the full-open flower. At this point, the electrostatic enhancement is significant i.e. up to 440 % at a nozzle-to-flower distance of 300 mm (see Fig. 6-10b where a lot of pollen are directed towards the stigma-style bush[3]). This enhancement is not realized at a stronger jet of 3 m/s (see Fig. 6-6c) because the drag force is more dominant. The comparison between Fig. 6-6a and 6-6c at the nozzle-to-flower distance of 100 mm indicates that it is more beneficial to use a higher jet velocity (i.e. 3 m/s) with no charging than a 1-m/s jet with electrostatics. The pollen trajectories are also more influenced by the behaviour of the jet. At the nozzle-to-flower distance of 300 mm, the artificial jet swinging (refer to earlier comments on this in section 5.2) occurs where the jet sways severely to one side and bypasses the flower (Fig. 6-10e). Although the jet also swings but to less extent at the nozzle-to-flower distance of 200 mm, it is enough to eliminate any enhancement offered by the electrostatic attraction (Fig. 6-6c). It must be noted that this enhancement may have been preserved in the absence of artificial jet swinging.

In contrast, the stigma of a bold flower enjoys greater collection of corona-charged pollen released in a 1-m/s jet for all nozzle-to-flower distances (Fig. 6-6b). Undesirable repulsion from an electrode placed too close to the flower does not seem to be an issue here. Fig. 6-9b suggests that the reason lies with the absence of petals on the bold

---

[3] This hints that with charge, the pollen collection by the stigma becomes less sensitive to the nozzle pointing direction.

flower. Even though pollen are still repelled extensively to the sides, the absence of petals has enabled more pollen to be attracted electrostatically to the stigma. The loss of petals has increased the electric field acting on the stigma, as shown in Table 6-1. In a way, this suggests an interaction between the petals and the stigma. The percentage of pollen collection decreases slightly with the increasing nozzle-to-flower distance (Fig. 6-6b). But, the electrostatic enhancement has increased at the same time, contributing 375 % increment at the nozzle-to-flower distance of 300 mm.

At the nozzle-to-flower distance of 100 mm, the trajectories of corona-charged pollen are significantly different in a 3-m/s jet compare to those in a 1-m/s jet (see Fig. 6-9b and e). The charged-pollen cloud released at 3 m/s receives small degree of repulsion away from the electrode (Fig. 6-9e). It proceeds further downstream before the pollen are attracted and deposited on the flower surfaces. However, the simulation predicts that the combination of aerodynamic drag and electrostatics at this nozzle-jet configuration worsens the pollen collection on the stigma (see Fig. 6-6d). Shifting the nozzle to 200 mm away from the flower centre sees a jet swinging (as mentioned above), in which the addition of electrostatic action has actually deteriorated the pollen collection. This is a rather unusual outcome which is also predicted on a full-open flower in Fig. 6-6c. When the jet is stable i.e. straight and not swaying as at the nozzle-to-flower distance of 300 mm in Fig. 6-6d (see trajectories in Fig. 6-11e), an electrostatic enhancement of 45 % is gained in the pollen collection. It is anticipated that, if the jet swinging has not occurred in the simulations, the data points of corona-charged pollen collection in Fig. 6-6c and d should follow the trends of those in Fig. 6-6a and b.

In general, Fig. 6-6 implies that, putting the jet swinging aside:
- a corona charger, but not a tribo-charger, is expected to improve the pollen deposition on the stigma. Furthermore, other parts of the flower are able to gather significantly more airborne pollen under the corona charging, as shown in Fig. 6-7. This is likely to promote additional pollen collection on stigma if the pollen landed on these locations are re-lifted by a gust of wind and transferred towards the stigma.
- it is more beneficial to carry out corona-charged pollen spraying during the bold flower opening stage.

- the electrode-fitted nozzle should not be placed too close to the flower. A nozzle-to-flower distance of 200 mm is considered suitable.

The results with jet swinging were rejected as being valid because of the suspicion that they were computer artefacts (refer to comments in section 5.2).

6.2.4. Discussion and recommendations

Comparisons with literature

The calculated trajectories of pollen under corona charging in this work are similar to those done by Ang & Lloyd (1987) on a corona powder coating gun i.e. the particles emerging from the nozzle are diverted outwards before reversing back to the grounded target.

Tribo-charging does not give improvement in pollen deposition in this work because of the low amount of pollen fed (3.8 mg/s). This feed rate is significantly less than a powder feed of 600 mg/s in the tribo-charged powder coating (Adamiak, 1998, 2001b, Adamiak & Mao, 1995; Adamiak *et al*, 1994). Since it is not economically viable to increase the electric field through higher pollen feed rate, this essentially renders tribo-charging as a non-feasible option in enhancing pollen collection.

The simulations in this work are more comprehensive than the flower models reported by Bechar *et al* (1999) and Dai & Law (1995). Dai & Law focussed on the initial electric field acting on the stigma when suddenly exposed to a charged cloud at an assumed constant space charge density of 25 $\mu g/m^3$. The flow of air and pollen were not included in their model. Their assumption of a constant space charge made their model resemble a tribo-charging scenario. They reported the most intense electric field near the stigma, which is also predicted in the tribo-charging simulations in this work (see Fig. 6-4 and 6-5). They speculated that this would preferentially attract the charged pollen to the stigma. The simulations in this work show that this is not necessary true as the tendency of pollen to be collected depends on the complex air flow field and the distribution of pollen mass fraction around the flower.

Bechar *et al* (1999) presented a more extensive model than Dai & Law (1995) where the trajectories of charged pollen were computed. However, the simplification to a constant velocity (0.5 m/s) all over the simulation domain and the exclusion of petals meant the influence of air flow field, which has been found important in this work, was not incorporated. Bechar *et al* represented the corona-charged pollen cloud by a pollen cloud having a constant charge flux of 33.3 μC/m^2. Their model did not include the electrode, which has also been demonstrated to be vital in creating the electric field between it and the flower. So, strictly speaking, Bechar *et al*'s model is more like a tribo-charging case, but with over-simplified aerodynamic effect. Their result indicated the highest electric field acting and maximum pollen deposition on the stigma. This result was claimed to be supported by their field trials where the stigma of date flowers received more deposition with charged pollen. In the author's opinion, based on the modelling in this work, the improvement in pollen deposition on the stigma of date flowers is more likely to be contributed by a strong electric field established by the electrode, rather than the charged pollen cloud itself. If Bechar *et al* had employed a detailed simulation of airflow around their flower model, they might have reached a different conclusion about the comparison between their theoretical and field results.

Recommendations

The theoretical studies in this section show the promise of raising the pollen collection efficiency of stigma by using a corona-charger gun. Perhaps the most exciting outcome from the simulation is that the enhancement in collection efficiency obtained even when the electrode-fitted nozzle is positioned further from the flowers. This would definitely translate into saving labour time as close-up individual flower targeting (e.g. at 100 mm) and accurate pointing are not needed. In addition, it enables the pollen to be transferred to those hard-to-reach flowers inside a patch of flowers.

Further advantage is expected when this attractive feature is used with a larger nozzle, say ϕ 90-mm nozzle. The benefits of using a large nozzle are that the jet tends not to swing (swinging does not favour electrostatic collection) and also it has the ability to cover more than one flower in a spray (i.e. time saving). The simulations using a ϕ 90-mm nozzle in the presence of an electrode have not been carried out here, but are certainly recommended for future works.

Even though a corona charging device looks promising, there are some concerns from a safety point of view. It is uncertain how comfortable the growers are with the carrying of a high voltage generator. Precautions are needed when spraying near wet foliage surfaces and the wires (and metallic components) of the training systems. However, it must be borne in mind that a corona sprayer has become a mature technology, in terms of safety, efficiency and portability, through its popularity in the powder coating industry. Bechar *et al* (1999) and Vaknin *et al* (2001a) have demonstrated that it can be used for applying the pollen on other crops. As with any electrical devices, safety consciousness is always required.

Tribo-electrification of pollen is preferred from the safety aspect. However, it is theoretically shown to not improve the pollen collection on the stigma. This will be further examined experimentally in the following section.

6.3. Pollen-loaded spraying experiment

This section describes a laboratory study of the collection of charged and uncharged pollen by the stigma of a single fresh Green kiwifruit flower. The pollen grains were tribo-charged using the Tribomatic II powder spraying system from Nordson Corporation.

6.3.1. Experimental methods and layout

Fig. 6-12 shows the equipment layout of the pollen charging and spraying system (see Fig. 6-13a). The Tribomatic II system requires a clean and dry compressed air supply. The in-house compressed air was first de-misted and de-oiled. The moisture was further removed by a 1-m long transparent column filled with molecular sieves, which are inter-mixed with blue-colour silica gels as indicators. A layer of glass wool was placed at the exit of the column for removing fine dusts. For greater assurance, a fine dust filter was installed downstream. The degree of drying was checked by using a Vaisala humidity sensor which indicated a reading of < 2 %RH. The Norgren FM13-
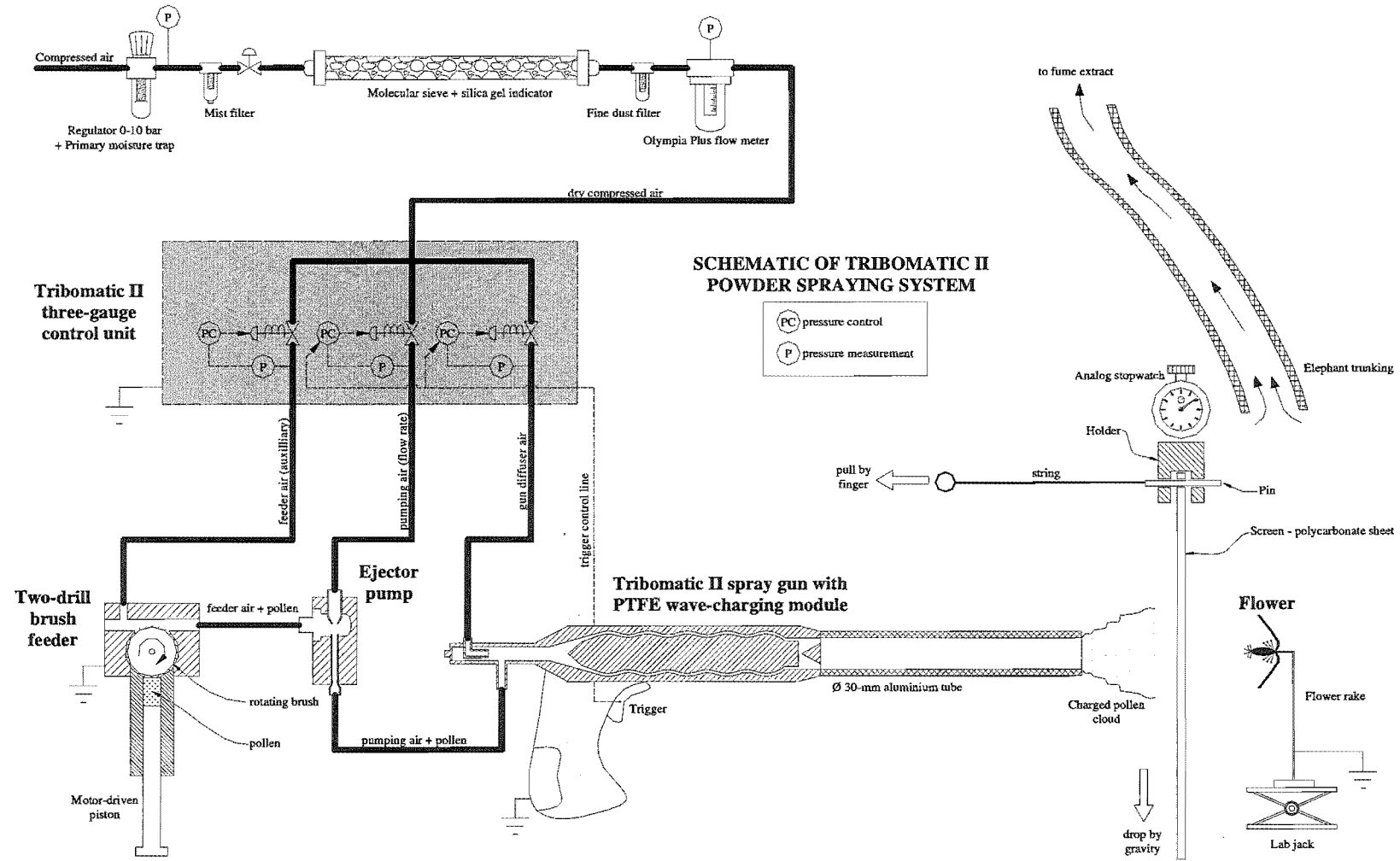
Fig. 6-12: Schematic diagram of Tribomatic II pollen spraying system and the placement of the flower.
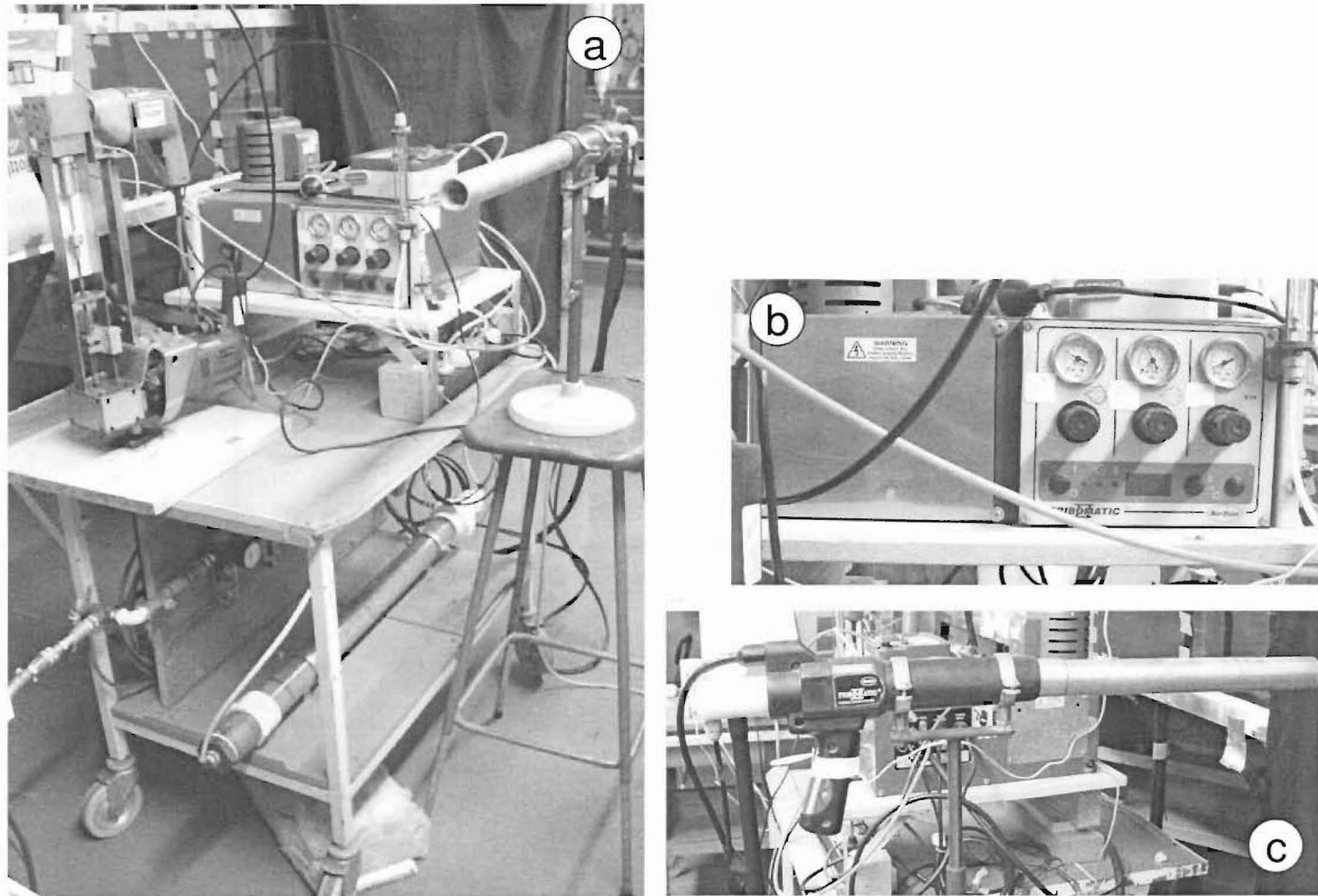
Fig. 6-13: (a) Overall view of the Tribomatic II pollen charging equipment layout on a trolley. The compressed air filtering system is installed below the deck of the trolley. (b) Tribomatic II three-gauge control unit. (c) Tribomatic II spray gun with φ 30-mm aluminium tube.

001-EOTO Olympia Plus flow meter gives the volumetric air flow reading in the range of 0 to 10 L/s.

The compressed air is then split into three streams, namely feeder air, pumping air and gun diffuser air; in order to drive the pollen feeding and spraying sections. The pneumatic and electrical controls are provided by the Nordson Tribomatic II three-gauge control unit (see Fig. 6-13b; Nordson Corporation, 1995).

Pollen feeder

A brush feeder can accurately apply kiwifruit pollen in small amounts (Ferguson & King, 1991). Fig. 6-14 shows the brush feeder driven by two drills. Pure pollen is tightly packed in a brass syringe of 6.4 mm ID. The bottom drill drives the piston upward. This pushes the pollen towards the rotating brush driven by the top drill. The speed of the bottom drill is controlled by varying the voltage supplied to the drill. A pollen feed rate of 2.5 ± 0.2 mg/s was used in this work[4].

The rotating brush picks up the pollen which are then blown off the brush and conveyed by the feeder air to an ejector pump (see Fig. 6-12). This is a high efficiency venturi type ejector powder pump (Nordson Corporation, 1992). After passing the venturi nozzle, the pumping air delivers the pollen to the Tribomatic II spray gun (Fig. 6-13c).

Gun spraying

The gun diffuser air pushes the pollen at an increased velocity through a small gap formed by the ribbed surfaces (see Fig. 6-12). The pollen grains are tribo-charged through collisions with the inner and outer wear sleeves inside the Teflon charge module (called a wave-charging design; Nordson Corporation, 1996). The chargeability of the pure pollen depends on the volumetric air flow through the spray gun, which is in turn determined by the combination of the pressures of pumping air, gun diffuser air and feeder air. This calibration had been carried out by Roberts (1997). For control experiments i.e. with uncharged pollen, the Teflon module was replaced with an aluminium module. The gun has a grounded ϕ 30-mm aluminium tube of 300 mm length fitted in the front to allow for a proper flow development before jet expulsion.

---

[4] Using the bulk density of 786 ± 70 kg/m^3 measured by Roberts (1997); cf. 630 kg/m^3 reported by Ferguson & King (1991).

A fresh kiwifruit flower was placed on a stainless steel rake which was grounded (see Fig. 6-12). It was found that it took 4 to 5 seconds initially for the pollen spray to stabilise. This start-up effect was unwanted in the experiments. To get around this, a light yet rigid polycarbonate sheet was used to screen the flower from the pollen-laden jet at start-up. The screen was held to a holder by two pins in the way shown in Fig. 6-12. The procedures of spraying are described below.

After the gun trigger was turned on and held by for approximately 5 seconds, the pin supporting the screen was pulled off using a string attached to a finger. The flower was exposed to the pollen cloud as the screen dropped down by gravity. The gun trigger was released after the second arm on an analogue stopwatch had indicated 3 seconds. The whole operation was done with a single person. The excess pollen around the workspace was vented to fume extract line through an elephant trunking. The purpose of this arrangement was to expose the flower to 3 seconds of fully laden jet flow.

The flower was sprayed from the front, side and back at different gun diffuser air pressures and different nozzle-to-flower distances. Three fresh full-open flowers were used at each experimental setting. Five styles were then removed randomly from each flower and the number of pollen grains deposited on each stigma was counted using the method described in section 6.3.2.

Flowers and pollen supplies

Fresh Green kiwifruit flowers at full-opening stage were obtained from cuttings picked in Nelson, New Zealand around one week before their projected blossom season. These cuttings, with unopened flower buds, were immediately half-immersed in a disinfected pail filled with distilled water. The pail was also jacketed with icy water during the transport back to Christchurch on the same day. The cuttings were pruned such that only the primary flower bud on the inflorescence was retained and not more than 3 buds were allowed per cutting. They were left in the open space of the laboratory. The nutrient reserve in the cuttings was found to be sufficient for sustaining the flower buds to full blossom. However, it was found that the flower buds obtained in this way did not maintain the full opening petals (~ 2 days) as long as the ones observed in the orchard (3 to 4 days).
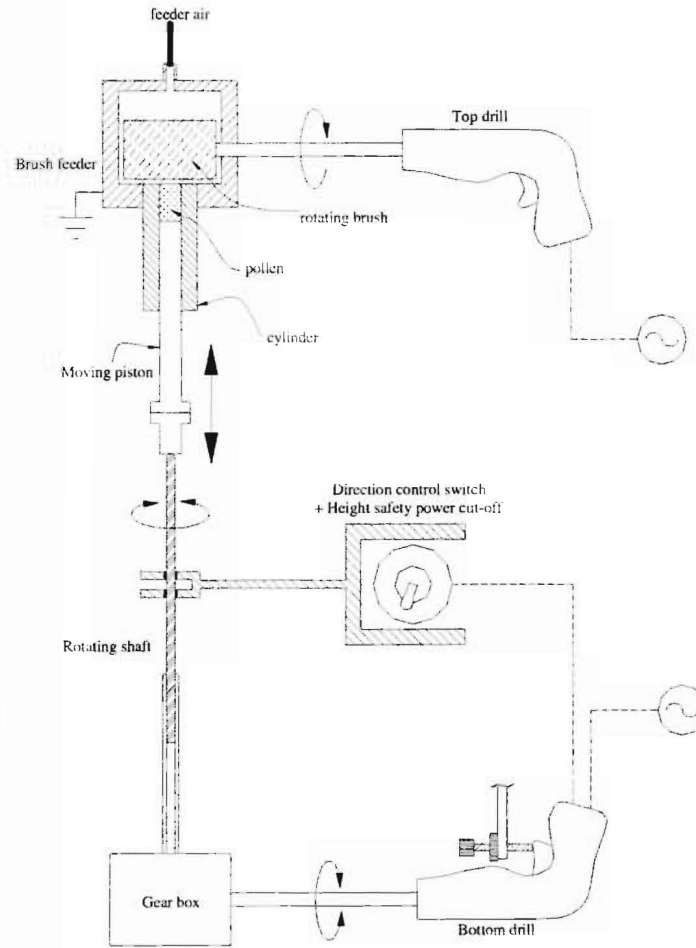
Fig. 6-14: Mechanism of two-drill brush feeder.

The alternative method that was previously tried but was less than satisfactory is the flower cultivation from the dormant canes (Snowball *et al*, 1996). With one end of the cuttings (>150 mm long) immersed in distilled water, the vegetative growth took place under the exposure to non-harmful UV light in a temperature-controlled chamber. Only one flower was allowed per cutting. This method offers the flexibility of obtaining fresh flowers outside normal flowering seasons. However, because most of the flowers did not develop fully, the method was abandoned.

The pure pollen grains were supplied by KiwiPollen Limited and stored at $-10\ ^{O}C$. They were thawed at room temperature one hour prior to the experiments.

6.3.2. Pollen counting method

It was found impractical to count the pollen directly on the stigma of kiwifruit flowers under a light microscope. This is because of the curved surface of stigma and the very similar colour between pollen and stigma. A literature search found that the methods of counting the pollen deposited on the stigma can be divided into two categories: (1) direct observation of intact stigma for pollen grains number; and (2) dislodging the pollen by some means prior to counting.

In method (1), the stigma preserved using FAA[5] are first squashed on the microscope slide, followed by the addition of annilin blue + K_2HPO_4 so that the pollen can be counted under a fluorescence light microscope (Fetscher *et al*, 2002). Murcia (1990) and Feinsinger *et al* (1986) mounted the stigma collected in the field using cellophane tape and counted the pollen later using either a dissecting microscope or Hoffman optics or epifluorescence illumination (see details in Kearns & Inouye, 1993).

In method (2), the pollen grains are removed in three ways:
1. Acetolysis method where the stigma are acetolyzed using acetic anhydride and concentrated sulphuric acid mixture, centrifuged and washed, leaving the pollen to be counted (Ornduff, 1975).

---

[5] Formalin-aceto-alcohol or formalin-acetic-acid; to prevent pollen tube growth (Kearns & Inouye, 1993) that can anchor the pollen to the stigma.

2. Sticking method where the stigma are dipped into melted basic fuchsin gel or glycerine jelly on a microscope slide to remove the pollen (Snow, 1982; Thomson & Plowing, 1980).

3. Liquid suspension method where the stigma are placed in vials with 70 % ethanol (or dilute saline solution) and the vials are sonicated or shaken using a vortex mixer for 5 s to remove the pollen (Bechar *et al*, 1997). To achieve uniform suspension without pollen clumping, cyclohexane or hexane is added to remove pollenkitt material and drops of detergent are added to neutralize the surface charges on the pollen (Shivanna & Rangaswarny, 1992).

The suspended pollen can either be counted manually or automatically:

1. Manual counting; Subsamples are placed on the microscope slide and after the ethanol has evaporated, the number of pollen grains are counted i.e. using an image analysis method (Bechar *et al*, 1997). The pollen can also be stained and the mixture of known volume is held on a hemacytometer for counting (Shore & Banett, 1984).

2. Automatic counting using electric counter; The pollen grains suspended in 0.1 % NaCl solution are drawn through a Coulter counter (Devlin, 1988) or a Particle Data Elzone 180XY particle counter (Harder, 1990) for counting[6]. Although significantly less time consuming than the manual counting, electric counters show drift in accuracy over the time of use, need to be free of debris, require pollen to be fully dispersed and must be verified using manual counting (Kearns & Inouye, 1993).

Hopping & Hacking (1983b) counted the pollen on 40 kiwifruit stigma by first dislodging the pollen three times from the stigma using a vortex mixer. The pollen were then washed in stain solutions and three 0.01-mL aliquots were taken for pollen counting under the microscope.

In this work, the number of pollen grains deposited on the individual stigma was counted. The amount of chemicals and plastic wares required in the liquid suspension method or acetolysis method is infeasible for that many samplings in this work (about

---

[6] Works on the principle of resistance changes between electrodes on either side of aperture when the pollen suspended in weak electrolyte solution pass through.

300 samples). Both the sticking method and the direct observation of intact stigma appeared promising but there was no fluorescence light microscope in place. Thus, the sticking method was modified where a sticky label (available off-the-shelf) was used to receive the pollen from each stigma.

Fig. 6-15 shows the preparation of the sticky surface on a microscope slide where the sticky surfaces are restricted to within each hole[7]. A single style was picked and the stigmatic end was brushed inside each hole. Almost all of the pollen grains were found to be collected only on the sticky surface with a negligible amount near the edge of the hole. Inspection of a few stigma afterwards found less than 1 % of the total pollen grains remaining on the stigma. To provide a contrast between the pollen and the background noise (such as dust) and to distinguish between male and female[8] pollen, a drop of staining solution[9] was introduced directly on the pollen stuck on the sticky surfaces. This was followed by drying in the oven at 40 °C for 1 to 2 hours. The male pollen appear either in crimson red or dark green and the female pollen in light green under the back lighted microscope.
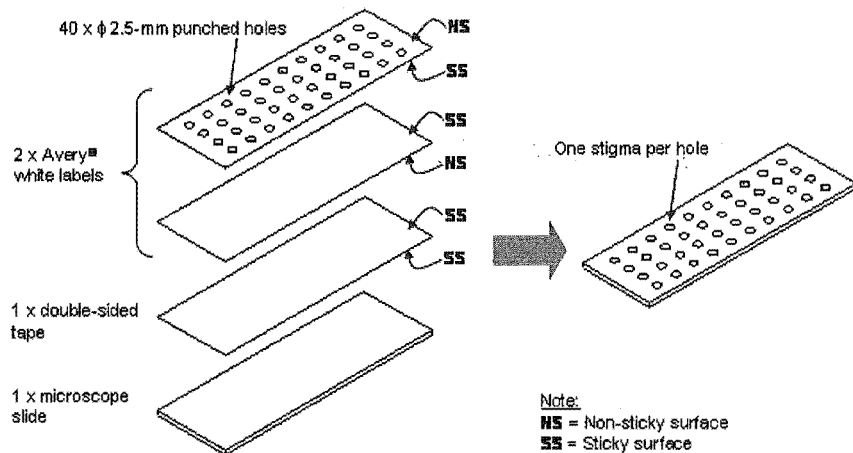
Fig. 6-15: Preparation of sticky surfaces on a microscope for collecting the pollen deposited on the stigma.

---

[7] Direct use of double-sided tape was found to give too much background interference due to the huge amount of bubbles created during the laying on the microscope slide. A cover slip was not used on top because it also caused bubbles trapping which greatly impaired the clarity.

[8] Female pollen from the anther bush around the style bush were also deposited on the stigma during the spraying.

[9] Based on Alexander's (1980) formula: 20 ml ethanol (95 %), 20 mg malachite green, 50 ml distilled water, 40 ml glycerol, 100 mg acid fuchsin, 5 g phenol and 3 ml lactic acid. The solution was stored for two weeks in a reagent bottle wrapped with aluminium foil before use. This staining solution has been used for kiwifruit pollen by Hopping & Hacking (1983) and Goodwin & McBrydie (2000).

The presence of female pollen and pollen clumps[10] rendered the automatic counting using image analysis impossible. The solution was to first mark the individual male pollen with red or blue felt pens on a printout of captured image. The ink of felt pens diffused to the back of A4 sheet, giving nicely separated red or blue dots. The back of the page was then scanned so that the number of dots could be counted using the image analysis software, Optimas® 6.5.

6.3.3. Results

Effect of pollen chargeability and initial jet velocity

Each point in Fig. 6-16 represents the number of pollen grains collected on individual stigma under a pollen-laden jet introduced at various gun diffuser pressures. Note that three flowers were sprayed at the same gun diffuser pressures and five stigma were then sampled from each flower. The pumping pressure was maintained at 25 psi. The nozzle was 200 mm in front of the flower.

Depending on the location of the stigma in the stigma-style bush, the number of pollen deposition on a stigma can vary significantly, as shown by the wide scatter in Fig. 6-16. It was observed that the stigma lying on the lower edges of the stigma-style bush typically captured less pollen than those in the middle. This matches the depositional patterns given in the simulations in Chapter 5.

The amount of data (i.e. number of pollen grains deposited per stigma) in Fig. 6-16 is reduced by taking the average of five stigma sampled from each flower. This is then multiplied by 36 (which is the average number of stigma per flower) and divided by 1.01 million (the number of pollen grains fed at a feed rate of 2.5 mg/s over 3 seconds). This gives the pollen collection efficiency of a flower and is plotted as percentages in Fig. 6-17.

---

[10] Could be from the process of brushing or the existing clumps on the stigma. The pollen in the clumps on the sticky surface were not found to overlay one another.
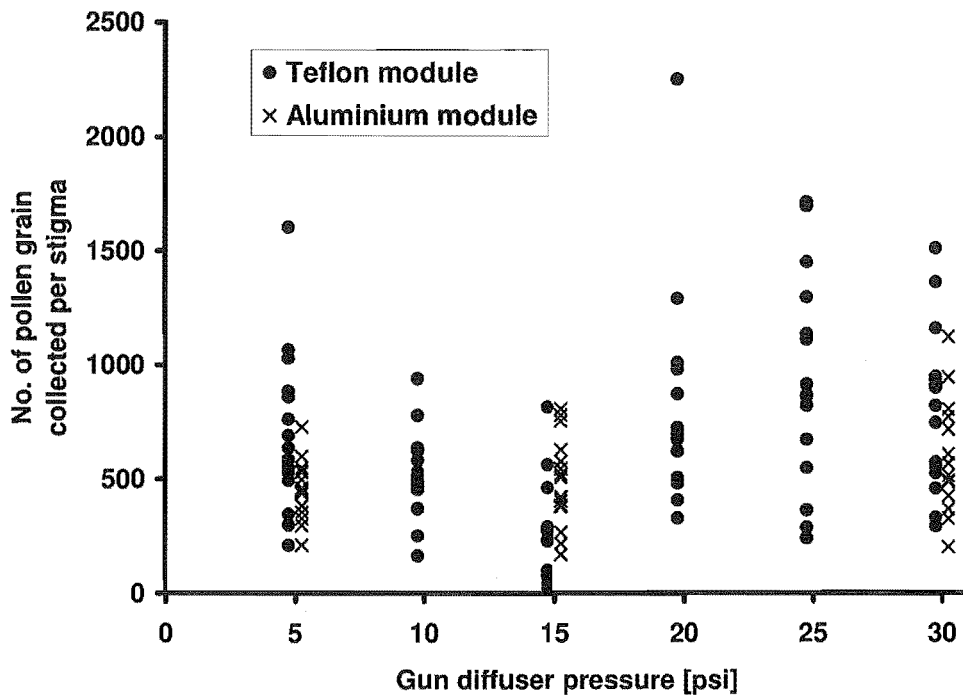
Fig. 6-16: Number of pollen captured by individual stigma of flowers exposed to a frontal jet at different gun diffuser pressures, with Teflon and aluminium charging modules. The nozzle-to-flower distance is 200 mm.

The gun diffuser pressure determines the initial jet velocities and the chargeability of the pollen. At increasing gun diffuser pressures, the pollen grains move at higher speed through the gun and hence gain more charges. The level of chargeability depends on the choice of Teflon or aluminium modules. This is plotted in Fig. 6-17 based on the calibration by Roberts (1997) up to a gun diffuser pressure of 15 psi[11]. Impaction on the aluminium module is not expected to tribo-charge the pollen. The upper scales in Fig. 6-17 show the background charges acquired by the pollen during the conveying in the system.

It appears that overall the stigma become more efficient in capturing airborne pollen with the increasing initial jet velocities in Fig. 6-17. However, the gain in efficiency depends on the level of charging. The pollen-capture performance of stigma drops at gun diffuser pressure of 15 psi before rebounding greatly with the more highly charged pollen i.e. by using the Teflon module. On the other hand, the pollen passed through

---

[11] This means the range above 15 psi is based on the extrapolated values.

the aluminium module display a steady but less extensive increase in collection efficiency with the faster jet speed.

The data in Fig. 6-17 are re-plotted at different pollen chargeability in Fig. 6-18. It appears that the more highly charged pollen display larger errors than the less charged ones. Fig. 6-18 hint that enhanced tribo-charging promotes greater pollen delivery to the stigma. This must however be taken cautiously as the succeeding analyses in Fig. 6-20 and 6-22 indicate a mixed result similar to that predicted in the CFD simulations in section 6.2.3 i.e. the pollen collection efficiency is indistinguishable with or without tribo-charging. In addition, when the correlation between the pollen chargeability and the collection efficiency in Fig. 6-18 is tested using the 'LINEST' function in Excel, pollen chargeability is only marginally significant as a factor at 95 % confidence level. In another words, the level of tribo-charging is not strongly influencing the collection efficiency here.

The overall trend of improved collection efficiency with faster initial jet velocity agrees with the CFD predictions in section 6.2.3, even though the range of experimental jet velocities are significantly higher i.e. maximum of 3 m/s in simulations cf. up to 7.5 m/s in the experiments (see Fig. 6-23). Spraying at gun diffuser pressures of above 10 psi saw aggressive vibration of petals, which is not feasible to be implemented in CFD models.

Effect of nozzle-to-flower distance

Here, the pressures of pumping air and gun diffuser are kept at 15 and 25 psi respectively. This gives an initial jet velocity of around 4.25 m/s. The pollen from both Teflon and aluminium modules are directed towards the front of a flower which is positioned 100 to 300 mm away from the nozzle. Again, large scatter is displayed in the number of pollen captured per stigma (see Fig. 6-19). As carried out for Fig. 6-17, the pollen collection efficiency of each sprayed flower is plotted in Fig. 6-20. The stigma gather less pollen as the jet is introduced further away from the flower. This confirms the theoretical predictions in Fig. 5-13 and 6-6. The pollen chargeability, i.e. depending on the use of Teflon or aluminium modules, does not emerge as a factor. The trend of collection shown by the pollen possessing different chargeability in
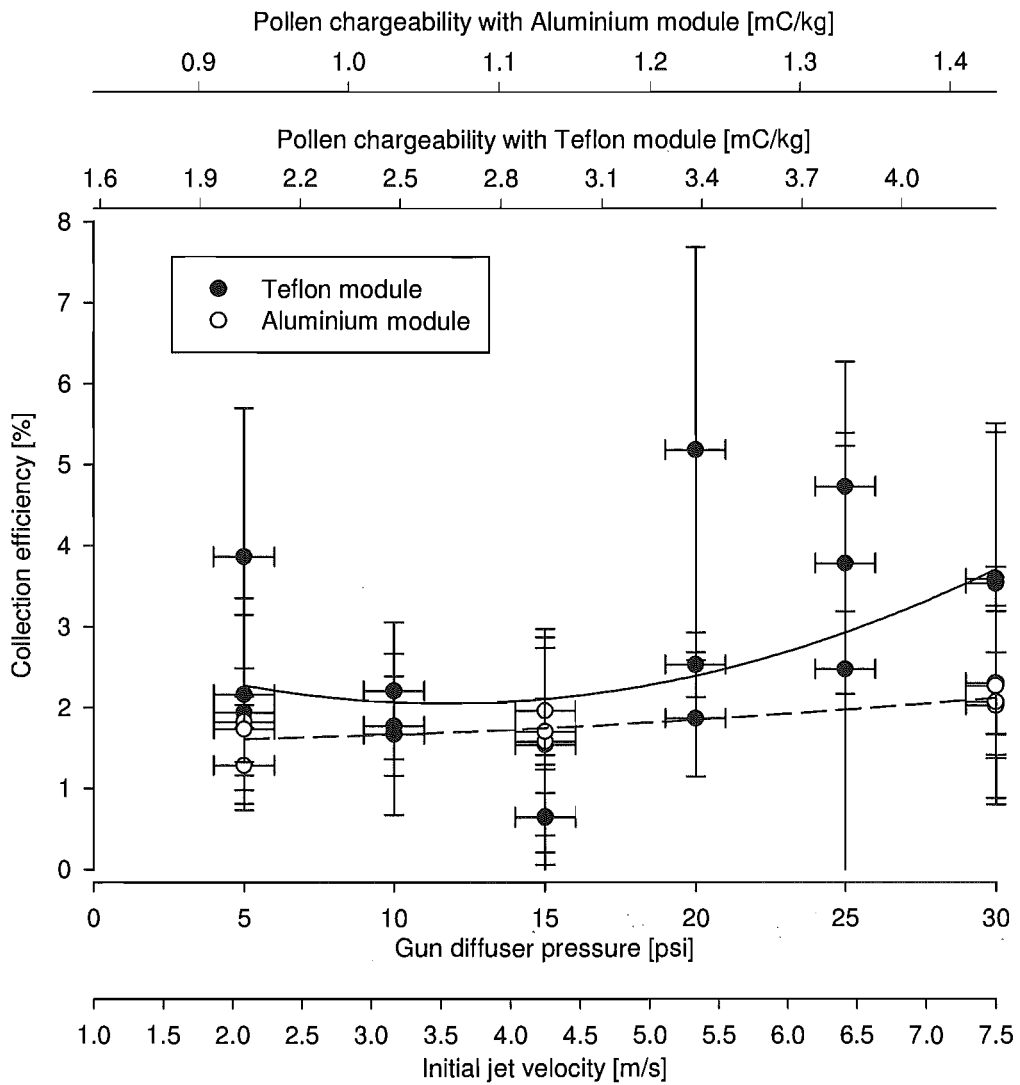
Fig. 6-17: Pollen collection efficiency by a full-open Green kiwifruit flower under a pollen-laden jet from the front. The jet exits the nozzle at different velocities and carries pollen of different chargeability depending on the types of charging module. The ϕ30-mm nozzle was placed 200 mm away from the flower. Efficiency = Collected / Fed in jet. Fitted polynomial lines are for indicative purpose only. Solid and dash lines are for the fitting of Teflon and aluminium modules respectively. The errors of collection efficiency are estimated using t-statistics at 95 % confidence limit. The gun diffuser pressure has a constant error of 1 psi.
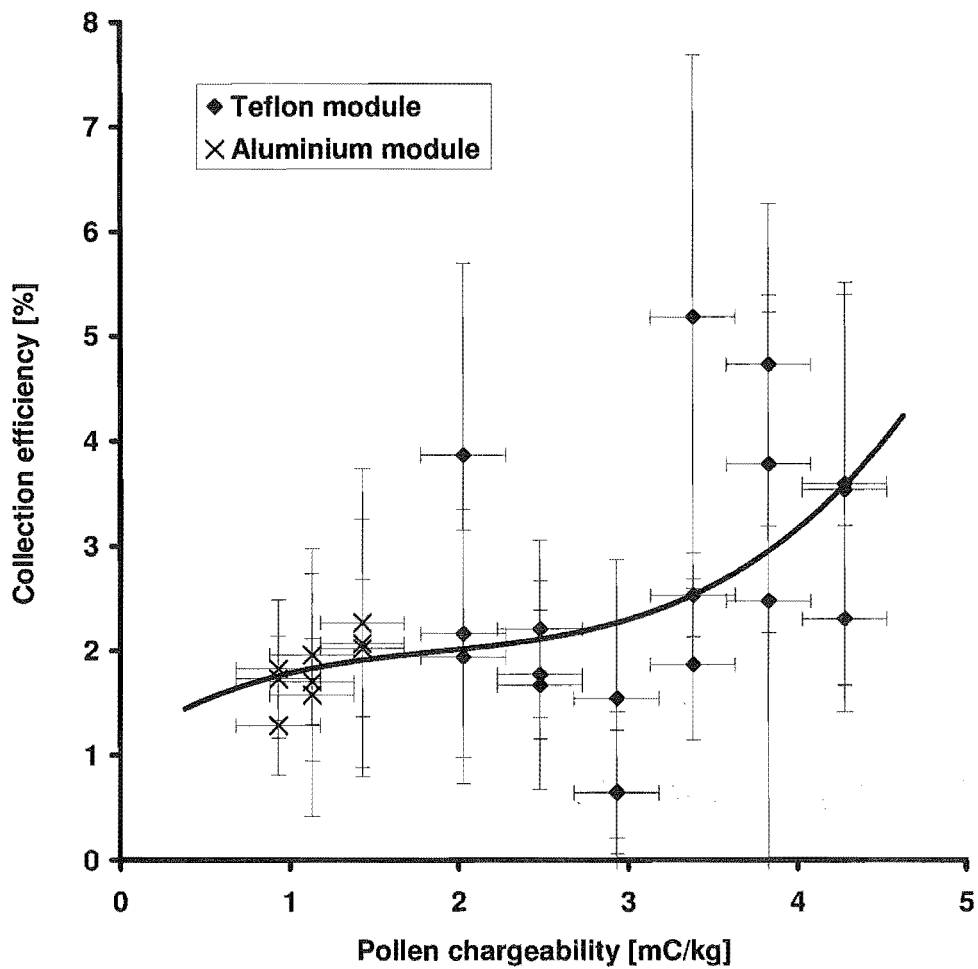
Fig. 6-18: Pollen collection efficiency by a full-open Green kiwifruit flower at different pollen chargeability. The chargeability of pollen dispersed by the frontal jet depends on the types of charging module used. The φ30-mm nozzle was placed 200 mm away from the flower. Efficiency = Collected / Fed in jet. Fitted polynomial line is for indicative purpose only. The errors of collection efficiency are estimated using t-statistics at 95 % confidence limit. The pollen chargeability has a constant error of 0.25 mC/kg.
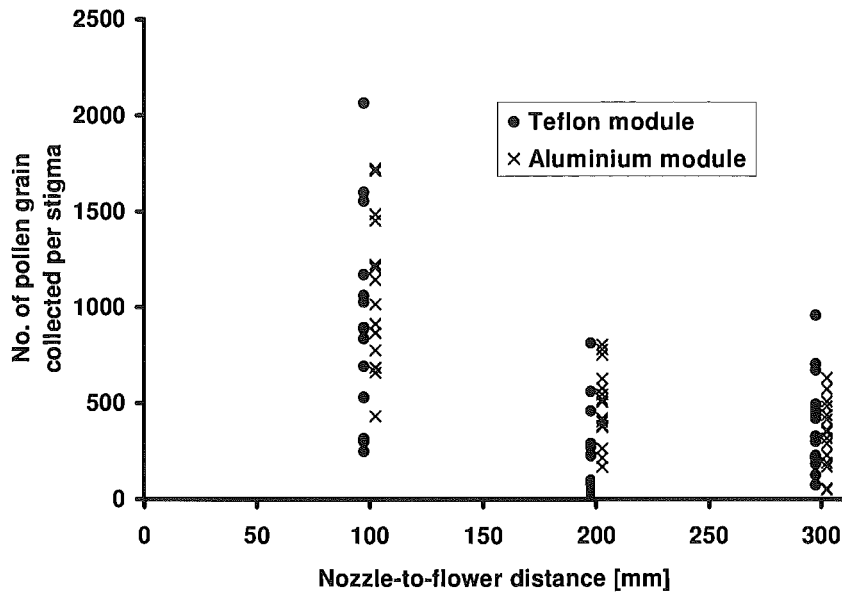
Fig. 6-19: Number of pollen captured by individual stigma of flowers exposed to a frontal jet at different nozzle-to-flower distances, with Teflon and aluminium charging modules. The pumping and gun diffuser pressures are 15 and 25 psi respectively.
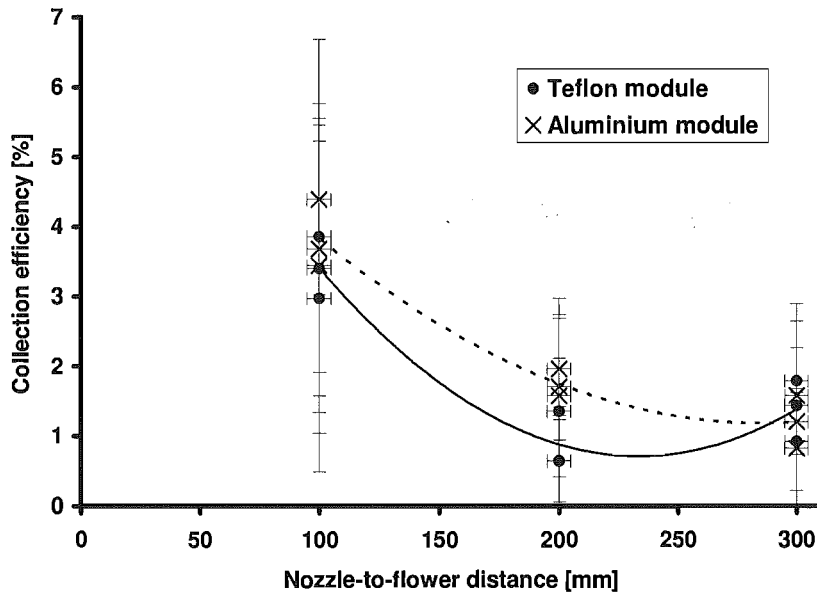
Fig. 6-20: Pollen collection efficiency by a full-open Green kiwifruit flower under a frontal jet at different nozzle-to-flower distances, with Teflon and aluminium charging modules. The pumping and gun diffuser pressures are 15 and 25 psi respectively. Efficiency = Collected / Fed in jet. Fitted polynomial lines are for indicative purpose only. Solid and dash lines are for the fitting of Teflon and aluminium modules respectively. The errors of collection efficiency are estimated using t-statistics at 95 % confidence limit. The nozzle-to-flower distance has a constant error of 5 mm.
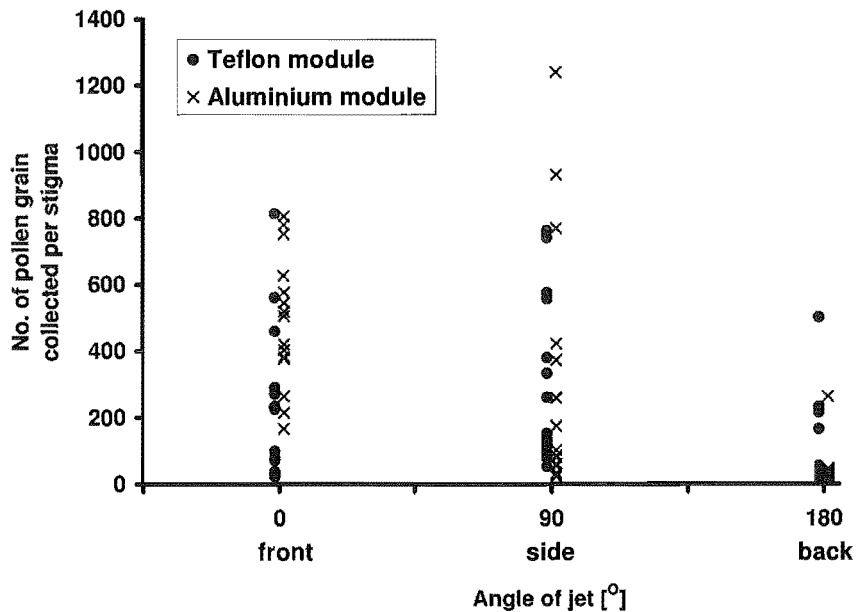
Fig. 6-21: Number of pollen captured by individual stigma of flowers exposed to a pollen-laden jet from the front, side and back, with Teflon and aluminium charging modules. The pumping and gun diffuser pressures are 15 and 25 psi respectively. The nozzle-to-flower distance is 200 mm.
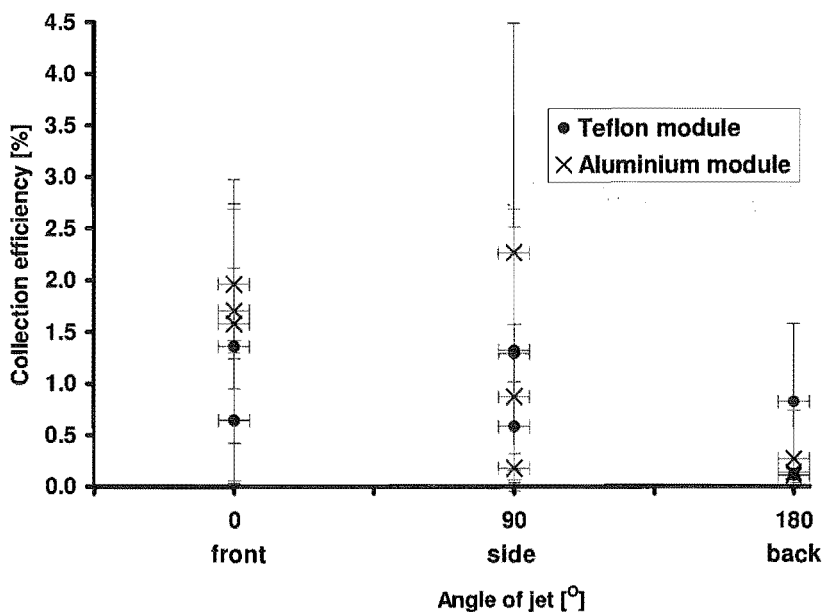
Fig. 6-22: Pollen collection efficiency by a full-open Green kiwifruit flower under a pollen-laden jet from the front, side and back, with Teflon and aluminium charging modules. The pumping and gun diffuser pressures are 15 and 25 psi respectively. Efficiency = Collected / Fed in jet. The nozzle-flower-distance is 200 mm. The errors of collection efficiency are estimated using t-statistics at 95 % confidence limit. The angle of jet has a constant error of 5 $^{\circ}$.
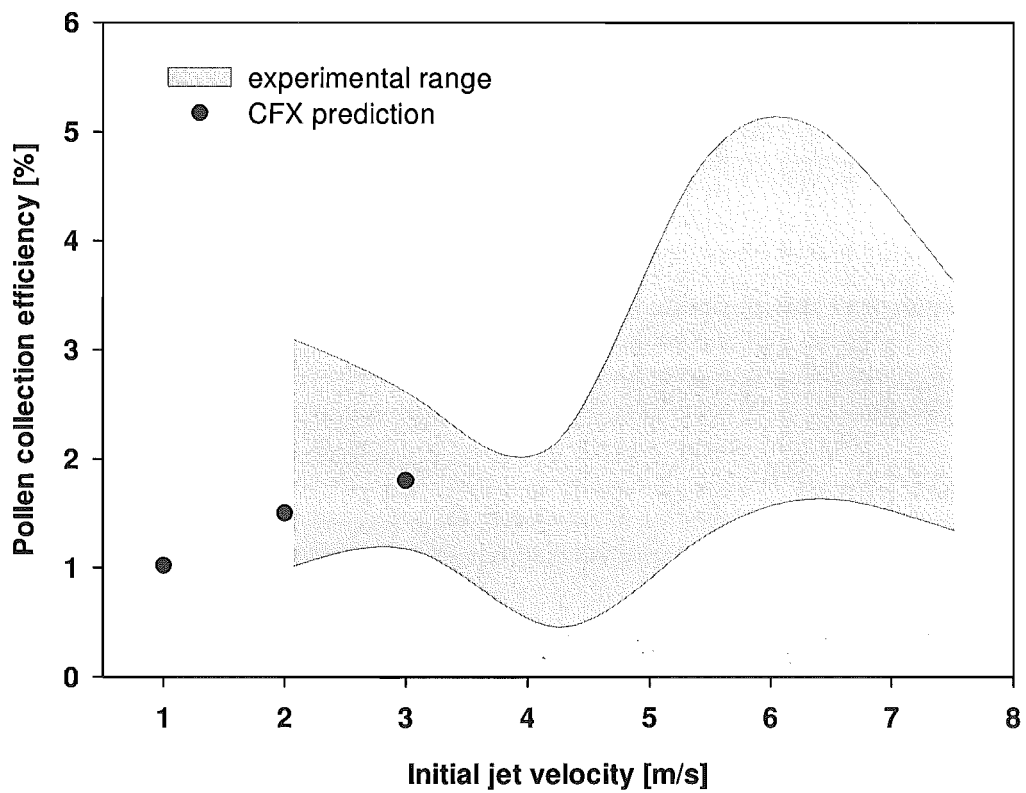
Fig. 6-23: Pollen collection efficiency (collected / fed by jet) by a full-open Green kiwifruit flower targeted by a pollen-laden jet from the front. The jet exits a φ30-mm nozzle placed 200 mm away from the flower. The experimental range refers to (mean ± one standard deviation).

Fig. 6-20 is similar to that predicted between the uncharged and charged pollen in Fig. 6-6, where the influence of charging is not apparent.

Effect of jet direction relative to flower

The same experiment is repeated but now the flowers are blown from three directions, namely front, side and back. The nozzle is fixed at 200 mm away from the flower. The quantity of pollen captured by a stigma is shown in Fig. 6-21 and the corresponding collection efficiency of a flower in Fig. 6-22. The stigma sampled from the flower subjected to a side spray display the largest scatter in the number of pollen collected per stigma (Fig. 6-21). This is because the sampling is affected by the position of stigma relative to the spray i.e. the stigma facing the spray receive more pollen than the leeward ones. Despite the awareness of this, random sampling of five stigma from each sprayed flower is still carried out. The averaging however has not minimized the scatter successfully as intended, as shown by the wide spread of data points for the collection efficiency under a side jet in Fig. 6-22.

Fig. 6-22 indicates that the frontal and side sprays yield better results than a back spray. Despite the large scatter exhibited under a side jet, a frontal spray seems to achieve better collection efficiency than a side jet. These results are in accordance to the predicted collection of uncharged pollen carried by a jet in Fig. 5-13.

Once again, as in Fig. 6-20, the pollen having only background charges (i.e. from the aluminium module) seems to occasionally outperform the more charged pollen in the deposition onto the stigma. There is no evidence in Fig. 6-22 to suggest an improved pollen collection by tribo-charging the pollen.

All the back-sprayed flowers have found pollen on the stigma. This is in contrast to the simulation outcome of uncharged pollen shown in Fig. 5-13 where no deposition is expected for an initial jet velocity of 3 m/s. One explanation offered for this discrepancy between the simulations and the experimental is the vibration of petals may have created a downstream flow pattern that assist the pollen deposition onto the stigma.

6.3.4. Discussion and recommendations

The order of magnitude of experimental pollen collection efficiency is comparable to the predicted efficiency. For example, in Fig. 6-17, at gun diffuser pressure of 5 psi i.e. at around 2.1-m/s initial jet velocity, the collection efficiency ranges from 1.3 to 2.2 % with an exception of a point at 3.9 %. The range of experimental efficiency is 1.7 to 2.2 % at gun diffuser pressure of 10 psi or initial jet velocity of around 3.2 m/s. The predicted efficiency at initial jet velocities of 2 and 3 m/s are 1.4 and 1.8 % respectively (see the curve for nozzle-to-flower distance of 200 mm in Fig. 5-13a), which are within the experimental ranges.

Under the illumination of a spotlight pointed across the exit of the nozzle, it was found that the pollen-laden jet displayed a small degree of oscillatory behaviour. The spotlight was originally intended to visually check whether the jet has stabilized i.e. the consistency of pollen cloud concentration. It was noted that there tended to be pulses of pollen cloud during the initial jet start-up. It is uncertain how the oscillating jet affected the pollen deposition on the flower. But its existence suggests that the jet swinging predicted in the steady state CFD simulations (note that the oscillatory behaviour can only be obtained in unsteady state models) is unlikely to be an erroneous computation.

The outcomes of the experiment suggest that:
- according to Fig. 6-18, tribo-charging the pollen appears beneficial in elevating the pollen deposition on the stigma. Greater charging gives more deposition. This may seem to contradict the findings from the tribo-charging simulations in section 6.2.3. However, it must be borne in mind that the benefit of tribo-charging is not clearly indicated in Fig. 6-20 and 6-22. In addition, the initial jet velocities used in the experiment (see Fig. 6-17) are mostly beyond the range in the simulations and have induced petal vibration, which may influence the pollen collection. Nevertheless, the encouraging gain in efficiency in Fig. 6-18 warrants further experiments with larger number of flowers to be sprayed and the refinement of the tribo-charging model that has used simplified assumptions in estimating the distribution of pollen mass fraction (see details in section 6.2.3).

- the trend exhibited in Fig. 6-20 validates the CFD predictions i.e. the pollen-laden jet should be discharged as close to the flower as possible. Increasing the nozzle-to-flower distance from 100 mm to 200 and 300 mm results in significant drop in collection efficiency.

- the experiments of targeting the flower with a jet from different directions (see Fig. 6-22) supports the CFD outcomes in that most pollen are delivered to the stigma under a frontal jet.

In addition, the future work is recommended to include the experimental spraying of pollen with a corona-charger onto both full-open and bold kiwifruit flowers in order to validate the outcomes of CFD simulations.

The pollen counting method used in this work is fairly labour intensive because of the need to mark individual pollen on the captured microscope images in order to facilitate automatic counting using the software. However, the technique of transferring the pollen from the stigma to a sticky surface for counting is thought to be practical. It has potential to be refined and made easy for use by growers. To the author's best knowledge, this method has not been applied by anyone else.

Currently, there is not a quick and convenient way for the growers to measure the pollen deposition on flowers. If desired, the growers may need to rely on laboratory personnel to come to the orchards to collect styles for counting in the laboratory. The service may not be available easily to all growers. The author's field trips to Te Puke and Nelson orchard areas in 2001 and 2003 respectively had not observed any growers using such services. Thus, it makes sense to come up with an assessment method that can be carried out by the growers themselves.

One suggested further development to the current pollen counting method is to have a circular sticky sampling label (say ϕ 12.5 mm, which is half of the diameter of stigma bush) attached to the end of a probe. Only one side of the label is sticky and it is covered with a protective seal before use. Within an hour after the machine spraying[12], the grower 'rubs' the sticky surface gently against the stigma of a randomly selected

---

[12] so that pollen can be removed before they start to germinate and anchor themselves to the stigma.

6-37

flower to transfer the pollen grains to the sticky surface. The grower can repeat this on as many flowers as appropriate, using a fresh sampling label for each flower. The sampling labels having the transferred pollen are removed from the probe and stored separately in a custom designed container before carrying out an indoor examination. Drops of staining solution, such as the one used in this work, are applied onto each sampling label. A period of one day is allowed for adequate staining to take place. Each label is then placed under a microscope illuminated with a low-power red laser (such as in laser pointers). Only the male pollen will then be visible. Instead of counting the actual number of pollen, the density of pollen on the sampling label is then compared to the 'standard' pictures of various pollen densities. The pollen density on the 'standard' pictures is pre-calibrated for the number of pollen grains. The comparison enables the growers to decide whether the artificial pollination has been adequate.

The idea is preliminary but is recommended to be looked at as it can be commercialized if successful. For instance, the 'standard' pictures will be bundled with the microscope and laser as a package. With the rapid drop in the cost, a digital camera can be fitted to the microscope so that the microscopic images can be displayed real time on a television (i.e. for easier assessment) and stored for future records.

6.4. Overall comments

A literature search finds that electrostatics have been applied successfully in artificial pollination of other agricultural crops. The reported cases are however limited to the corona charger method.

Simulations of the stigma collection of corona-charged and tribo-charged pollen dispersed in an air jet indicates that the use of only a corona charger is expected to improve the collection efficiency. The difference lies in the strong electric field established between the high-voltage electrode and the grounded flower.

Experimental spraying of tribo-charged pollen onto fresh flowers shows that the aerodynamic factors i.e. the initial jet velocity and the direction of jet are significantly

more dominant than the pollen chargeability in determining the pollen collection efficiency. There are signs that tribo-charging pollen may enhance pollen collection provided the jet is introduced at the certain conditions. For this reason, further work either in theoretical refinement of the model or more extensive experimental tests are recommended.

CHAPTER 7: STUDY OF STIGMA STICKINESS

7.1. Background

The growers usually spray the dry pollen using air before 10 am because the abundant presence of exudates on the stigma before 10 am is thought to enhance the collection of air-borne pollen by the stigma (personal communication with a grower in Te Puke, 2001). The growers found that spraying pollen in the afternoon did not yield as good crop as that carried out in the morning (personal communication with Steven Spark[1], 2003). One of the suggested reasons[2] is the lower number of pollen collected by the stigma due to the absence of exudates in the afternoon.

Craig & Stewart (1988) observed that the stigma were very wet and sticky over the early morning period from 2300 h to 0900 h but remained dry during much of the day. Observation by Corbet *et al* (1988) found that the presence of stigmatic exudates was dependent on ambient humidity. The stigma were covered by abundant exudates above 71 %RH but the presence of exudates was detected at down to 55 %RH. Gonzalez *et al* (1996) suggested that the abundant stigmatic secretion in the pistilar tract is important in supporting pollen tube growth. King & Ferguson (1991) also noted the abundant existence of exudates at high humidity and they suggested that the exudates would not only aid pollen germination but also assist the pollen collection.

This work aims to answer two questions:
1. *Is there any variation in stigma stickiness at different flower ages after blossom?*
2. *Is there any variation in stigma stickiness at different times of the day?*

The stickiness tests were carried out with the stigma of Gold and Green kiwifruit flowers. Gold kiwifruit flowers blossom about one month earlier than the Green flowers. All the flowers were picked from an orchard in Motueka in 2003 (see the dates below).

---

[1] Horticultural consultant, Agfirst, Motueka, New Zealand.
[2] Another suggested reason is the lower receptivity of stigma in the afternoon. This has yet to be verified. However, Gonzalez et al. (1995) showed that the receptivity is fairly constant over 5 days after blossom.

7.2. Experiment on stigma stickiness

7.2.1. Design of stickiness testing device

The stickiness or the force of adhesion of a particle on a surface is equal in magnitude and opposite in sign to the force needed to detach the particle (Zimon, 1982). There are several ways of measuring the particle adhesion by detaching the single particles on a surface. They include inclined-plane method, centrifugal method, vibration method, microbalance weight method, pendulum method, aerodynamic and hydrodynamic method (Boehme et al, 1962; Corn, 1966; Mullins et al, 1992; Zimon, 1982).

The aim is to determine the stickiness (or adhesion) of the male pollen on the stigma. In order to use the fresh styles, a portable, simple-operating, reliable and relatively quick testing device that can be used in the orchard needs to be designed. Among the abovementioned methods, only centrifugal method was considered suitable.

However, the detachment of a single pollen (~ 13 – 26 micron; see section 1.2) from the stigmatic surface will require an enormous level of centrifugal acceleration. Both Boehme et al (1962) and Corn (1966) applied a centrifugal acceleration of up to ~ 10^5 g to separate 13 to 15-μm starch powders from a starch-coated brass substrate and 20-μm glass spheres from a glass slide respectively. Separation of sticky starch powders is expected to resemble the removal of pollen from the sticky stigma. An initial estimation indicates that approximately 240000 RPM is needed to detach a single pollen grain from a stigma spinning horizontally. This certainly pushes the centrifugal device design to the limit and is considered impractical for a portable device.

In order to decrease the rotational speed required, instead of detaching the pollen from the stigma, the stigma were to be detached from the side wall of a spinning disc. The side wall was coated with the commercial pollen from KiwiPollen Limited to maintain a pollen-stigma contact or interaction.

Fig. 7-1 are the schematic diagram and photo of the designed testing device based on the centrifugal method. 10 to 13 stigma were placed circumferential evenly on the vertical side wall coated with viable male pollen. After the application of a certain centrifugal force, the number of stigma that were still attached to the side wall was recorded.
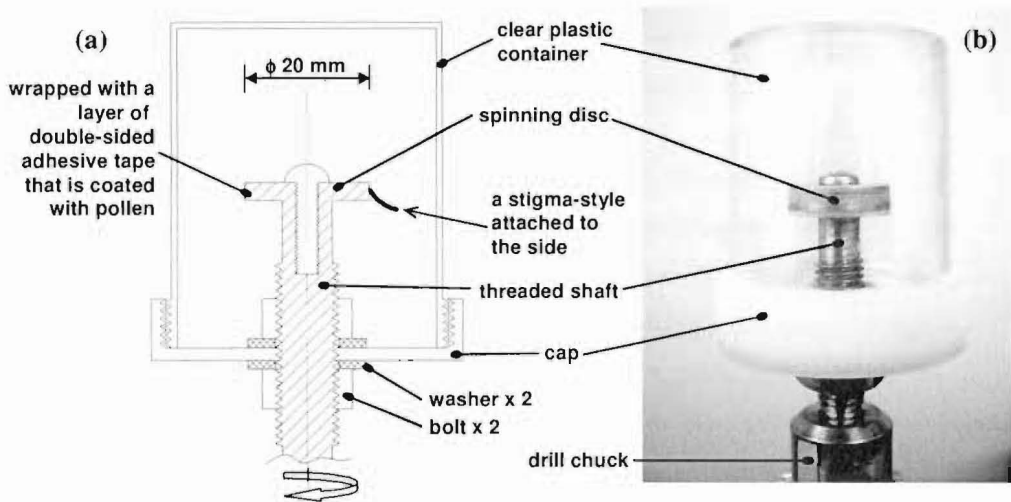
Fig. 7-1: (a) Schematic diagram and (b) photo of the centrifugal testing device used to measure the stigma stickiness.

The φ 20-mm spinning disc was fixed to the top of the 8-mm threaded shaft. The lower end of the shaft was inserted into the drill chuck of a variable speed spinning motor (Heldolph, Type RZR 1, from Victor Watson Limited, Germany). The speed was calibrated using SKF Digital Tachometer 729155 and ranged from 287 to 2283 RPM. However, the tests using the stigma from Gold kiwifruit flowers showed that 2283 RPM was insufficient to remove all the stigma. Thus, an additional motor (from AEI, Newcastle, England) that gave a speed range of 2385 – 14000 RPM was used for the stigma of Green kiwifruit flowers. The speed was varied by controlling the voltage supply to the motor.

A cage, modified from a clear plastic sampling container, helped to trap the air inside the cage and cause it to rotate with the cage, so that there was no air shearing effect on the detachment of the stigma.

7-3

7.2.2. Description of stigma stickiness tests

Below are the stickiness test procedures carried out for both Gold and Green kiwifruit flowers. The fresh flowers were used within an hour after picking.

1. The first step was the preparation of a pollen coating. A piece of double-sided adhesive tape was laid on the side of the spinning disc. The thawed pollen were dusted onto the tape using a water colour paint brush until the double-sided tape was not sticky anymore. The surface was then pressed with a piece of stainless steel sheet to consolidate the adhesion of pollen layer to the tape. The surface was dusted again with pollen to make sure the whole surface was completely covered with pollen. The excess pollen on the surface were removed by aggressive brushing using a soft brush. This process took about 15 minutes.

Examination under the light microscope showed that there was only a monolayer of pollen with no interstices larger than the pollen.

2. 10 to 13 styles were removed randomly from a single flower using a pair of tweezers. The stigma (the tip of the styles) were dabbed gently on the pollen coated wall. The stigmatic surface was identified as the front surface of the spoon-shaped tip (see Fig. 2-4i and j in section 2.4).
3. After the cage of the device was put on, the disc was spun and the number of stigma that were still attached to the pollen coated wall was recorded after 5 seconds of spinning at a particular speed. The speed increment was approximately 50 RPM, between successive levels.

The effect of stigma stickiness in capturing the air-borne pollen is thought to be most critical during the short moment of impaction of pollen on the stigma. If the rebounding pollen has enough energy to overcome the stigma surface stickiness, then the pollen will become air-borne again. On the other hand, the deposited pollen is unlikely to become elutriated, and thus will remain and germinate. Based on this reasoning, the waiting time at each motor speed is decided to be not more than 5 seconds. To prevent a sudden

start of spinning, each speed setting was achieved by gradually increasing the speed upwards from the lowest speed. This was done in about 5 – 8 seconds.

4. The same pollen coated surface was used for 3 or 4 flower replicates. Before the new batch of stigma were placed on it, the surface was dusted again with pollen followed by the removal of excess pollen as described before.

Assumptions made were:

• The variations in weight and length of individual stigma of different ages were minimal and thus did not affect the stickiness tests significantly.

• The applied force in dabbing the stigma onto the pollen coated wall did not introduce any variability to the stickiness tests.

• Since the bonding between the pollen and the adhesive tape was significantly greater than the bonding between the pollen layer and the stigmatic surface, the force required to detach a stigma were based only on the contact between the pollen and the stigma.

7.2.3. Scheduling of tests

Kiwifruit flowers were marked using colour-coded wire in order to identify their ages after blossom. The stickiness tests were carried out in the morning, at noon and late in the afternoon using the open-pollinated (i.e. not bagged) flowers. The planned times are shown in Tables 7-1 and 7-2 for Gold and Green kiwifruit flowers respectively. The actual times might differ by up to one hour e.g. due to the wet weather. The weather conditions were also recorded.

Each test comprised of 3 – 4 replicates where each replicate used only the stigma selected randomly from one single flower (i.e. one flower per replicate). A test took about 1 hour 45 minutes to 2 hours. The flowers of ages of 0, 1, 2, 3, 4 days were selected[3]. There were repetitions of 0-day-old and 1-day-old flowers in order to check the repeatability of the test on different days.

---

[3] This is the period where the stigma have maximum receptivity and before the stigma become completely dry.

Table 7-1: Timetable of the stickiness tests and the records of temperature and relative humidity when the Gold kiwifruit flowers were picked.

		8:00-9:30 am			12:00-1:30 pm			4:00-5:30 pm		
Date	Flower age	Replicates			Replicates			Replicates		
		1	2	3	1	2	3	1	2	3
27-Oct	0 day	12.6 °C, 52.6 %RH			20.0 °C, 28.9 %RH			18.3 °C, 37.0 %RH		
28-Oct	1 day	14.2 °C, 70.7 %RH [i, ii]			18.4 °C, 57.1 %RH [iii]			18.8 °C, 63.0 %RH		
29-Oct	0 day	13.3 °C, 74.0 %RH [i, iii]			23.6 °C, 52.4 %RH			19.5 °C, 49.7 %RH		
	2 days [v]	13.3 °C, 74.0 %RH [i, iii]			23.6 °C, 52.4 %RH			19.5 °C, 49.7 %RH		
30-Oct	3 days [v]	14.4 °C, 71.0 %RH [i]			16.5 °C, 70.0 %RH [ii]			13.2 °C, 81.7 %RH [iv]		
31-Oct	4 days [v]	13.5 °C, 77.8 %RH [i]			19.0 °C, 45.3 %RH			18.1 °C, 58.9 %RH [iii]		

[i] presence of morning dew observed;
[ii] flowers picked under light shower;
[iii] flowers picked after shower;
[iv] flowers picked under heavy shower;
[v] brownish stigma observed;

Table 7-2: Timetable of the stickiness tests and the records of temperature and relative humidity when the Green kiwifruit flowers were picked. Some tests only consisted of 3 replicates.

		8:00-10:30 am				12:00-1:30 pm				4:00-6:00 pm			
Date	Flower age	Replicates				Replicates				Replicates			
		1	2	3	4	1	2	3	4	1	2	3	4
25-Nov	0 day	14.9 °C, 66.9 %RH				21.8 °C, 37.7 %RH				20.2 °C, 46.0 %RH			
26-Nov	1 day	14.0 °C, 66.0 %RH				17.8 °C, 50.0 %RH [ii]				15.6 °C, 63.8 %RH [ii]			
27-Nov	0 day	18.3 °C, 47.1 %RH [iv]				15.6 °C, 61.6 %RH [iii]				15.6 °C, 61.6 %RH [ii]			
	2 days [vii]	13.8 °C, 75.0 %RH [iv]				19.5 °C, 45.7 %RH [iii]				15.6 °C, 61.6 %RH [ii]			
28-Nov	1 day	–				17.5 °C, 57.5 %RH				17.8 °C, 55.6 %RH [iii]			
	3 days [vii]	14.2 °C, 56.6 %RH [vi]				17.5 °C, 57.5 %RH				17.8 °C, 55.6 %RH [iii]			
29-Nov	0 day	13.6 °C, 56.3 %RH [i]				–				–			
	4 days [vii]	13.6 °C, 56.3 %RH [i]				18.9 °C, 60.5 %RH				20.8 °C, 39.4 %RH			

[i] presence of morning dew observed;
[ii] flowers picked under light shower;
[iii] flowers picked after light shower;
[iv] flowers picked after heavy shower;
[v] flowers picked under heavy shower;
[vi] flowers picked after overnight shower;
[vii] brownish stigma observed;

7-6

7.3. Analysis methods and results of stickiness tests

The percentage of stigma remaining at different rotational speeds are shown in Fig. 7-2 and 7-3 for the Gold and Green kiwifruit flowers respectively. Note that the repetitions using the flowers of same age but on different days are also shown. The stigma stickiness seems to increase with the flower age after blossom. It is however difficult to identify any difference in stickiness at different times during the day.

The data in Fig. 7-2 and 7-3 are further processed qualitatively and quantitatively below to answer the two questions raised in section 7.1.

7.3.1. Method 1: qualitative assessments

According to Zimon (1982), the adhesion on particles on a substrate is better evaluated on the basis of the detachment force for an adhesion number of 50 %. Adhesion number is the ratio of the number of particles remaining on a surface after the application of force to the number initially there (Mullins et al, 1992).

Thus, only the RPM at which 50 % stigma remains are considered for the stigma stickiness analysis below. Since some of the Gold kiwifruit flower tests, particularly the ones using the older flowers, did not have all the stigma detached at the maximum RPM (2283 RPM), 2283 RPM is then taken as the 50 % cut.

The Gold kiwifruit stigma tend to become much stickier from day 2 onwards (Fig. 7-4). The trend is more clearly shown in Fig. 7-5, a distribution plot of RPM at 50 % stigma remaining for flowers at different age. The same trend is also observed for Green kiwifruit stigma in Fig. 7-8 and 7-9.

To examine the variation of stickiness during the day, the data of RPM at 50 % remaining are categorized into the morning, noon and afternoon tests regardless of the flower ages in Fig. 7-6 and 7-10. Both graphs do not show variation in stickiness

during the day. However, the box plots in Fig. 7-7 and 7-11 hint that as the stigma get older, their stickiness may not be constant from the morning to the afternoon.

7.3.2. Method 2: paired comparisons

The means of RPM at 50 % stigma remaining are computed for each morning, noon and afternoon tests. They are then assigned as M_i, N_i and A_i respectively, where i is the flower age in day(s). These means are plotted in Fig. 7-13 and 7-15 with respect to the flower ages and test time during the day, for both Gold and Green kiwifruit flowers respectively.

Three ratios, namely N_i/M_i, A_i/M_i and A_i/N_i, are calculated to compare the stickiness of stigma used in the morning, noon and afternoon tests. The box plots of these comparison ratios are shown in Fig. 7-12 and 7-14 for the Gold and Green kiwifruit flowers respectively.

Both contour plots in Fig. 7-13 and 7-15 indicate that the stickiness increases with the stigma aging. The more mature stigma appear to become stickier towards the afternoon.

Fig. 7-13 shows that the Gold kiwifruit flower stigma are stickier at noon and in the afternoon. There is however no significant change in stickiness moving into the afternoon. For the Green kiwifruit flowers (Fig. 7-14), the stigma stickiness seems significantly higher in the afternoon. Stigma picked at noon are as sticky as the ones collected in the morning.

Overall, this section finds that the aging of stigma not only increase their overall stickiness but also their daily stickiness as the day progresses into the afternoon. There is a possibility of interaction between flower age and test time during the day.
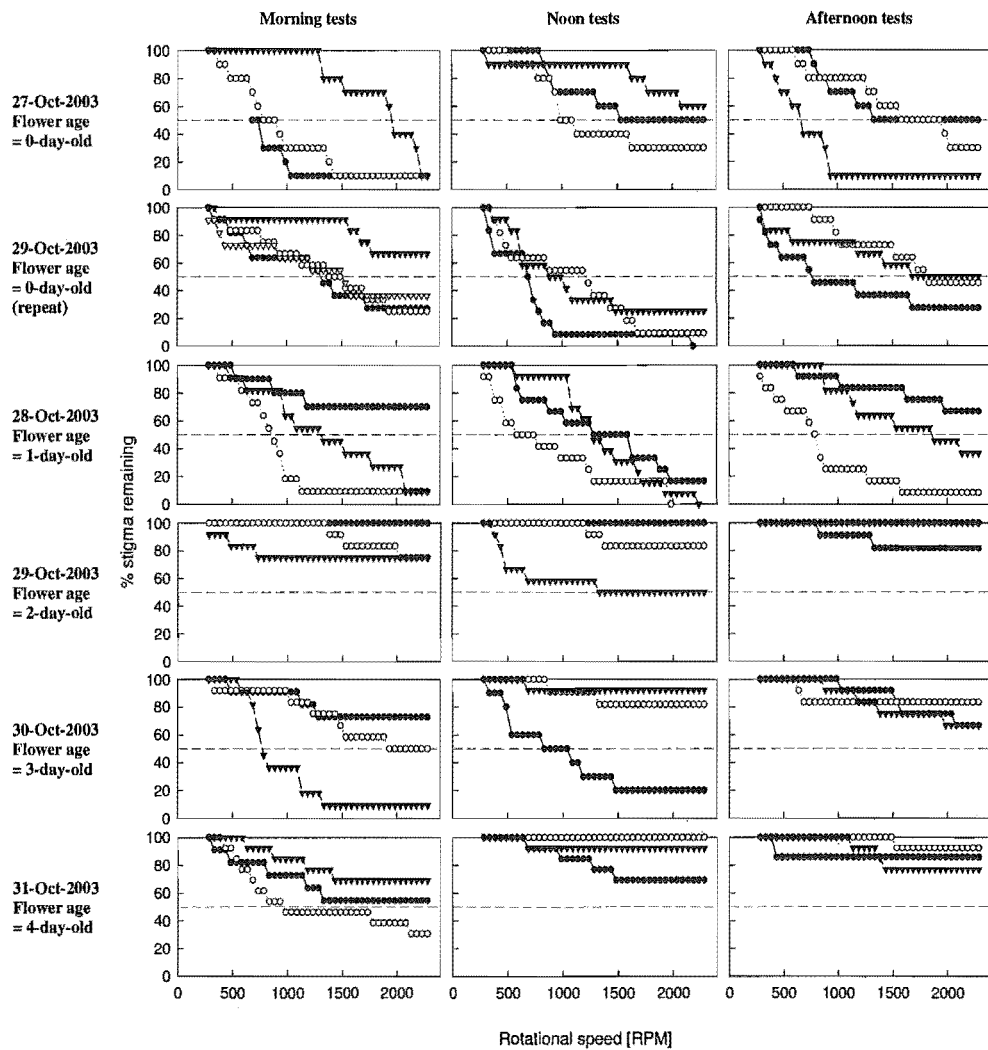
Fig. 7-2: Centrifugal tests of the stickiness of stigma sourced from the Gold kiwifruit flowers of different ages. The tests were carried out at different times of the day. Shown are the % of stigma that remained at different speeds. Each curve is given by one replicate using the stigma from one flower.
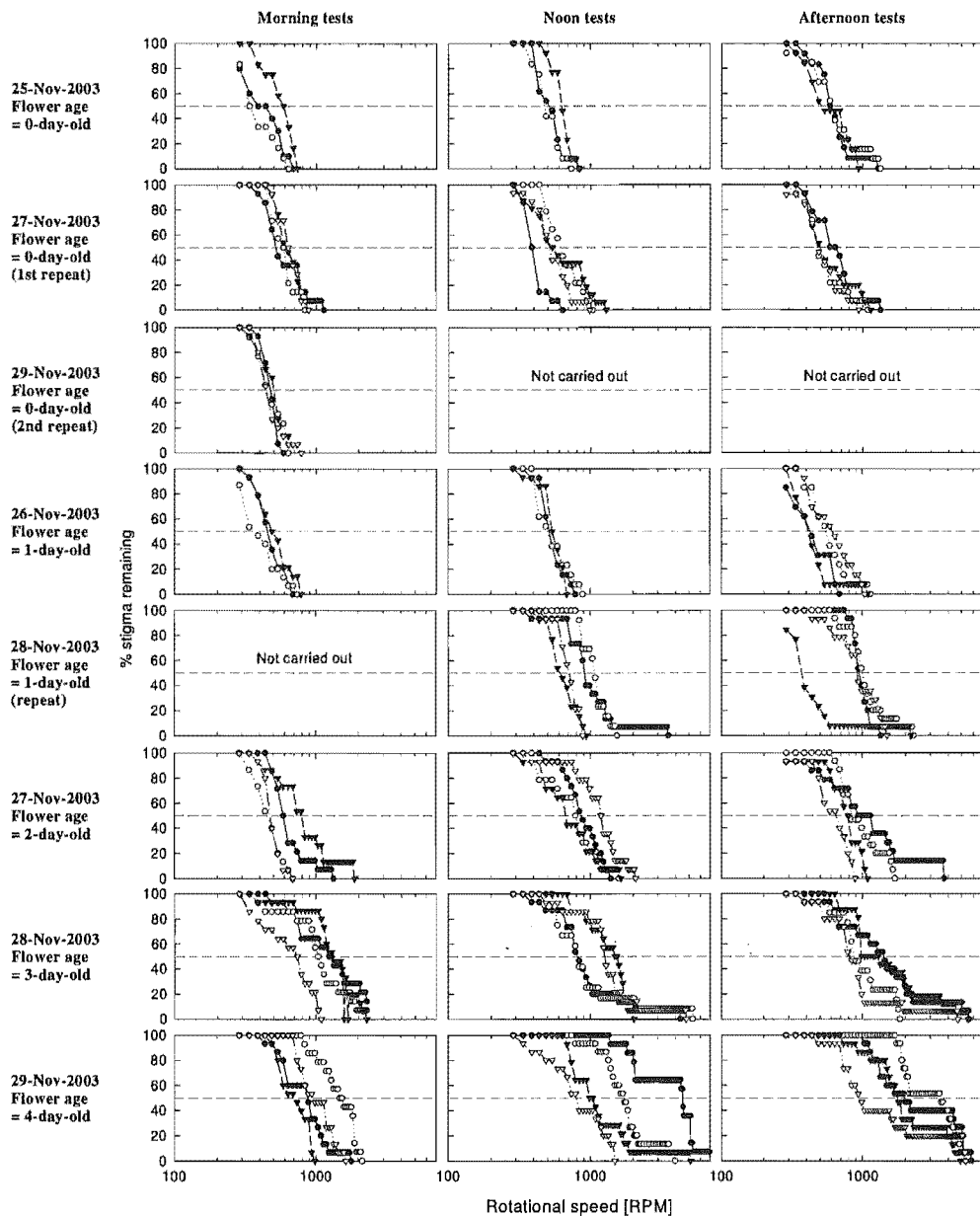
Fig. 7-3: Centrifugal tests of the stickiness of stigma sourced from the Green kiwifruit flowers of different ages. The tests were carried out at different times of the day. Shown are the % of stigma that remained at different speeds. Each curve is given by one replicate using the stigma from one flower. Note that the log scale is used for Rotational speed [RPM].
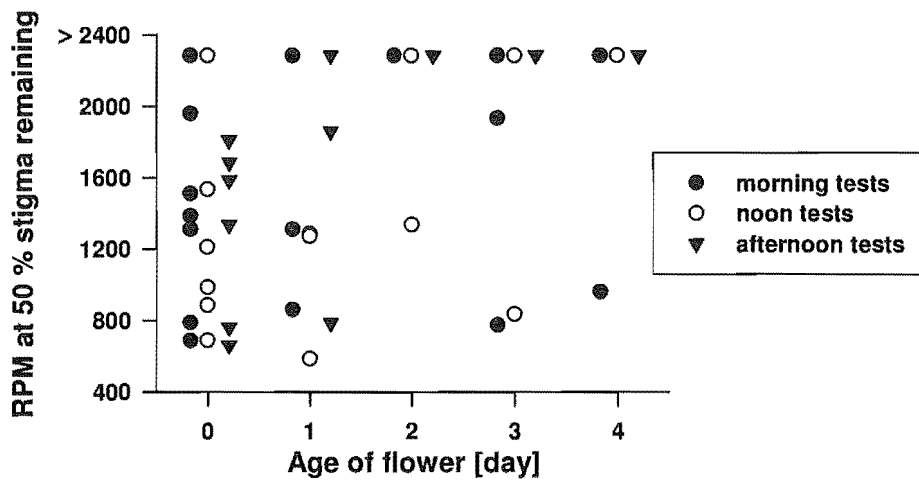
Fig. 7-4: RPM at 50 % stigma remaining in the morning, noon and afternoon tests using the stigma from the Gold kiwifruit flowers of different age.
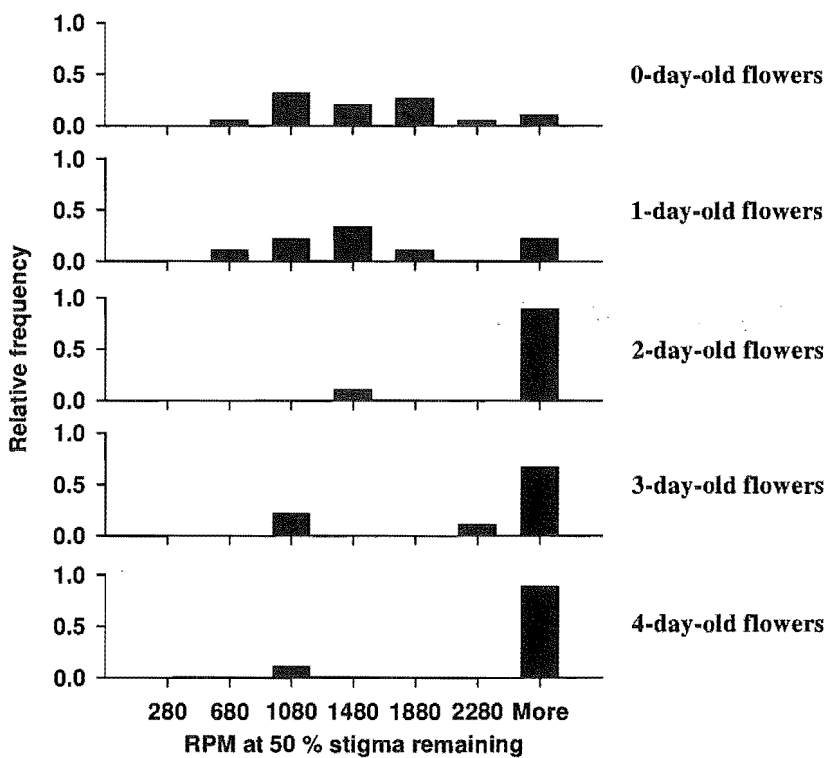
Fig. 7-5: The distribution of RPM at 50 % stigma remaining using the stigma picked from the Gold kiwifruit flowers of different age. The data of morning, noon and afternoon tests are lumped here.
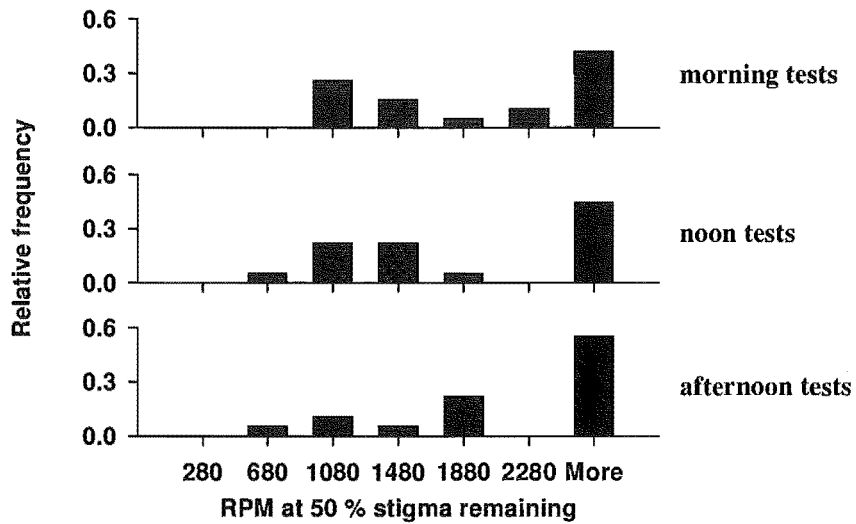
Fig. 7-6: The distribution of RPM at 50 % stigma remaining categorized based on the morning, noon and afternoon tests. The data of Gold kiwifruit flowers of different age are lumped here.
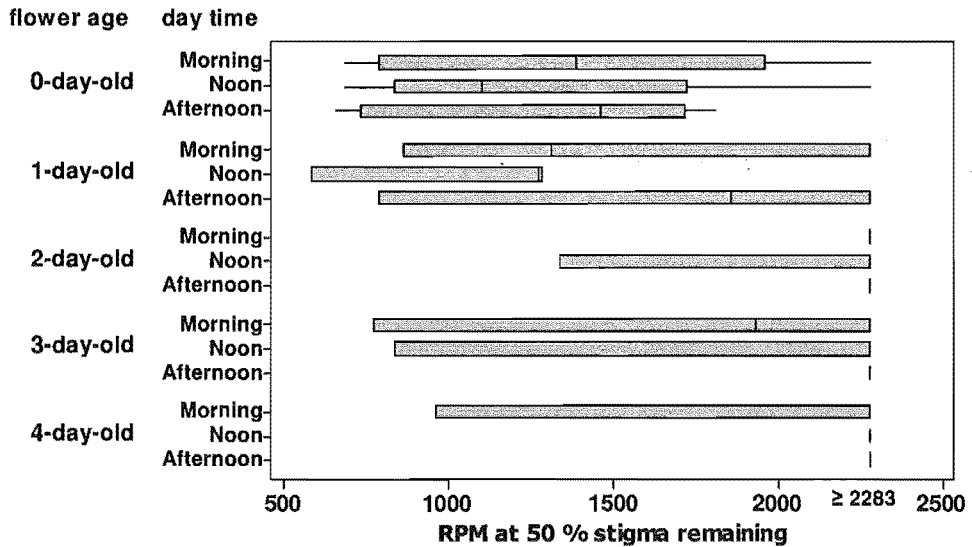
Fig. 7-7: Box plot of RPM at 50 % stigma remaining against the Gold kiwifruit flower age and the time during the day. Note: solid line inside the box = median; left box boundary = 25th percentiles; right box boundary = 75th percentiles; left whisker= 10th percentiles; right whisker = 90 % percentiles. Note that 2283 is the maximum available RPM.
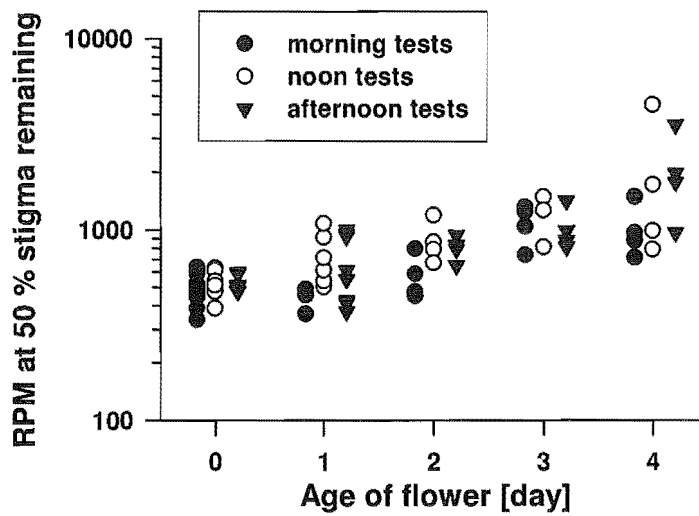
Fig. 7-8: RPM at 50 % stigma remaining in the morning, noon and afternoon tests using the stigma from the Green kiwifruit flowers of different age. Note that the log scale is used for RPM at 50 % stigma remaining.
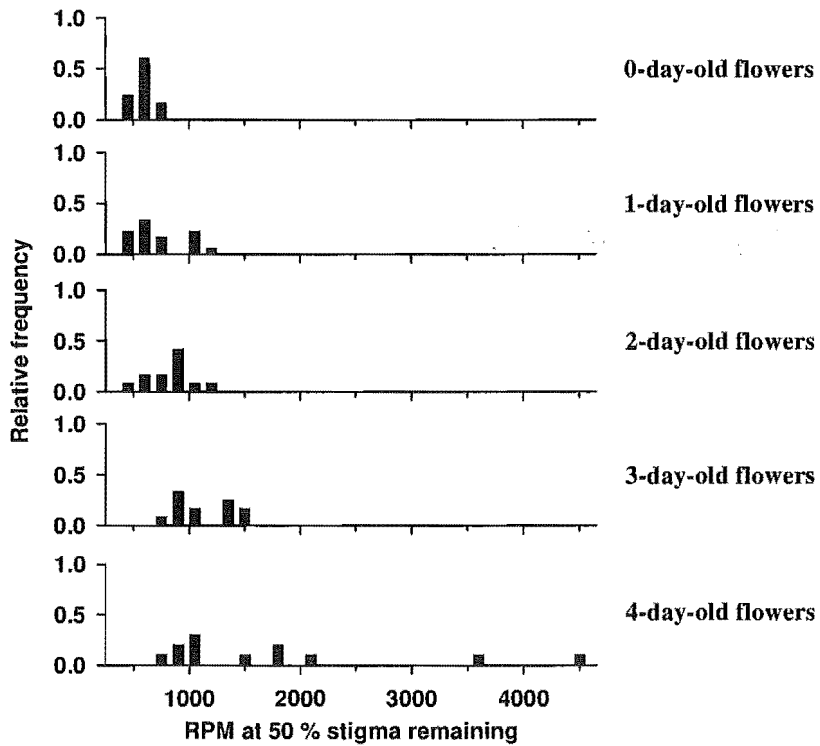
Fig. 7-9: The distribution of RPM at 50 % stigma remaining using the stigma picked from the Green kiwifruit flowers of different age. The data of morning, noon and afternoon tests are lumped here.
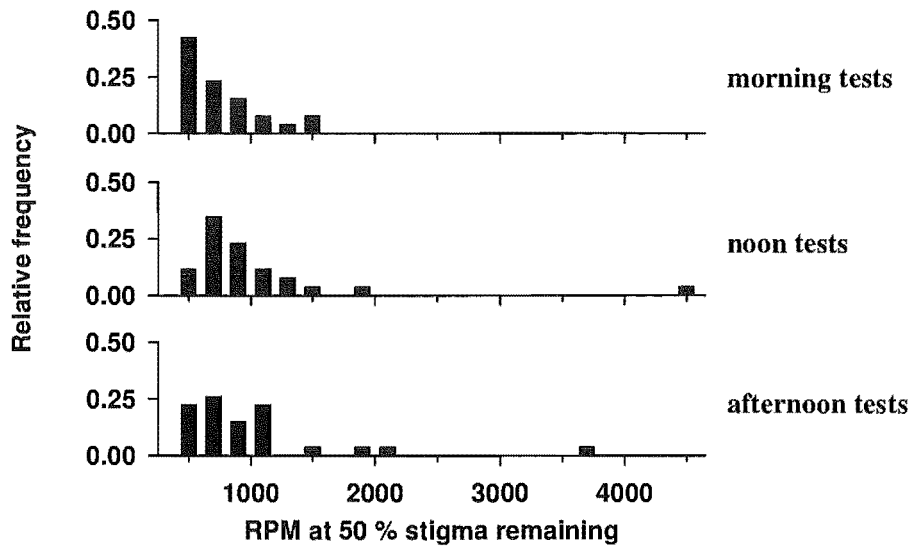
Fig. 7-10: The distribution of RPM at 50 % stigma remaining categorized based on the morning, noon and afternoon tests. The data of Green kiwifruit flowers of different age are lumped here.
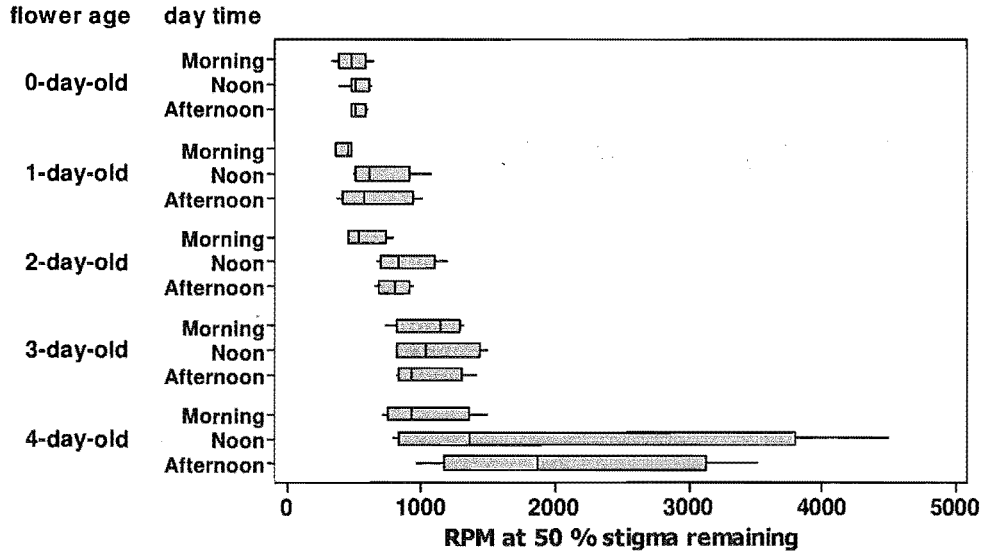
Fig. 7-11: Box plot of RPM at 50 % stigma remaining against the Green kiwifruit flower age and the time during the day. Note: solid line inside the box = median; left box boundary = 25th percentiles; right box boundary = 75th percentiles; left whisker= 10th percentiles; right whisker = 90 % percentiles.
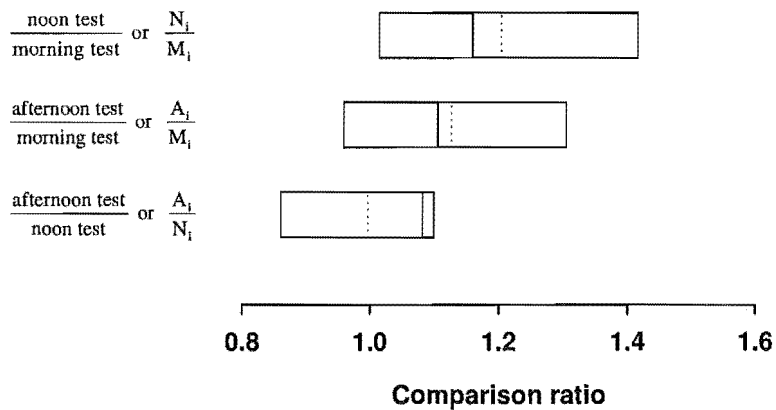
Fig. 7-12: Box plot of comparison ratios N_i/M_i, A_i/M_i and A_i/N_i for the stigma from Gold kiwifruit flowers of different ages. M_i, N_i and A_i refer to the mean of the stickiness readings (i.e. RPM at 50 % stigma remaining) taken in the morning, noon and afternoon tests respectively. i is the flower age in day(s). Note: solid line inside the box = median; dotted line inside the box = mean; left box boundary = 25th percentiles; right box boundary = 75th percentiles.
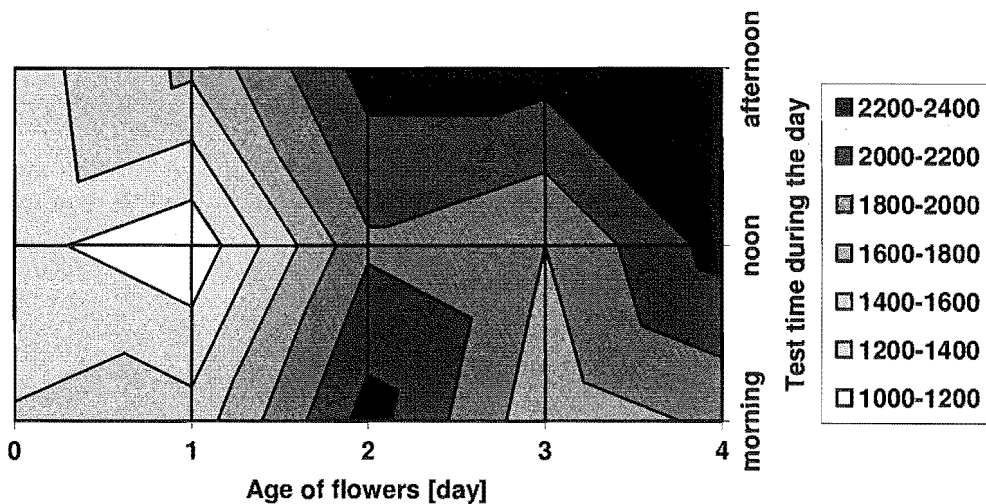
Fig. 7-13: Contour plot of 'RPM at 50 % stigma remaining' for the stickiness tests carried out at three different time during the day and using the stigma from Gold kiwifruit flowers of different ages.
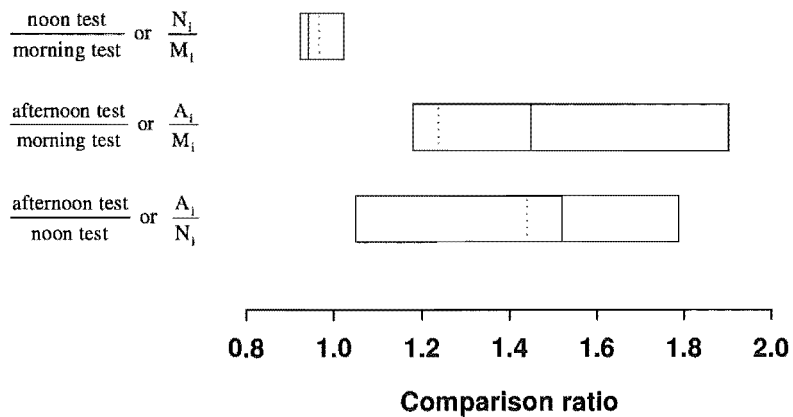
Fig. 7-14: Box plot of comparison ratios N_i/M_i, A_i/M_i and A_i/N_i for the stigma from Green kiwifruit flowers of different ages. M_i, N_i and A_i refer to the mean of the stickiness readings (i.e. RPM at 50 % stigma remaining) taken in the morning, noon and afternoon tests respectively. i is the flower age in day(s). Note: solid line inside the box = median; dotted line inside the box = mean; left box boundary = 25th percentiles; right box boundary = 75th percentiles.
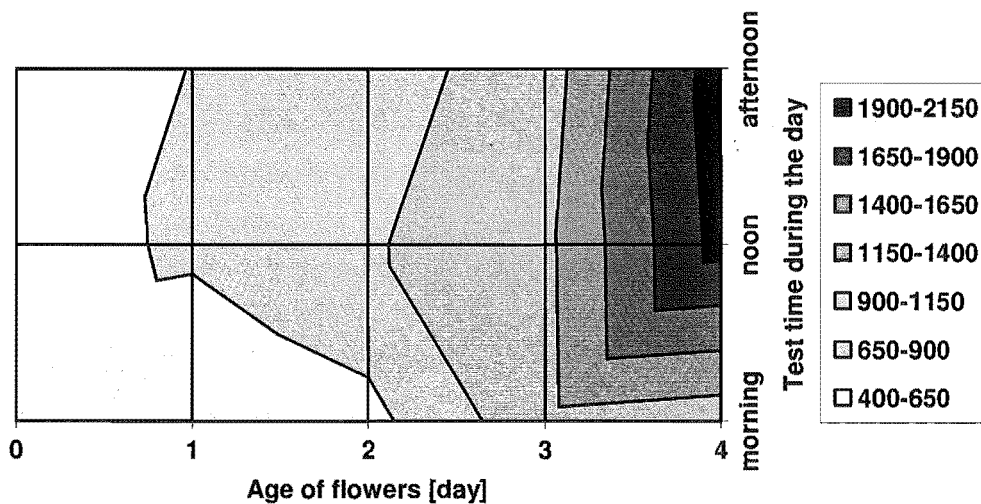
Fig. 7-15: Contour plot of 'RPM at 50 % stigma remaining' for the stickiness tests carried out at three different time during the day and using the stigma from Green kiwifruit flowers of different ages.

7.3.3. Method 3: ANOVA

Analysis of variance (ANOVA) is a statistical methodology to compare the means of populations according to one or more factors (refer to more details in Moore & McCabe, 1999). There are two factors here, namely flower age and day time. Flower age has 5 levels representing 0-day-old to 4-day-old flowers. Day time has 3 levels representing the tests carried out in the morning, noon and afternoon. RPM at 50 % stigma remaining is the response. The standard two-way ANOVA is not suitable because the data set does not contain the same number of observations for each combination of factor levels i.e. the data are 'unbalanced'. Thus, the ANOVA is performed using the General Linear Model (GLM) in Minitab 14. The printouts from Minitab 14 are shown in Fig. 7-16 and 7-17 for the stigma of Gold and Green kiwifruit flowers respectively.

The comparison of the p-values in Fig. 7-16 and 7-17 to the commonly used confidence level (α) of 0.05 show that[4], for both Gold and Green kiwifruit flowers:
- there is no interaction between the flower age and day time. This is in contrast to the findings from Methods 1 and 2.
- the stigma stickiness differs significantly among the flowers of different age.
- there is no significant variation in stigma stickiness in the tests carried out in the morning, noon and afternoon. The p-value for 'day time' effect in Fig. 7-17 is essentially same as the α level, which means there is not enough confidence to reject the null hypothesis that there is no difference in stickiness during the day.

7.3.4. Method 4: t-statistics

The means plotted in Fig. 7-13 and 7-15 are surface-fitted using the built-in LINEST function in Microsoft Excel. Flower age and day time are the independent variables while RPM at 50 % stigma remaining is the dependent variable. In addition, the surrounding humidity at the times the flowers were picked is introduced as the third

---

[4] A factor is statistically significant if p-value is less than α.

independent variable. The significance of surrounding humidity is examined here because it was thought to cause the fluctuations in the data shown in Fig. 7-4 and 7-8.

As in ANOVA calculations in section 7.3.3, flower age is assigned value 1 to 5 to represent 0-day-old to 4-day-old flowers. Day time is assigned value 1 to 3 to represent morning, noon and afternoon. The recorded relative humidity readings, as shown in Tables 7-1 and 7-2, are used in the fitting.

The equation used for the fit is

$$y = m_1x_1 + m_2x_2 + m_3x_3 + b$$

Equation 7-1

Where y is the independent variable; x is the dependent variable; m is the slope coefficient; and b is the constant.

Here, the LINEST function uses the 'least square' method to calculate a 'linear' surface that best fits the data. It then returns the slope coefficients of the independent variables and the regression statistics of the fitted equation. For each independent variable, the division of the slope coefficient by the estimated standard error of the slope coefficient gives a t-observed value. This t-observed value can be used to test whether a particular independent variable is statistically significant in predicting the dependent variable. This is done by comparing it to the two-tailed t-critical value at the specified degree of freedom and α. The calculations for the stigma of Gold and Green kiwifruit flowers at the commonly used α of 0.05 are shown in Tables 7-3 and 7-4 respectively.

Table 7-3: t-statistics calculation for the stickiness data using the stigma from Gold kiwifruit flowers.
Degree of freedom = 52 and α = 0.05

Independent variables	t-observed	t-critical	Is t-observed > t-critical?	Statistically significant?
Flower age	3.76	2.01	yes	yes
Day time	0.95		no	no
Surrounding humidity	0.37		no	no

General Linear Model: RPM at 50 % stig versus flower age, day time

```
Factor        Type   Levels  Values
flower age    fixed       5  1, 2, 3, 4, 5
day time      fixed       3  1, 2, 3


Analysis of Variance for RPM at 50 % stigma remaining, using Adjusted SS for
    Tests

Source                 DF    Seq SS     Adj SS    Adj MS      F      P
flower age              4   7585771    7637640   1909410   6.46  0.000
day time                2    561440     754035    377018   1.27  0.291
flower age*day time     8   1313567    1313567    164196   0.56  0.808
Error                  40  11831220   11831220    295781
Total                  54  21291998


S = 543.857   R-Sq = 44.43%   R-Sq(adj) = 24.99%
```

Fig. 7-16: Minitab 14 printout of ANOVA carried out to test the dependence of the stickiness of the stigma of Gold kiwifruit flower on the age of flower and the time during the day.

General Linear Model: RPM at 50 % stig versus flower age, day time

```
Factor        Type   Levels  Values
flower age    fixed       5  1, 2, 3, 4, 5
day time      fixed       3  1, 2, 3


Analysis of Variance for RPM at 50 % stigma remaining, using Adjusted SS for
    Tests

Source                 DF    Seq SS     Adj SS    Adj MS      F      P
flower age              4  12775226   12706327   3176582  13.98  0.000
day time                2   1082016    1412343    706172   3.11  0.051
flower age*day time     8   2033670    2033670    254209   1.12  0.363
Error                  64  14541392   14541392    227209
Total                  78  30432303


S = 476.665   R-Sq = 52.22%   R-Sq(adj) = 41.76%
```

Fig. 7-17: Minitab 14 printout of ANOVA carried out to test the dependence of the stickiness of the stigma of Green kiwifruit flower on the age of flower and the time during the day.

Table 7-4: t-statistics calculation for the stickiness data using the stigma from Green kiwifruit flowers.

Degree of freedom = 76 and α = 0.05

Independent variables	t-observed	t-critical	Is t-observed > t-critical?	Statistically significant?
Flower age	6.78	1.99	yes	yes
Day time	1.07		no	no
Surrounding humidity	-1.89		no *	no

* Since this is a two-tailed t-statistics, the absolute values of t-observed and t-critical are compared.

Both t-statistics tests in Tables 7-3 and 7-4 indicate that the stickiness of the stigma from Gold and Green kiwifruit flowers is correlated to the flower age but not to the time during the day. This agrees with the outcomes from the ANOVA method.

The influence of surrounding humidity is statistically rejected for both flowers. However, the rejection is very marginal for Green kiwifruit flowers because the absolute value of t-observed is very close to the t-critical in Table 7-4. In fact, the surrounding humidity can be considered as a factor if the α level is relaxed to 0.10 in Table 7-4. The negative t-observed in Table 7-4 implies that the stigma of Green kiwifruit flower become stickier with the decreasing surrounding humidity. It seems that the change in surrounding humidity may be a potential factor for the Green kiwifruit flower.

7.4. Discussion of stickiness test

1. Is there any variation in stigma stickiness at different flower ages after blossom?

Yes, all four methods found that the older Gold and Green kiwifruit flowers had stickier stigma as the age increased up to 4 days.

2. Is there any variation in stigma stickiness at different times of the day?

The dependence of stigma stickiness on the day time show mixed results among the four methods. Methods 1 and 2 found that the more matured stigma become stickier in the afternoon. The more comprehensive statistical tests in Method 3 and 4 that take into account the variance of the data however indicate that there is no significant interaction between flower age and day time, and also no significant variation in stigma stickiness during the day. Thus, from a statistical significance point of view, the answer is 'no'.

The stickiness measured here will be the total stickiness due to any exudates covering the stigma and the papillae on the stigma. The 2000 papillae on each stigma (Hopping & Jerram, 1979) will provide large contact surfaces for pollen grains via van deer Waals force.

The overall increase in stigma stickiness after the blossom is likely due to the change in stigmatic surfaces, which in turn depends on the aging of stigma and the pollination. According to Stevens & Forsyth (1982), unpollinated stigma appeared white while pollinated stigma became brown and withered after 4 – 5 days. Observations in Motueka orchard area in 2003 found that, for both Gold and Green kiwifruit, the stigma of the open-pollinated flowers (as in this work) became brownish as early as on the 2nd day after opening. The bagged flowers had brownish stigma one day later. The degeneration of stigmatic arm is a result of gradual loss of papillae turgidity during the lifetime of flower (Gonzalez *et al*, 1995a).

Despite the statistical rejection, there are signs in Method 2 that the young stigma display consistent daily stickiness but the older ones gain stickiness towards the

afternoon. This is in opposite to the general perceptions that the presence of exudates in the morning makes it a better time to apply spray pollination.

The daily changes in stickiness may be related to the exudates' film covering the stigma. Abundant of exudates are present early in the morning but they are still rather watery. Since they are sweet, presence of sugars are anticipated[5]. The exudates' film is expected to contribute to the stickiness significantly after the evaporation of water during the day has reduced it to a highly viscous and saturated thin film. Craig & Stewart (1988a) reported only dry stigma in the afternoon. So, it is likely that the secretion takes place only in the morning[6]. The secretion quantity declines when the flowers age (Gonzalez et al, 1995a) and are pollinated (Gonzalez et al, 1996). Minute amount of exudates had been observed on the white but not the brown stigma in fine weather from 1200h to 1700h in Motueka orchard area in 2003. These observations may be used to explain why the more matured stigma exhibit higher stickiness in the afternoon i.e. the reduced secretion on the older stigmatic surface means after the morning, the exudates' film becomes saturated and hence stickier in shorter time. If only water is lost through evaporation, the non-volatile sticky components from the previous days' exudates are likely to accumulate and hence enhance the stickiness of the aging stigma.

Two uncontrolled factors in the tests are variation among flowers and surrounding humidity. The variation among flowers can be seen by the difference among the replicates in each test (see Fig. 7-2 and 7-3). In addition to the fluctuations in the data, the humidity effect is also thought to cause the discrepancy among the repetition tests, as shown in Fig. 7-18 and 7-19.

The morning test of 0-day-old Green kiwifruit stigma on 27th November 2003 (520 – 636 RPM at 50 % stigma remaining) showed much higher stickiness than the morning tests on 25th November and 29th November 2003 (337 – 387 and 443 – 502 RPM at 50

---

[5] Analyses on the exudates collected from the freshly opened *Actinidia eriantha* flowers had detected the presence of fructose but no sucrose or glucose. The exudates of Green kiwifruit flowers (*Actinidia deliciosa*) had been sampled but are not yet analysed at this writing. However, fructose is anticipated in the exudates of Green kiwifruit flower.

[6] On 25th November 2003, although there was no morning dew, the presence of exudates was observed on the stigma of Green kiwifruit flowers. This means the release of exudates does not totally depend on the presence of morning dew or surrounding humidity.

% stigma remaining respectively). It was observed that before the flowers were picked for the tests on 27th November 2003, the strong sunlight came out suddenly and this caused rapid evaporation of rain water from overnight shower. There was also a sudden drop of humidity from 75.0 %RH to 47.1 %RH. It was thought that this was the cause of the unusually high stickiness observed here i.e. the rapid moisture evaporation of exudates made the exudates to become concentrated and sticky. Thus, this suggests that:

(a)   the exudates do contribute to the stickiness of stigma, but more significantly at saturated thin liquid film state than in the abundant liquid state;

(b)   the exudates become very sticky when there is a rapid dry out of exudates due to the sudden drop in surrounding humidity.

This observation also suggests that, to take advantage of the maximum stickiness, it is desirable to apply pollen when there is a sudden dry out of exudates rather than when there is abundant of liquid exudates.

This view is consistent with the negative correlation between the surrounding humidity and the stickiness obtained from the LINEST fitting in section 7.3.4. If the exudation is limited to the early morning, then any drop in humidity afterwards will dehydrate the exudates' film, resulting in stickier stigma.

Woittiez & Willemse (1979) stated that surface tension force from the exudates played an important role in the staying of pollen to the wet stigmata. They observed that the decayed stigma were dry and less sticky.

Surface tension force is only significant when a liquid exudates bridge of substantial size exists between the pollen and the stigmatic surface. This reflects the benefit of the short presence of abundant exudates in the morning. The role of surface tension is expected to be greatly discounted following the moisture loss afterwards.

Their observations may also appear in contrast to the findings from this work that aged stigma were stickier. However, it must be pointed out that the maximum stickiness is likely to exist between the two extreme exudates' coverage on the stigma – completely wet and completely dry. Woittiez & Willemse (1979) manually placed pollen on the
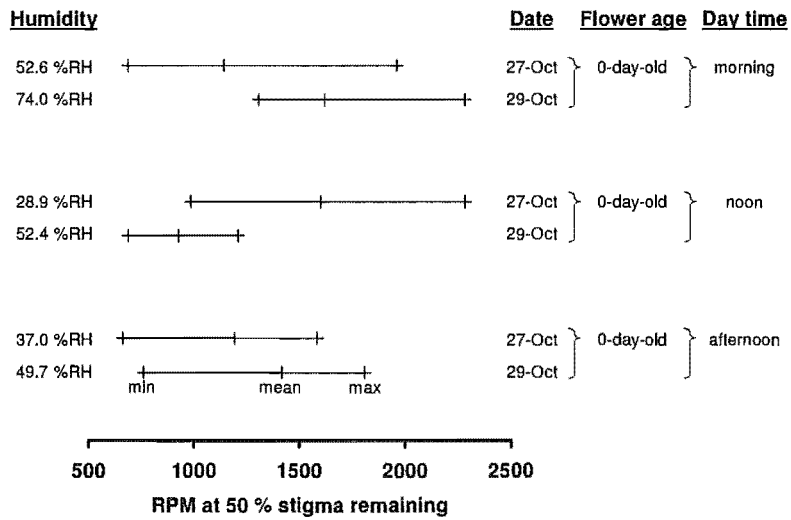
Fig. 7-18: Repetition tests for stigma of the 0-day-old Gold kiwifruit flowers.
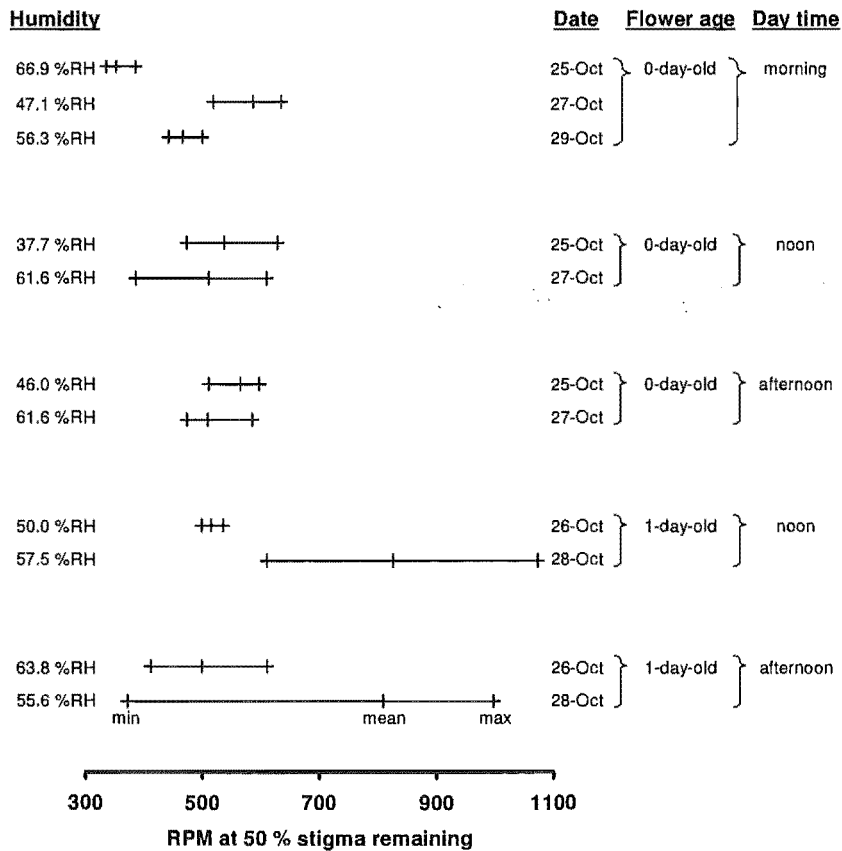
Fig. 7-19: Repetition tests for stigma of the 0-day-old and 1-day-old Green kiwifruit flowers.

fresh stigma which were completely wet and observed that the pollen stayed in place until the stigma were decayed and completely dry. This means any change in the magnitude of stickiness during this period was not studied. What this work has shown is that the dehydration during the day and the reduced secretion during the aging of stigma produce a partially wet exudates' film that gains stickiness in the process. This work did not sample any stigma of more than 4-day-old. The gradual cessation of exudation beyond this period is expected to render the stigma un-sticky to the pollen eventually.

Justification of assumptions

For both Gold and Green kiwifruit flowers, more than 50 % of their styles are within 15 % of the average length and weight (see Fig. 7-20a, c, e, f and g). Thus, the natural differences in length and weight among the styles are unlikely to influence the stickiness tests.

Fig. 7-20a, c and g randomly sampled the flowers of age from 0 to 4 days old. Fig. 7-20e and f used two groups of Green kiwifruit styles which are less than and more than 2 days old respectively. A comparison between them shows that the older styles are heavier, which means the older styles should be easier to be detached upon the application of centrifugal force. However, it was the lighter young styles that were detached at lower RPM, as shown in Fig. 7-20. This further consolidates the finding before that the older stigma are stickier.

The consistency of the applied force when dabbing the styles onto the pollen coated wall was examined by repeating the same process on the pollen coated platform of a digital force gauge (Model MG2 from Mark-10 Corporation, USA; resolution is 0.01 N). Since the styles became softer with the aging, 0-day-old to 2-day-old styles were used here. It appears in Fig. 7-21 that younger styles were dabbed more strongly. The fact that younger styles were easier to be detached at lower RPM despite the higher applied force indicates the slight inconsistency of the dabbing did not introduce variability into the stickiness tests and the more matured stigma were stickier.
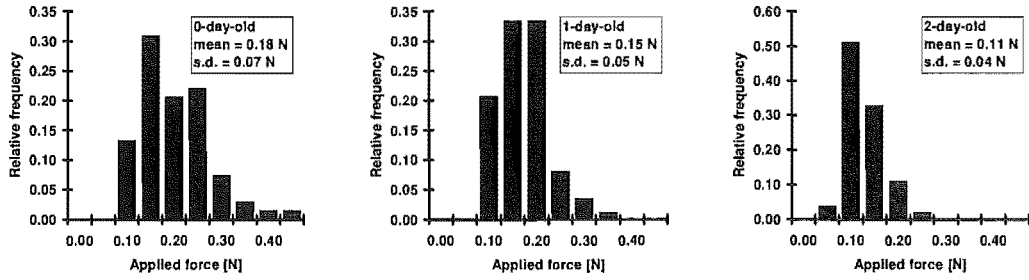
Fig. 7-21: Measured applied force in dabbing the styles of different age onto a pollen coated wall.

Sticky forces between a single pollen grain and stigma

The force needed to detach a style from the pollen coated wall (F_{s-w}) is given by

$$F_{s-w} = m_s \left(\frac{2\pi N}{60} \right)^2 R \qquad \text{Equation 7-2}$$

Where m_s is the weight of a single style; N is speed of rotation in RPM; and R is the distance from the centrifuge axis of rotation to the centre of the style. R is then the radius of the spinning disc (10 mm) plus the half length of a single style.

The ranges of RPM at 50 % stigma remaining are 286 – 2283 and 337 – 4495 for the Gold and Green kiwifruit flowers respectively (refer to Fig. 7-4 and 7-8). Based on the average length and weight of styles from Fig. 7-20 (take 5.36 mg for Green kiwifruit style), this corresponds to F_{s-w} of $(10.4 - 663.1) \times 10^{-6}$ N and $(0.1 - 17.8) \times 10^{-3}$ N for the Gold and Green kiwifruit flowers respectively.

For a pollen grain that is deposited on the stigma, the force required to detach it from the stigmatic surface (F_{p-s}) can be estimated by correcting F_{s-w} with the contact area ratio:

$$F_{p-s} = F_{s-w} \times \frac{A_{p-s}}{A_{s-w}} \qquad \text{Equation 7-3}$$

Where A_{p-s} is the contact area between a pollen grain and the stigmatic surface; and A_{s-w} is the contact area between the stigma and the pollen coated wall in the stickiness test.

The contact area between a Gold kiwifruit stigma and the pollen coated wall was rectangular of approximately 0.75 mm × 0.5 mm = 0.375 mm². For Green kiwifruit, it was roughly 1.75 mm × 1.0 mm = 1.75 mm². Assuming that a pollen grain is a 22-

7-16
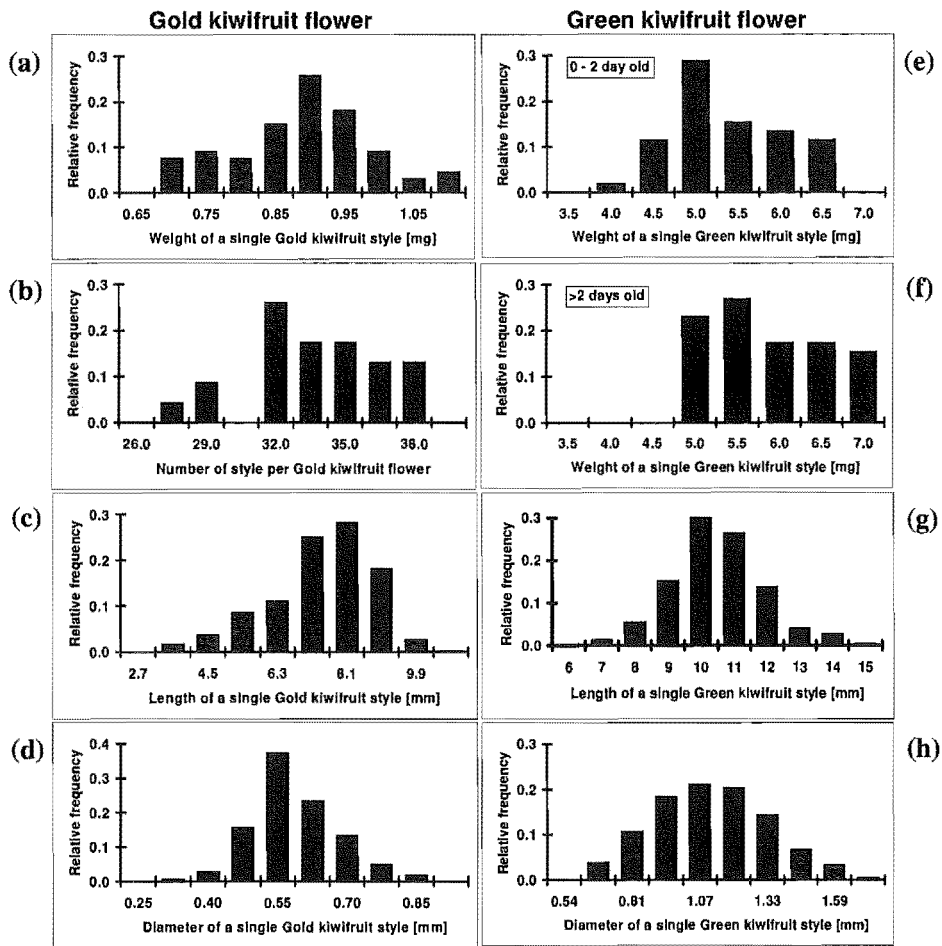
Fig.			mean	s.d.	count	min	max
Gold kiwifruit style	(a)	Weight [mg]	0.86	0.10	66	0.66	1.08
	(b)	Style number	33.3	2.9	2.3	27	28
	(c)	Length [mm]	6.98	1.37	290	2.87	10.16
	(d)	Diameter [mm]	0.55	0.09	179	0.32	0.84
Green kiwifruit style	(e)	Weight [mg] 0-2 day old	5.12	0.66	43	3.52	6.29
	(f)	>2 days old	5.60	0.71	52	4.51	6.98
	(g)	Length [mm]	9.98	1.41	670	5.07	14.27
	(h)	Diameter [mm]	1.06	0.23	667	0.55	1.83

Fig. 7-20: The weight, length and diameter of a single Gold kiwifruit style (a, c and d) and a single Green kiwifruit style (e, f, g and h). (b) the number of style per single Gold kiwifruit flower. (g) and (h) also appear in Fig. 2-6.

micron sphere with 1/5 of its surface touching the stigma, F_{p-s} are then $(8 - 538) \times 10^{-9}$ N and $(17 - 3094) \times 10^{-9}$ N for Gold and Green kiwifruit stigma respectively.

It must be noted that the stickiness tests of Gold kiwifruit stigma were limited to the maximum speed of rotation available (2283 RPM). Judging from the calculated ranges of F_{p-s}, it is likely that Gold kiwifruit stigma are as sticky as the Green kiwifruit stigma.

Recommendations

Based on the results above, it seems more advantageous to apply machine pollination when most of the Gold and Green kiwifruit flowers are between 3-day and 5-day-old.

During the discussion of preliminary results with a grower in Motueka (Bill Stevens, 2003), it was suggested that since an increase in stickiness was observed when there was a sudden drying out of exudates and the presence of morning dew seemed to encourage the release of exudates, it might be feasible to turn on irrigation early in the morning, say before 6 am, to promote the exudates secretion. The strong morning sunlight then caused the rapid moisture evaporation which would make the exudates sticky.

The author was also informed by another grower in Motueka (2003) there were abundance of exudates observed at night. The grower did not mind spraying the pollen at night when there was no potential disturbance from the honey bees to the workers. The level of exudates at night had not been examined in this work. The pollen spraying in the late evening may be feasible during the pro-longed daylight in early summer. It is recommended to carry out similar stickiness tests in the late evening, say between 9 pm and midnight, to identify any gain in stickiness in this time frame. However, it must be pointed out that any exudation at night will tend to re-wet the stigmatic surface and hence reduce the stickiness. From this point of view, pollen spraying is better to be completed before the night release of exudates.

7-17

CHAPTER 8: STUDY OF LARGE JET SPRAYING

IN THE ORCHARD

8.1. Background

Individual flower spraying (such as with the small dry air jet used in this project and the wet Pollenaid system; see section 1.6) is labour intensive and slow. A desired alternative is to apply a big pollen-laden spray that targets a large number of flowers at a time. Among the dry-based systems described in section 1.6, the Turbobee and Variflo air pollinator covers significantly more flowers than the Airflo pollinator that directs pollen only at small groups of flowers.

One of the many prototype sprayers developed in 1980s is the boom sprayer that was mounted on a tractor for rapid application of dry or wet pollen to either T-bars or Pergola trained vines. The version proposed by Ensor (1986) discharged the dry pollen from a row of five nozzles fitted along a horizontal boom. King & Ferguson (1991) tested a boom sprayer fitted with a pair of fan shaped nozzles discharging air at 500 – 850 m/s[1] in commercial orchards.

The boom sprayer by Hopping et al (1985) comprised of 6 pneumatic atomising nozzles spaced along a 2-m boom. Hopping & Hacking (1983b) used it to spray pollen suspended solution on a tractor operated at 3 km/h but found that the mechanical pumping decreased pollen viability substantially (see also Hopping, 1982a).

Boom sprayer was not fully commercialized because it needed excessive amount of pollen (Hopping & Hacking, 1983a; Hopping & Martyn, 1986a) and was thus considered uneconomic with the expensive pure pollen supply (Anon., 1991). Successful trials, i.e. achieving satisfactory fruit set and size, had been reported using bee collected pollen at 1.5 kg/ha (Anon., 1993), pure pollen at 1 kg/ha (Anon, 1985; Hopping, 1985b, Hopping et al, 1985) and pure pollen at 1.5 – 4 kg/ha (King &

---

[1] The reported speed range is likely to be in error because the maximum attainable velocity by a nozzle is the sonic velocity i.e. ~ 346 m/s. The expected range is 500 – 800 m/min i.e. 8.3 – 13.3 m/s.

Ferguson, 1991), which were comparatively higher levels of application than other machine pollinators (see Table 1-2). Nevertheless, its quickness of 1 h/ha (wet system; Hopping & Martyn, 1986a), which is comparable to that of the Turbobee (see Table 1-2), is a plausible advantage. It is considered worth further study in combination with the simple jet-like sprayer like Variflo air pollinator.

The idea in this chapter orients around the use of large air jets to deliver the pollen. For example, the air jets are released from the nozzles mounted on a tractor that moves along the row of vines. The tractor will need to be fitted with a blower of required flow and pressure drop, and a pollen feeding system. The design of the nozzles such as the orientations and sizes will depend on the types of vines training system.

The kiwifruit vines are either supported on T-bar fences or pergolas (see Fig. 8-1d). Each has advantages in term of labour-intensity in maintenance, the risk of wind damage and diseases, and the ease in pollinating (Sale & Lyford, 1990). For both T-bar and Pergola systems, the trunks are established along the row of posts with the leaders creeping horizontally along the same row (refer to Fig. 8-1c for the vine structure). The fruiting arms and canes expand horizontally across the framework of supporting wires in the Pergola system, creating a flat "roof type" canopy on top (Fig. 8-1a). On the other hand, the fruiting arms and canes of T-bar trained vines do not stretch as far but hang down gradually, creating a near parabolic-shaped canopy (Fig. 8-1b). Details of the assemblies of T-bar fences and pergolas can be found in Sale (1983a, 1983b, 1990). The dimensions of the canopies trained on these two systems are given in Fig. 8-2 and 8-3. Each range is based on 10 random sampling measurements carried out in the Motueka orchard area, 2003.

8.2. Equipment layout

Since both training systems present canopies of different structures, they require different ways of applying bulk pollen-loaded air jet. In this work, a single vertical jet under the Pergola-trained Gold kiwifruit vines and a single horizontal jet beside the T-bar-trained Green kiwifruit vines (both in Motueka orchard area, 2003) were studied for jet coverage and penetration.

(a)
Pergola

(b)
T-bar

(c)
leader
fruiting arm
or cane
lateral
trunk

(d)
T-bar
Pergola
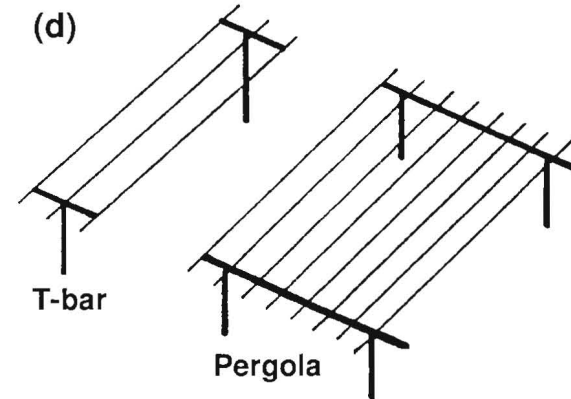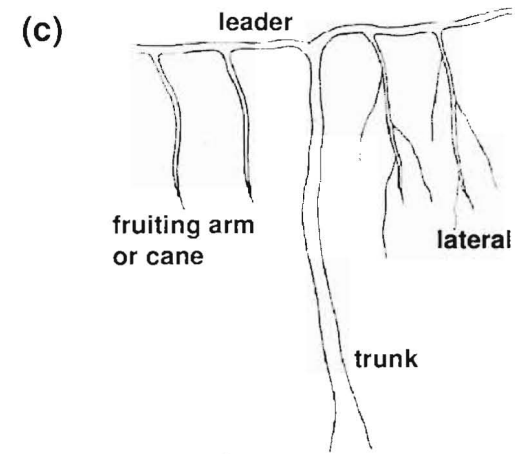
Fig. 8-1: (a) and (b) photos of kiwifruit vines trained on T-bar fences and a pergola system respectively (taken in Motueka orchard area, 2003). (c) basic vine structure of kiwifruit (Sale, 1983b). (d) illustration of T-bar and Pergola systems (Kumeu Kiwifruit Nurseries Ltd., 1981).
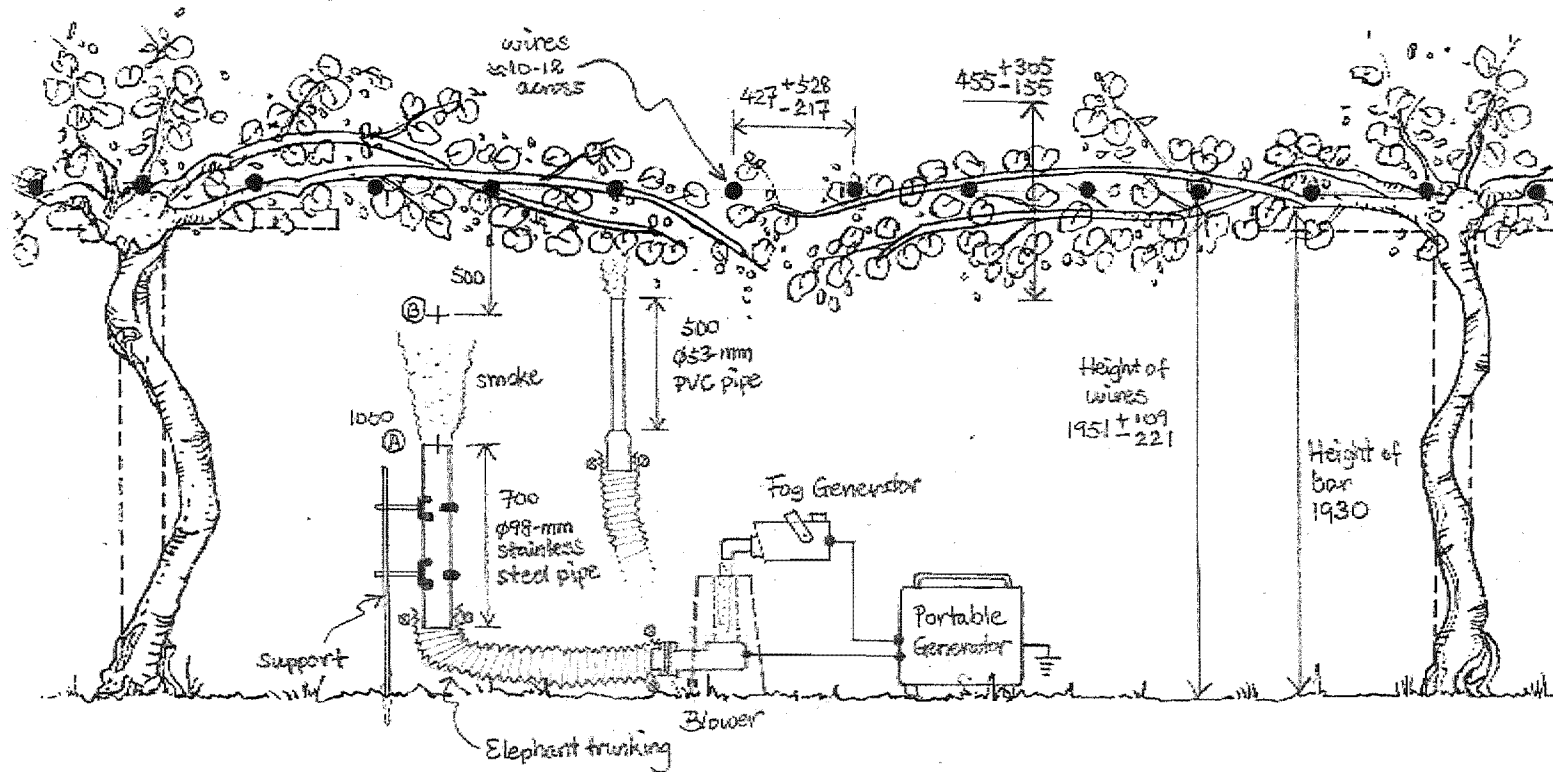
Fig. 8-2: Equipment setup under the vine trained on the Pergola system to visualize the single jets discharged from either φ 53-mm or φ 98-mm nozzle using the smoke. The velocity profiles were measured using the same setup in the absence of smoke. Marks A and B refer to the distances between the nozzle and the wires. Also shown are the dimensions of the vines and the Pergola training structure in [mm].
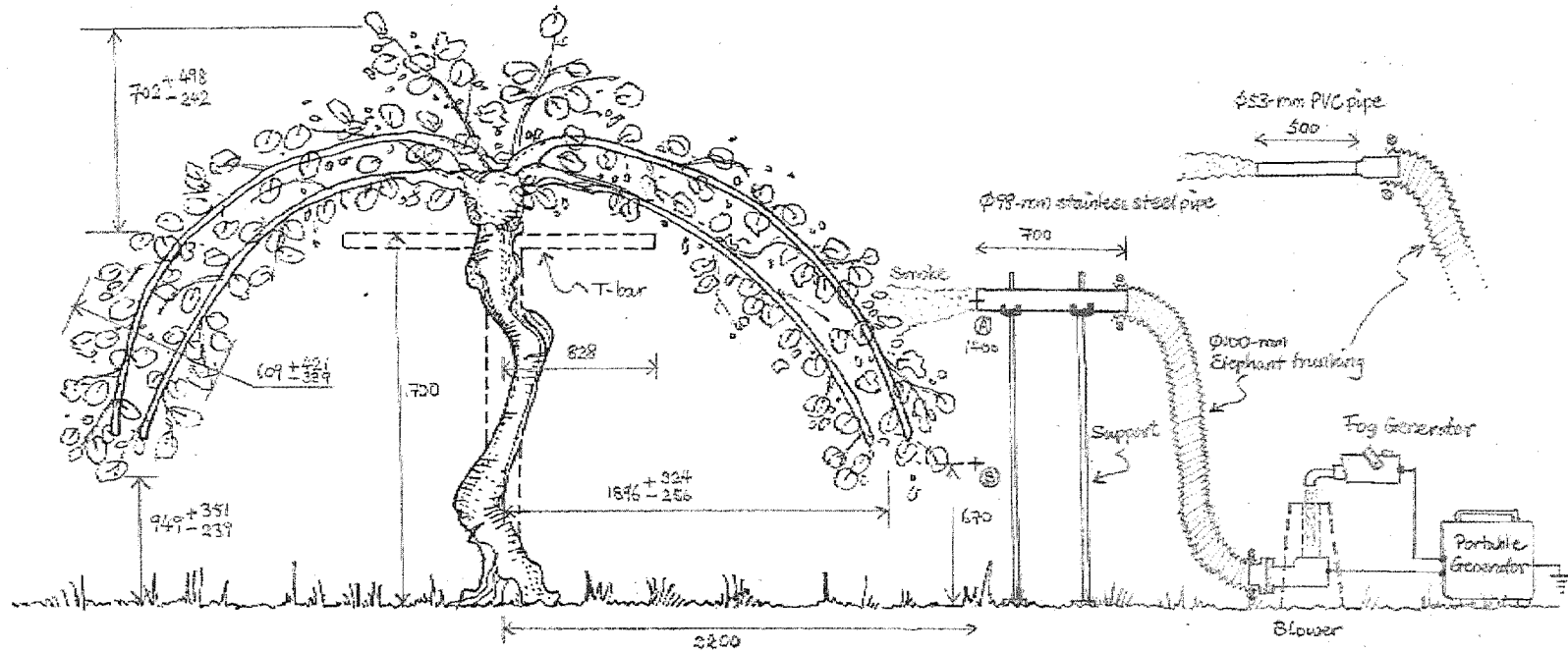
Fig. 8-3: Equipment setup beside the vine trained on the T-bar system to visualize the single jets discharged from either φ 53-mm or φ 98-mm nozzle using the smoke. The velocity profiles were measured using the same setup in the absence of smoke. Marks A and B refer to the heights of the nozzle. Also shown are the dimensions of the vines and the T-bar training structure in [mm].

Fig. 8-2 shows the equipment layout under the vines where a φ 53-mm PVC or a φ 98-mm stainless steel pipe was connected to a 360-W fan blower. The centreline and longitudinal velocity profiles of the vertical jet were measured using a pitot tube (4 mm OD) with a Solomat Zephyr digital micro-manometer (± 0.1 m/s). The profiles were obtained for the blower operating at its maximum and half of its maximum outputs (called full speed and half speed respectively in the following). The nozzles were placed at 500 mm and 1000 mm away from the supporting wires (marked by A and B in Fig. 8-2) to study the effect of distance between the nozzle and the canopy. Supporting wires were merely used as convenient reference locators. To visualize the jet, white smoke from a fog generator was introduced at the in-flow of the blower. The flow patterns were captured with a Sony Digital Handycam DCR-TRV33E at 30 fps.

The same flow measurement and visualization techniques were carried out for the jets released beside the vines grown on T-bar fences (Fig. 8-3). However, both pipes were placed horizontally with their nozzles at 2200 mm away from the centre of the fence row. The velocity profiles and flow patterns of the jets directed to the middle of the canopy were recorded for the blower at its half and full speeds. The position of these jets is marked as 'A' in Fig. 8-3, which is 1400 mm from the ground. In addition, smoked jets that were discharged from the φ 53-mm nozzle at two blower speeds and directed towards the bottom edge of the canopy (670 mm elevation from the ground; mark 'B' in Fig. 8-3) were also captured.

It must be noted that the density or porosity of the canopy varies across the block. The chosen canopy parts were considered to be visually representative of them. Occasional gusts of wind were experienced during the work.

8.3. Results

Single vertical jet introduced under Pergola system

Fig. 8-4 shows the centreline velocities of a single jet discharged from nozzle of two sizes at two nozzle-to-wire distances and two blower speeds. The approximate location where the single jet met the canopy is also shown. The respective longitudinal

velocities measured at near the supporting wires and half way between the nozzle and the supporting wires are in Fig. 8-5 and 8-6.

Fig. 8-7 is a collection of images from the captured video clips of the smoked single jets. The diameters of the nozzles were used as the reference scales here. These images were analysed for the side angle of jet (Fig. 8-8a) and longitudinal coverage of canopy (Fig. 8-8b).

The jet side angles range from 4 to 15 ^{O}C and appear to be independent of initial jet velocities and nozzle diameters. Fig. 8-8b indicates that the coverage of canopy increases with larger nozzle-to-wire distances, but not the initial jet velocities nor the nozzle diameters.

Single horizontal jet introduced beside T-bar fences

Fig. 8-9 shows the centreline velocities of a single jet directed towards the middle of the sides of the vines trained on T-bar fences, for a combination of two nozzle sizes and two blower speeds. The jets entered and exited the canopies at approximately 1100 mm and 1450 mm away from the nozzles respectively. The vertical longitudinal velocity profiles were also recorded before and after penetrating the canopies, as shown in Fig. 8-10 and 8-11.

The snapshots of videos captured for jets towards the middle and the bottom edge of the sides of T-bar trained canopies are assembled in Fig. 8-12. It must be noted that Fig. 8-12c to d and Fig. 8-12g to h are the pairs of snapshots using the same experiment settings. They were included to demonstrate the two possible jet behaviours after penetrating the canopies.

The flow patterns in Fig. 8-12a to h are schematically illustrated in the respective Fig. 8-13a to h.
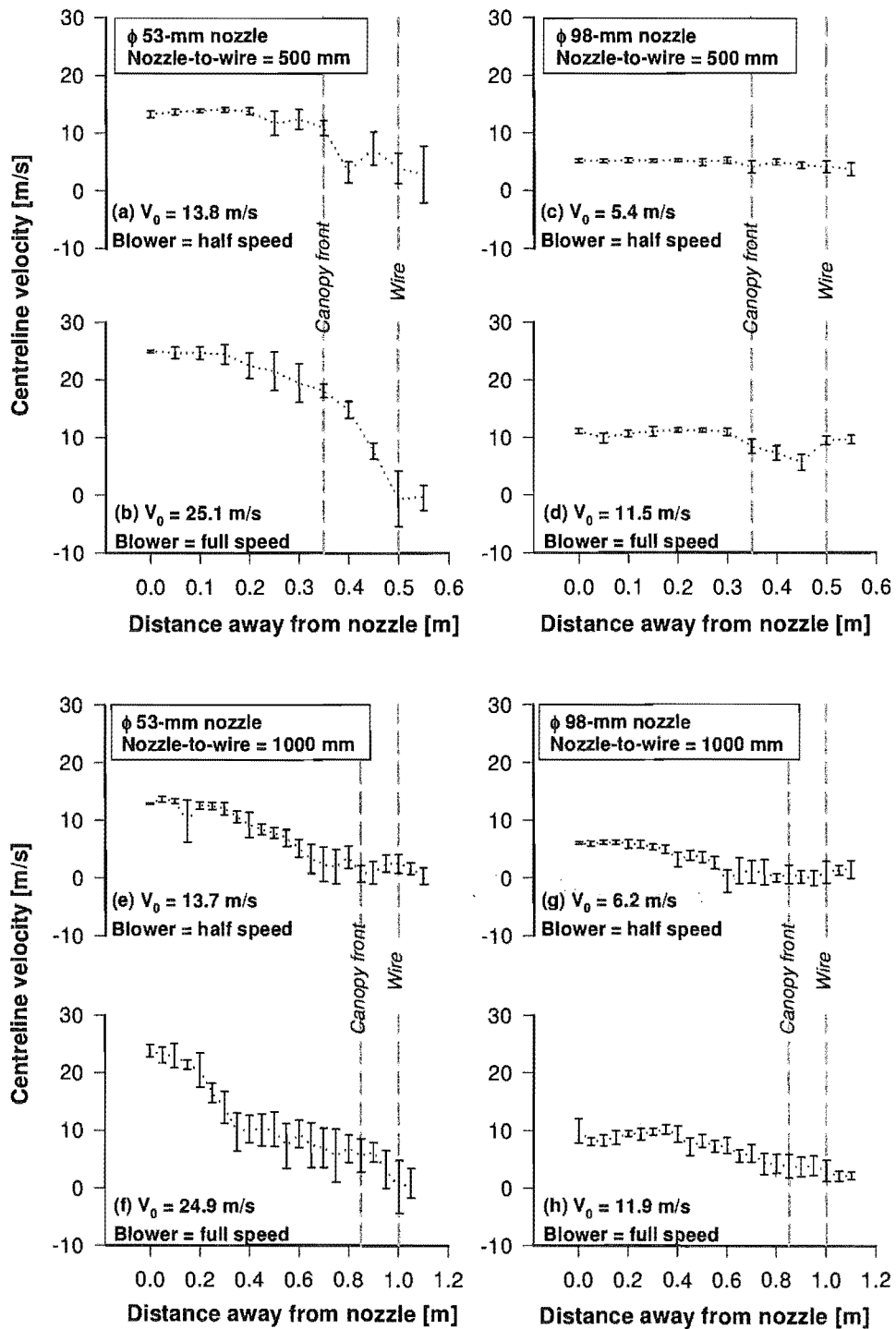
Fig. 8-4: Centreline velocities of the single jets applied vertically at different blower speeds under Pergola system trained vines. The error bars refer to the max and min velocities recorded. Shown also are the approximate locations of canopy front and wire, and the initial jet velocities (V_0).
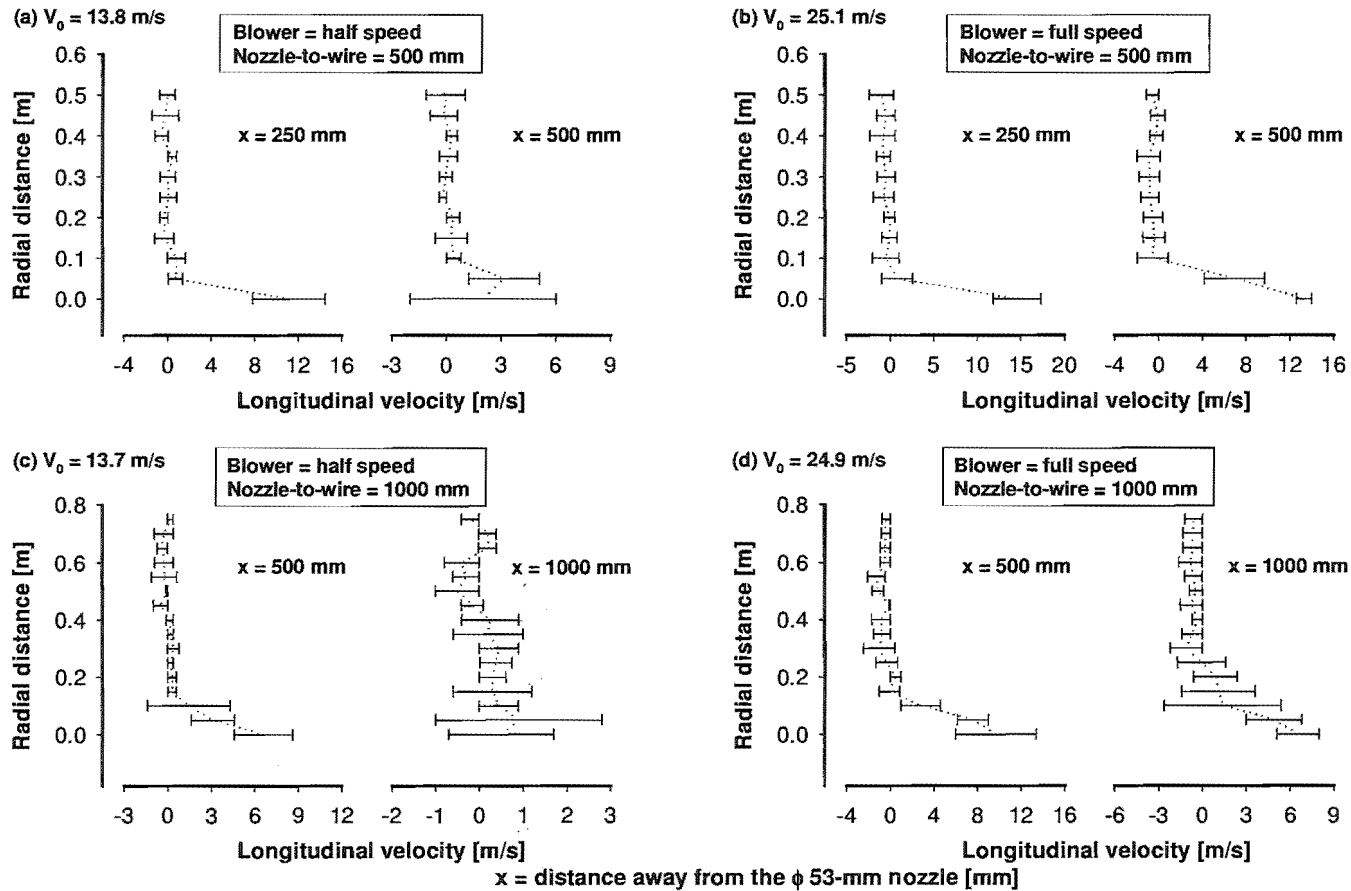
Fig. 8-5: Longitudinal velocity profiles of the single jets measured at different distances away from the φ 53-mm nozzle with different blower speeds. The jets were introduced vertically under the vines trained on Pergola system. The error bars refer to the max and min velocities recorded. Shown also are the initial jet velocities (V₀).
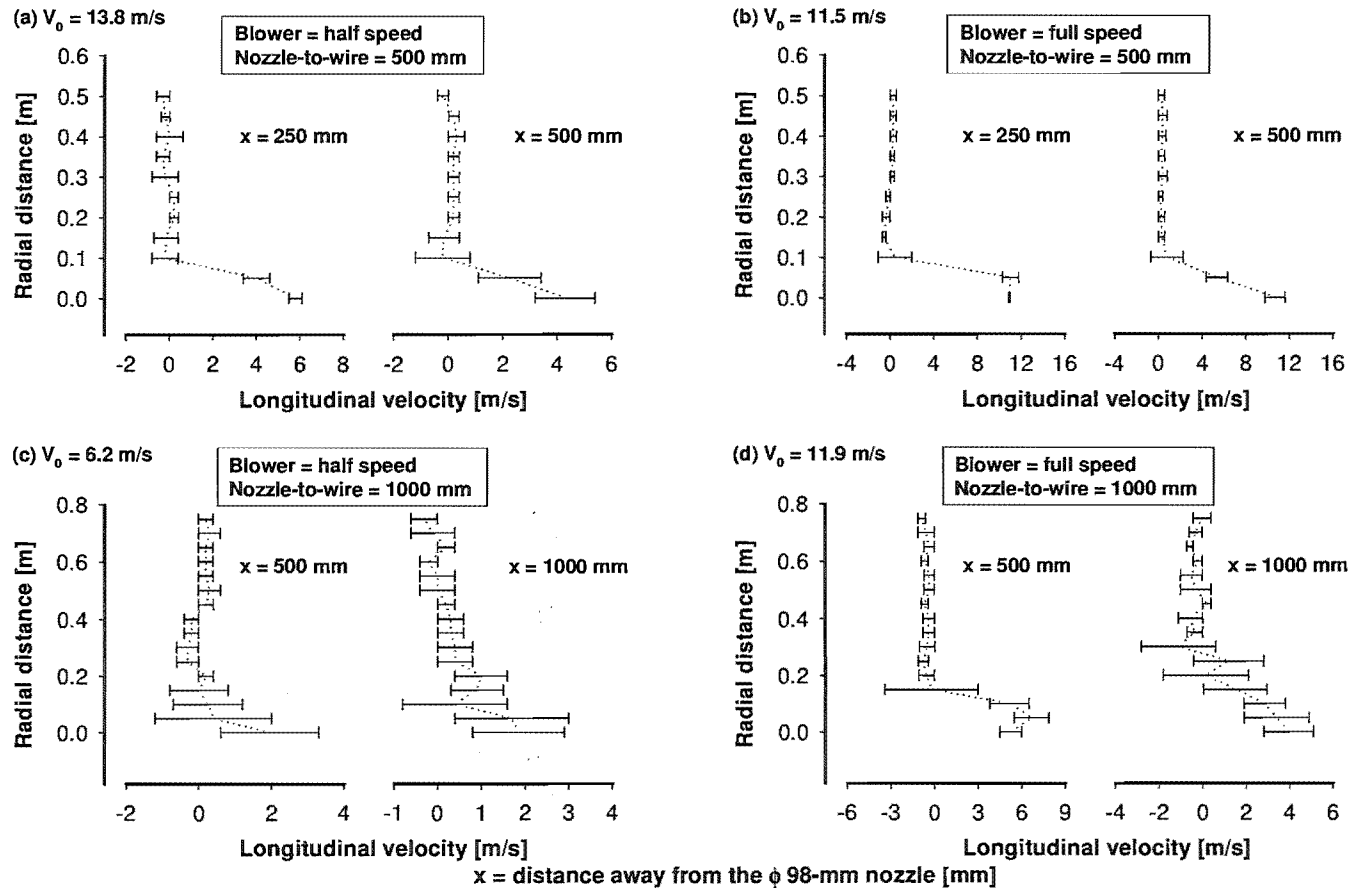
Fig. 8-6: Longitudinal velocity profiles of the single jets measured at different distances away from the φ 98-mm nozzle with different blower speeds. The jets were introduced vertically under the vines trained on Pergola system. The error bars refer to the max and min velocities recorded. Shown also are the initial jet velocities (V_0).
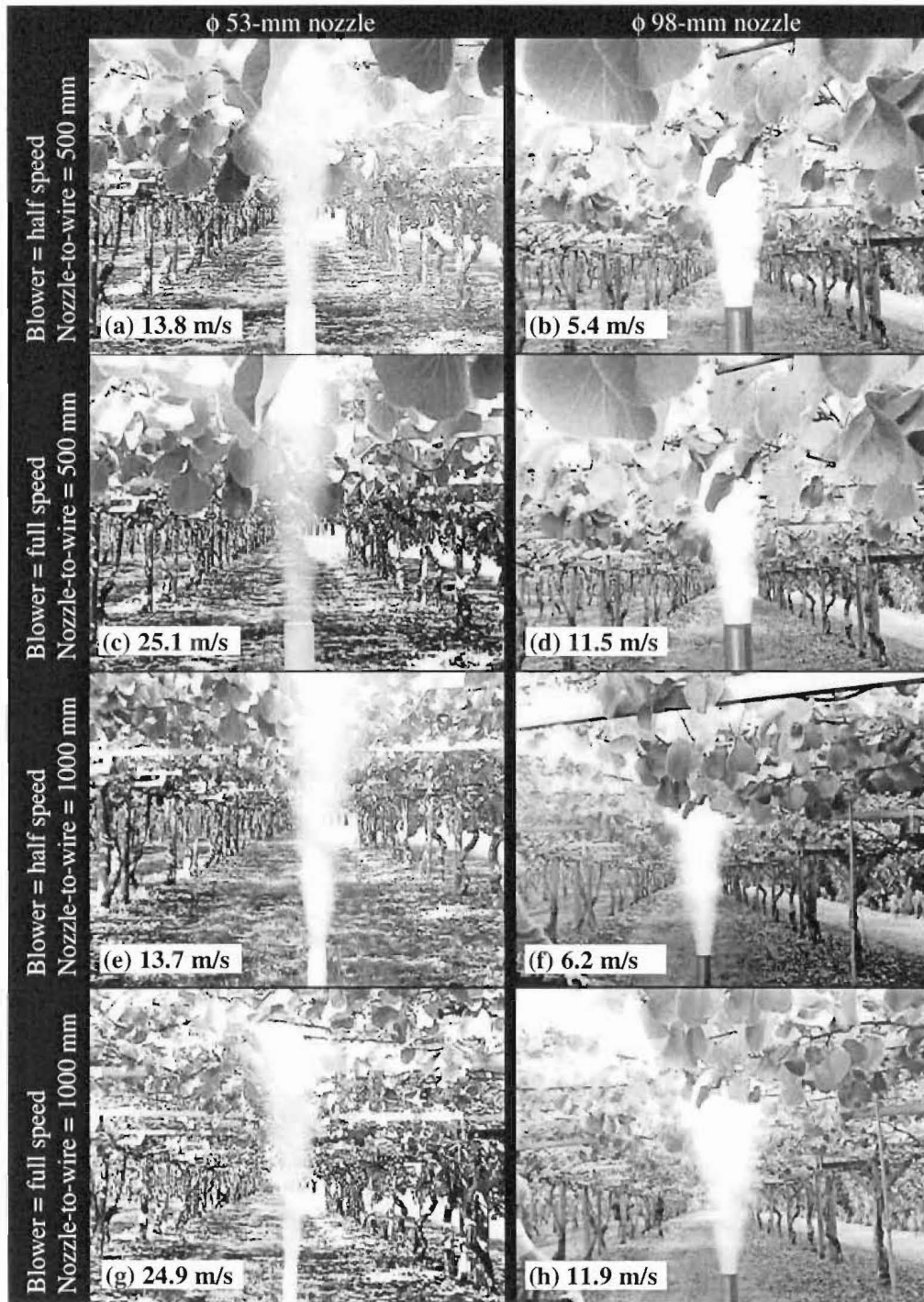
Fig. 8-7: Smoke visualization of single jets from nozzle of two sizes, at two different blower speeds and two different nozzle-to-wire distances under the vines trained on Pergola system. The initial jet velocities are shown.
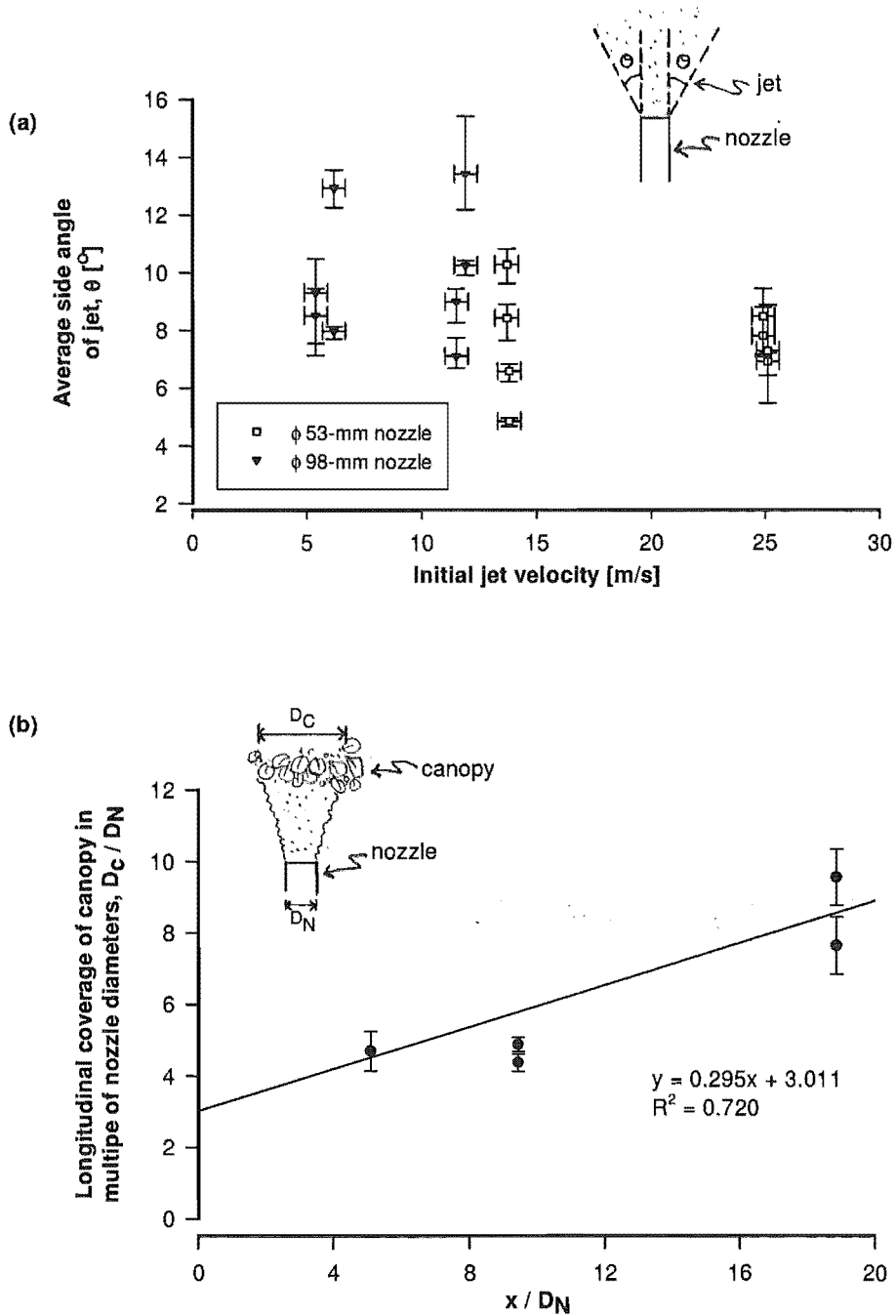
Fig. 8-8: Characteristics of the single jets introduced vertically under the vines trained on Pergola system. The jets were discharged from nozzle of two sizes at two different blower speeds and two different nozzle-to-wire distances (x). (a) Average side angle of jet; (b) Longitudinal coverage of canopy in multiple of nozzle diameters.
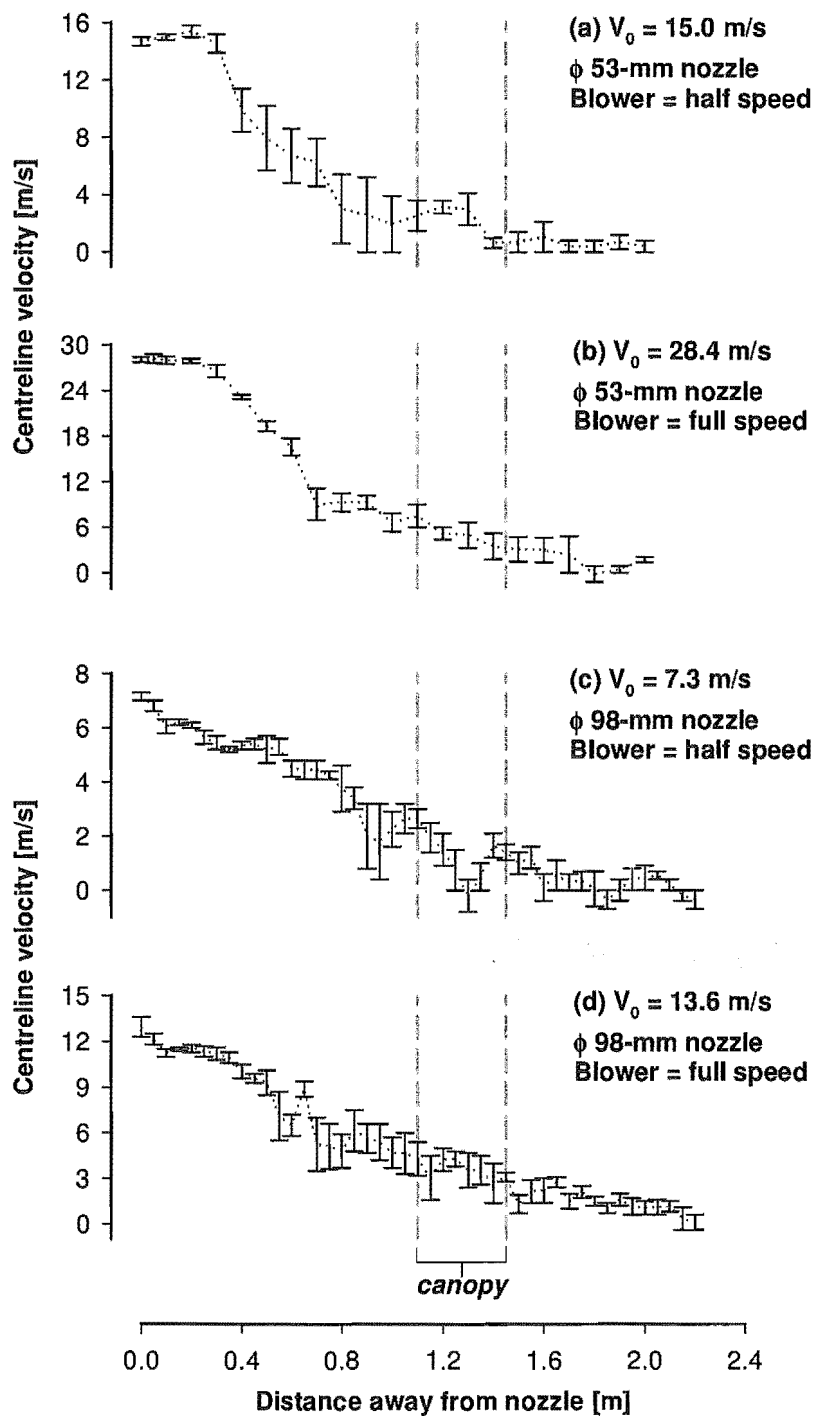
Fig. 8-9: Centreline velocities of the single jets applied horizontally at different blower speeds towards T-bar system trained vines. The jets were centred towards approximately the middle of the side canopy. The error bars refer to the max and min velocities recorded. Shown also are the approximate locations where the jets reached and left the canopy, and the initial jet velocities (V_0).
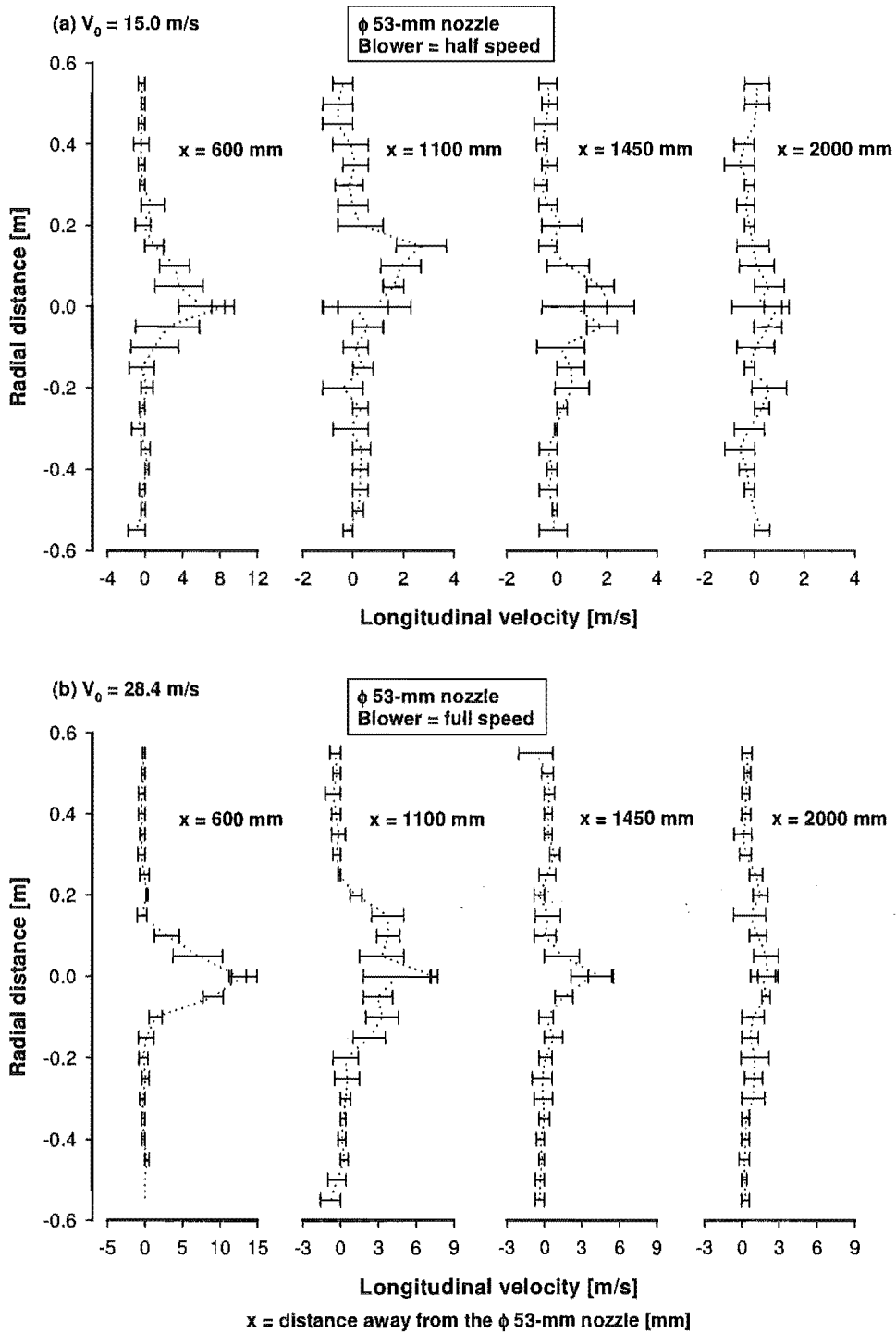
Fig. 8-10: Longitudinal velocity profiles of the single jets measured at different distances away from the φ 53-mm nozzle with different blower speeds. The jets were introduced horizontally towards the vines trained on T-bar system. The error bars refer to the max and min velocities recorded. Shown also are the initial jet velocities (V₀).
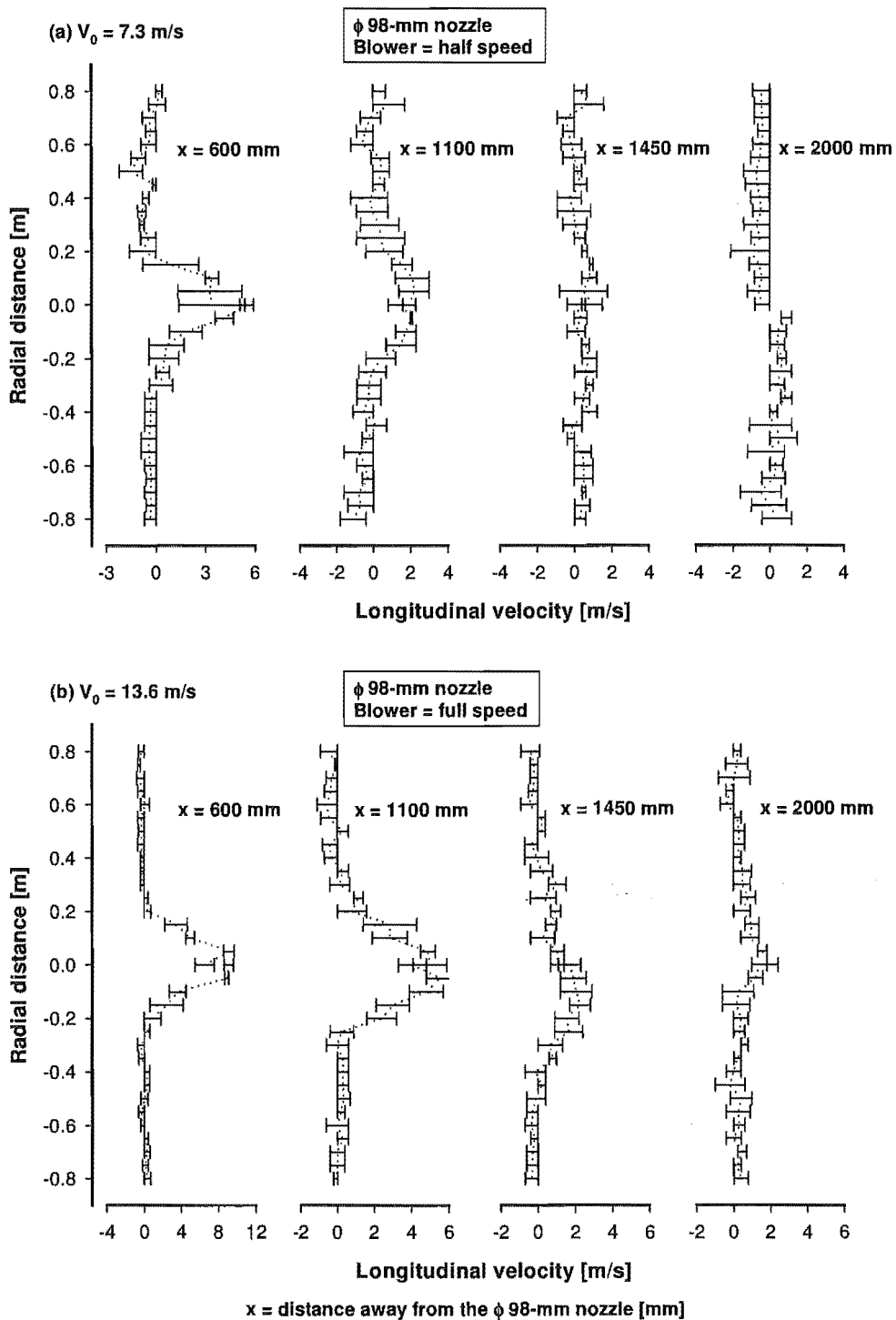
Fig. 8-11: Longitudinal velocity profiles of the single jets measured at different distances away from the φ 98-mm nozzle with different blower speeds. The jets were introduced horizontally towards the vines trained on T-bar system. The error bars refer to the max and min velocities recorded. Shown also are the initial jet velocities (V_0).
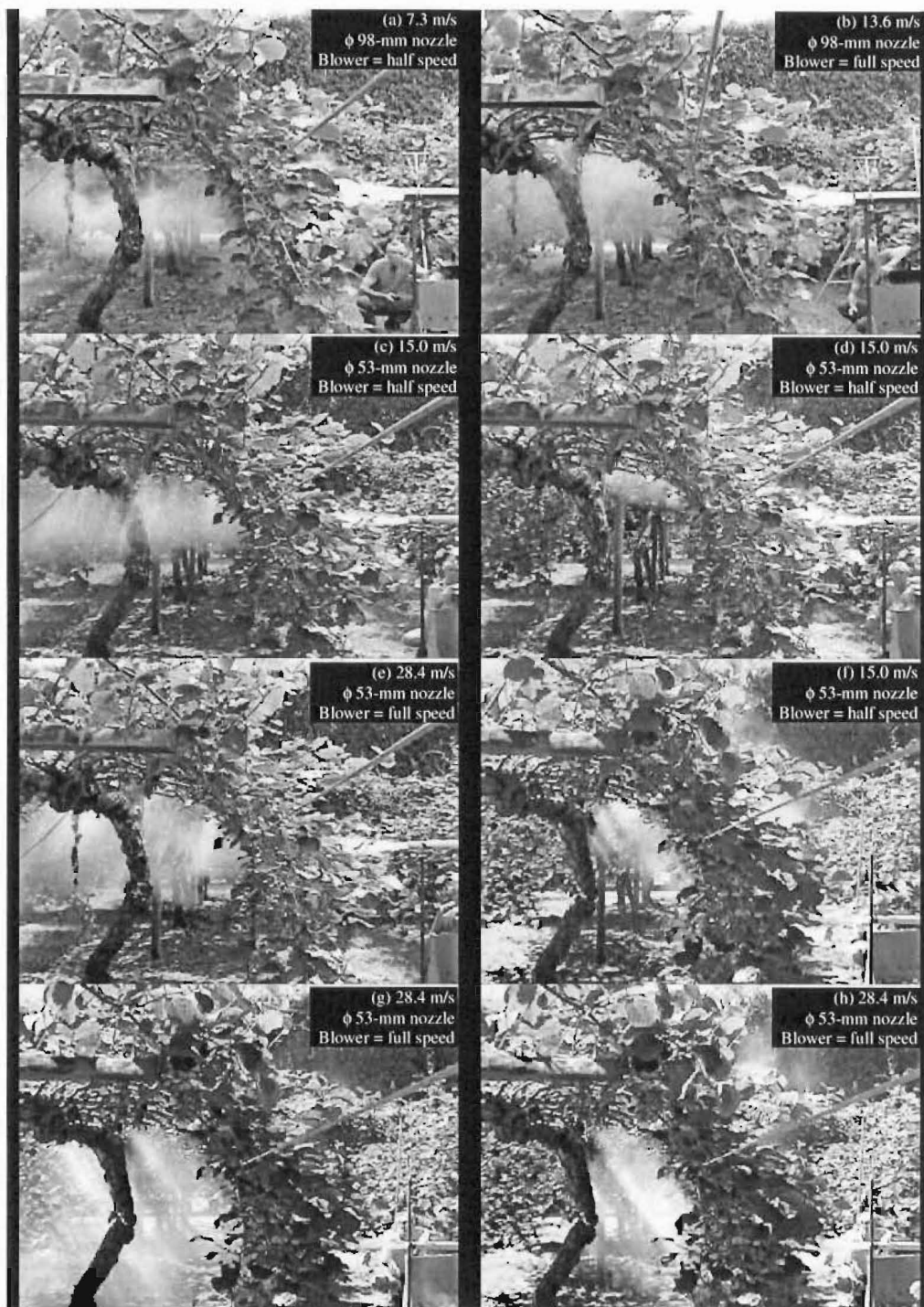
Fig. 8-12: Smoke visualization of single jets from nozzle of two sizes, at two different blower speeds and two different nozzle-to-wire distances towards the vines trained on T-bar system. The initial jet velocities are shown. Jets were introduced towards the middle of canopy in (a) to (e) and the bottom edge of canopy in (f) to (h).
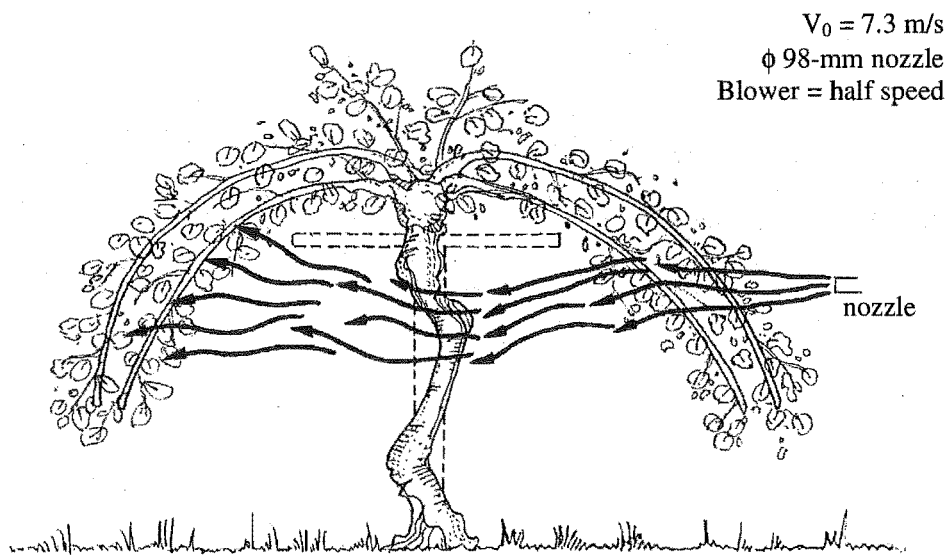
Fig. 8-13a: Behaviour of a single jet released from a φ 98-mm round nozzle towards the middle of the canopy trained on T-bar system. The blower was set at half of its maximum speed. V_0 = initial jet velocity. Refer to Fig. 8-12a.
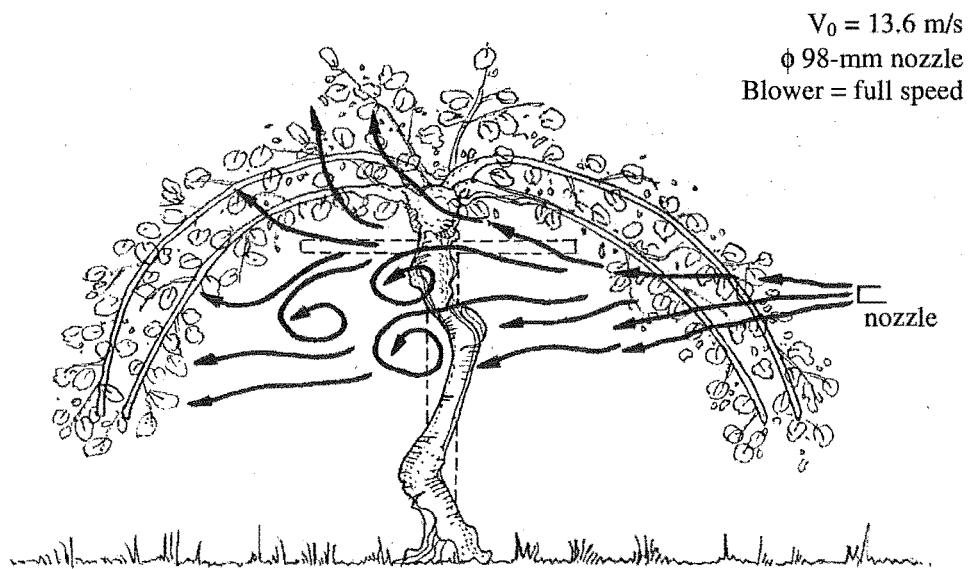
Fig. 8-13b: Behaviour of a single jet released from a φ 98-mm round nozzle towards the middle of the canopy trained on T-bar system. The blower was set at its maximum speed. V_0 = initial jet velocity. Refer to Fig. 8-12b.
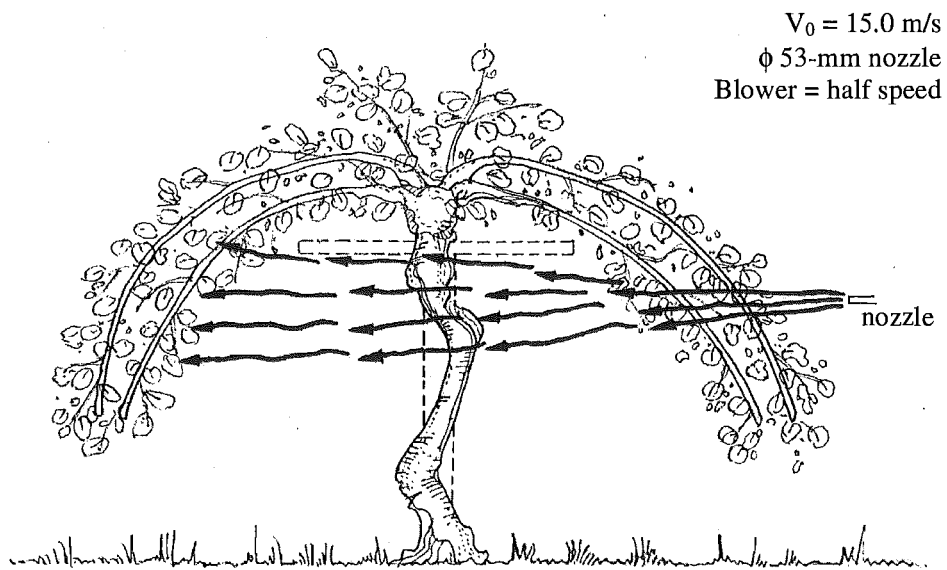
Fig. 8-13c: Behaviour of a single jet released from a φ 53-mm round nozzle towards the middle of the canopy trained on T-bar system. The blower was set at half of its maximum speed. V_0 = initial jet velocity. Refer to Fig. 8-12c.
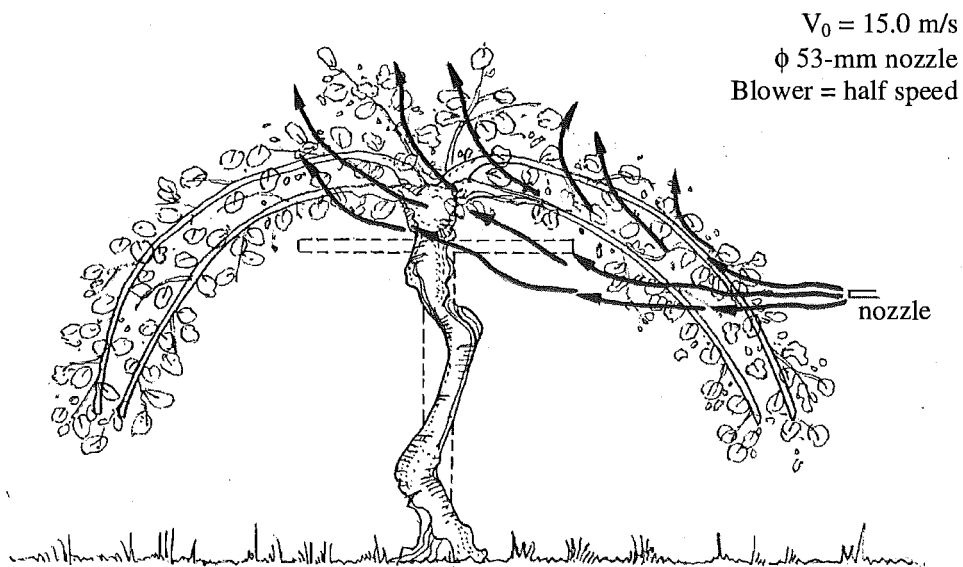
Fig. 8-13d: Behaviour of a single jet released from a φ 53-mm round nozzle towards the middle of the canopy trained on T-bar system. The blower was set at half of its maximum speed. V_0 = initial jet velocity. Refer to Fig. 8-12d.

$V_0 = 28.4$ m/s
ϕ 53-mm nozzle
Blower = full speed
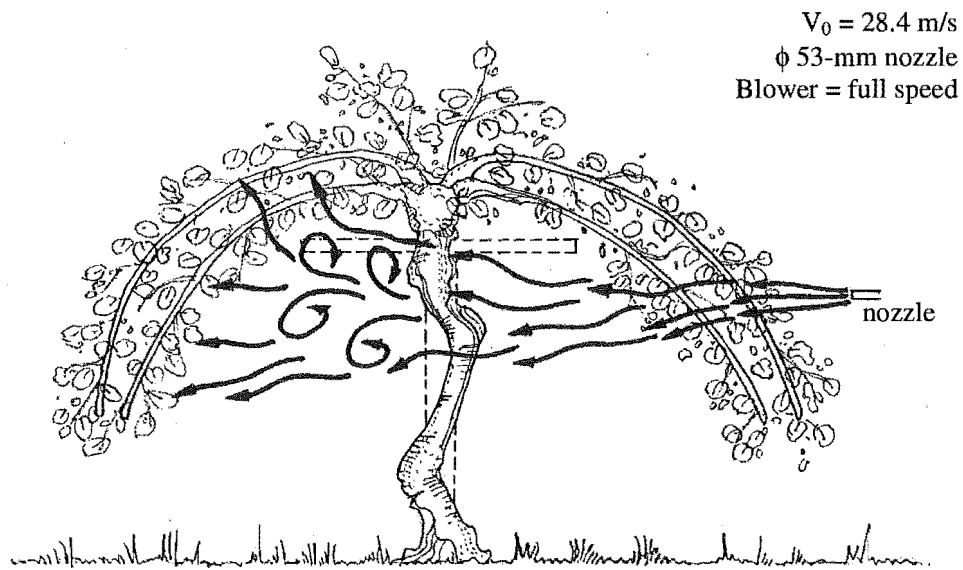
nozzle

Fig. 8-13e: Behaviour of a single jet released from a ϕ 53-mm round nozzle towards the middle of the canopy trained on T-bar system. The blower was set at its maximum speed. V_0 = initial jet velocity. Refer to Fig. 8-12e.

$V_0 = 15.0$ m/s
ϕ 53-mm nozzle
Blower = half speed
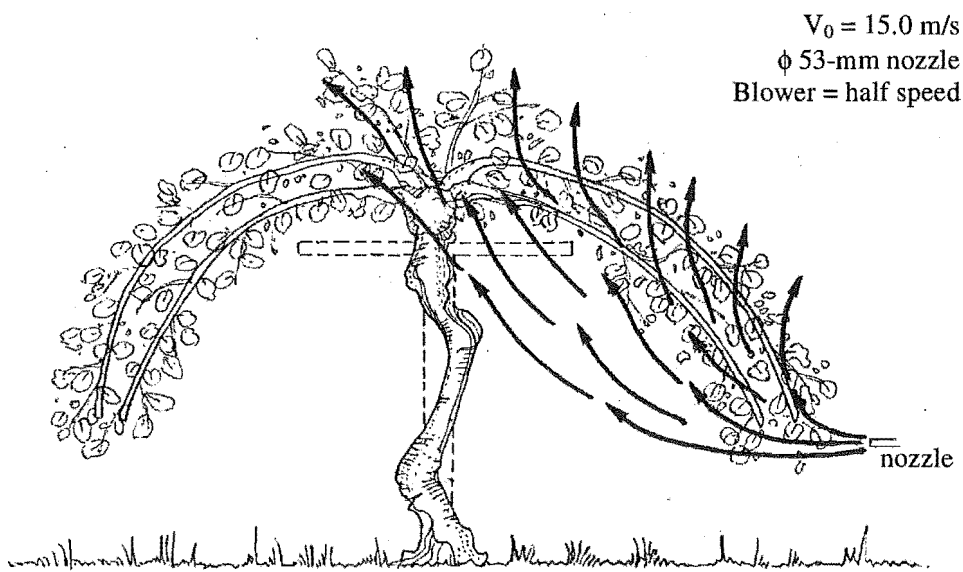
nozzle

Fig. 8-13f: Behaviour of a single jet released from a ϕ 53-mm round nozzle towards the bottom edge of the canopy trained on T-bar system. The blower was set at half of its maximum speed. V_0 = initial jet velocity. Refer to Fig. 8-12f.
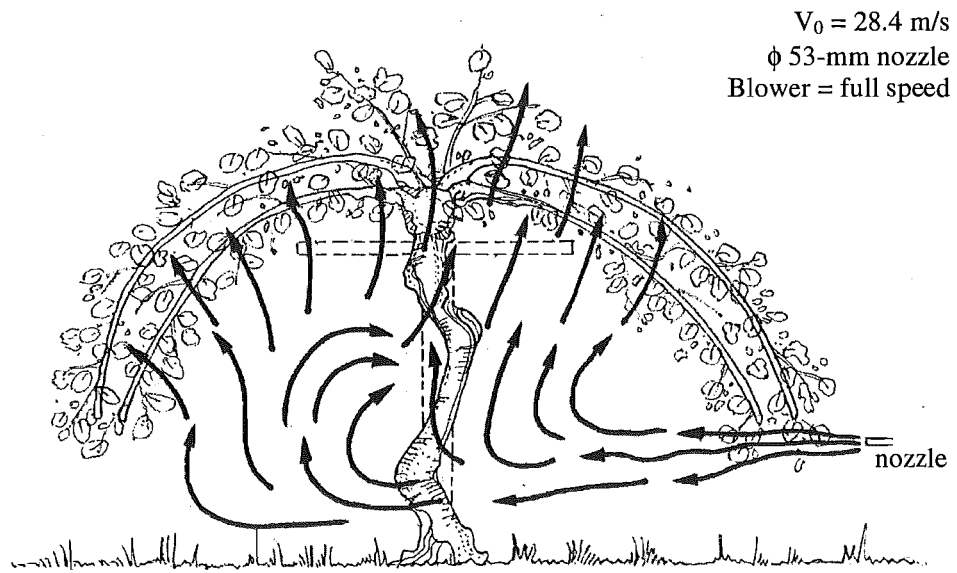
Fig. 8-13g: Behaviour of a single jet released from a ϕ 53-mm round nozzle towards the bottom edge of the canopy trained on T-bar system. The blower was set at its maximum speed. V_0 = initial jet velocity. Refer to Fig. 8-12g.
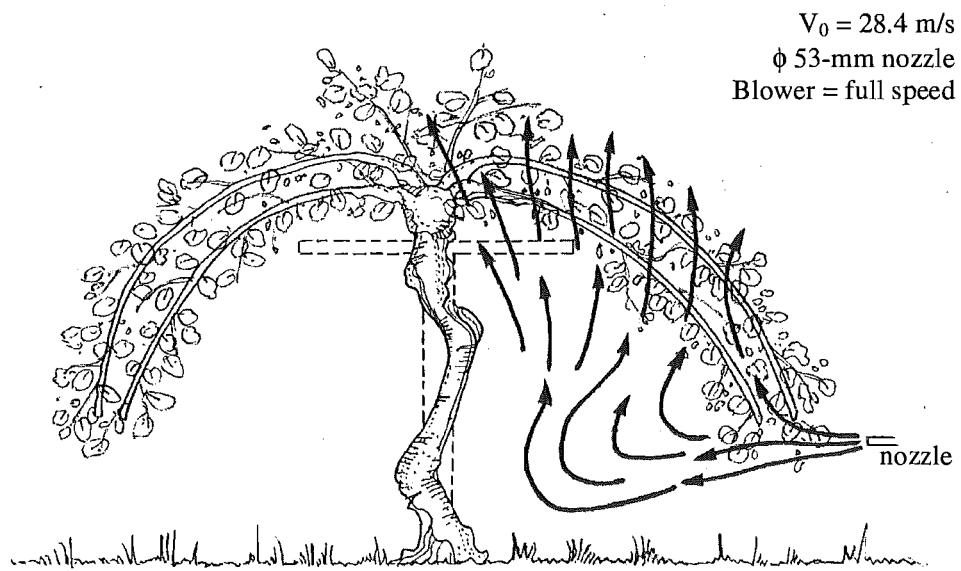
Fig. 8-13h: Behaviour of a single jet released from a ϕ 53-mm round nozzle towards the bottom edge of the canopy trained on T-bar system. The blower was set at its maximum speed. V_0 = initial jet velocity. Refer to Fig. 8-12h.

8.4. Discussion

Single vertical jet introduced under Pergola system

At the nozzle-to-wire distance of 500 mm, the centreline velocities of jets were almost constant from the ϕ 98-mm nozzle to the supporting wires (Fig. 8-4c and d). The variations were also minimal even at longer nozzle-to-wire distance of 1000 mm (see Fig. 8-4g and h) compared to the decay of jets from the ϕ 53-mm nozzle (Fig. 8-4a, b, c and d).

Assuming that the supporting wires are located at the middle of the canopies, the velocities near the wires can be considered as an average measure of the approaching velocities experienced by all the flower within the canopies. Higher collection efficiencies of airborne pollen by the flowers are expected with the higher approaching velocities of pollen-laden air jet.

Comparisons among Fig 8-4a, b, c and d show that, at the nozzle-to-wire distance of 500 mm, the jets from the ϕ 53-mm nozzle reached the canopy front at higher velocity than those from the ϕ 98-mm nozzle. It must be noted here that the comparisons are done at the same volumetric flow. However, the velocities of these jets were greatly reduced within the canopy until their magnitudes near the supporting wires became comparable to the jets from the ϕ 98-mm nozzle (shown also by the longitudinal velocities at x = 500 mm in Fig. 8-5a, b and Fig. 8-6a, b).

For the case of nozzle-to-wire distance of 1000 mm, Fig 8-4e, f, g and h show that the jets from both nozzle sizes approached the canopy front and the supporting wires at similar velocities (see also the longitudinal velocities at x = 1000 mm in Fig. 8-5c, d and Fig. 8-6c, d).

Hence, it appears that despite the higher initial jet velocities achieved by shifting from the ϕ 98-mm nozzle to the ϕ 53-mm nozzle, these advantages were not preserved into the canopies.

The comparisons of Fig. 8-5a to Fig. 8-5c, Fig. 8-5b to Fig. 8-5d, Fig. 8-6a to Fig. 8-6c and Fig. 8-6b to Fig. 8-6d found that the jet velocities near the supporting wires were nearly halved when the nozzle-to-wire distance was doubled from 500 mm to 1000 mm.

Most of the flowers are facing downwards meaning the flowers are exposed to the air jet from the front. The CFD simulations in section 3.6 show that, for a full open flower under frontal flow, there is no significant gain in airborne pollen collection efficiency by the stigma when spraying at initial jet velocity of more than 3 m/s. Viewed from another perspective, it can be conservatively said that the pollen-laden air jet should be aimed to approach the supporting wires at $\geq$ 3 m/s in order to maximize the pollen deposition on the stigma. However, as pointed out in section 3.7, the flowers had been observed to undulate in the strong draft and this is thought to increase the pollen uptake by the stigma. The velocity at which the undulation occurs has not been measured. It is also unknown whether higher jet speed may introduce physical damage to the flowers.

The canopy coverage of jets shown in Fig. 8-8b needs to be further examined in conjunction with the longitudinal velocities near the supporting wires in Fig. 8-5 and 8-6. If 3 m/s is considered as a threshold for desired approaching jet velocity, then the effective radius of canopy coverage near the wire, i.e. at x = 500 mm or 1000 mm depending on the nozzle-to-wire distance, is defined as the radial distance before the longitudinal velocities drop below 3 m/s.

For both ϕ 53-mm and 98-mm nozzles, operating the blower at half speed and with nozzles being 1000 mm away from the wires did not give jets that passed the threshold (see Fig. 8-5c and 8-6c). For both nozzles, spraying at 500 mm away from the supporting wires at both blower speeds gave an effective canopy coverage diameter of 100 – 140 mm (Fig. 8-5a, b and Fig. 8-6a, b). This range is doubled to around 300 mm when the jets were released at 1000 mm away and with blower at full speed (Fig. 8-5d and 8-6d).

This brief exercise shows that although spraying at closer distance has jets approaching the canopies at higher velocities, the effective canopy coverage radius is reduced. So, there has to be a compromise between the desired approaching jet velocity and the effective canopy coverage. Here, it seems that introducing jets at 1000 mm away from

8-6

the supporting wires will give the most canopy coverage provided the right initial jet velocities.

Single horizontal jet introduced beside T-bar fences

Several flow behaviours of jet were observed for the six cases studied (refer to Table 8-1).

Table 8-1: Settings in the smoke visualization of large jet discharged beside T-bar trained vines.

Case	Nozzle diameter [mm]	Blower setting	V_o [m/s]	Target location	Figures
A	98	H/S	7.3	Middle of canopy	Fig. 8-12a, 8-13a
B	98	F/S	13.6	Middle of canopy	Fig. 8-12b
C	53	H/S	15.0	Middle of canopy	Fig. 8-12c, d; 8-13c, d
D	53	F/S	28.4	Middle of canopy	Fig. 8-12e
E	53	H/S	15.0	Bottom edge of canopy	Fig. 8-12f
F	53	F/S	28.4	Bottom edge of canopy	Fig. 8-12g, h; 8-13g, h

V_o = initial jet velocity; H/S = half speed; F/S = full speed

If the jets were too weak, occasional strong draft outside the vine was observed to prevent them from reaching the front canopy in Cases A, C and E. The front canopy is the first canopy along the curved fruiting canes that the jets met e.g. the right side of the canopy in Fig. 8-13a. Likewise, the back canopy is the opposite canopy side on the left in Fig. 8-13a. The canopy roof refers to the top part in the middle. Since the failure to reach the front canopy represents wastage of pollen, the initial jet velocity must be kept above 15.0 m/s.

After penetrating through the front canopy, the level of dispersion of the jets depended on the strength of jet. The weak jet in Case A (Fig. 8-13a) did not spread as widely as the stronger jet in Cases B, C and D (Fig. 8-13b, c, e). The wider dispersions in Cases B, C and D gave good coverage of the back canopy and the canopy roof, which

presented chances for recollection of pollen that were not captured by the flowers in the front canopy.

However, the presence of draft under the vine could deflect and prevent the jets from reaching the back canopy (Fig. 8-13d). Instead, the smoked jets were observed to creep along the front canopy to the canopy roof. This was thought to give a good coverage of the front of the canopy. This flow pattern was further studied by targeting the jets at the bottom edge of the front canopy in Cases E and F.

At an initial jet velocity of 15.0 m/s (Case E), the smoked jets blanketed the front canopy where they climbed from the bottom tip to the top of the front canopy (Fig. 8-13d). When the jets were made stronger in Case F, large vortices were created under the middle of the vine (Fig. 8-13g). The smoke was then found to progress to the front, back and roof of the canopy. The draft under the vine however could push the recirculations closer to the front canopy and thus only give coverage of the front canopy (Fig. 8-13h). Large recirculations that increased the residence time of pollen under the vine were not observed in Cases A, B, C and D. Thus, it appears that directing the pollen-loaded jets towards the bottom edge of the front canopy will yield more efficient coverage of the canopy.

The jets from the ϕ 53-mm nozzle decayed more quickly prior to the canopy than those from the ϕ 98-mm nozzle (Fig. 8-9). There is not much drop in velocity across the canopy. For all cases, the jet centreline velocity exited the canopy at 12.5 – 16.7 % of the initial jet velocity and experienced gradual decay afterwards. The jet velocities were reduced close to zero below the middle of the canopy roof (see the changes in vertical longitudinal velocity from x = 600 to 2000 mm in Fig. 8-10 and 8-11). The vertical longitudinal velocity profiles at x = 1100 mm in Fig. 8-10 and 8-11 show that

• spraying at the middle of the front canopy using either nozzle sizes used in this study was insufficient to provide enough coverage to the front of the canopy;

• at the nozzle-to-canopy distance of 1100 mm, the initial jet velocity must be above 13.6 m/s (based on Fig. 8-11b) in order to have the jets arriving the front canopy at 3 m/s or more.

8.5. Recommendations

Design of large jet spraying for Pergola system

A quick way of applying dry pollen is by having a tractor that carries a row of vertically mounted nozzles and moves in the middle between the pergola rows. The tractor has a pollen feeder and a blower that supplies the air to convey and disperse the pollen. The data of the jet from the ϕ 98-mm nozzle at 1000 mm away from the wire can be used in the design here. A wide opening slot nozzle is preferred to a round nozzle here because the tractor is moving in parallel to the pergola rows. If the nozzle thickness is chosen as 30 mm, the nozzle width is then 251 mm in order to maintain the same cross sectional area as the ϕ 98-mm nozzle. Based on the longitudinal velocity profiles estimated using the correlations given by Elrod (1954), a slot nozzle of 251 mm in width is expected to provide a canopy coverage diameter of 300 mm at 3 m/s (refer to the curve 'slot; x-direction' in Fig. 8-14; note that here, coverage diameter refers to 2 × radial distance at 3 m/s in Fig. 8-14). The distance between the pergola rows is 5000 mm, which means 17 evenly spaced slot nozzles that are 1000 mm away from the support wires are required. The initial jet velocity must be at least 12 m/s in order to have pollen grains arriving the canopy at desired velocity (see Fig. 8-6d). The required blower capacity is then $(251\,\text{mm} \times 30\,\text{mm}) \times 17\,\text{nozzles} \times 12\,\text{m/s} \approx 1.54\,\text{m}^3/\text{s} \approx 92\,\text{m}^3/\text{min}.$
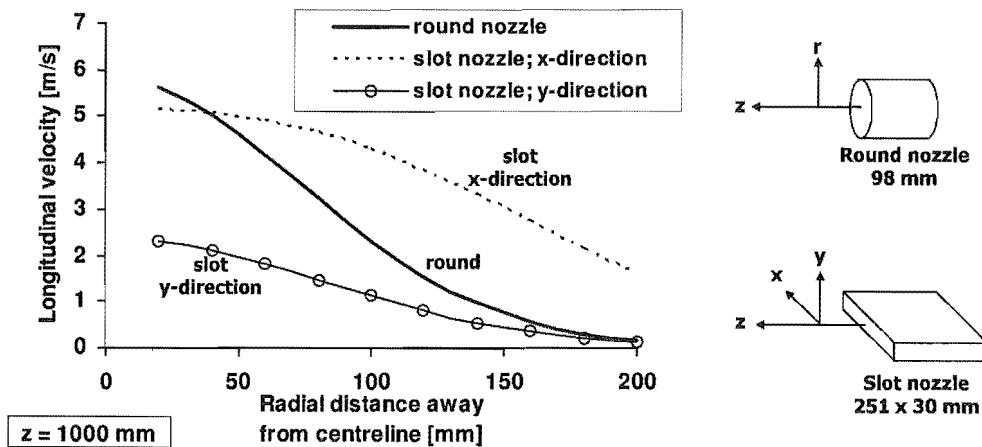
Fig. 8-14: Longitudinal velocity profiles of a ϕ 98-mm round nozzle and a 251 × 30 slot nozzle, estimated based on the correlations in Tuve (1953) and Elrod (1954). The initial jet velocity is 11.9 m/s.

8-9

If the tractor moves at 3 km/h as done by Hopping & Hacking (1983b), the time to pollinate a hectare of orchard is $\dfrac{1\,\text{ha}}{3\,\text{km/h} \times 5000\,\text{mm}} \times (\text{safety factor of } 1.5) = 1\,\text{h/ha}$.

Each flower needs to be fertilized by at least 7900 pollen grains to develop into a 100-g fruit (see section 1.3) and there are about 400,000 flowers per hectare of vines (Goodwin, 2000). Based on the simulated pollen collection efficiency of 1.5 %, an average pollen diameter of 22 micron and the pollen density of 1330 kg/m^3 (Ferguson & Pusch, 1991), the amount of pollen grains that need to be sprayed is

$$\dfrac{\dfrac{\pi}{6}(22\,\text{micron})^3}{\text{pollen}} \times 1330\,\text{kg/m}^3 \times \dfrac{7900\,\text{pollen/flower}}{1.5\,\%} \times 400000\,\text{flower/ha} \approx 1.56\,\text{kg/ha}.$$

The pollen consumption is high and similar to those reported in the literature (see section 8.1). But the cost of the pollen can be offset by the saving in the number of workers and the labour time. More significantly, the direct application of dry pollen (i.e. without liquid mixing as in Pollenaid system) and the application rate of 1 h/ha will offer great flexibility to growers when encountering a wet season.

The number of nozzles designed in this example can be reduced by increasing the nozzle width and initial jet velocity. It must be noted that an excessively high jet velocity may lead to wastage of pollen because of no further gain in collection efficiency.

Design of large jets spraying for T-bar system

The idea is similar but with the tractor moving in the middle between the rows of T-bar fences (see Fig. 8-15).

8-10
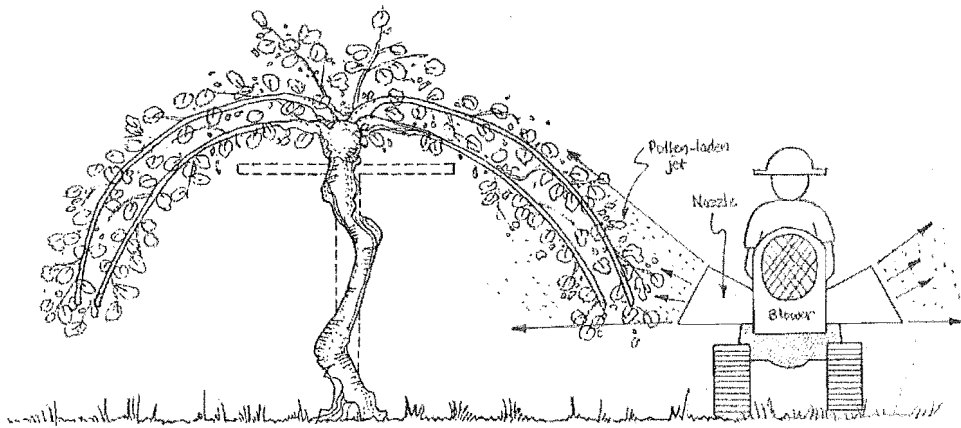
Fig. 8-15: Illustration of large jets pollen spraying for T-bar trained vines.

The jet is directed towards the bottom edge of the canopy for the reasons discussed in section 8.4. Likewise, instead of using a round nozzle, a slot nozzle with a thickness of 30 mm is more suitable here. To obtain a more effective coverage of the front canopy, a wider opening of say, 500 mm is suggested arbitrarily here. If the jets are introduced at 1100 mm away from the front canopy, the preferred initial jet velocity is 28.4 m/s. This is chosen for the jets to approach the front canopy at 3 m/s or more (see Fig. 8-10b) and getting the coverage to the back canopy and canopy roof in the way shown in Fig. 8-13g. The required blower capacity is (500 mm × 30 mm) × 28.4 m/s $\approx$ 0.43 m^3/s $\approx$ 26 m^3/min. This means for those orchards that have a mix of T-bar and Pergola-trained blocks, the same blower can be fitted with different nozzle configurations to suit each training system.

Since the average distance between the T-bar fences is 5000 mm and the flower loading on the T-bar trained vines is around 370000 flowers per hectare, the pollen application rate and quantity are likely to be similar to that for Pergola system.

Future work

Apart from the vertically mounted nozzles, jets introduced at different inclined angles can be looked at under the Pergola-trained vines because they are likely to give more coverage to the canopies at same air flow rate. The aim is then to determine the optimum angles that will yield the most effective coverage areas on canopies, say using

8-11

the approaching velocity threshold discussed above. Likewise, for the T-bar trained vines, it is recommended to look the variations from the horizontal jets studied in this work.

Future tests may include the evaluation of different wide-angle nozzles available off-the-shelf either using the flow measurement and visualization techniques as used in this work or using a full-scale pollen-loaded field trial.

CONCLUSIONS AND RECOMMENDATIONS

Artificial pollination is an important supplement to ensure adequate pollination of kiwifruit. This work looks at the dry air jet spraying of kiwifruit pollen, which is promising because of its simplicity but in the past has had a lack of quantification of its mechanism and efficiency.

CFD simulations – wind pollination

This study began with the computational fluid dynamic (CFD) modelling of air and pollen flow around a full scale flower model. The steady state CFD models predict the efficiency of pollen collection by the stigma under the typical wind speed recorded in the orchard, 1 to 3 m/s. Four different bud openings, namely half-open, full-open, flip-back and bold, are included to represent the gradual changes in flower geometry over the flowering season. The main outcomes of the models are:

- Each flower displays different flow patterns in the wind approaching from the front, side and back.

- With the exception of the cup-shaped half-open flower, the stigma of all flowers are predicted to harvest the most windborne pollen grains in a frontal wind and the least in a back flow. Large downstream recirculations are responsible for conveying all the airborne pollen to the stigma in back flow.

- In a front-approaching pollen cloud, the pollen collection efficiency improves with the faster wind speed. The predicted efficiency rises as the bud opens wider and loses its petals.

- For the side flow, except for a half-open bud due its petal shielding, more pollen grains deposit on the stigma as the draft becomes stronger.

- In the absence of petals to deflect the pollen towards the stigmatic region, a bold flower collects least pollen in a back wind. In contrast to the frontal and side flows, for back flow the pollen capture deteriorates at higher wind speed.

- Based on the highest pollen collection efficiency obtained i.e. from a bold flower under a frontal wind at 3 m/s, a deposition of 2000 pollen is estimated by using the "natural" maximum pollen flux in the orchard reported in the literature. This is inadequate to produce a minimum export size fruit, which agrees with field results from other researchers that wind pollination alone is insufficient.

- The high predicted pollen capture efficiency by stigma, the gain in pollen capture efficiency after the natural de-petalling (i.e. bold flower) and the increase in the stickiness of stigma with aging (see below) suggest that the kiwifruit flower is adapted to wind pollination.

Experimental – flow validation in wind tunnel

The flow fields predicted above compare well with the smoke visualization of flows around a real Green kiwifruit flower under a uniform incoming air flow in a wind tunnel.

CFD simulations – pollen-loaded jet

The CFD work was then extended to predict the pollen capture efficiency of a single flower under a pollen-laden air jet. Full-open and bold flower models were selected to study the effect of different jet-nozzle configurations – the jet direction, nozzle-to-flower distance, diameter of nozzle and initial jet velocity. It is found that:

- Jet swinging, which was unexpected prior to the simulations, appeared randomly in different jet-nozzle combinations. Its occurrence is repeatable within a scenario and is thought to be due to the interaction between the jet and the domain boundaries.

- For both full-open and bold flowers, a frontal jet gives the most pollen collection on the stigma compared to a side and back jet.

- Applying the pollen after the petal loss enables more efficient pollen delivery to the stigma.

- Stigma capture less pollen as the nozzle-to-flower distance increases from 100 mm to 300 mm.

- At the same total pollen mass flow rate, the use of a ϕ 30-mm nozzle places more pollen grains on the stigma than a ϕ 90-mm nozzle.

- A stronger jet, i.e. by increasing the initial jet velocity from 0.5 to 3 m/s, elevates the pollen collection efficiency. The gain in efficiency levels off above 3 m/s.

These findings suggest pollen spraying should be carried out using a ϕ 30-mm nozzle at 3 m/s and 100 mm in front of a bold flower. However, considering the practicality of using a ϕ 30-mm nozzle (such as the labour intensiveness in targeting individual flowers) and the fact that most flowers appear in patches on the vine, a ϕ 90-mm nozzle

is recommended here since its larger jet coverage is estimated to produce the equivalent results on an array of flowers packed close to one another.

CFD simulations – electrostatic spraying

The electrostatic influence is assessed in the last part of the CFD work. This work simulates the collection of corona-charged and tribo-charged pollen by the stigma of a single full-open and bold flower. Frontal jets, of different initial jet velocities and positioned at various nozzle-to-flower distances, disperse the charged pollen cloud from a ϕ 30-mm nozzle. The comparisons with the uncharged pollen indicate that:

- No enhancement in pollen collection efficiency is predicted with the tribo-charging of pollen. This is due to the weak electric field between the nozzle and the grounded flower.

- On the other hand, a strong electric field between the corona electrode and the grounded flower leads to an improved pollen deposition on the stigma. The electrode needs to be positioned $\geq$ 100 mm away from the flower in order to eliminate an unwanted repulsion effect from the electrode.

- It is more beneficial to spray charged pollen during the bold flower opening stage.

Experimental – electrostatic spraying

Individual real Green kiwifruit flowers were sprayed with tribo-charged pollen and 'control' pollen that held only background charges. The experimental results showed that there are some indications that increased pollen chargeability may raise the collection efficiency by the stigma. However, this benefit may not be significant as it is not consistently realized in all the conditions studied in the experiment. Thus, further refinement of tribo-charging CFD model and more detailed tests may be needed. The results of CFD simulations are also validated in that the pollen deposition on the stigma:

- Increases with the higher initial jet velocity;
- Decreases with the longer nozzle-to-flower distance;
- Is the highest in a frontal jet, followed by a side and back jet; and
- Has the collection efficiency in the same order of magnitude (1.3 to 2.2 % at initial jet velocities below 3 m/s) comparable to that predicted by the CFD computations.

Experimental – stickiness of stigma

The variation of Gold and Green kiwifruit stigma stickiness was measured using a centrifugal device over five days during the flowering season. This test gave the cohesiveness of pollen to the stigma receptive area. The stickiness tests show that:

- The stigma of Gold and Green kiwifruit flowers become stickier as they age. This is attributed to the physical changes to the stigma and the accumulation of sugar from the exudates on the stigma.

- The change in stigma stickiness during the day is not statistically significant. However, parts of the results hint that the older stigma appear stickier towards the afternoon. This is in contrast to the general perceptions among growers that the stigma are stickier in the early morning.

- Stigma were observed to be stickiest just after most of the exudate has evaporated, rather than when the exudate is in abundant liquid state. A suggested reason is that the loss of moisture has left a thin exudate film saturated with sugar on the stigma.

- The Gold kiwifruit stigma are as sticky as the Green kiwifruit stigma.

Experimental – study of large jet spraying in the orchard

The flow patterns and velocity profiles were recorded for a large air jet (without pollen) targeted at the T-bar and pergola trained vines. Suggestions have been made for the designs of jet (such as the positioning of the jet relative to the vine structure, the nozzle size and the initial jet velocity) to achieve an effective coverage of vines and desired jet velocity to deliver the pollen to the flowers.

Recommendations for spraying pollen

Detail recommendations can be found in each chapter. More notable ones are summarized below:

- Carry out artificial pollination when most of the flowers have lost their petals, say three days after opening. This is to take advantage of the higher pollen collection efficiency and the stickier stigma.

- Spray the pollen from a 90 mm diameter nozzle.

- Place the nozzle 100 mm in front of the flowers.

- Set the initial jet velocity to ≥ 3 m/s.

- Based on the theoretical study, apply the pollen with a corona charger at 200 mm away from the flowers.

GLOSSARY

anemophilous   Wind-pollinated.

anthesis   The period of flowering in plants; more specifically, the time of flower bud opening and expansion when pollination takes place (Hopping, 1990a).

bold   Used in this thesis to refer to the flowers that have lost their petals.

dehisce   The breakdown of the anther wall to expose the pollen (Goodwin, 2000).

evocation   The induction of flowering i.e. the changing of a meristem to begin reproductive development (Hopping, 1990a).

inflorescences   The reproductive shoot; the part of a plant that consists of the flower-bearing stalks and their flowers (Hopping, 1990a).

papillae   Small projection of tissues (Hopping, 1990a).

peduncle   The stalk of a flower cluster or inflorescence, or of a single flower (Hopping, 1990a).

pollenkitt   A sticky material, produced by the tapetum, that may hold pollen grains together during dispersal.

staminoid   A pollenless stamen.

REFERENCES

Abrahamson J. & Marshall J. (2002) Permanent electric dipoles on gas-suspended particles and the production of filamentary aggregates, *Journal of Electrostatics*, 55(1): 43-63.

Adamiak K. (1997a) Numerical Modelling of Tribo-Charge Powder Coating Systems, *Journal of Electrostatics*, 40-41:395-400.

Adamiak K. (1998) Numerical investigation of powder trajectories and deposition in tribo-charge powder coating, *Industry Applications Conference, Thirty-Third IAS Annual Meeting. The 1998 IEEE*, vol.3, pp. 1898-1905.

Adamiak K. (2001b) Numerical investigation of powder trajectories and deposition in tribocharge powder coating, *Industry Applications, IEEE Transactions on*, 37(6):1603-1609.

Adamiak K. & Mao J. (1995) Simulation of particle trajectories in tribo-powder coating, *Industry Applications Conference, Thirtieth IAS Annual Meeting, IAS '95., Conference Record of the 1995 IEEE*, pp. 1273-1279.

Adamiak K., Castle G.S.P., Inculet I.I. & Pierz E. (1992) Numerical simulation of electrical field distribution in tribo-powder coating of conducting cylindrical objects, *Industry Applications Society Annual Meeting, Conference Record of the 1992 IEEE*, vol.2, pp. 1513-1520.

Adamiak K., Castle G.S.P., Inculet I.I. & Pierz E. (1994) Numerical simulation of the electric field distribution in tribo-powder coating of conducting cylindrical objects, *Industry Applications, IEEE Transactions on*, 30(1):215-221.

Alexander M.P. (1980) A versatile stain for pollen fungi, yeast and bacteria, *Stain Technology*, 55(1): 13-18.

Ali F.S., Base T. E. & Inculet I. I. (2000). Mathematical modeling of powder paint particle trajectories in electrostatic painting, *Industry Applications, IEEE Transactions on*, 36(4):992-997.

Alspach P.A., Pyke N.B., Morgan C.G.T. & Ruth J.E. (1991) Influence of application rates of bee-collected pollen on the fruit size of kiwifruit, *New Zealand Journal of Crop and Horticultural Science*, 19: 19-24.

Ang M.L. & Lloyd P.J. (1987) Investigation of charged particle trajectories in electrostatic powder coating systems, *International Journal of Multiphase Flow*, 13(6): 823-836.

Anon. (1983) Artificial pollination of kiwifruit, *New Zealand Ministry of Agriculture and Fisheries Agricultural Research Division Annual Report 1982/83*, New Zealand Ministry of Agriculture and Fisheries, pp. 14.

Anon. (1984) Artificial pollination of kiwifruit, *New Zealand Ministry of Agriculture and Fisheries Agricultural Research Division Annual Report 1983/84*, New Zealand Ministry of Agriculture and Fisheries, pp. 8-9.

Anon. (1985) Kiwifruit pollination, *New Zealand Ministry of Agriculture and Fisheries Agricultural Research Division Annual Report 1984/85*, New Zealand Ministry of Agriculture and Fisheries, pp. 7-8.

Anon. (1987) Airflow pollination raises yields, *New Zealand Kiwifruit*, September: 26.

Anon. (1988a) Spray pollination: cheaper alternatives, *New Zealand Kiwifruit*, August: 7.

Anon. (1989a) Good artificial pollination without bees, *New Zealand Kiwifruit*, July: 7.

Anon. (1988b) Vacuuming off and rolling on, *New Zealand Kiwifruit*, August: 7, 9.

Anon. (1989b) Airflo pollinators, *New Zealand Kiwifruit*, October: 19.

Anon. (1989c) Another pollination aid, *New Zealand Kiwifruit*, October: 19.

Anon. (1991) A one-person backpack sprayer, *New Zealand Kiwifruit*, September: 21.

Anon. (1992) A new rollon pollinator, *New Zealand Kiwifruit*, September: 13.

Anon. (1993) Artificial pollination does well, *New Zealand Kiwifruit*, April/May: 28-29.

Atkinson D. (1989) Note from the manufacturer, *New Zealand Kiwifruit*, July: 7.

Aylor D.E. & Ferrandino F.J. (1985) Rebound of pollen and spores during deposition on cylinders by inertial impaction, *Atmospheric Environment*, 19(5): 803-806.

Bailey A.G. (1998) The science and technology of electrostatic powder spraying, transport and coating, *Journal of Electrostatics*, 45(2):85-120.

Bakker A., Haidari A.H. & Oshinowo L.M. (2001) Realize greater benefits from CFD, *Chemical Engineering Progress*, 97(3): 45-53.

Banerjee S. & Law S.E. (1995) Characterization of chargeability of biological particulates by triboelectrification, *Conference Record of the 1995 IEEE Industry Applications 30th IAS Annual Meeting*, Part 2 (of 3) M1 1995 Oct 8-12, pp. 1295-1301.

Banerjee S. & Law S.E. (1996) Electrostatic induction charging of pollen suspensions, *Conference Record of the 1996 IEEE Industry Applications 31th IAS Annual Meeting*, Part 3 (of 4) M1 1996 Oct 6-10, pp. 1775-1781.

Banerjee S. & Law S.E. (1998) Characterization of chargeability of biological particulates by triboelectrification, *IEEE Transactions on Industry Applications*, 34(6): 1201-1205.

Baughn J. & Shimizu S. (1989) Heat transfer measurements from a surface with uniform heat flux and an impinging jet, *Journal of Heat Transfer*, 111: 1096-1098.

Bay of Plenty Pollen Limited (n.d.) *Supplementary Pollination Technical Guide*, promotional brochure.

Bechar A., Gan-Mor S., VakninY. Shmulevich I., Ronen B. & Eisikowitch D. (1997) An image analysis technique for accurate counting of pollen on stigmas, *The New Phytologist*, 137(4): 639-643.

Bechar A., Shmulevich I., Eisikowitch D., Vaknin Y., Ronen B. & Gan-Mor S. (1999) Modeling and experiment analysis of electrostatic data pollination, *Transactions of the ASAE*, 42:1511-1516.

Bellini E., Rotundo A. & Pilone N. (1991) Observations on self-fertile clones of kiwifruit, *New Zealand Journal of Crop and Horticultural Science*, 19:337-339.

Blanchet P. (1990) Kiwifruit (Actinidia deliciosa Chev.) pollination: honeybee behavior and its influence on the fruit, *Acta Horticulturae 282*, pp. 105-110.

Boehme I.G., Krupp H., Rabenhorst H. & Sanstede G. (1962) Adhesion measurements involving small particles, *Transactions of The Institutions of Chemical Engineers*, 40: 252-259.

Bomben C., Malossini C., Cipriani G. & Testolin R. (1999) Long term storage of kiwifruit pollen, *Proceedings of 4th International Kiwifruit Symposium, Acta Horticulture 498*, ISHS, pp. 105-108.

Bottner C.-U. & Sommerfeld M. (2002) Numerical calculation of electrostatic powder painting using the Euler/Lagrange approach, *Powder Technology*, 125(2-3): 206-216.

Brach R.M. & Dunn P.F. (1992) Mathematical model of the impact and adhesion of microspheres, *Aerosol Science and Technology*, 16(1): 51-64.

Brach R.M. & Dunn P.F. (1995) Macrodynamics of microparticles, *Aerosol Science and Technology*, 23(1): 51-71.

Brach R.M. & Dunn P.F. (1998) Models of rebound and capture for oblique microparticle impacts, *Aerosol Science and Technology*, 29(5): 379-388.

Bradshaw P.F., Ferriss D.H. & Atwell N.P. (1967) Calculation of boundary layer development using the turbulent energy equation, *Journal of Fluid Mechanics*, 28:593-616.

Brandon D.J. & Aggarwal S.K. (2001) A numerical investigation of particle deposition on a square cylinder placed in a channel flow, *Aerosol Science and Technology*, 34: 340-352.

Brewer R. (1988) Kiwifruit spray pollination, *Agrisearch*, May: 2-3.

Bright A.W., Corbett R.P. & Hughes J.F. (1978) *Electrostatics*, Oxford University Press, Oxford.

Brundell D.J. (1973) *Flower development of the Chinese gooseberry (Actinidia chiensis Planch.) and some factors influencing it*, M. Hort. Sc. Thesis, Department of Horticulture, Massey University, Palmerston North, N.Z.

Brundell D.J. (1975a) Flower development of the Chinese Gooseberry (*Actinidia chinensis* Planch.) I. Development of the flowering shoot, *New Zealand Journal of Botany*, 13: 473-483.

Brundell D.J. (1975b) Flower development of the Chinese Gooseberry (*Actinidia chinensis* Planch.) II. Development of the flower bud, *New Zealand Journal of Botany*, 13: 485-496.

Brundell D.J. (1975c) Effect of defoliation, shading, and tipping of shoots on flower bud development and vegetative growth of Chinese gooseberry (*Actinidia chinensis* Planch.), *New Zealand Journal of Agricultural Research*, 18: 365-370.

Brundell D.J. (1975d) Quantitative aspects of flowering in the Chinese gooseberry (*Actinidia chinensis* Planch.), *New Zealand Journal of Agricultural Research*, 18: 371-374.

Brundell D.J. (1976) The effect of chilling on the termination of rest and flower bud development of the Chinese Gooseberry, *Scientia Horticulturae*, 4: 175-182.

Bryant T.G. (1986) The use of honey bees as pollinators of kiwifruit, *Kiwifruit Pollination Seminar Proceedings*, Ministry of Agriculture and Fisheries, Tauranga, New Zealand, pp. 9 pp.

Bryant T. & Vardy C. (1985) Pollination of crops with honey bees, *Proceedings of Kiwifruit Seminar*, Ministry of Agriculture and Fisheries, Te Puke, New Zealand, pp. 44-52.

Buchmann S.L. (1983) Buzz pollination in agiosperms, In: C.E. Jones and L.R. John (Editors), *Handbook of Experimental Pollination Biology*, Scientific and Academic Editions. Van Nosrand Reinhold Company Inc., pp.73-113.

Buchmann S.L., O'Rourke M.K. & Niklas K.J. (1989) Aerodynamics of Ephedra trifurca. III. Selective pollen capture by pollination droplets, *Botanical Gazette*, 150(2): 122-131.

Burge G., Spence C. & Pallesen J. (1988) Laying more pollination myths to rest, *New Zealand Kiwifruit*, May: 7.

Burrows F.M. (1975) Calculation of primary trajectories of dust seeds, spores and pollen in unsteady winds, *New Phytologist*, 75(2): 389-403.

Camazine S. & Niklas K.J. (1984) Aerobiology of *Symplocarpus foetidus*: interactions between the spathe and spadix, *American Journal of Botany*, 71(6): 843-850.

Castro I.P., Cowan I.R. & Robins A.G. (1999) Simulations of flow and dispersion around buildings, *Journal of Aerospace Engineering*, 12(4): 145-160.

Cebeci T. & Smith A.M.O. (1974) *Analysis of turbulent boundary layers*, Academic Press, N.Y.

CFX-4.4 Solver Manual (2001), AEA Technology.

CFX-5.6 Manual (2003), AEA Technology.

CFX-5.7 Manual (2004), Ansys Inc.

CFX Consultants (2002) *Simulation of Particles Under The Influence of Electric Field*, version 1.0, unpublished, 25 pp., AEA Technology Plc, Harwell, United Kingdowm.

Choi B.S. & Fletcher C.A.J. (1998) Turbulent particle dispersion in an electrostatic precipitator, *Applied Mathematical Modelling*, 22(12):1009-1021.

Clark C.J. & Lintas C. (1992) Chemical composition of pollen from kiwifruit vines, *New Zealand Journal of Crop and Horticultural Science*, 20(3): 337-44.

Clinch P.G. (1979) Honey bees and kiwifruit pollination, *Proceedings of Kiwifruit Seminar. Ministry of Agriculture and Fisheries*, Tauranga, New Zealand, pp. 4-7.

Clinch P.G. (1982) Some factos influencing the pollination of kiwifruit by honey bees, *Proceedings of Kiwifruit Pollination Seminars*, Ministry of Agriculture and Fisheries, Hamilton & Tauranga, New Zealand, pp. 26-29.

Clinch P.G. (1984a) Kiwifruit pollination by honeybees, 1. Taurange observations, 1978-1981., *New Zealand Journal of Experimental Agriculture*, 12:29-38.

Clinch P.G. (1984b) Effect of pollen traps on kiwifruit pollen collection by honey bees, *New Zealand MAF Agricultural Research Division Annual Report 1983/84*, New Zealand Ministry of Agriculture and Fisheries, pp. 184.

Clinch P.G. (1990) Honey-bee management for kiwifruit pollination, In: I.J. Warrington and G.C. Weston (Editors), *Kiwifruit: Science and Management*, Ray Richards Publisher, Auckland, pp. 347-361.

Clinch P.G. & Heath A. (1985) Wind and bee pollination research, *New Zealand Kiwifruit*, November: 15.

Clinch P.G., Heath A.C.G., Schrader M., Bishop D.M. & Tenquist J.D. (1985) Pollination of pastures and crops - kiwifruit. Honey bees - wind, *New Zealand MAF Agricultural Research Division Annual Report 1984/85*, New Zealand Ministry of Agriculture and Fisheries, pp. 110.

Clinch P.G. & Schrader M. (1984) Competing pollen sources, *New Zealand MAF Agricultural Research Division Annual Report 1983/84*, New Zealand Ministry of Agriculture and Fisheries, pp. 183.

Clinch P.G. & Ten Houten A. (1986) Pollination of pastures and crops - kiwifruit. Honey Bees, *New Zealand MAF Agricultural Research Division Annual Report 1985/86*, New Zealand Ministry of Agriculture and Fisheries, pp. 41-42.

Coffee R.A. (1974) Depositional control of macroscopic particles by high-strength electric-field propulsion, *IEEE Transactions on Industry Applications*, IA-10(4): 511-519.

Collie S.J., Gerritsen M. & Jackson P.S. (2001) A review of turbulence modelling for use in sail flow analysis, *School of Engineering Report no. 603*, Department of Engineering Science, University of Auckland.

Comer J.K., Kleinstreuer C. & Kim C.S. (2001) Flow structures and particle deposition patterns in double-bifurcation airway models. Part 2. Aerosol transport and deposition, *Journal of Fluid Mechanics*, 435: 55-80.

Cooke J.R. & Law S.E. (2001) Finite-element analysis of space-charge suppression of electrostatic-induction spray charging, *IEEE Transactions on Industry Applications*, 37(3):751-758.

Corbet S.A., Beament J. & Eisikowitch D. (1982) Are electrostatic forces involved in pollen transfer? *Plant, Cell and Environment*, 5:125-129.

Corbet S.A., Chapman H. & Saville N. (1988) Vibratory pollen collection and flower form: bumble-bees on *Actinidia, Symphytum, Borago* and *Polygonatum, Functional Ecology*, 2: 147-155.

Corn M. (1966) Adhesion of particles, In: C.N. Davies (Editor), *Aerosol Science*, Chapter XI, pp. 359-392, Academic Press, London.

Costa G., Testolin R. & Vizzotto G. (1993) Kiwifruit pollination: an unbiased estimate of wind and bee contribution, *New Zealand Journal of Crop and Horticultural Science*, 21(2): 189-195.

Craig J.L. & Stewart A.M. (1988a) A review of kiwifruit pollination: where to next? *New Zealand Journal of Experimental Agriculture*, 16: 385-399.

Craig J.L. & Stewart A.M. (1988b) Pollination - proven facts or mythology, *New Zealand Kiwifruit*, February: 22-23.

Cross, J. (1987). *Electrostatics : principles, problems and applications*, Hilger, Bristol.

Dai Y. & Law S.E. (1992) Modeling the transient electric field produced by a charged pollen cloud entering a flower, *IEEE/IAS Conference*, pp. 1395-1402.

Davison R.M. (1974) Flowering of kiwifruit, *Proceedings of Kiwifruit Seminar. Ministry of Agriculture and Fisheries*, Tauranga, New Zealand, pp. 13-16.

Davison R.M. (1977) Some factos affecting flowering and cropping in kiwifruit, *Proceedings of Kiwifruit Seminar*, Ministry of Agriculture and Fisheries, Tauranga, New Zealand, pp. 23-27.

Delnoij E., Lammers F.A., Kuipers J.A.M. & van Swaaij W.P.M. (1997) Dynamic simulation of dispersed gas-liquid two-phase flow using a discrete bubble model, *Chemical Engineering Science*, 52(9): 1429-1458.

Devlin B. (1988) The effects of stress on reproductive characters of *Lobelia Cardinalis*, *Ecology*, 69(6): 1716-1720.

Dickison W.C., Nowicke J.W. & Skvarla J.J. (1982) Pollen morphology of the Dilleniaceae and Actinidiaceae, *American Journal of Botany*, 69:1055-1073.

Di-Giovanni F. & Beckett P.M. (1990) On the mathematical-modeling of pollen dispersal and deposition, *Journal of Applied Meteorology*, 29(12): 1352-1357.

Donovan B.J. (1983) Kiwifruit pollination, *Proceedings of MAF Beekeepers' Seminar*, Ministry of Agriculture and Fisheries, Nelson, New Zealand, pp. 18-24.

Donovan B.J. (1987) Give native bees a helping hand, *New Zealand Kiwifruit*, May: 19, 20, 22.

Dunn P.F., Brach R.M. & Caylor M.J. (1995) Experiments on the low-velocity impact of microspheres with planar surfaces, *Aerosol Science and Technology*, 23(1): 80-95.

Dunn P.F., Brach R.M. & Janson G.G. (1996) Surface-contact mechanics during oblique impact of microspheres with planar surfaces, *Aerosol Science and Technology*, 25(4): 445-465.

Elrod H.G. (1954) Computation charts and theory for rectangular and circular jets, *Heating, Piping & Air Conditioning*, 26:149-155.

Ensor I. (1986) *Assessment of kiwifruit pollinator*, unpublished, Department of Scientific and Industrial Research, Christchurch Industrial Development Division, Christchurch.

Erickson E.H. & Buchmann S.L. (1983) Electrostatics and pollination, In: C.E. Jones and L.R. John (Editors), *Handbook of Experimental Pollination Biology*, Scientific and Academic Editions, Van Nosrand Reinhold Company Inc., pp. 173-84.

Esch T., Menter F. & Vieser W. (2003) Heat transfer predictions based on two-equation turbulence models, *6th ASME-JSME Thermal Engineering Joint Conference*, TED-AJ03-542.

Feinsinger P., Murray, K.G., Kinsman, S. & Busby, W.H., 1986. Floral neighborhood and pollination success in four hummingbird-pollinated cloud forest plant species. Ecology, 67(2): 449-464.

Ferguson A.M. & King M.J. (1991) A system to accurately apply fine powders, *Proceedings of the 44th New Zealand Weed and Pest Control Conference*, pp. 268-269.

Ferguson A.M. & Pusch W.M. (1991) Development of mechanical dry-pollen application to kiwifruit, *Kiwifruit II, Acta Horticulturae 297*, ISHS, pp. 299-304.

Ferguson A.R. (1990a) The genus *Actinidia*, In *Kiwifruit: Science and Management*, Warrington I.J. & Weston G.C. (eds), 15-35, Ray Richards Publisher, Auckland.

Ferguson A.R. (1990b) Botanical nomenclature: *Actinidia chinensis*, *Actinidia deliciosa*, and *Actinidia setosa*, In *Kiwifruit: Science and Management*, Warrington I.J. & Weston G.C. (eds), 36-57, Ray Richards Publisher, Auckland.

Ferguson A.R. & Bollard E.G. (1990) Domestication of the kiwifruit, In *Kiwifruit: Science and Management*, Warrington I.J. & Weston G.C. (eds), 165-246, Ray Richards Publisher, Auckland.

Ferguson A.R. & Davison R.M. (1986) *Actinidia Deliciosa*, In: A.H. Halevy (Editor), *CRC Handbook of Flowering*, CRC Press, Boca Raton, Florida, pp. 1-14.

Ferguson L. & Bradley J. (1991) Hand-held pollinators compared in Takaka orchard trial, *New Zealand Kiwifruit*, October: 20-22.

Ferziger J.H. & Peric M. (1999) *Computational methods for fluid dynamics*, 2nd edn, pp 257-297, Springer-Verlag, Berlin.

Fetscher A.E., Rupert S.M. & Kohn J.R. (2002) Hummingbird foraging position is altered by the touch-sensitive stigma of bush monkeyflower, *Oecologia*, 133: 551-558.

Fluent User Guide (2003) Vol 2, 20, 21, 22, Fluent Incorporated.

Ford I. (1971) Chinese gooseberry pollination, *New Zealand Journal of Agricultural*, 122(2): 34-35.

Fruitfed Limited (n.d.) *Airflo Pollinator*, promotional brochure.

Ganmor S., Schwartz Y., Bechar A., Eisikowitch D. & Manor G. (1995) Relevance of Electrostatic Forces in Natural and Artificial Pollination, *Canadian Agricultural Engineering*, 37(3):189-194.

Gonzalez M.V., Coque M. & Herrero M. (1994) Pollinator selection in kiwifruit (*Actinidia deliciosa*), *Journal of Horticultural Science*, 69: 697-702.

Gonzalez M.V., Coque M. & Herrero M. (1995a) Papillar integrity as an indicator of stigmatic receptivity in kiwifruit (*Actinidia deliciosa*), *Journal of Experimental Botany*, 46(283): 263-269.

Gonzalez M.V., Coque M. & Herrero M. (1995b) Stigmatic Receptivity Limits the Effective Pollination Period in Kiwifruit, *Journal of the American Society for Horticultural Science*, 120(2): 199-202.

Gonzalez M.V., Coque M. & Herrero M. (1996) Pollen-pistil interaction in kiwifruit (*Actinidia delicisiosa*; *Actinidiaceae*), *American Journal of Botany*, 83(2): 148-154.

Gonzalez M.V., Coque M. & Herrero M. (1997) Kiwifruit flower biology and its implications on fruit set, In: E. Sfakiotakis and J. Porlingis (Editors), *Proceedings of Third International Symposium on Kiwifruit, Acta Horticulture 444*, ISHS, pp. 425-429.

Goodwin R.M. (1986a) Kiwifruit flowers: anther dehiscence and daily collection of pollen by honey bees, *New Zealand Journal of Experimental Agriculture*, 14: 449-452.

Goodwin R.M. (1986b) Increased kiwifruit pollen collection after feeding sugar syrup to honey bees within their hive, *New Zealand Journal of Experimental Agriculture*, 14:57-61.

Goodwin R.M. (1986c) Honey bee pollination of kiwifruit, *Kiwifruit Pollination Seminar Proceedings*, Ministry of Agriculture and Fisheries, Tauranga, pp. 18 pp.

Goodwin R.M. (1986d) Honey bee pollination of kiwifruit, *Proceedings from The Horowhenua Kiwifruit Production Seminar held at the Levin Horticultural Research Centre*, Ministry of Agriculture and Fisheries, Levin, New Zealand, pp. 4-15.

Goodwin R.M. (1987) Sugar feeding doubles pollen collection, *New Zealand Kiwifruit*, October: 20.

Goodwin R.M. (1995a) Afternoon decline in kiwifruit pollen collection, *New Zealand Journal of Crop and Horticultural Science*, 23(2): 163-171.

Goodwin R.M. (1995b) Pollination check list, *New Zealand Kiwifruit*, October: 4.

Goodwin R.M. (2000) *Zespri Innovation Kiwifruit Pollination Manual*, Zespri Innovation Company Limited & The Horticulture and Food Research Institute of New Zealand Limited.

Goodwin R.M. & Haine H. (1995) How many bee visits to fully pollinate kiwifruit, *New Zealand Kiwifruit*, October: 5.

Goodwin R.M. & McBrydie H.M. (2000) *Artificial pollination of Hort16A*, HortResearch Client Report No. 2000/357, unpublished, The Horticulture & Food Research Institute of New Zealand Ltd, Ruakura Research Centre, Hamilton.

Goodwin R.M., McBrydie H.M. & Taylor M. (2000) Pollination of Hort16A, *Interim Report to Zespri Group Ltd, Project No 404-00*, The Horticulture & Food Research Institute of New Zealand Ltd, Ruakara Research Centre, Hamilton.

Goodwin R.M., Perry J.H. & Ten Houten A. (1992a) The effect of male distribution on the size of fruit, *New Zealand Kiwifruit*, September: 14-15.

Goodwin R.M., Perry J.H., Ten Houten A., Haine H. & Brown P. (1992b) A comparison of pollinators, *New Zealand Kiwifruit*, September: 12.

Goodwin R.M., Perry J.H., Haine H. & Brown P. (1994) An evaluation of kiwifruit pollination systems, *New Zealand Kiwifruit*, April/May: 22-23.

Goodwin R.M. & Ten Houten A. (1988) Sugar syrup feeding to improve kiwifruit pollination, *New Zealand Kiwifruit Authority National Research Conference, New Zealand Kiwifruit Special Publication No. 2*, Rotorua, New Zealand, pp. 44-45.

Goodwin R.M. & Ten Houten A. (1989) Maximising pollination in poor weather, *New Zealand Kiwifruit*, February: 20, 22.

Goodwin R.M. & Ten Houten A. (1991) Feeding sugar syrup to honey bee (Apis mellifera L.) colonies to increase kiwifruit pollen collection: Effect of frequency, quantity and time of day, *Journal of Apicultural Research*, 30(1): 41-48.

Goodwin R.M., Ten Houten A. & Perry J. (1990) Hydrogen cyanamide and kiwifruit pollination, *New Zealand Kiwifruit Authority National Research Conference 1990, New Zealand Kiwifruit Special Publication No. 3*, Rotorua, New Zealand, pp. 14.

Goodwin R.M., Ten Houten A. & Perry J.H. (1991) Effect of variations in sugar presentation to honey bees (Apis mellifera) on their collection of kiwifruit (*Actinidia deliciosa*) pollen, *New Zealand Journal of Crop and Horticultural Science*, 19: 259-262.

Goodwin R.M., Ten Houten A. & Perry J.H. (1999) Effect of staminate kiwifruit vine distribution and flower number on kiwifruit pollination, *New Zealand Journal of Crop and Horticultural Science*, 27(1): 63-67.

Harder L.D. (1990) Pollen removal by bumble bees and its implications for pollen dispersal, *Ecology*, 71(3): 1110-1125.

Hardin G.B. (1976) Better charge, better pollination, *Agricultural Research (U.S. Department of Agriculture)*, December 25(6):15.

Harvey C.F., Fraser L.G., Pavis S.E. & Considine J.A. (1987) Floral biology of two species of Actinidia (Actinidiaceae) I. The stigma, pollination and fertilization, *Botanical Gazette*, 148(3): 426-432.

Hathaway R.L. (1990) Shelter for kiwifruit production, In: I.J. Warrington and G.C. Weston (Editors), *Kiwifruit: Science and Management*, Ray Richards Publisher, Auckland, pp. 322-346.

Hawes L. & Lupton T. (1982) Setting out a kiwifruit orchard, *Proceedings of Kiwifruit Pollination Seminars*, Ministry of Agriculture and Fisheries, Hamilton & Tauranga, New Zealand, pp. 11-20.

Heath A.C.G. (1984) Viability of kiwifruit pollen, *New Zealand MAF Agricultural Research Division Annual Report 1983/84*, New Zealand Ministry of Agriculture and Fisheries, pp. 184.

Heath A.C.G. & Tenquist J.D. (1984) Dispersal of kiwifruit pollen, *New Zealand MAF Agricultural Research Division Annual Report 1983/84*, New Zealand Ministry of Agriculture and Fisheries, pp. 183.

Heath A.C.G., Tenquist J.D. & Bishop D.M. (1984) Wind pollination, *New Zealand MAF Agricultural Research Division Annual Report 1983/84*, New Zealand Ministry of Agriculture and Fisheries, pp. 184.

Henzell R. & Allison P. (1993) Reducing side flowers for increased export production, *New Zealand Kiwifruit*, August/September: 16-17.

Hongladarom K. (1988) *Development of biosensor for kiwifruit pollination*, unpublished BE report, University of Canterbury, Christchurch, New Zealand.

Hopping M.E. (1976) Effect of exogenous auxins, gibberellins, and cytokinins on fruit development in Chinese gooseberry (*Actinidia chinensis* Planch.), *New Zealand Journal of Botany*, 14:69-75.

Hopping M.E. (1979) Supplemental pollination, *Proceedings of Kiwifruit Seminar. Ministry of Agriculture and Fisheries*, Tauranga, New Zealand, pp. 8-14.

Hopping M. (1981a) Kiwifruit pollination: Influence of male clones, *Kiwifruit Seminar*, Ministry of Agriculture and Fisheries, Tauranga.

Hopping M. (1981b) Kiwifruit: hand pollination to improve fruit size, *The Orchardist of New Zealand*, 54: 258.

Hopping M.E. (1982a) Spray pollination of kiwifruit, *New Zealand Agricultural Science*, 16: 46-48.

Hopping M.E. (1982b) Kiwifruit, Hand pollination for size improvement, *Aglink HPP260*, Ministry of Agriculture and Fisheries, 2 pp.

Hopping M.E. (1985a) Kiwifruit pollination, *New Zealand MAF Agricultural Research Division Annual Report 1984/85*, New Zealand Ministry of Agriculture and Fisheries, pp. 63.

Hopping M.E. (1985b) New pollination developments, *Proceedings of Kiwifruit Seminar. Ministry of Agriculture and Fisheries*, Te Puke, New Zealand, pp. 41-43.

Hopping M.E. (1986) Kiwifruit, In *CRC Handbook of Fruit Set and Development*, Monselise S.P. (eds), pp. 217-232, CRC Press, Boca Raton, Florida.

Hopping M.E. (1990a) Floral biology, pollination, and fruit set. In *Kiwifruit: Science and Management*, Warrington I.J. & Weston G.C. (eds), 71-96, Ray Richards Publisher, Auckland.

Hopping M.E. (1990b) Is pollination the real problem? *New Zealand Kiwifruit Authority National Research Conference 1990, New Zealand Kiwifruit Special Publication No. 3*, Rotorua, New Zealand, pp. 13.

Hopping M.E. & Hacking N.J.A. (1983a) Artificial pollination: progress and future direction. In: A.G. Matheson (Editor), Proceedings of Ministry of Agriculture and Fisheries Beekeepers Seminar. Ministry of Agriculture and Fisheries, Nelson, pp. 9-17.

Hopping M.E. & Hacking N.J.A. (1983b) A comparison of pollen application methods for the artificial pollination of kiwifruit, In: G. Bunemann (Editor), *Fruit Set and Development, XXI IHC, Acta Horticulturae 139*, ISHS, Hamburg, Germany, pp. 41-50.

Hopping M.E. & Hacking N.J.A. (1983c) Artificial pollination of kiwifruit, *New Zealand MAF Agricultural Research Division Annual Report 1982/83*, New Zealand Ministry of Agriculture and Fisheries, pp. 89.

Hopping M.E. & Hacking N.J.A. (1983d) Kiwifruit pollen physiology, *New Zealand MAF Agricultural Research Division Annual Report 1982/83*, New Zealand Ministry of Agriculture and Fisheries, pp. 89-90.

Hopping M.E. & Hacking N.J.A. (1984) Kiwifruit pollen physiology, *New Zealand MAF Agricultural Research Division Annual Report 1983/84*, New Zealand Ministry of Agriculture and Fisheries, pp. 83-84.

Hopping M.E., Hacking N.J.A. & Martyn J.A.K. (1985) Spray pollination: progress and likely economics, *Proceedings of Ruakura Horticultural Conference on Kiwifruit. Minisitry of Agriculture and Fisheries*, Hamilton, New Zealand, pp. 9-12.

Hopping M.E., Hacking N.J.A. & Stevenson B.E. (1984) Artificial pollination of kiwifruit, *New Zealand MAF Agricultural Research Division Annual Report 1983/84*, New Zealand Ministry of Agriculture and Fisheries, pp. 82-83.

Hopping M.E. & Jerram E.M. (1979) Pollination of kiwifruit (*Actinidia chinensis* Planch.): stigma-style structure and pollen tube growth, *New Zealand Journal of Botany*, 17:233-240.

Hopping M.E. & Jerram E.M. (1980a) Supplementary pollination of tree fruits. I. Development of suspension media, *New Zealand Journal of Agricultural Research*, 23(4): 509-515.

Hopping M.E. & Jerram E.M. (1980b) Supplementary pollination of tree fruits. II. Field trials on kiwifruit and Japanese plums, *New Zealand Journal of Agricultural Research*, 23: 517-521.

Hopping M.E. & Martyn J.A.K. (1986a) Spray pollination, *New Zealand MAF Agricultural Research Division Annual Report 1985/86*, New Zealand Ministry of Agriculture and Fisheries, pp. 66.

Hopping M.E. & Martyn J.A.K. (1986b) Spray pollination and superior males, *Proceedings from The Horowhenua Kiwifruit Production Seminar held at the Levin Horticultural Research Centre*, Ministry of Agriculture and Fisheries, Levin, New Zealand, pp. 16-22.

Hopping M.E. & Martyn J.A.K. (1986c) Spray pollination - method, cost, and benefits, *Kiwifruit Pollination Seminar Proceedings*, Ministry of Agriculture and Fisheries, Tauranga, New Zealand, pp. 13 pp.

Hopping M., Martyn J.A.K., Mills R.A. & Stevenson B.E. (1987) Spray it on and count the savings, *New Zealand Kiwifruit*, September: 25.

Hopping M.E. & Simpson L.M. (1982) Supplementary pollination of tree fruits. III. Suspension media for kiwifruit pollen, *New Zealand Journal of Agricultural Research*, 25: 245-250.

Howpage D., Spooner-Hart R.N. & Vithanage V. (2001) Influence of honey bee (Apis mellifera) on kiwifruit pollination and fruit quality under Australian conditions, *New Zealand Journal of Crop and Horticultural Science*, 29(1): 51-59.

Huang H. & Ferguson A.R. (2001) Kiwifruit in China, *New Zealand Journal of Crop and Horticultural Science*, 29: 1-14.

ICEM CFD 4.CFX Manual (2003), ANSYS Inc.

International Standardisation of Fruit and Vegetables (1992) Organisation for Economic Co-operation and Development (OECD), pp. 47, France.

Ivens J. (1982) Kiwifruit Pollination, *Development Finance Corporation of New Zealand*, 52 pp, Wellington.

Jansson D.M. & Warrington I.J. (1988) The influence of temperature during floral development and germination in vitro on the germinability of kiwifruit pollen, *New Zealand Journal of Experimental Agriculture*, 16: 225-230.

Jay S.C. (1982) Honey bees as pollinators, *Proceedings of Kiwifruit Pollination Seminars*, Ministry of Agriculture and Fisheries, Hamilton & Tauranga, New Zealand, pp. 21-25.

John W. (1995) Particle-Surface Interactions - Charge-Transfer, Energy-Loss, Resuspension, and Deagglomeration, *Aerosol Science and Technology*, 23(1): 2-24.

Jonassen N. (1998) *Electrostatics*, Chapman & Hall, United States, pp. 48-58.

Jones W.P. & Launder B.E. (1972) The prediction of laminarization with a two-equation model of turbulence, *International Journal of Heat and Mass Transfer*, 15: 301-313.

Joshi J.B. & Ranade V.V. (2003) Computational fluid dynamics for designing process equipment: expectations, current status, and path forward, *Industrial and Engineering Chemistry Research*, 42: 1115-1128.

Kardos O.N. (1998) *Enhancing kiwifruit pollination*, unpublished project report, Chemical and Process Engineering, University of Canterbury, Christchurch, New Zealand.

Kearns C.A. & Inouye D.W. (1993) *Techniques for Pollination Biologists*, pp 94-97, 115-119, 123, University Press of Colorado, Colorado.

Keene H. (2000a) Bee mite menaces seed industry, *The Press*, 20 April 2000, Christchurch, pp. 16.

Keene H. (2000b) Push urged to find other pollinators, *The Press*, 20 April 2000, Christchurch, pp. 16.

King M.J. (1993) Buzz foraging mechanism of bumble bees, *Journal of Apicultural Research*, 32(1): 41-49.

King M.J. & Ferguson A.M. (1991) Collection and use of dry pollen for pollination of kiwifruit, *New Zealand Journal of Crop and Horticultural Science*, 19: 385-389.

King M.J. & Ferguson A.M. (1994) Vibratory collection of *Actinidia deliciosa* (Kiwifruit) pollen, *Annals of Botany*, 74: 479-482.

King M.J. & Lengoc L. (1993) Vibratory pollen collection dynamics, *Transactions of the ASAE*, 36(1): 135-140.

Kiwi Pollen Limited (n.d. 1) *Evaluation of the Kiwi Pollen Blower as a means of delivery for kiwifruit pollen in supplementray pollination 1997-98*, promotional brochure.

Kiwi Pollen Limited (n.d. 2) *Kiwi Pollen Variflo Air Pollinator*, promotional brochure.

Kiwi Pollen Limited (n.d. 3) *Kiwi Pollen Sprayer*, promotional brochure.

Kiwi Pollen Limited (1993) *Pollenaid Application, Pollenaid: Spray Pollination, Technical Guide Number 1*, Te Puke, New Zealand.

Kiwi Pollen Limited (2002) *Pollenaid Application - Technical Guide*, Te Puke, New Zealand.

Kiwi Pollen Limited (2004) http://www.kiwipollen.com [online accessed 1 February 2004].

Koumoutsakos P. & Shiels D. (1996) Simulations of the viscous flow normal to an impulsively started and uniformly accelerated flat plate, *Journal of Fluid Mechanics*, 328: 177-227.

Kumeu Kiwifruit Nurseries Ltd. (1981) Whenuapai, New Zealand, information booklet, pp. 19.

Lasher W.C. (2001) Computation of two-dimensional blocked flow normal to a flat plate, *Journal of Wind Engineering and Industrial Aerodynamics*, 89(6): 493-513.

Launder B.E. & Spalding D.B. (1972) *Lectures in Mathematical Models of Turbulence*, Academic Press, pp 90-110, London, England.

Launder B.E. & Spalding D.B. (1974) The numerical computation of turbulent flows, *Computer Methods in Applied Mechanics And Engineering*, 3(2): 269-289.

Laurence D. (1993) Modelling flows around bluff bodies by Reynolds averaged transport equations, *Journal of Wind Engineering and Industrial Aerodynamics*, 46 & 47: 53-68.

Laurence D. (2002) Limitations of current RANS models and progress perspectives, *The Second QNET-CFD Workshop Proceedings*, Lucerne.

Law S.E. (1983) Electrostatic pesticide spraying: Concepts and practice, *IEEE Transactions of Industry Applications*, IA-19: 160-168.

Law S.E. (1995a) Electrostatics technology for agricultural and biological applications: Status and trends, In: S. Cunningham (Editor), *Electrostatics 1995*, Institute of Physics Conference Series, IOP PUBLISHING LTD, Bristol, pp. 1-12.

Law S.E. (1995b) Electrostatic atomization and spraying, In: J.S. Chang, A.J. Kelly & J.M. Crowley (Editors), *Handbook of Electrostatic Processes*, Marcel Dekker, Inc., United States, pp. 413-440.

Law S.E. & Cooper S.C. (2001) Air-assisted electrostatic sprays for postharvest control of fruit and vegetable spoilage microorganisms, *IEEE Transactions on Industry Applications*, 37(6):1597-1602.

Law S.E., Banerjee S., Wetzstein H.Y. & Eisikowitch D. (1996) Electrostatic application of pollen sprays: Effects of charging field intensity and aerodynamic shear upon deposition and germinability, *Conference Record of the 1996 IEEE Industry Applications 31st IAS Annual Meeting*, Part 4 (of 4) M1 1996 Oct 6-10, pp. 1940-1948.

Law S.E., Wetzstein H.Y., Banerjee S. & Eisikowitch D. (2000) Electrostatic application of pollen sprays: Effects of charging field intensity and aerodynamic shear upon deposition and germinability, *IEEE Transactions on Industry Applications*, 36(4): 998-1009.

Lawes G.S., Woolley D.J. & Lai R. (1990) Seeds and other factors affecting fruit size in kiwifruit, *Acta Horticulturae 282*, pp. 257-264.

Lees N. (1986) Growing export kiwifruit, *Kiwifruit Pollination Seminar Proceedings*, Ministry of Agriculture and Fisheries, Tauranga, New Zealand, pp. 6 pp.

Li X., Dunn P.F. & Brach R.M. (1999) Experimental and numerical studies on the normal impact of microspheres with surfaces, *Journal of Aerosol Science*, 30(4): 439-449.

Linder H.P. & Midgley J. (1996) Anemophilous plants select pollen from their own species from the air, *Oecologia*, 108(1): 85-87.

Lu W.Z., Howarth A.T., Adams N.M. & Riffat S.B. (1999) CFD modeling and measurement of aerosol particle distributions in ventilated multizone rooms, *ASHRAE Transactions: Research*, 105(2): 116-127.

Luchini P. & Tognaccini R. (2002) The start-up vortex issuing from a semi-infinite flat plate. Journal of Fluid Mechanics, 455: 175-193.

Lyford P. & Goodwin R.M. (1989) Pollination - the big P, *Kiwifruit Cropping with Hi-Cane Conference 1989*, MAFTech, Tauranga, Kerikeri, pp. 35-37.

Lyford P. & Underwood R. (1992) The quest for larger fruit, *New Zealand Kiwifruit*, September: 11.

Lytle D. & Webb B.W. (1994) Air-Jet Impingement Heat-Transfer at Low Nozzle Plate Spacings, *International Journal of Heat and Mass Transfer*, 37(12): 1687-1697.

Malaboeuf F., Vaissiere B.E. & Cour P. (1997) Pollen flow in the atmosphere of kiwifruit (*Actinidia deliciosa*) orchards. In: E. Sfakiotakis and J. Porlingis (Editors), Third International Symposium on Kiwifruit. Acta Horticulture, pp. 413-420.

Martyn J. & Hopping, M. (1988) How to identify superior males, *New Zealand Kiwifruit*, February: 29.

McAneney K.J., Judd M.J. & Trought M.C.T. (1984) Wind damage to kiwifruit (*Actinidia chinensis* Planch.) in relation to windbreak performance, *New Zealand Journal of Agricultural Research*, 27:255-263.

McNeilage M. & Seal A. (1990) Developing and testing new males, *New Zealand Kiwifruit*, February: 25.

McNeilage M.A., Seal A.G., Steinhagen S. & McGowan J. (1991) Evaluation of kiwifruit pollinizers, *Acta Horticulturae 297 - Kiwifruit II*, pp 277-282, ISHS.

McPherson H.G., Richardson A.C., Snelgar W.P., Patterson K.J. & Currie M.B. (2001) Flower quality and fruit size in kiwifruit (*Actinidia deliciosa*), *New Zealand Journal of Crop and Horticultural Science*, 29(2): 93-101.

McPherson H.G., Stanley C.J., Warrington I.J. & Jansson D. (1988) Dynamics of budbreak and flowering, *New Zealand Kiwifruit Authority National Research Conference, New Zealand Kiwifruit Special Publication No. 2*, Rotorua, New Zealand, pp. 9-11.

Menter F.R. (1992a) Influence of freestream values on k-w turbulence model predictions, *American Institute of Aeronautics and Astronautics Journal*, 30(6): 1657-1659.

Menter F.R. (1992b) Performance of popular turbulence models for attached and separated adverse pressure gradient flows, *American Institute of Aeronautics and Astronautics Journal*, 30(8): 2066-2072.

Menter F.R. (1994) Two-equation eddy-viscosity turbulence models for engineering applications, *American Institute of Aeronautics and Astronautics Journal*, 32(8): 1598-1605.

Menter F.R. (1996). A comparison of some recent eddy-viscosity turbulence models, *Transaction of the ASME - Journal of Fluids Engineering*, 118:514-19.

Menter F.R. & Grotjans H. (2000) Application of advanced turbulence models to complex industrial flows, In: G. Tzabiras (Editor), Calculation of Complex Turbulent Flows, *Advances in Fluid Mechanics*, WIT Press, Southampton, UK., pp. 167-207.

Merzkirch W. (1987) *Flow Visualization*, pp. 14-114, Academic Press, Orlando.

Mills R.A., Stevenson B.E. & Ward B.Q. (1986) Spray pollination, *New Zealand MAF Agricultural Research Division Annual Report 1985/86*, New Zealand Ministry of Agriculture and Fisheries, pp 41-42.

Moore D.S. & McCabe G.P. (1999) *Introduction to The Practice of Statistics*, 3rd edn, pp. 799-825, W.H. Freeman and Company, New York.

Morgans R.C., Dally B.B., Nathan G.J., Lanspeary P.V. & Fletcher D.F. Application of the revised Wilcox (1998) k-ω turbulence model to a jet in co-flow, *Second International Conference on CFD in the Minerals and Process Industries*, Melbourne, Australia, pp 479-484.

Morley-Bunker M.J. & Salinger M.J. (1987) Kiwifruit development The effect of temperature on budburst and flowering, *Weather and Climate*, 7: 26-30.

Mueller T.J. (1983a) Smoke visualization in wind tunnels, *Astronautics & Aeronautics*, pp. 50-54&62.

Mueller T.J. (1983b) Recent developments in smoke flow visualization, *Third International Symposium on Flow Visualization*, University of Michigan, pp. 30-40.

Mueller T.J., Nelson R.C., Kegelman J.T. & Zehentner R.J. (1983) A new single filament smoke tube injection device, *Third International Symposium on Flow Visualization*, University of Michigan, pp. 45-48.

Mullins M.E., Michaels L.P., Menon V., Locke B. & Ranade M.B. (1992) Effect of geometry on particle adhesion, *Aerosol Science and Technology*, 17: 105-118.

Murakami S. (1993) Comparison of various turbulence models applied to a bluff body, *Journal of Wind Engineering and Industrial Aerodynamics*, 46 & 47: 21-36.

Murakami S. (1998) Overview of turbulence models applied in CWE-1997, *Journal of Wind Engineering and Industrial Aerodynamics*, 74-76: 1-24.

Murcia C. (1990) Effect of floral morphology and temperature on pollen receipt and removal in *Ipomoea Trichocarpa*, *Ecology*, 71(3): 1098-1109.

Nee C.C. (1991) Breaking dormancy in kiwifruit with chilling or chemical treatment, *New Zealand Journal of Crop and Horticultural Science*, 19: 419-421.

New Zealand Horticulture Facts & Figures - Fruits, Flowers & Vegetables 2002 (2002) compiled by Kerr J.P., Hewett E.W. & Aitken A.G., The Horticulture & Food Research Institute of New Zealand Ltd., Palmerston North, New Zealand.

Niklas K.J. (1981a) Airflow patterns around some early seed plant ovules and cupules: implications concerning efficiency in wind pollination, *American Journal of Botany*, 68(5): 635-650.

Niklas K.J. (1981b) Simulated wind pollination and airflow around ovules of some early seed plants, *Science*, 211(4479): 275-277.

Niklas K.J. (1982) Simulated and empiric wind pollination patterns of conifer ovulate cones, *Proceedings of the National Academy of Sciences of the United States of America*, 79(2): 510-514.

Niklas K.J. (1983a) The influence of paleozoic ovule and cupule morphologies on wind pollination, *Evolution*, 37(5): 968-986.

Niklas K.J. (1984) The motion of windborne pollen grains around conifer ovulate cones - implications on wind pollination, *American Journal of Botany*, 71(3): 356-374.

Niklas K.J. (1985a) Wind pollination - a study in controlled chaos, *American Scientist*, 73(5): 462-470.

Niklas K.J. (1985b) The aerodynamics of wind pollination, *Botanical Review*, 51(3): 328-386.

Niklas K.J. (1985c) Wind pollination of *Taxus-Cuspidata*, *American Journal of Botany*, 72(1): 1-13.

Niklas K.J. (1987b) Aerodynamics of wind pollination, *Scientific American*, 255(7): 90-95.

Niklas K.J. (1988) Equations for the motion of airborne pollen grains near the ovulate organs of wind-pollinated plants, *American Journal of Botany*, 75(3): 433-444.

Niklas K.J. (1992) *Plant Biomechanics - An Engineering Approach to Plant Form and Function*, The University of Chicago Press, pp. 29-33, 178-187, 424-473, 519-525 pp.

Niklas K.J. & Buchmann S.L. (1985) Aerodynamics of wind pollination in *Simmondsia-Chinensis* (Link) Schneider, *American Journal of Botany*, 72(4): 530-539.

Niklas K.J. & Buchmann S.L. (1986) Wind pollination in 2 Sympatric species of Ephedra, *American Journal of Botany*, 73(5): 674-674.

Niklas K.J. & Buchmann S.L. (1987) The aerodynamics of pollen capture in 2 Sympatric *Ephedra* species, *Evolution*, 41(1): 104-123.

Niklas K.J. & Buchmann S.L. (1988) Aerobiology and pollen capture of orchard-grown *Pistacia vera* (*anacardiaceae*), *American Journal of Botany*, 75(12): 1813-1829.

Niklas K.J. & Kerchner V. (1986) Aerodynamics of Ephedra-Trifurca .2. Computer modeling of pollination efficiencies, *Journal of Mathematical Biology*, 24(1): 1-24.

Niklas K.J. & Norstog K. (1984) Aerodynamics and pollen grain depositional patterns on *Cycad Megastrobili* - Implications on the reproduction of 3 Cycad Genera (*Cycas, Dioon,* and *Zamia*), *Botanical Gazette*, 145(1): 92-104.

Niklas K.J. & Paw U K.T. (1982) Pollination and airflow patterns around conifer ovulate cones, *Science*, 217(4558): 442-444.

Niklas K.J. & Paw U K.T. (1983) Conifer ovulate cone morphology - Implications on pollen impaction patterns, *American Journal of Botany*, 70(4): 568-577.

Niklas K.J., Buchmann S.L. & Kerchner V. (1986) Aerodynamics of *Ephedra Trifurca* .1. pollen grain velocity-fields around stems bearing ovules, *American Journal of Botany*, 73(7): 966-979.

Nordson Corporation (1992) *Tribomatic II Powder Pump Manual.*

Nordson Corporation (1995) *Tribomatic II Three-Gauge Control Unit Manual.*

Nordson Corporation (1996) *Tribomatic II Manual Spray Gun Manual.*

Olmos E., Gentric C., Vial C., Wild G. & Midoux N. (2001) Numerical simulation of multiphase flow in bubble column reactors. Influence of bubble coalescence and break-up, *Chemical Engineering Science*, 56(21-22): 6359-6365.

Ornduff R. (1975) Pollen flow in *Lythrum Junceum*, a tristylous species, *New Phytologist*, 75(1): 161-166.

Palmer-Jones T. (1974) Pollination of kiwifruit, *Proceedings of Kiwifruit Seminar. Ministry of Agriculture and Fisheries*, Tauranga, New Zealand, pp. 17-19.

Palmer-Jones T. & Clinch P.G. (1974) Observations on the pollination of Chinese gooseberries variety 'Hayward', *New Zealand Journal of Experimental Agriculture*, 2:455-458.

Palmer-Jones T. & Clinch P.G. (1975) Honey bees essential for kiwifruit pollination, *The Orchardist of New Zealand*, 48: 347.

Palmer-Jones T. & Clinch P.G. (1976) Effect of honey bee saturation on the pollination of Chinese gooseberries variety 'Hayward', *New Zealand Journal of Experimental Agriculture*, 4:255-256.

Paterson F. (1995) Spring pollination strategies, *New Zealand Kiwifruit*, October: 7.

Patterson K.J. (2000) *Proceedings of a workshop to review the use of Hicane and alternatives to promote fruitful budbreak in kiwifruit*, HortResearch Client Report No. 2001/62, unpublished, The Horticulture and Food Research Institute of New Zealand Ltd, Mt Albert Research Centre, Auckland.

Patterson K.J., Gould K.S., Watson M., Barker K.A. & Martin P.J. (1991) Does the timing of flowering affect fruit size, *New Zealand Kiwifruit*, December: 14-15.

Patterson K.J., Snelgar W.P., Richardson A.C. & McPherson H.G. (1999) Flower quality and fruit size of Hayward kiwifruit, *Acta Horticulturae 498*, pp. 143-150.

Pauthenier M. M. & Moreau-Hanot M. (1932) Charging of spherical particles in an ionizing field, *Journal de physique et le radium*, Ser. 7(3), 590-613.

Paw U K.T. (1983) The rebound of particles from natural surfaces, *Journal of Colloid and Interface Science*, 93(2): 442-452.

Penrose J. & Hamill I.S. (2003) *Algebraic Slip Model Design in CFX-5.6*, version 1.0, unpublished, 10 pp., CFX Ltd., United Kingdom.

Philippe G. & Baldet P. (1997) Electrostatic dusting: an efficient technique of pollination in larch, *Annales des Sciences Forestieres*, 54:301-310.

Pomeroy N. (1988) Comment to A review of kiwifruit pollination: where to next?, *New Zealand Journal of Experimental Agriculture*, 16: 392-393.

Pomeroy N. (2001) *Quantitative assessment of stocking rates for kiwifruit pollination by bumble bees*, unpublished, Research Contract 422/00 between Zespri Innovation Company Ltd and Nelson Pomeroy Ltd.

Poppe T., Blum J. & Henning T. (2000) Analogous experiments on the stickiness of micron-sized preplanetary dust, *Astrophysical Journal*, 533(1): 454-471.

Pyke N.B. & Alspach P.A. (1986) Inter-relations on the pollination of chinese gooseberries variety 'Hayward', *New Zealand Agricultural Science*, 20:153-156.

Ranade V.V. (2002) *Computational flow modeling for chemical reactor engineering.* pp 57-83, San Diego, Academic Press.

Richardson A.C. & McAneney K.J. (1990) Influence of fruit number on fruit weight and yield of kiwifruit, *Scientia Horticulturae*, 42: 233-241.

Richardson A.C., Dawson T.E., Hampton R.E. & Blank R.H. (1994) The effects of hydrogen cyanamide and mineral oil on kiwifruit performance, *Proceedings of the 47th NZPPS Conference*, The New Zealand Plant Protection Society, Waitangi.

Reid M. (1982) Protecting everyone's interest, *Proceedings of Kiwifruit Pollination Seminars*, Ministry of Agriculture and Fisheries, Hamilton & Tauranga, New Zealand, pp. 39-43.

Roberts S. (1997) *Enhancement of Kiwifruit Pollination by Triboelectric Charging*, unpublished project report, University of Canterbury, Christchurch, New Zealand.

Rodi W. (1980) *Turbulence models and their application in hydraulics - a state of the art review*, pp 26-33, International Association for Hydraulic Research Publication.

Rodi W. (1993) On the simulation of turbulent flow past bluff bodies, *Journal of Wind Engineering and Industrial Aerodynamics*, 46 & 47: 3-19.

Rodi W. & Scheurer G. (1986) Scrutinizing the k-ε model under adverse pressure gradient conditions, *Journal of Fluids Engineering*, 108:174-179.

Ryan K. & Rhoades D. (1988) Airflo pollinator results analysed, *New Zealand Kiwifruit*, October: 16-18.

Ryugo K., Okuse I. & Saga K. (1988) Influence of floral morphology, hand-pollination, and xylem sap loss on the harvest size of kiwifruit, *HortScience: a publication of the Americal Society for Horticultural Science*, 23(3): 745.

Sale P.R. (1981) Kiwifruit Pollination, male to female ratios and bee activity, *Aglink HPP233*, New Zealand Ministry of Agriculture and Fisheries, 3 pp.

Sale P.R. (1983a) *Kiwifruit Culture*, pp 23-32, 39-41, Government Printer, Wellington, New Zealand.

Sale P.R. (1983b) Kiwifruit training and pruning, on T-bar and Pergola systems, *Aglink HPP234*, New Zealand Ministry of Agriculture and Fisheries, pp. 3 pp.

Sale P.R. (1983c) Subtropical fruit pollination, an introduction, *Aglink HPP97*, New Zealand Ministry of Agriculture and Fisheries, pp. 2 pp.

Sale P.R. (1986) Factors which influence fruit size, *Kiwifruit Pollination Seminar Proceedings*, Ministry of Agriculture and Fisheries, Tauranga, New Zealand, pp. 6 pp.

Sale P.R. (1990) *Kiwifruit Growing*, pp 14, 20-27, 34-36, GP Books, Wellington, New Zealand.

Sale P.R. & Lyford P.B. (1990) Cultural, management and harvesting practices for kiwifruit in New Zealand. In: I.J. Warrington and G.C. Weston (Editors), *Kiwifruit: Science and Management*, Chapter 9, pp 247-296, Ray Richards Publisher, Auckland.

Salinger M.J. & Morley-Bunker M.J. (1988) The effect of climate on kiwifruit flowering and fruit maturity, *New Zealand Kiwifruit Authority National Research Conference, New Zealand Kiwifruit Special Publication No. 2*, Rotorua, New Zealand, pp. 46-47.

Schmid R. (1978) Reproductive anatomy of *Actinidia chinensis* (*Actinidiaceae*), *Botanischer Jahrbucher fur Systematick, Pflanzengeschichte und Pflanzengeographie*, 100(2):149-195.

Sheat D.S., Hopping M.E. & Smith J. (1982) Spray pollination of kiwifruit, *New Zealand MAF Agricultural Research Division Annual Report 1981/82*, New Zealand Ministry of Agriculture and Fisheries, pp. 80.

Shivanna K.R. & Rangaswamy N.S. (1992) *Pollen Biology - A Laboratory Manual*, pp 91-92, Springer-Verlag, Germany.

Shore J.S. & Barrett S.C.H. (1984) The effect of pollination intensity and incompatible pollen on seed set in *Turnera Ulmifolia* (Turneraceae), *Canadian Journal of Botany*, 62(6): 1298-1303.

Simiu E. & Scanlan R.H. (1986) *Wind Effects on Structures - An Introduction to Wind Engineering*, John Wiley & Sons, USA, pp. 123-178.

Snow A.A. (1982) Pollination intensity and potential seed set in *Passiflora vitifolia*, *Oecologia*, 55: 231-237.

Snowball A.M. (1996) The timing of flower evocation in kiwifruit, *Journal of Horticultural Science*, 71(2): 335-347.

Snowball A.M., Smith R.C. & Considine J.A. (1996) Flowering and fruiting rootless cuttings of kiwifruit, *New Zealand Journal of Crop and Horticultural Science*, 24: 355-60.

Sotiropoulos F. (2000) Progress in modeling 3D shear flows using RANS equations and advanced turbulence models, in *Calculation of Complex Turbulent Flows*, edited by Tzabiras G., Advances in Fluid Mechanics, Chapter 6, pp 209-248, WIT Press, Southampton, UK.

Stevens I. & Forsyth M. (1982) Pollination, fertilisation, and fruit development, *Proceedings of Kiwifruit Pollination Seminars*, Ministry of Agriculture and Fisheries, Hamilton & Tauranga, New Zealand, pp. 2-10.

Stremler F.G., Klein S.A., Luo F.F. & Liao Y. (1990) Numerical solutions and mapping of electrostatic fields using the Apple MacIntosh computer, *Education, IEEE Transactions on*, 33:104-110.

Taylor B. (1986) *Triboelectric charging of pollen*, unpublished BE report, Chemical and Process Engineering, University of Canterbury, Christchurch, New Zealand.

Testolin R., Vizzotto G. & Costa G. (1991) Kiwifruit pollination by wind and insects in Italy, *New Zealand Journal of Crop and Horticultural Science*, 19:381-384.

The Visualization Society of Japan (1993) *Fantasy of Flow: The World of Fluid Flow Captured in Photographs*, Nakayama Y. (eds.), pp. 118-120, IOS Press, Amsterdam, Netherlands.

Thomson J.D. & Plowright R.C. (1980) Pollen carryover, nectar rewards, and pollinator behaviour with special reference to *Diervilla Ionicera*, *Oecologia*, 46(1): 68-74.

Tsirakoglou V., Thrasyvoulou A. & Hatjina F. (1997) Techniques to increase the attractiveness of kiwi flowers to honey bees, In: E. Sfakiotakis and J. Porlingis (Editors), *Proceedings of Third International Symposium on Kiwifruit, Acta Horticulture, 444*, ISHS, pp. 439-443.

Tu J.Y. & Fletcher C.A.J. (1995) Continuum hypothesis in the computation of gas-solid flows, In: D. Leutloff and R.C. Srivastava (Editors), *Computational Fluid Dynamics*, Springer-Verlag, Germany, pp. 1-11.

Tuve G.L. (1953) Air velocities in ventilating jets, *Heating, Piping & Air Conditioning*, 25:181-191.

Tyler J. & Mees P. (1999) Using CFD to model the interaction of a horizontal feed jet on fluidized bed hydrodynamics, *Second International Conference on CFD in the Minerals and Process Industries*, CSIRO, Melbourne, Australia, pp. 113-117.

Underwood R. (2001) Pollination of kiwifruit, *New Zealand Kiwifruit Journal*, 44-46.

Vaissiere B.E., Rodet G., Cousin M., Botella L. & Grossa J.P.T. (1996) Pollination effectiveness of honey bees (Hymenoptera: Apidae) in a kiwifruit orchard, *Journal of Economic Entomology*, 89(2): 453-461.

Vaknin Y., Gan-Mor S., Bechar A., Ronen B. & Eisikowitch D. (2000) The role of electrostatic forces in pollination, *Plant Systematics and Evolution*, 222:133-142.

Vaknin Y., Gan-Mor S., Bechar A., Ronen B. & Eisikowitch D. (2001a) Improving pollination of almond (Amygdalus communis L., Rosaceae) using electrostatic techniques, *Journal of Horticultural Science & Biotechnology*, 76(2): 208-212.

Vaknin Y., Gan-mor S., Bechar A., Ronen B. & Eisikowitch D. (2001b), Are flowers morphologically adapted to take advantage of electrostatic forces in pollination, *New Phytologist*, 152:301-6.

Versteeg H. & Malalasekera W. (1995) *An introduction to computational fluid dynamics : the finite volume method*, Longman Scientific & Technical, New York.

Vieser W., Esch T. & Menter F. (2002) *Heat transfer predictions using advanced two-equation turbulence models*, CFX-VAL10/0602, Germany.

Wakelin R. (1985a) *Report on investigations relating to an artificial spray pollinating machine conducted at the University of Canterbury over November 1984*, unpublished, Chemical and Process Engineering, University of Canterbury, Christchurch, New Zealand.

Wakelin R. (1985b) *Artificial pollination of kiwifruit*, unpublished project report, University of Canterbury, Christchurch, New Zealand.

Waki K. & Takeuchi K. (1990) Pollen collecting method for artificial kiwifruit pollination: 1. Washing method by organic solvents, *Bulletin of the Faculty of Agriculture Tamagawa University*, (30): 59-72.

Wall S., John W. & Wang H.C. (1990) Measurements of kinetic energy loss for particles impacting surfaces, *Aerosol Science and Technology*, 12: 926-946.

Warrington I.J. & Stanley C.J. (1986) The influence of pre- and post-budbreak temperatures on flowering in kiwifruit, *Acta Horticulturae 175*, pp. 103-107.

Warsi Z.U.A. (1999) *Fluid dynamics: theoretical and computational approaches*, 2nd edn, pp 421-608, CRC Press, Boca Raton.

Werner H., Balashazy I. & Heistracher T. (2001) The relationship between secondary flows and particle deposition patterns in airway bifurcations, *Aerosol Science and Technology*, 35: 958-968.

Wesseling P (2001) *Principles of computational fluid dynamics*, pp 1-52, Springer Berlin.

Wilcox D.C. (1988) Reassessment of the Scale-Determining Equation for Advanced Turbulence Models, *American Institute of Aeronautics and Astronautics Journal*, 26(11): 1299-1310.

Wilcox D.C. (1993) *Turbulence Modelling for CFD*, DCW Industries Inc, La Canada, 460 pp.

Williams R.R. & Legge A.P. (1979) Pollen application by mechanical dusting in English apple orchards, *Journal for Horticultural Science*, 54(1):67-74.

Wilson G. (1990) Pollination: don't depend on the wind, *New Zealand Kiwifruit*, April: 14-15.

Woittiez R.D. & Willemse M.T.M. (1979) Sticking of pollen on stigmas: the factors and a model, *Phytomorphology*, 29:57-63.

Woolley D.J., Lawes G.J. & Lai R. (1988) Factors affecting fruit size, *New Zealand Kiwifruit Authority National Research Conference, New Zealand Kiwifruit Special Publication No. 2*, Rotorua, New Zealand, pp. 11-14.

Wright N.G. & Easom G.J. (1999) Comparison of several computational turbulence models with full-scale measurements of flow around a building, *Wind and Structures*, 2(4): 305-323.

Yakhot V. & Orszag S.A. (1986) Renormalisation group analysis of turbulence: I. Basic theory, *Journal of Scientific Computing*, 1(1): 3-51.

Yakhot V., Orszag S.A., Thangam S., Gatski T.B. & Speziale C.G. (1992) Development of turbulence models for shear flows by a double expansion technique, *Physics of Fluids A: Fluid Dynamics*, 4(7): 1510-1520.

Yakhot V. & Smith L.M. (1992) The renormalization group, the ε-expansion and derivation of turbulence models, *Journal of Scientific Computing*, 7(1): 35-60.

Ye Q., Steigleder T., Scheibe A. & Domnick J. (2002) Numerical simulation of the electrostatic powder coating process with a corona spray gun, *Journal of Electrostatics*, 54(2):189-205.

Zespri Kiwifruit Annual Report (2003) ZESPRI International Ltd, Mount Maunganui, New Zealand, 45 pp.

Zhang J. & Thorp T.G. (1986) Morphology of nine pistillate and three staminate New Zealand clones of kiwifruit, *New Zealand Journal of Botany*, 24: 589-613.

Zimon, A.D. (1982) *Adhesion of Dust and Powder*, 2nd edn, pp. 10, 69-91, Consultants Bureau, New York.

Appendix A

Paper presented in 3rd International Conference on CFD in the Minerals and Process Industries, Melbourne, Australia (2003)

MODELLING OF AIR FLOW AND POLLEN COLLECTION BY A SINGLE KIWIFRUIT FLOWER UNDER WIND AND AN AIR JET

Michael J.W. HII, John ABRAHAMSON and Patrick J. JORDAN

Chemical and Process Engineering, University of Canterbury, Christchurch, New Zealand.

ABSTRACT

Pollen capture by kiwifruit flowers is a central problem in the kiwifruit industry, both by natural wind flow and by artificial air jet application. A commercial CFD code is used here to simulate the 3-dimensional air flow field around a single female kiwifruit flower at full bloom. The flow solutions from these models are compared in the air velocity range measured in kiwifruit orchards and at various flow-attacking angles. Particle transport models are then used in order to build a robust predictive model of pollen behaviour around a kiwifruit flower under a pollen-loaded air-jet.

NOMENCLATURE

A_f projected area of flower $= 3.42 \times 10^{-3}$ m^2
N_p number of pollen collected
Re Reynolds number
η_f pollen collection efficiency

INTRODUCTION

To produce an exportable 100-g kiwifruit (*Actinidia deliciosa*), between 6000 and 12000 viable male pollens need to be deposited on the stigma of a female kiwifruit flower (estimated from the data by Goodwin, 2000). Insufficient fertilization is known to lead to unsatisfactory fruit size, shape and uniformity, which represents a decreased marketable value. However, this pollination level must be completed in the limited six-day flowering period annually when the stigma are receptive (Gonzalez et al., 1995). This imposes serious constraints on the natural wind and bee pollinators which are often hampered by the wet weather, the delay in flowering between male and female flowers and the lack of attraction by flowers to bees. As a result, artificial pollination has become more popular because it offers great flexibility in timing and is used to supplement the inadequate pollination by wind and bee pollinators. Among different types of wet or dry spray-based machine application (see review by Goodwin, 2000), the dry air jet appears to be more promising due to its simplicity. The major cost of artificial pollination comes from the relatively expensive pure pollen supply and the labour. There is a need to optimise the pollen collection efficiency. We studied the air flow and pollen transport around a single kiwifruit flower using the commercial CFD code, CFX-5, with the pollen concentration at the background level in an orchard and at a more concentrated level as in an air jet application. The artificial pollination is usually applied when there is 30 to 40 % flower opening. Thus, in previous work (Hii et al., 2002), we looked at the air flow field around the buds at different opening stages, namely half-open, full-open and flip-back. Results of pollen capture only for a full-open female flower are presented here.

MODEL DESCRIPTION

Figure 1 shows one of the more than 200 female kiwifruit flowers photographed in Te Puke orchard area, New Zealand from 9-10 November 2001. This collection was studied to extract the detailed geometry for a model flower.
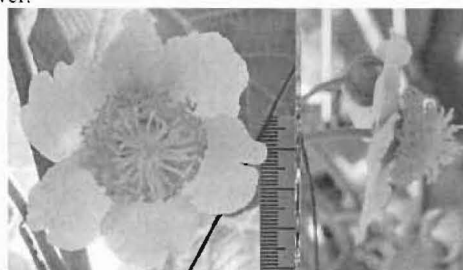
Figure 1: Front and side views of a full-open female kiwifruit flower (cv Hayward).

The flower model has an ovary, which is a truncated oblate spheroid 9.3 mm high, 9.0 mm diameter, and 3 and 7 mm diameter top and bottom (Figure 2).
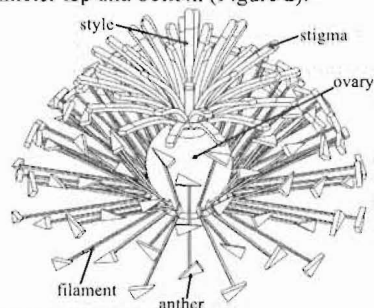
Figure 2: Flower model showing ovary, 36 stigma, 84 filaments and anthers. The filaments are 0.205×0.205 mm square rods, 14.2-15 mm long.

The ovary top has an expanding bush of 36 evenly spaced styles which are slightly curled but otherwise flat (0.9 mm in width, 0.5 mm in thickness and 9.5-10.5 mm in length). For economy of mesh, we did not fillet the edges of the style nor model it as a cylinder. Each style on an actual flower has a stigma at its tip (see Figure 3), which is the area of interest because only the pollen deposited here will germinate. A real stigma occupies about half of the style's circumferential surface. We define a pair of stigmatic surfaces at the tip of each style i.e. one on top and another on the bottom, to take into account that a real stigma can orient in any direction. Eighty four filaments, with a triangular anther (1.25 mm width $\times$ 2.7 mm high $\times$ 0.58 mm thick) at each end, extend from the base of the ovary and surround it. Although for ease of computation

the number of filaments is reduced from an average of 183 on a real flower (Hopping and Jerram, 1979), its density is visually comparable to that of an actual flower shown in Figure 1. The model flower has 6 petals, the average on most female flowers but some may have >7 petals. 3 pairs of overlapped 0.75-mm-thick petals (primary and secondary), with a gap along the overlap, are evenly spaced around the ovary in order to include the effect of flow leakage through the gap between the primary and secondary petals. The primary petal is constructed using the radial variation profile obtained by analysing a photo such as Figure 1. The secondary petal is then drawn to obtain a linear gap along the overlap up to a maximum gap of 5 mm. 6 sepals with their base and a 77-mm long stem (ϕ 2.73 mm) are placed under the petals. Any small gaps or isolated regions are eliminated manually for efficient meshing and better solver convergence.
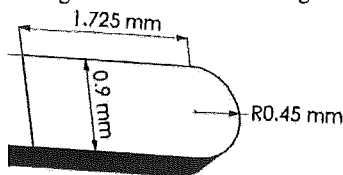
Figure 3: Shape of the model's planar stigmatic surface.

Simulation of wind pollination

We first studied the collection mechanism of windborne pollen by the flower under the average measured air velocity of 1 m/s (cf. maximum of 1.25 m/s recorded by Costa et al., 1993) from different directions, namely front, side and back. These simulate the wind pollination under the vine with the draft in random directions. The flower is treated as a bluff body in a computational domain shown in Figure 4 for a frontal flow (note that the air jet nozzle is not included in this wind simulation). The preliminary observations in a wind tunnel found that the petals of a 1-day-old flower remain rigid up to 1.8±0.1 m/s. The inlet and outlet boundaries (section 400 × 400 mm) are 200 mm and 350 mm away from the centre of the flower respectively. Other boundaries of the domain are of the "Opening" type with the Cartesian velocities set to be parallel to the inlet flow. The outlet boundary has a relative pressure of 0 Pa. The flower surfaces including the stigma are smooth with no slip.
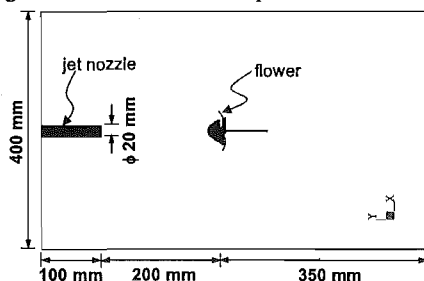
Figure 4: Schematic diagram of full-scale computational domain with an air jet nozzle in front of the flower.

The localized characteristic Re ranges from 50 to 4400 based on the dimension of style and the largest overall flower diameter (ϕ 66 mm). Since the localized flow varies from laminar coherent eddying to turbulent, we considered laminar, RNG k-ϵ (Yakhot et al., 1992) and SST (Menter, 1994) models. We found that all models gave a similar overall flow pattern but different

magnitudes. RNG k-ϵ is chosen because its flow prediction is consistently between the other two models. It is applied with the built-in scalable wall treatment (Vieser et al., 2002). The incompressible air flow field is solved at steady state and isothermally at 25 °C, with a uniform inlet velocity and an assumed inlet turbulence intensity of 3.7 % in the absence of field data.

A maximum daily male pollen loading of 14.5 million grain/m^2/day in the orchard air has been reported by Malaboeuf et al. (1997), but the authors did not specify the average daily draft velocity. So, we decided to use our measured average velocity of 1 m/s in the orchard and this gives ~ 168 grain pollen/m^3 air. This means in our computational domain of 88 × 10^{-3} m^3, there are only ~ 15 pollen grains at any time and thus only the one-way fluid-particle coupling is considered. Since the injection of 15 pollen on the inlet boundary is not going to give a representative estimation of pollen collection efficiency from wind, 30000 pollens are injected uniformly on a ϕ 66-mm circular plane (with centre at the centre of the inlet boundary) which represents a projected area of the flower. The pollen passing through this circular plane may possibly collide and collect inertially on the flower. The pollen, having a solid density of 1330 kg/m^3 (Ferguson & Pusch, 1991) and an average diameter of 22 µm (Hopping, 1990; actual pollen are oblate spheroidal) are introduced at 1 m/s.

With the air as the continuous phase, the pollen (dispersed phase) trajectories are calculated in steady state using the Lagrangian framework (CFX-5.6 Manual, 2003; see the general equations in Ranade, 2002). The simulated pollen experience drag force and turbulent dispersion, but not gravitational force (the pollen settling velocity is low (~ 10 mm/s) compare to its superficial velocity of 1 m/s). The presence of papillar (Gonzalez et al., 1995) and liquid exudate (in the early morning) mean the pollen will stay on the stigma upon collision. Since it is unknown how the pollen will behave on the other surfaces of the flower, we assume that all the contacted pollen are captured. Other pollen leave the domain through the Opening and outlet boundaries.

Simulation of air jet sprayer

Following the results from the simulation of wind pollination, here we focus on introducing a pollen-loaded air jet onto the front of the flower (see domain setup in Figure 4). There are four initial air jet velocities - 0.5, 1.0, 2.0 and 3.0 m/s. The tubular flow is allowed to develop for 100 mm before being discharged from the ϕ 20-mm circular nozzle. The nozzle is located at the centre of the indicated domain boundary in Figure 4. All the side boundaries of the domain are assigned to be of the Opening type with a relative pressure of 0 Pa to handle the expanding air jet. The same turbulence model and wall treatment are applied to the air flow which is solved as in previous case, with all the walls regarded as smooth with no slip.

To find the pollen collection efficiency, the air jet releases 30000 non-coupled pollen which are tracked using the steady state Lagrangian approach. To estimate the effect of momentum coupling between the air and the pollen, we assume that 12000 pollen need to be collected by each flower at a collection efficiency of 5 % i.e. 240000 pollen

516

or 1.78-mg pollen/flower to be sprayed. A 1-second spray per flower gives a mass loading of 0.92-0.16 %wt in an air jet of 0.5-3.0 m/s. Despite this low mass loading, we still included the two-way coupling by employing a smaller set of pollen number (1000; using the recommendation in CFX-5.6 Manual, 2003) with a specified pollen mass flow rate of 1.78 mg/s. It has been found that this does not alter the air flow field. The particle-particle interaction is unlikely because the pollen volume fraction is 8.5×10^{-6} to 1.4×10^{-6} in this initial jet velocity range. All the walls, except for the jet nozzle, are assumed to be sticky to the pollen. The particle tracking also finishes at Opening boundaries.

Gridding

Figure 5 shows the gradual refinement of unstructured mesh closer to the flower surfaces. The number of elements is about 1 to 1.4 million with the maximum cell edge length ≤ 13 mm and the finest 0.1 mm. To promote better flow prediction in the region of interest, the styles and stigmas are covered with fine prismatic cells.
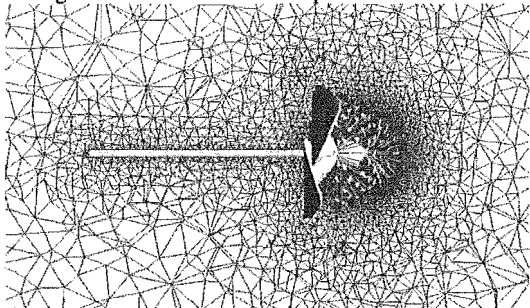
Figure 5: Generated mesh around a full-open flower.

RESULTS AND DISCUSSION

Collection of airborne pollen from wind

The streamline plots in Figure 6(a) to 6(c) for different approach directions show that the predicted flow fields are non-symmetrical and there are at least two recirculation regions, a larger recirculation downstream of the flower and some small eddies in the airspace between the stigma and the petals. The spiralling large wakes extend up to ~ 1.6 flower diameters downstream from the flower centre for the front and back flows. The pollen tracking calculations with side flow (Figure 6(e)) show that these large wakes help to redirect the pollen back to the stigmatic areas for secondary collection after the primary collection through the approaching flow. Under back flow, the role of the downstream wake becomes very important because all of the collected pollen on stigma rely on them. Figure 6(f) shows that most of the pollen follow the streamlines that are diverted to the sides by the petals. The large downstream vortices are found to incorporate these pollen grains and direct them straight to the stigma. This kind of backwards pollen collection has also been observed on other plants e.g. conifer ovulate cones (Niklas, 1984). However, this recirculated pollen collection is not important in front flow because of the impedance from the petals (Figure 6(d)). On the other hand, the eddies in the vicinity of the filament and stigma bushes have been found to trap the pollen. Although we expected that this will present more chances for trapped pollen to be deposited on the stigma, the simulations did not find any pollen collected in this way. This is because we assume that the filament and anther surfaces are sticky like the stigma. Thus the trapped pollen grains are filtered by the filament and anther surfaces before they reach the stigma.
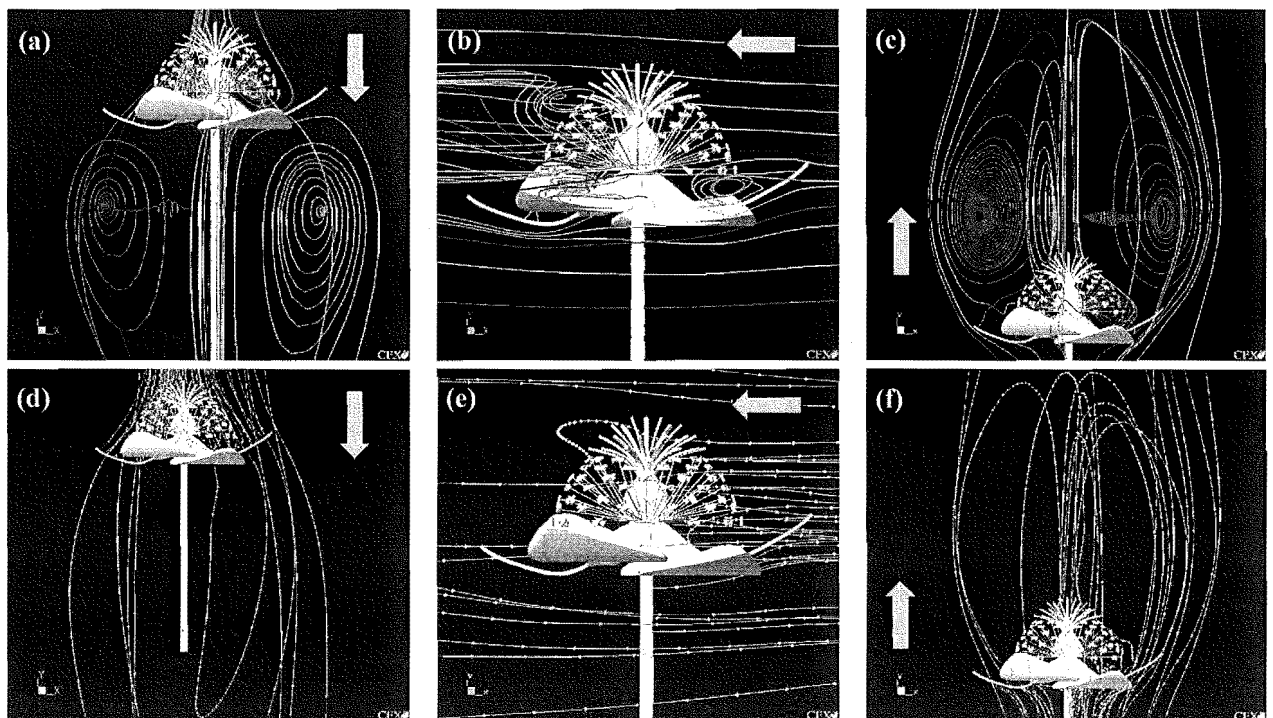
Figure 6: (a), (b) and (c) are the predicted air flow field around a single full-open flower under 1-m/s flow from the front, side and back respectively (as shown by the arrows). The corresponding calculated trajectories of a cloud of pollen are shown in (d), (e) and (f). The separation between pollen along a trajectory is 0.01 s.

The pollen collection efficiencies of stigma calculated based on the total number of pollen injected in different directions (through a circle the same diameter as the flower) are shown in Figure 7. It must be noted that these efficiencies have been halved because we defined a pair of stigmatic surfaces at the end of each style.
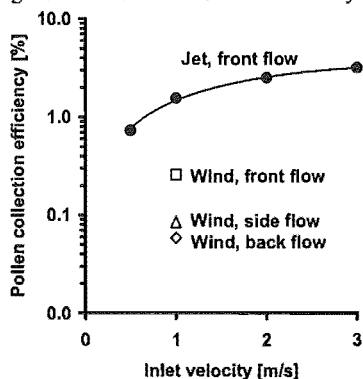
Figure 7: Calculated collection efficiency of windborne pollen and air-jet sprayed pollen by stigma of a full-open flower. The log scale is used for pollen collection efficiency.

According to Figure 7, the stigma capture the most pollen from a pollen cloud approaching in front flow (0.26 %), predominantly by direct impaction. The opposite is true for back flow. Due to our assumption of sticky surfaces, other surfaces of flower have been found to collect 10, 12 and 5 % of total pollen under front, side and back flows respectively, particularly on the petals. So, the actual pollen collection efficiency on the stigma may be higher than those shown in Figure 7 if the pollen rebound elastically on other flower surfaces.

Based on the efficiencies (η_f) in Figure 7, we estimate the number of windborne pollen collected by inertial impaction over 6 days under the maximum pollen loading reported by Malaboeuf et al. (1997) using Equation (1).

$$N_p = 14.5 \times 10^6 \text{ pollen/m}^2\text{/day} \times A_f \times \eta_f \times 6 \text{ days} \qquad (1)$$

A single female flower is expected to receive only 774, 238 and 179 windborne pollen grains in front, side and back flows respectively. This agrees with the experimental results from Costa et al. (1993) that wind pollination alone is insufficient.

We examined the number of pollen collected on each pair of stigma at the end of each style after 30000 pollen fed, and found that less than half of the 72 defined stigma have collected pollen (see Figure 8). No pollen is found to be deposited on the bottom face in each pair of stigma. If the bottom stigmatic face is regarded as leeward face, then all of the simulated pollens are deposited by direct interception on the forward faces (see particularly Figure 6(d) and (f)). The results with the bottom stigmatic surfaces may be different if the filaments and anthers are assumed to be non-sticky i.e. the small eddies within the flower enclosure can then deliver the pollen to the bottom stigmatic surfaces.

Although the draft in the vine is likely to have larger eddies than the flower itself, our simulated flow fields based on a uniform incoming flow are not expected to be

significantly different to the actual ones. Since the simulation of wind pollination shows that pollen collection is favoured by the front flow, we now focus on spraying the concentrated pollen flow onto the front of a single female flower.
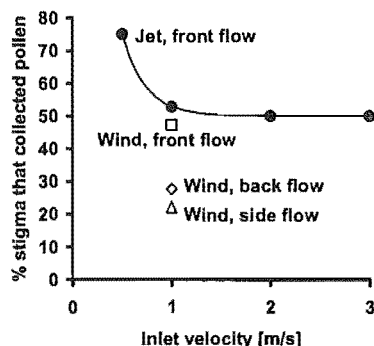
Figure 8: Percentage of 72 stigma that has windborne or sprayed pollen deposited on it, after 30000 were trialled in the simulation.

Collection of airborne pollen from air jet

With an air jet, the simulations show that the downstream eddies (see Figures 9(a) and 9(b)) are not as tidy and axisymmetrical as in the previous simulations with a uniform flow inlet where the downstream vortices have their centres along the ring of about the same diameter as the flower (see Figure 6(a)). This ring is ~ 0.54 flower diameters away from the flower centre. The pollen-loaded air jet also spreads more widely than is the case with uniform front flow after the impingement on the petals, likely due to the absence of surrounding flow. The comparison between Figure 9(a) and 9(b) shows that the degree of spread depends on the strength of jet.

Figure 10 is the profile of predicted centreline jet velocity from the discharge to the top of the ovary. The profile displays a slightly higher than initial jet velocity in the immediate discharge region. All four initial jet velocities then exhibit quite similar exponential decay although the lower initial jet velocity seems to have a faster decay. At around 160 mm away from the nozzle, there is a sudden drop of velocity due to the close distance approaching the ovary. This distance (~10 mm from the stigma) may be regarded as the stopping distance for the pollens to decelerate and be collected by the stigma. A plot of velocity profile across the stigma-style bush (Figure 11) shows that there is a stagnation region in the central bush. The velocity in the outer parts of the bush then increases up to ~ 60 % of the initial jet velocity before decreasing again, where the air flow sweeps past the stigma bush.

The jet Re number in this work ranges from 667 to 4000 based on the range of initial jet velocity used. So, strictly speaking the laminar model should be considered. However, we decided to select RNG k-ε based on the flower Re number. We compare the centreline velocity profile at initial jet velocity of 3 m/s with the turbulent free-jet formulae from Tuve (1953) and this is plotted between 140 and 160mm in Figure 10, the range where Tuve's formulae is valid. Our calculated velocity decay is under-estimated by 10.7 to 23.8 %. This may be because the RNG k-ε model has under-predicted the dissipation rate at this intermediate Re range here.
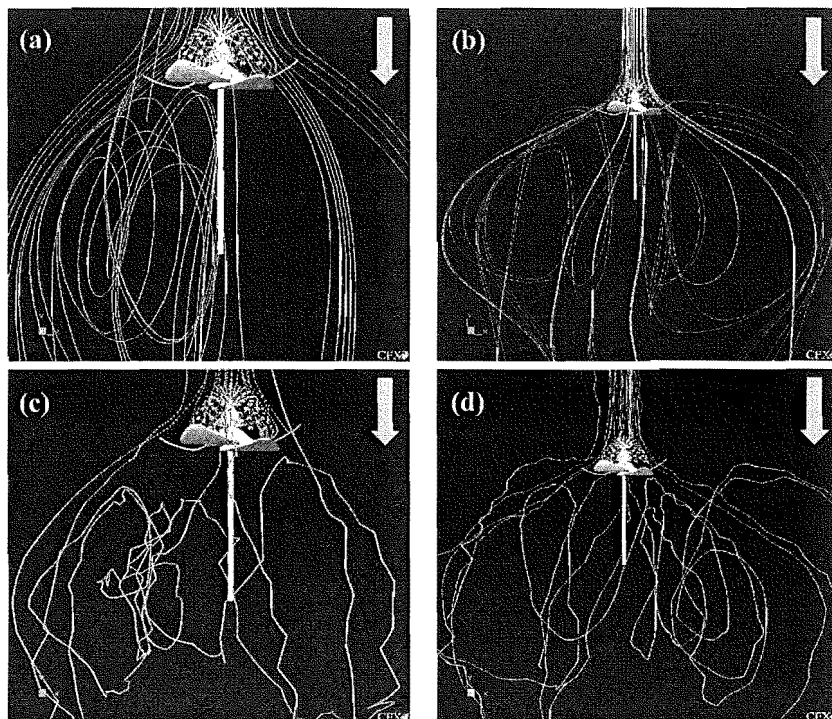
Figure 9: Simulations; (a) and (b) are the streamline plots from an air jet directed towards the front of the flower at 0.5 and 2.0 m/s respectively. The pollen movement around the flower under the respective jet velocities are shown in (c) and (d). The arrows indicate the direction of the air jet.
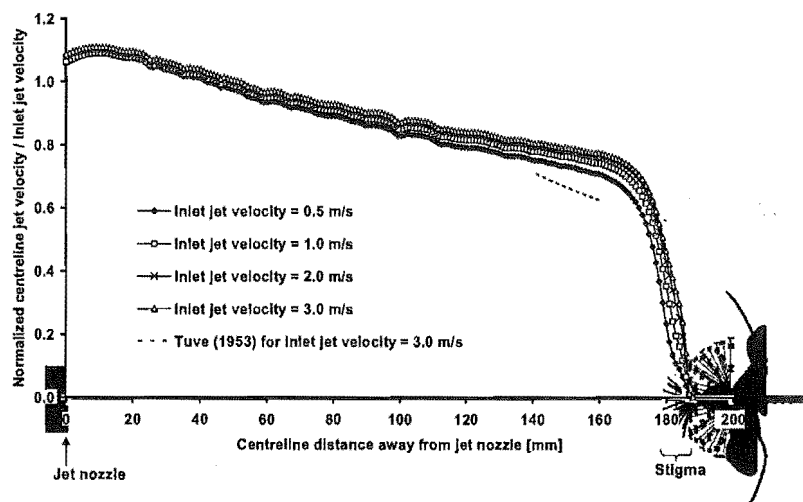
Figure 10: Jet centreline velocity.

The pollen trajectories under an air jet (Figure 9(c) and 9(d)) follow the overall pattern of streamlines to some degree but not the exact path. They appear to be more zigzagging, random and chaotic than those under the uniform velocity inlet (Figure 6(d)). There are a significant number of pollen grains trapped in the downstream vortices. But as mentioned before, the petals prevent any of this pollen from being re-collected by the stigma.

A higher velocity jet is found to give better collection efficiency as shown in Figure 7 (refer to values in Table 1). However, the gain in collection efficiency decreases with the increasing jet velocity. Considering the front flow in Figure 7, a possible reason why the flower collects more pollen in an air jet than in wind simulation is because in the latter case, the pollens are released over a larger projected area (ϕ 66 mm) compare to the nozzle diameter (ϕ 20 mm).

Based on the collection efficiencies in Figure 7 and the minimum required pollen capture of 6000 per flower, we estimate the minimum pollen loading of spray at different initial air jet velocities onto a single flower for one second (Table 1). Table 1 indicates that, for a circular ϕ 20-mm nozzle, by an increase of air jet from 0.5 m/s to 3.0 m/s will enable at least 3 more flowers to be sprayed for the equivalent amount of pollen.

Referring to Figure 8, it is found that only in air jets of 0.5 and 1.0 m/s have the bottom surface of each stigma pair at the end of each style been predicted to collect any pollen. This is indicated by the points with % stigma that collected pollen of more than 50 %. For an air jet at 0.5 m/s, about half of the bottom stigmatic faces are shown to have pollen deposited. It may be that at higher air jet velocity, the inertia of the pollen grains is too high to allow them to be collected by back-recirculation behind a single style. The effect of electrostatic in enhancing this type of collection is being studied.

Since the orientation of actual stigma is random, a lower air jet should be used, despite the lower collection efficiency, if a more consistent deposition over all the stigma is desired. Although the required total number of pollen for full fertilization does not have to be collected evenly by all the stigma (Howpage et al., 1995), it is known that the collection of too many pollen on a single flower can cause a lower number of seeds due to competition between pollen tube germinations (Hopping, 1990). From this perspective, there should be a compromise between the consistent pollen deposition and the collection efficiency in order to avoid local congestion on a stigma.
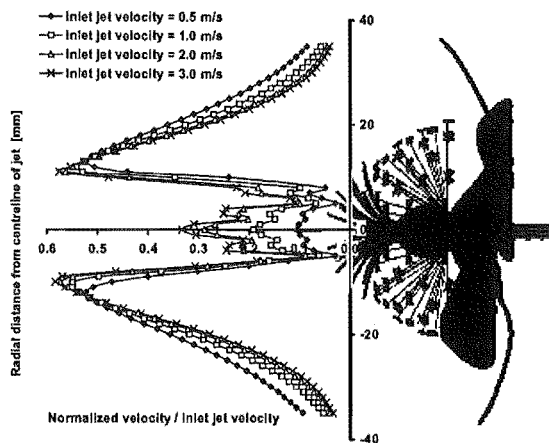
Figure 11: Velocity profile across the stigma bush.

In this flower model, the stigma are positioned at 2.3, 5.9, 8.6 and 10.6 mm along the horizontal stigma bush radius. The average number of pollen collected by each stigma generally increases towards the outer edge of the bush, but the maximum are predicted on stigma at either 5.9 or 8.6 mm.

Air jet velocity [m/s]	η [%]	Min. number of pollen per spray of one flower	Mass flow rate of pollen [mg/s]
0.5	0.73	8.2×10^5	6.1
1.0	1.54	3.9×10^5	2.9
2.0	2.48	2.4×10^5	1.8
3.0	3.17	1.9×10^5	1.4

Table 1: Minimum pollen loading required for capture of 6000 at different air jet velocities for a ϕ 20-mm circular nozzle.

Considering the practicality in placing a ϕ 20-mm jet nozzle accurately in front of a flower in the orchard, a larger nozzle size is expected to be exercised between this and the pollen injection area in wind simulation.

CONCLUSION

The simulations of wind pollination at the average draft velocity in an orchard show that a single female flower collects the most pollen in front flow compared to side and back flows. Large downstream recirculations are responsible for conveying the airborne pollen to the stigma in back flow. The depositions of pollen on stigma with uniform inlet velocity are from direct impaction only. On the other hand, the local eddies around each style are shown to assist the pollen collection at a low air jet velocity. This effect disappears at higher jet velocity as the bulk inertia from the incoming air jet dominates. The pollen collection increases with the increasing air jet velocity but with a gradual decrease in the gain in efficiency. An example of the pollen loading recommended for a ϕ 20-mm circular nozzle at different jet velocities has been provided.

ACKNOWLEDGEMENT

REFERENCES

CFX-5.6 Manual (2003), ANSYS.

COSTA, G., TESTOLIN, R. and VIZZOTO, G., (1993), "Kiwifruit pollination: an unbiased estimate of wind and bee contribution", *NZ J. of Crop and Hort. Sci.*, **21**, 189-195.

FERGUSON, A.M. and PUSCH, W.M., (1991), "Development of mechanical dry-pollen application to kiwifruit", *Acta Horticulturae 297*, ISHS, 299-304.

GONZALEZ, M.V., COQUE, M. and HERRERO, M., (1995), "Papillar integrity as an indicator of stigmatic receptivity in kiwifruit (*Actinidia deliciosa*)", *J. Exp. Bot.*, **46**, 263-269.

GOODWIN, R.M., (2000), *Zespri Innovation Kiwifruit Pollination Manual*, Zespri Innovation & The Hort. Research of New Zealand, New Zealand.

HII, M.J.W., ABRAHAMSON, J. and JORDAN, P.J., (2002), "CFD simulation of flow around a single kiwifruit flower", *5th Int. Symp. on Kiwifruit*, ISHS, Wuhan, China, September 15-20.

HOPPING, M.E., (1990), "Floral biology, pollination, and fruit set", In: WARRINGTON, I.J. and WESTON, G.C. (eds.), *Kiwifruit: Science and Management*, Ray Richards Publisher, Auckland, 71-96.

HOPPING, M.E. and JERRAM, E.M., (1979), "Pollination of kiwifruit (*Actinidia chinensis Planch.*): stigma-style structure and pollen tube growth", *NZ J. Botany*, **17**, 233-240.

HOWPAGE, D., VITHANAGE, V. and SPOONER-HART, R.N., (1998), "Pollen tube distribution in the Kiwifruit (*Actinidia deliciosa* A. Chev. C. F. Liang) pistil in relation to its reproductive process", *Annals of Botany*, **81**, 697-703.

MENTER, F.R., (1994), "Two-equation eddy-viscosity turbulence models for engineering applications", *AIAA J.*, **32**, 1598-1605.

MALABOEUF, F., VAISSIERE, B.E. and COUR, P., (1997), "Pollen flow in the atmosphere of kiwifruit (*Actinidia deliciosa*) orchards", In: SFAKIOTAKIS, E. and PORLINGIS, J. (eds.), *3rd Int. Symp. on Kiwifruit, Acta Horticulture*, 413-420.

NIKLAS, K.J., (1984), "The motion of windborne pollen grains around conifer ovulate cones: implications on wind pollination", *Amer. J. Bot.*, **71**, 356-374.

RANADE, V.V., (2002), *Computational Flow Modelling for Chemical Reactor Engineering*, Academic Press, San Diego, 85-122.

TUVE, G.L., (1953), "Air Velocities in Ventilating Jets", *Heat. Piping Air Cond.*, **25**, 181-191.

VIESER, W., ESCH, T. and MENTER, F., (2002), "Heat transfer predictions using advanced two-equation turbulence models", *AEA Technology validation report CFX-VAL10/0602*, Germany, www.software.aeat.com, 1-69.

YAKHOT, V., ORSZAG, S.A., THANGAM, S., GATSKI, T.B. and SPEZIALE, C.G., (1992), "Development of turbulence models for shear flows by a double expansion technique", *Physics of Fluids A: Fluid Dynamics*, **4**, 1510-1520.

Appendix B

Paper presented in 3rd International Symposium on Kiwifruit, Wuhan,

China (2002)

CFD Simulation of Flow Around a Single Kiwifruit Flower

M.J.W. Hii, J. Abrahamson and P.J. Jordan
Department of Chemical & Process Engineering
University of Canterbury
Christchurch, New Zealand

Abstract

Pollination by using air jets offers flexibility in timing and other advantages, and is becoming increasingly popular in the kiwifruit industry. A quantitative analysis of the parameters affecting collection of pollen by flowers from the air is expected to be valuable to improve the pollination efficiency. A commercially available computational fluid dynamics (CFD) code is used here to simulate the 3-dimensional air flow field around a kiwifruit flower. The volume around the complex flower geometry at different bud opening stages is divided ("meshed") using an unstructured grid. Due to the large ratio of the biggest to the smallest dimensions of the flower components, both laminar and turbulent models have been used. The flow solutions from these models are compared in the air velocity range measured in kiwifruit orchards and at various flow-attacking angles. Inertial collection of pollen by the stigma from normally loaded orchard air is found to be inadequate to achieve satisfactory pollination, confirming general experience.

INTRODUCTION

Artificial pollination is an important supplement to ensure adequate pollination of kiwifruit (*Actinidia deliciosa*). The performances of natural vectors (wind and bees) are affected by the adverse weather, non-ideal timing of anther dehiscence/pollen release (Goodwin, 1986) and, for bees, lack of attraction by flowers (Palmer-Jones and Clinch, 1974). The use of a machine pollinator offers high flexibility to use the few days (about 6; Gonzalez et al., 1995) of stigma receptivity to deliver the >3000 and >6000 viable male pollen needed for a marketable ($\geq$70 g) and a 100-g fruit respectively (estimated from the data by Goodwin, 2000). Among many currently used wet or dry spray-based machine applications (see review by Goodwin, 2000), the dry air sprayer appears to be the more promising because of its simplicity. There is however a lack of quantification of the mechanism and efficiency of air spraying, and also natural wind pollination. For this reason, we look at both natural pollination, and artificial pollination with a jet of air. Here, we report the air flow field around a single female kiwifruit flower simulated using a commercially available computational flow dynamics (CFD) package, CFX-5.5.

MATERIALS AND METHODS

Full scale flowers with three different opening configurations (half-open, full-open and flip-back) were constructed in Solidworks 2001. Each had an ovary modelled as a truncated oblate spheroid 9.3 mm high, 9.0 mm diameter, and 3 and 7 mm diameter top and bottom. 36 slightly curled and flat stigma-styles (the average number on a flower, see Hopping and Jerram, 1979) were evenly spaced on top of the ovary to form an 'expanding bush' (Fig. 1). They were 0.9 mm in width and 0.5 mm in thickness, with a length of 11.1

mm, with semi-spherical ends. The ovary was surrounded by 84 filaments, less than the average number on a flower (183; Hopping and Jerram, 1979) for ease of computation. The density of this reduced number of filaments was found visually to be comparable to that of a real flower (Fig. 1 (b)). Each filament extends from the bottom of the ovary. The filament spacing evolves from alternate (a) and (b) rows around the ovary as shown in Fig. 2.

Although a female flower may have 5 to 7 petals (occasionally more than 7), 6 petals are chosen because this is the most frequent number. Each petal, 0.75 mm thick as taken from the measured mean thickness of the petal middle, is generated by a straight line perpendicular to a chosen petal centreline profile. The length of the line and the profile followed detailed geometry parameters obtained from the study of > 200 Hayward flowers during in a field trip to Te Puke orchard area, New Zealand, 9 to 20 November 2001. This radial variation data is extracted by analyzing photos (see an example in Fig. 1 (b)) taken during the field trip. In order to simulate the flow leakage through the gap between petals, a pair of petals (primary and secondary) was modelled (see Fig. 3 (a) and (b)) and 3 pairs evenly spaced around the ovary. The secondary petal was drawn such that the petal gap was linear with distance along the overlap with a maximum gap of 5 mm. The edges of the petal are rounded. The sepal width follows the radial variation of their respective primary and secondary petals until about 5 mm from the ovary, reducing to zero at around 15 mm.

A sepal base and a 77-mm long stem (ϕ 2.73 mm) are also included under the ovary. Any isolated or small gaps, particularly in the space between the sepals and the stem, are filled to promote better solver convergence. More details can be obtained form the authors.

The volume around the flower model was then meshed using unstructured grids in a 550 mm long bounding domain with the centre of the ovary bottom 200 mm away from the inlet boundary (section 400 × 400 mm). CFX-5.5 works with small volume elements where the mass and momentum balances are solved. Finer prismatic elements (constituting an "inflated boundary"; see AEA, 2001) were applied at the surfaces of stigma and styles for better flow prediction in this region of interest. The total number of volume elements (tetrahedral, pyramidal and prisms) is about 10^6 for all configurations with the maximum cell edge length of all ≤ 15 mm, and the finest 0.1 mm. Fig. 4 shows for flowers of different opening the gradual refinement of meshes (using multiple mesh controls) closer to the surfaces.

The flow past the rigid flower was solved at steady state and isothermally for incompressible air at the reference pressure of 10^5 kPa and temperature of 20 °C. We set the air flow to flow onto the flowers from the front, side and back, at 1 and 3 m/s. These two velocities were the average and the maximum recorded respectively under the vine during the abovementioned field trip (cf. maximum of 1.25 m/s recorded by Costa et al., 1993). At 1 m/s, the localized characteristic Reynolds number, Re, describing inertial effect compared to viscous effect ranges from 143 to 5291, based on the smallest dimension of filament and the largest overall diameter of the flip-back flower (ϕ 75.71 mm) respectively. This Re range is tripled at 3 m/s i.e. 430 to 15873. This means the localized flow varies from laminar coherent eddying (for Re of several 100) to turbulent.

This prompted us to use both laminar and turbulence models here. A laminar model is suitable only for low Re number where viscous fluid force is dominant. For turbulence, the widely used industry standard linear two-equation k-ε turbulence model is reasonably accurate and numerically robust (AEA, 2001). However, the ε-equation has

severe limitations in the near-wall region where it over-predicts the turbulent length scale giving late onset of separation and under-predicted amount of separation ("separation" refers to situations involving recirculation eddies). The alternative is to use the k-ω turbulence model that is robust for complex applications and allows reduced resolution for the near-wall calculations. But solutions of the ω-equation show too strong a sensitivity to values of ω outside the boundary layer in the main stream. We decided to compare the laminar model, RNG k-ε model (an improved k-ε based on Renormalization Group theory, which is more successful for some separated flows) and the Shear Stress Transport model (SST) that shows highly accurate onset and amount of flow separation under adverse pressure gradients). This latter uses the k-ω model near the wall and k-ε model away from the wall with a blending factor to make the transition gradual.

Uniform velocity was assumed on the inlet boundary with *relative* pressure of 0 kPa on the outlet boundary and no slip (zero velocity) at the surface of the flowers. The other boundaries of the flow domain were represented as symmetry planes. For turbulent models, the program default inlet turbulence intensity of 3.7 % and an auto-computed length scale for grid generation were used in the absence of proper user data. In the RNG k-ε model, we chose the built-in scalable wall-function in which the grid can be refined consistently and independent of the Re number of the application. The SST model carries out an automatic close-to-wall treatment.

RESULTS AND DISCUSSION

Comparison of flow models

We found for the open flower with flow from the back, that all models (laminar, RNG k-ε and SST) displayed the same flow pattern but gave different magnitude (Fig. 5). RNG k-ε was found to consistently show a flow prediction consistently between the other two models, as shown by the example of v- (vertical) velocity profile at the stigmatic region (Fig. 5 (b)). Their differences mean that 54 combinations (based on 3 flow models, 3 flower openings, 2 velocities and 3 flow directions relative to flowers) need to be simulated with some of them to be validated through the experimental flow visualizations.

Convergence and computational time

A root-mean-square residual target of 10^{-3} is satisfactory in solving mass and momentum balances for the laminar and RNG k-ε models, but 10^{-4} is needed for the SST model. Depending on the complexity of the petal opening and the type of flow models, the solver requires 3 to 9 hours for satisfactory solutions.

Flow field around a single kiwifruit flower

Fig. 6 (a) to (i) show the flow patterns around the flowers of 3 different petal openings for 3 different flow directions, predicted by the RNG k-ε model at an approach velocity of 1 m/s. All petal openings show at least two regions of recirculation, a larger recirculation downstream of the flower and smaller eddies in the airspace between the stigma and the petals. The predicted non-symmetrical flow fields here agree well with the smoke tests on kiwifruit flowers and models of them carried out by Hongladarom (1988) (Fig. 7). The spiralling large wakes direct the pollen backwards to the stigma area for a secondary pollen collection after the primary collection through the approaching flow. This pollen 'recycle' phenomenon has also been observed on other plants e.g. conifer ovulate cones (Niklas, 1984). This secondary collection is more important with back flow than for front and side flow because the petals are not expected to greatly impede the

latter flows. The eddies in the vicinity of the filament and stigma bushes give longer residence time and more chances for pollen to be deposited on the stigma.

Since the Stokes numbers (Stk) (describing the inertial pollen deviation from the streamline) for all flowers are < 0.1 (see Stk_f in Table 1), the pollen trajectories are not expected to deviate significantly from the streamlines shown in Fig. 6. The streamlines past the stigma are found to be perpendicular to their receptive surfaces, which suggests a genetic selection of the kiwifruit flower where stigma are oriented to give the maximum pollen collection through inertial impact. Our simulations show that the side flow towards full-open and flip-back flowers gave the highest average localised velocity around stigma (see U_s in Table 1) and hence the highest localized collection efficiency (see η_s in Table 1). This is contratory to our first expectation that the front flow will provide the maximum inertial collection. In fact, the front flow towards a half-open flower gives the lowest η_s, possibly due to the stagnation effect of an impinging air jet.

Our estimation of the overall flower collection efficiency (η_f in Table 1) shows that 7 to 159 out of 10000 pollen will be captured by the stigma of flowers for different openings at 1 m/s approach velocity. Using the maximum daily pollen loading in the air of 14.5×10^6 grain/m^2/day from Malaboeuf et al. (1997), 133 to 1740 pollen are expected to be deposited through inertial impaction on the stigmatic surface of a single pistillate flower over 6 days (Fig. 8). This indicates that the inertial collection from normally loaded wind is insufficient to achieve the required pollination level, agreeing with the experimentation results from Costa et al. (1993). Thus, in order to deliver >3000 pollen by inertial collection on a full-open ϕ 68-mm pistillate flower (from Hopping, 1990) with a front air jet at 1 m/s, >0.57 billion grain/m^3 (or 4 mg-pollen/L-air) needs to be sprayed, if the jet is on the flower for one second. This pollen loading can be reduced with the use electrostatic charging which is known to enhance the pollen collection (Cobert et al., 1982). Since the pollen is larger than 1 μm, Brownian motion is not expected to contribute any pollen collection.

In the vine, although the incoming flow is likely to have larger eddies than the flower itself, the actual flow field is not expected to be significantly different to the prediction here. Our simulations at 1 and 3 m/s found that both approach velocities give similar recirculation patterns with their magnitudes in proportion to the approach velocity. These flower models will also be used in the near future to simulate pollen transport under an electrostatic influence.

CONCLUSION

The CFD-simulated flow fields around a single kiwifruit flower of different petal openings and under different approaching airflow directions show large eddies formed downstream of the flower and small eddies in the airspace close to the stigma. Based on these flow fields, the inertial collection of pollen from normally loaded wind is estimated to be inadequate to achieve sufficient pollination. The pollen loading possible using an air-jet sprayer has been recommended.

Literature Cited

AEA Technology. 2001. CFX-5 Documentation.

Corbet, S.A., Beament, J. and Eisikowitch, D. 1982. Are electrostatic forces involved in pollen transfer? Plant, Cell and Environ. 5:125-129.

Costa, G., Testolin, R. and Vizzotto, G. 1993. Kiwifruit pollination: an unbiased estimate of wind and bee contribution. New Zealand J. Crop and Hort. Sci. 21:189-195.

Ferguson, A.M. and Pusch, W.M. 1991. Development of mechanical dry-pollen application to kiwifruit, Second Int'l Symp. On Kiwifruit, Acta Hort. Palmerston North, New Zealand 18-20 February. p. 299-303.

Gonzalez, M.V., Coque, M. and Herrero, M. 1995. Papillar integrity as an indicator of stigmatic receptivity in kiwifruit (*Actinidia deliciosa*). J. Exp. Bot. 46: 263-269.

Goodwin R.M. 1986. Kiwifruit flowers: anther dehiscence and daily collection of pollen by honey bees. New Zealand J. Exp. Agri. 14:449-452.

Goodwin, R.M. 2000. Zespri Innovation Kiwifruit Pollination Manual. Zespri Innovation Company Limited & The Horticulture and Food Research Institute of New Zealand Limited.

Hongladarom, K. 1988. Development of a biosensor for kiwifruit pollination. Honours project. Department of Chemical and Process Engineering, University of Canterbury. (Fig. 7 from video of this work).

Hopping, M.E. 1990. p. 71-96. In: I.J. Warrington and G.C. Weston (eds.), Kiwifruit: Science and Management, Ray Richards Publisher.

Hopping, M.E. and Jerram, M.E. 1979. Pollination of kiwifruit (*Actinidia chinensis* Planch.): stigma-style structure and pollen tube growth. New Zealand J. Bot. 17:233-240.

Kanaoka, C. 1997. p. 680-682. In: K. Gotoh, H. Masuda and K. Higashitani (eds.), Powder Technology Handbook, 2nd edn, Marcel Dekker, Inc.

Malaboeuf, F., Vaissiere, B.E. and Cour, P. 1997. Pollen flow in the atmosphere of kiwifruit (*Actinidia deliciosa*) orchards. Proc. Third Int'l Symp. On Kiwifruit, Acta Hort. 444. 1:413-418.

Niklas, K.J. 1984. The motion of windborne pollen grains around conifer ovulate cones: implications on wind pollination. Amer. J. Bot. 71:356-374.

Palmer-Jones, T. and Clinch, P.G. 1974. Observations on the pollination of Chinese gooseberries variety "Hayward". New Zealand J. of Exp. Agri. 2:455-458.

Symbols

A	projected area [m]
C_p	concentration of pollen [g/m^3]
D	characteristic diameter [m]
d_p	average pollen diameter = 22 µm (from Hopping, 1990)
f	subscript for flower
k	turbulence kinetic energy
Re	Reynolds number = $\rho_a \cdot U \cdot D / \mu_a$ [dimensionless]
s	subscript for stigma
Stk	Stokes number = $\dfrac{d_p^2 \times (\rho_p - \rho_a) \times U}{18\mu \times D}$ [dimensionless]

	U	approaching air velocity [m/s]

U   approaching air velocity [m/s]
ε turbulence eddy dissipation
η inertial collection efficiency
μ_a air viscosity $= 1.7 \times 10^{-5}$ kg/m.s
ρ_p pollen density $= 1330$ kg/m^3 (Ferguson and Pusch, 1991)
ρ_a air density $= 1.2$ kg/m^3
ω turbulent frequency

Tables

Table 1. Calculated Stk, η of stigma (s) and their flowers (f) shown in Fig. 6. Refer to Symbols.

	Half-open flower			Full-open flower			Flip-back flower		
	Front flow	Side flow	Back flow	Front flow	Side flow	Back flow	Front flow	Side flow	Back flow
$Stk_f \times 10^3$ ♥	32	35	32	38	37	38	29	31	29
U_s	0.25	0.63	0.35	0.16	0.25	0.34	0.28	0.59	0.33
Stk_s	0.58	1.44	0.81	0.37	0.58	0.77	0.64	1.36	0.77
η_s *	0.23	0.48	0.32	0.14	0.23	0.30	0.28	0.45	0.30
$\eta_f \times 10^4$ ♦	14	159	28	7	33	32	16	114	21

* assuming that the pollen is captured stigma-style like an inertial collection by a circular cylinder (Kanaoka, 1997).

♦ calculated by the ratio of $\dfrac{\text{local stigma collection}}{\text{overall flower collection}} = \dfrac{C_p \times U_s \times A_s \times \eta_s}{C_p \times U_f \times A_f}$

♥ for example, $Stk_f = 0.032$ for half-open flower and front flow.

Figures
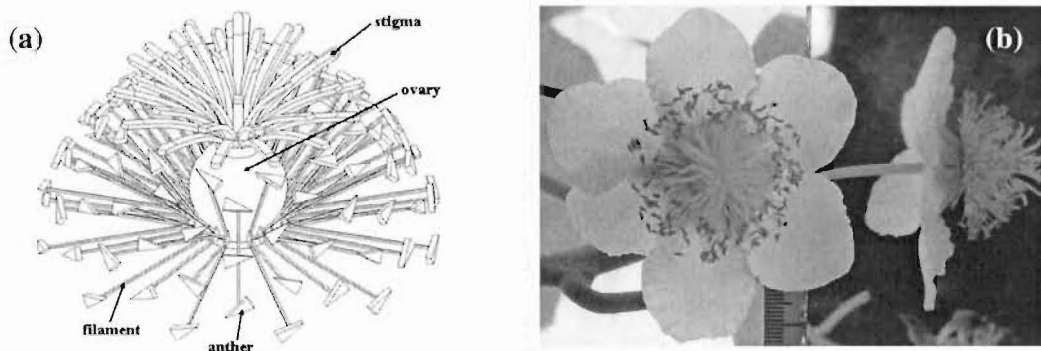
Fig. 1. (a) Solid model of flower ovary, 36-stigma, 84 filaments and anthers. (b) Front and side views of a female flower opening at flip-back stage.
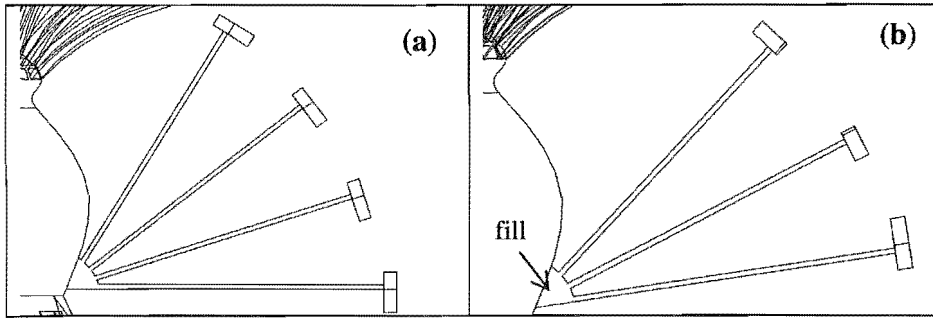
Fig. 2. Vertical side views of 3- and 4-filament row, captured in Solidworks 2001. Another triangular wedge (1.25 mm base × 2.7 mm high, 0.58 mm thick) on end of 0.205 × 0.205 mm square rod, 14.2–15 mm long.
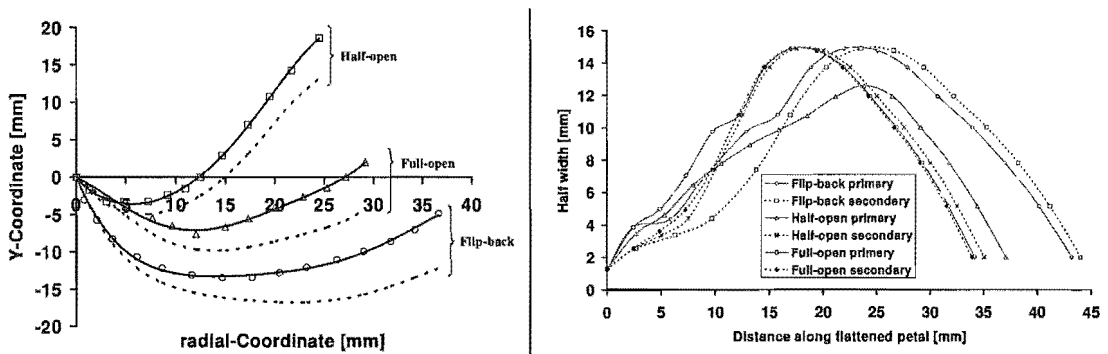
Fig. 3. (a) Radial profiles of the centreline of petals at 3 opening stages. Solid lines represent primary petal while dotted lines represent secondary petal. (b) Half width profile of the symmetrical petal when flattened, at different bud opening (some minor differences used for ease of meshing).
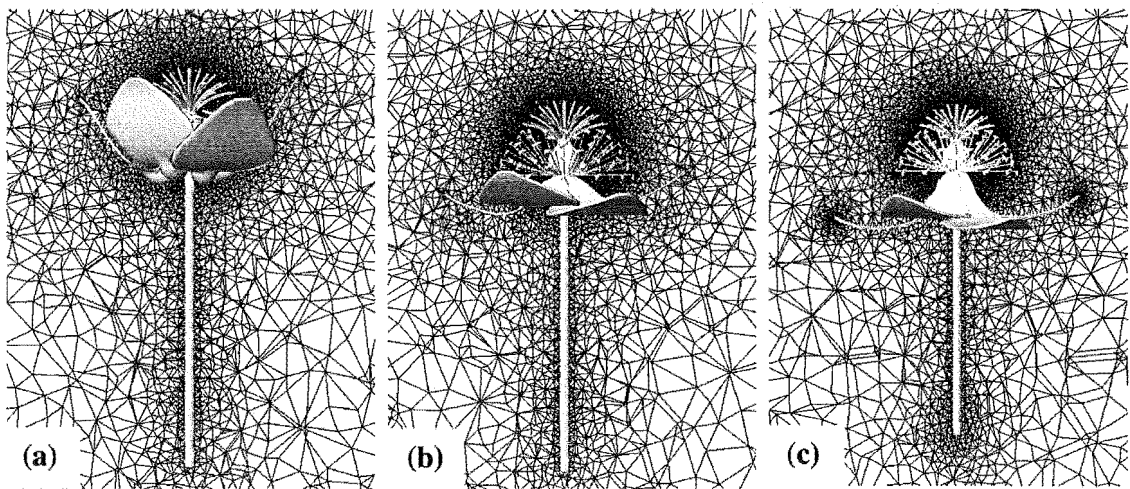
Fig. 4. Generated mesh around flowers of different opening. (a) half-open. (b) full-open. (c) flip-back.
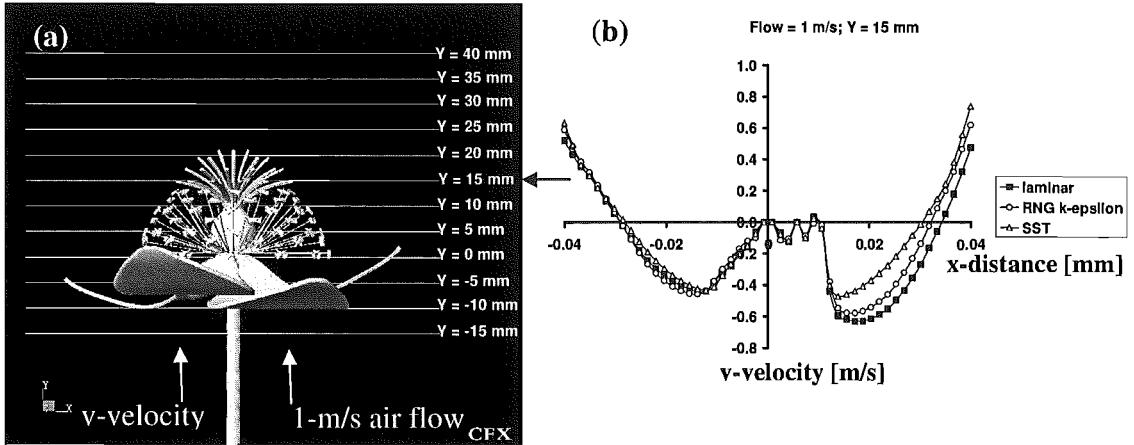
Fig. 5. Comparison of laminar, RNG k-ε and SST models using the v-velocity profile (shown in (b)) at Y = 15 mm (shown in (a)), on a full-open flower with a back-coming bulk velocity of 1 m/s.
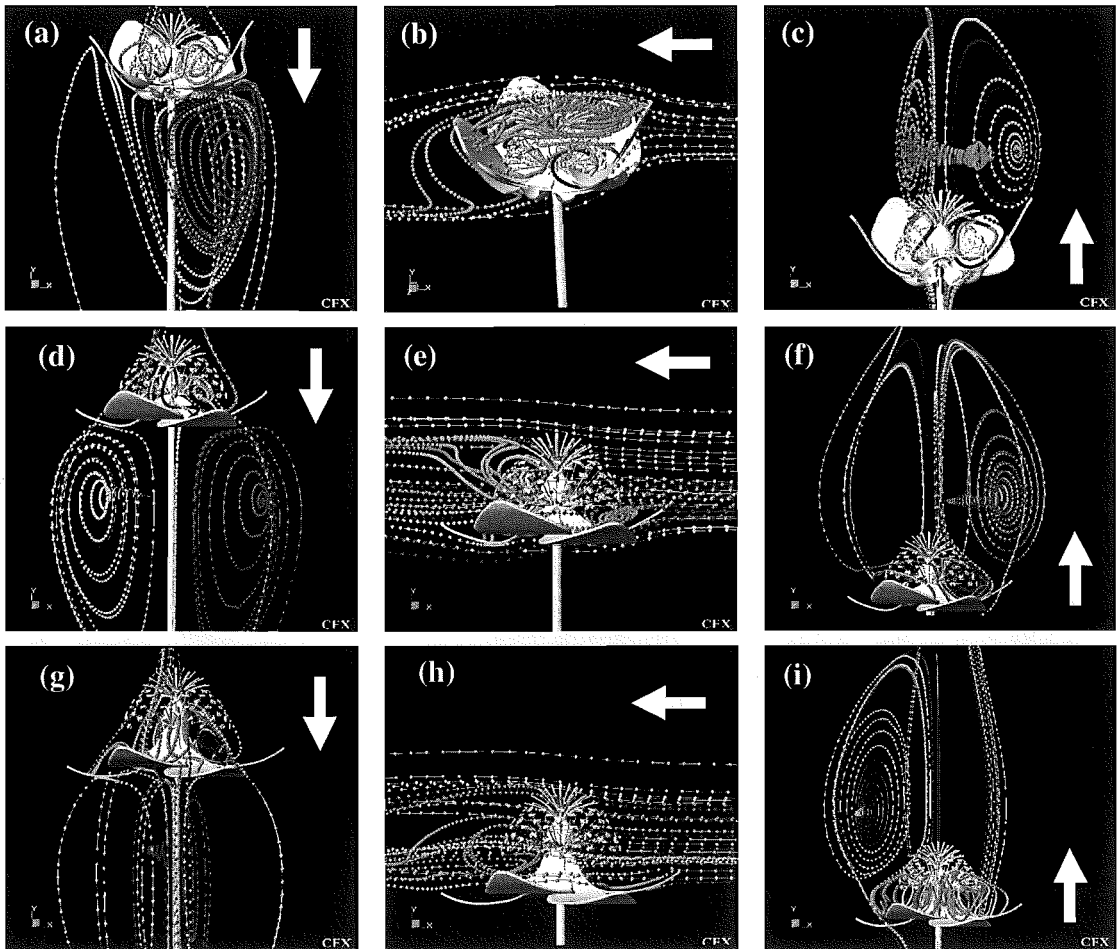
Fig . 6. Predicted flow fields around a single flower of different openings and attacked at different 1-m/s flow directions (shown by the arrows), using RNG k-ε model. (a) half-

open, front flow. (b) half-open, side flow. (c) half-open, back flow. (d) full-open, front flow. (e) full-open, side flow. (f) full-open, back flow. (g) flip-back, front flow. (h) flip-back, side flow. (i) flip-back, back flow.
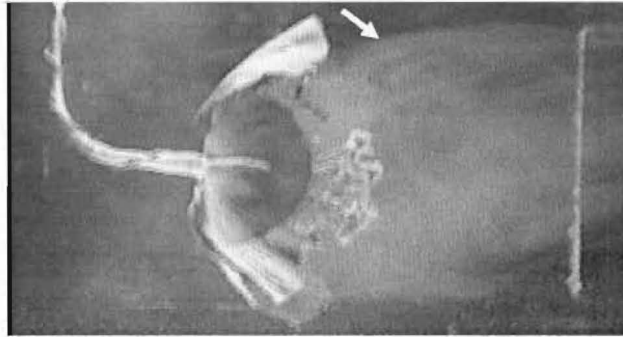
Fig. 7. Smoke visualization photo from Hongladarom (1988) with an arrow indicating an eddy downstream of an artificial half-open kiwifruit flower under a back flow of 0.16 m/s. The shape of this flower is close to that in Fig. 6(c).
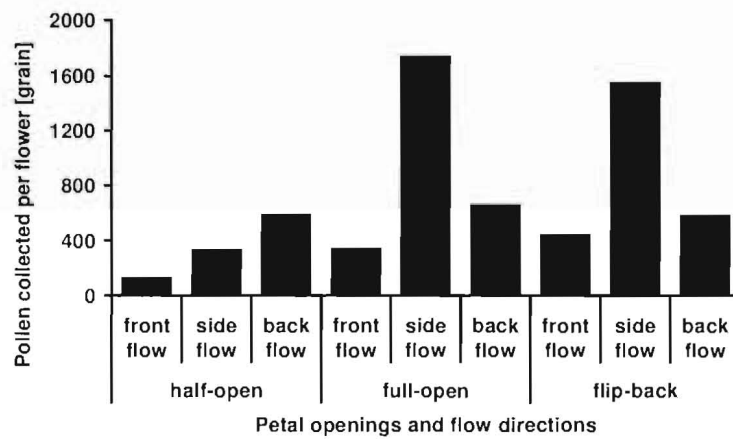
Fig. 8. Calculated number of pollen collected by inertial impaction ($= 14.5 \times 10^6$ grain/m^2/day $\times A_p \times \eta_p \times 6$ days) for flowers of different opening and at 1 m/s under different flow directions.